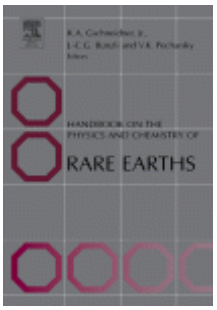

Handbook on the Physics and Chemistry of Rare Earths volume 8

Elsevier, 1986

Edited by: Karl A. Gschneidner, Jr. and LeRoy Eyring
ISBN: 978-0-444-86971-5

Handbook on the Physics and Chemistry of Rare Earths, edited by K.A. Gschneidner, Jr. and L. Eyring

PREFACE

Karl A. GSCHNEIDNER, Jr., and LeRoy EYRING

These elements perplex us in our rearches [sic], *baffle us in our speculations, and haunt us in our very dreams. They stretch like an unknown sea before us – mocking, mystifying, and murmuring strange revelations and possibilities.*

Sir William Crookes (February 16, 1887)

As in the previous seven volumes of the "Handbook" this volume continues our coverage of a wide spectrum of topics. Although these topics (intra rare earth alloys, polarographic analysis, complex inorganic compounds and use in organic synthesis) seem diverse and unrelated, they are indeed unified by the fact that the chemical, metallurgical and most physical properties and behaviors of the lanthanide elements vary in a regular and systematic manner due to the sequential filling of the 4f levels. For those which do not show this variation (e.g. the magnetic and optical properties, heats of sublimation, etc.) the observed behaviors can also be understood in terms of the filling of the 4f orbitals by electrons and the coupling between them. But still many surprises, twists and turns are found each year and many still lie ahead of us; and the words of Sir William Crookes (above), written nearly 100 years ago, are even more appropriate today than in 1887.

In the first chapter of this volume Gschneidner and Calderwood review the phase relationships in the binary intra rare earth alloy systems and the variation in their lattice spacings due to alloying. Systematization of these data resulted in (1) a single generalized phase diagram which represents 91 possible binary intra rare earth phase diagrams both at 1 atmosphere and high pressures (up to 4 GPa), and (2) some interesting correlations concerning the variation of their lattice spacings. The polarographic analysis of the rare earth elements is described next by Gao, who points out that before 1980 this technique was difficult to carry out for the rare earths except for Eu and Yb. But recent developments in this field have led to polarographic methods which are simple and easy to perform, and can be used to determine at micro molar levels either the individual elements or the total amount of rare earths. The inorganic, crystal and physical chemistry of complex inorganic compounds is examined by Leskelä and Niinistö in two separate articles. The first, which appears in this volume, deals with the borates, carbonates, silicates, germanates and nitrates, and their derivatives. The second part of their review covers phosphates, arsenates, sulfates, selenates, selenites, vanadates, chromates, complexes involving the halides, sulfur and nitrogen, and structures in solutions, and is scheduled to appear in volume 9. In the last chapter Long describes the use of rare earth ions and

compounds in organic synthesis. A relatively young field, Long points out that the unique properties of the lanthanides—the contracted and shielded 4f levels and large ionic size—have opened new approaches for forming standard and unique organic molecules, many of which have important and/or unusual commercial applications.

In this volume two new items make their appearance. One is an errata. Readers are urged to send us any errors that they may have encountered in reading the "Handbook". The other new innovation is color figures which appear near the end of the first chapter (ch. 54). We hope future authors will consider using color figures where it is appropriate.

CONTENTS

CONTENTS OF VOLUMES 1–7

VOLUME 1: METALS

VOLUME 2: ALLOYS AND INTERMETALLICS

VOLUME 3: NON-METALLIC COMPOUNDS – I

VOLUME 4: NON-METALLIC COMPOUNDS–II

VOLUME 5

VOLUME 6

VOLUME 7

Handbook on the Physics and Chemistry of Rare Earths, edited by K.A. Gschneidner, Jr. and L. Eyring

Chapter 54

INTRA RARE EARTH BINARY ALLOYS: PHASE RELATIONSHIPS, LATTICE PARAMETERS AND SYSTEMATICS*

K.A. GSCHNEIDNER, JR. and F.W. CALDERWOOD
Rare-Earth Information Center and Ames Laboratory†, Iowa State University
Ames, IA 50011, U.S.A.

Dedication

This paper is dedicated to the memory of Professor Frank H. Spedding, Iowa State University, who died on December 15, 1984 at the age of 82. It is especially appropriate to the subject of this paper because a fair fraction of his many scientific endeavors was devoted to the study of the rare earth metals—especially their preparation, properties and alloying behavior of the intra rare earth binary alloys. His contributions (along with his many collaborators) in this area include: the first to prepare metallic Sm metal; the determination of its unique crystal structure; the discovery of the Sm-type structure in an intermediate alloy phase formed by a light and a heavy lanthanide; the first to ascertain that the crystal structure of the high temperature phase was bcc; and the first to show that there is no detectable separation between liquidus and solidus ($< 1°C$) in binary alloy systems of the lanthanide metals that have atomic numbers within four of each other.

Contents

*This work was partially supported by Department of Energy funds through the Joint Program on Critical Compilation of Physical and Chemical Data, Office of Standard Reference Data, National Bureau of Standards, Washington, DC; Th. Goldschmidt, AG (Essen, West Germany); Molycorp, Inc., Union Oil Co. of California (Los Angeles, CA); Reactive Metals & Alloys Corp. (West Pittsburg, PA); Ronson Metals Corp. (Newark, NJ); and Santoku Metal Industry Co., Ltd. (Kobe, Japan).

†Operated for the U.S. Department of Energy by Iowa State University under contract no. W-7405-ENG-82. This work was supported by the Office of Basic Energy Sciences.

1. Introduction

The known phase relationships, crystallographic and thermodynamic data of the known rare earth binary phase diagrams have been critically evaluated. The intra rare earth binary alloy systems will be reported in order of increasing atomic number with the exception of scandium and yttrium, which will follow lutetium in that order. The first system to be considered is lanthanum–cerium (atomic numbers 57 and 58) followed by lanthanum–praseodymium (atomic numbers 57 and 59), etc. Following

this order, scandium–yttrium will be the last intra rare earth alloy system discussed. Following the presentation of the information on the binary diagram a section is devoted to the interrelationships and systematics of these alloys including a generalized phase diagram as a function of pressure.

The information on the various binary alloy systems will be presented in the following order: the phase diagram, the lattice spacings, phase relationships as a function of pressure, thermodynamic data, and the pertinent references.

1.1. *Melting and transition temperatures*

As a part of the Introduction a list of the important properties of the pure rare earth elements, as pertaining to phase equilibria are presented. These data are included here since a wide variation of melting point and transition point data exists in the literature. The phase relationships that follow will be standardized to these data.

Phase transformations (only those that occur near or above room temperature) and the melting point of each rare earth metal are shown in table 1 using data from Beaudry and Gschneidner (1978) and from Koskenmaki and Gschneidner (1978).

TABLE 1
Transition temperatures, phases and melting point of rare earth metals (after Beaudry and Gschneidner, 1978, unless otherwise noted).

	Transition I (α–β)[a]		Transition II (β–γ)[a]		Melting point
Metal	T (°C)	Phases	T (°C)	Phases	(°C)
La[b]	310	dhcp → fcc	865	fcc ⇆ bcc	918
Ce[c]	139	dhcp → fcc (β–γ)	726	fcc ⇆ bcc (γ–δ)	798
Pr	795	dhcp ⇆ bcc	—	—	931
Nd	863	dhcp ⇆ bcc	—	—	1021
Pm	890	dhcp ⇆ bcc	—	—	1042
Sm[d]	734	rhom → hcp	922	hcp ⇆ bcc	1074
Eu	—	—	—	—	822
Gd	1235	hcp ⇆ bcc	—	—	1313
Tb	1289	hcp ⇆ bcc	—	—	1356
Dy	1381	hcp ⇆ bcc	—	—	1412
Ho	—	—	—	—	1474
Er	—	—	—	—	1529
Tm	—	—	—	—	1545
Yb[e]	7	hcp → fcc	795	fcc ⇆ bcc	819
Lu	—	—	—	—	1663
Sc	1337	hcp ⇆ bcc	—	—	1541
Y	1478	hcp ⇆ bcc	—	—	1522

[a] For all the transformations listed, unless otherwise noted.
[b] On cooling, fcc → dhcp ($\beta \rightarrow \alpha$), 260°C.
[c] On cooling, fcc → dhcp ($\gamma \rightarrow \beta$), −16°C (Koskenmaki and Gschneidner, 1978).
[d] On cooling, hcp → rhomb ($\beta \rightarrow \alpha$), 727°C.
[e] On cooling, fcc → hcp ($\beta \rightarrow \alpha$), −13°C.

Five of the rare earth elements do not exhibit a high temperature phase transition while others have one or more transitions. However, several of the lanthanide metals undergo transitions below room temperature—cerium (2), terbium, dysprosium, and ytterbium—see Beaudry and Gschneidner (1978).

1.2. *Crystal structures, lattice constants, atomic volumes and radii*

1.2.1. *Pure rare earth metals*

The crystal structures, lattice parameters, metallic radii for a coordination number of 12, atomic volumes and the densities of the rare earth metals at 24°C or below are

TABLE 2
Crystal structure and related properties of rare earth metals at 24°C or below (Beaudry and Gschneidner, 1978).

Rare earth metal	Crystal structure[a]	Lattice constants (Å)			Metallic radius CN = 12 (Å)	Atomic volume (cm^3/mol)	Density (g/cm^3)
		a_0	b_0	c_0			
αLa	dhcp	3.7740	—	12.171	1.8791	22.602	6.146
αCe[b]	fcc	4.85[c]	—	—	1.71	28.5	8.16
βCe[b]	dhcp	3.6810	—	11.857	1.8321	20.947	6.689
γCe	fcc	5.1610	—	—	1.8247	20.696	6.770
αPr	dhcp	3.6721	—	11.8326	1.8279	20.803	6.773
αNd	dhcp	3.6582	—	11.7966	1.8214	20.583	7.008
αPm	dhcp	3.65	—	11.65	1.811	20.24	7.264
αSm	rhomb[d]	3.6290	—	26.207	1.8041	20.000	7.520
Eu	bcc	4.5827	—	—	2.0418	28.979	5.244
αGd	hcp	3.6336	—	5.7810	1.8013	19.903	7.901
α′Tb[e]	ortho	3.605	6.244	5.706	1.784	19.34	8.219
αTb	hcp	3.6055	—	5.6966	1.7833	19.310	8.230
α′Dy[f]	ortho	3.595	6.184	5.678	1.775	19.00	8.551
αDy	hcp	3.5915	—	5.6501	1.7740	19.004	8.551
Ho	hcp	3.5778	—	5.6178	1.7661	18.752	8.795
Er	hcp	3.5592	—	5.5850	1.7566	18.449	9.066
Tm	hcp	3.5375	—	5.5540	1.7462	18.124	9.321
αYb[g]	hcp	3.8799	—	6.3859	1.9451	25.067	6.903
βYb	fcc	5.4848	—	—	1.9392	24.841	6.966
Lu	hcp	3.5052	—	5.5494	1.7349	17.779	9.841
αSc	hcp	3.3088	—	5.2680	1.6406	15.039	2.989
αY	hcp	3.6482	—	5.7318	1.8012	19.893	4.469

[a] dhcp = double-*c* hexagonal close-packed; fcc = face-centered cubic; bcc = body-centered cubic; hcp = hexagonal close-packed.
[b] After Koskenmaki and Gschneidner (1978).
[c] At 77 K (−196°C).
[d] Rhombohedral is the primitive cell. Lattice parameters given are for the nonprimitive hexagonal cell.
[e] At 220 K (−53°C), after Darnell (1963).
[f] At 86 K (−187°C), after Darnell and Moore (1963).
[g] At 23°C.

TABLE 3
High temperature crystal structures of the rare earth metals (Beaudry and Gschneidner, 1978).

Rare earth	Structure	Lattice parameter (Å)	Temp. (°C)
βLa	fcc	5.303	325
γLa	bcc	4.26	887
δCe	bcc	4.12	757
βPr	bcc	4.13	821
βNd	bcc	4.13	883
βPm	bcc	4.10 (est.)	865
βSm	hcp	$a = 3.6630$ $c = 5.8448$	450[a]
γSm	bcc	4.10 (est.)	897
βGd	bcc	4.05[b] 4.06	24 1265
βTb	bcc	4.02[b]	24
βDy	bcc	3.98[b]	24
γYb	bcc	4.44	763[c]
βSc	bcc	3.73 (est.)	1312
βY	bcc	4.11[d] 4.04[b]	24 24

[a] The hcp phase was stabilized by impurities and the temperature of measurement was below the transition temperature listed in table 1.
[b] Determined by extrapolation to 0% solute of a vs. composition data for R–Mg alloys.
[c] The bcc phase was stabilized by impurities and the temperature of measurement was below the transition temperature listed in table 1.
[d] Determined by extrapolation to 0% solute of a vs. composition data for Y–Th alloys.

presented in table 2. The crystal structures of the high temperature phases, and the lattice constants are found in table 3.

1.2.2. *Effect of impurities on lattice parameters of the rare earth metals*

The large deviations in the values of room temperature lattice constants as found in the literature are thought to be due to impurities since many of the reported values were determined on low purity metals. However, Spedding and Beaudry (1971) observed that parameters determined on metals of the same purity by different workers also varied, suggesting that impurities were introduced in the preparation of X-ray samples. After an extensive study of sample preparation methods, they showed that impurities were introduced in the preparation of annealed filings. They found that hydrogen had a large effect on room temperature lattice parameters, especially for the heavy lanthanides, and Sc and Y.

Since the light lanthanide metals are reactive in air, one might expect—depending on the handling technique used in the determination of lattice constants—a greater change in their lattice parameters than that observed in the less reactive hcp-type rare earth metals. However there is little, if any, change due to the use of filings as

TABLE 4
Boiling points and heat of sublimation of rare earth metals (Beaudry and Gschneidner, 1978).

Metal	Boiling point (°C)	Heat of sublimation at 25°C (kJ/mol)
La	3464	431.0
Ce	3443	422.6
Pr	3520	355.6
Nd	3074	327.6
Pm	3000[a]	348[a]
Sm	1794	206.7
Eu	1527	175.3
Gd	3273	397.5
Tb	3230	388.7
Dy	2567	290.4
Ho	2700	300.8
Er	2868	317.1
Tm	1950	232.2
Yb	1196	152.1
Lu	3402	427.6
Sc	2836	377.8
Y	3338	424.7

[a]Estimated.

compared with a solid sample for the light lanthanide metals. The change between lattice parameters determined from filings versus those determined from a bulk sample is significant in the lanthanides from Tb to Lu (excluding Yb) and Sc and Y. Beaudry and Spedding (1975) showed that the solubility of hydrogen at room temperature increases from less than 0.1 at% in Gd to 20.6 at% in Lu while the effect of H on the lattice parameters increases from practically zero in Gd to a maximum in Lu. These facts need to be kept in mind when one is comparing lattice parameter data for solid solution alloys from various sources, especially if a late heavy lanthanide metal or Sc or Y is involved.

1.3. *Boiling points and heats of sublimation*

The boiling point temperatures and the heats of sublimation for rare earth metals are listed in table 4.

References

Beaudry, B.J. and K.A. Gschneidner, Jr., 1978, in: Gschneidner, Jr., K.A. and L. Eyring, eds., Handbook on the Physics and Chemistry of Rare Earths, Vol. 1, Metals (North-Holland, Amsterdam) p. 215.
Beaudry, B.J. and F.H. Spedding, 1975, Metall. Trans. **6B**, 419.
Darnell, F.J., 1963, Phys. Rev. **132**, 1098.
Darnell, F.J. and E.P. Moore, 1963, J. Appl. Phys. **34**, 1337.
Koskenmaki, D.C. and K.A. Gschneidner, Jr., 1978, in: Gschneidner, Jr., K.A. and L. Eyring, eds.,

Handbook on the Physics and Chemistry of Rare Earths, Vol. 1, Metals (North-Holland, Amsterdam) p. 337.
Spedding, F.H. and B.J. Beaudry, 1971, J. Less-Common Met. **25**, 61.

2. Intra Rare Earth Phase Diagrams

2.1. *Introduction*

2.1.1. *Ideal liquid and solid solution behavior*

As is well known, neighboring lanthanide elements are quite similar in their physical and chemical properties (except for those that depend directly on the 4f electrons) because of the filling of the inner 4f level as the nuclear charge increases on going from one element to the next in increasing atomic number. This similarity has an important effect on the intra rare earth binary alloys, i.e., if neighboring or near neighboring elements are alloyed, they behave as ideal alloys at high temperatures. Thus there is no measurable difference in the liquidus and solidus temperature, i.e., the two-phase liquid plus solid region is quite narrow (a few degrees at most). Furthermore, the liquidus–solidus line between the two end-members is a straight line connecting the respective melting points of the pure metals. The same is true for the close-packed (dhcp, fcc or hcp) to bcc transformation, which occurs near the melting point. This behavior only holds if the two components are trivalent and have atomic numbers within $\sim \pm 4$ of each other. This has been observed experimentally for the Tb–Ho, Tb–Er, Dy–Ho, Dy–Er and Ho–Er systems (Spedding et al., 1973). The other important factor is that this behavior is only observed if high purity metals (> 99.9 at% pure) are used. Another verification of this is found in the study of the physical properties of pure mischmetal (approximate composition is 50% Ce, 25% La, 15% Nd, 5% Pr and 5% other rare earth metals) by Palmer et al. (1982), who found that if the mischmetal did not contain any heavy lanthanides and the cerium contents were less than 40%, then the observed melting and transition temperatures agreed with those calculated from the sum of the products of the transition and melting points of the pure metals times their respective atomic fractions.

Since many of the reported phase diagrams were based on studies using impure metals, the phase diagrams reported here have been modified to show this ideal behavior. *But if scientists use commercially available metals, the experimental alloying behavior they experience may not be exactly the same as expected from the phase diagrams given here.*

2.1.2. *Nonideal behavior*

For binary alloys involving yttrium or scandium with one of the other rare earth metals, or if the atomic numbers of the two lanthanide metals differ by more than ± 4 then departures from ideal behavior, as discussed above (section 2.1.1) are to be expected. The departures are expected to vary depending upon the alloying partners —the further apart the two metals are in the Periodic Table, the greater the difference. An example is the Er–Y system which was also studied by Spedding et al.

(1973). They found that both the transition and melting point variations with alloying exhibited a minimum, but no separation of the liquidus–solidus and the two solvus lines were observed.

Nonideal behaviors are also expected for rare earth metals that are alloyed with the two divalent lanthanide metals europium and ytterbium. Cerium and samarium may also be anomalous because these two metals have a tendency to exhibit other valence states rather than the normal 3^+ state (2^+ for Sm and 4^+ for Ce). However, the mischmetal study reported by Palmer et al. (1982) did not indicate any anomalous behavior for cerium in this polycomponent system.

2.1.3. *Formation of the δ phase (Sm-type intermediate phase)*

In the early 1960s Spedding et al. (1962) discovered the existence of an intermediate phase that has the Sm-type crystal structure in intra rare earth alloys formed by a light lanthanide (La, Ce, Pr or Nd) with a heavy lanthanide (Gd thru Tm, Lu) or Y. The authors called this phase the "δ phase". The early phase diagrams showed that the Sm-type structure decomposed peritectoidally on heating to the dhcp phase (of the light lanthanide) and the hcp phase (of the heavy lanthanide or Y). Lundin (1966) made a systematic study of the nature and formation of the Sm-type structure in 13 intra rare earth alloy systems. Since annealing and quenching, thermal analysis, dilatometry and resistivity studies failed to confirm the assumed peritectoid reaction of the earlier phase studies, Lundin concluded that the Sm-type structure is a recrystallization phenomenon formed by strains set up within the solid solution in the range of existence of the structure. Koch et al. (1971) studied in detail this transformation in the similar Ce–Gd alloy system using electrical resistivity, X-ray diffraction, optical metallography and transmission electron microscopy. They concluded that the formation of the Sm-type phase is a shear-type transformation that resembles a martensitic reaction.

As a result of these studies the reviewers have concluded that the δ phase decomposes congruently to a dhcp–hcp solid solution. This, of course, implies a continuous change from dhcp to hcp when alloying a light lanthanide with a heavy lanthanide or Y. This is discussed below in the next section.

2.1.4. *The dhcp–hcp solid solution*

The proposed continuous change from the dhcp to hcp structure proposed above (section 2.1.3) is unusual, but it has been clearly established in the Nd–Sc system (section 2.37). Both structures belong to the same space group ($P6_3/mmc$); we know of no requirement that there be a first or higher order phase transition between them (also see Franzen and Gerstein, 1966). We feel that the continuous change from dhcp to hcp might be accounted for through a stacking-fault mechanism.

References

Franzen, H.F. and B.C. Gerstein, 1966, Am. Inst. Chem. Eng. **12**, 364.

Koch, C.C., P.G. Mardon and C.J. McHargue, 1971, Metall. Trans. **2**, 1095.

Lundin, C.E., 1966, Final Report, Denver Research Institute Rept. AD-633558, Denver University, Denver, CO (also given as DRI-2326).

Palmer, P.E., H.R. Burkholder, B.J. Beaudry and K.A. Gschneidner, Jr., 1982, J. Less-Common Met. **87**, 135.
Spedding, F.H., B. Sandeen and B.J. Beaudry, 1973, J. Less-Common Met. **31**, 1.
Spedding, F.H., R.M. Valletta and A.H. Daane, 1962, Trans. Quarterly (Am. Soc. Met.) **55**, 483.

2.2. *La–Ce: Lanthanum–cerium*

2.2.1. *Phase diagram*

The liquidus and fcc to bcc transformation data of Vogel and Klose (1954) is the basis for the phase diagram of the lanthanum–cerium system. Their lanthanum was reported to have a purity of 97% (the major impurities were 1.4% Fe, 0.3% each Si and Mg, and 1% miscellaneous) and their cerium a purity of 99.5%. Savitskii and Terekhova (1958) reported data on the liquidus and solidus for this system but did not include information on the solid state transformations. They claimed a purity of 98.6% for their lanthanum and 97 to 99% for their cerium. Impurity elements were listed but no concentrations were given (Fe and Pr in lanthanum; Fe, La, Pr and Nd in cerium). Terekhova (1963) later published a similar phase diagram for this system that seems to be a repetition of that earlier reported by Savitskii and Terekhova.

Lanthanum and cerium form a continuous series of solid solutions as shown in fig. 1. The melting points of the pure metals have been adjusted to the accepted values (table 1) from those given with the reported lanthanum–cerium phase diagrams. Lanthanum undergoes two phase transformations on heating: from the double-hexagonal close-packed form (dhcp) to the face-centered cubic (fcc) form at 310°C and then to the body-centered cubic (bcc) form at 865°C. Cerium exhibits only the

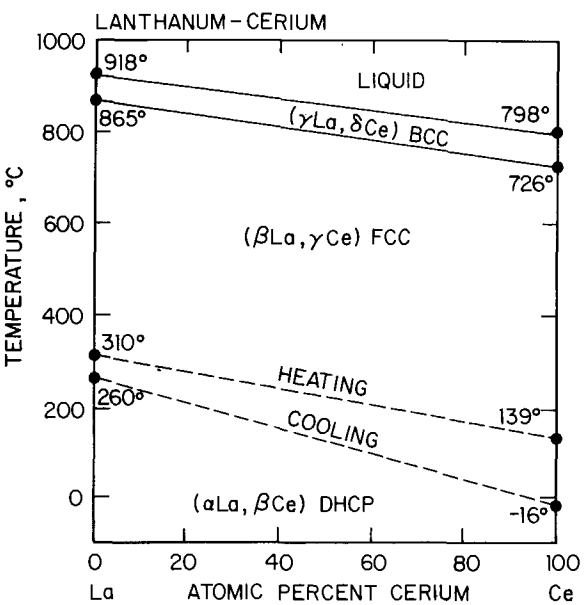

Fig. 1. Phase diagram of the lanthanum–cerium system.

latter transformation at 726°C since it is normally face-centered cubic at room temperature. On cooling, the fcc → dhcp transformation occurs at lower temperatures (260°C for lanthanum and −16°C for cerium) than the dhcp → fcc transition on heating. Since lanthanum and cerium form a continuous series of solid solutions and are adjacent elements in the Periodic Table, the liquidus and solidus, and the heating and cooling lines of the fcc ⇄ bcc transformation, respectively, were drawn as a single straight line connecting the two melting or the two transformation points of lanthanum and cerium (see section 2.1.1). There is no information available concerning the dhcp ⇄ fcc transformation for the lanthanum–cerium alloys other than for the pure elements (see §1.1). Thus a dashed line has been drawn connecting the heating and cooling transformation temperatures of αLa–βLa and βCe–γCe. But in a study of the magnetic and electrical properties of some cerium–lanthanum alloys, Peterson et al. (1978) found that at room temperature alloys containing 30 to 70 at% Ce contained at least some of the fcc phase, while alloys containing 0 to 30 at% Ce and 70 to 100% Ce could be prepared as the pure dhcp phase (βCe and αLa, respectively). These alloys were prepared by normal melting procedures followed by low temperature (< 25°C) cycling. This suggests that the dhcp ⇄ fcc transformation lines may go through a minimum in the center of the diagram. However, the inability to prepare the dhcp alloys between 30 and 70 at% Ce may be a kinetics problem and not a lowering of the fcc to dhcp transformation temperature.

2.2.2. *Lattice spacings*

Several investigators have reported lattice spacings for lanthanum–cerium alloys. Ellinger (1958) presented parameter data for alloys that were quenched from 400 and 500°C. More recent results were reported by Evans and Raynor (1962), Gschneidner et al. (1962a), Norman et al. (1967), and King and Harris (1972). Evans and Raynor prepared alloys in an arc furnace from lanthanum (negligible impurities except for 0.001 wt% iron) and cerium (metallic impurities 0.002 wt% iron and less than 0.05 wt% lithium). After homogenizing for 10 days at 700°C, their alloys were rapidly cooled, then filings for X-ray diffraction work were stress-relieved for 2 hr at 400°C and furnace-cooled to room temperature. Gschneidner et al. did not report purities for their metals. Alloys were prepared by melting the metals in MgO crucibles followed by annealing in evacuated Pyrex tubes for 300 hr at 450°C. Filings were sealed in Pyrex capillary tubes for 15 min to 2 hr at 450°C and water-quenched. Norman et al., who used lanthanum and cerium that contained less than 0.01 wt% other rare earths and about 0.02 wt% other metallic impurities, stated that their procedures were identical to those used by Evans and Raynor. King and Harris reported that their lanthanum and cerium were the same as used by Norman et al. King and Harris, however, homogenized their alloys at 600°C under vacuum, stress-relieved their powders for X-ray diffraction at 600°C under vacuum, sealed the powders in silica capillaries and then rapidly cooled the samples to room temperature. As seen in fig. 2, all of these lattice spacing data are in good agreement. The lattice spacings exhibit a small positive deviation from ideality (Vegard's law) for all compositions.

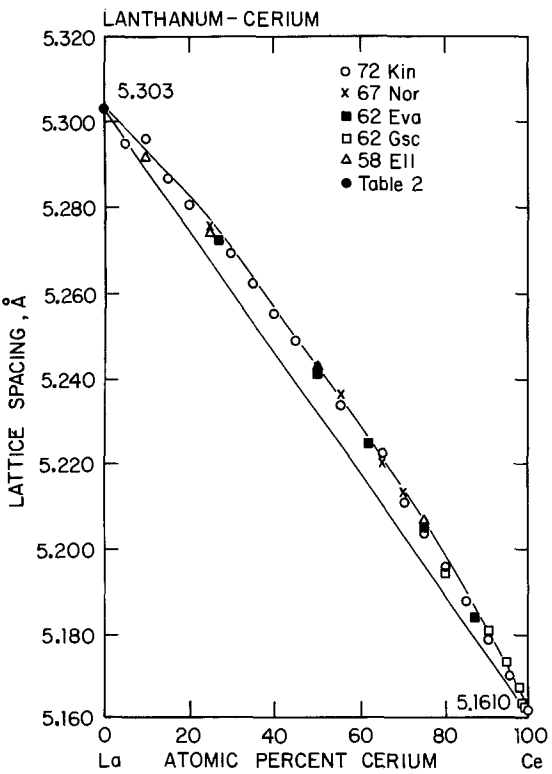

Fig. 2. Lattice spacings for the lanthanum–cerium system. The straight line connecting the end-members is the Vegard's law relationship based on the values listed in table 2.

2.2.3. *Phase relationships as a function of pressure*

King and Harris (1972) used resistance measurements to study the $\gamma \rightleftarrows \alpha$ transition in La–Ce alloys at low temperatures where the normal metastable fcc γ phase changes to the collapsed fcc α phase at about 100 K (−173°C). This change also occurs at room temperature under a pressure of about 0.7 GPa. Gschneidner et al. (1962b) studied the $\alpha \rightleftarrows \gamma$ transformation in cerium-based alloys using a high pressure piston–cylinder device and found that lanthanum, which was the largest solute atom, raised the transformation pressure more rapidly than did solutes with a smaller radius. Oomi (1980) determined the $\gamma \rightleftarrows \alpha$ transition pressure, temperature and critical point of $La_{1-x}Ce_x$ alloys by electrical resistance measurements under pressure up to 1.0 GPa at temperatures between 50 K (−223°C) and 300 K (27°C).

2.2.4. *Thermodynamic data*

Roberts and Lock (1957) measured the heat capacity between 1.5 and 20 K on four lanthanum–cerium alloys (5.0, 27.0, 37.6 and 78.9 at% Ce) and found anomalies which moved to lower temperatures with decreasing cerium content. Nikulin and Patrikeev (1971) studied the nuclear heat capacity of lanthanum–cerium alloys at low temperatures (0.08 to 0.18 K). Culbert and Edelstein (1974) examined several

lanthanum-rich alloys containing between 1.25 and 20 at% Ce and found an anomaly in the heat capacity at about 1.2 K that could not be explained.

References

Culbert, H.V. and A.S. Edelstein, 1974, Solid State Commun. **15**, 1633.
Ellinger, F.H., 1958, private communication, cited in K.A. Gschneidner, Jr., Rare Earth Alloys, (Van Nostrand, New York), p. 82.
Evans, D.S. and G.V. Raynor, 1962, J. Nucl. Mater. **5**, 308.
Gschneidner, K.A., Jr., R.O. Elliott and M.Y. Prince, 1962a, in: Nachman, J.F. and C.E. Lundin, eds., Rare Earth Research (Gordon and Breach, New York) p. 71.
Gschneidner, K.A., Jr., R.O. Elliott and R.R. McDonald, 1962b, J. Phys. Chem. Solids **23**, 1201.
King, E. and I.R. Harris, 1972, J. Less-Common Met. **27**, 51.
Nikulin, E.I. and Yu.B. Patrikeev, 1971, Fiz. Tverd. Tela **13**, 1824 [English transl.: Sov. Phys.—Solid State **13**, 1819].
Norman, M., I.R. Harris and G.V. Raynor, 1967, J. Less-Common Met. **13**, 24.
Oomi, G., 1980, J. Phys. Soc. Jpn. **48**, 857.
Peterson, T.S., S. Legvold, K.A. Gschneidner, Jr., T.-W.E. Tsang and J.O. Moorman, 1978, J. Appl. Phys. **49**, 2115.
Roberts, L.M. and J.M. Lock, 1957, Phil. Mag. **2**, 811.
Savitskii, E.M. and V.F. Terekhova, 1958, Zh. Neorg. Khim. **3**, 756 [English transl.: Russ. J. Inorg. Chem. **3**, 1].
Terekhova, V.F., 1963, Metalloved. Term. Obrab. Met. [8], 47 [English transl.: Met. Sci. Heat Treat. [8], 465].
Vogel, R. and H. Klose, 1954, Z. Metallkd. **45**, 633.

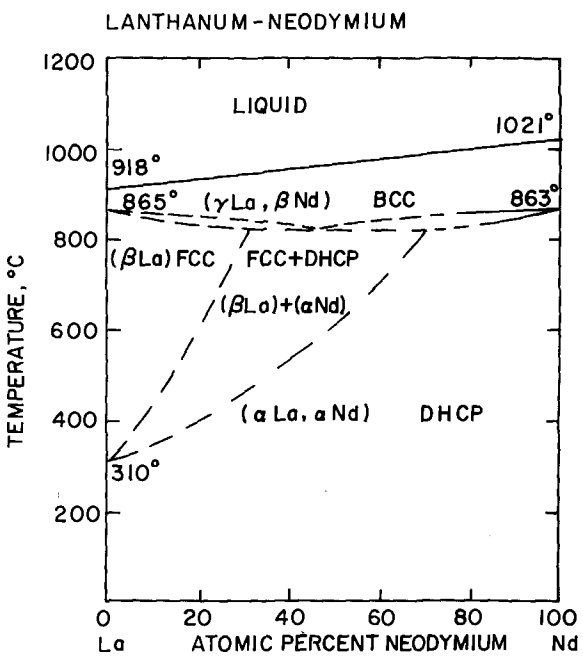

Fig. 3. Phase diagram of the lanthanum–neodymium system.

2.3. *La–Nd: Lanthanum–neodymium*

2.3.1. *Phase diagram*

The phase diagram for the lanthanum–neodymium system, shown in fig. 3, is derived from Gschneidner (1961), who modified a diagram reported by Daane and Spedding (1954). The purity of the starting materials was not given. The melting points of the pure metals and the transformation temperatures have been adjusted slightly in fig. 3 to conform with values listed in table 1. Since the two components are trivalent and have atomic numbers which differ by only three, the liquidus–solidus line has been drawn as a straight line connecting the two end-members (see section 2.1.1). The diagram reported by Daane and Spedding showed the bcc solid solution of γLa and βNd that transformed to another region of complete solid solubility. Gschneidner found this to be unlikely because of the difference in crystal structures (βLa is fcc and αNd is dhcp). Instead, he suggested that the γLa and βNd solid solution decomposes eutectoidally at ~ 825°C with βLa forming a closed field and αLa and αNd forming a complete dhcp solid solution below 310°C. Peterson et al. (1978) studied magnetic and electrical properties of La–Nd alloys at low temperatures and found, unlike La–Ce alloys, only the dhcp allotrope.

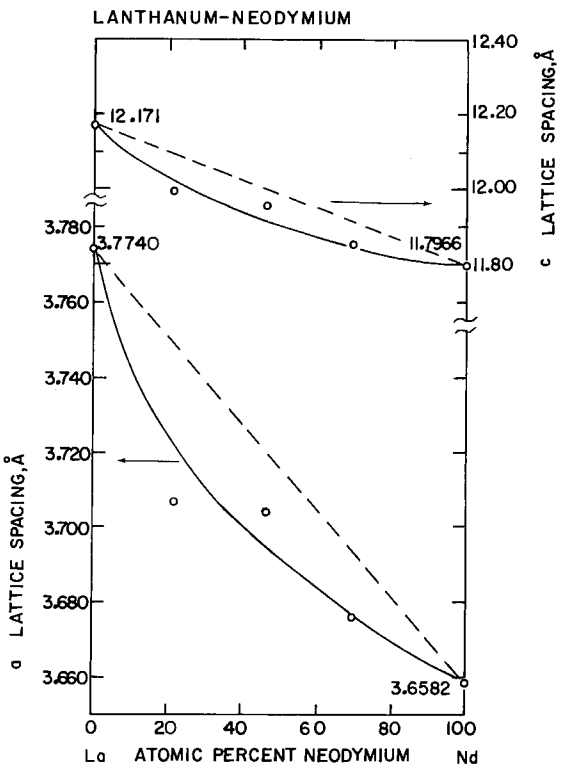

Fig. 4. Lattice spacings in the lanthanum–neodymium system. The dashed straight lines connecting the end-members are the Vegard's law relationships based on data from table 2.

2.3.2. *Lattice spacings*

Room temperature lattice spacings determined by Daane and Spedding (1954) in the lanthanum–neodymium system were reported by Gschneidner (1961). The reported spacings are slightly larger than those shown in table 2 for the pure components, possibly due to impurities in their specimens. A prorated correction has been applied to these data and these modified values are plotted in fig. 4. The difference between the dotted and solid lines indicates a negative deviation from ideality in contrast to the positive deviation observed for La–Ce (see fig. 2).

References

Daane, A.H. and F.H. Spedding, 1954, Ames Laboratory Rept. ISC-530, Iowa State University (declassified September 1955.)

Gschneidner, K.A., Jr., 1961, Rare Earth Alloys (Van Nostrand, New York) p. 87.

Peterson, T.S., S. Legvold, K.A. Gschneidner, Jr., T.-W.E. Tsang and J.O. Moorman, 1978, J. Appl. Phys. **49**, 2115.

2.4. *La–Gd: Lanthanum–gadolinium*

2.4.1. *Phase diagram*

The lanthanum–gadolinium alloy system presents an intermediate phase that has the same structure as samarium metal: a primitive rhombohedral crystal

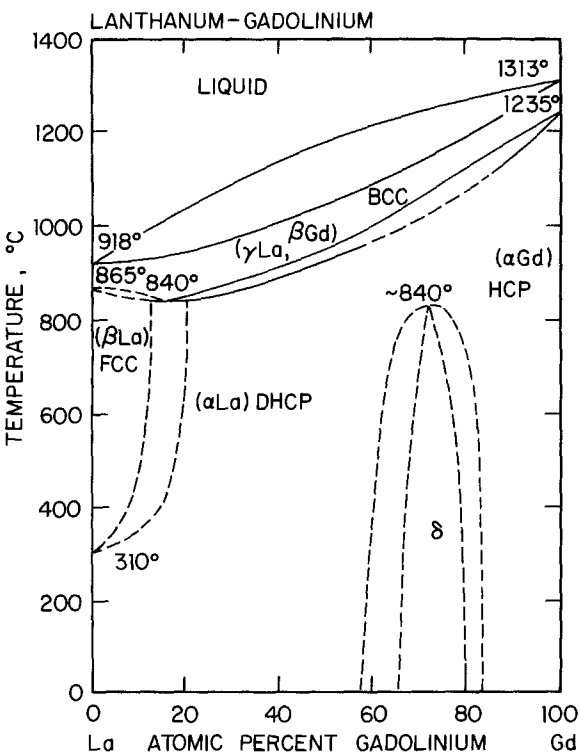

Fig. 5. Phase diagram of the lanthanum–gadolinium system.

structure that is generally referred to in terms of its nonprimitive hexagonal axes. The nonprimitive hexagonal unit cell has a c axis four and one-half times that of the normal hexagonal structure with a stacking sequence of ABABCBCAC, ABABCBCAC, etc. This structure is observed in other alloy systems of a light lanthanide metal with a heavy lanthanide or yttrium metal. These intra rare earth alloy systems follow, across their binary phase diagrams, a series of phases in which the percentage of hexagonal stacking increases from 0% in the fcc to 50% in the dhcp to 66.7% in the Sm-type to 100% in the hcp structure as the concentration of the heavy lanthanide or yttrium metal in the light lanthanide metal increases.

Spedding et al. (1962) proposed a phase diagram for the lanthanum–gadolinium system that indicates that the intermediate Sm-type (δ) phase is formed by a peritectoidal reaction between αLa and αGd. But on the basis of the detailed studies of Lundin (1966) and Koch et al. (1971), see section 2.1.3, the reviewers have modified the lanthanum–gadolinium phase diagram as originally proposed by Spedding et al. (1962). The modified phase diagram, fig. 5, shows the δ phase (Sm-type structure) forms congruently from the αLa–αGd solid solution; also see comments in Section 2.1.4. Some of the melting point and transformation temperatures of the pure metals have been slightly adjusted to conform with table 1. The purities of the starting materials were stated to be as follows: Spedding et al. reported La 99.96% pure (0.02% Ca and 0.01% Si as major impurities) and Gd 99.8% pure (0.1% Ta, 0.03% Si and 0.01% Fe as major impurities); and Lundin gave La 99.9% pure (0.051% O and 0.033% other rare earths as major impurities) and Gd 99.9% pure (0.021% O and 0.032% other rare earths as major impurities).

2.4.2. *Lattice spacings*

Several investigators have reported room temperature lattice spacings for alloys in the lanthanum–gadolinium system and are generally in good agreement. Before the stacking arrangement for alloys in the Sm-type region had been worked out, Thoburn et al. (1958) reported lattice spacings that agreed well with the eventual phase diagram except for the stacking factor in the δ-phase region. Valletta (1959) reported lattice spacings for nine alloys in this system including three alloys in the δ-phase region and his c-axis lattice spacing values reflect the accepted stacking. In his report on the investigation of the nature and formation of the Sm-type structure, Lundin (1970) included lattice spacings for La–Gd alloys over the composition range 62 to 90 at% gadolinium at 2% intervals. His data generally had less scatter than Valletta's and his spacing values are slightly smaller and include one more significant figure. Lundin also X-rayed alloys in the 40 to 60 at% region but these films contained α, β and γLa lines and were too complicated to be fully interpreted. Speight (1970) investigated the rapid quenching of certain intra rare earth alloys and reported spacings for a lanthanum–70 at% gadolinium alloy which has the δ-phase structure under normal conditions. His spacings agreed well with the data of Valletta and of Lundin. Jayaraman et al. (1966), who investigated the effect of pressure on several rare earth alloys, reported lattice constants for the δ phase 25 at% La–75 at% Gd alloy that also agreed with Lundin's values. Beznosov and Nikol'skii (1973) reported lattice spacings for lanthanum–gadolinium alloys over the range 90 to

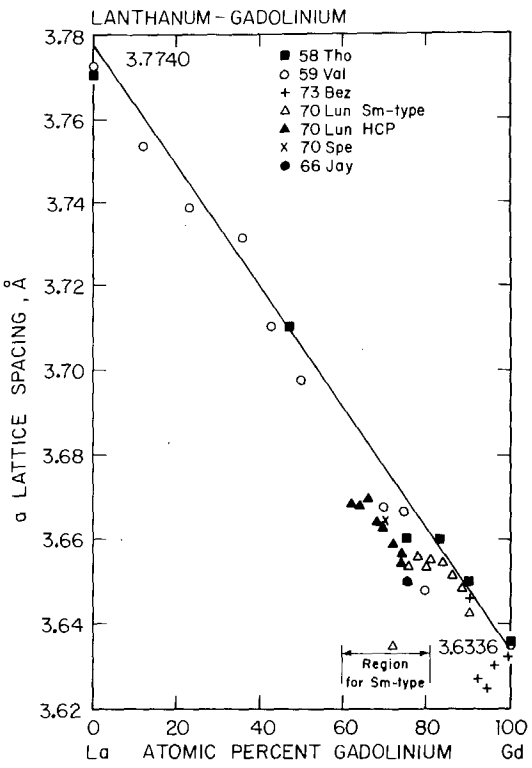

Fig. 6. *a* lattice spacings in the lanthanum–gadolinium system. The solid line connecting end-members represents the Vegard's law relationship as calculated from data given in table 2. The lattice parameters for the Sm-type at 75% Gd reported by Jayaraman (1966) and Lundin (1970) coincide.

100 at% gadolinium. Their reported spacings for both the *a* and the *c* lattice parameters decreased slightly as lanthanum was added up to 7.83 at%, then increased rapidly and were in good agreement with other data at 10 at% La. The *a*-axis lattice parameter for all of the lattice spacing data is shown in fig. 6. Certain data points from the different sets of data overlay each other so closely that in some cases they are not distinguishable. The solid line drawn in fig. 6 is the Vegard's law behavior expected using the lattice constants given in table 2. It is noted that the *a* lattice parameter for the Sm-type phase lies significantly below the Vegard line, while *a* values for the hcp and dhcp phases tend to scatter about this line. The *c* spacing data of these investigators are presented in fig. 7. Only a few data points overlay one another in this plot. The solid lines represent the Vegard's law values (adjusted for the appropriate crystal structure) as calculated from the accepted *c* values for Gd and La (see table 2). In this case the lattice parameters for the dhcp and the Sm-type phases generally lie above the Vegard line and those for the hcp phase lie below it.

2.4.3. *Phase relationships as a function of pressure*

Jayaraman et al. (1966) studied pressure-induced transformations for several intra rare earth alloy systems including the lanthanum–gadolinium system. The appropriate amounts of metals were arc-melted under argon, then sealed in evacuated

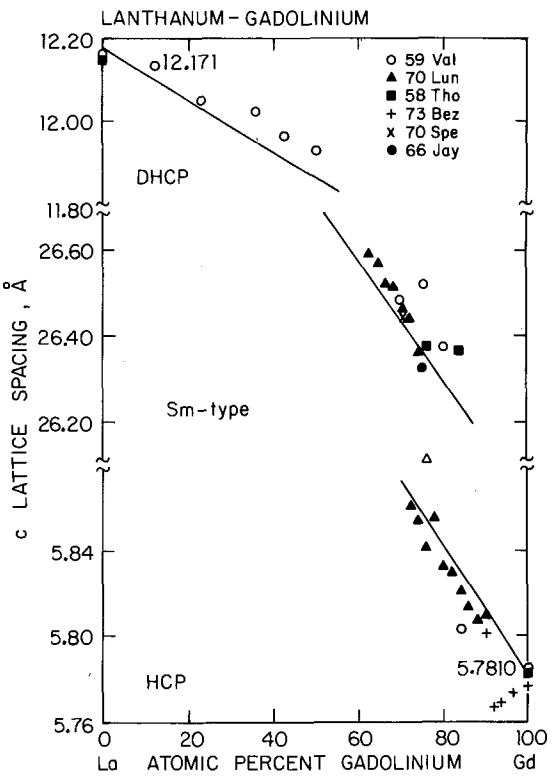

Fig. 7. c lattice spacings in the lanthanum–gadolinium system. The straight lines represent the Vegard's law relationships for each region in the phase diagram and are calculated from the data given in table 2.

quartz tubes and heat-treated at about 500°C for several days. X-ray patterns revealed that the specimens were single-phase material of the expected structure. A piston–cylinder apparatus was used to subject specimens to about 4.0 GPa pressure and 450°C for about 5 hr, after which the specimens were again X-rayed and magnetic-susceptibility measurements were made down to 1.4 K. The 75 at% Gd–La alloy with a normal structure of the Sm-type, transformed under the conditions of the experiment to the dhcp structure. Other intra rare earth alloys also underwent pressure-induced transformations in the sequence hcp → Sm-type → dhcp → fcc. Magnetic measurements indicated that the metastably retained δ phase of some of the La–Gd alloys reverted to hcp structure on cooling. The temperature of reversion to hcp structure was found to be dependent upon the La concentration.

2.4.4. *Thermodynamic data*

Lundin (1966) measured heat of solution and calculated the heat of mixing for alloys in the La–Gd system. A plot of the heat of mixing versus composition for a binary system should show abrupt inflections at major phase boundaries. Lundin used a liquid-metal-solution calorimeter that employed a liquid indium bath. The calorimeter was calibrated using solid indium samples and to avoid alloying between the rare earth metals and the molten indium, the indium bath was changed after

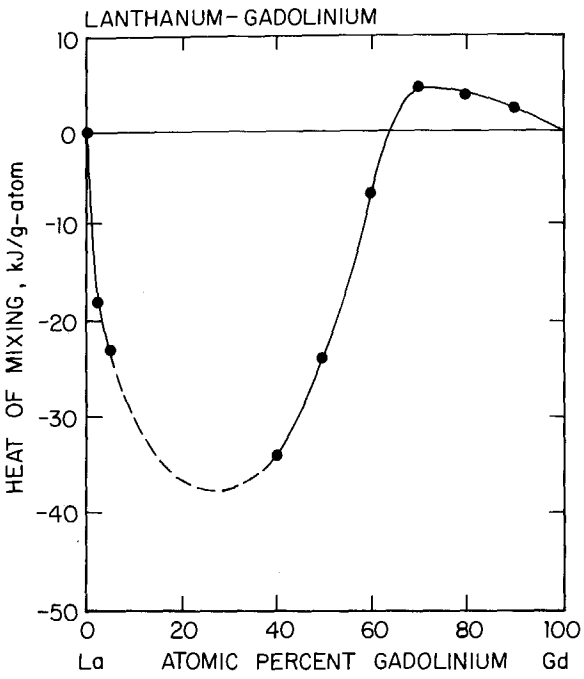

Fig. 8. Heat of mixing at 273 K for the lanthanum–gadolinium system (after Lundin, 1966). The dotted curve is the expected behavior, but no data points could be obtained in this region because of the slow dissolution of the alloys in the liquid indium. The heat of formation of the δ phase, which exists from ~ 65 to ~ 80 at% Gd, is not evident.

every three rare earth specimens. Values for the heat of mixing were referred to 0°C, the initial temperature of the alloys and the elements. The measured heats of solution of the alloys in indium were large and negative: The calculations of the heat of mixing involved differences between large numbers, which increased the chance for error in the calculated values.

Lundin's data for the calculated heat of mixing in the lanthanum–gadolinium systems is plotted in fig. 8. An anomaly exists in the diagram because lanthanum-rich alloys went into solution slowly—too slowly for accurate results. Between 40 and 60 at% Gd the dissolution slowed down abruptly. Between 7.5 and 30 at% Gd the dissolution was extremely slow but a normal rate of dissolution was observed when less than 5 at% Gd was present. This slowdown of dissolution is not related to the Sm-type phase since it occurs at the other end of the diagram. Lundin deduced that tighter bonding in the lattice occurred over this composition range.

Phillips and Matthias (1961) made heat capacity measurements at low temperatures (< 4 K) on solid solutions of small amounts of gadolinium in lanthanum and concluded that superconductivity and ferromagnetism extended throughout the sample. Finnemore et al. (1965a) measured the specific heat of superconducting La doped with magnetic impurity Gd and found inconclusive evidence for "gapless" superconductivity. Finnemore et al. (1965b) reported the heat capacity data on La doped with 0.8 at% Gd. They concluded that Gd ions order in a sample that shows

bulk superconductivity and that antiferromagnetism and superconductivity coexist in their sample.

References

Beznosov, A.B. and G.S. Nikol'skii, 1973, Fiz. Tverd. Tela **15**, 2808 [English transl.: Sov. Phys.—Solid State **15**, 1873].

Finnemore, K.D., D.L. Johnson, J.E. Ostenson, F.H. Spedding and B.J. Beaudry, 1965a, Phys. Rev. **137**, A550.

Finnemore, D.K., D.C. Hopkins and P.E. Palmer, 1965b, Phys. Rev. Lett. **15**, 891.

Jayaraman, A., R.C. Sherwood, H.J. Williams and E. Corenzwit, 1966, Phys. Rev. **148**, 502.

Koch, C.C., P.G. Mardon and C.J. McHargue, 1971, Metall. Trans. **2**, 1095.

Lundin, C.E., 1966, Final Report, Denver Research Institute Rept. AD-633558, Denver University, Denver, CO (also given as DRI-2326).

Lundin, C.E., 1970, in: Les Elements des Terres Rares, Vol. 1 (Centre National de la Recherche Scientifique, Paris) p. 151.

Phillips, N.E. and B.T. Matthias, 1961, Phys. Rev. **121** 105.

Spedding, F.H., R.M. Valletta and A.H. Daane, 1962, Trans. Quarterly (Am. Soc. Met.) **55**, 483.

Speight, J.D., 1970, J. Less-Common Met. **20**, 251.

Thoburn, W.C., S. Legvold and F.H. Spedding, 1958, Phys. Rev. **110**, 1298.

Valletta, R.M., 1959, Ph.D. thesis, Iowa State University, Ames, IA.

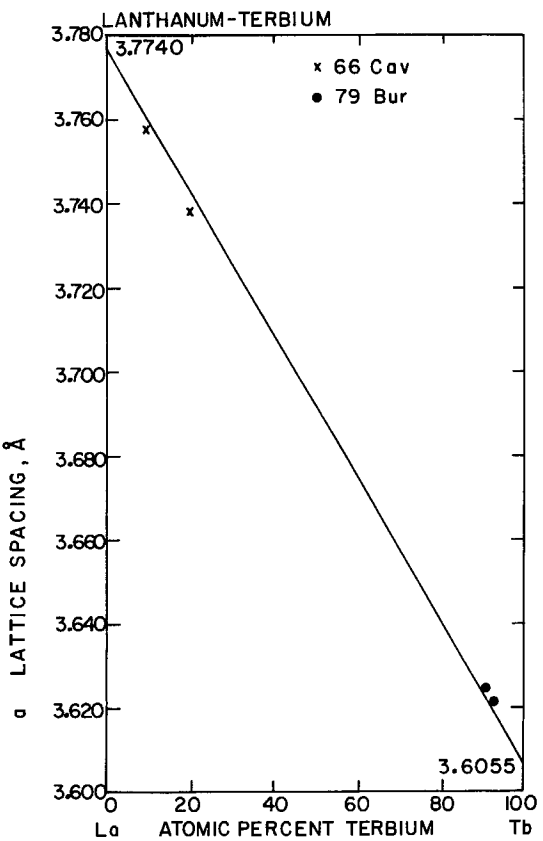

Fig. 9. *a* lattice spacings in the lanthanum–terbium system. The straight line connecting end-members represents the Vegard's law relationship for the *a* lattice spacing in this system based on the values listed in table 2 for the two end-members.

2.5. *La–Tb: Lanthanum–terbium*

2.5.1. *Lattice spacings*

No phase diagram has been found for the lanthanum–terbium system but some information has been published on the structures of the phases that exist in various parts of this system. Koehler et al. (1968), using neutron-diffraction methods, found that alloys having 15 at% or less of La had the simple hcp structure. At the lanthanum-rich end of the system, compositions containing 20, 40 and 50 at% Tb formed single-phase alloys with the dhcp structure. The X-ray pattern of a specimen that contained 75 at% Tb showed lines that were identified as being from the hcp and dhcp structures as well as from a third phase which was thought to be Sm-type structure. In a 10 at% Tb alloy, both dhcp and fcc phases were observed at room temperature. Achiwa and Kawano (1972, 1973) reported a Sm-type structure for an 80 at% Tb alloy with La. Cavin et al. (1966), who reported lattice spacing data for 10 and 20 at% Tb alloys of lanthanum, found that both of these compositions had dhcp structure. Burgardt et al. (1979) reported lattice spacing for Tb-rich alloys which had the hcp structure.

The lattice spacing information that has been reported for the lanthanum–terbium system is shown in figs. 9 and 10 for the *a* and *c* lattice parameters, respectively. The reported data are concentrated in the lanthanum- and terbium-rich ends of the system with no data between 20 and 90 at% terbium.

References

Achiwa, N. and S. Kawano, 1972, Acta Crystallogr. **28A**, 599.
Achiwa, N. and S. Kawano, 1973, J. Phys. Soc. Jpn. **35**, 303.

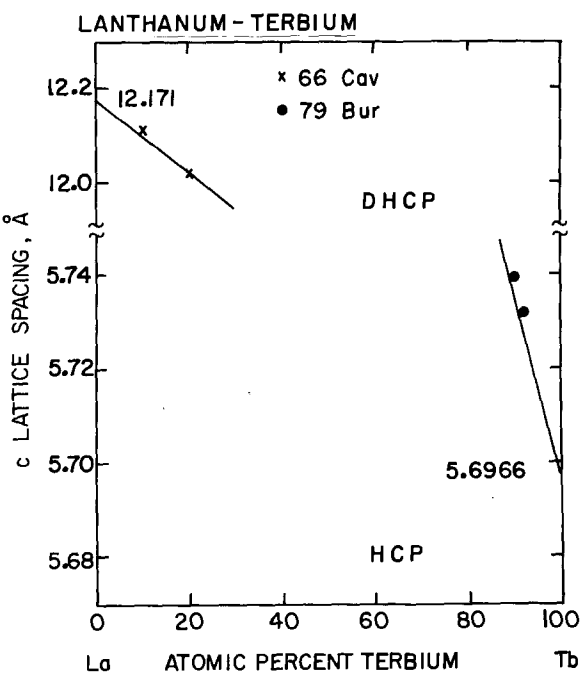

Fig. 10. *c* lattice spacings for the lanthanum–terbium system. The straight lines represent Vegard's law relationships for this system based on the values listed in table 2 for La and Tb.

Burgardt, P., S. Legvold, B.J. Beaudry and B.N. Harmon, 1979, Phys. Rev. B **20**, 3787.
Cavin, O.B., R.M. Steele, L.A. Harris and H.L. Yakel, 1966, Oak Ridge National Laboratory Rept. ORNL-3970, Oak Ridge, TN, p. 54.
Koehler, W.C., H.R. Child, E.O. Wollan and J.W. Cable, 1968, J. Appl. Phys. **39**, 1331.

2.6. *La–Dy: Lanthanum–dysprosium*

2.6.1. *Phase relationships*

No complete phase diagram for the lanthanum–dysprosium system was found, but Krizek and Taylor (1974), who measured lattice spacings in this system, reported rough phase boundaries at room temperature. The authors prepared their alloys by arc-melting 99.9% pure ingots of lanthanum and dysprosium. Their bulk samples were annealed 14 days at 200°C to convert the fcc phase to the appropriate close-packed hexagonal structures (dhcp, δ or Sm, and hcp). The fcc phase, according to the authors, is stable above 280°C. The authors suggest that the dhcp phase exists from 0 to 21 at% Dy, the δ (Sm) phase from 21 to 38 at% Dy and the hcp phase from 38 to 100 at% Dy.

2.6.2. *Lattice parameters*

The lattice parameters for this system as observed by Krizek and Taylor are plotted in figs. 11 and 12. The straight line connecting the *a* lattice spacings for the pure metals in fig. 11 indicates a negative deviation from Vegard's law in the hcp-phase region and a strong negative deviation in the Sm-type phase region. This

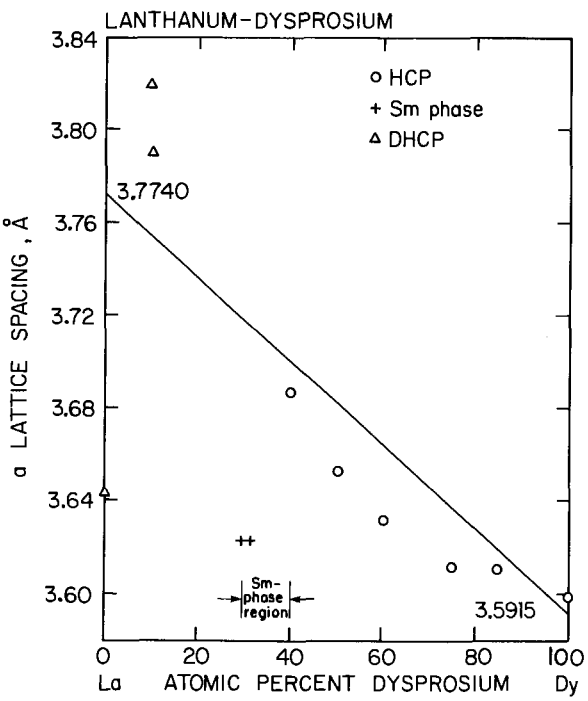

Fig. 11. *a* lattice spacings in the lanthanum–dysprosium system. The straight line connecting the end-members is the Vegard's law relationship based on the data in table 2.

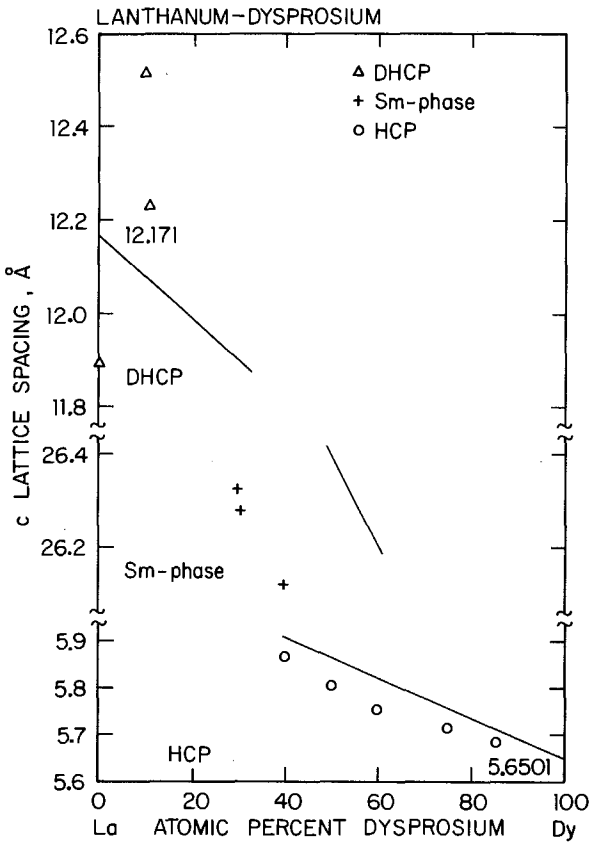

Fig. 12. *c* lattice spacings in the lanthanum–dysprosium system. The straight lines in the three phase areas are the Vegard's law relationships based on the data from table 2.

is also the case for the *c* lattice spacing data in the same regions (fig. 12). There is wide scatter among the three points in the dhcp region with two points indicating a positive deviation for both *a* and *c*; their value for pure lanthanum lies well below the accepted value for the pure metal, as listed in table. 2.

Reference

Krizek, H. and K.N.R. Taylor, 1974, J. Less-Common Met. **38**, 263.

2.7. *La–Ho: Lanthanum–holmium*

2.7.1. *Lattice spacings*

Lundin (1966), in a systematic study of the formation of the Sm-type structure in intra rare earth binary alloys, measured lattice spacings for several lanthanum–holmium compositions in and near the range of existence of that structure. His X-ray films of the 60 and 65 at% Ho alloys had insufficient lines for a lattice spacing determination. He reported boundaries for the Sm-type structure in

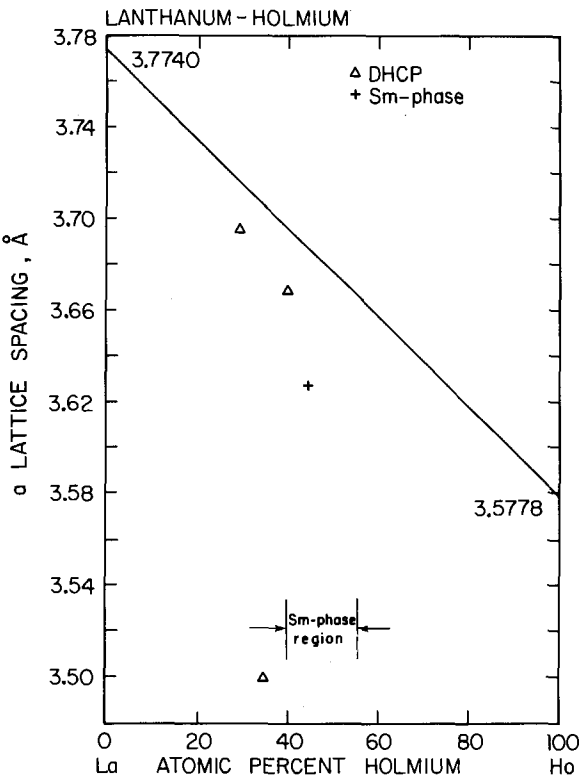

Fig. 13. *a* lattice spacings in the lanthanum–holmium system. The straight line connecting the end-members is Vegard's law based on the lattice parameters given in table 2.

this system as 40 and 55 at% Ho. The structure was dhcp at high lanthanum concentrations and hcp at lanthanum concentrations below 35 at% La. The data for the *a* and *c* lattice spacings are plotted in figs. 13 and 14, respectively.

Reference

Lundin, C.E., 1966, Final Report, Denver Research Institute Rept. AD-633558, Denver University, Denver, CO (also given as DRI-2326).

2.8. *La–Lu: Lanthanum–lutetium*

2.8.1. *Phase relationships*

Lundin (1966) tried to include alloys of the lanthanum–lutetium system in his study of the formation of the samarium-type structure in intra rare earth alloys. The wide differences in the melting points (La: 918°C; Lu: 1663°C) and densities (La: 6.146 g/cm^3; Lu: 9.841 g/cm^3) allowed the lutetium to settle to the bottom of molten lanthanum during the alloying process. Alloys were inverted and remelted several times to improve the homogeneity. Lundin reported: (1) lanthanum–lutetium alloys formed a complex microstructure that had a different appearance than that of the samarium-type structure formed in the other alloy systems between a light and a heavy lanthanide or yttrium metal; and (2) X-ray analysis failed to confirm the

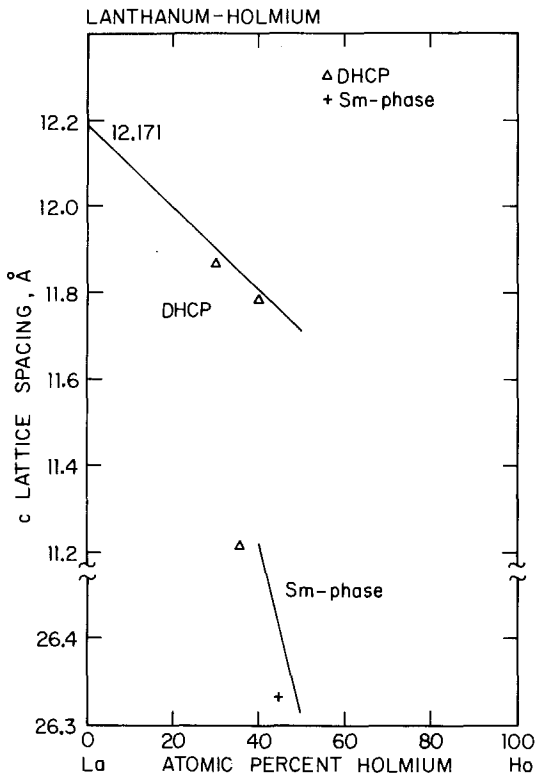

Fig. 14. *c* lattice spacings in the lanthanum–holmium system. The straight lines represent the Vegard's law relationships for the spacings in the Sm-phase and dhcp regions based on the lattice parameters given in table 2.

presence of the samarium-type structure in this system. The X-ray pattern from a 34 at% La–66 at% Lu alloy could be indexed on the basis of the coexistence of lanthanum (dhcp) and lutetium (hcp) solid solutions. These data suggest that a two-phase immiscibility gap exists in the low temperature region of this system. Lundin proposed that the most probable phase equilibria to accommodate this immiscibility gap would be a eutectoid reaction of the high temperature body-centered cubic allotrope to the two terminal (lanthanum plus lutetium) solid solutions. On the basis of the two-phase character of the microstructure, Lundin deduced that the assumed eutectoid would be near 34 at% La–66 at% Lu.

The reviewers, however, suggest an alternate model for the phase equilibria in this region of the lanthanum–lutetium system. At high temperature we propose that the dhcp La and hcp Lu phases form a continuous series of solid solutions, which upon cooling form a solid miscibility gap of the two terminal solid solutions. This construction would be essentially identical to the phase relationships observed in the Nd–Sc system by Beaudry et al. (1965) (see section 2.37 and fig. 65) and similar to that observed in the La–Gd system in that the dhcp La phase forms a continuous series of solid solutions with the hcp Gd phase at high temperatures (see section 2.4 and fig. 5). Clearly a careful experimental study needs to be made of the 20 to 50 at% La region of the lanthanum–lutetium system, especially at high temperatures.

Anderson et al. (1958) measured the effect of lutetium additions on the superconducting transition temperature of lanthanum and reported that alloys containing 55 and 80 at% La each had the lanthanum dhcp structure. These results are consistent with those reported above by Lundin.

2.8.2. *Lattice spacings*

Lundin (1966) reported lattice spacings for the two phases found in a 34 at% La–66 at% Lu alloy. For the lanthanum solid solution he found $a = 3.727$ Å and $c = 12.028$ Å. For the lutetium solid solution he reported a and c lattice spacings of 3.547 and 5.642 Å, respectively.

References

Anderson, G.S., S. Legvold and F.H. Spedding, 1958, Phys. Rev. **109**, 243.

Beaudry, B.J., M. Michel, A.H. Daane and F.H. Spedding, 1965, in: Eyring, L., ed., Rare Earth Research III (Gordon and Breach, New York) p. 247.

Lundin, C.E., 1966, Denver Research Institute Rept. AD-633558, University of Denver, Denver, CO (also given as DRI-2326).

2.9. *La–Sc: Lanthanum–scandium*

2.9.1. *Phase diagram*

Lundin (1970), in an investigation of the formation of samarium–type structure in intra rare earth binary alloys included six compositions in the lanthanum–scandium system ranging from 10 to 85 at% La. Lundin prepared his alloys using 99.8 (wt?)% pure lanthanum metal (major impurities, 330 ppm other rare earths, 510 ppm O, 50 ppm each Si, Mg and Zn) and 99 + (wt?)% pure scandium for which there were no details given on the impurities. Lundin found two-phase immiscibility at low temperatures in the lanthanum–scandium system and, since no samarium-type structure was found, he concluded that scandium behaves more like the neighboring transition elements than it does as a rare earth metal.

The phase diagram for this system, as reported by Naumkin et al. (1970) and Savitskii et al. (1970) is shown in fig. 15. Savitskii et al. did not reveal the purity of their alloying materials but Naumkin et al. reported a 99.7 wt% purity for their lanthanum (impurities, reported in wt%, were 0.04 Ce, 0.07 each Pr and Nd and 0.012 Fe). Their scandium was reported to be 99.7 wt% pure (impurities included 0.11 wt% O). Their alloys were formed by arc-melting the metals under an atmosphere of purified helium. Below the solidus, the body-centered cubic γLa and βSc form a solid solution. Two eutectoid transformations at about 750°C and 45 at% Sc and 233°C and 14 at% Sc result in regions of two-phase immiscibility.

2.9.2. *Thermodynamic properties*

DeBoer et al. (1980) presented calculated values for the enthalpy of formation, the limiting partial heats of solution and the heat of mixing of several binary alloys based on scandium. The authors pointed out that the scarcity of experimental information on the heat of alloying of scandium alloys makes the comparison of the

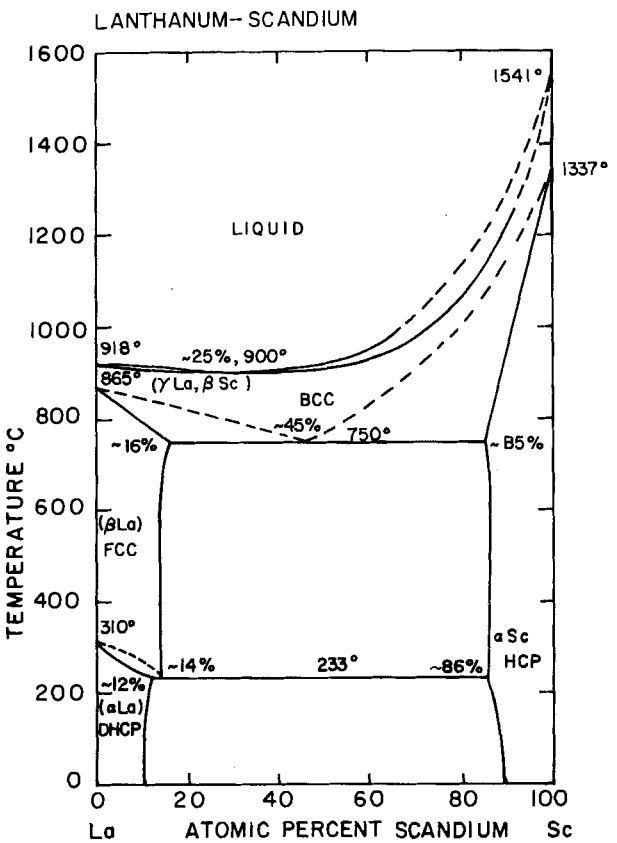

Fig. 15. Phase diagram of the lanthanum–scandium system.

calculations with experimental results difficult. They assumed that enthalpies of formation and of mixing are independent of temperature. For compounds, the reference state used was the pure solid metals and for liquid alloys, the reference states used were the pure liquid metals.

Their calculated values for the heat of formation, ΔH_f, for the compositions $ScLa_5$, $ScLa_2$, ScLa, Sc_2La and Sc_5La were, respectively, +4, +9, +11, +10 and +6 kJ per mole of atoms. These positive values for ΔH_f are consistent with the known La–Sc phase diagram in that no intermediate phases are known. The limiting partial heats of solution, $\Delta \bar{H}°$, for Sc in La and for La in Sc were, respectively, +27 and +35 kJ/mol, and the integral heat of mixing ΔH_{mix}, for ScLa was calculated to be +8 kJ/mol.

References

DeBoer, F.R., R. Boom and A.R. Miedema, 1980, Physica **101B**, 294.

Lundin, C.E., 1970, in: Les Elements des Terres Rares, Vol. 1 (Centre National de la Recherche Scientifique, Paris) p. 151.

Naumkin, O.P., V.F. Terekhova and E.M. Savitskii, 1970, Izv. Akad. Nauk SSSR, Met. [4], 137 [English transl.: Russ. Metall. [4], 99].

Savitskii, E.M, V.F. Terekhova, R.S. Torchinova, I.A. Markhova, O.P. Naumkin, V.E. Kolesnichenko and V.F. Stroganova, 1970, in: Les Elements des Terres Rares, Vol. 1 (Centre National de la Recherche Scientifique, Paris) p. 47.

2.10. *La–Y: Lanthanum–yttrium*

2.10.1. *Phase diagram*

The phase diagram for the lanthanum–yttrium alloy system, fig. 16, is based on the data of Spedding et al. (1962), but has been revised somewhat in light of the investigation by Lundin (1966) on the formation of the samarium-type structure in intra rare earth binary alloys. The metals used by Spedding et al. were more than 99.9(wt?)% pure with respect to other rare earths and contained small amounts of tantalum and oxygen as impurities. In the case of yttrium, the oxygen and tantalum contents were 1800 and 2000 ppm, respectively, and in the lanthanum each was less than 500 ppm. Their alloys were prepared by co-melting the components in a tantalum crucible using an induction furnace. Lundin used 99.9 wt% pure lanthanum

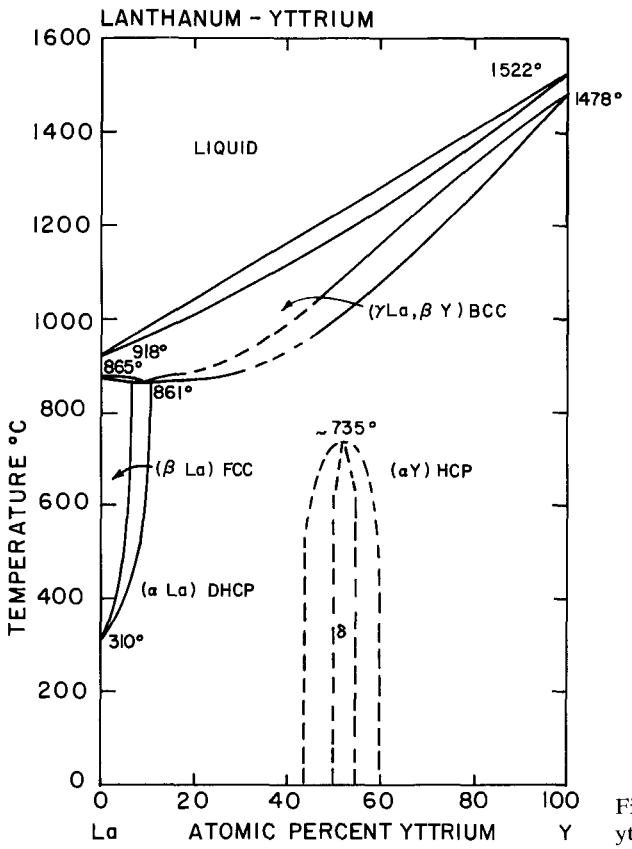

Fig. 16. Phase diagram of lanthanum–yttrium system.

that contained 520 ppm O, 330 ppm other rare earths and 50 ppm each Si, Mg and Zn. His yttrium which was 99.4 wt% pure, contained 1850 ppm O, 3000 ppm Zr, 330 ppm other rare earths, 80 ppm C and 60 ppm each Fe, Ta and Ni. Melting of component metals was done under a positive pressure of purified argon in a nonconsumable electrode arc furnace. As proposed by Spedding et al., the phase diagram showed a peritectoid reaction which formed the intermediate samarium-type phase from βLa and αY. An extensive investigation, that included thermal analyses, dilatometry, resistivity measurements and isothermal annealing and quenching treatments, failed to confirm the peritectoidal reaction. Lundin concluded that the samarium-type structure results from a recrystallization phenomenon formed by strains set up within the solid solution in the composition range where this structure exists, also see sections 2.1.3 and 2.1.4. In fig. 16 the peritectoid reaction has been replaced by a congruent transformation. Lundin reported the compositional range for the Sm-type structure in the La–Y system to run from ~ 40 at% La to ~ 65 at% La, a range that is somewhat wider than that given by Spedding et al. Jayaraman et al. (1966) reported that a 60 at% Y alloy has the hcp phase, which is consistent with the results shown in fig. 16. Some of the melting and transformation temperatures of the pure metals have been adjusted to conform with table 1.

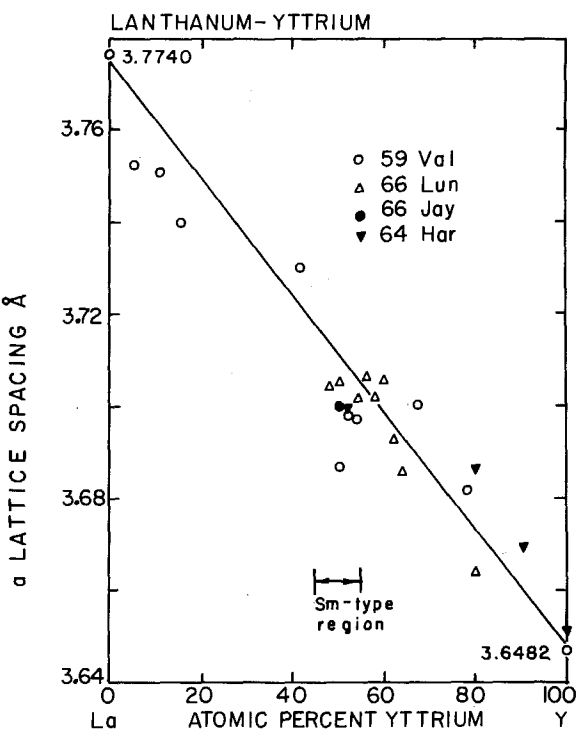

Fig. 17. *a* lattice spacings in the lanthanum–yttrium system. The straight line represents the Vegard's law relationship for the *a* lattice spacings based on the lattice parameters given in table 2.

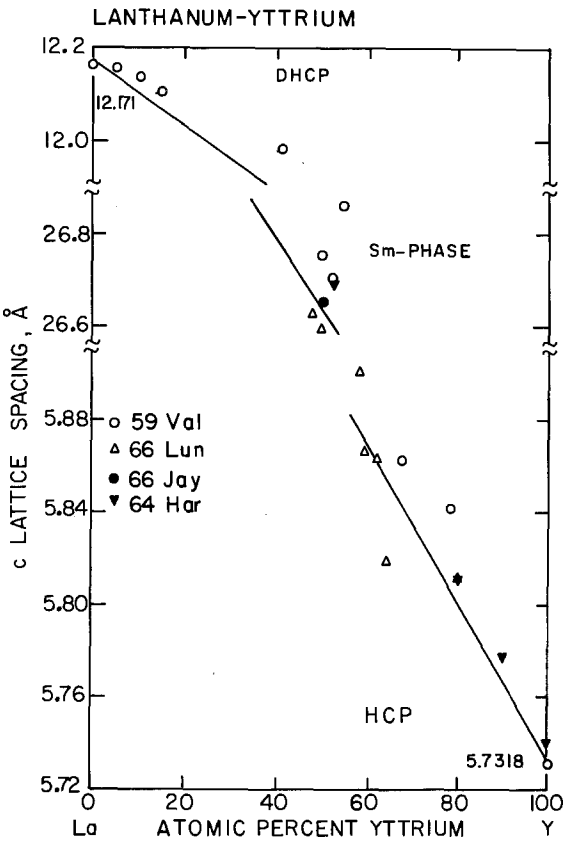

Fig. 18. *c* lattice spacings in the lanthanum–yttrium system. The straight lines represent the Vegard's law relationships for the *c* lattice spacings in each phase region as calculated from the lattice parameters of the pure metals given in table 2.

2.10.2. *Lattice spacings*

The lattice spacings for alloys in the lanthanum–yttrium system as reported by several investigators (Valletta, 1959; Harris and Raynor, 1964; Jayaraman et al., 1966; Lundin, 1966) are plotted in figs. 17 and 18. The solid line drawn in each graph represents the expected Vegard's law behavior and is based on the lattice spacings for the pure metals listed in table 2. In fig. 17 the *a* lattice spacings appeared to have a slight negative deviation in the dhcp region. In the Sm-type region the negative deviation trend appears to continue since more points fall below the Vegard's law line than above. In the hcp region scatter still exists, but here more points fall above the Vegard's law line indicating a positive deviation. The *c* lattice spacings are shown in fig. 18 and here a positive deviation is found in the dhcp and hcp regions. In the Sm-type region the data of Lundin fall just below the Vegard's law line, but Valletta's data, all of which lie above this line, show considerable

scatter. Lundin did not index the film of a sample containing 52 at% yttrium because of poor resolution of the lines; he observed that two phases were present. Jayaraman et al. (1966) did not give spacings for specimens having 60 and 70 at% Y but observed that each had hcp structure.

2.10.3. *Phase relationships as a function of pressure*

Jayaraman et al. (1966) studied pressure-induced transformations in the lanthanum–yttrium system using a piston–cylinder apparatus. Appropriate amounts of the metals (no purities stated) were arc-melted under an argon atmosphere, then heat-treated at 500°C for several days in sealed evacuated quartz tubes. The annealed specimens were single-phase materials of the expected structure. After a 5 hr anneal at 4.0 GPa pressure and 450°C, temperature was reduced to ambient and pressure was released. The X-ray patterns were again recorded and magnetic-susceptibility measurements down to 1.4 K were made by using a pendulum magnetometer. A 30 at% La specimen, normally having a hcp structure, underwent no phase transition; a 40 at% La specimen, also normally having hcp structure was transformed to Sm-type structure; a 50 at% La specimen, normally having Sm-type structure, transformed to the dhcp structure. The transformations are sluggish and conversion to the high pressure form is temperature- and time-dependent; therefore, no attempt was made to identify the transition pressure.

References

Harris, I.R. and G.V. Raynor, 1964, J. Less-Common Met. **7**, 1.
Jayaraman, A., R.C. Sherwood, H.J. Williams and E. Corenzwit, 1966, Phys. Rev. **148**, 502.
Lundin, C.E., 1966, Final Report, Denver Research Institute Rept. AD-633558, University of Denver, CO (also given as DRI-2326).
Spedding, F.H., R.M. Valletta and A.H. Daane, 1962, Trans. Quarterly (Am. Soc. Met.) **55**, 483.
Valletta, R.M., 1959, Ph.D. thesis, Iowa State University, Ames, IA.

2.11. *Ce–Pr: Cerium–praseodymium*

2.11.1. *Phase diagram*

Altunbas and Harris (1980) studied the cerium–praseodymium alloy system using electrical resistivity, *X*-ray diffraction and differential thermal analysis (DTA) techniques. In most of the research they used "standard commercial" material but some "relatively pure" praseodymium (purified by solid state electrolysis) was used in the DTA measurements. Appropriate amounts of the component metals were arc-melted in purified argon, turned and remelted several times. This was followed by a seven day vacuum anneal at 600°C with slow cooling to room temperature. Their electrical resistivity curves for the praseodymium sample indicated only one solid phase transformation (dhcp $\rightleftarrows$ bcc) whereas the curves for cerium and the Ce–Pr alloys exhibited two transitions, dhcp $\rightleftarrows$ fcc (below 61°C for pure cerium) and fcc $\rightleftarrows$ bcc.

The hysteresis that accompanied the dhcp–fcc transition increased as the cerium content increased. The resistivity data for praseodymium were in good agreement with those of Spedding et al. (1957) and their transition temperature for the γ–β (fcc–dhcp) phase change in cerium was similar to values reported by Gschneidner et al. (1962a) and by McHargue and Yakel (1960). The spread in these reported values is probably due to different impurity levels in the alloys investigated. An X-ray diffraction study (Altunbas and Harris) on powders that had been annealed at 600°C for 2 hr and quickly cooled to room temperature showed that: (1) alloys in the range 0 to 65 at% Pr have fcc structure; (2) alloys in the range 74 to 100 at% Pr have dhcp structure; and (3) alloys containing 66 to 74 at% Pr contained both the dhcp and fcc phases. Altunbas and Harris correlated the predominance of the fcc structure with the hysteresis characteristics of these alloys. They found considerable hysteresis associated with the fcc–dhcp transformation in Ce-rich alloys, which they associated with a change in the transformation mechanism from a martensitic to diffusion-controlled process. They observed a rapid nonlinear increase for the linear increase for the temperature dependence of the solvus lines that separate the fcc from the dhcp-phase regions. They postulated that either the dhcp + fcc-phase field meets the bcc + fcc-phase field just before 100% Pr to give a high temperature eutectoid or peritectoid reaction, or that the dhcp–fcc transition occurs in commercial praseodymium just below a bcc–fcc transition. If the latter were true, the resistivity and DTA effects associated with the dhcp–fcc phase change merged with the effects due to the bcc $\rightleftarrows$ fcc transformation. Altunbas and Harris believed that if

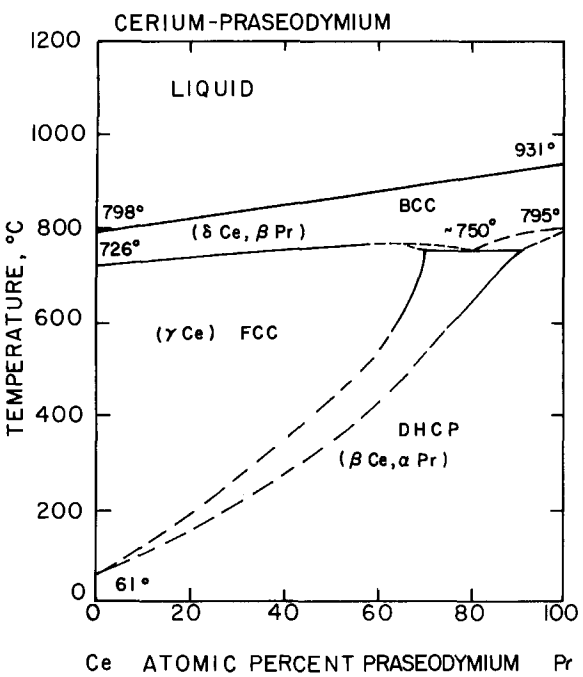

Fig. 19. Phase diagram of the cerium–praseodymium system. The 61°C value for the γ–β (fcc–dhcp) transformation for pure cerium is the midpoint value of the heating (139°C) and cooling (−16°C) transformation temperatures (see table 1).

the Ce–Pr alloys could be prepared from pure components the fcc–dhcp-phase field would shift to lower Pr contents and a phase diagram similar to that of the La–Nd system (see section 2.3 and fig. 3) would be anticipated. Their DTA and solidification data indicated a narrow liquidus–solidus separation, as expected in an intra rare earth alloy system of this kind.

Gschneidner et al. (1961 and 1962b) investigated the effect of alloying on the $\gamma \rightarrow \alpha$ transition temperature of cerium and found that the addition of 2 at% Pr lowers this transition temperature. At high pressures, this addition of Pr raised the transformation pressure of pure cerium.

Figure 19 is the reviewers' interpretation of the phase relationships in the cerium–praseodymium system based on the experimental data presented by Altunbas and Harris. Melting and transition temperatures of the pure component metals have been adjusted to conform with table 1.

2.11.2. *Lattice spacings*

Published lattice spacing data for the cerium–praseodymium system are limited to the pure components and to several cerium-rich alloys. Gschneidner et al. (1962c) examined lattice spacings for several cerium-rich alloys containing up to 5 at% of several rare earth metals. The experimental details are given in section 2.2.2. They found that the lattice spacings for all of these alloys except those with praseodymium showed a positive deviation from Vegard's linear approximation whereas the lattice spacings for the cerium–praseodymium alloys, shown in fig. 20, followed Vegard's law quite well.

References

Altunbas, M. and I.R. Harris, 1980, J. Mater. Sci. **15**, 693.
Gschneidner, K.A., Jr., R.R. McDonald and R.O. Elliott, 1961, Phys. Rev. Lett. **6**, 218.
Gschneidner, K.A., Jr., R.O. Elliott and R.R. McDonald, 1962a, J. Phys. Chem. Solids **23**, 555.
Gschneidner, K.A., Jr., R.O. Elliott and R.R. McDonald, 1962b, J. Phys. Chem. Solids **23**, 1201.
Gschneidner, K.A., Jr., R.O. Elliott and M.Y. Prince, 1962c, in: Nachman, J.F. and C.E. Lundin, eds., Rare Earth Research (Gordon and Breach, New York) p. 71.
McHargue, C.J. and H.L. Yakel, 1960, Acta Metall. **8**, 637.
Spedding, F.H., A.H. Daane and K.W. Hermann, 1957, J. Met. **9**, 895.

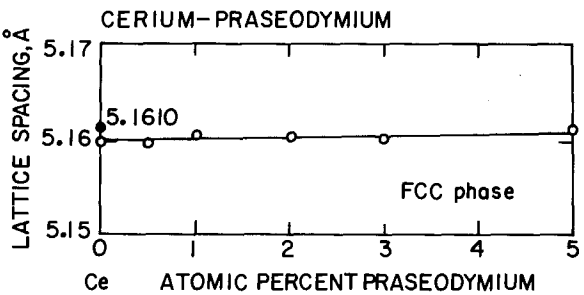

Fig. 20. Lattice spacings in the cerium-rich end of the cerium–praseodymium system.

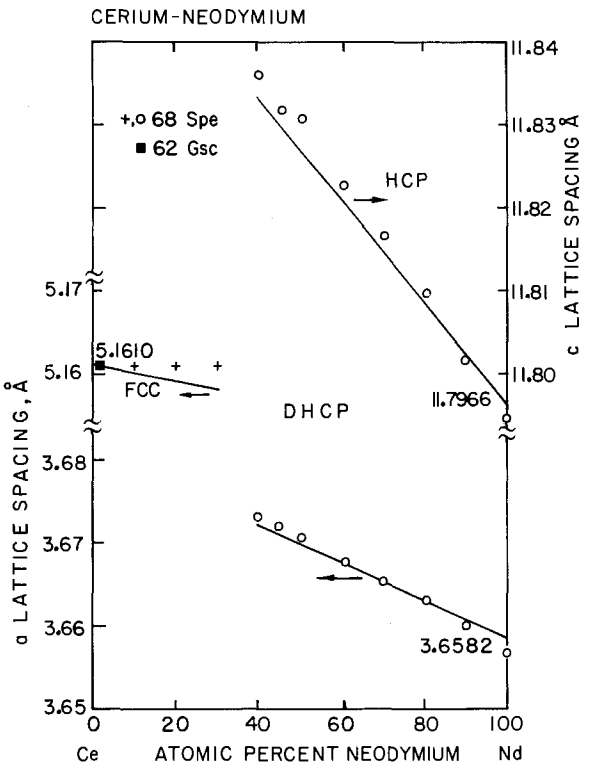

Fig. 21. Lattice spacings in the cerium–neodymium system. The straight lines show Vegard's law relationships based on data from table 2.

2.12. *Ce–Nd: Cerium–neodymium*

2.12.1. *Lattice spacings*

No phase diagram for the cerium–neodymium system was found in the literature, but Speight et al. (1968) have measured the room temperature lattice spacings for this alloy system. Their alloy specimens were made from the cerium metal that contained no more than 100 ppm of other rare earth metals and from neodymium metal that contained approximately 200 ppm of non-rare earth metals and < 1000 ppm of other rare earth metals. Lattice spacings were determined by X-ray diffraction and a Nelson–Riley extrapolation was used to eliminate systematic errors. Their data for the cerium–neodymium system, reported in kX units, have been converted to angstrom units and are plotted in fig. 21. In the cerium-rich fcc region, the lattice spacings appear to be independent of composition. A small deviation from ideality exists for both the a and the c lattice spacings in the dhcp region except at Nd content greater than 90 at% where a small negative deviation from ideality exists.

In addition to this work (Speight et al.), Gschneidner et al. (1962) reported the lattice parameter of a cerium-rich alloy containing 2 at% Nd. The experimental details are given in section 2.2.2.

References

Gschneidner, K.A., Jr., R.O. Elliott and M.Y. Prince, 1962, in: Nachman J.R. and C.E. Lundin, eds., Rare Earth Research (Gordon and Breach, New York) p. 71.

Speight, J.D., I.R. Harris and G.V. Raynor, 1968, J. Less-Common Met. **15**, 317.

2.13. *Ce–Sm: Cerium–samarium*

2.13.1. *Phase diagram*

A partial phase diagram for the cerium–samarium alloy system has been reported by Terekhova et al. (1968) and by Torchinova et al. (1971). A comparison of the two published phase diagrams indicates that each is based on the same research. The purity of the cerium and samarium metals was not reported. The phase relationships were determined by metallographic, X-ray diffraction, thermal analysis, hardness, thermal expansion and magnetic-susceptibility measurements. Neither Terekhova et al. nor Torchinova et al. considered the existence of the high temperature hcp form of samarium (βSm) in the construction of their phase diagram. Consequently, the reviewers have made revisions in their phase diagram to include the βSm phase. The revised diagram is shown in fig. 22. Here, the liquidus–solidus is shown as a single straight line connecting the melting points of the pure components since their atomic numbers differ by only four (see discussion in section 2.1.1). The solid solution ranges at room temperature shown in fig. 22 are based on the lattice parameter data (see section 2.13.2) reported by Speight et al. (1968). The temperature shown for the

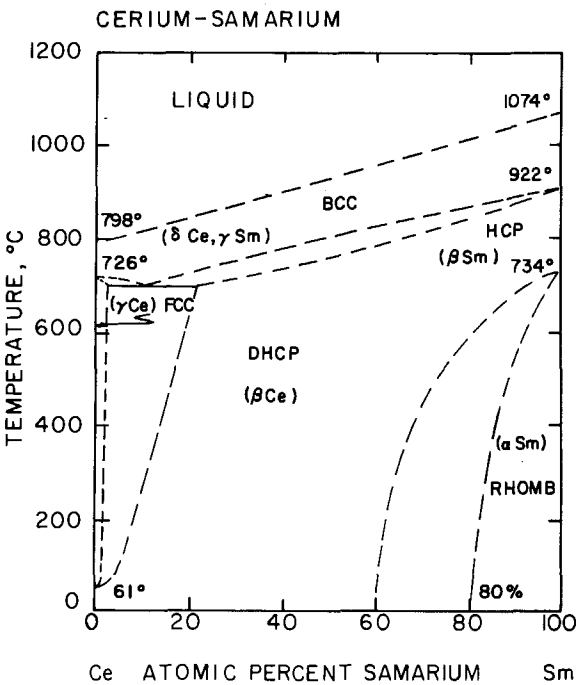

Fig. 22. Phase diagram of the cerium–samarium system.

transformation of γ Ce to β Ce (61°C) is the average temperature of this transformation on heating and on cooling. Much of the phase diagram between the liquidus and the room temperature region is uncertain but the diagram presented here is a logical interpretation of the reported data and the existence of a continuous series of solid solutions between dhcp and hcp rare earth metals, see section 2.1.4. The original diagram presented by Terekhova et al. and Torchinova et al. showed bcc solid solution reacting with the rhombohedral αSm phase to form the dhcp βCe solid solution by a peritectoid reaction. However, the thermal analysis data points given by these investigators are in good agreement with the solvus lines separating the bcc phase from the dhcp–hcp solid solution shown in fig. 22.

Clinard (1967) used electrical resistivity measurements to study the β-phase forming tendencies of cerium alloys between 300 and 1.5 K. The addition of 2 at% samarium to cerium resulted in a hysteresis loop in the temperature vs. resistivity curve between approximately 40 and 170 K. This was attributed to the formation of some αCe during thermal cycling.

2.13.2. *Lattice spacings*

Speight et al. (1968) reported lattice spacings at room temperature for cerium–samarium alloys that had been rapidly cooled from 600°C. Their samarium

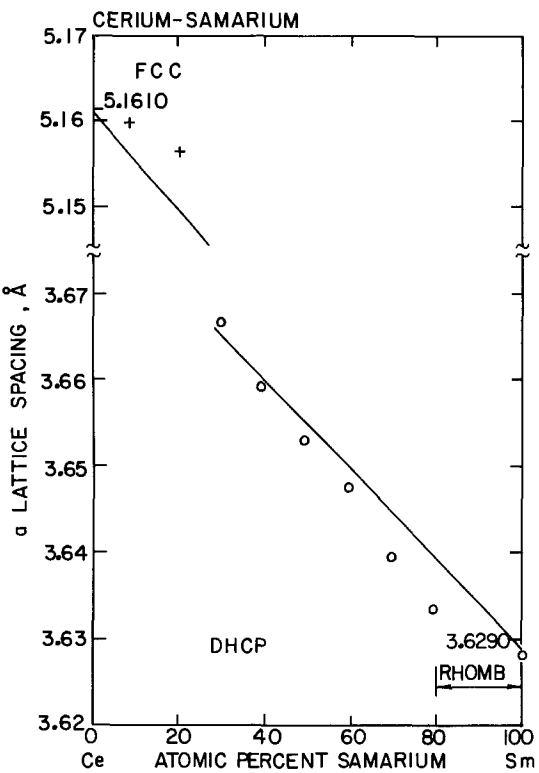

Fig. 23. *a* lattice spacings in the cerium–samarium system. The straight line represents the Vegard's law relationship for the *a* lattice spacing in this system based on the data given in table 2.

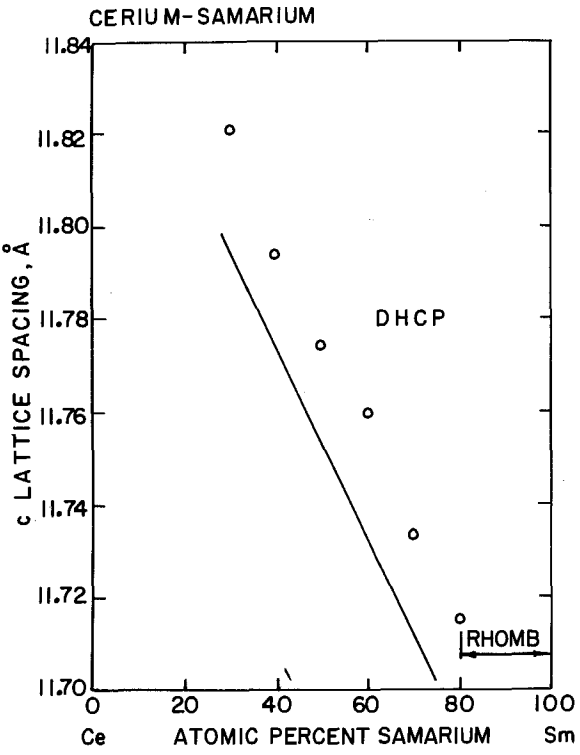

Fig. 24. *c* lattice spacings for the cerium–samarium system. The straight lines represent the Vegard's law relationships for *c* lattice spacings in this system based on the data given in table 2.

contained approximately 200 ppm of base metals and < 1000 ppm of other rare earth metals. Impurities in their cerium did not exceed 100 ppm of other rare earth metals. The lattice spacings were obtained by X-ray diffraction methods at room temperature and systematic errors were eliminated by use of a Nelson–Riley extrapolation function. At compositions between 80 and 100% Sm, Speight et al. found the alloys to be of Sm-type structure but the diffraction patterns were of insufficient quality for accurate lattice parameter measurements. Their data for the other alloys are plotted in figs. 23 and 24 along with a line showing the Vegard's law relationship for each part of the plot. The dhcp structure was found to persist over the composition range 30 to 80 at% Sm. A large positive deviation from the Vegard's law relationship exists in the *c* spacing data. Most of the *a* spacing data in the same region showed a negative deviation from the appropriate straight line relationship but one datum point, at 29.6 at% Sm, showed a slight positive deviation. All three of the *a* spacing data points in the fcc region exhibit positive deviations that increased with samarium content.

References

Clinard, F.W., Jr., 1967, J. Appl. Phys. **38**, 1694.
Speight, J.D., I.R. Harris and G.V. Raynor, 1968, J. Less-Common Met. **15**, 317.
Terekhova, V.F., E.M. Savitskii and R.S. Torchinova, 1968, in: Gulyaev, B.B., ed., Diagrammy Sostoyaniya

Metallich Sistem [Constitutional Diagrams of Metallic Systems] (Nauka, Moscow) p. 200.
Torchinova, R.S., V.F. Terekhova and E.M. Savitskii, 1971, in: Savitskii, E.M. and V.F. Terekhova, eds., Redkozemel'nye Metally i Splavy (Nauka, Moscow) p. 39 [English transl.: Rare Earth Metals and Alloys, Rept. AEC-tr-7408, National Technical Information Service, Springfield, VA, 1974].

2.14. *Ce–Eu: Cerium–europium*

2.14.1. *Phase diagram*

A partial phase diagram for the cerium–europium system has been proposed by Savitskii et al. (1967). There is no information on the purity of their cerium metal but they state that their metallic europium contained < 0.1 (wt?)% Sm and Gd, 0.075% Ca, 0.01% Fe, 0.005% Cu and 0.04% Ta. They assumed that bcc Eu and bcc δCe form a continuous series of solid solutions at high temperatures. A two-phase region was assumed for Eu and γCe, the fcc structure that exists below 726°C. Savitskii et al. studied the microstructure of their Ce–Eu alloys and found that oxide inclusions in samples containing more than 40 at% Eu prevented the observation of the structure of high europium composition. They found a single-phase region at compositions varying between 10 to 20 at% Eu. This is in conflict with the results of Arajs et al. (1963) who found only 4.4 at% Eu is soluble in γCe (see section 2.14.2).

An alternate and more logical interpretation, which is consistent with the data given by Savitskii et al., is presented in fig. 25. The reviewers believe that the divalent Eu and trivalent Ce form immiscible liquids, just as divalent Yb with trivalent Lu

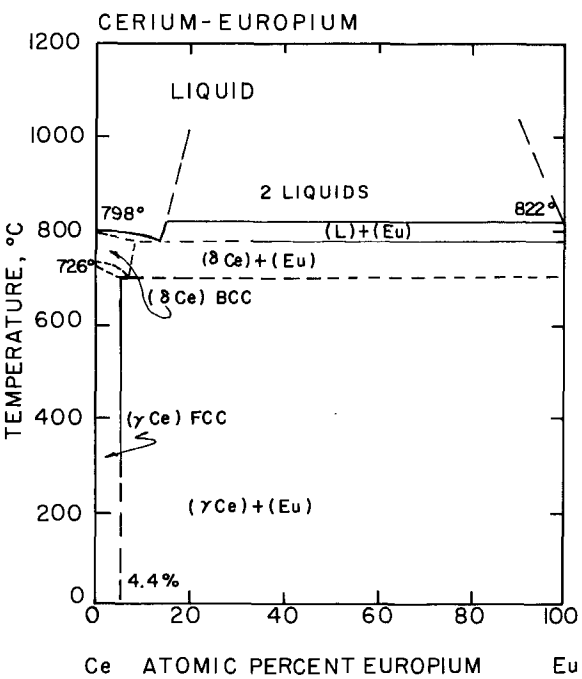

Fig. 25. Phase diagram for the cerium–europium system.

(Beaudry, 1974) and divalent Ca with trivalent Ce and La (Zverev, 1955; Savitskii and Terekhova, 1958, respectively). In these four alloy systems the divalent metals are 5 to 10% larger than the trivalent metal (~ 5% for Ca–La and Ca–Ce and ~ 10% for Eu–Ce and Yb–Lu).

2.14.2. *Lattice spacings*

Lattice spacings for a few cerium-rich alloys in the cerium–europium system were reported by Arajs et al. (1963). They found that europium forms a solid solution with cerium up to 4.4 at% Eu. The lattice spacings increased with europium concentration over this range; hence they concluded that the lattice spacing data support the idea of divalent europium dissolved in cerium. Figure 26 is a plot of their lattice spacing data in which the solid lines and the open circles represent their data. Since their *a* spacing value for cerium is smaller than the accepted value listed in table 2 (section 1.2), a uniform adjustment has been made to the data as presented by Arajs et al. and this is shown in fig. 26 by solid circles and a dashed line. The plot indicates that only about 4.4 at% Eu dissolves in γCe.

References

Arajs, S., H. Chessin, R.V. Colvin and G.R. Dunmyre, 1963, J. Appl. Phys. **34**, 1668.
Beaudry, B.J. and F.H. Spedding, 1974, Metall. Trans. **5**, 1631.
Savitskii, E.M. and V.F. Terekhova, 1958, Zh. Neorg. Khim. **3**, 756.
Savitskii, E.M., V.F. Terekhova and R.S. Torchinova, 1967, Metalloved. Term. Obrab. Metal. [2], 25 [English transl.: Met. Sci. Heat Treat. [1/2], 100].
Zverev, G.V., 1955, Dokl. Akad. Nauk SSSR **104**, 242.

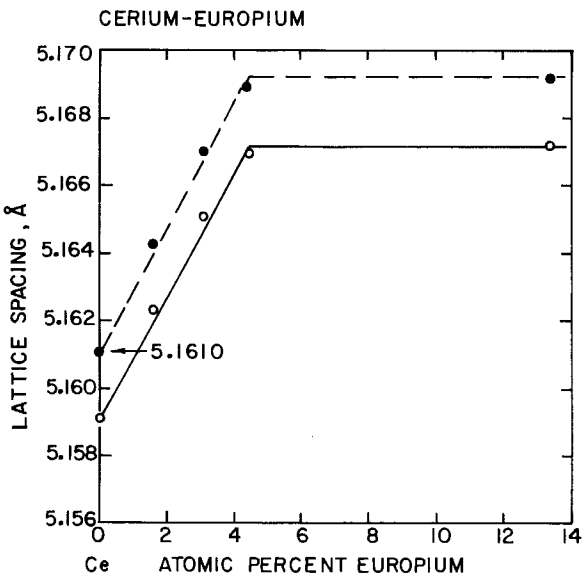

Fig. 26. Lattice spacings for cerium–europium alloys in cerium-rich region. The solid line is data as presented by Arajs et al. The dashed line is data adjusted to the pure γCe value listed in table 2.

2.15. *Ce–Gd: Cerium–gadolinium*

2.15.1. *Phase diagram*

Partial phase diagrams for the cerium–gadolinium system have been presented by several researchers (Burov et al., 1963, 1964; Terekhova, 1963). These earlier phase diagrams indicate that an intermediate Sm-type (δ) phase is formed by a peritectoid reaction. More recent research has altered this concept (see below and also sections 2.1.3 and 2.1.4). Harris et al. (1966) defined through X-ray studies the range of composition over which the close-packed hcp, δ and dhcp phases exist in Ce–Gd alloys at room temperature. Lundin (1966) studied several binary alloy systems consisting of a light rare earth metal and a heavy rare earth metal (including Ce–Gd) in an intensive investigation of the formation of the intermediate δ phase. Koch et al. (1971) studied the nature of this phase in the Ce–Gd system since this system is typical of the intra rare earth alloys that contain the δ-phase structure. In their investigation, Koch et al. utilized electric resistance measurements, X-ray diffraction and both optical and electron microscopy. Neither Lundin nor Koch found any evidence to support the assumed peritectoid reaction in the formation of the δ phase. Rather, their studies implied that the transformation to the samarium-type

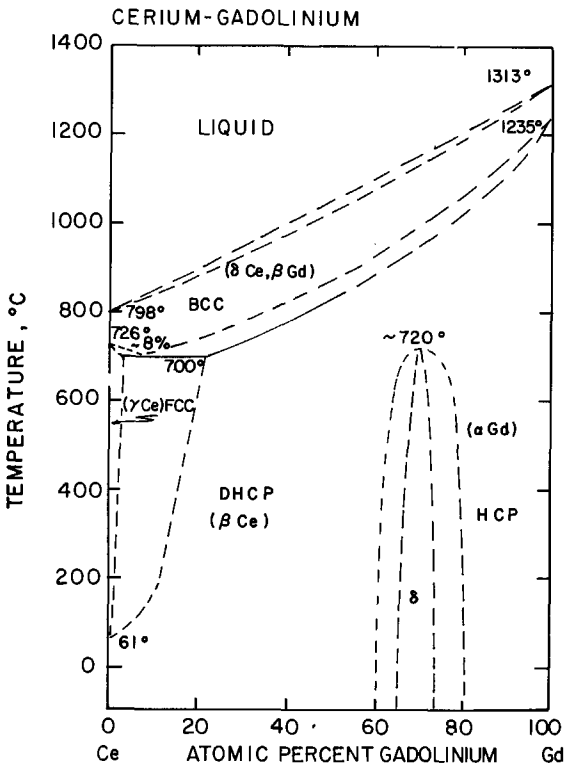

Fig. 27. Phase diagram of cerium–gadolinium system.

structure is martensitic in nature. Harris et al. (1967) have investigated the effects of filing at room temperature and at −196°C on the X-ray diffraction patterns of some Ce–Gd alloys. Their study suggested that the Sm-type and the dhcp structures can be stabilized at significantly lower cerium content by cold-working. The phase diagram for the cerium–gadolinium system, presented in fig. 27, combines features of the phase diagram as proposed by Burov et al. (1963) with revisions that bring it into harmony with the findings of Lundin and Koch et al. The melting points and the transition temperatures of the pure metals have been adjusted to the values listed in table 1. The widths of the two-phase regions between the liquidus–solidus and between the bcc–close-packed solvus lines have been narrowed slightly from the Burov et al. diagram, in keeping with the tendency toward ideal behavior for these closely related lanthanide elements, see section 2.1.1.

2.15.2. *Lattice spacings*

Lattice spacings for the cerium–gadolinium system have been reported by Harris et al. (1966) for compositions across the phase system. Lundin (1966) has reported lattice spacings at several compositions above and below the δ-phase composition range but his patterns contained an insufficient number of lines for reliable lattice parameter measurements between 60 and 75 at% Gd. Burov et al. (1963) reported the spacings for a specimen containing ~ 80 at% Gd. Gschneidner et al. (1962) reported

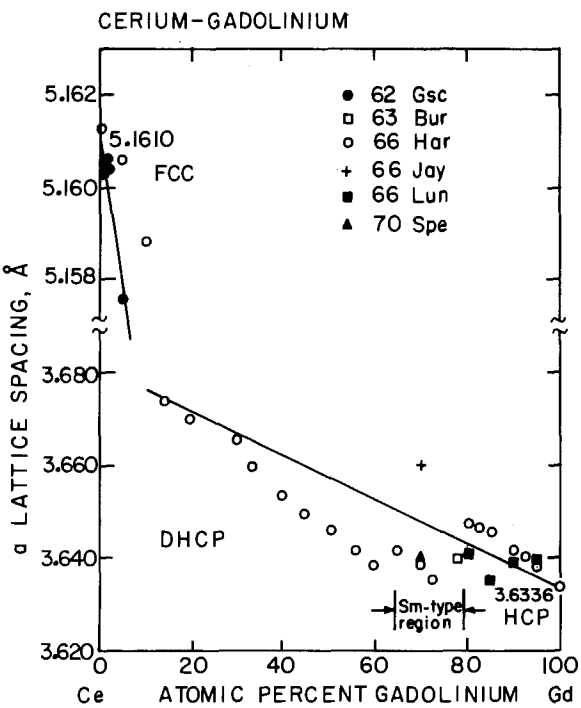

Fig. 28. *a* lattice spacings in the cerium–gadolinium system. The straight lines indicate the Vegard's law relationships based on the pure metal values given in table 2.

spacings for cerium-rich Ce–Gd alloys up to 5 at% Gd. Jayaraman et al. (1966) studied effects of pressure on various pairs of light and heavy rare earth binary alloys and reported the lattice spacings of a Ce–70 at% Gd alloy for both the normal and the pressure-induced phases. Speight (1970) also reported lattice spacings for a Ce–70 at% Gd alloy for both the homogenized and rapidly quenched states.

The room temperature *a* lattice spacings of normal phases in the cerium–gadolinium system are shown in fig. 28. Straight lines represent the Vegard's law relationships in both the cubic and hexagonal composition ranges. In the fcc range, the data of Harris et al. show a positive deviation from the Vegard's law line whereas the data reported by Gschneidner et al. lie close to this line. In the gadolinium-rich end of the system, the data of Harris et al. for the hcp phase also have a positive deviation from the Vegard's law line but Lundin's data for this phase are scattered both above and below this line. In the Sm-type phase range all of the data, except for the one datum point given by Jayaraman et al. at Ce–70 at% Gd, showed a significant negative deviation. In the dhcp region, three of the data points from Harris et al. (from about 15 to 30 at% Gd) fall close to the Vegard's law line but their remaining data show a strong negative deviation that increases with gadolinium content.

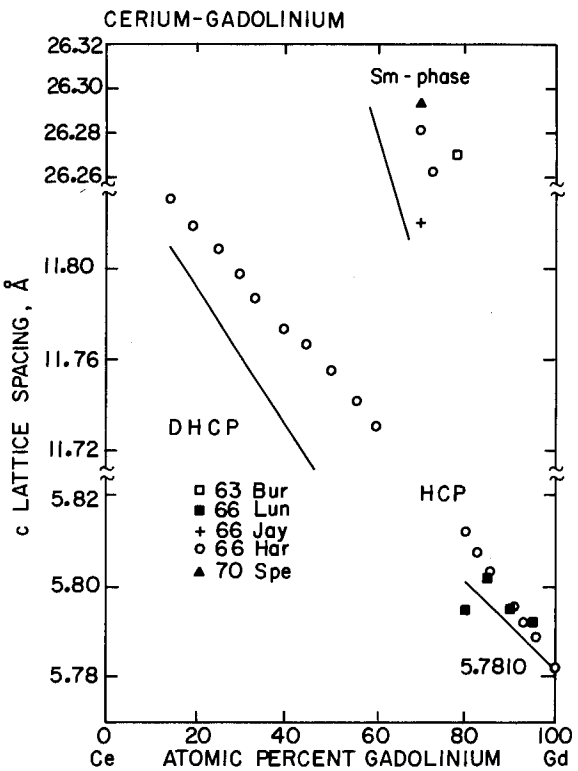

Fig. 29. *c* lattice spacings in the cerium–gadolinium system. The straight lines show the Vegard's law relationships based on the pure metal values given in table 2.

The c spacings for the hexagonal phases in this system are shown in fig. 29. Positive deviations from ideality are encountered for all structures with only one datum point exhibiting a negative deviation.

2.15.3. *Phase relationships as a function of pressure*

Jayaraman et al. (1966) examined several binary alloys of a light rare earth metal with a heavy rare earth metal and found that a Ce–70 at% Gd specimen transformed from its normal Sm-type structure to dhcp structure during a 5 hr treatment at 4.0 GPa and 450°C. Since this alloy did not decompose to the elements during the heating-pressure cycle, Jayaraman et al. concluded that cerium remains in its trivalent state under the above conditions.

2.15.4. *Metastable solid solutions*

Wang (1976) investigated phase stability of intra rare earth alloys by splat-cooling of hcp solid solutions, which contained elements with both hcp and bcc allotropic forms, including alloys in the Ce–Gd system. Wang found that, through splat-cooling, the hcp-phase field was extended into the composition range that, under equilibrium conditions, should have the Sm-type structure. The latter structure was not suppressed by the hcp phase but was pushed toward higher concentrations of cerium. He observed that extension of the hcp-phase field is limited by a c/a ratio of about 1.597.

References

Burov, I.V., V.F. Terekhova and E.M. Savitskii, 1963, Zh. Neorg. Khim. **8**, 2685 [English transl.: Russ. J. Inorg. Chem. **8**, 1408].

Burov, I.V., V.I. Cherchernikov, E.M. Savitskii and P. Iuliu, 1964, Zh. Neorg. Khim. **9**, 2594 [English transl.: Russ. J. Inorg. Chem. **9**, 1401].

Gschneidner, K.A. Jr., R.O. Elliott and M.Y. Prince, 1962, in: Nachman, J.F. and C.E. Lundin, eds., Rare Earth Research (Gordon and Breach, New York) p. 71.

Harris, I.R., C.C. Koch and G.V. Raynor, 1966, J. Less-Common Met. **11**, 436.

Harris, I.R., C.C. Koch and G.V. Raynor, 1967, J. Less-Common Met. **12**, 239.

Jayaraman, A., R.C. Sherwood, H.J. Williams and E. Corenzwit, 1966, Phys. Rev. **148**, 502.

Koch, C.C., P.G. Mardon and C.J. McHargue, 1971, Metall. Trans. **2**, 1095.

Lundin, C.E., 1966, Denver Research Institute Final Rept., AD-633558 University of Denver, Denver, CO (also given as DRI-2326).

Speight, J.D., 1970, J. Less-Common Met. **20**, 251.

Terekhova, V.F., 1963, Metalloved. Term. Obrab. Met. [8], 47 [English transl.: Met. Sci. Heat Treat. [8], 465].

Wang, R., 1976, Mater. Sci. Eng. **23**, 135.

2.16. *Ce–Tb: Cerium–terbium*

2.16.1. *Lattice spacings*

Lattice spacings for alloys in the cerium–terbium system have been reported by Speight et al. (1968). Gschneidner et al. (1962) measured lattice spacings of several cerium-rich binary alloys with the other rare earth metals and reported the a spacing for the Ce–2 at% Tb alloy. There is no report on the purity of the metals used in the

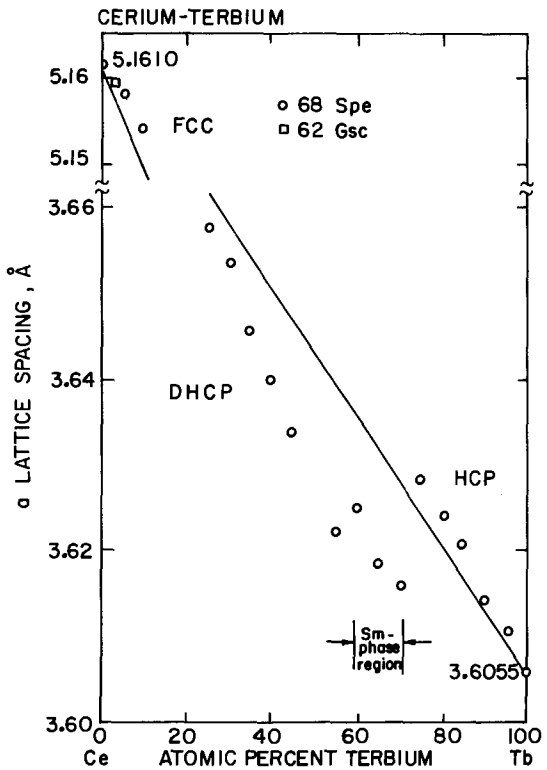

Fig. 30. *a* lattice spacings of alloys in the cerium–terbium system. The straight lines indicate the Vegard's law relationships calculated from the data given in table 2.

latter research. The experimental details are given in section 2.2.2. Speight et al. used terbium containing about 200 ppm of the common metals and less than 1000 ppm of other rare earth metals. Their cerium metal had no more than 100 ppm of other rare earth metals. Lattice spacings were determined by X-ray diffraction techniques and a Nelson–Riley extrapolation was used to eliminate systematic errors. The lattice spacing data reported by Speight et al. and by Gschneidner et al. are presented in figs. 30 and 31 for the *a* and *c* spacings, respectively.

In the cerium-rich fcc region, all data points show a positive deviation from the Vegard's law line. At somewhat higher terbium content where the structure is dhcp (from about 25 to 55 at% Tb), all data points show a negative deviation that increases as the terbium content increases. The negative deviation from ideality continues in the Sm-phase region (up to about 70 at% Tb), but in the hcp region (75 at% Tb and higher) a small positive deviation exists. The *c* lattice spacing data show positive deviations in all three of the noncubic phase regions.

References

Gschneidner, K.A., Jr., R.O. Elliott and M.Y. Prince, 1962, in: Nachman, J.F. and C.E. Lundin, eds., Rare Earth Research (Gordon and Breach, New York) p. 71.

Speight, J.D., I.R. Harris and G.V. Raynor, 1968, J. Less-Common Met. **15**, 317.

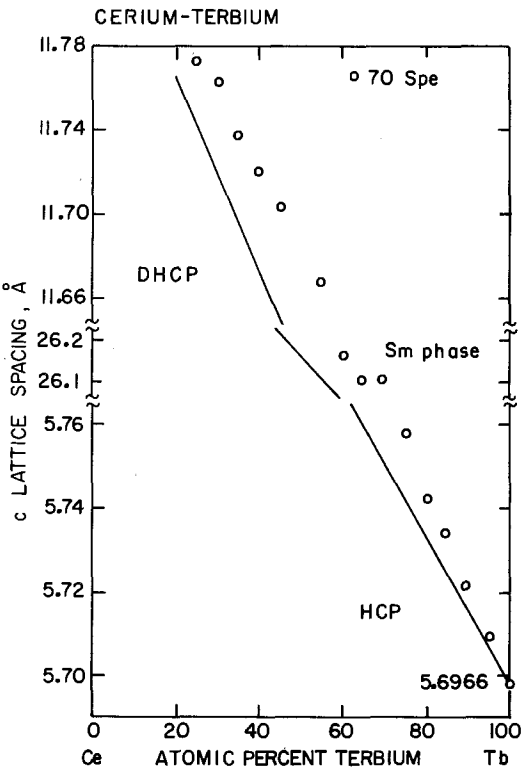

Fig. 31. *c* lattice spacings of alloys in the cerium–terbium system. The straight lines indicate the Vegard's law relationships calculated from the data given in table 2.

2.17. *Ce–Dy: Cerium–dysprosium*

2.17.1. *Lattice spacings*

Gschneidner et al. (1962) have measured lattice spacings of several cerium–dysprosium alloys in the cerium-rich portion of the system. The experimental details are given in section 2.2.2. Alloys containing up to 3 at% Dy, when quenched from 450°C, had face-centered cubic structure and their lattice spacings showed a positive

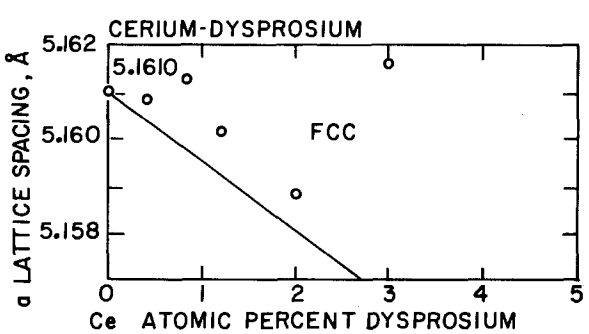

Fig. 32. Lattice spacings in the cerium-rich region of the cerium–dysprosium system. The solid line represents Vegard's linear approximation as calculated from the data given in table 2.

deviation from Vegard's linear approximation. Their data, as presented in fig. 32, have been adjusted by the addition of a small uniform increment to each point to bring the lattice spacing for pure γCe to 5.1610 Å, the accepted value listed in table 2 (see section 1.2).

Reference

Gschneidner, K.A., Jr., R.O. Elliott and M.Y. Prince, 1962, in: Nachman, J.F. and C.E. Lundin, eds., Rare Earth Research (Gordon and Breach, New York) p. 71.

2.18. *Ce–Ho: Cerium–holmium*

2.18.1. *Lattice spacings*

Lundin (1966) studied nine compositions in the cerium–holmium alloy system and reported lattice spacings for four of his alloys. He used 99.9 wt% pure cerium (principal impurities were C, O, Fe, Al, Si, Cu, Mo and W) and 99.9 + wt% pure holmium (principal impurities were O, Zn, Ca and other rare earths) in the preparation of his alloys, which were melted under purified argon in a nonconsumable electrode arc furnace, then homogenized at 650°C for 32 hr followed by rapid cooling. Jayaraman et al. (1966) also reported lattice spacings for a δ phase

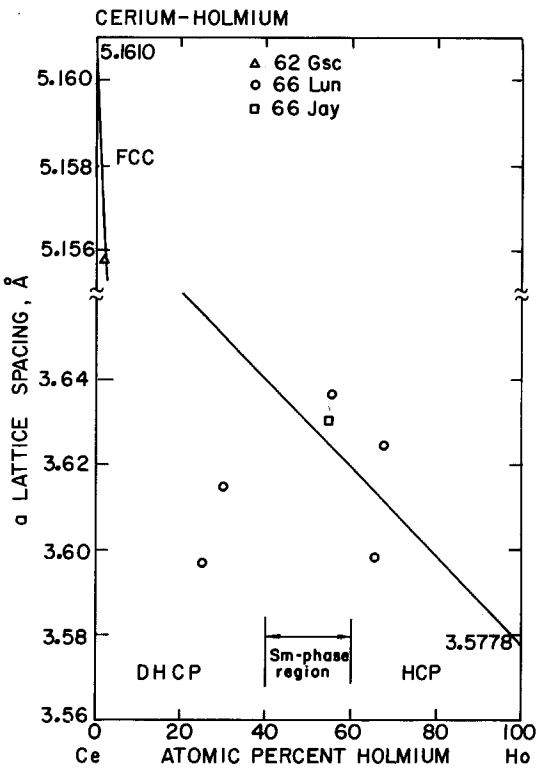

Fig. 33. *a* lattice spacings in the cerium–holmium system. The straight lines are the Vegard's law relationships based on the accepted values for the pure metals as shown in table 2.

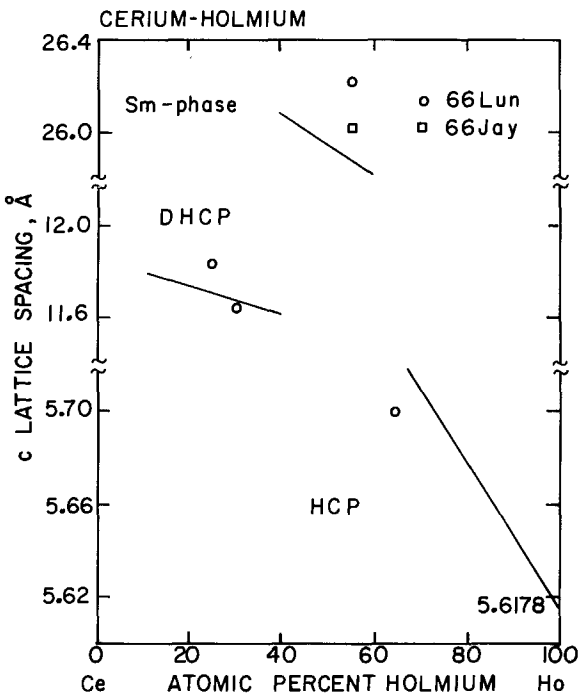

Fig. 34. *c* lattice spacings in the cerium–holmium system. The straight lines are the Vegard's law relationships for each phase region based on the accepted values for the pure metals as shown in table 2.

Ce–55 at% Ho specimen under ambient conditions and under pressure, see section 2.18.2. Gschneidner et al. (1962) reported on a specimen in the face-centered cubic cerium-rich region. The data from the above sources are plotted in figs. 33 and 34 for the *a* and *c* lattice spacings, respectively. The one datum point for *a* spacings in the fcc region falls on the Vegard's law line. The number of data points in the other phase regions is also small. A positive deviation from the Vegard's law line is observed in the δ-phase region for the Ce–55 at% Ho alloys as determined by Lundin and by Jayaraman et al. The values in both the hcp and dhcp regions show a negative deviation for the *a* spacings. The *c* spacings for both δ-phase specimens likewise show a positive deviation from the Vegard's law line. In the hcp region, the one specimen reported has a negative deviation, but in the dhcp region one specimen had a positive deviation while the other fell just below this line. Lundin did not attempt to present a phase diagram for this system but reported that the compositional range for the δ phase lies between 45 and 60 at% Ce, with 100% δ-phase structure existing at 55 at% Ce.

2.18.2. *Phase relationships as a function of pressure*

Jayaraman et al. (1966) included a Ce–55 at% Ho alloy in a study of the effects of pressure and temperature (4.0 GPa, 450°C) on the structure of several rare earth binary alloys. The Ce–55 at% Ho alloy, which under ambient conditions has the Sm-type structure, transformed under the conditions of this experiment to the dhcp structure.

References

Gschneidner, K.A., Jr., R.O. Elliott and M.Y. Prince, 1962, in: Nachman, J.F. and C.E. Lundin, eds., Rare Earth Research (Gordon and Breach, New York) p. 71.

Jayaraman, A., R.C. Sherwood, H.J. Williams and E. Corenzwit, 1966, Phys. Rev. **148**, 502.

Lundin, C.E., 1966, Final Report, Denver Research Institute Rept. AD-633558, University of Denver, Denver, CO (also given as DRI-2326).

2.19. *Ce–Er: Cerium–erbium*

2.19.1. *Lattice spacings*

The lattice spacing of a 2 at% Er–Ce alloy has been reported by Gschneidner et al. (1962). Information on the purity of their materials is not available. The experimental procedures are summarized in section 2.2.2. Lattice spacings for the erbium-rich portion of the cerium–erbium system have been measured by Norman et al. (1967). Their alloys were made from metals that contained less than 100 ppm (by wt?) of other rare earths with approximately 200 ppm of the common metals impurities. No information regarding nonmetallic impurities was given.

The above data are presented in figs. 35 and 36, which show the *a* and *c* spacings, respectively. In fig. 35, the one datum for the *a* spacings in the fcc region falls

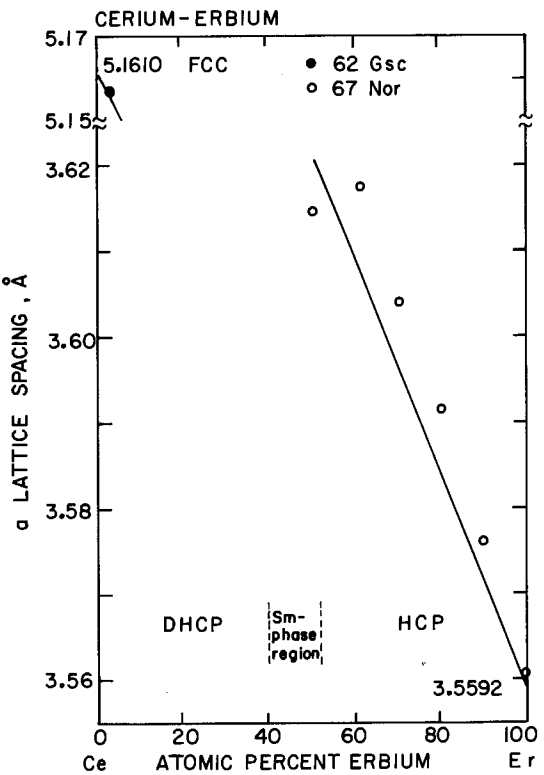

Fig. 35. *a* lattice spacings in the cerium–erbium system. The straight lines show the Vegard's law relationships based on the accepted values for the pure metals listed in table 2.

directly on the Vegard's law line. There are no available data for spacings in the dhcp-phase region and only one set of lattice spacings (a and c) in the δ-phase region. The room temperature composition range of the δ-phase (Sm-type) phase was not defined by this study. However, Harris and Raynor (1969) have noted a correlation between phase structures and the mean atomic number (Z_m) of an alloy in an intra rare earth binary system. According to their observations, the Sm-type structure is expected to form in this system between 40 and 50 at% Er; and indeed, their alloy, which contains about 50 at% Er, does have this structure (Norman et al., 1967). This one alloy exhibits a negative deviation from Vegard's law behavior in the a lattice spacing and a large positive deviation in the c spacing. The a spacings for alloys in the hcp region exhibit a positive deviation from ideality that decreases as the cerium content decreases (fig. 35). The c spacings in the hcp range are close to ideality with a slight negative deviation as the cerium content increases (fig. 36).

References

Gschneidner, K.A. Jr., R.O. Elliott and M.Y. Prince, 1962, in: Nachman, J.F. and C.E. Lundin, eds., Rare Earth Research (Gordon and Breach, New York) p. 71.

Harris, I.R. and G.V. Raynor, 1969, J. Less-Common Met. **17**, 336.

Norman, M., I.R. Harris and G.V. Raynor, 1967, J. Less-Common Met. **13**, 24.

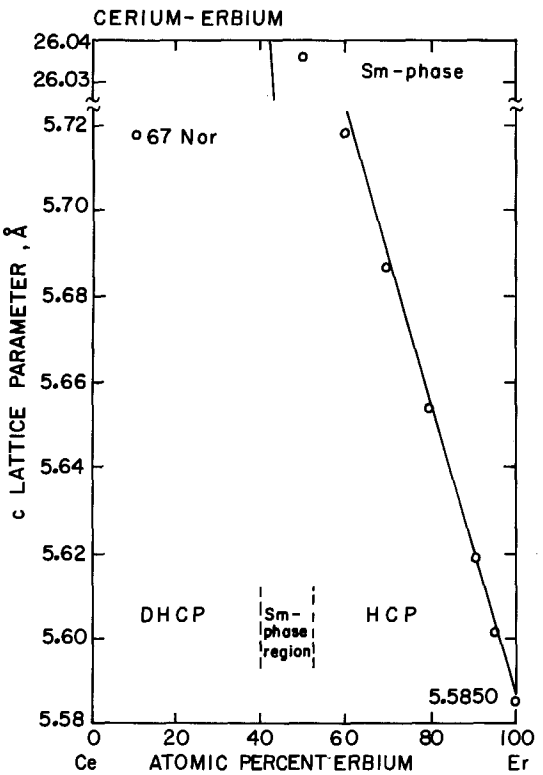

Fig. 36. c lattice spacings in the cerium–erbium system. The straight lines show the Vegard's law relationships based on the accepted values for the pure metals listed in table 2.

2.20. *Ce–Tm: Cerium–thulium*

2.20.1. *Lattice spacing*

In their study of lattice spacings of cerium-rich alloys, Gschneidner et al. (1962) list the lattice spacing ($a = 5.1575$ Å) for a Ce–2 at% Tm alloy. The a value for this alloy exhibits a positive deviation from the Vegard's law line.

Reference

Gschneidner, K.A. Jr., R.O. Elliott and M.Y. Prince, 1962, in: Nachman, J.F. and C.E. Lundin, eds., Rare Earth Research (Gordon and Breach, New York) p. 71.

2.21. *Ce–Yb: Cerium–ytterbium*

2.21.1. *Phase relationships*

Spedding and Daane (1961) have reported that a 50% alloy of ytterbium in cerium was observed to contain two immiscible liquids. An X-ray study of these phases indicated a solubility of ~ 1 at% Ce in Yb and ~ 3 at% Yb in Ce. King (1969) studied electrical resistance of ytterbium-rich alloys of the cerium–ytterbium phase diagram and observed that an addition of 10 at% cerium moved the resistance peak in pure ytterbium from 3.937 to ~ 5.27 GPa at room temperature.

References

King, E., 1969, Atomic Energy Research Establishment Rept. AERE – R5954, Harwell.
Spedding, F.H. and A.H. Daane, 1961, Ames Laboratory Rept. IS-350, Iowa State University, Ames, IA, p. 27.

2.22. *Ce–Lu: Cerium–lutetium*

2.22.1. *Lattice spacings*

Lattice spacings for several cerium–lutetium alloys containing up to 4 at% Lu have been determined by Gschneidner et al. (1962). The experimental details are summarized in section 2.2.2. They also observed that a Ce–10 at% Lu alloy, quenched from 450°C, contained both the γCe (fcc) and the βCe (dhcp) phases whereas a Ce–20 at% Lu alloy contained only the β phase. No lattice spacings were reported for the 10 and 20 at% Lu alloys. Harris and Raynor (1969) reported lattice spacings for lutetium metal and for a Ce–92.3 at% Lu alloy (both hcp phase). Both the a and c lattice spacings for their lutetium metal are higher than the accepted values listed in table 2. This would seem to indicate some contamination of their metal, probably by hydrogen (see section 1.2.2). Both sets of data are plotted in fig. 37. All of the data as plotted have been adjusted by a small increment so that the spacings for the pure metals would agree with the accepted lattice spacing values. The cerium-rich

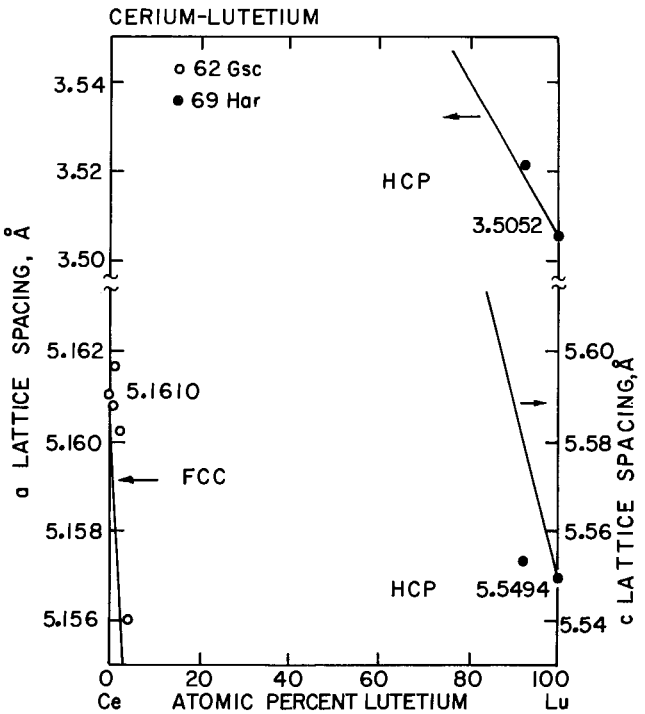

Fig. 37. Lattice spacings in the cerium–lutetium alloy system. The straight lines represent the Vegard's law relationships in the various phase regions based on the accepted parameters listed in table 2.

alloys show a positive deviation from the Vegard's law. The lutetium-rich alloy had a large negative deviation in the *c* spacing but was close to ideality in the *a* spacing.

References

Gschneidner, K.A., Jr., R.O. Elliott and M.Y. Prince, 1962, in: Nachman, J.F. and C.E. Lundin, eds., Rare Earth Research (Gordon and Breach, New York) p. 71.
Harris, I.R. and G.V. Raynor, 1969, J. Less-Common Met. **17**, 336.

2.23. *Ce–Sc: Cerium–scandium*

2.23.1. *Phase diagram*

A phase diagram for the cerium–scandium system has been reported by Naumkin et al. (1964). Distilled scandium of 99.5(wt?)% purity (major impurities: 0.2% O, 0.15% Cu, 0.06% Fe, 0.03% N, 0.1% Ti, 0.01% each Al, H, Ca) and 99.5% cerium (major impurities: 0.02% each C and Ca and 0.01% each Ta and Fe) were used to prepare the alloys. The alloys were prepared in an arc furnace under helium, remelted three times, then annealed 240 hr at 500°C in vacuum. The phase diagram

was determined by means of thermal analysis, X-ray diffraction, metallography, hardness and density measurements. Cerium and scandium were found to be miscible in the liquid state over the entire composition range, and a continuous region of high temperature solid solutions (bcc) extended from pure cerium to pure scandium (see fig. 38). At about 680°C, this high temperature solid solution was observed to decompose eutectoidally to γCe (fcc) and αSc (hcp) solid solutions. They stated that the room temperature solid solubility limit of scandium in cerium is about 17 at% Sc and that of cerium in scandium is about 12 at% Ce. X-ray diffraction analysis of alloys in the two-phase region revealed that all lines that occur can be accounted for as belonging to either γCe or αSc and no Sm-type structure exists in this system. Naumkin et al. state that the addition of scandium to cerium broadens the γCe (fcc) region and narrows the βCe (dhcp) region, which was not shown on their phase diagram. The melting points and transformation temperatures of the pure metals have been adjusted to conform with the accepted values listed in table 1.

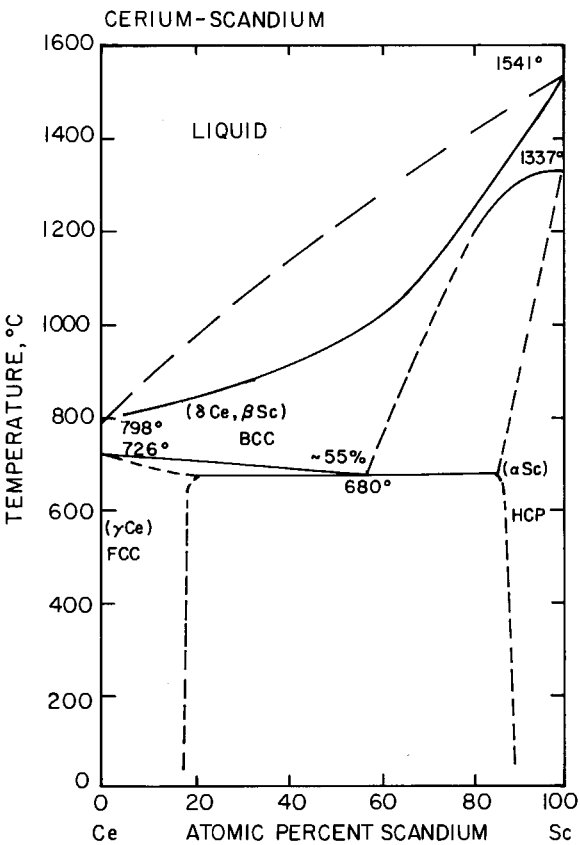

Fig. 38. Phase diagram of the cerium–scandium system.

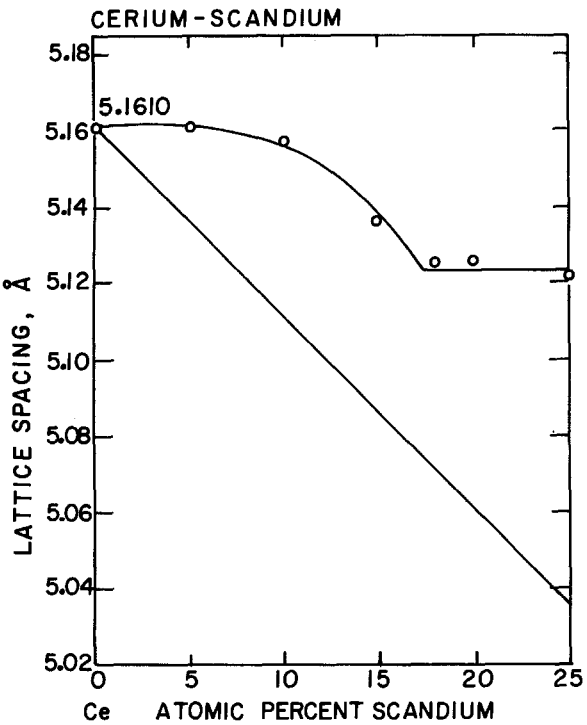

Fig. 39. Lattice spacings in the cerium–rich end of the cerium–scandium system. The straight line indicates the Vegard's law relationship for this system based on the accepted values for the pure metals as listed in table 2.

2.23.2. *Lattice spacings*

Figure 39 is a plot of lattice spacing data for the cerium-rich portion of the cerium–scandium system as reported by Gschneidner et al. (1962). The experimental details are given in section 2.2.2. They found the solubility limit for scandium in cerium to be 17.2 at% Sc at 450°C. The second phase present in alloys containing more than 17.2 at% Sc is hcp scandium. They observed that cerium alloys that contain more than 18 at% Sc do not oxidize on exposure to the atmosphere at 23°C.

References

Gschneidner, K.A., Jr., R.O. Elliott and M.Y. Prince, 1962, in: Nachman, J.F. and C.E. Lundin, eds., Rare Earth Research (Gordon and Breach, New York) p. 71.

Naumkin, O.P., V.F. Terekhova and E.M. Savitskii, 1964, Zh., Neorg. Khim. **9**, 2497 [English transl.: Russ. J. Inorg. Chem. **9**, 1347].

2.24. *Ce–Y: Cerium–yttrium*

2.24.1. *Phase diagram*

The cerium–yttrium system as reported by Lundin and Klodt (1958) showed the intermediate Sm-type phase to be formed by a peritectoid reaction. Later, a systematic study of the formation of the Sm-type structure by Lundin (1966) and by Nachman et al. (1963), using metallographic, X-ray diffraction, thermal, dilatomet-

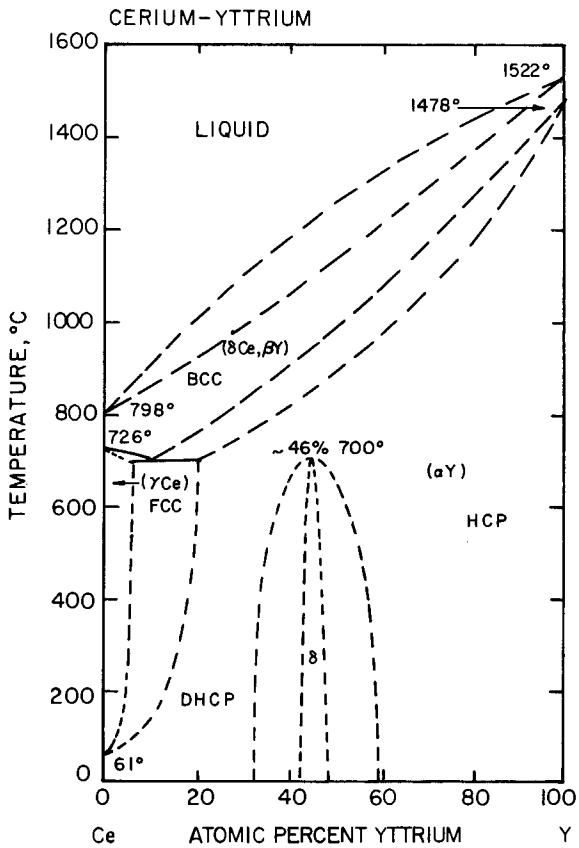

Fig. 40. Phase diagram of the cerium–yttrium system. The symbol "δ" used by itself refers to the Sm-type phase, while the bcc high temperature phase of cerium is defined as "δCe".

ric, calorimetric and microprobe studies, failed to confirm the assumed peritectoid reaction in any of 13 binary systems composed of a light and a heavy rare earth metal including the Ce–Y system, also see sections 2.1.3 and 2.1.4.

The equilibrium phase diagram for the cerium–yttrium system is presented in fig. 40. This diagram does not show a peritectoid reaction to form the Sm phase as did that of Lundin and Klodt. Instead, a congruent transformation is presented, based on the results of the investigations into the nature of the formation of the δ phase. The melting points and transformation temperatures of the pure metals have been adjusted to conform with the accepted data listed in table 1.

2.24.2. *Lattice spacings*

Lattice spacing data for the fcc cerium-rich portion of this system has been reported by Gschneidner et al. (1962) and by Harris et al. (1966). Several investigators have reported lattice spacings for the hexagonal portions of this system. No purities were listed by Gschneidner et al. but the experimental details were given and are summarized in section 2.2.2. Harris et al. (1966) reported that impurities in their

yttrium metal included < 0.10 wt% other rare earth metals, 0.1 wt% Ta and a total of 0.03 wt% common metals; their cerium contained < 0.01 wt% other rare earth metals and a total of 0.02 wt% common metals. Harris and Raynor (1964) used yttrium containing 0.03 wt% Fe and "negligible amounts" of metallic impurities. Nachman et al. (1963) used yttrium in which the impurities were: 2175 ppm O, 3000 ppm Zr, 330 ppm other rare earths, 200 ppm Si and 108 ppm Fe. Their cerium contained 500 ppm C, 220 ppm Fe and 140 ppm Al.

The *a* lattice spacing data for the cerium–yttrium system are shown in fig. 41. A positive deviation from Vegard's law is observed for the data in the fcc region. In the hcp region, all of the *a* lattice spacing data showed a strong positive deviation from the Vegard's law relationship. Nachman et al. reported that alloys having more than 65 at% Y had the αY (hcp) solid solution structure and alloys having 54 to 60 at% Y had both αY- and Sm-type structures. X-ray films of alloys having 30 to 40 at% Y could not be interpreted on the basis of only the Sm phase and βCe solid solution. Their alloy with 25 at% Y had the βCe structure. The alloys in the 54 to 60 at% Y composition range showed a positive deviation for the *a* lattice spacings of the hcp αY phase and negative deviations for the *a* spacings of the Sm phase. Two *a* spacing data points listed by Harris et al. for Sm-type structures fell almost on the Vegard's law line. The *a* spacing for 55.5 at% Y (Sm phase), which was listed by Spedding et

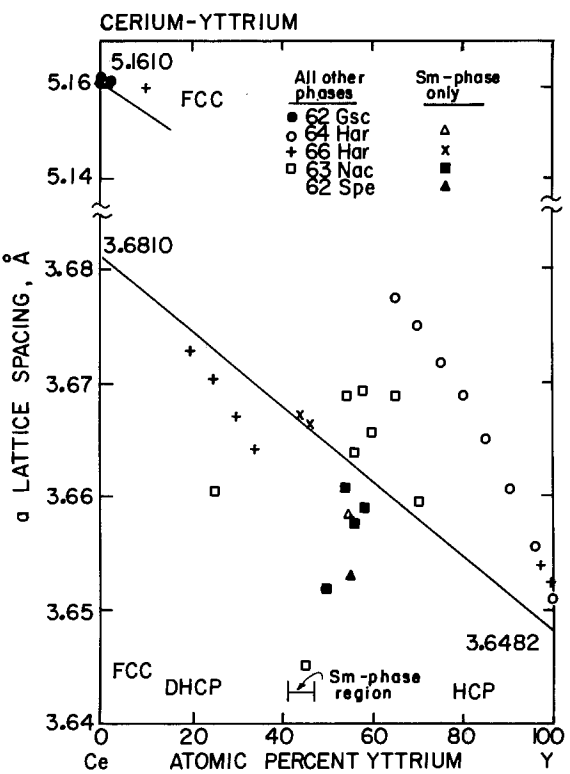

Fig. 41. *a* lattice spacings in the cerium–yttrium system. The straight lines show the Vegard's law relationships for the cubic and hexagonal structures in this system based on the accepted values for the pure metals as listed in table 2.

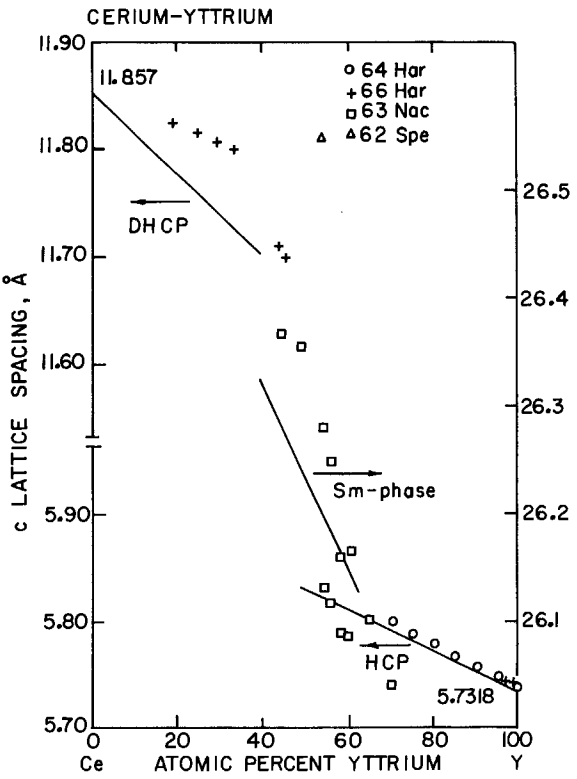

Fig. 42. *c* lattice spacings in the cerium–yttrium system. The straight lines show the Vegard's law relationships for the various structures as calculated from values for the pure metals as listed in table 2.

al. (1962), had a large negative deviation from ideality. All of the *a* lattice data for specimens with the dhcp structure showed negative deviations.

The *c* lattice spacings for the Ce–Y system are shown in fig. 42. In the three hexagonal phase regions, the data show a positive deviation from Vegard's law relationship with the exception of the three alloys of Nachman et al., two of which lie in the two-phase region where the αY solid solution was mixed with Sm-type structure. The observed negative deviation for these two-phase alloys with the hcp α-Y structure is expected. In the Sm-phase region, the 55.5 at% Y specimen reported by Spedding et al. had such a large positive deviation from ideality that, when plotted, it lies closer to the field of the dhcp data. The points for the hcp data lie quite close to the Vegard's law line.

2.24.3. *Effect of pressure on phase relationships*

Jayaraman et al. (1966) in a study of the effects of high pressure and temperature on binary cerium–rare earth alloys, tested three cerium–yttrium alloys that, under normal conditions, had the hcp: the Sm-type and the dhcp structures. Pressure-induced phase transformations in the sequence hcp → Sm type → dhcp → fcc were observed in several other intra rare earth alloy systems tested but in the Ce–Y

system: one composition, Ce–75 at% Y, retained the hcp structure at all pressures and the other two compositions, Ce–50 at% Y and Ce–25 at% Y, decomposed into two phases, γCe and αY. The decompositions were attributed to a change under temperature and pressure of normally trivalent cerium to tetravalent cerium with a subsequent reduction in metallic radius. The collapsed cerium atoms apparently diffused through the alloy under the influence of high temperature and formed pockets of αCe that reverted to γCe when the pressure was released.

2.24.4. *Metastable solid solutions*

Wang (1976) splat-cooled samples from five intra rare earth alloy systems including Ce–Y. He found that by splat-cooling, the hcp phase was extended into the composition range that, under equilibrium conditions, should have the Sm-type structure. The Sm-type structure was not suppressed by the hcp phase but was pushed toward higher concentrations of cerium. Wang observed that the extension of the hcp-phase field was limited by a c/a ratio of about 1.597.

References

Gschneidner, K.A., Jr., R.O. Elliott and M.Y. Prince, 1962, in: Nachman, J.F. and C.E. Lundin, eds. Rare Earth Research (Gordon and Breach, New York) p. 71.

Harris, I.R. and G.V. Raynor, 1964, J. Less-Common Met. **7**, 1.

Harris, I.R., C.C. Koch and G.V. Raynor, 1966, J. Less-Common Met. **11**, 502.

Jayaraman, A., R.C. Sherwood, H.J. Williams and E. Corenzwit, 1966, Phys. Rev. **148**, 502.

Lundin, C.E., 1966, Final Report, Denver Research Institute Rept. AD-633558, University of Denver, Denver CO (also given as DRI-2326).

Lundin, C.E. and D.T. Klodt, 1958, APEX Rept. 424 (August 1958); XDC Rept. 59-8-187 (November 1958); XDC Rept. 59-8-188 (February 1959), Denver Research Institute, University of Denver, Denver, CO.

Nachman, J.F., C.E. Lundin and G.P. Rauscher, Jr., 1963, Denver Research Institute Rept., DRI-2080, University of Denver, Denver, CO.

Spedding, F.H., R.M. Valletta and A.H. Daane, 1962, Trans. Quarterly (Am. Soc. Met.) **55**, 483.

Wang, R., 1976, Mater. Sci. Eng. **23**, 135.

2.25. *Pr–Nd: Praseodymium–neodymium*

2.25.1. *Phase diagram*

The phase diagram for the praseodymium–neodymium system has been investigated by Markova et al. (1963) and by Lundin et al. (1964). Markova et al. used 97 (wt?)% pure praseodymium and 98% pure neodymium. The impurities present in their metals consisted of other rare earth metals, plus Cu, Fe and Ca in unspecified amounts. Their methods of investigation included thermal analysis, metallography, X-ray diffraction and hardness measurements. Their alloys were annealed at 600°C for 20 hr before measurements were made. Terekhova (1963) has published a similar phase diagram that would appear to be based on the same research. Both Russian diagrams show complete solid solubility for both the dhcp and the bcc structures and a definite two-phase region (liquid plus solid) between the liquidus and solidus lines.

Lundin et al. (1964) determined the phase diagram for this system using metallography, thermal analysis, X-ray diffraction and density measurements. The total content of other rare earths in their starting metals did not exceed 0.16 wt%. Impurities reported in their praseodymium were: 65 ppm C, 50 ppm N, 27 ppm F, < 0.02% Ca, < 0.025% Si, < 0.01% Mg and ~ 0.05% Ta. Impurities in their neodymium included: 62 ppm C, 39 ppm N, 200 ppm F, 0.01% Fe, < 0.03% Ca, < 0.025% Si, < 0.01% Mg, and 0.05% Ta. Alloys were arc-melted under purified argon and remelted four times to improve the homogeneity. Care was taken in the preparation of metallographic specimens to avoid reaction products and disturbed metal. Screened filings for X-ray diffraction studies were annealed to relieve cold-working. Densities were determined by displacement in monobromobenzene as well as by calculation from lattice parameters.

The phase diagram for the praseodymium–neodymium system is shown in fig. 43. The equilibrium diagram as presented by Lundin et al. showed a narrow two-phase region between the liquidus and solidus lines and also between the $\alpha \rightleftarrows \beta$ transformation lines. Their diagram showed complete solubility for both the dhcp and the bcc allotropes. Since praseodymium and neodymium are both trivalent, have adjacent atomic numbers and exhibit a continuous series of solid solutions, the liquidus and solidus in fig. 43, and the heating and cooling solvus lines of the dhcp $\rightleftarrows$ bcc transition, respectively, were drawn as a single straight line connecting the two melting points or the two transformation points of praseodymium and neodymium

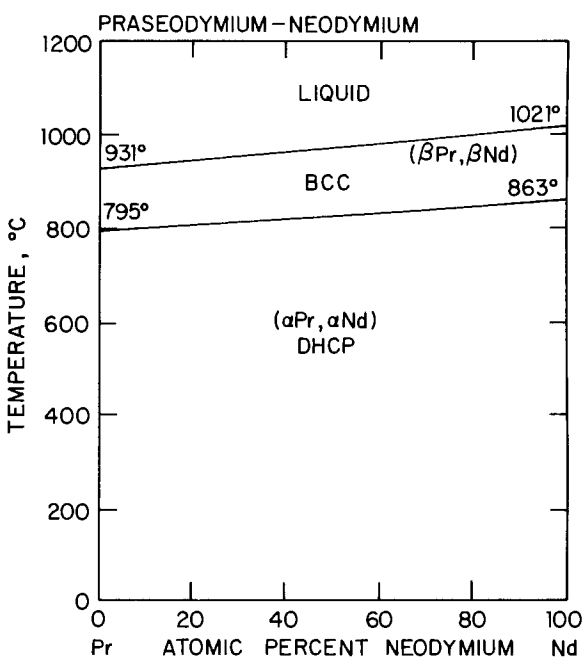

Fig. 43. Phase diagram of the praseodymium–neodymium system.

(see section 2.1.1). In addition, the melting point temperatures and the transformation temperatures of the pure metals have been adjusted to the accepted values listed in table 1.

In addition to the experimental determinations of the phase diagrams described above, Shiflet et al. (1979) calculated the phase diagram for the praseodymium–neodymium system using the differences in enthalpy and entropy between the different crystal structures in the pure elements and the regular solution constant for the enthalpy of mixing. The paths of two-phase fields that Shiflet et al. calculated for this diagram were in good agreement with those determined experimentally by Markova et al. and by Lundin et al., but the widths of those fields were appreciably smaller than those experimentally observed. These wide two-phase fields would be expected to occur because of impurities present in metals used in the experimental research (see section 2.1.1).

2.25.2. *Lattice spacings*

Lundin et al. (1964) determined lattice spacings of their pure metals and of a series of alloys. Since the *a* and the *c* spacings of their pure metals differ slightly from the accepted values for these spacings (see table 2), adjustments have been made in the spacing data of the alloys on the basis of the observed differences in the

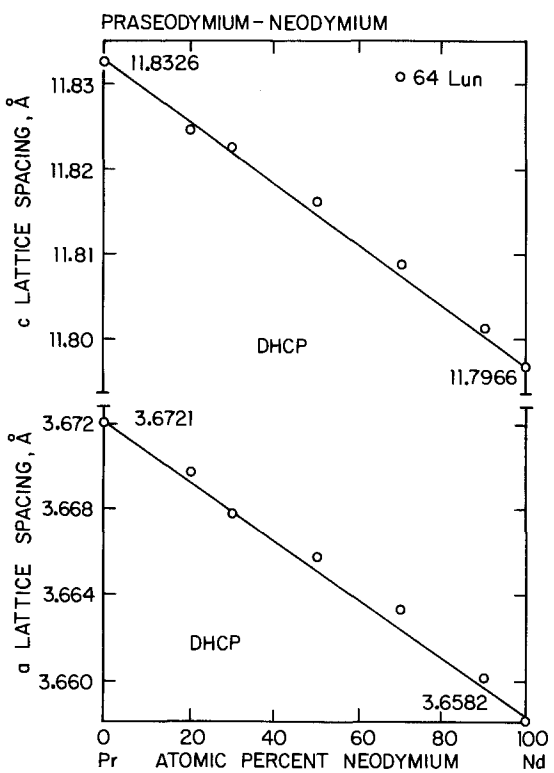

Fig. 44. Lattice spacings in the praseodymium–neodymium system. The straight lines represent the Vegard's law relationships based on the accepted data for the pure metals as shown in table 2.

spacings for the pure metals and the mole fraction of each component in the alloy. These adjusted values for the *a* and *c* lattice spacings are plotted in fig. 44. These investigators also measured density of the various alloys by displacement in monobromobenzene and found excellent agreement with densities determined by calculations using their lattice spacings. Their density vs. composition plot was linear, another evidence of ideality that is unusual in binary metal systems.

2.25.3. *Thermodynamic properties*

Lundin et al. (1965) measured the thermodynamic activities at 1475, 1500 and 1525°C of liquid solutions of praseodymium–neodymium. Vapors from eight alloys were condensed and the compositions were determined by X-ray spectrographic analysis and from these data the activity of each component was calculated. Figure 45 is a plot of the activity of liquid praseodymium and of liquid neodymium as a function of the neodymium concentration in the liquid state at 1500°C. The activities vs. composition at the other two temperatures are similar to the results obtained at 1500°C. The linear relationship observed in the plot indicates that the solutions are essentially ideal since the activity is equal to the mole fraction.

References

Lundin, C.E., J.F. Nachman and A.S. Yamamoto, 1964, in: Vorres, K.S., ed., Rare Earth Research II (Gordon and Breach, New York) p. 315.

Lundin, C.E., A.S. Yamamoto and J.F. Nachman, 1965, Acta Metall. **13**, 149.

Markova, I.A., V.F. Terekhova and E.M. Savitskii, 1963, Zh. Neorg. Khim. **8**, 1998 [English transl.: Russ. J. Inorg. Chem. **8**, 1041].

Shiflet, G.J., J.K. Lee and H.I. Aaronson, 1979, Calphad **3**, 129.

Terekhova, V.F., 1963, Metalloved. Term. Obrab. Met. [8], 47 [English transl.: Met. Sci. Heat Treat. [8], 465].

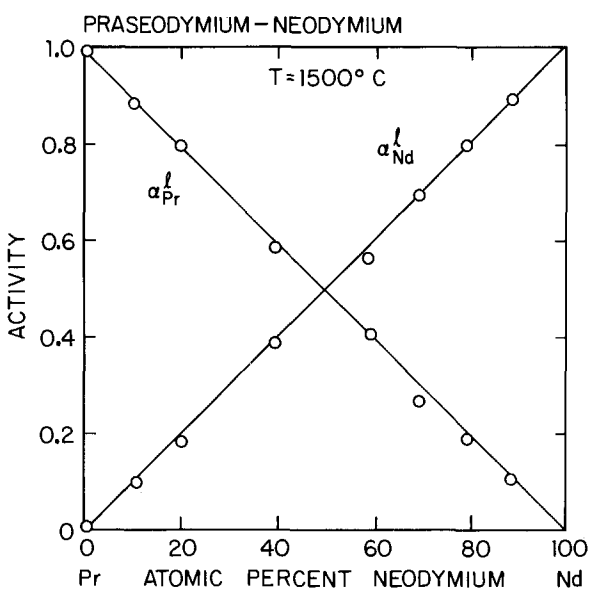

Fig. 45. Activities of praseodymium and neodymium in liquid Pr–Nd alloys at 1500°C. Essentially identical results were obtained at 1475 and 1525°C.

2.26. *Pr–Gd: Praseodymium–gadolinium*

2.26.1. *Lattice spacings*

Harris et al. (1966) measured lattice spacings for a selection of alloys that included several compositions in the Pr–Gd system. The impurities in their praseodymium–gadolinium were each given as < 0.01 wt% other rare earth metals, 0.10 wt% Ta, and other common metals 0.02 wt%. Alloys were arc-melted under an argon atmosphere, then homogenized 14 days at 600 to 1000°C and quenched. Filings were stress-relieved prior to X-ray diffraction analysis and systematic errors in their X-ray data were eliminated by use of the Nelson–Riley extrapolation function. Tissot and Blaise (1970) also studied magnetic and crystallographic properties of alloys in the Pr–Gd system. They melted nine compositions of "specpure" elements under helium in an induction furnace followed by quenching. Traces of Fe and Mn (100 ppm) were detected in their ingots. X-ray diffraction measurements were performed on the surface of their ingots (heat treatment details were not published). Speight (1970) also reported the *a* and *c* lattice spacings of one composition in this system. He prepared his alloys by induction melting 99.9% pure metals under an argon atmosphere, then homogenizing at 600°C for four days and quenching.

The *a* lattice spacings for praseodymium–gadolinium alloys are presented in fig. 46 and the *c* lattice spacings in fig. 47. In the dhcp region (0 to ~ 50 at% Gd), the *a*

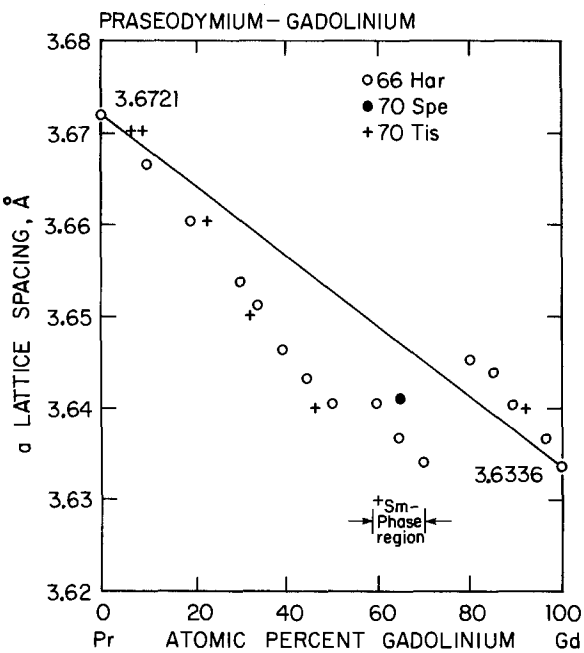

Fig. 46. *a* lattice spacings in the praseodymium–gadolinium system. The straight line connecting the end-members is the Vegard's law relationship based on the accepted values of the pure metals listed in table 2.

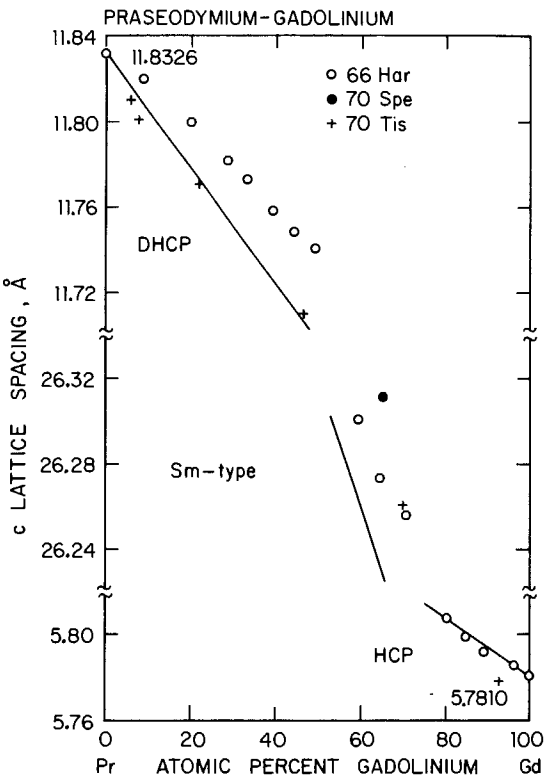

Fig. 47. *c* lattice spacings in the praseodymium–gadolinium system. The straight lines represent the Vegard's law relationships for each structure region and are based on the accepted values for the pure metals as listed in table 2.

spacings exhibit a negative deviation from Vegard's Law and the *c* spacings a positive deviation. Two of the *a* spacings presented by Tissot and Blaise, at compositions less than 10 at% Gd, exhibit the opposite behavior, having a small positive deviation, and their *c* lattice spacings for the same alloys in the dhcp region fall below the Vegard's law line, which is again the opposite observed for the majority of points. In the Sm-type phase region (~ 60 to 70 at% Gd), the *a* spacings exhibit a large negative deviation while the *c* spacings have a large positive deviation from the Vegard's law relationship. In contrast to this behavior the *a* spacings show a positive deviation from the Vegard's law relationship for all specimens having the hcp structure (~ 80 to 100 at% Pr), and the *c* spacings fall close to the Vegard's law line.

Harris et al. stated that the Sm-type phase occurs between 59.8 and 70.1 at% Gd. Their alloys with compositions 55.0 and 74.8 at% Gd were reported to be mixtures of dhcp with Sm-type and Sm-type with hcp, respectively, and no lattice spacings were reported for these compositions. However, Tissot and Blaise reported the Sm-phase structure for an alloy of 70.5 at% Gd but found the X-ray patterns for the 63.8 and 80.4 at% Gd alloys to be too complex to index.

2.26.2. *Metastable solid solutions*

Wang (1976) splat-cooled Pr–Gd alloys that had compositions normally in the hcp-phase field. By splat-cooling, the hcp-phase field was extended into the composition range that under equilibrium conditions would have the Sm-type structure. The Sm-type structure was not suppressed but the hcp phase was extended to higher Pr concentrations. Wang found that the extension of the hcp-phase field was limited by a c/a ratio of about 1.597.

2.26.3. *Thermodynamic properties*

Dreyfus et al. (1963) measured the heat capacity of a Pr–73 at% Gd alloy from 1.4 to 4 K. Their data were fitted to the following equation:

$$C = AT^{-2} + \gamma T + \beta T^3,$$

where the first term is the nuclear contribution, the second term is the electronic contribution and the third term is the lattice contribution to the heat capacity. The values obtained for the constants are: $A = 228 \pm 2.2$ mJ K/mol, $\gamma = 26.3 \pm 0.6$ mJ/mol K^2 and $\beta = 1.16 \pm 0.06$ mJ/mol K^4.

References

Dreyfus, B., A. Lacaze and J.C. Michel, 1963, Compt. Rend. **257**, 3355.
Harris, I.R., C.C. Koch and G.V. Raynor, 1966, J. Less-Common Met. **11**, 436.
Speight, J.D., 1970, J. Less-Common Met. **20**, 251.
Tissot, L. and A. Blaise, 1970, J. Appl. Phys. **41**, 1180.
Wang, R., 1976, Mater. Sci. Eng. **23**, 135.

2.27. *Pr–Tb: Praseodymium–terbium*

2.27.1. *Lattice spacings*

Lattice spacings in the praseodymium–terbium system have been determined by Speight et al. (1968). The praseodymium and terbium metals from which their specimens were prepared contained approximately 0.02 wt% of common metals and less than 0.10 wt% of other rare earth metals. Weighed amounts of the constituent metals were melted under a purified argon atmosphere in a nonconsumable electrode arc furnace. Alloys were homogenized at 700 to 1000°C for two weeks and rapidly quenched. Filings for X-ray analysis were annealed to relieve stresses. Systematic errors were eliminated by use of the Nelson–Riley extrapolation function.

The lattice spacings for the pure metals observed by Speight et al. vary slightly from the accepted values for these metals as listed in table 2 (section 1.2.1). The lattice spacings of the alloys have been adjusted by prorating the variations from the spacings of the pure metals on the basis of mole fraction of each constituent in the alloy. These adjusted data are plotted in figs. 48 and 49 showing a and c lattice

spacings, respectively. In the praseodymium-rich region (up to about 40 at% Tb), the *a* lattice spacings for the dhcp phase show a negative deviation from the Vegard's law relationship while the *c* lattice spacings for this phase exhibit a positive deviation. Likewise in the Sm-type region, the *a* spacings exhibit a negative deviation and the *c* spacings a positive deviation. In the terbium-rich region (from 75 to 100 at% Tb) the *a* spacings for the hcp phase show a positive deviation from Vegard's law while the *c* spacings lay almost directly on the Vegard's law line.

According to Achiwa and Kawano (1972, 1973), a Pr–80 at% Tb alloy had Sm-type structure. This does not agree with the work of Speight et al. (1968) nor does it agree with the criteria proposed by Harris and Raynor (1969) for the prediction of the crystal structure of an alloy based on the mean atomic number. On the basis of the Harris–Raynor method the Sm-type structure in the Pr–Tb system would be expected to exist between 50 and 66.5 at% Tb (range of mean atomic numbers from about 62 to 63).

References

Achiwa, N. and S. Kawano, 1972, Acta Crystallogr. **28A**, 599.
Achiwa, N. and S. Kawano, 1973, J. Phys. Soc. Jpn. **35**, 303.
Harris, I.R. and G.V. Raynor, 1969, J. Less-Common Met. **17**, 336.
Sleight, J.D., I.R. Harris and G.V. Raynor, 1968, J. Less-Common Met. **15**, 317.

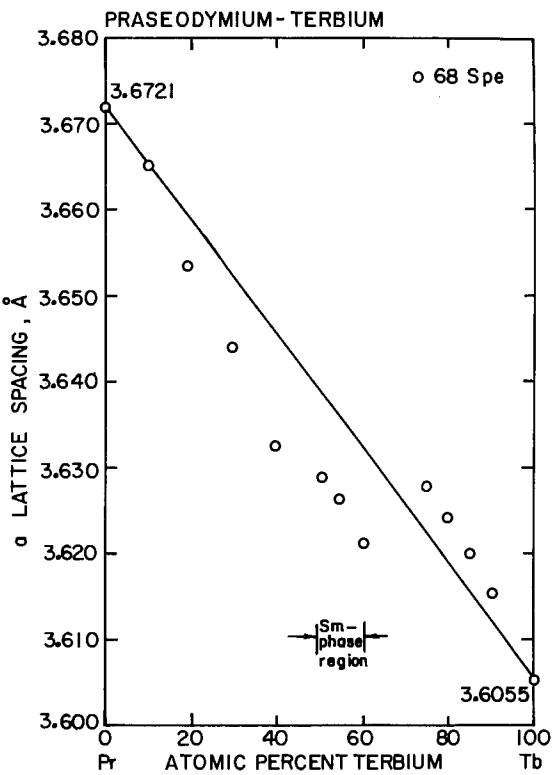

Fig. 48. *a* lattice spacings in the praseodymium–terbium system. The straight line represents the Vegard's law relationship based on the accepted values for the pure metals as listed in table 2.

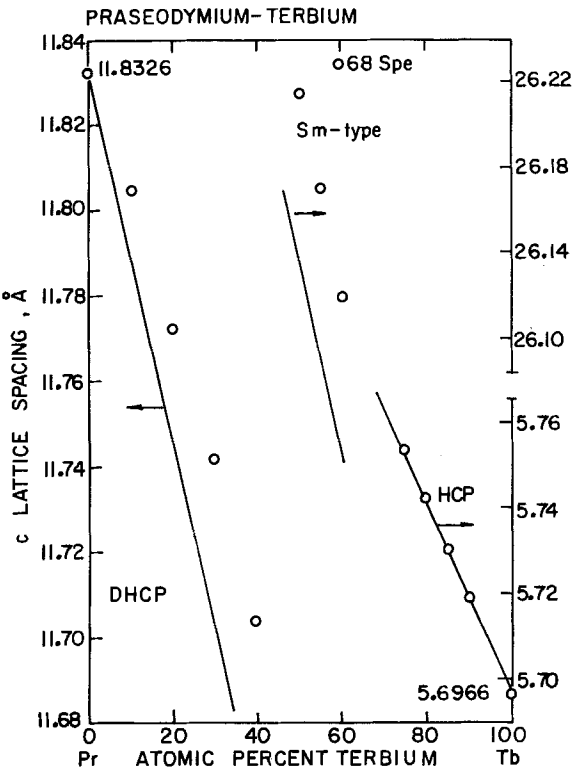

Fig. 49. *c* lattice spacings in the praseodymium–terbium system. The straight lines in each phase region represent the Vegard's law relationships based on the accepted values for the pure metals as shown in table 2.

2.28. *Pr–Y: Praseodymium–yttrium*

2.28.1. *Lattice spacings*

Lattice spacings in the praseodymium–yttrium system have been measured by Harris et al. (1966). Their alloys were prepared from praseodymium and yttrium, which each contained less than 0.10 wt% other rare earth metals and 0.1 wt% Ta. Their praseodymium and yttrium contained 0.02 and 0.03 wt% total common metals, respectively. The weighed portions of the pure metals were arc-melted under purified argon, homogenized at 800°C and quenched. Filings for X-ray diffraction analysis were stress-relieved before exposure to Cu-, Co- or Cr-$K\alpha$ radiation. Systematic errors were eliminated by use of the Nelson–Riley extrapolation function.

Figures 50 and 51 are, respectively, the plots of the *a* and *c* spacing data for this system. Since the lattice spacing data of Harris et al. for the pure metals deviated from the accepted values listed in table 2, the lattice spacings for their alloys were adjusted before plotting by prorating the deviations in the lattice spacings for the pure metals on the basis of the molar composition of each alloy. A negative deviation from the Vegard's law relationship is observed in fig. 50 for all of the praseodymium-rich dhcp *a* lattice spacings. The yttrium-rich hcp alloys all show a

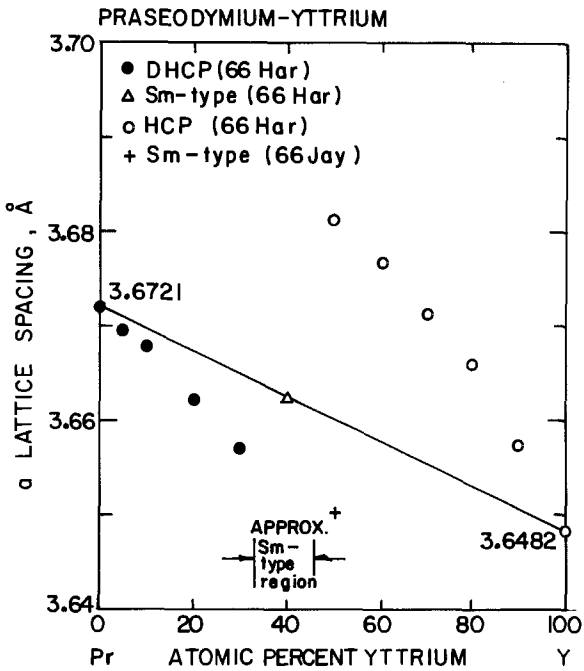

Fig. 50. *a* lattice spacings in the praseodymium–yttrium system. The straight line represents the Vegard's law relationship, based on the accepted values for the pure metals as listed in table 2.

large positive deviation in the *a* spacings. The alloy with an Sm-type structure which Harris et al. reported (45 at% Y) had an *a* spacing that followed Vegard's law. However, Jayaraman et al. (1966) reported that a PrY alloy (Pr–50 at% Y) normally had the Sm-type structure and listed an *a* lattice spacing with a large negative deviation from ideality. It must be noted that Harris et al. found hcp structure in an alloy of similar composition (49.8 at% Y); however, the difference in annealing temperatures (800°C for the Harris et al. alloy and 500°C for the Jayaraman et al. alloy) could account for this difference, since the Sm-type phase would be expected to exist over a wider composition range at lower temperatures.

In fig. 51, the *c* lattice spacings for the praseodymium-rich dhcp structure alloys (0 to 30 at% Y) have a positive deviation from Vegard's law that increases with the yttrium content. The yttrium-rich hcp alloys (50 to 100 at% Y) have a small barely noticeable positive deviation. The *c* lattice spacing for the Sm-type structure alloy that Harris et al. reported (40 at% Y) has a large positive deviation and lies so far from the Vegard's law line that it is difficult to relate it to the Vegard's law line. Likewise, the *c* spacing for the Pr–50 at% Y alloy reported by Jayaraman et al. has a large positive deviation.

2.28.2. *Phase relationships as a function of pressure*

Jayaraman et al. (1966) investigated pressure-induced phase changes in several intra rare earth alloy systems including the Pr–Y system. A Pr–50 at% Y alloy was

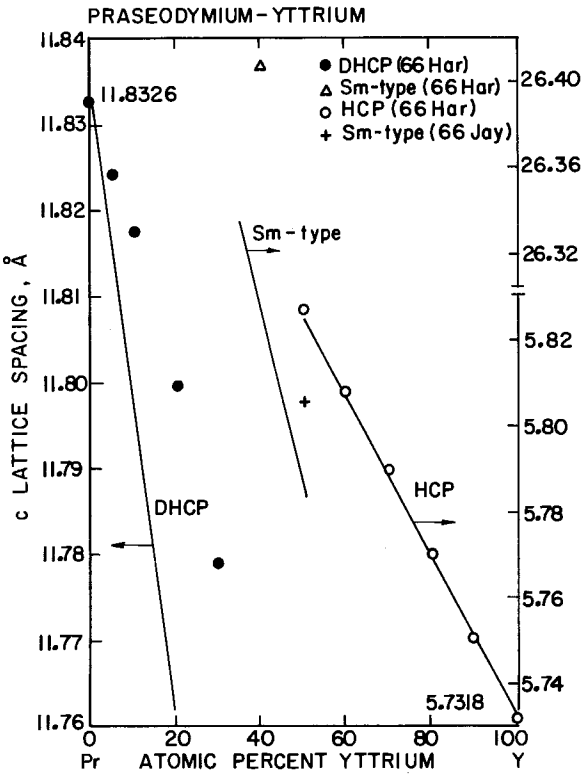

Fig. 51. *c* lattice spacings for the praseodymium–yttrium system. The straight lines represent the Vegard's law relationships for the three structures and are based on the accepted values for the pure metals as listed in table 2.

observed to have Sm-type structure after an annealing treatment at 500°C for several days. It was then subjected to 4.0 GPa pressure at 450°C for 5 hr in a piston–cylinder apparatus. This alloy transformed to the dhcp structure and retained this form at room temperature and atmospheric pressure. No attempt was made to locate transition pressures but Jayaraman et al. suggest that transition pressures for the Sm-type phases increase in the sequence LaY < PrY < NdY.

2.28.3. *Metastable solid solutions*

Wang (1976) splat-cooled alloys in the Pr–Y system and found that by splat-cooling, the hcp-phase range was extended to compositions that, under equilibrium conditions, should have the Sm-type structure. The Sm-type structure was pushed toward higher concentrations of praseodymium. Wang observed that extensions of the hcp-phase fields are limited by a c/a ratio of 1.597.

References

Harris, I.R., C.C. Koch and G.V. Raynor, 1966, J. Less-Common Met. **11**, 436.
Jayaraman, A., R.C. Sherwood, H.J. Williams and E. Corenzwit, 1966, Phys. Rev. **148**, 502.
Wang, R., 1976, Mater. Sci. Eng. **23**, 135.

2.29. *Nd–Sm: Neodymium–samarium*

2.29.1. *Phase diagram*

Kobzenko and Martynchuk (1975) investigated the neodymium–samarium phase system using thermal analysis, X-ray diffraction and metallography. Their alloys were cast using neodymium metal that had greater than 99.34(wt?)% purity and that also contained < 0.19% other rare earths, < 0.11% common metals and < 0.042% O. Their samarium metal contained < 0.10(wt?)% other rare earths, < 0.014% common metals, 0.003% N and 0.09% O. Alloys were heat-treated at 600 to 750°C for 100 hr under an argon atmosphere.

The phase diagram for the neodymium–samarium system, presented in fig. 52 is based on the work of Kobzenko and Martynchuk and on the accepted melting and transition temperatures for the pure metals listed in table 1. Kobzenko and Martynchuk showed a narrow two-phase region between the liquidus and solidus lines and also between the solvus lines. Their diagram showed complete solid solubility for the high temperature alloys. There was no indication of three allotropic forms of samarium in their diagram. A two-phase region for the coexistence of αNd (dhcp) and αSm (the Sm-type) was partially indicated by dotted lines. Since Nd and Sm are trivalent metals having atomic numbers that differ by two and since complete solid solubility was demonstrated for the high temperature (bcc) phase, the melting

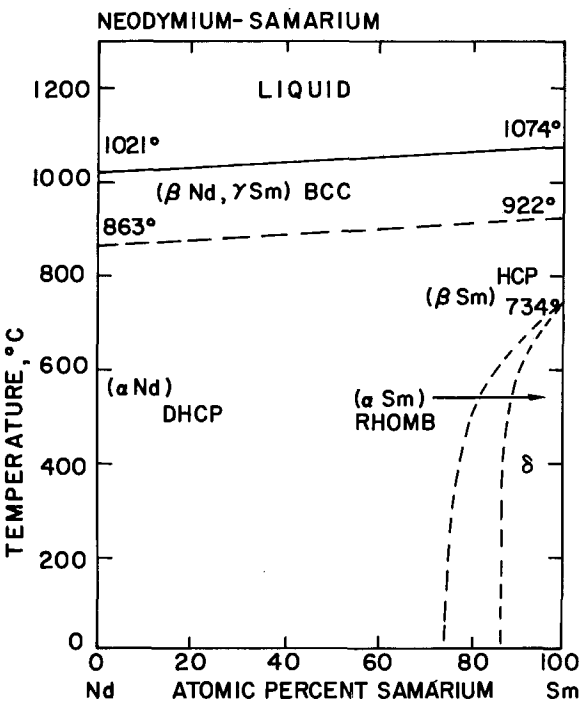

Fig. 52. Phase diagram of the neodymium–samarium system.

points of the end-members have been joined by a straight line in fig. 52, eliminating the liquidus–solidus gap (see section 2.1.1). For the same reason, the transformation temperatures of the pure metals to the bcc form are also joined by a straight line and the solvus gap is thus eliminated. The phase boundaries in the samarium-rich regions below the $\beta Sm \rightleftarrows \gamma Sm$ transformation have been drawn with dashed lines to indicate the uncertainty in their location.

Reference

Kobzenko, G.F. and E.L. Martynchuk, 1975, Dopov. Akad. Nauk Ukr. RSR, Ser. A, 263.

2.30. *Nd–Gd: Neodymium–gadolinium*

2.30.1. *Phase diagram*

Svechnikov et al. (1975) using thermal analysis, X-ray diffraction and metallography, investigated the neodymium–gadolinium phase system. The purity of their metals was not given. Cast alloys were annealed at 600 to 750°C for 300 hr under a gettered argon atmosphere. The phase diagram presented by the authors shows complete solid solubility at all compositions in the high temperature body-centered cubic phase. They found a narrow two-phase region between the liquidus and

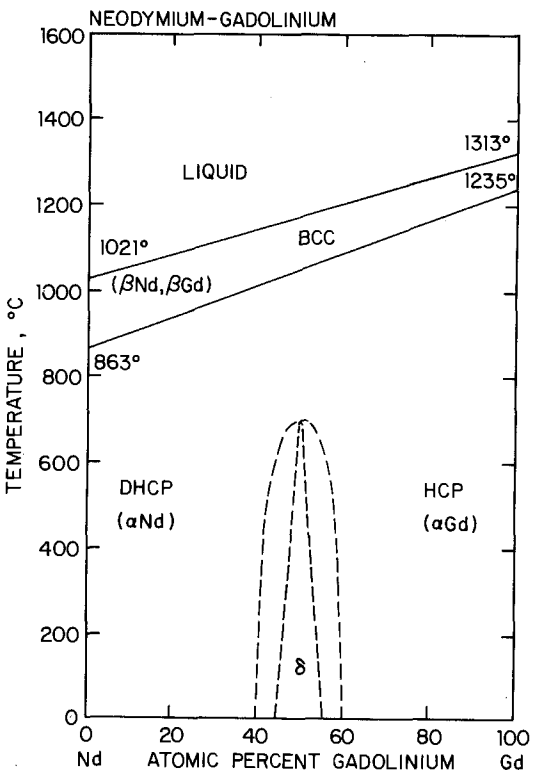

Fig. 53. Phase diagram of the neodymium–gadolinium system.

solidus lines and between the solvus lines at the transformation from the hcp structures to the bcc structure. They showed by dashed lines a single-phase region containing the samarium-type (δ) structure, surrounded by a two-phase region containing the δ phase mixed with αNd on one side and by the δ phase mixed with αGd on the other side. In their diagram, the region containing Sm-type structure existed from ~ 48 to ~ 80 at% Gd at 200°C and disappeared completely at about 700°C. Lundin (1966) in his systematic study of the nature of the formation of Sm-type structure in alloys of light lanthanide metals with heavy lanthanide and yttrium metals included a study of alloys in this system. He found that the compositional range for the Sm-type structure is from 40 to 60 at% Gd.

The phase diagram of the neodymium–gadoliniium system, shown in fig. 53, has features from both Svechnikov et al. and Lundin. Based on the fact that both end-members are trivalent metals, that the atomic numbers of the end-members differ by only four and that complete solid solubility exists in the high temperature phase (bcc) region, a straight line has replaced the narrow gap that Svechnikov et al. showed between the liquidus and the solidus as well as between the solvus lines at the transformation of the hcp phases to the bcc phase (see section 2.1.1). The Sm-type structure for this system is placed in the compositional range stated by Lundin instead of at a somewhat higher gadolinium content as indicated by Svechnikov et al.

2.30.2. *Lattice spacings*

Lundin (1966) measured lattice spacings of neodymium–gadolinium alloys over the composition range Nd–30 at% Gd through Nd–70 at% Gd. His neodymium metal was 99.9 + wt% pure and contained 140 ppm O and 50 ppm each B, Zn and other rare earths. His gadolinium was also reported to be 99.9 + wt% pure and had 375 ppm other rare earths (including 50 ppm Ce), 210 ppm O and 50 ppm each Mg and Zn. The alloys were homogenized at 800°C for 16 hr and filings were annealed to relieve stress. Since Lundin's values for the a and c lattice spacings of the end-members varied from the accepted values as listed in table 2, the a and c lattice spacing for each alloy were adjusted by prorating the deviations in the spacing of the end-members according to the mole fraction of each metal in each alloy. The adjusted a lattice spacings for Lundin's alloys are plotted in fig. 54 along with a spacing data for a Nd–50 at% Gd alloy as reported by Jayaraman et al. (1966) and by Speight (1970). Since Lundin's objective was to study the formation of the Sm-type structure, he did not prepare alloys in the 0 to 30 and 70 to 100 at% Gd ranges. Instead he concentrated on the 30 to 70 at% Gd composition range and the pure metals. In the part of the hcp structure region that he did cover, his three alloys had a lattice spacings that fell both above and below the Vegard's law behavior line, so no trend is established. Lundin reported a spacings for two alloys with the dhcp structure and both had strong negative deviations from Vegard's law. Lundin, Jayaraman et al. and Speight each reported lattice spacings for the Sm-type Nd–50 at% Gd alloy. The a spacings reported by the first two researchers for this composition both showed positive deviations from ideality while the a spacing reported by the latter exhibited a negative deviation. The c spacings for the

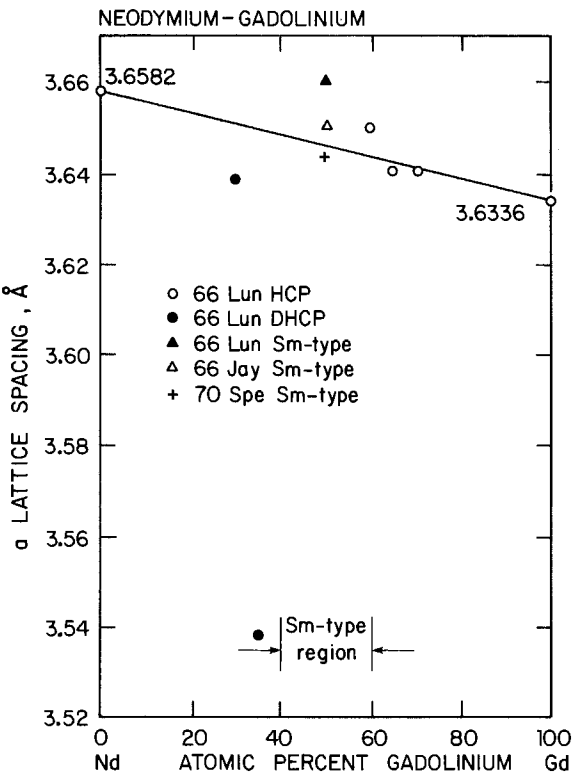

Fig. 54. *a* lattice spacings in the neodymium–gadolinium system. The straight line shows the Vegard's law relationship based on the accepted values for the pure metals as listed in table 2.

neodymium–gadolinium system are shown in fig. 55. It is noted that in the Sm-type region those alloys that showed positive deviations from Vegard's law behavior in the *a* lattice spacing had negative deviations in their *c* lattice spacing and vice versa. In the hcp structure region, the *c* lattice spacings showed large scatter, both positively and negatively, from Vegard's law behavior, but in the dhcp structure region the deviation is negative for *a* and positive for *c*.

2.30.3. *Phase relationships as a function of pressure*

Jayaraman et al. (1966) investigated pressure-induced transformations in several intra rare earth alloy systems and included the Sm-type Nd–50 at% Gd alloy. Equal molar amounts of neodymium and gadolinium metals were arc-melted in an argon atmosphere, then heat treated at 500°C for several days in sealed evacuated quartz tubes. X-ray patterns established that this alloy had the Sm-type structure under equilibrium conditions. After this alloy had been subjected to 4.0 GPa pressure at 450°C for 5 hr, the pressure was related and the temperature was reduced to ambient. X-ray patterns revealed that the alloy had transformed to dhcp structure that was retained metastably after the release of pressure.

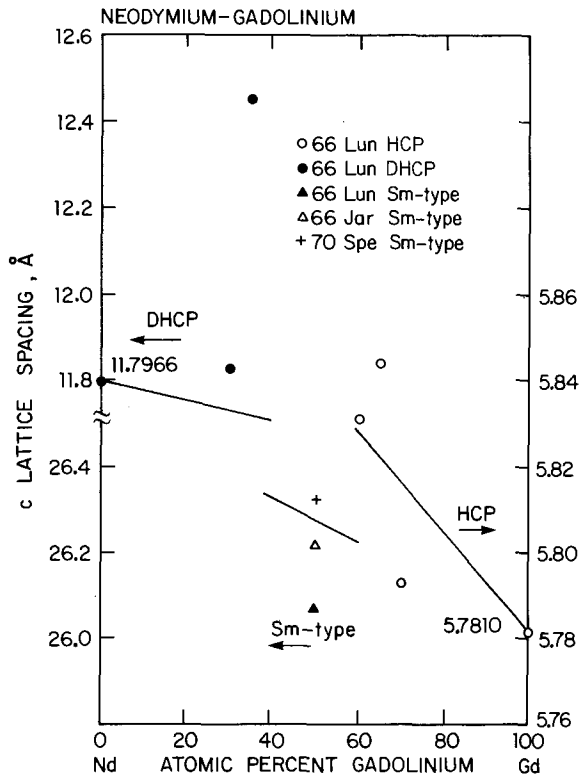

Fig. 55. c lattice spacings in the neodymium–gadolinium system. The straight lines illustrate the Vegard's law relationships in each phase region based on accepted values for the pure metals as listed in table 2.

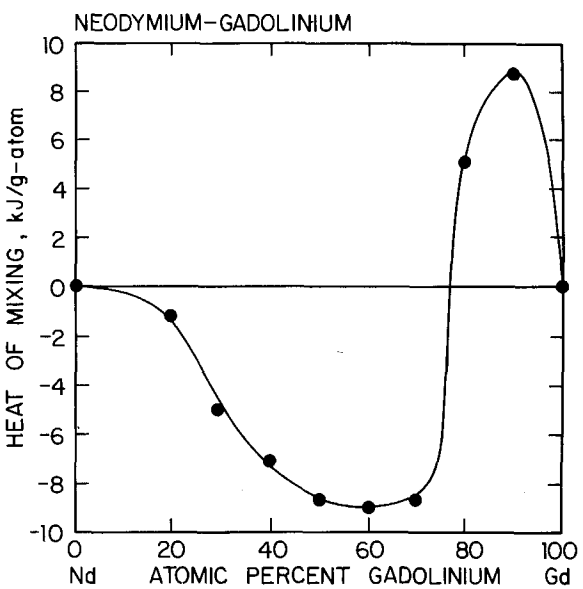

Fig. 56. Heat of mixing of neodymium and gadolinium referred to 0°C. The heat of formation of the δ phase, which exists from 45 to 55 at% Gd, is not evident.

2.30.4. *Metastable solid solutions*

Speight (1970) investigated the effect of rapid quenching on the Sm-type crystal structure of a Nd–50 at% Gd alloy. The purity of the metals used was reported to be 99.9%. The alloy was homogenized at 600°C for four days in sealed capsules. Small amounts of the alloy were induction melted under argon then ejected at high velocity onto a curved copper strip. X-ray patterns revealed that the quenched alloys were single phase and had the hcp structure. The a lattice spacing was observed to be greater than that of the normal Sm-type phase having the same composition.

Wang (1976) splat-cooled several alloys in intra rare earth systems, including Nd–Gd. As in other systems that contain a Sm-type phase, he found that by liquid quenching the hcp-phase field was extended into the composition range which under equilibrium conditions would show Sm-type structure. Here again the extension of the hcp-phase field was limited by a c/a ratio of ~ 1.597.

2.30.5. *Thermodynamic properties*

Lundin (1966) measured heat of solution and calculated the heat of mixing for Nd–Gd alloys using liquid metal calorimetry. His data for the heat of mixing at 0°C are presented in fig. 56. For more details of Lundin's calorimetry measurements see section 2.4.4, La–Gd system.

References

Jayaraman, A., R.C. Sherwood, H.J. Williams and E. Corenzwit, 1966, Phys. Rev. **148**, 502.
Lundin, C.E., 1966, Final report, Denver Research Institute Rept. AD-633558, University of Denver, Denver, CO (also given as DRI-2326).
Speight, J.D., 1970, J. Less-Common Met. **20**, 251.
Svechnikov, V.N., G.F. Kobzenko and E.L. Martynchuk, 1975, Dopov. Akad. Nauk Ukr. RSR, Ser. B, 79.
Wang, R., 1976, Mater. Sci. Eng. **23**, 135.

2.31. *Nd–Dy: Neodymium–dysprosium*

2.31.1. *Phase diagram*

Kobzenko et al. (1972) investigated the neodymium–dysprosium system by means of thermal analyses, X-ray diffraction, metallography and dilatometry. Their neodymium metal was reported to be 99.34(wt?)% pure and contained no more than 0.21% other rare earths (La, Ce, Pr, Sm), and no more than 0.03% total Fe, Ca, Cu and 0.08% Ta. Their dysprosium was reported to be 99.76(wt?)% pure and contained 0.1% other rare earth metals (Tb, Ho, Er), a total of 0.09% Fe, Ca and Cu, and 0.05% Ta or Mo. Appropriate amounts of these metals were arc-melted then annealed at 550 to 800°C.

The phase diagram shown in fig. 57 is based on that presented by Kobzenko et al. but with adjustments in the melting point and transformation temperatures of the pure metals based on the accepted values listed in table 1, and a revision of the shape of the diagram around the Sm-type phase region based on Lundin's (1966) investigation of the formation of this phase in binary alloys of light and heavy rare earth metals. The phase diagram presented by Kobzenko et al. showed the formation of the δ phase through a peritectoid reaction of the two solid solutions of αNd and

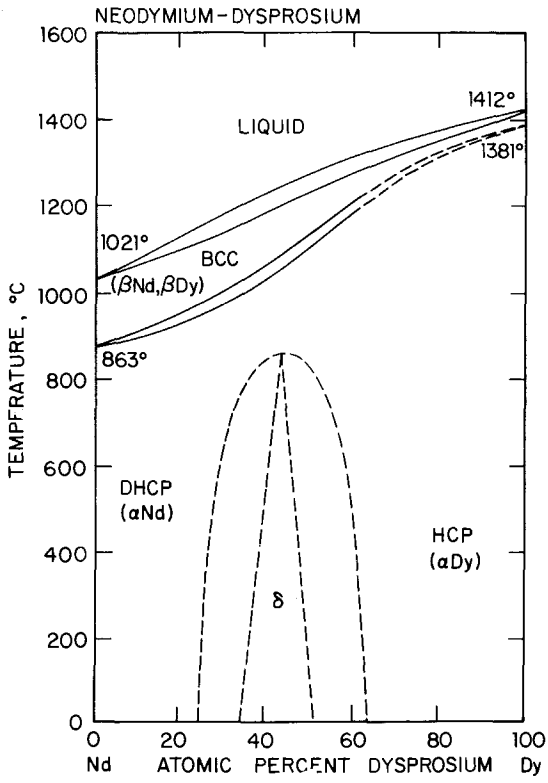

Fig. 57. Phase diagram of the neodymium–dysprosium system.

αDy at about 860°C. Since earlier research had already disproven the peritectoid-type reaction for the formation of the Sm-type structure in intra rare earth alloys (see section 2.1.3 and 2.1.4), the peritectoid reaction put forward by Kobzenko et al. has been replaced with a congruent transformation to account for the formation of the δ-phase structure. The shape of the two-phase regions on either side of the Sm-type field, shown here in dashed lines, has been adjusted to bring it into accord with the lattice spacing data of Chatterjee and Taylor (1972) which is presented in the next section (2.31.2). The diagram presented by Kobzenko et al. completely ignored the hcp ⇄ bcc transition in dysprosium at 1381°C, showing instead the melting point of dysprosium at about this temperature. Even with these major modifications the diagram presented in fig. 57 is in good agreement with their listed data points and makes use of one point that lies in a single liquid phase region well away from a single-phase/two-phase boundary line.

2.31.2. *Lattice spacings*

Chatterjee and Taylor (1972) examined physical properties associated with different crystal structures in the neodymium–dysprosium alloy system. The purity of their starting metals was not reported. Alloys were prepared by arc melting the

constituents under an argon atmosphere. Observations were made on as-cast as well as on annealed specimens. Lattice spacings were determined for neodymium and dysprosium as well as for several intermediate alloy compositions. The alloy containing 70 at% Dy showed extensive line broadening, but was successfully indexed to the hcp structure. The 60 at% Dy alloy had a complex X-ray pattern (mixture of hcp- and δ-phase lines) and could not be indexed with sufficient precision to yield reliable lattice constants.

Arajs et al. (1965) studied lattice spacings of neodymium-rich alloys at 22°C after quenching from 550°C. Their neodymium contained < 0.02 wt% Pr, 0.001 wt% Mg, no other metallics and 0.16 wt% O; their dysprosium contained < 0.002 wt% Mg, 0.002 wt% Si, < 0.004 wt% Ca, no other metallics and 0.16 wt% O. The arc-melted alloys were homogenized at 777°C for three days in sealed capsules then dropped into liquid nitrogen. Filings for X-ray studies were again annealed and quenched in ice water.

Adjustments were made to the spacings data from both sources by prorating on the basis of molar composition of the alloys the differences between the lattice spacings of the end-members as reported by the investigators and the accepted values for the pure metals as listed in table 2. The *a* lattice spacings, as adjusted, are shown in fig. 58. With two exceptions these data show a negative deviation from

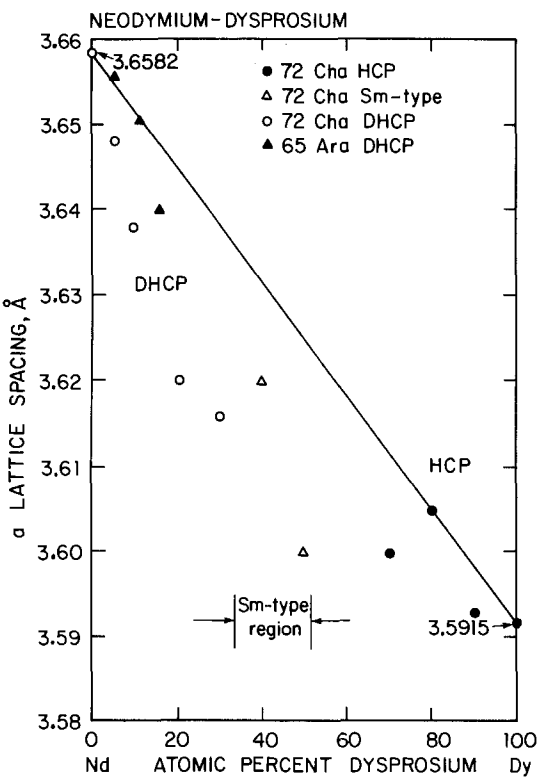

Fig. 58. *a* lattice spacings in the neodymium–dysprosium alloy system. The straight line represents the Vegard's law relationship as based on the accepted values for the pure metals as listed in table 2.

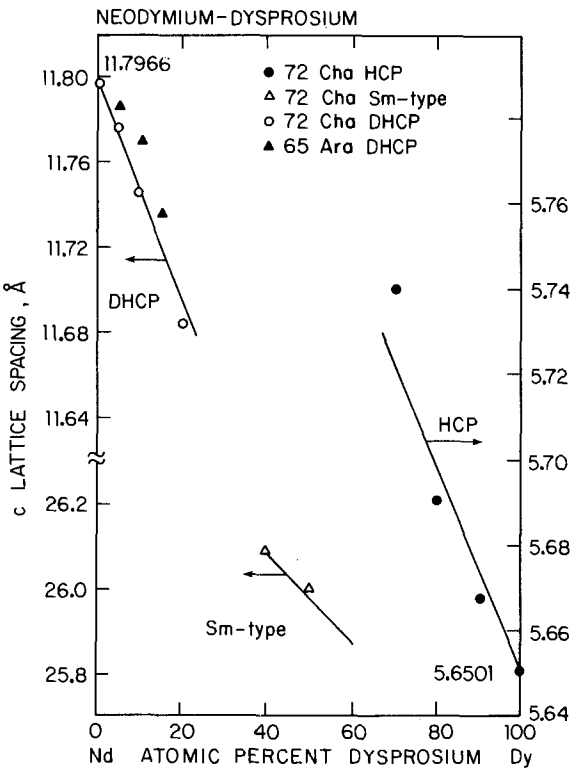

Fig. 59. *c* lattice spacings in the neodymium–dysprosium system. The straight lines represent the Vegard's law relationships for each phase region as calculated from the accepted values for the pure metals listed in table 2.

Vegard's law behavior: the 80 at% Dy alloy of Chatterjee and Taylor (hcp structure) had an *a* spacing which agreed with Vegard's law, and the quenched 5.5 at% Dy alloy (dhcp structure) of Arajs et al. had a small positive deviation.

The *c* lattice spacings as adjusted are shown in fig. 59. These data points lie close to the Vegard's law behavior line. In the dhcp structure region the quenched alloys of Arajs et al. have a small positive deviation from ideality.

References

Arajs, S., R.V. Colvin and H. Chessin, 1965, J. Less-Common Met. **8**, 186.

Chatterjee, D. and K.N.R. Taylor, 1972, J. Phys. F **2**, 151.

Kobzenko, G.F., V.N. Svechnikov and E.L. Martynchuk, 1972, Dopov. Akad. Nauk Ukr. RSR, Ser. A, 563.

Lundin, C.E., 1966, Final Report, Denver Research Institute Rept. AD-633558, University of Denver, Denver, CO (also given as DRI-2326).

2.32. *Nd–Ho: Neodymium–holmium*

2.32.1. *Lattice spacings*

Lundin (1966) measured lattice spacings of neodymium–holmium alloys in the neodymium-rich part of this system during his investigation of the nature and formation of the Sm-type structure. Both the neodymium and the holmium metal

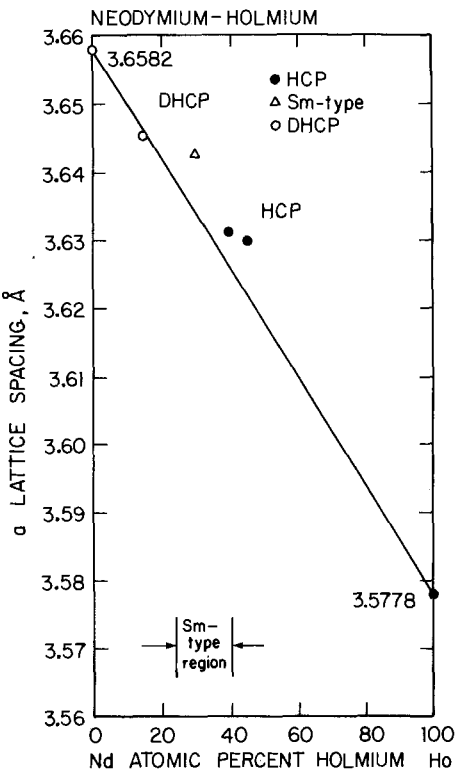

Fig. 60. *a* lattice spacings in the neodymium–holmium system. The straight line represents the Vegard's law relationship based on the accepted data for the pure metals as listed in table 2.

were reported to be 99.9 + wt% pure. The principal impurities in his neodymium were 140 ppm O and 50 ppm each of B, Zn and other rare earths; his holmium contained 110 ppm other rare earths, 125 ppm O and 50 ppm Zn. Lundin found that in this system the Sm-type structure occurs at compositions ranging between 25 and 40 at% Ho.

Since Lundin's spacings for the pure neodymium and holmium metals did not quite match the accepted lattice spacings for these metals as listed in table 2, the spacings for his alloys were adjusted by prorating the difference on the basis of composition. The adjusted *a* lattice spacings are shown in fig. 60. All of the data presented in this figure show a small positive deviation from Vegard's law behavior. However the *a* lattice spacing for an alloy having 20 at% Ho is not shown because its large negative deviation (*a* of 3.551 Å for this alloy as compared with the Vegard's law value of 3.641 Å) brought it below the range of the graph. The *c* lattice spacings, which were also adjusted to bring the *c* spacings for the pure metals into agreement with table 2, are shown in fig. 61. Both points in the hcp-phase field show a large negative deviation from Vegard's law while the one point in the Sm-phase field shows a large positive deviation. The two points in the dhcp field have large deviations, negative at 20 at% Ho and positive at 15 at% Ho. His specimen, having 50 at% Ho, had insufficient lines for accurate lattice parameter determination.

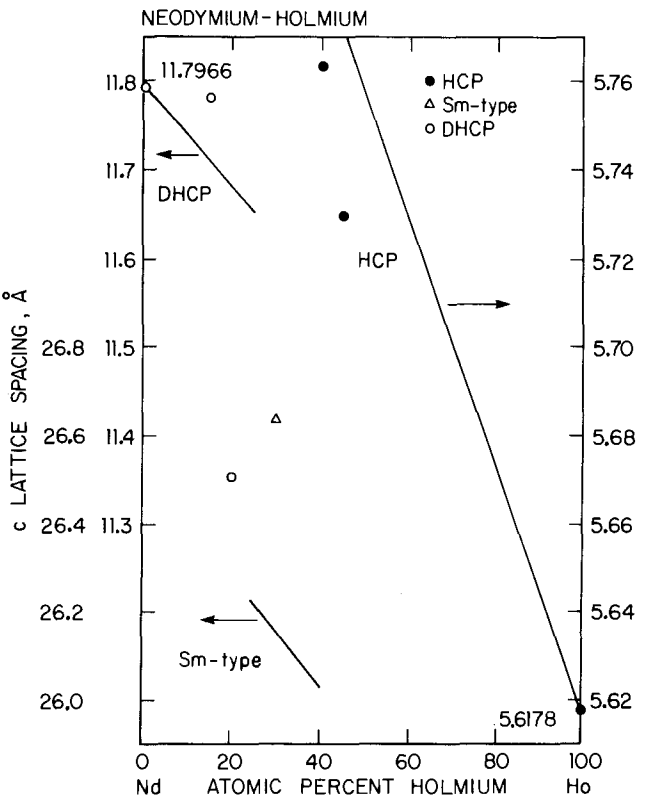

Fig. 61. *c* lattice spacings in the neodymium–holmium system. The straight lines represent the Vegard's law relationships for each phase field as calculated from the accepted data for the pure metals as listed in table 2.

2.32.2. *Thermodynamic properties*

Lundin (1966) also determined the heat of mixing for neodymium–holmium alloys from measurements of the heats of solution obtained in a liquid indium calorimeter (see section 2.4.4). His curve for heat of mixing, referred to 0°C, is reproduced in fig. 62.

Reference

Lundin, C.E., 1966, Final Report, Denver Research Institute Rept. AD-633558, University of Denver, Denver, CO (also given as DRI-2326).

2.33. *Nd–Er: Neodymium–erbium*

2.33.1. *Phase diagram*

Kobzenko et al. (1972) have investigated phase relationships in the neodymium–erbium system using thermal analysis, X-ray diffraction and metallographic observations. The neodymium metal used in their alloys was 99.4(wt?)% pure (impurities were reported to be 0.05% La, 0.05% Ce, 0.21% Pr, $\ll$ 0.1% Sm, 0.03% Cu, 0.011% Fe, 0.03% Ca and 0.2% Ta). Their erbium was 99.7(wt?)% pure

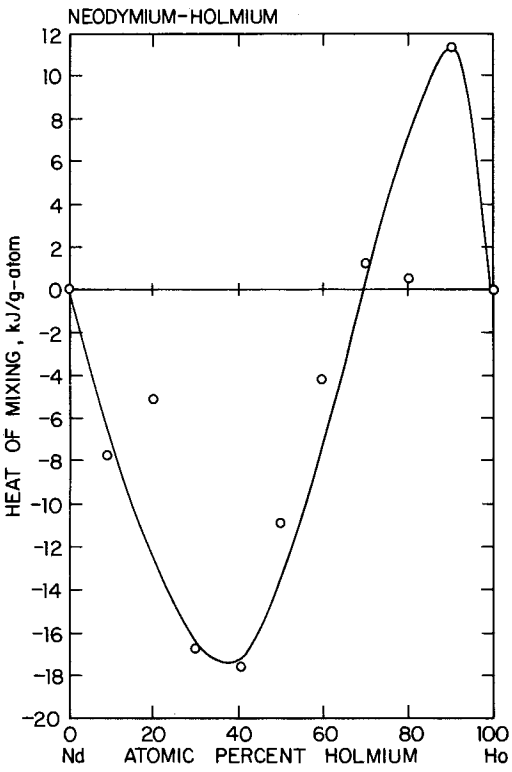

Fig. 62. Heat of mixing of alloys in the neodymium–holmium system at 0°C. The heat of formation of the δ phase, which exists from ~ 20 to ~ 40 at% Ho, is not evident.

(impurities 0.015% Tm, 0.01% Ho, 0.02% Dy, 0.02% Y, < 0.01% Cu, 0.02% Fe and 0.004% Ca). The cast alloys were annealed for a long period before the examination. The phase diagram as reported by these investigators showed the Sm-type structure as a Nd_3Er_2 compound formed by a peritectoid reaction during the cooling of two phases based on the solid solutions of αNd and Er (dhcp and hcp structures). Also, their melting points for the pure metals were given as 995 and 1445°C, respectively, for Nd and Er instead of the accepted values of 1021 and 1529°C (see table 1).

The phase diagram shown in fig. 63 for this system has been modified to avoid these defects. Based on Lundin's (1966) study of the nature of the formation of Sm-type structure, the δ phase is shown here to be formed by a congruent transformation (see sections 2.1.3. and 2.1.4.). The upper portion of the diagram has been revised to bring melting temperatures and the αNd $\rightleftarrows$ βNd transition temperature into accord with table 1 while utilizing as many of the data points listed by Kobzenko et al. as possible.

References

Kobzenko, G.F., E.L. Martynschuk and I.V. Moiseeva, 1972, Dopov. Akad. Nauk Ukr. RSR, Ser. A, 374.
Lundin, C.E., 1966, Final Report, Denver Research Institute Rept. AD-633558, University of Denver, Denver, CO (also given as DRI-2326).

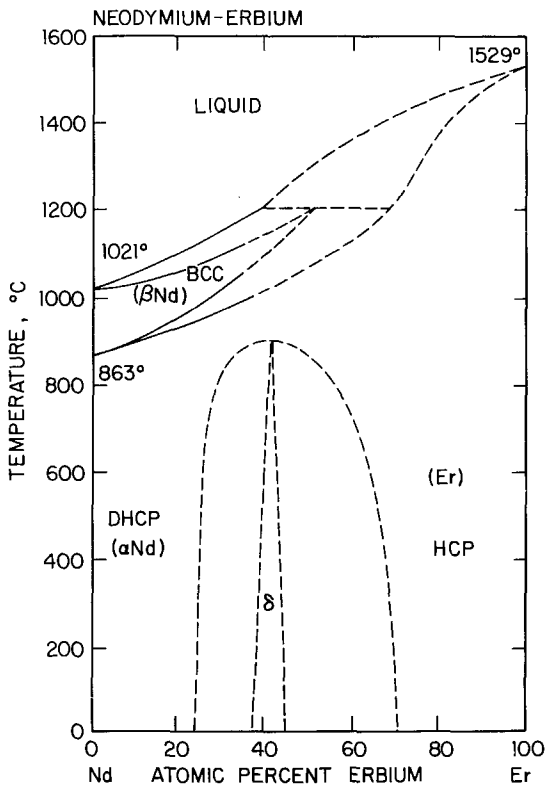

Fig. 63. Phase diagram of the neodymium–erbium system.

2.34. *Nd–Tm: Neodymium–thulium*

2.34.1. *Lattice spacings*

Spedding et al. (1962) indexed the powder pattern of a Nd–37 at% Tm alloy as a mixture of dhcp and Sm-type structures. The a and c lattice spacings for the δ phase were 3.656 and 26.36 Å, respectively while the dhcp phase had a and c spacings of 3.763 and 12.32 Å, respectively. The metals used in their study were better than 99.9 (wt?)% pure with respect to other rare earths and in addition contained small amounts of oxygen and tantalum as impurities.

2.34.2. *Phase relationships as a function of pressure*

Jayaraman et al. (1966) studied pressure-induced transformation in several rare earth alloys, including a Nd–Tm alloy, which they stated was considerably less rich in Tm than $Nd_{0.5}Tm_{0.5}$ due to loss of Tm as vapor in the preparation of their alloy. They stated that the Sm-type phase is centered at $Nd_{0.63}Tm_{0.37}$. Their alloy had the Sm-type structure under normal conditions ($a = 3.50$ Å, $c = 26.00$ Å) but transformed to the dhcp structure ($a = 3.60$ Å, $c = 11.50$ Å) during treatment for 5 hr at 4.0 GPa and 450°C in a piston–cylinder apparatus.

References
Jayaraman, A., R.C. Sherwood, H.J. Williams and E. Corenzwit, 1966, Phys. Rev. **148**, 502.
Spedding, F.H., R.M. Valletta and A.H. Daane, 1962, Trans. Quarterly (Am. Soc. Met.) **55**, 483.

2.35. *Nd–Yb: Neodymium–ytterbium*

2.35.1. *Phase diagram*

By means of thermal analysis, metallography and X-ray diffraction studies, Svechnikov et al. (1975) have investigated the properties of cast and annealed Nd–Yb alloys. Alloys were prepared by melting the metals in an electric arc furnace under an argon atmosphere. The interaction between the two metals was represented by a monotectic-type phase diagram (fig. 64). These two elements were found to have limited solubilities in each other in the solid state and also in the liquid state near the melting points.

The melting points and the $\beta \rightleftarrows \gamma$ transformation temperatures of neodymium were 21 and 13°C, respectively, below the accepted values while the $\beta \rightleftarrows \gamma$ transformation temperature of ytterbium was 115°C below the accepted value (table 1), indicating substantial impurities in their starting materials. The melting point of their ytterbium was only 1°C higher than the accepted value (see table 1). Because of the substantial differences in the melting and transformation temperature of the pure metals, three of the four invariant points were adjusted: from 665 to 780°C for the $\gamma Yb \rightarrow \alpha Nd + \beta Yb$ eutectoid reaction; from 840 to 855°C for the $\beta Nd \rightarrow \alpha Nd + L_2$ inverted peritectic reaction; from 985 to 1005°C for the $L_1 \rightarrow \beta Nd + L_2$ monotectic reaction, while the 810°C temperature for the $L_2 \rightarrow \alpha Nd + \gamma Yb$ eutectic reaction was left unchanged. The compositions of the four invariant points are not well established and are shown as approximate values in fig. 64.

Svechnikov et al. (1975) also presented lattice spacing data for Nd–Yb alloys that had been quenched from 550°C. Their data indicate there is no change in the c lattice parameter of βNd with Yb additions and also for the a lattice parameters of the βYb for Nd additions, at least within the experimental scatter of their data. The a lattice parameter shows a slight increase from their pure αNd value of 3.656 to 3.672 Å, which indicated that the solid solubility of ytterbium is < 9 at% in Nd.

Reference
Svechnikov, V.N., G.F. Kobzenko and E.L. Martynchuk, 1975, Akad. Nauk Ukr. SSR, Metallofiz., 71

2.36. *Nd–Lu: Neodymium–lutetium*

2.36.1. *Phase relationships*

In his investigation of the nature of the formation of the Sm-type structure, Lundin (1966) included some alloys in the neodymium–lutetium system that combine the heaviest of the heavy lanthanides with the heaviest of the light lanthanides that still have the dhcp structure. His neodymium metal was 99.9 + wt% pure

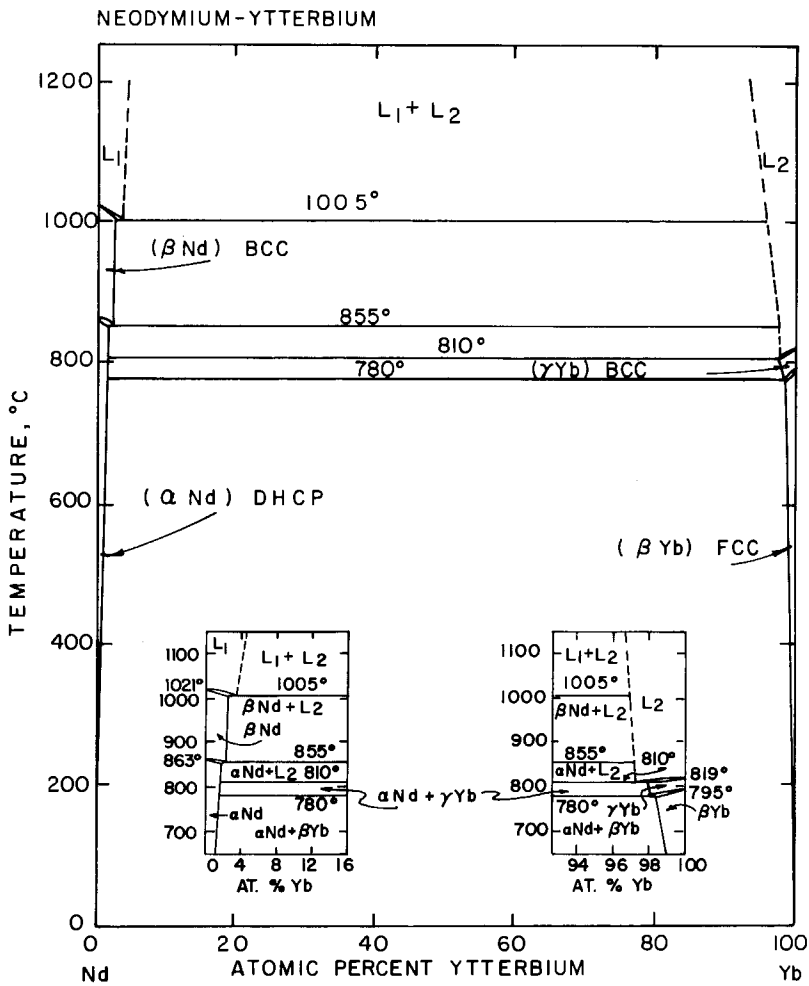

Fig. 64. Phase diagram of the neodymium–ytterbium system.

(impurities: 0.014% O, 0.005% other rare earths, 0.005% B and 0.005% Zn; the lutetium was 99.9 wt% pure but no detailed analysis of the impurities was given. Some difficulty was encountered in the melting of these alloys due to the large differences in the melting points and the densities of the starting materials, but by inverting and remelting a total of 12 times most of the inhomogeneity was eliminated.

Lundin failed to confirm by X-ray analysis the existence of the Sm-type structure in this system but found evidence for the presence of two phases. Metallographic examination showed that the alloys in the composition range where the Sm-type structure would be expected (Nd–18 at% Lu, for instance) had a complex structure with a different appearance compared with that expected if a Sm-type structure had

formed. Because of the metallographic differences observed as compared with nine other systems, the Nd–Lu system was carefully analyzed by X-ray diffraction. The conclusion was reached that a two-phase miscibility gap exists in this system. The X-ray pattern from a Nd–23 at% Lu alloy could not be indexed as that of the Sm-type structure. A good fit was obtained by indexing some of the lines as associated with the neodymium solid solution phase ($a = 3.696$ Å, $c = 11.916$ Å) but the assignment of the remaining lines to the lutetium solid solution phase was not reasonable. Lundin proposed a eutectoid reaction of the high temperature bcc allotrope as the most probable phase equilibria to accommodate an immiscibility gap. However the reviewers feel that the phase relationships found in the Nd–Sc system (section 2.37.1, fig. 65) are more likely than those proposed by Lundin because of the similarity of the physical properties and alloying behavior of lutetium and scandium.

Reference

Lundin, C.E., 1966, Final Report, Denver Research Institute Rept. AD-633558, University of Denver, Denver, CO (also given as DRI-2326).

2.37. *Nd–Sc: Neodymium–scandium*

2.37.1. *Phase diagram*

Beaudry et al. (1965) investigated the neodymium–scandium phase system using differential thermal analysis, X-ray diffraction and metallography. A typical analysis of their neodymium showed 0.018 wt% O, 0.015 wt% each N and Mg, 0.01 wt% each C and Ta, 0.006 wt% F, 0.005 wt% each Ni and Fe, and 0.003 wt% each H and Ca. Their scandium metal contained 0.065 wt% O, 0.035 wt% F, 0.025 wt% Ta, 0.01 wt% C, 0.005 wt% N, 0.004 wt% Ni, 0.003 wt% each H and Ca, and 0.001 wt% Mg. Alloys were prepared by melting weighed portions of the two metals under purified argon or helium in a nonconsumable electrode arc furnace, then inverting and remelting several times to improve homogeneity of the alloys. The solidus and the liquidus lines as well as the solid state transformation temperatures were determined by thermal analysis. X-ray methods were used in the establishment of phase boundaries below 600°C and metallographic techniques were used to establish phase boundaries between 600 and 1060°C. Filings for X-ray analysis were sealed in tantalum capsules and heat-treated at temperatures ranging from 450 to 1060°C for a time period that varied inversely with the temperature (260 hr at 450°C, 16 hr at 1060°C), then quenched. Samples for metallographic examination received a similar heat treatment before quenching.

The phase diagram that Beaudry et al. established is shown in fig. 65. The boundary for the transformation from the hcp solid solution to the bcc form goes through a minimum at 22 at% Sc and 800°C as determined by differential thermal analysis data taken at 5 at% intervals. The thermal analysis established the existence of the continuous series of bcc solid solutions. The shape of the miscibility gap was established by metallographic examination of annealed alloys quenched from various temperatures. Anomalies were noted in the heating and cooling curves between

30 and 70 at% Nd because of the large change in mutual solubility over a narrow temperature range. Thermal arrests were found to occur 20 to 40°C higher on heating than on cooling. To obtain consistent results, all of the thermal arrests were approached from a temperature above that of the arrest because equilibrium conditions were easier to establish in the high temperature single-phase region. There was no evidence of the Sm-type structure in the Nd–Sc alloys even when annealed two weeks at 350°C or one month at 250°C.

The absence of a two-phase region above 700°C in the Nd–Sc system as determined by metallography strongly indicates a continuous series of solid solution between the dhcp (ABAC) structure of neodymium and the hcp (ABAB) structure of scandium, and this necessitates a continuous change in symmetry in passing from 0 to 100% Sc. Since both structures belong to the same space group ($P6_3/mmc$ D_6^4h), we know of no requirement that there be a first or higher order phase transition between them. The absence of a first or higher order transition is also consistent with thermodynamics, i.e., Gibbs–Konovalov equations, Franzen and Gerstein (1966).

Shiflet et al. (1979) attempted to apply the Kaufman approach to the construction of phase diagrams of several binary rare earth systems. While good agreement with experimentally determined phase diagrams was obtained with some systems, phase

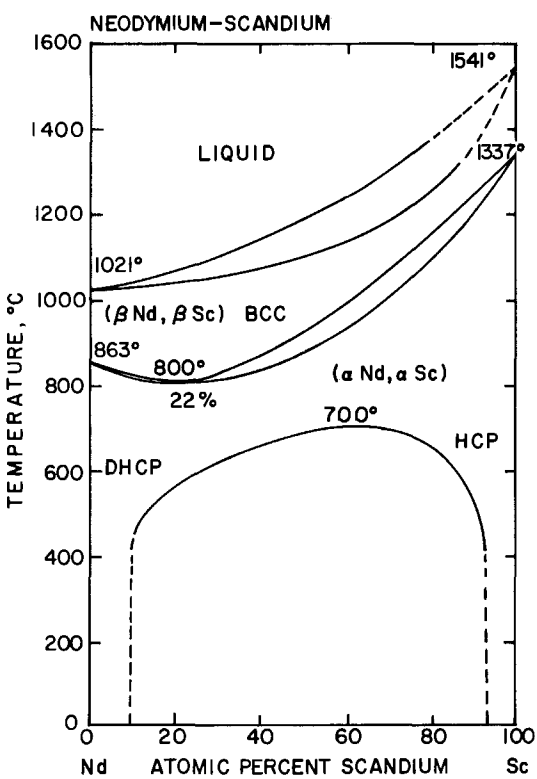

Fig. 65. Phase diagram of the neodymium–scandium system.

diagrams for Sc with Nd, Gd and Y were unsatisfactory. The calculate liquid + bcc-phase field was wider for Nd–Sc than that determined experimentally and lay at a somewhat lower temperature. The calculated maximum of the solid miscibility gap (at ~ 50 at% Sc and 980°C) deviated from the experimental maximum (at ~ 60 at% Sc and 700°C), and lacked the asymmetry of the experimental gap. A particularly disturbing feature of this theoretical phase diagram was that the calculated two-phase region (liquid + bcc) overlapped the calculated bcc + hcp(dhcp) two-phase region.

References

Beaudry, B.J., M. Michel, A.H. Daane and F.H. Spedding, 1965, in: Eyring, L., ed., Rare Earth Research III (Gordon and Breach, New York) p. 247.
Franzen, H.F. and B.C. Gerstein, 1966, A.I.Ch.E. Journal **12**, 364.
Shiflet, G.J., J.K. Lee and H.I. Aaronson, 1979, Calphad **3**, 129.

2.38. *Nd–Y: Neodymium–yttrium*

2.38.1. *Phase diagram*

Several investigators have contributed to the understanding of the neodymium–yttrium system. Spedding et al. (1962) noted the formation of the δ-phase structure in a Nd–47 at% Y alloy. Kirkpatrick and Love (1962) reported the δ phase at "nearly equal mole percent". Beaudry et al. (1965) and Svechnikov et al. (1972) made thorough examinations of this system and prepared phase diagrams each of which indicated the formation of the δ phase by a peritectoid reaction. Svechnikov et al. reported their neodymium metal to be 99.4(wt?)% pure and contained 0.05% each La and Ce, 0.21% Pr, 0.1% Sm, < 0.05% Cu, 0.011% Fe, < 0.03% Ca and 0.2% Ta; their 99.76% pure Y contained < 0.005% Tb, < 0.001% each Dy and Ho, and < 0.01% each Ca and Cu. They used thermal analysis, metallography, X-ray diffraction and dilatometry in their investigation. The melting point and the $\alpha \rightleftarrows \beta$ phase transformation temperatures for pure yttrium as shown on their phase diagram (~ 1440 and ~ 1400°C, respectively) are considerably below the accepted values for these temperatures as listed in table 1 (1522 and 1478°C, respectively). Their reported melting and transition temperatures for pure neodymium (~ 1000 and ~ 840°C, respectively) are also lower than the accepted values in table 1 (1021 and 863°C, respectively). These low values indicate that the impurity concentrations are probably higher than that listed above. Thus more reliance will be placed on the study by Beaudry et al. that utilized metals that had melting point and transition temperatures close to the accepted values (Y: 1525 and 1460°C; Nd: 1010 and 850°C). The yttrium metal used by Beaudry et al. contained 0.053 wt% O, 0.02 wt% Fe, 0.026 wt% N, ~ 0.012 wt% each C, H and F, and 0.01 wt% Ta; the neodymium metal used had 0.018 wt% O, 0.015 wt% each N and Mg, and 0.01 wt% each Ca and Ta. Alloys were prepared by melting the metals in an electric arc furnace under a purified helium or argon atmosphere. Alloys were inverted and remelted several times and further homogenized by heat treatment. Solidus and liquidus lines were determined by an optical pyrometer method; most of the solid transformation

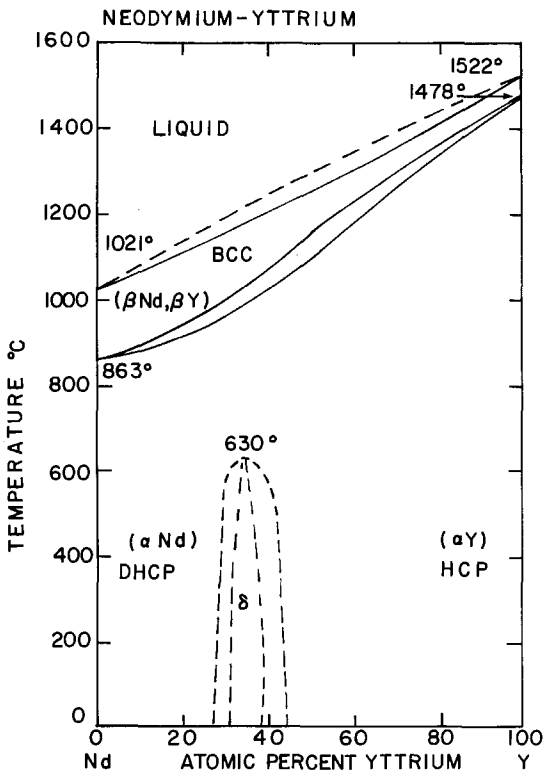

Fig. 66. Phase diagram of the neodymium–yttrium system.

temperatures were determined by thermal analysis. X-ray methods were used to determine boundaries below 600°C.

The phase diagram for the neodymium–yttrium system, based largely on the work of Beaudry et al., is shown in fig. 66. A nearly straight line relationship exists for the liquidus–solidus curves. The transformation temperature from the hexagonal forms of Nd and Y to their bcc form also varies in a nearly linear mode. The authors showed by dashed lines a peritectoid horizontal to account for decomposition of the δ phase upon heating. A short nonisothermal thermal arrest is said to have been observed at 630°C but no thermal arrests were observed on either side of that point. The authors suggested the possibility of a congruent transformation of the δ phase to a single-phase hexagonal solid solution. Since Lundin (1966) researched the nature of the δ phase and disproved its formation by a peritectoid reaction, fig. 66 has been drawn to indicate the δ phase to be the result of a congruent transformation. The room temperature phase boundaries around the δ-phase region were established by X-ray diffraction patterns taken at 2 at% intervals in the region. The δ-phase lines only were observed in the 31 to 38 at% Y range, while δ-phase and αNd lines were observed in the 27 to 31 at% Y range. This is in fair agreement with a similar study conducted by Nachman et al. (1963).

2.38.2. *Lattice spacings*

Beaudry et al. (1965) reported lattice spacings for neodymium and yttrium metal and for alloys ranging in composition from 0 to 60.8 at% Y. The purity of their metals and the preparation of their alloys were discussed above. To further homogenize the alloys for X-ray analysis, each alloy was wrapped in tantalum, sealed in quartz and held at a high temperature: Those between 0 and 50 at% Y were heated at 900°C for 20 hr, and those with greater than 50 at% Y were heated to 950°C for 100 hr. After filing, the sieved filings were sealed in capsules and stress-relieved at 450°C for 70 hr. Lattice constants were refined using a least squares method.

Lundin (1966) also reported lattice spacings for the neodymium–yttrium alloys over the composition range 0 to 60 at% Y and for the pure metals. His 99.9+ wt% pure neodymium had 0.014% O, 0.005% each Zn, B and other rare earths. His 99.4 wt% pure yttrium contained 0.185% O, 0.3% Zr, 0.033% other rare earths, 0.012% N, < 0.01% each Co and Zn, 0.008% C, 0.006% each Fe, Ta and Ni. Lundin's alloys were prepared by melting in an arc furnace under an argon atmosphere, inverting and remelting several times. Filings for X-ray analysis were sieved through a 325 mesh screen, sealed in capillary tubes and annealed for 2 hr at 300°C to relieve stresses. Film data were reduced on a computer using a least squares technique to provide precise lattice spacings.

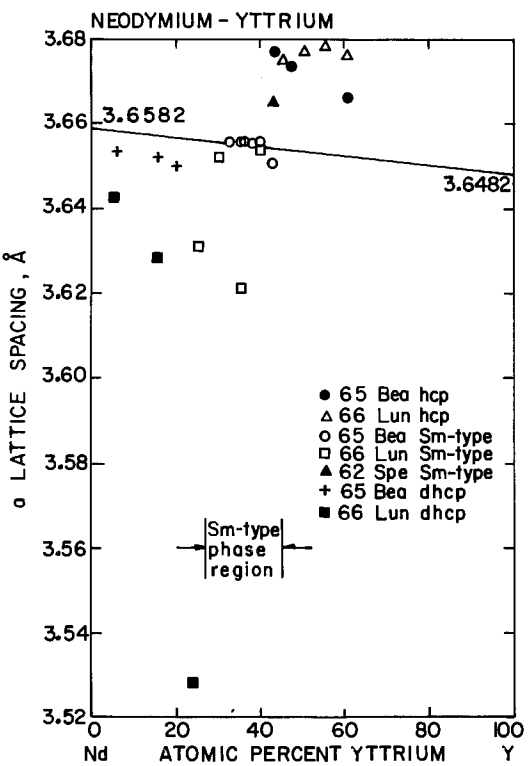

Fig. 67. *a* lattice spacings in the neodymium–yttrium system. The straight line represents the Vegard's law relationship based on the accepted values for the pure metals as shown in table 2.

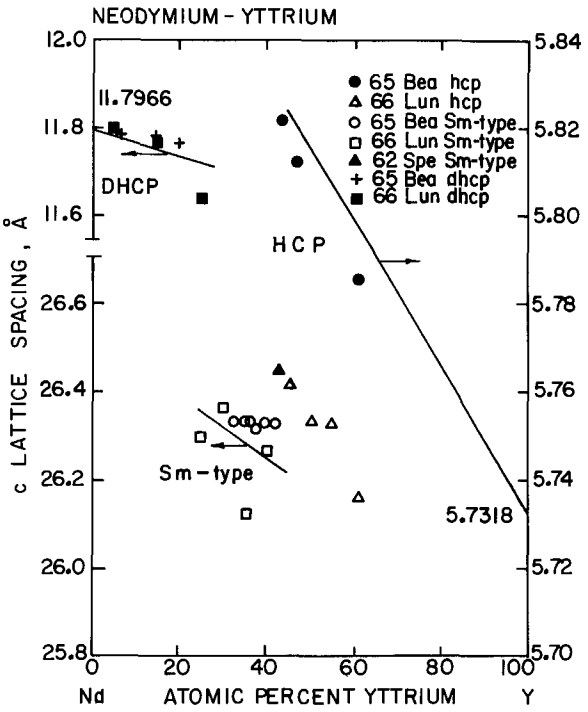

Fig. 68. *c* lattice spacings in the neodymium–yttrium system. The straight lines show the Vegard's law relationships for each phase as calculated from the accepted values for the pure metals as listed in table 2.

There was a rather large difference between the lattice spacings of the pure metals as reported by both of the above investigators and the accepted values for these spacings as listed in table 2. Each set of alloy lattice spacing data was adjusted on the basis of the molar compositions and the differences between the lattice spacings observed for the pure metals and the accepted value for each. The *a* lattice spacings, as adjusted, are plotted in fig. 67 and the *c* spacings in fig. 68.

All of the *a* spacing data for the neodymium-rich dhcp phase shows a negative deviation from Vegard's law. In the δ-phase region, most of the data of Beaudry et al. fall close to the Vegard's law line but the data of Lundin for this phase region have mostly a negative deviation from Vegard's law. In addition to the data from these two sources, one alloy reported by Spedding et al. (1962) is shown on these plots. The *a* lattice spacing for the Sm phase observed in this alloy showed a positive deviation from Vegard's law behavior. All of the *a* spacing data in the hcp-phase region showed large positive deviations from the Vegard's law line.

The *c* lattice spacing data in the neodymium-rich dhcp region show small positive deviations from the Vegard's law relationship except for Lundin's alloy at 25 at% Y, which has a negative deviation. In the Sm-type region, all of the data of Beaudry et al. have a small positive deviation, Lundin's data are split between positive and negative deviations and the alloy reported by Spedding et al. has a positive deviation. In the hcp region all of the data show a negative deviation from Vegard's law behavior with the deviations being much greater for the alloys reported by

Lundin as compared with those reported by Beaudry et al. No adjustments were made to the *a* and *c* lattice spacings of the alloy reported by Spedding et al. since no information was available on the measured *a* and *c* lattice spacings of the end-members.

2.38.3. *Phase relationships as a function of pressure*

Jayaraman et al. (1966) investigated the effect of pressure and temperature upon the phase transformation sequence of several intra rare earth alloy systems and included the δ-phase-type NdY. The alloys were subjected to 4.0 GPa pressure at 450°C for about 5 hr in a piston-cylinder apparatus. After the pressure had been released and the temperature reduced to ambient, X-ray patterns of the NdY specimen revealed a partial conversion of the Sm-type phase to a pressure-induced dhcp phase under conditions of the experiment. Such a transformation is sluggish and the conversion to the high pressure form is temperature- and time-dependent. Transition pressures were not determined, but the authors state that the transition pressure for the Sm-type phase increases in the sequence LaY < PrY < NdY.

References

Beaudry, B.J., M. Michel, A.H. Daane and F.H. Spedding, 1965, in: Eyring, L., ed., Rare Earth Research III (Gordon and Breach, New York) p. 247.

Jayaraman, A., R.C. Sherwood, H.J. Williams and E. Corenzwit, 1966, Phys. Rev. **148**, 502.

Kirkpatrick, C.G. and B. Love, 1962, in: Nachman, J.F. and C.E. Lundin, eds., Rare Earth Research (Gordon and Breach, New York) p. 87.

Lundin, C.E., 1966, Final Report, Denver Research Institute Rept. AD-633558, University of Denver, Denver, CO (also given as DRI-2326).

Nachman, J.F., C.E. Lundin and G.P. Rauscher, Jr., 1963, Technical Rept. No. 1 (DRI-2080), Denver Research Institute, University of Denver, Denver, CO.

Spedding, F.H., R.M. Valletta and A.H. Daane, 1962, Trans. Quarterly (Am. Soc. Met.) **55**, 483.

Svechnikov, V.N., G.V. Kobzenko and E.L. Martynchuk, 1972, Dopov. Akad. Nauk, Ukr. RSR, Ser. A, 754.

2.39. *Sm–Gd: Samarium–gadolinium*

2.39.1. *Phase diagram*

Lundin and Yamamoto (1967) investigated the samarium–gadolinium system as part of a program to further the understanding of alloy formation, in particular to elucidate the effect of the difference in crystal structures on the various thermodynamic properties.

The samarium and gadolinium metals were reported to include no more than 0.1 wt% total impurities in either metal, but a detailed chemical analysis was not reported. Alloys were prepared by standard arc-melting techniques, and since samarium has a high vapor pressure, the alloys were analyzed by X-ray fluorescence to assess loss of samarium. Loss of gadolinium was not a problem in the alloy preparation since the vapor pressure of gadolinium is at least four orders of magnitude less than that of samarium. The phase relations in this system were established by metallography, X-ray diffraction, thermal analysis, density and microhardness measurements and effusion experiments.

Lundin and Yamamoto (1967) investigated the liquidus–solidus and the hcp ⇄ bcc transformation temperatures in the samarium–gadolinium system by thermal analysis of the two component metals and eleven alloys whose compositions varied by about 10 at% across the range from samarium to gadolinium. Their data indicated a narrow gap between the liquidus and the solidus as well as between the hcp and bcc fields. Furthermore, each of the lines involved is close to being a straight line. Since both components are trivalent, have similar atomic numbers (62 and 64 for samarium and gadolinium, respectively) and have the same structures at high temperatures, the liquidus–solidus line and the bcc ⇄ hcp transformation line in fig. 69 are each drawn as a single straight line connecting the corresponding temperatures of the end-members in accordance with section 2.1.1. The phase diagram presented by these authors covers only the high temperature (above 850°C) portion of the system. The area in their phase diagram labeled "α phase" would appear to consist of αGd and βSm, both hcp structure, and the area labeled "β phase" would be βGd and γSm, both having the bcc structure. The melting temperatures and transition temperatures in fig. 69 have been adjusted slightly to bring these properties of the pure metals into agreement with the accepted values listed in table 1.

The phase diagram presented by Lundin and Yamamoto did not show the transformation of the δ-phase structure to the hcp structure. However, they con-

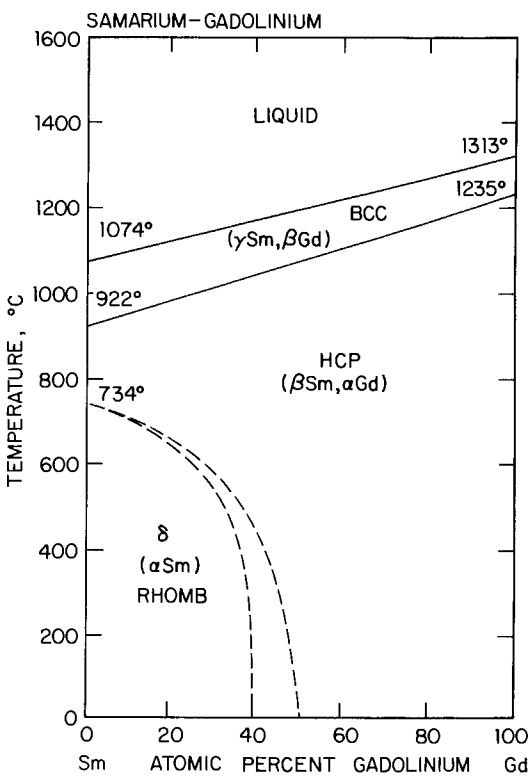

Fig. 69. Phase diagram of the samarium–gadolinium system.

cluded that based on their determination of the thermodynamic activities of the components in the Sm–Gd alloys and the state functions of mixing, the transition from the hcp to the δ-phase solid solution begins at 40 at% Gd. Other data that supported this conclusion were lattice parameters, atomic volumes, microhardness and metallographic observations. The δ-phase solid solution area in fig. 69 is bounded by a dashed line beginning at room temperature at the 40 at% Gd composition and curving upward to join the 100 at% Sm line at 734°C, the temperature listed in table 1 for the $\alpha \rightleftarrows \beta$ (rhomb $\rightleftarrows$ hcp) transition in samarium.

Torchinova et al. (1971) also studied the Gd–Sm phase system. The purity of their metals, their methods of alloy preparation and their methods of investigation were not disclosed. The partial phase diagram that they published is in reasonable accord with the diagram presented by Lundin and Yamamoto, except that Torchinova et al. suggest the δ-phase (αSm) phase exists from 0 to 58.1 at% Gd—a wider range than that reported by Lundin and Yamamoto, who give the range as 0 to 40 at% Gd. We believe the results of Lundin and Yamamoto are the more reliable because they made a more extensive study and probably had purer starting materials.

2.39.2. *Lattice spacings*

Lundin and Yamamoto (1967) reported lattice spacings for samarium, gadolinium and 11 alloy compositions in this system. Filings from their specimens were passed

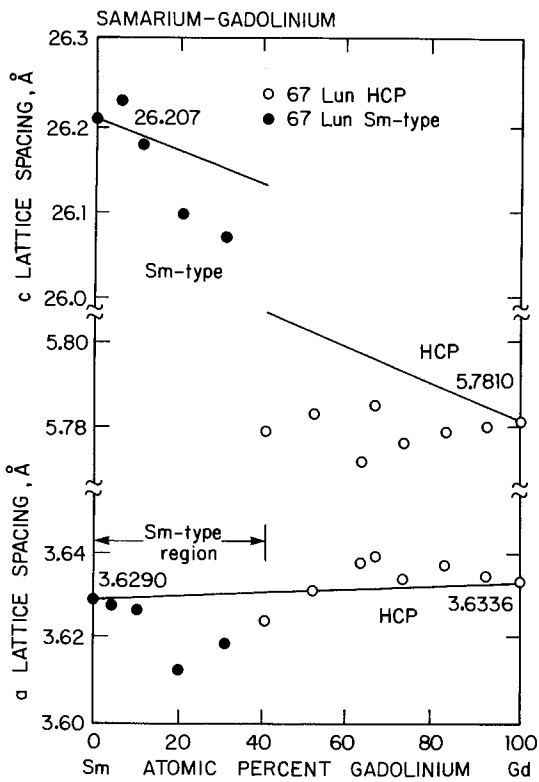

Fig. 70. Lattice spacings in the samarium–gadolinium system. The straight lines represent the Vegard's law relationships and are based on the accepted values for the pure metals as listed in table 2.

through a 325 mesh screen, sealed in Pyrex capsules under an inert atmosphere and annealed at 350°C for 24 hr to relieve stress. Since no mention of quenching was made in their report, it is assumed that their data apply to room temperature equilibrium conditions. The lattice spacings were calculated using a modified Cohen's least squares method. Their *a* and *c* lattice spacing data, as adjusted for the discrepancies between the accepted values for the spacings in the pure metals and the corresponding values reported by these authors, are plotted in fig. 70. The *a* lattice spacings of the δ-phase (Sm-type) alloys show a negative deviation from Vegard's law behavior at each composition while those in the hcp region show a positive deviation from about 50 to 100 at% Gd. The *c* lattice spacings of the alloys with hcp structure all show negative deviations as do most of the alloys with the δ-phase Sm structure. Although the authors state that the δ-phase solid solution field begins at 40 at% Gd, their alloy of this composition was indexed to fit the hcp-phase structure.

2.39.3. *Thermodynamic data*

Lundin and Yamamoto (1967) calculated thermodynamic activities of samarium in the hcp phase in the temperature range 800 to 1100°C from vapor pressure data obtained in Knudsen effusion studies. The activity of gadolinium was derived from the activity of samarium using the Gibbs–Duhem equation. These activities are presented in fig. 71 where a negative deviation from Raoult's law is evident for both metals. The authors concluded that the difference in crystal structure is responsible for the large negative deviation. This explanation is unreasonable since Sm and Gd both have the hcp structure (and so do all their intermediate compositions) at the temperature of measurement, 900°C (see fig. 69). A more likely explanation is that

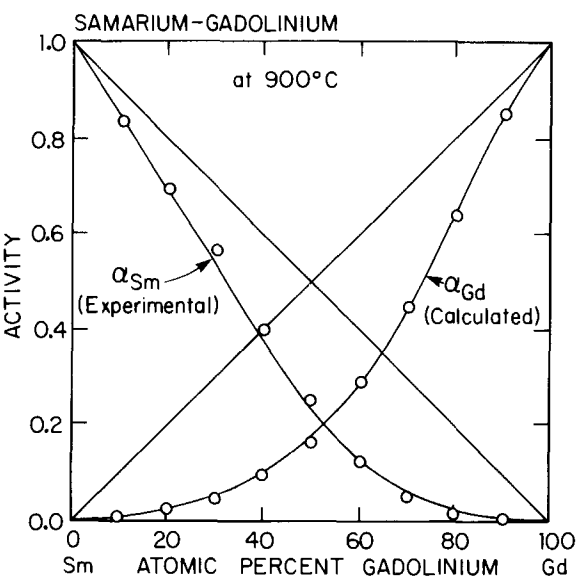

Fig. 71. Activities of alloys in the samarium–gadolinium system at 900°C. The straight diagonal lines represent ideal behavior as indicated by Raoult's law.

the negative deviations are due to the tendency of Sm to become divalent (see section 3.6).

Relative partial and integral free energies, enthalpies and entropies were calculated from the activity data. Integral free energies, enthalpies and entropies of mixing at 900°C are shown in fig. 72. The integral free energy of mixing is negative while the excess enthalpy and excess entropy are each positive with the maxima in either case occurring at 40 at% Gd. The authors postulated that the excess positive entropy may be due to a vibrational contribution caused by a strain in the lattice that is thought to arise from the impingement of the two different lattices of gadolinium and samarium. Lundin and Yamamoto also suggested that magnetic contributions may contribute due to the ferromagnetic character of gadolinium and its alloys at lower temperatures (< 20°C) and the transition to a paramagnetic state at higher temperatures. Neither of these explanations is reasonable because the temperature at which the measurements (900°C) were made is too high for these effects to have any importance. For the former, the crystal structure of Sm and Gd and all intermediate alloy compositions are the same (hcp) at 900°C (see fig. 69). For the latter, the magnetic transition occurs at room temperature or below. A more likely explanation is that these excess energies are due to the tendency toward divalency in samarium (see section 3.6).

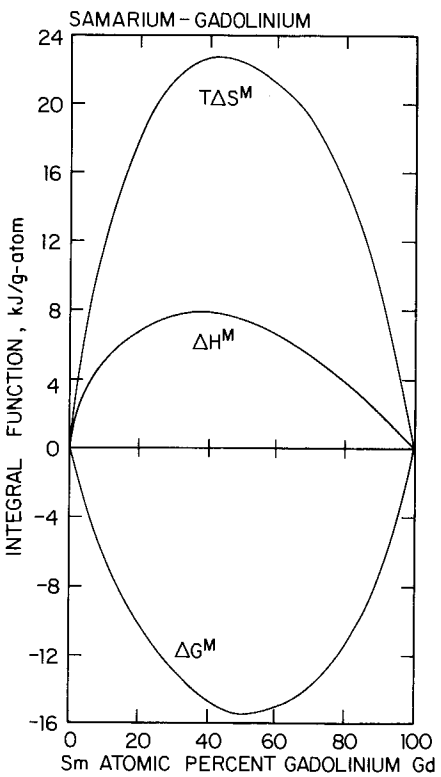

Fig. 72. Integral free energy, enthalpy and entropy of mixing for samarium–gadolinium alloys at 900°C.

References

Lundin, C.E. and A.S. Yamamoto, 1967, Final Report, Denver Research Institute, Rept. DRI-2437, University of Denver, Denver, CO.

Torchinova, R.S., V.F. Terekhova and E.M. Savitskii, 1971, in: Savitskii, E.M. and V.F. Terekhova, eds., Redkozemel. Metally i Splavy (Nauka, Moscow) p. 39 [English transl.: Rare Earth Metals and Alloys, AEC-tr-7408, National Technical Information Service, Springfield, VA 22151 (1974)].

2.40. *Sm–Y: Samarium–yttrium*

2.40.1. *Phase diagram*

Lundin and Yamamoto (1967), employing thermal analysis, metallography, X-ray diffraction, density and hardness studies and Knudsen effusion analysis, established phase equilibria and calculated thermodynamic properties for the Sm–Y system.

Lundin and Yamamoto formed their alloys from metals of "select purity". Major impurities in their samarium were: < 0.038 wt% O, 0.02 wt% Ca, 0.005 wt% each Ce, Nd, Pr, B, Si and Zn and 0.003 wt% Zr. Their yttrium metal contained 0.037 wt% O, 0.01 wt% each Er and Tb and 0.005 wt% each Ce, Ho, Tb, Pr, B and Si. Alloys were prepared at ~ 10 at% intervals and melted in sealed tantalum crucibles. Three or more melting cycles, well above the melting temperature, were performed before the thermal analysis of each alloy was carried out.

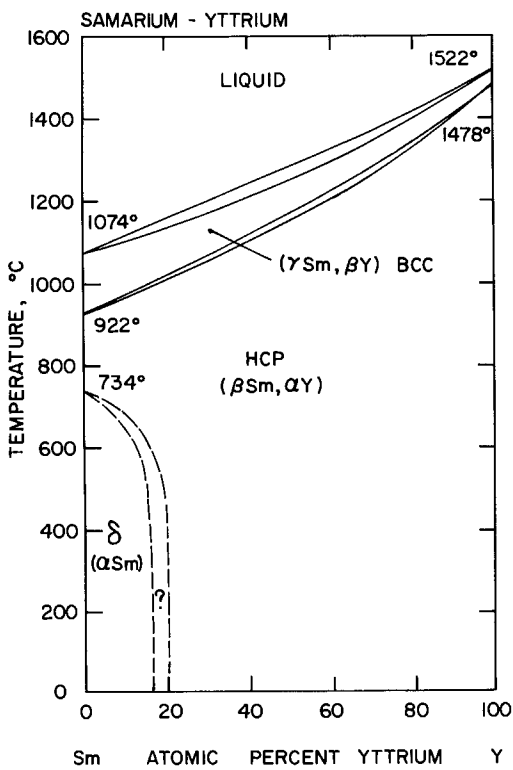

Fig. 73. Phase diagram of the samarium–yttrium system.

Lundin and Yamamoto presented a phase diagram for the high temperature (above 800°C) portion of this system based on their thermal analysis data. Their diagram showed relatively narrow gaps both between the liquidus and solidus lines and between the solvus lines that separate the bcc and the hcp fields. The upper portion of fig. 73 is a reproduction of their diagram with minor adjustments in the melting point and transition temperatures of the end-members to bring these temperatures into agreement with the accepted values for the pure metals as listed in table 1. Complete solubility was observed in the liquid phase in the bcc and hcp solid solutions. Although Harris and Raynor (1975), working with 99(wt?)% pure samarium and yttrium, found the composition range for the hcp structure to extend from 0 to 90 at% Sm, Lundin and Yamamoto, by microscopic examination of the microstructure, observed the appearance of the δ phase at about 80 at% Sm. An X-ray study over short intervals in this composition range showed that the transition from the hcp solid solution to the δ phase occurs abruptly between 80 and 81 at% Sm and no coexistence of the two was found in any of their X-ray patterns. However, a two-phase region has been found in similar intra rare earth systems, so fig. 73 was drawn with dashed lines enclosing a narrow two-phase region. As drawn, this postulated two-phase region is shown at room temperature at compositions between 16 and 20 at% Y and narrowing at higher temperatures until it meets the 100% Sm boundary at 734°C where pure Sm transforms from rhombohedral to hcp structure. All compositions on the Sm-rich side of the two-phase field have the rhombohedral Sm-structure below 734°C. It should be emphasized that the two-phase region has not been confirmed experimentally and should be the subject of further investigation.

2.40.2. *Lattice spacings*

Both the a and the c lattice spacing data presented by Lundin and Yamamoto (1967) and by Harris and Raynor (1975) are shown in fig. 74. The latter authors presented their lattice data in graphic rather than in tabular form and their values were retrieved by scaling their plot. Adjustments to the reported data were made by prorating deviations between the accepted values for the lattice spacings of the pure metals and the reported values for the corresponding end-members on the basis of the composition of the alloys. Since Harris and Raynor did not report lattice spacings for their samarium metal, adjustments to their data are based on the assumption that the deviation for their samarium is the same as for their yttrium metal. The adjusted data as plotted in fig. 74 show positive deviations from Vegard's law behavior for the a lattice spacings for all compositions except Lundin and Yamamoto's alloy containing 80 at% Y. The c lattice spacing data for the hcp structure alloys have a large deviation from the Vegard's law relationship, but the as-adjusted c spacing data from the two sources agree fairly well. In the Sm-type structure region, the c lattice spacing for the 10 at% Y alloy as reported by Lundin and Yamamoto has a large positive deviation. But a similar alloy composition, as reported by Harris and Raynor, has a large negative deviation, which is increased by the adjustment of the data. However, even the unadjusted value exhibits a large negative deviation.

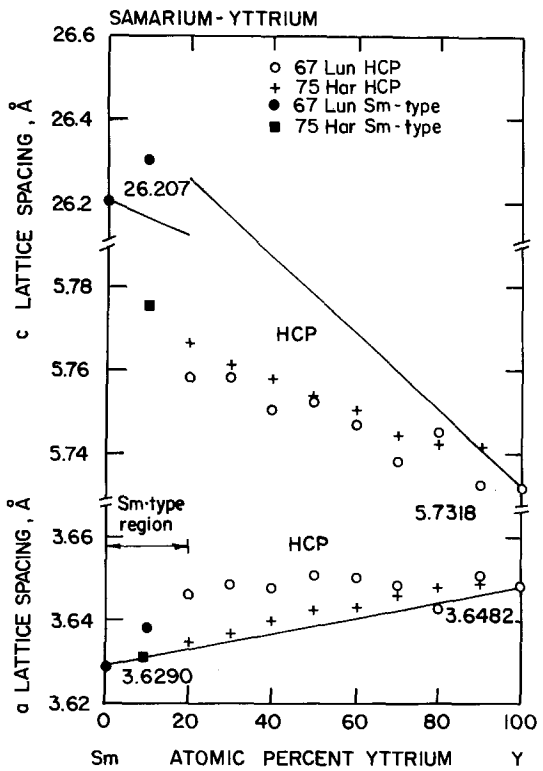

Fig. 74. Lattice spacings in the samarium–yttrium system. The straight lines represent the Vegard's law relationships for the various phases and are calculated from the accepted values for the pure metals shown in table 2.

2.40.3. *Thermodynamic data*

Lundin and Yamamoto (1967) conducted Knudsen effusion studies at 10 at% increments in the hcp region of the Sm–Y system. The high vapor pressure of samarium precluded an effusion study in the δ-phase region and Knudsen flow conditions were not valid in the temperature range of the bcc region. Since the vapor pressures of samarium and yttrium differ by several orders of magnitude, only the vapor loss for samarium was measured. Activity of samarium in the alloys was calculated from the vapor pressure data on the assumption that this vapor behaves as an ideal gas. The corresponding activity of yttrium at the same temperature was obtained through a graphical integration of the Gibbs–Duhem equation. Figure 75 shows their activity data for solid Sm–Y alloys at 900°C. A large negative deviation from ideality exists for each component and, based on comparison with the results for other systems, Lundin and Yamamoto concluded that the crystal structure difference between the components caused these deviations. This explanation is not reasonable since at the temperature of measurement the entire binary system from pure Sm to pure Y has the hcp structure (see fig. 73). A more reasonable explanation is proposed based on the tendency of Sm to become divalent (see section 3.6).

Partial molal free energies, enthalpies and entropies were calculated from the activity data. The integral free energy, enthalpy and entropy of mixing were

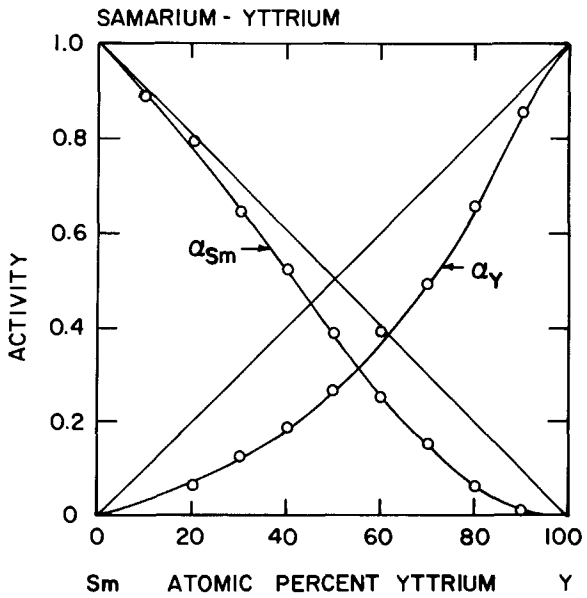

Fig. 75. Activity of samarium and yttrium in solid samarium–yttrium alloys at 900°C.

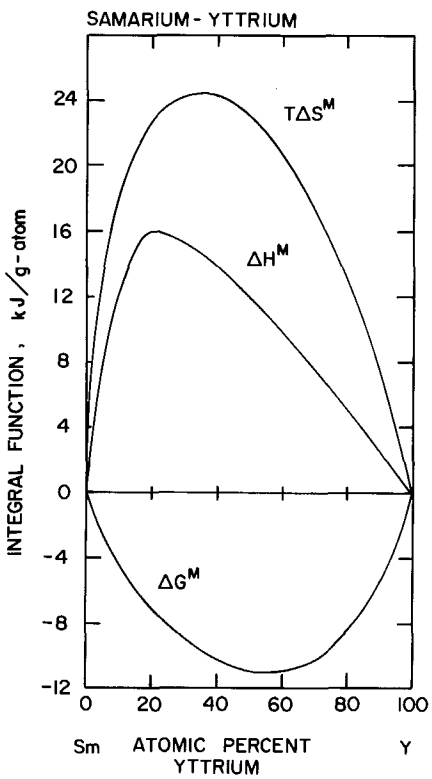

Fig. 76. Integral free energy, enthalpy and entropy of mixing for samarium–yttrium alloys at 900°C.

calculated from the partial quantities at 900°C and are shown in fig. 76 where the entropy is presented as $T\Delta S$ so that the plots can be drawn using the same energy scale. Asymmetry exists in the enthalpy and entropy plots toward the Sm-rich region. The maxima of these curves occur in the region where the stacking sequence changes from hcp to δ-phase solid solutions at lower temperatures, < 700°C. The authors conclude that the strain due to the mismatch in lattices at the point of transition in the solid solution is the major contributor to excess energy. This explanation is not likely since at the temperature of measurement the alloys from pure Sm to pure Y have the hcp structure. This excess energy is probably due to the tendency of Sm to be divalent (see section 3.6).

References

Harris, I.R. and G.V. Raynor, 1975, J. Less-Common Met. **43**, 147.
Lundin, C.E. and A.S. Yamamoto, 1967, Final Report, Denver Research Institute Rept. DRI-2437, University of Denver, Denver, CO.

2.41. *Eu–Ho: Europium–holmium*

2.41.1. *Phase relationships*

Savitskii et al. (1967) attempted to prepare four alloys in the europium–holmium system with compositions ranging from 0 to 51 at% Eu (49 wt% Eu). Despite a protective atmosphere of argon in their arc furnace, the high vapor pressure of these metals, particularly europium, caused a large weight loss to occur and the final compositions contained significantly less europium than was present in the original weighed-out samples. The weight loss was determined to be about 20 wt% in pure holmium metal and 50 wt% in the alloy that had 51 at% Eu in the original batch. The as-cast alloys were reported to be single phase with many oxide inclusions. Savitskii et al. stated that alloys in this system are characterized by high mutual solubility in the liquid and solid states. However, in view of the difficulty in preparing Eu–Ho alloys and the fact that the size disparity between divalent Eu and trivalent Ho is 15.5%, it is quite unlikely that much Eu is soluble in solid Ho as implied by Savitskii et al. Their assumption of a continuous series of solid solutions of a high temperature bcc modification is wrong since Spedding et al. (1973) showed that holmium does not have a bcc form.

References

Savitskii, E.M., V.F. Terekhova and R.S. Torchinova, 1967, Metalloved. Term. Obrab. Met. [2], 25 [English transl.: Met. Sci. Heat Treat. [1/2], 100].
Spedding, F.H., B. Sandeen and B.J. Beaudry, 1973, J. Less-Common Met. **31**, 1.

2.42. *Eu–Yb: Europium–ytterbium*

2.42.1. *Phase relationships*

Savitskii et al. (1967) presented a photomicrograph showing the structure of a Yb–33 at% Eu alloy which appears to be a single-phase alloy. No details were given on the purity of their metals nor on the preparation treatment of this specimen. King

and Harris (1970) investigated the effect of pressure on the electrical conductivity of a series of alloys in the Eu–Yb system up to 8.0 GPa. Their Eu metal contained < 1 wt% other rare earth metals while their Yb metal contained < 0.1 wt% other rare earth metals. Each contained ~ 0.02 wt% "other base metals". Alloys were arc-melted under argon, homogenized one week at 500°C, then examined by X-ray diffraction. In the composition range 60 to 100 at% Yb, alloys had the fcc structure at 500°C and in the range 0 to 50 at% Yb, alloys had bcc structure at that temperature. Legvold and Beaver (1979), who made magnetization measurements on as-cast alloys containing 60 to 90 at% Yb reported that alloys in this composition range had fcc structure. This is in good agreement with the results of King and Harris.

2.42.2. *Phase relationships as a function of pressure*

King (1969) measured electrical resistance as a function of pressure on alloys in the Yb-rich portion of the Eu–Yb system. Alloys in this system were difficult to prepare because of the volatility of europium and so it was necessary to confirm the compositions on the basis of lattice spacing data, none of which were presented in King's paper. Additions of europium lowered the fcc(β) $\rightleftarrows$ bcc(γ) transformation that occurred at 3.94 GPa for pure ytterbium to ~ 3.1 GPa for the 70 at% Yb alloy.

References

King, E., 1969, Atomic Energy Research Establishment Rept. AERE-R5954, Harwell.
King, E. and I.R. Harris, 1970, J. Less-Common Met. **20**, 237.
Legvold, S. and J.P. Beaver, 1979, Solid state Commun. **31**, 727.
Savitskii, E.M., V.F. Terekhova and R.S. Torchinova, 1967, Metalloved. Term. Obrab. Met. [2], 25 [English transl.: Met. Sci. Heat Treat. [1/2], 100].

2.43. *Eu–Sc: Europium–scandium*

2.43.1. *Phase relationships*

No experimental data for the europium–scandium phase diagram were found. However, Miedema (1976), using Gschneidner's (1969) value for the energy difference between divalent and trivalent europium (96 kJ/g-at) found his method would account for the known information on the valence state of europium in intermetallic compounds. The application of his thermodynamic calculations to the europium–scandium alloy system predicted that no stable compounds exist in this system.

A complicating factor in an investigation of the Eu–Sc alloy system is the fact that the melting point of scandium (1541°C, see table 1) is 14°C higher than the boiling point of europium (1527°C see table 4).

References

Gschneidner, K.A., Jr., 1969, J. Less-Common Met. **17**, 13.
Miedema, A.R., 1976, J. Less-Common Met. **46**, 176.

2.44. *Eu–Y: Europium–yttrium*

2.44.1. *Phase relationships*

No experimental data for the europium–yttrium phase diagram were found. However, Miedema (1976), using Gschneidner's (1969) value for the energy difference between divalent and trivalent europium (96 kJ/g-at), found his method would account for the known information on the valence state of europium in intermetallic compounds. The application of his thermodynamic calculations to the europium–yttrium alloy system predicted that no stable compounds exist in this system.

An investigation of the europium–yttrium alloy system would be complicated by the fact that the melting point of yttrium (1522°C, see table 1) is only 5°C below the boiling point of europium (1527°C, see table 4).

References

Gschneidner, K.A., Jr., 1969, J. Less-Common Met. **17**, 13.
Miedema, A.R., 1976, J. Less-Common Met. **46**, 176.

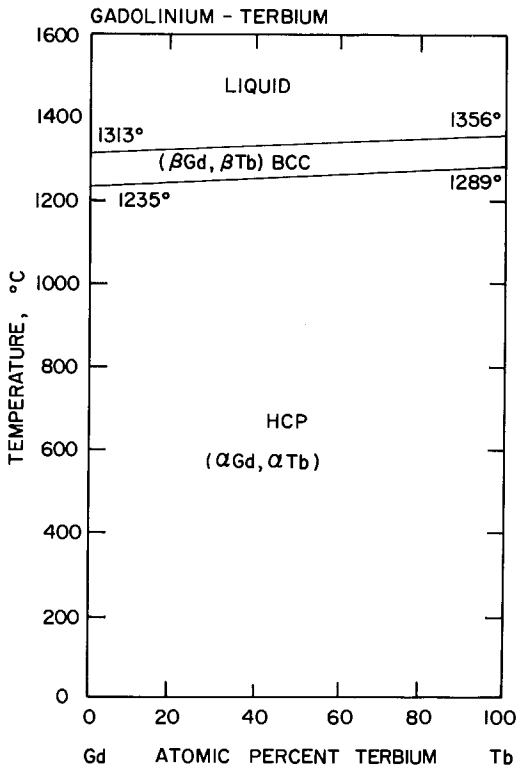

Fig. 77. Phase diagram of the gadolinium–terbium system.

2.45. *Gd–Tb: Gadolinium–terbium*

2.45.1. *Phase diagram*

Burov et al. (1964) have investigated the Gd–Tb phase system using thermal analysis, metallography, X-ray diffraction, hardness, electrical resistivity and magnetic susceptibility. Their starting materials were 98.5 to 99.0 wt% pure. Alloys were prepared in an arc furnace and were annealed 50 hr at 1000°C. Complete solid solubility was observed for the low temperature allotrope. The phase diagram which they presented showed a slight gap between nearly linear liquidus and solidus lines as well as between nearly linear solvus lines for the hcp ⇄ bcc transformation. Savitskii et al. (1965) presented an identical phase diagram for this system, but with no information regarding purity of materials or the procedure used. It appears to be based on the same research as reported by Burov et al. It was shown in section 2.1.1 that when highly pure (99.9+ at% pure) trivalent lanthanide metals that have atomic numbers that differ by no more than four are alloyed, the liquidus–solidus line is a straight line connecting the melting points of the pure metals, and the same relationship is true for the high temperature transformation from hcp to bcc structures. Gadolinium and terbium satisfy the requirements for this behavior and therefore fig. 77 has been drawn to show the relationships that would be expected with high purity metals. Although Burov et al. did not use metals that approached

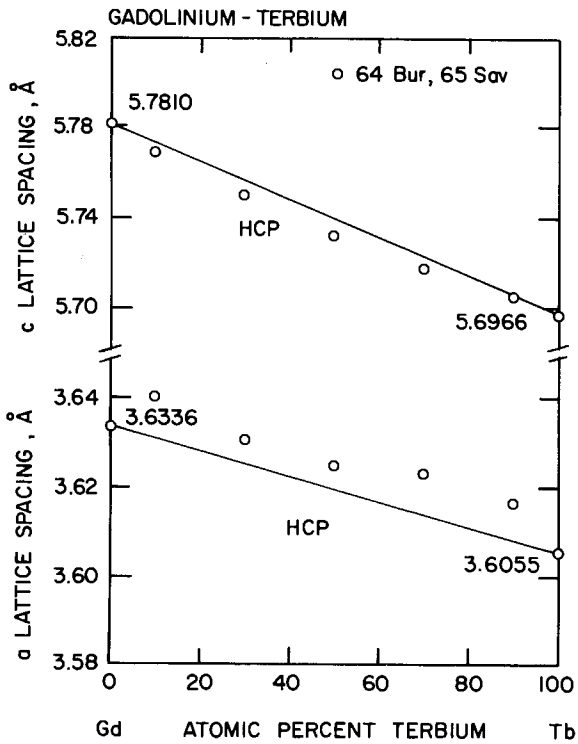

Fig. 78. Lattice spacings in the gadolinium–terbium system. The straight lines represent the Vegard's law relationships for the *a* and *c* lattice spacings and are based on the accepted values for the pure metals as listed in table 2.

this purity, their results were surprisingly close to this behavior. The temperature for the melting and transformation points of the pure metals have been adjusted to conform with table 1.

2.45.2. *Lattice spacings*

Burov et al. (1964) and Savitskii et al. (1965) presented lattice spacing data for the Gd–Tb system in the form of a graph and did not list their data. The data shown in fig. 78 were obtained by scaling their plot, converting from kX to Å units, then prorating the deviations between their values for the *a* and *c* lattice spacings for the end-members and the accepted values listed in table 2 to each alloy on the basis of composition. The adjusted data show a positive deviation from the Vegard's law relationship in the *a* lattice spacing at all compositions. The *c* lattice spacings show a slight negative deviations from Vegard's law behavior.

References

Burov, I.V., V.F. Terekhova and E.M. Savitskii, 1964, Zh. Neorg. Khim. **9**, 2036 [English transl.: Russ. J. Inorg. Chem. **9**, 1100].

Savitskii, E.M., V.F. Terekhova and I.V. Burov, 1965, Izv. Akad. Nauk SSSR, Neorg. Mater. **1**, 1648 [English transl.: Inorg. Mater. **1**, 1503].

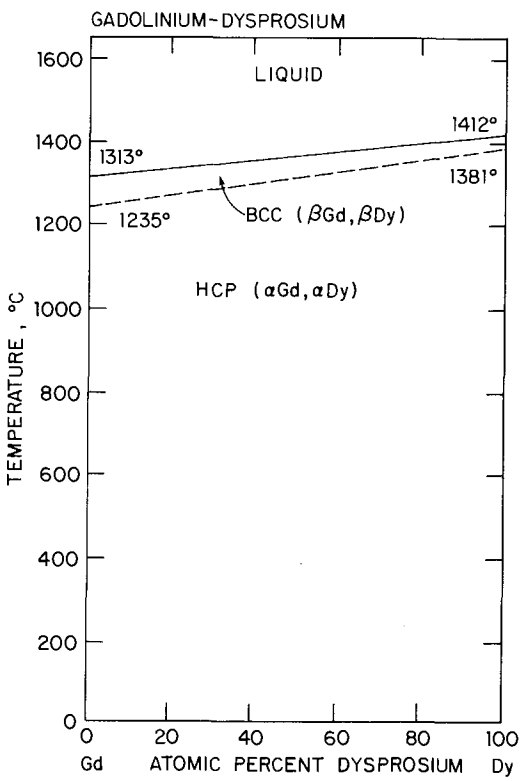

Fig. 79. Phase diagram for the gadolinium–dysprosium system.

2.46. *Gd–Dy: Gadolinium–dysprosium*

2.46.1. *Phase diagram*

Markova et al. (1971) reproduced the phase diagram for the Gd–Dy system and two other binary rare earth alloy systems in a report dealing with alloys of the lanthanide metals and yttrium, but did not reveal the source of their diagrams. Levitin et al. (1974) also showed this phase diagram and cited Markova et al. Details of the investigation that produced these diagrams were not found.

The phase diagram for the Gd–Dy system as presented by Markova et al. showed six data points that formed a smooth curve defining the solidus of the system. This solidus has a slight downward curvature and the liquidus was drawn as a dashed straight line that connected the melting points of the end-members. Dashed solvus lines having a small gap between them indicated the probable temperature–composition relationship for the hcp ⇄ bcc transformation but no data were presented in support of these lines.

Dysprosium and gadolinium are both trivalent lanthanide metals with atomic numbers that differ by 2 ($Z = 66$ and 64, respectively). Therefore, when prepared from high purity metals, alloys in this system would be expected to exhibit ideal behavior (see section 2.1.1). The phase diagram for the Gd–Dy system, shown in fig. 79, reflects the expected phase relationships for alloys prepared from high purity

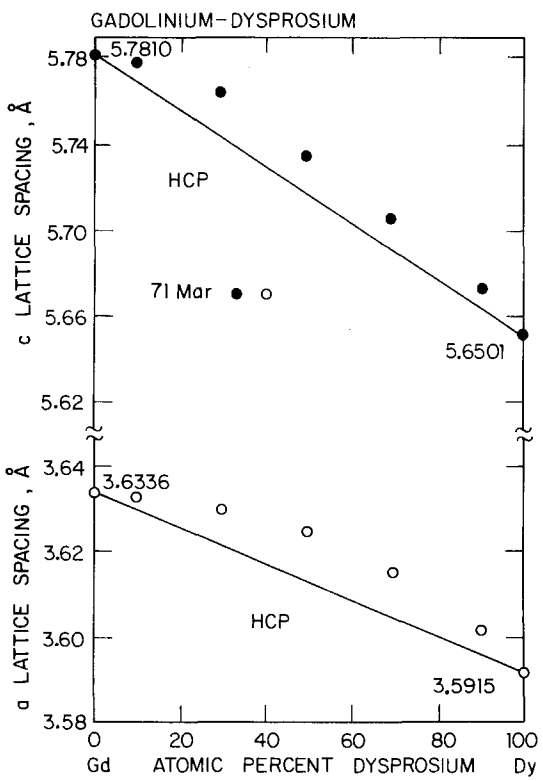

Fig. 80. Lattice spacings in the gadolinium–dysprosium system. The straight line in each section represents the Vegard's law relationship based on the accepted values for the pure metals listed in table 2.

(99.9+ at% pure) materials. Less pure alloys would be expected to perform more in accord with the diagram of Markova.

2.46.2. *Lattice spacings*

Markova et al. (1971) presented a plot of the *a* and *c* lattice spacings in the Gd–Dy system. The data shown in fig. 80 were obtained by scaling their plot. Their dysprosium metal has an *a* spacing that is close to the corresponding value in table 2, but the *c* spacing for dysprosium and both the *a* and *c* spacings for gadolinium show large negative deviations from the accepted values for the pure metals. Therefore, their data were adjusted to bring the lattice spacings of the end-members into agreement with the accepted values for the pure metals. The adjusted data, as shown in fig. 80, deviate in a positive direction at all compositions for both the *a* and the *c* lattice spacings.

References

Levitin, R.Z., E.M. Savitskii, V.F. Terekhova, O.D. Chistyakov and V.L. Yakovenko, 1974, in: Savitskii, E.M., ed., Splavy Redkikh Metallov s Osobymi Fizicheskimi Svoistvami [Alloys of Rare Earth Metals with Special Properties] (Nauka, Moscow) p. 100.

Markova, I.A., R.S. Torchinova, V.F. Terekhova and E.M. Savitskii, 1971, in: Ageev, N.V. and O.S. Ivanov, eds., Diagrammy Sostoyaniya Metallicheskikh Sistem [Constitutional Diagrams of Metallic Systems] (Nauka, Moscow) p. 170.

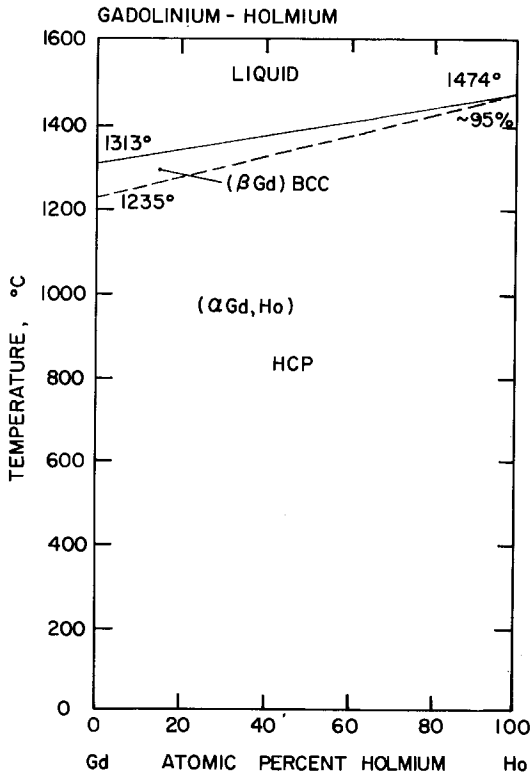

Fig. 81. Phase diagram for the gadolinium–holmium system.

2.47. *Gd–Ho: Gadolinium–holmium*

2.47.1. *Phase diagram*

Markova et al. (1971), in a report on the nature of alloys of rare earth metals with yttrium, presented a phase diagram for the gadolinium–holmium system. No details were given on the source of this diagram, the purity of the metals from which the alloys were made or the methods of investigation. The plot indicated five alloy compositions plus the gadolinium and holmium end-members. The data points shown on their phase diagram lie on a nearly straight line that defines the solidus. The liquidus and the solvus lines are drawn with dashes and no supporting data are shown. This diagram indicates complete solid solubility across the composition range from 0 to 100% Ho for both α(hcp) and β(bcc) phases. However, Spedding et al. (1973) have shown conclusively that high purity holmium does not have a bcc form despite earlier published results on less pure metals that suggested a high temperature transformation. The phase diagram for the Gd–Ho system presented in fig. 81 has been drawn to reflect the behavior of high purity metals. The phase boundary for the hcp $\rightleftarrows$ bcc transformation is shown by a dashed line beginning at 1235°C, the temperature for this transition in pure gadolinium, and intersecting the liquidus–solidus line somewhere near 95 at% Ho. This construction conforms to that

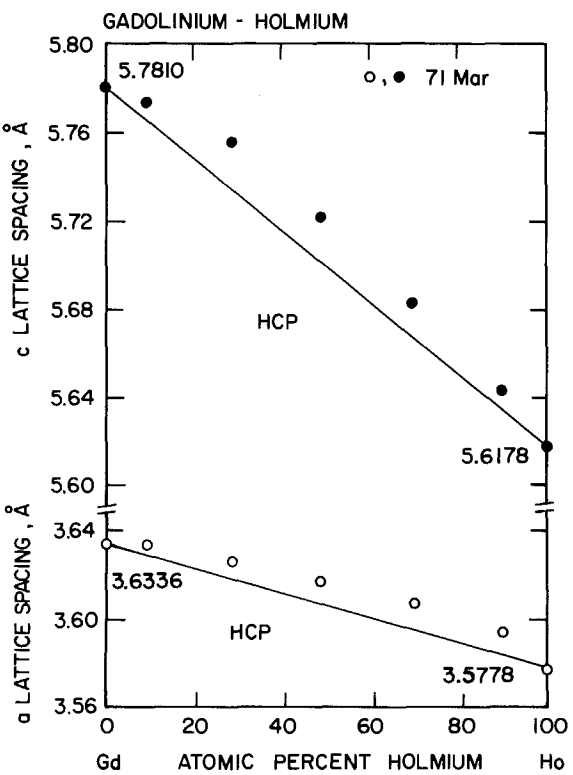

Fig. 82. Lattice spacings in the gadolinium–holmium system. The straight line in each section represents the Vegard's law relationship and is based on the accepted values for the pure metals listed in table 2.

observed by Spedding et al. for the related Tb–Ho and Dy–Ho alloy systems (see sections 2.54.1 and 2.60.1).

2.47.2. *Lattice spacings*

Markova et al. (1971) presented some data on the a and c lattice spacings in the Gd–Ho system in the form of a graph. Figure 82 is a plot of their data, which were obtained by scaling their plot and adjusting the results to bring the lattice spacings of the end-members into agreement with the accepted values for the pure metals as shown in table 2. Their values for the a and c lattice spacings of gadolinium and the c lattice spacing of holmium had large negative deviations from the accepted values for the pure metals. The values for the lattice spacings of the intermediate compositions were accordingly adjusted. Positive deviations from Vegard's law behavior for all of the alloy compositions are noted.

References

Markova, I.A., R.S. Torchinova, V.F. Terekhova and E.M. Savitskii, 1971, in: Ageev, N.V. and O.S. Ivanov, eds., Diagrammy Sostoyaniya Metallicheskikh Sistem [Constitutional Diagrams of Metallic Systems] (Nauka, Moscow) p. 170.

Spedding, F.H., B. Sandeen and B.J. Beaudry, 1973, J. Less-Common Met. **31**, 1.

2.48. *Gd–Er: Gadolinium–erbium*

2.48.1. *Phase diagram*

Burov et al. (1964) investigated phase equilibria in the Gd–Er system by using alloys made from 98.5 to 99.0 wt% pure metals. Specimens weighing 8 to 10 g were prepared in an arc furnace. Alloys were annealed at 1000°C for 50 hr. Their phase diagram was established by means of thermal analysis, X-ray diffraction, metallography, and measurements of hardness, electrical resistivity and magnetic properties. Their analyses showed that the Gd–Er phase diagram is characterized by a continuous region of single-phase (hcp) solid solution. The high temperature region of their diagram consisted of a slightly wavy solidus line drawn through six data points across the diagram. The liquidus was indicated by a wavy dashed line that formed a narrow gap with the solidus. Another dashed line below the solidus indicated a solvus line for the hcp $\rightleftarrows$ bcc transformation. This dashed solvus line extended from the transformation temperature in gadolinium to an intersection with the solidus line at about 68.7 at% Er.

Savitskii et al. (1965) also discussed this system in a review article but did not reveal details of the investigation or show the phase diagram. They did present a diagram for the Gd–Tb system, which they stated was similar to the Gd–Er system.

It has been shown in section 2.1.1. that when high purity (+99.9 at%) trivalent rare earth metals are alloyed, ideal behavior may be expected provided the atomic numbers of the component metals differ by no more than ± 4. The Er–Gd system fits these criteria, so fig. 83 was drawn to show the behavior expected of pure metals. It was demonstrated by Spedding et al. (1973) that Er does not have a high temperature bcc structure and when alloyed with a lanthanide metal that has a high temperature bcc form, the solvus transformation temperature line in the system

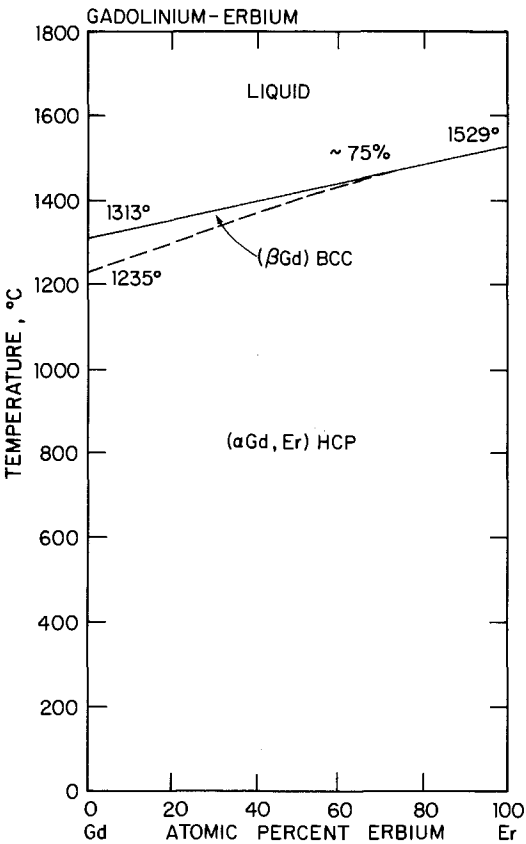

Fig. 83. Phase diagram of the gadolinium–erbium system.

intersects the solidus line at a composition where the alloy has an effective atomic number slightly below that of holmium ($Z = 67$). In this particular case for the Er–Gd system, that composition would be 75 at% Er. This construction of the phase diagram for the Gd–Er system is in good agreement with the diagram presented by Burov et al. considering the low purity of their metals.

2.48.2. *Lattice spacings*

Lattice spacings in the Gd–Er system from three sources are shown in fig. 84. The lattice spacings from the investigation by Burov et al. (1964) were obtained by scaling their plot. These data, as presented here, have been adjusted by prorating the differences between the observed lattice spacings for gadolinium and erbium and the accepted values for these pure metals as shown in table 2 to each alloy on the basis of composition. Smidt and Daane (1963) measured lattice spacings on four Gd–Er alloys that had been arc-melted under an argon atmosphere. These data are also presented in fig. 84 as adjusted to bring the lattice spacings of their pure metals into agreement with table 2. McWhan and Stevens (1967), who measured magnetic properties of several rare earth alloys as a function of pressure, included lattice

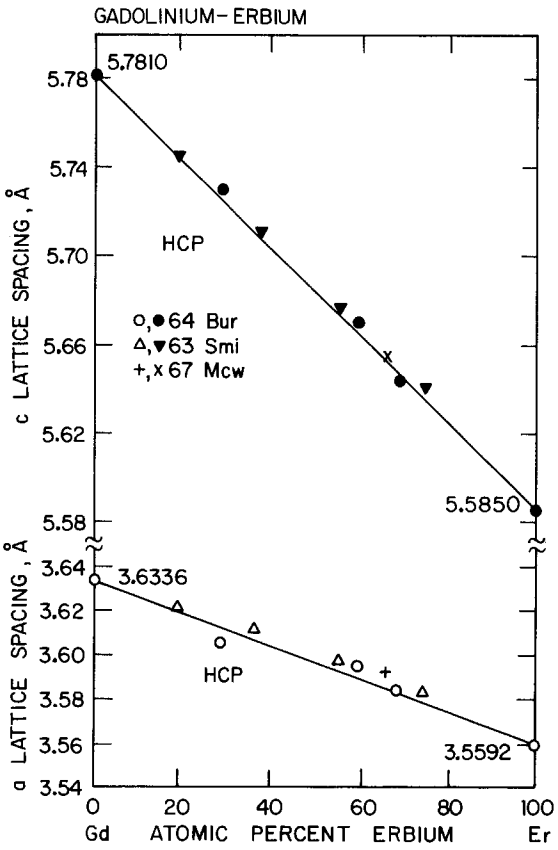

Fig. 84. Lattice spacings in the gadolinium–erbium system. The straight lines indicate the Vegard's law relationships in each section based on the accepted values for the pure metals as listed in table 2.

constant data on a 65.7 at% Er alloy in terms of the ratio of the spacings for the alloy to those of pure terbium. Since they did not show their values for pure terbium, the ratios for this alloy were multiplied by the accepted values for terbium as listed in table 2.

All of the above data, which are graphed in fig. 84, fall fairly close to the lines that depict the Vegard's law relationship. Only two points, *a* spacing for the ~ 28 at% Er alloy of Burov et al. and their *c* spacing for the ~ 68 at% Er alloy, show a negative deviation. All other data points fall on the Vegard's law line or show a small positive deviation.

References

Burov, I.V., V.F. Terekhova and E.M. Savitskii, 1964, Zh. Neorg. Khim. **9**, 2036 [English transl.: Russ. J. Inorg. Chem. **9**, 1100].

McWhan D.B. and A.L. Stevens, 1967, Phys. Rev. **154**, 438.

Savitskii, E.M., V.F. Terekhova, I.V. Burov and O.P. Naumkin, 1965, in: Eyring, L., ed., Rare Earth Research III (Gordon and Breach, New York) p. 301.

Smidt, F. A., Jr. and A.H. Daane, 1963, J. Phys. Chem. Solids **24**, 361.

Spedding, F.H., B. Sandeen and B.J. Beaudry, 1973, J. Less-Common Met. **31**, 1.

2.49. *Gd–Yb: Gadolinium–ytterbium*

2.49.1. *Phase diagram*

Beaudry and Spedding (1974) investigated phase relationships in the Gd–Yb system by means of thermal analysis, electron microprobe, metallography, X-ray diffraction and chemical analysis. The gadolinium metal contained the following impurities (in at ppm): 1050 O, 157 C, 155 H, 45 N, 33 F and 20 each Al, Cl, La and Ta. The impurities in their ytterbium metal included (in at ppm): 2570 H, 324 O, 210 Cl, 80 Ca, 62 N, 30 Dy, 29 C, 22 Fe and 20 each Mg and Lu.

The phase diagram presented by Beaudry and Spedding is shown in fig. 85. They observed that the solubility of ytterbium in gadolinium ranges from 6.5 at% at 500°C to 19 at% at 1161°C. The addition of ytterbium lowers the β(bcc) $\rightleftarrows$ α(hcp) transformation temperature of gadolinium by means of an inverted peritectic reaction at 20 at% Yb and 1161°C and lowers the melting point of gadolinium to a monotectic horizontal at 1183°C. This horizontal extends from 21 to 71 at% Yb. Solid solubility of gadolinium in ytterbium ranges from 0.2 at% at 500°C to 2.3 at% at 822°C. Beaudry and Spedding's phase diagram also shows that the melting point of ytterbium is raised 3°C by the addition of gadolinium. The melting point of ytterbium was reported to be 3°C lower than the accepted value, see table 1, and thus the melting point and the γYb peritectic horizontal were raised by this amount in fig. 85.

The addition of gadolinium to ytterbium also lowered the γ(bcc $\rightleftarrows$ β(fcc) transformation temperature from 795 to 780°C. Solubility of gadolinium in liquid ytterbium was found to be quite low, ranging from 1.6 at% at 850°C to 12.3 at% at 1150°C.

The intermediate compositions in this system form two phases. The authors concluded that the tendency to form trivalent ytterbium in gadolinium is small. Although X-ray diffraction measurements were used in this investigation, the only lattice spacing data reported were plots of a vs. at% Yb for several compositions that had been heat-treated and quenched from 500, 750 and 810°C to establish the solubility of gadolinium in ytterbium at these temperatures.

Reference

Beaudry, B.J. and F.H. Spedding, 1974, Metall. Trans. **5**, 1631.

2.50. *Gd–Lu: Gadolinium–lutetium*

2.50.1. *Phase relationships*

Smidt (1962) investigated electrical resistivity of several rare earth alloys including the Gd–Lu system. His investigation established the existence of complete solid solubility for the hcp phase (αGd and Lu) of this system. But since there is no high temperature bcc phase for lutetium, the βGd phase must terminate somewhere in the Gd–Lu system; we estimate it to be ~ 40 at% Lu (see section 3.3).

2.50.2. *Lattice spacings*

Smidt and Daane (1963) reported lattice spacings for gadolinium and lutetium metals and for four alloy compositions in this system. According to the chemical

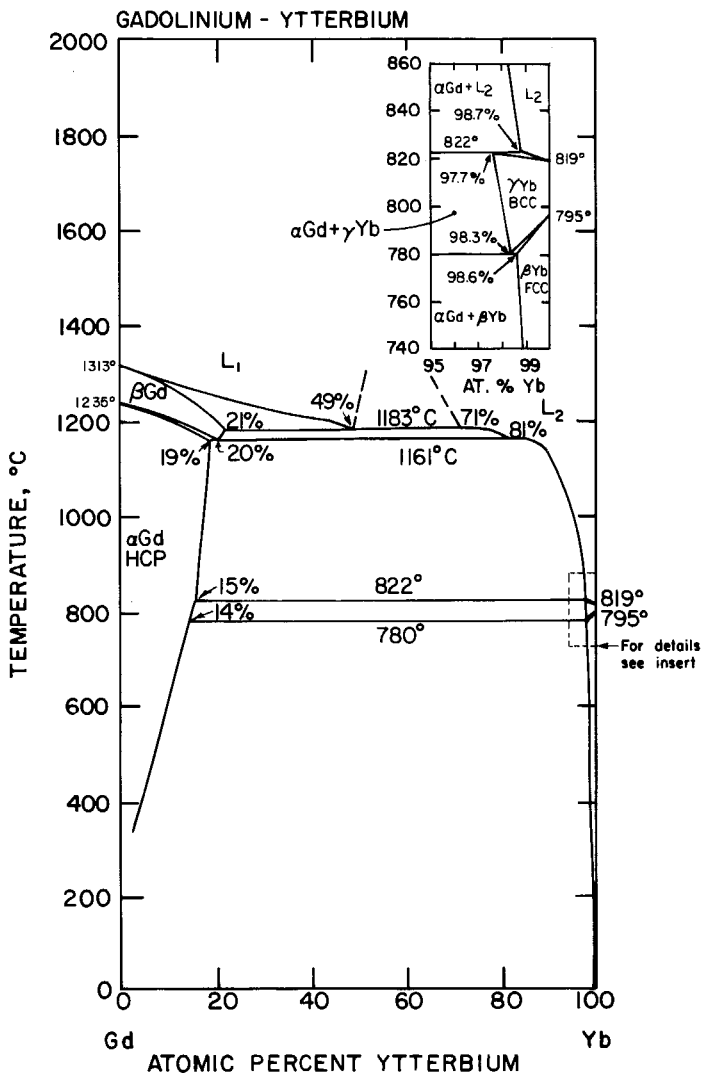

Fig. 85. Phase diagram of the gadolinium–ytterbium system.

analysis reported by Smidt (1962), the principal impurities in their lutetium (in wt ppm) were: 800 N, 735 O, 300 Mg, 250 Si, 200 Ca, 106 C, 50 Fe, 48 F and 70 other rare earth metals. The gadolinium metal contained 1150 wt ppm O, 500 Ta, 250 Si, 200 Mg, 170 F, 160 C, 150 Fe, 147 N, 50 Ca and 1110 total other rare earth metals. As would be expected from the chemical analysis there were significant differences between the accepted *a* and *c* lattice spacings that they listed for their metals and the accepted values for the pure metals as listed in table 2. The lattice spacings that they reported for their alloys were adjusted by prorating the deviations in the corresponding spacings of the end-members according the mole fraction of

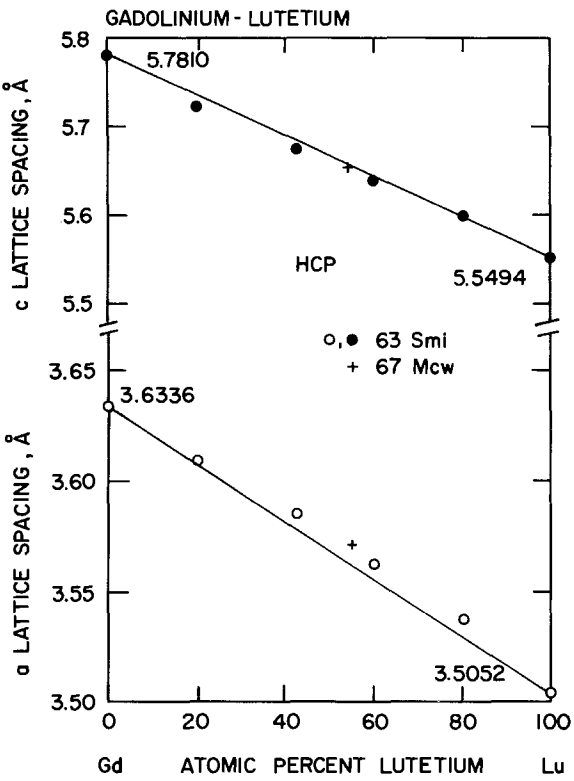

Fig. 86. Lattice spacings in the gadolinium–lutetium system. The straight lines show the Vegard's law relationships and are based on the accepted values for the pure metals as listed in table 2.

each metal in the alloys. These modified data are plotted in fig. 86 where the spacings of the alloys can be compared with the ideal behavior indicated by Vegard's law. A small positive deviation from ideal behavior exists for the *a* lattice spacings and a small negative deviation exists in the *c* lattice spacings for the Gd-rich alloys. This plot also shows lattice spacings reported by McWhan and Stevens (1967) for a Gd–55 at% Lu alloy. These authors reported their lattice spacings in terms of the ratio of the spacing for this alloy to the corresponding spacing of terbium. In evaluating their parameters, the accepted values for pure terbium (table 2) were employed. Bauminger et al. (1975) reported a set of lattice spacings for $Gd_{0.03}Lu_{0.97}$ measured at 30 K. Their values exhibit a small deviation from the room temperature Vegard's law lines despite the low temperature of the measurement.

2.50.3. *Thermodynamic data*

Kogan et al. (1971) measured heat capacity of magnetic Gd–Lu alloys in the 0.06 to 0.16 K range. Specimens having 10, 25, 40, 55, 70, 85 and 90% Lu were used. The heat capacity of the alloys was described by the relationship

$$C = AT + B/T^2,$$

where the first term corresponds to the electronic and the second to the nuclear hyperfine heat capacity.

References

Bauminger, E.R., A. Diamant, I. Felner, I. Nowik and S. Ofer, 1975, Phys. Rev. Lett. **34**, 962.
Kogan, A.V., E.I. Nikulin and Yu. B. Patrikeev, 1971, Fiz. Tverd. Tela **12**, 1969 [English transl.: Sov. Phys.—Solid State **12**, 1565].
McWhan, D.B. and A.L. Stevens, 1967, Phys. Rev. **154**, 438.
Smidt, F.A., Jr., 1962, Ph.D. thesis, Iowa State University, Ames, IA.
Smidt, F.A., Jr. and A.H. Daane, 1963, J. Phys. Chem. Solids **24**, 361.

2.51. *Gd–Sc: Gadolinium–scandium*

2.51.1. *Phase diagram*

Beaudry and Daane (1964) investigated the gadolinium–scandium system using thermal and X-ray methods. Impurities in their gadolinium after distillation were (in ppm): 500 O, 800 F, < 500 Ta, 200 Fe, 100 each Si and Cr, < 50 Ca, 40 N and 25 Mg. The scandium metal, after distillation, contained (in ppm), 800 O, 475 F, 250 Ta, 180 Fe, 125 Mg, 50 Si, < 50 Cr, 30 each Al and N, and ~ 10 Ca. Weighed portions of the two metals were melted in an arc furnace under an atmosphere of

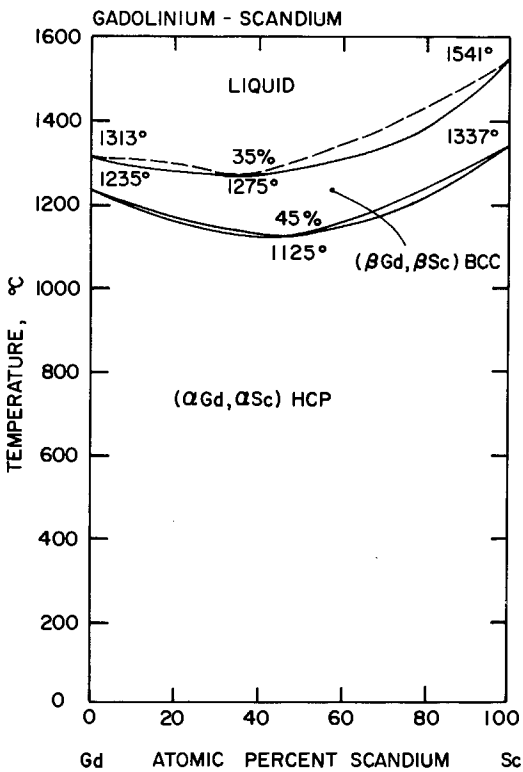

Fig. 87. Phase diagram of the gadolinium–scandium system.

purified argon or helium, then inverted and remelted several times. To further improve homogeneity, the alloys were wrapped in tantalum foil, sealed in quartz capsules and held at 1150°C for 15 hr, then cooled at the rate of 8°C/min. Filings for X-ray diffraction analysis were taken from these annealed alloys, sealed in tantalum capsules under helium and again annealed at 800°C for 15 hr followed by slow cooling.

The phase diagram for the Gd–Sc system, presented in fig. 87, is taken from the work of Beaudry and Daane. The melting point and the $\alpha(\text{hcp}) \rightleftarrows \beta(\text{bcc})$ transformation temperatures of scandium were each raised 2°C to bring them into conformity with the accepted values listed in table 1. The melting temperature of gadolinium was raised 3°C for the same reason. The solidus line was established by Beaudry and Daane using an optical pyrometer method. Since no data were obtained on the liquidus, it was presented as a dashed line. The transformation temperatures for the alloys were established by differential thermal analysis. Complete solubility exists in all three single-phase regions: the liquid state, the bcc high temperature region, and in the hcp region that exists at lower temperatures.

Lundin (1966) included Gd–Sc alloys in his investigation of the nature of the formation of the Sm-type structure in binary alloys composed of light and heavy rare earths. Since no Sm-type structure was observed by Lundin in any of his alloys, no further effort was spent on this system. He observed complete solid solubility in this system, which is consistent with the findings of Beaudry and Daane.

Shiflet et al. (1979) attempted to use the Kaufman method to calculate the Gd–Sc phase diagram but, as with Nd–Sc (see section 2.37.1), the results were not satisfactory. The composition of the congruently melting bcc phase was predicted with fair accuracy but the melting temperature was 150°C low. Also, the calculated two-phase liquid + bcc region overlapped the calculated two-phase bcc + hcp field.

2.51.2. *Lattice spacings*

Lattice spacing data for alloys in the gadolinium–scandium system have been reported by Beaudry and Daane (1963) and by Yakel (1968, 1969). The data of Beaudry and Daane have been modified by prorating the deviations between the values reported by these investigators and the accepted values for the lattice spacings of the pure metals as listed in table 2 for each alloy on the basis of its composition. The adjusted lattice spacing data are plotted in fig. 88 along with the Vegard's law lines for the hcp allotrope, which are based on the accepted lattice spacing data for the pure metals. As adjusted, both the a and the c spacing data agree well with Vegard's law: A slight positive deviation exists for the a spacings while the c spacing data fall on the Vegard's law line. The data from Yakel could not be adjusted since no lattice spacing values were presented for the end-members, but his unadjusted data agree well with the adjusted data of Beaudry and Daane.

2.51.3. *Thermodynamic properties*

Isaacs (1973) measured the specific heat of a series of dilute gadolinium in scandium alloys in the temperature range 0.5 to 4.2 K. In alloys with less than 0.2 at% Gd, he observed a contribution to specific heat due to a solute–matrix

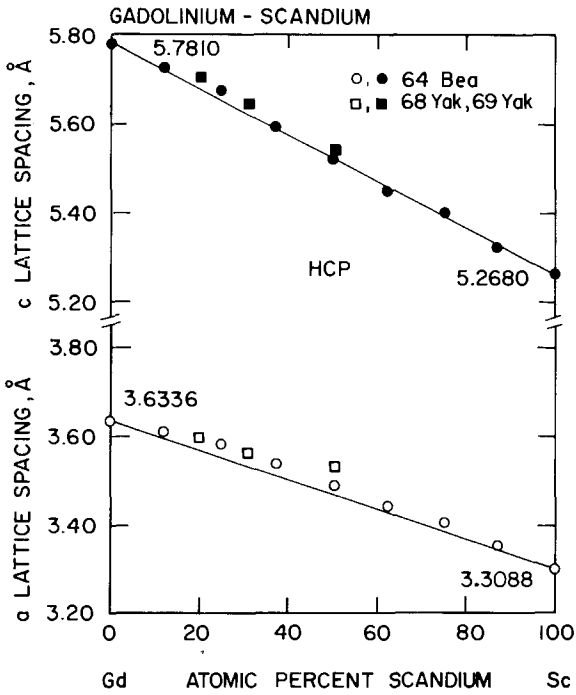

Fig. 88. Lattice spacings in the gadolinium–scandium system. The straight lines represent Vegard's law relationships and are based on the accepted values for the pure metals as listed in table 2.

interaction. At higher concentrations of Gd, the major contribution is due to long-range solute spin–spin interactions. The phase transformation due to magnetic ordering was observed in a 1.0 at% Gd alloy. The electronic specific heat coefficient increased rapidly with Gd content. Caudron et al. (1981) determined specific heats down to 0.030 K on a 3 at% Gd–Sc spin glass. Their data, presented in a log–log plot of specific heat vs. temperature, demonstrated a $T^{1.7}$ relationship.

References

Beaudry, B.J. and A.H. Daane, 1964, J. Less-Common Met. **6**, 322.
Caudron, R., P. Costa, J.C. Lasjaunias and B. Levesque, 1981, J. Phys. F **11**, 451.
Isaacs, L.L., 1973, Phys. Rev. B **8**, 3301.
Lundin, C.E., 1966, Final report, Denver Research Institute Rept. AD-633558, University of Denver, Denver, CO (also given as DRI-2326).
Shiflet, G.J., J.K. Lee and H.I. Aaronson, 1979, Calphad **3**, 129.
Yakel, H.L., 1968, Oak Ridge National Laboratory Rept. ORNL-4370, Oak Ridge, TN.
Yakel, H.L., 1969, Oak Ridge National Laboratory Rept. ORNL-4470, Oak Ridge, TN.

2.52. *Gd–Y: Gadolinium–yttrium*

2.52.1. *Phase diagram*

Spedding et al. (1962) examined the gadolinium–yttrium alloy system using metals that were 99.9+ wt% pure with respect to other rare earth metals. The yttrium metal

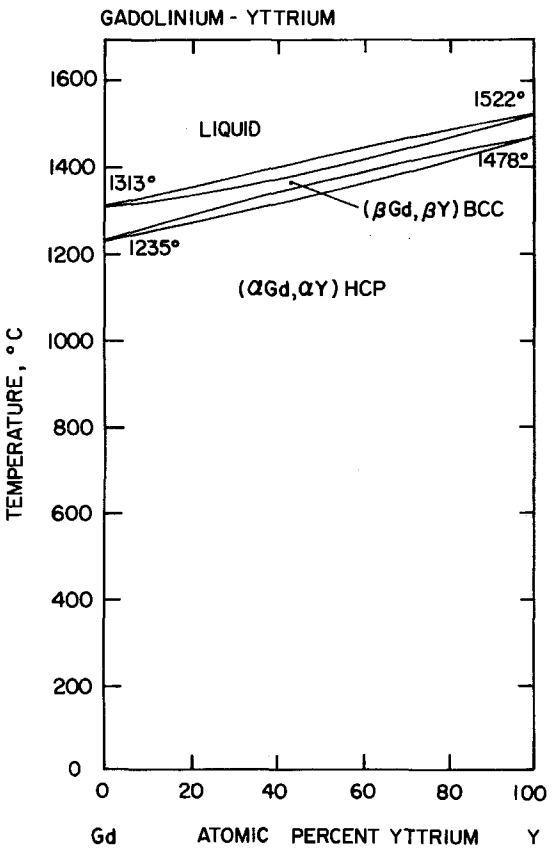

Fig. 89. Phase diagram of the gadolinium–yttrium system.

contained 1800 ppm oxygen and 2000 ppm tantalum as impurities while the gadolinium had less than 500 ppm of each. The tantalum, present as primary dendrites, was believed to have no effect on the equilibrium between gadolinium and yttrium. X-ray powder patterns showed that the annealed alloys were homogeneous. Equilibrium data were obtained by differential thermal analysis, by microscopy and by X-ray examination.

The phase diagram for the gadolinium–yttrium system is shown in fig. 89. Both room temperature (hcp) and high temperature (bcc) forms show complete solid solubility. The authors could not retain the high temperature bcc structure at room temperature by quenching.

Shiflet et al. (1979) calculated the phase diagram for this system using the Kaufman method. The calculated liquidus and solidus lines and the solvus lines that define the two-phase field at the bcc $\rightleftarrows$ hcp transformation were generally in good agreement with the experimentally determined lines but the width of the two-phase field between each set of lines was too narrow.

2.52.2. *Lattice spacings*

The lattice spacing data from Spedding et al. (1962) for the gadolinium–yttrium system are shown in fig. 90. These data were obtained by scaling their published graphs and have been adjusted to bring their observed *a* and *c* spacings for both gadolinium and yttrium into agreement with the accepted values for the pure metals (see table 2). The *a* lattice spacings show a small positive deviation from Vegard's law behavior and the *c* lattice spacings exhibit a slightly larger negative deviation.

McWhan and Stevens (1967), who measured magnetic properties of several rare earth alloys at high pressures, reported lattice spacings for a Gd–55 at% Y alloy at atmospheric pressure in terms of the ratio of the spacing for the alloy to the corresponding spacing in pure terbium. The *a* and *c* lattice spacings for their alloy are included in fig. 100 and agree with the data of Spedding et al. Yakel (1968, 1969) reported lattice spacings for four compositions in this system but did not report lattice spacings for the end-members. His unadjusted data agree well with the other data in fig. 90. Bauminger et al. (1975) reported lattice spacings for a Gd–97 at% Y

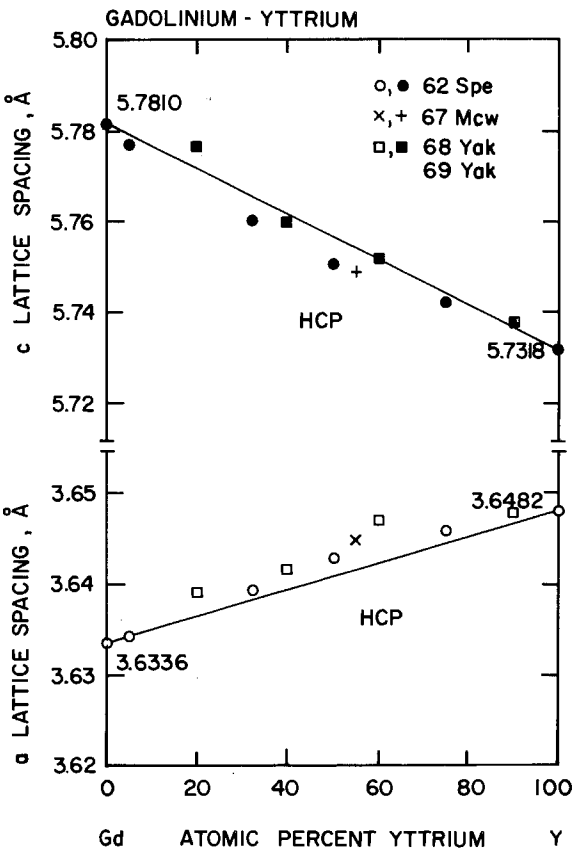

Fig. 90. Lattice spacings in the gadolinium–yttrium system. The straight lines represent the Vegard's law relationships for the pure metals based on the accepted values listed in table 2.

alloy measured at 30 K. Their values for the a and c lattice spacings, measured at this low temperature, are 0.06 and 0.16% greater, respectively, then the room temperature values calculated using Vegard's law.

2.52.3. *Amorphous alloys*

Laridjani and Sadoc (1981) studied amorphous Gd–Y alloys in the composition range 10 to 90 at% Y by X-ray diffraction. The amorphous alloys were prepared by sputtering onto an aluminum substrate at 78 K under argon pressure. Uniform foils having a thickness of 5 to 10 μm were obtained. A chemical short-range order was indicated by the interference and radial distribution function. These authors found that the radial distribution function could be accounted for by a mixture of tetrahedra and octahedra. At low concentrations of Y in Gd or Gd in Y there were four tetrahedra for one octahedra, but the number of tetrahedra increased as the concentration approached an equiatomic mixture of yttrium and gadolinium.

2.52.4. *Thermodynamic properties*

Lundin and Yamamoto (1967) used the Knudsen effusion technique to determine the thermodynamic activities in the Gd–Y alloy system. The vapor pressures of both Gd and Y in the solid state are well below the measuring ability of this technique; hence it was necessary to employ the molten state. Before analyses of the alloys, the vapor pressures of the pure components were measured. Vapors effused from nine liquid Gd–Y alloys at 1600°C were collected and subjected to X-ray spectrometer analysis. Activities of both components were determined from the ratio of the

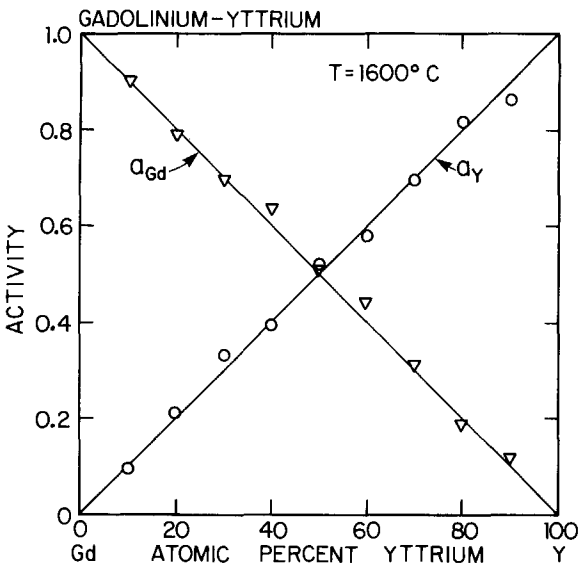

Fig. 91. Activities of gadolinium and yttrium in liquid Gd–Y alloys at 1600°C.

components in the condensed vapor phase using a modified Gibbs–Duhem relation. Their activity data are presented in fig. 91 where it is observed that the data fit a straight line and Raoult's law is obeyed in the liquid state. Thus the liquid alloy solutions at 1600°C are thermodynamically ideal. The enthalpy of mixing is zero. The only difference in these two elements is electronic structure, which does not affect the solution ideality in the Gd–Y system. This solution ideality would be expected because of the similarity of atomic diameters, electronegativities, valences and crystal structures.

References

Bauminger, E.R., A. Diamant, I. Felner, I. Nowik and S. Ofer, 1975, Phys. Rev. Lett. **34**, 962.
Laridjani, M. and J.F. Sadoc, 1981, J. Phys. (Paris) **42**, 1293.
Lundin, C.E. and A.S. Yamamoto, 1967, Final report, Denver Research Institute Rept. DRI-2437, University of Denver, Denver, CO.
McWhan, D.B. and A.L. Stevens, 1967, Phys. Rev. **154**, 438.
Shiflet, G.J., J.K. Lee and H.I. Aaronson, 1979, Calphad **3**, 129.
Spedding, F.H., R.M. Valletta and A.H. Daane, 1962, Trans. Quarterly (Am. Soc. Met.) **55**, 483.
Yakel, H.L., 1968, Oak Ridge National Laboratory Rept. ORNL-4370, Oak Ridge, TN.
Yakel, H.L., 1969, Oak Ridge National Laboratory Rept. ORNL-4470, Oak Ridge, TN.

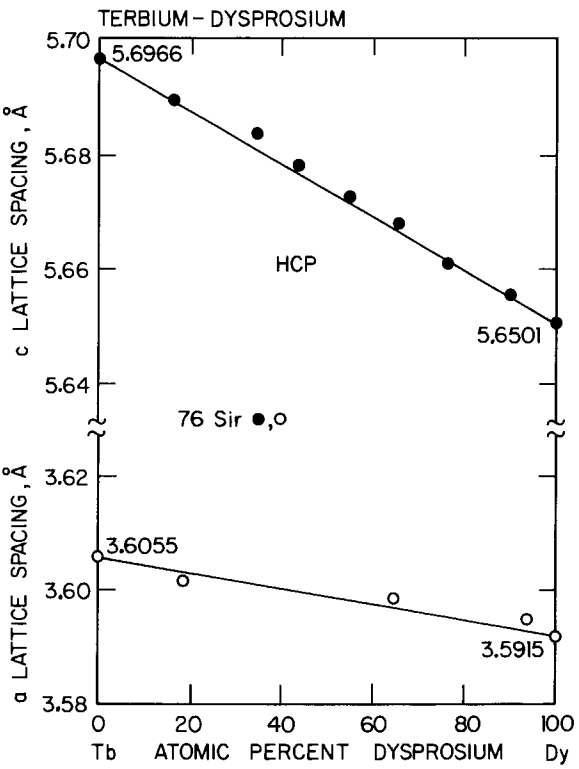

Fig. 92. Lattice spacings in the terbium–dysprosium system. The straight lines show the Vegard's law relationships for the pure metals and are based on the data in table 2.

2.53. *Tb–Dy: Terbium–dysprosium*

2.53.1. *Lattice spacings*

Sirota and Semirenko (1976) studied ternary terbium–dysprosium–holmium alloys and included diagrams that showed lines of equal value of the lattice spacings in this ternary system. Binary lattice spacing data in the terbium–dysprosium system were obtained by scaling the Tb–Dy side of their diagram. The data shown in fig. 92 have been adjusted to being the lattice spacings observed by these authors into agreement with the accepted values for these pure metals as listed in table 2. Both the *a* and *c* lattice spacing data appear to be in agreement with the Vegard's law relationship, which is depicted by the straight lines between the data for pure terbium and dysprosium.

Reference

Sirota, N.N. and V.V. Semirenko, 1976, Izv. Akad. Nauk SSSR, Met. [6], 209 [English transl.: Russ. Metall. [6], 167].

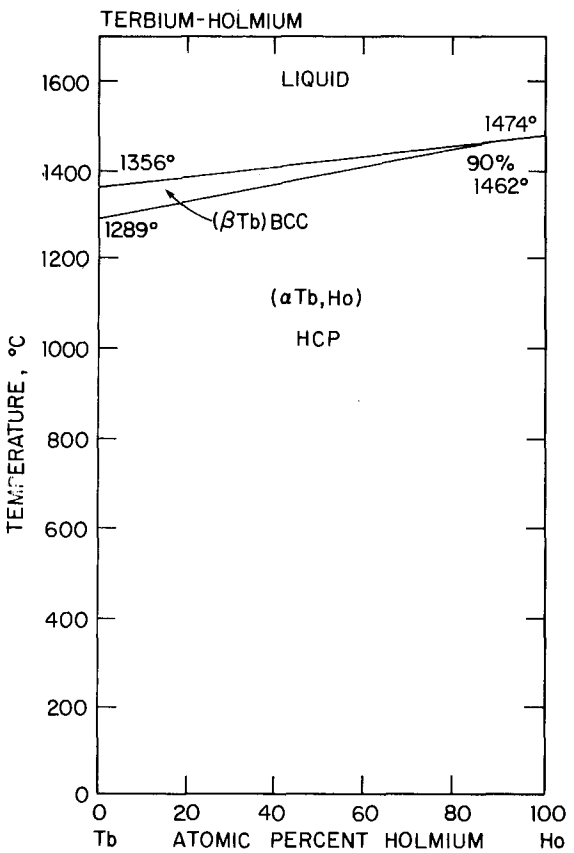

Fig. 93. Phase diagram of the terbium–holmium system.

2.54. *Tb–Ho: Terbium–holmium*

2.54.1. *Phase diagram*

The phase diagram for the terbium–holmium system has been reported by Spedding et al. (1973). Impurities present in their holmium metal (in at ppm) were: 816 H, 556 O, 59 each N and Si, 30 Fe, 27 C, 26 F, 22 Sc and 20 each Cu and Er. Their terbium metal contained (in at ppm) at 1340 O, 315 H, 66 C, 57 Fe, 53 Ta, 46 N, 33 F and 20 each Ca and Cu.

This system was studied by thermal, X-ray and metallographic methods. Care was taken in the preparation of specimens and in the design of equipment and experimental runs to assure accuracy in the reported results, which include the phase diagram shown in fig. 93.

Since the thermal arrests were within 1.5°C on both the heating and cooling curves, as is the case for pure metals, the liquidus–solidus line and the solvus line for the bcc ⇄ hcp transformation were drawn as single lines. The transformation temperature of terbium was found to be raised linearly by the addition of holmium but at a greater slope than the melting temperature. Extrapolation of the transformation temperature curve to the solidus showed that the two curves intersect at 90 at% Ho. This confirms the absence of the bcc form at high temperatures in holmium.

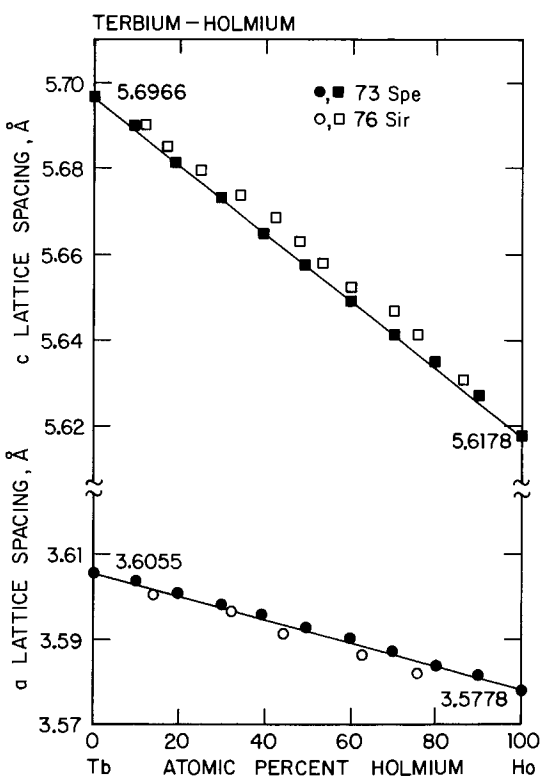

Fig. 94. Lattice spacings in the terbium–holmium system. The straight lines represent the Vegard's law relationships in this system based on the data for the pure metals listed in table 2.

Shiflet et al. (1979) have applied the Kaufman approach to the calculation of the Tb–Ho phase diagram and have compared their results with those obtained experimentally by Spedding et al. Their calculated peritectic point in this system fell at a somewhat lower temperature and holmium concentration than did the experimentally determined peritectic point.

2.54.2. *Lattice spacings*

Lattice spacing data from the report by Spedding et al. (1973) and from Sirota and Semirenko (1976) are presented in fig. 94. The data of Sirota and Semirenko were presented in the form of a ternary diagram showing lines of equal value of the lattice parameters in the Tb–Dy–Ho alloy system. The data presented here were obtained by scaling the Tb–Ho side of their diagram, then adjusting this data so that the lattice spacings for the end-members agreed with the accepted values for the pure metals as shown in table 2. No adjustments were required on the data of Spedding et al. The data, as plotted, show good agreement with Vegard's law. The presence of small deviations in the data of Sirota and Semirenko (a, negative; c, positive) is probably due to higher impurity levels in their alloys.

References

Shiflet, G.J., J.K. Lee and H.I. Aaronson, 1979, Calphad **3**, 129.

Sirota, N.N. and V.V. Semirenko, 1976, Izv. Akad. Nauk SSSR, Met. [6], 209 [English transl.: Russ. Metall. [6], 167].

Spedding, F.H., B. Sandeen and B.J. Beaudry, 1973, J. Less-Common Met. **31**, 1.

2.55. *Tb–Er: Terbium–erbium*

2.55.1. *Phase diagram*

Spedding et al. (1973) have investigated the terbium–erbium system using metallography, X-ray and thermal analysis methods. The terbium used in preparation of their alloys contained the following impurities (in at ppm): 1340 O, 315 H, 66 C, 57 Fe, 53 Ta, 46 N, 33 F and 20 each Ca and Cu. Impurities in their erbium (also in at ppm) were: 368 O, 331 H, 145 Cu, 97 C, 60 Ta, 28 Y and 26 F. Specially designed thermal analysis equipment was used to precisely establish the melting and transition temperatures of the alloys in this system. Their phase diagram is shown in fig. 95. As anticipated, each component was entirely soluble in the other over the entire composition range. The melting point of Tb–Er alloys was observed to increase linearly with increasing erbium concentration. The bcc phase terminates at 66 at% Er. The transformation temperature for the bcc $\rightleftarrows$ hcp transition was lowered linearly from 66 at% Er with increasing terbium content to the transition temperature of pure terbium, 1289°C. No bcc $\rightleftarrows$ hcp transition was observed in pure erbium metal or in alloys containing more than 66 at% Er.

Shiflet et al. (1979) combined the Kaufman approach with values of the enthalpies and entropies of melting and transformation of the pure rare earth metals and calculated the phase diagram for the Tb–Er system. The peritectic point in the

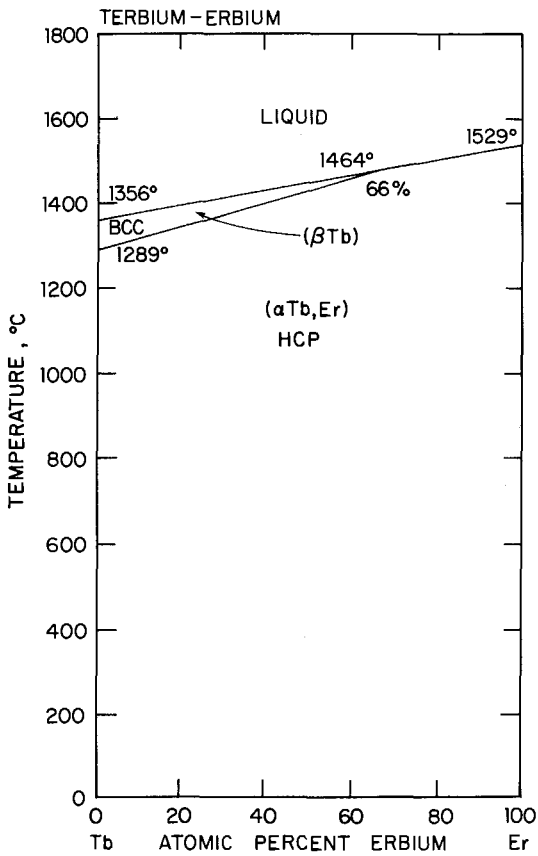

Fig. 95. Phase diagram of the terbium–erbium system.

calculated Tb–Er diagram fell at a higher temperature and at a higher erbium concentration than did the experimentally determined peritectic point.

2.55.2. *Lattice spacings*

Spedding et al. (1973) measured lattice spacings on their carefully prepared Tb–Er alloys. Although their spacings, shown in fig. 96, are nearly linear, they observed a distinct deviation from linearity that was positive for the *a* lattice spacings and slightly negative for the *c* lattice spacings.

McWhan and Stevens (1967), who measured magnetic properties of several rare earth alloys as a function of pressure, reported the lattice spacings at atmospheric pressure for an alloy containing 43 at% Er. The *a* and *c* lattice spacings for this alloy are included on fig. 96. The *c* spacing for their alloy is in fair agreement with the data of Spedding et al. but has a small positive deviation from linearity. The *a* spacing for their alloy has a large positive deviation from linearity, which would appear to indicate the presence of nonmetallic impurities in their alloy (see section 1.2.2).

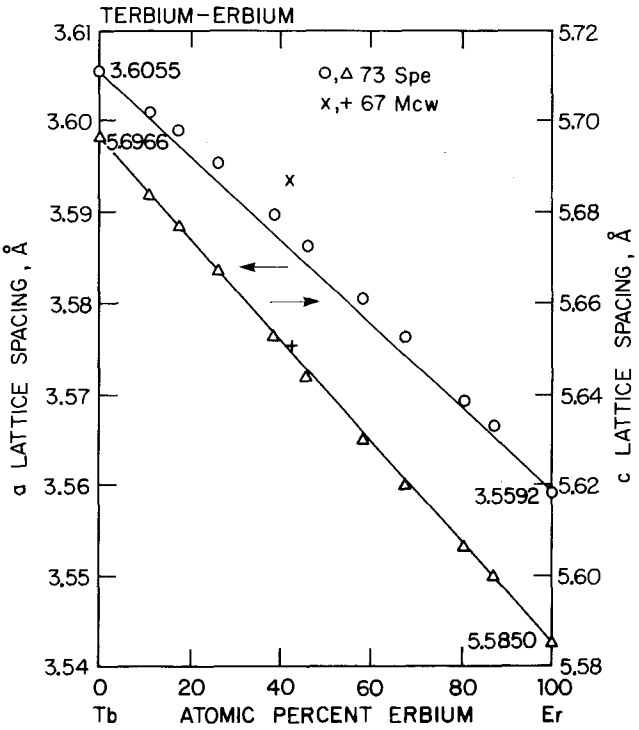

Fig. 96. Lattice spacings in the terbium–erbium system. The straight lines illustrate Vegard's law behavior and are based on accepted values for the pure metals as listed in table 2.

References

McWhan, D.B. and A.L. Stevens, 1967, Phys. Rev. **154**, 438.
Shiflet, G.J., J.K. Lee and H.I. Aaronson, 1979, Calphad **3**, 129.
Spedding, F.H., B. Sandeen and B.J. Beaudry, J., 1973, Less-Common Met. **31**, 1.

2.56. *Tb–Yb: Terbium–ytterbium*

2.56.1. *Lattice spacings*

Burgardt et al. (1979) studied magnetic ordering in terbium alloys with several nonmagnetic diluents and reported lattice spacings for several alloy compositions. Ytterbium, which exists in the nonmagnetic divalent state, did not form a wide range of solid solutions. The lattice spacing data reported for this system by Burgardt et al. are presented in fig. 97 along with the accepted values of the lattice spacings for pure terbium metal from table 2. A negative deviation from Vegard's law behavior is observed in both the *a* and *c* lattice spacings in fig. 97. These authors found that the addition of a nonmagnetic solute such as ytterbium, which expands the *c* lattice spacings of terbium, promotes ferromagnetism, whereas the addition of a solute, which shrinks the *c* parameter of terbium, favors helical magnetic structure.

Reference

Burgardt, P., S. Legvold, B.J. Beaudry and B.N. Harmon, 1979, Phys. Rev. B **20**, 3787.

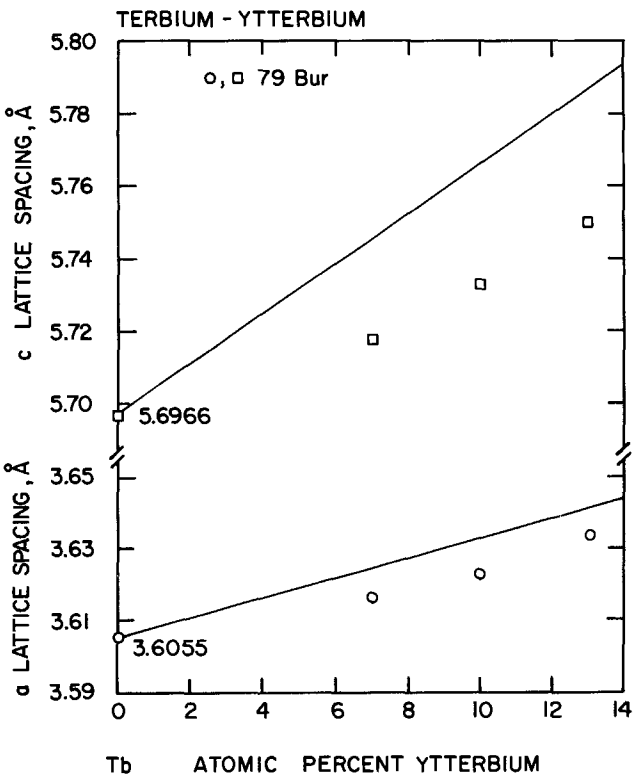

Fig. 97. Lattice spacings in the terbium-rich portion of the terbium–ytterbium system. The Vegard's lines are based on the accepted values for the pure metals as listed in table 2.

2.57. *Tb–Lu: Terbium–lutetium*

2.57.1. *Phase relationships*

Smidt (1962) and Smidt and Daane (1963) investigated electrical resistivity of several rare earth alloy systems and reported the existence of complete solubility in the terbium–lutetium system as confirmed by X-ray diffraction and resistivity methods. This result was not unexpected since these metals satisfy the Hume–Rothery requirements for formation of extensive solid solutions: similar valence, electronegativities and crystal structures, and have a difference in metallic radii of less than 3%.

2.57.2. *Lattice spacings*

Smidt and Daane (1963) reported lattice spacings for four alloy compositions and for the pure metals in the Tb–Lu system. Their observed lattice spacings have been adjusted on the basis of composition to bring the observed values for the end-members into agreement with the accepted values for the pure metals as shown in table 2. These adjusted values are presented in fig. 98 along with a set of lattice spacings for a 32.5 at% Lu alloy from McWhan and Stevens (1967) and a set for a 10 at% Lu alloy from Burgardt et al. (1979). The *a* lattice spacings of Smidt and Daane have a

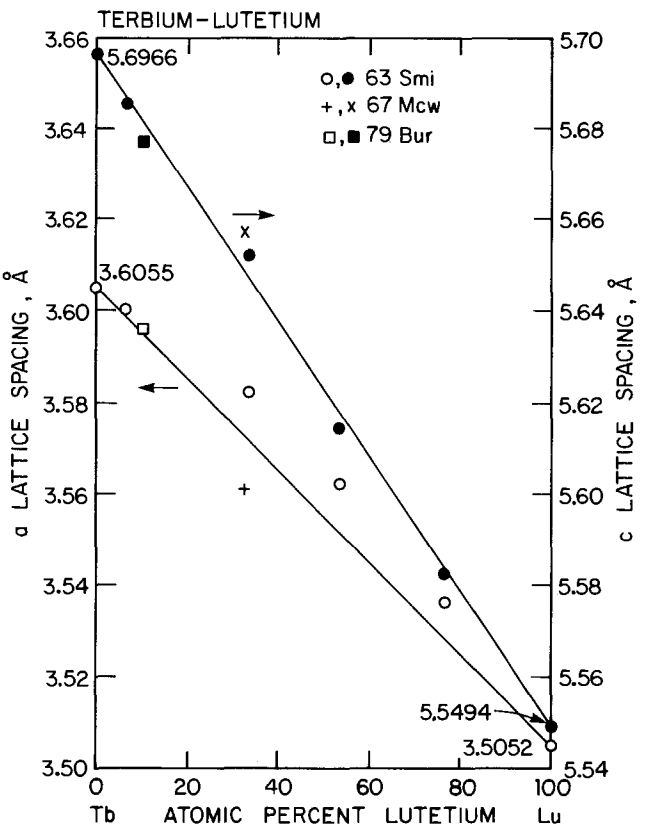

Fig. 98. Lattice spacings in the terbium–lutetium system. The straight lines illustrate the Vegard's law relationships and are based on the accepted values for the lattice spacings of the pure metals, shown in table 2.

positive deviation from Vegard's law behavior over most of this composition range. Their *c* lattice spacing data points scatter about the Vegard's law line and generally are in good agreement. The lattice spacings for the alloy reported by McWhan and Stevens had a negative deviation in the *a* spacing. The data for the 10 at% Lu alloy reported by Burgardt et al. had an *a* spacing that agreed with Vegard's law and a *c* spacing that showed a negative deviation.

References

Burgardt, P., S. Legvold, B.J. Beaudry and B.N. Harmon, 1979, Phys. Rev. B **20**, 3787.
McWhan, D.B. and A.L. Stevens, 1967, Phys. Rev. **154**, 438.
Smidt, F.A., Jr., 1962, Ph.D. thesis, Iowa State University, Ames, IA.
Smidt, F.A., Jr. and A.H. Daane, 1963, J. Phys. Chem. Solids **24**, 361.

2.58. *Tb–Sc: Terbium–scandium*

2.58.1. *Lattice spacings*

Chatterjee and Corner (1971) measured lattice spacings of Tb–Sc single crystal specimens containing 11.0, 17.5 and 30.5 at% Sc as well as polycrystalline specimens containing 50 and 75 at% Sc. The latter were prepared by repeated arc-melting of the

raw materials to attain homogeneity. Absorption spectroscopy showed the compositions to be accurate to within ± 0.5 at%. Lattice spacings at room temperature were determined by the X-ray powder method. The data shown in fig. 99 have been adjusted so that the spacings for terbium and scandium agree with the accepted values for these pure metals as shown in table 2. The terbium–scandium alloys have hcp structure and the *a* lattice spacings appear to follow Vegard's law within experimental error. A slight negative deviation from Vegard's law behavior is observed for most of the *c* spacing data. Burgardt et al. (1979) reported the lattice spacings for a 10 at% Sc alloy that also had been prepared by arc-melting the constituent metals. Their lattice spacing data agreed with those of Chatterjee and Corner. Cavin et al. (1966) reported lattice spacings for five compositions in the Tb–Sc system. Since no spacing data were included for the end-members, no adjustments could be made on the data for the alloys. However, with one exception, these data agree well with those from the other sources. Their *c* lattice spacing for the 75 at% Sc alloy is so far out of line (it cannot be plotted in fig. 99) as to suggest a typographical error, particularly when the *a* lattice spacing for this composition and all of their other *c* lattice data lie about where anticipated.

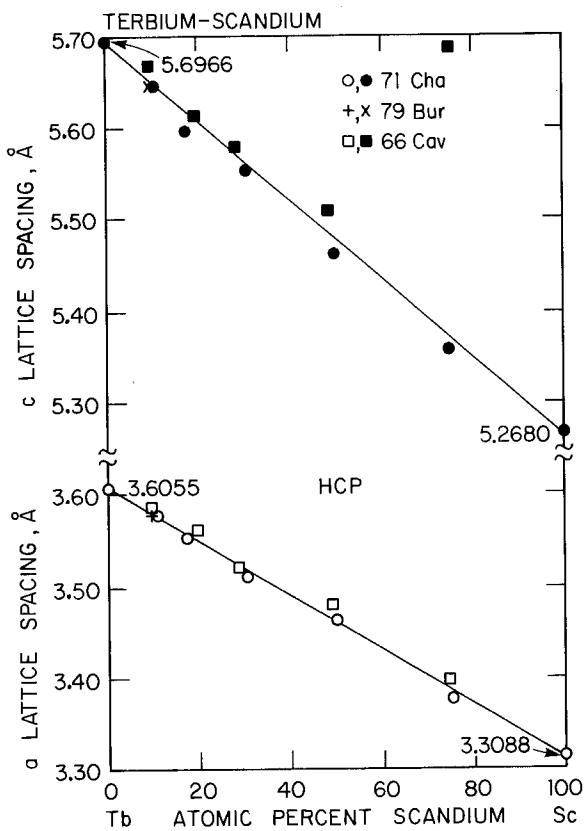

Fig. 99. Lattice spacings in the terbium–scandium system. The straight lines, based on the accepted values for the pure metals as listed in table 2, show the Vegard's law relationships for this system.

Chatterjee and Corner measured thermal expansion on their 11 at% Sc alloy and found that the *a* spacing contracted from 300 K down to the Curie temperature (136 K) where there was a sharp contraction and a continued contraction in the ferromagnetic state. The *c* spacing contracted down to the Neel point then expanded upon further cooling. It was observed by Burgardt et al. that scandium diluents in terbium suppress the ferromagnetic state relative to the helical state.

References

Burgardt, P., S. Legvold, B.J. Beaudry and B.N. Harmon, 1979, Phys. Rev. B **20**, 3787.
Cavin, O.B., R.M. Steele, L.A. Harris and H.L. Yakel, 1966, Oak Ridge National Laboratory Rept. ORNL-3970 (October), Oak Ridge, TN.
Chatterjee, D. and W.D. Corner, 1971, J. Phys. (Paris), Suppl. **32**, C1-243.

2.59. *Tb–Y: Terbium–yttrium*

2.59.1. *Phase diagram*

Markova et al. (1967) investigated the terbium–yttrium system by means of microscopy, X-ray diffraction, thermal analysis, hardness and electrical resistance measurements. Their starting materials were distilled yttrium of 99.6 to 99.7 (wt?)% purity and terbium of 98.5 to 99% purity. Impurities in their terbium included yttrium, gadolinium, dysprosium, calcium, copper, iron and tantalum. Both metals contained gaseous impurities. Alloys were melted in an arc furnace under a helium atmosphere and annealed at 850°C for 70 hr.

All alloys in the system were single phase and had hcp structure at room temperature. The solidus temperature for each alloy was determined in vacuum using a calibrated optical pyrometer focused on a 1 mm hole drilled to a depth of 3–4 mm in an attempt to achieve black body conditions (normally a 10 : 1 ratio of depth to diameter is required for black body conditions).

The phase diagram for this system is presented in fig. 100. Since their value for the melting point of yttrium (1502°C vs. the accepted value of 1522°C) and for the transition (bcc $\rightleftarrows$ hcp) temperature of both metals (Tb: 1317°C and Y: 1490°C) did not agree with the accepted values for the pure metals (1289 and 1478°C, respectively) as listed in table 1, the melting and transition temperatures of the alloys were adjusted on the basis of composition. These discrepancies may be due to the gaseous materials present in their metals and suggested that purities of their metals are significantly lower than reported. As noted above, only the solidus line was established by experimental data. The other phase boundaries in their diagram are presented as dashed lines, which conform to the anticipated phase relationships. Complete solid solubility exists at all compositions below the solidus including a narrow single-phase bcc region at high temperatures and hcp structure at lower temperatures.

2.59.2. *Lattice spacings*

McWhan and Stevens (1967) studied the effect of high pressures on several rare earth alloys including compositions ranging from 100% Tb to Tb–70 at% Y. They reported lattice spacings in terms of the ratio of the lattice spacing of the alloy to the

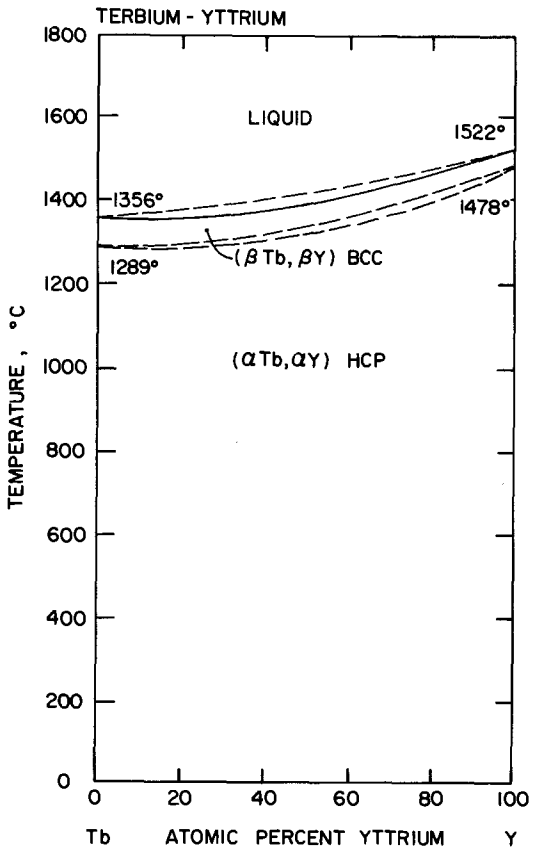

Fig. 100. Phase diagram of the terbium–yttrium system.

corresponding lattice spacing for pure terbium. The values for the lattice constants of pure terbium given in table 2 were used to obtain the data for the alloys. Their samples were prepared by arc-melting appropriate mixtures of terbium and yttrium [stated purity 99.9(wt?)%]. Weight loss during preparation ranged from 0.02 to 0.24% and this was taken as the maximum deviation in composition that may have occurred. Lattice spacings were determined from Guinier X-ray powder patterns.

Burgardt et al. (1979), who investigated magnetic ordering in terbium alloys, reported lattice spacings for a Tb–10 at% Y alloy. This alloy, made from high purity metals, was also prepared by arc-melting, followed by a three day anneal and a cold water quench.

Belovol et al. (1975) investigated crystal structure of terbium–yttrium alloys in the 0 to 50 at% Y composition range over the 77 to 300 K temperature range. A plot of lattice spacings vs. temperature for six compositions was reported and it was necessary to scale the plot to retrieve their data, then adjust the retrieved data to bring the lattice spacings for terbium and yttrium into agreement with the accepted values for the pure metals as listed in table 2. The alloy data were then adjusted

accordingly by prorating the differences of the pure metals by the respective compositions.

Finkel' and Vorob'ev (1967) studied the structure of several Tb–Y solid solutions over the temperature range −196 to 57°C (77 to 330 K) by X-ray diffraction. Their alloys were made from terbium of 99.5 (wt?)% purity and yttrium of 99.8 (wt?)% purity. After arc-melting, their samples were cut to size then annealed at 1200°C in vacuum for 10 to 50 hr. Their data, also retrieved by scaling their plots, have been adjusted to bring the lattice spacings for terbium and yttrium into agreement with the table 2 values. Cavin et al. (1966) reported lattice spacings for four compositions in the Tb–Y system, but did not report spacings for the end-members and did not indicate the purity of the metals involved or the measurement methods employed.

The lattice spacing data from all five references are shown in fig. 101. The data from McWhan and Stevens show a positive deviation from Vegard's law behavior in both the *a* and *c* lattice spacings. Several of the adjusted data points from Belovol

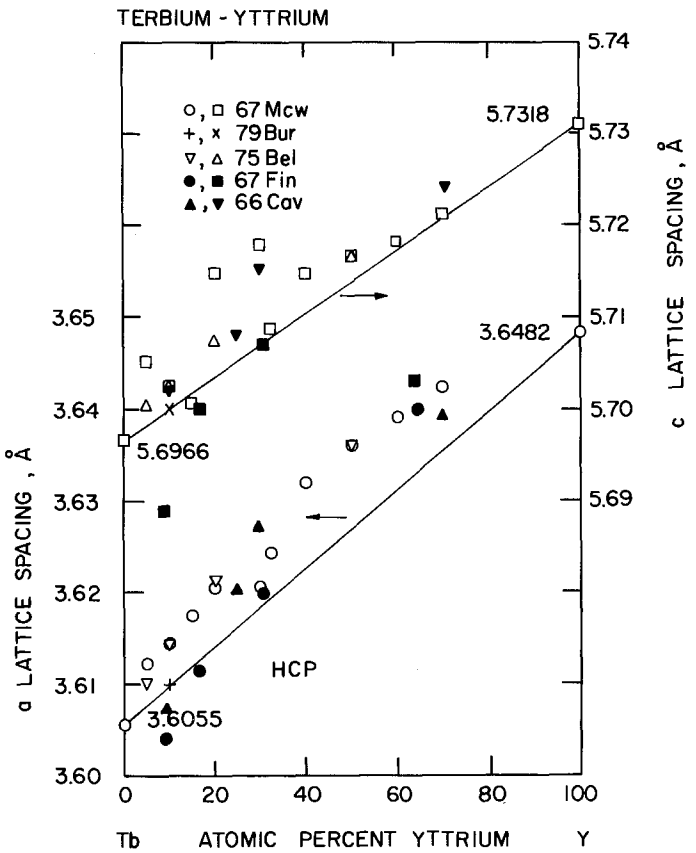

Fig. 101. Lattice spacings in the terbium–yttrium system. The straight lines represent Vegard's law behavior and are based on the accepted values for the pure metals as listed in table 2.

et al. fall directly on corresponding data points from McWhan and Stevens. The lattice spacings for the 90 at% Tb–10 at% Y alloy reported by Burgardt et al. lie on the Vegard's law line and may thus reflect higher purity in this alloy. As can be seen in fig. 101, the addition of yttrium expands the *c* lattice spacing of terbium. Unlike lanthanum and ytterbium, which also expanded the *c* lattice and promoted ferromagnetism in the alloys, Burgardt et al. observed that yttrium additions favored helical magnetic structure. The data of Finkel' and Vorob'ev, even after adjustment, show more scatter than the data from the other sources, particularly along the *c* axis where three of their compositions have a negative deviation from the Vegard's law relationship. The unadjusted data of Cavin et al. follow the same trend as the data from the other sources with the exception of the *a*-lattice spacing for the Tb–10 at% Y alloy, which has a negative rather than a positive deviation from Vegard's law behavior.

2.59.3. *Thermodynamic properties*

Naigovzin et al. (1979) made a mass-spectrometric study of the vaporization of terbium–yttrium alloys. The activity coefficients of yttrium were calculated graphically and those of terbium were calculated using the Gibb–Duhem equation. The activities of yttrium and terbium, shown for 1577°C (1850 K) in fig. 102, deviate from ideal solution behavior, according to the authors, because of the differences in the polarizabilities and the electronegativities of terbium and yttrium.

References

Belovol, V.S., V.A. Finkel' and V.E. Sivokon', 1975, Zh. Eksp. Teor. Fiz. **69**, 1734 [English transl.: Sov. Phys.–JETP **42**, 880].

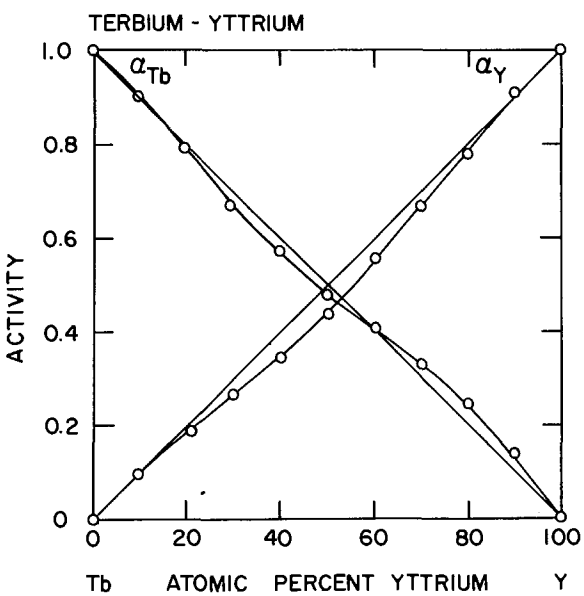

Fig. 102. Activities of terbium and yttrium alloys at 1577°C (1850 K).

Burgardt, P., S. Legvold, B.J. Beaudry and B.N. Harmon, 1979, Phys. Rev. B **20**, 3787.
Cavin, O.B., R.M. Steele, L.A. Harris and H.L. Yakel, 1966, Oak Ridge National Laboratory Rept. ORNL-3970 (October), Oak Ridge, TN.
Finkel', V.A. and V.V. Vorob'ev, 1968, Zh. Eksp. Teor. Fiz. **53**, 1913 [English transl.: Sov. Phys.–JETP **26**, 1086].
Markova, I.A., V.F. Terekhova and E.M. Savitskii, 1967, Izv. Akad. Nauk SSSR, Neorg. Mater. **3**, 392 [English transl.: Inorg. Mater. **3**, 343].
McWhan, D.B. and A.L. Stevens, 1967, Phys. Rev. **154**, 438.
Naigovzin, I.A., V.S. Kutsev, M.L. Grachev and G.E. Chuprikov, 1979, Zh. Fiz. Khim. **53**, 2118 [English transl.: Russ. J. Phys. Chem. **53**, 1210].

2.60. *Dy–Ho: Dysprosium–holmium*

2.60.1. *Phase diagram*

Spedding et al. (1973) investigated the dysprosium–holmium system by thermal, X-ray and metallographic methods. They used dysprosium metal which had the

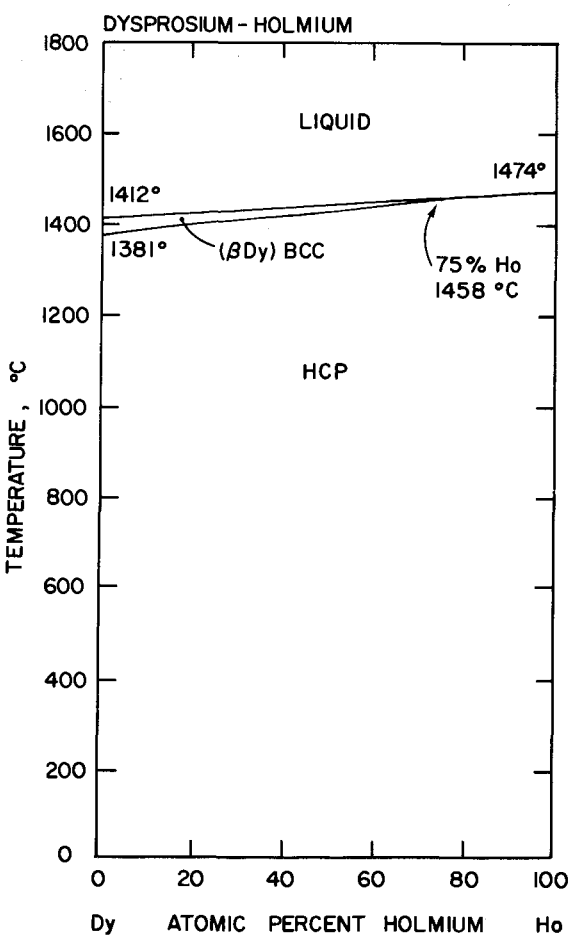

Fig. 103. Phase diagram of the dysprosium–holmium system.

following impurities (at ppm): 581 O, 189 C, 161 H, 46 N, 41 Fe and 20 each Cu and Ho. Their holmium metal contained these impurities (at ppm): 816 H, 556 O, 59 each N and Si, 30 Fe, 27 C, 26 F, 22 Sc and 20 each Cu and Er. Great care was taken to assure accurate determination of melting points and transformation temperatures. Weighed portions of the metals were placed in a tantalum crucible, which was evacuated and back filled with helium and a lid welded in place. The charge was then heated 50°C above the highest melting point.

The phase diagram shown in fig. 103 was the result of thermal and X-ray studies. The liquidus–solidus line is drawn as a single line because the thermal arrests on both the heating and cooling curves were within 1.5°C. Likewise, the solvus line for the bcc $\rightleftarrows$ hcp transformation is a single line. The transformation temperature of dysprosium is raised linearly by the addition of holmium, but at a greater rate than the melting temperature. The point of intersection, determined by extrapolating the transformation temperature curve to the solidus, is 75 at% Ho and 1458°C.

A continuous series of liquid and solid solutions was observed in this investigation. The study showed no bcc form for holmium metal.

Shiflet et al. (1979) applied the Kaufman approach to the calculation of the Dy–Ho phase diagram. Their calculated peritectic point fell at a lower temperature and concentration of holmium than the experimentally determined peritectic point.

2.60.2. *Lattice spacings*

Spedding et al. (1973) also reported lattice spacings at approximately 10 at% intervals across the dysprosium–holmium system. Cylindrical specimens with diameters of about 0.3 mm were prepared for the X-ray diffraction study. Samples were electropolished to remove the cold-worked surface. Lattice spacings were obtained by the application of a least square fit to the extrapolation of back reflection data using a Nelson–Riley function.

Sirota and Semirenko (1976) studied the ternary Tb–Dy–Ho system and presented a triangular plot showing lattice spacings as a function of composition. Lattice spacing data for the dysprosium–holmium system were retrieved by scaling the appropriate side of their diagram. Since their lattice spacings for dysprosium and holmium deviated from the accepted values for the pure metals as listed in table 2, it was necessary to adjust their data by prorating the deviations in the spacings of the end-members to each alloy on the basis of composition.

The lattice spacings in the dysprosium–holmium system are shown in fig. 104. The adjusted data of Sirota and Semirenko show a small scatter around the Vegard's law line for the a lattice spacings and a positive deviation from Vegard's law behavior for the c lattice spacings. However, the data presented by Spedding et al. show a variation of a and c with composition that is essentially linear and obeys Vegard's law.

References

Shiflet, G.J., L.K. Lee and H.I. Aaronson, 1979, Calphad **3**, 129.

Sirota, N.N. and V.V. Semirenko, 1970, Izv. Akad. Nauk SSSR, Met. [6], 209 [English transl.: Russ. Metall. [6], 167].

Spedding, F.H., B. Sandeen and B.J. Beaudry, 1973, J. Less-Common Met. **31**, 1.

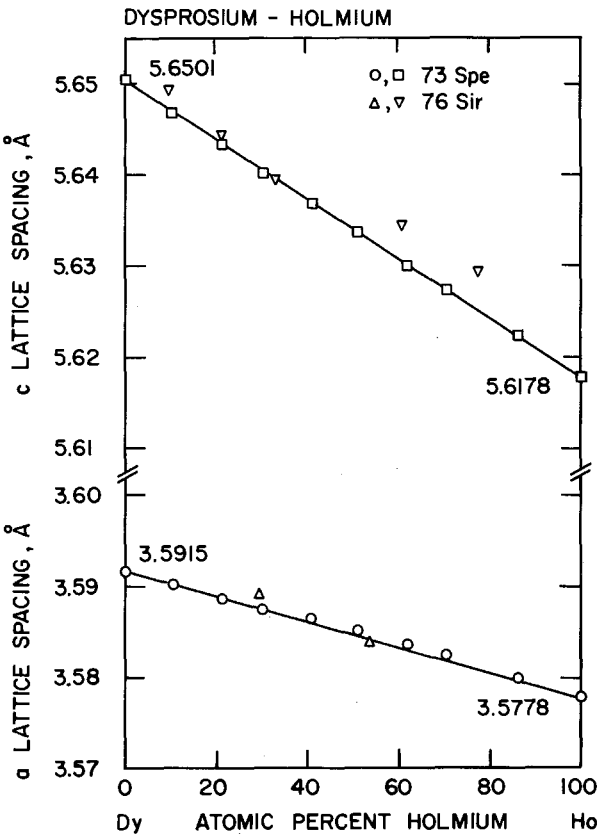

Fig. 104. Lattice spacings in the dysprosium–holmium system. The straight lines represent Vegard's law relationships and are based on the accepted values for the spacings of the pure metals as listed in table 2.

2.61. *Dy–Er: Dysprosium–erbium*

2.61.1. *Phase diagram*

The phase equilibria for the dysprosium–erbium system has been studied by Spedding et al. (1973). The metals used in the investigation were prepared by the calcium reduction of the fluoride of these metals. The reduced metals were purified by sublimation. Impurities present in their dysprosium (in at ppm) were: 581 O, 189 C, 161 H, 46 N, 41 Fe and 20 each Cu and Ho. Impurities in their erbium (also in at ppm) were: 368 O, 331 H, 145 Cu, 97 C, 60 Ta, 28 Y and 26 F. Great care was taken in the design of experimental equipment and research techniques to avoid error in the determination of melting points and transition temperatures.

The phase diagram for the dysprosium–erbium system as determined by Spedding et al. is shown in fig. 105. The melting point of the alloys decreases almost linearly with increase of the dysprosium content with a slight negative deviation that reaches its maximum where the bcc structure first starts to form from the melt (50 at% Dy). The transformation temperature is lowered linearly from this point with increasing dysprosium content to 1381°C, the transition temperature in pure dysprosium. The system was characterized by complete mutual solubility in both the solid (hcp) and liquid states.

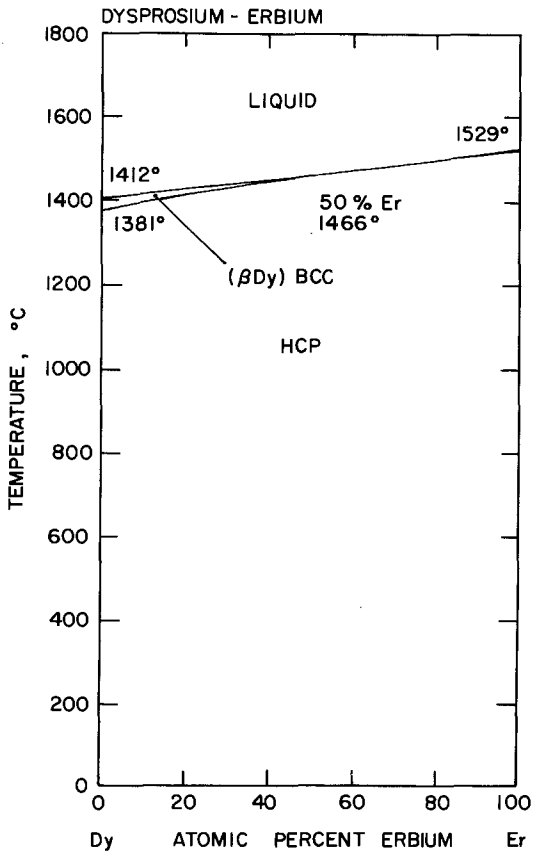

Fig. 105. Phase diagram of the dysprosium–erbium system.

Shiflet et al. (1979) were fairly successful in their calculation of the Dy–Er phase diagram using the Kaufman approach. The solidus and liquidus lines on their calculated phase diagram showed a slight gap and each had a slight positive deviation from linearity. The peritectic point on the calculated diagram falls at a slightly higher temperature and at a slightly greater erbium concentration than is the case with the experimentally determined diagram.

2.61.2. *Lattice spacings*

Spedding et al. (1973) determined lattice spacings at approximately 10 at% intervals in the dysprosium–erbium system using carefully prepared cylindrical specimens. The latter spacings were obtained by applying a least squares fit to the extrapolation of back reflection X-ray data. Their lattice spacing data are shown in fig. 106. The *a* and *c* spacings vary nearly linearly with composition within the limits of the experimental errors. The *a* lattice spacings appear to exhibit a positive deviation from Vegard's law.

References

Shiflet, G.J., J.K. Lee and H.I. Aaronson, 1979, Calphad **3**, 129.
Spedding, F.H., B. Sandeen and B.J. Beaudry, 1973, J. Less-Common Met. **31**, 1.

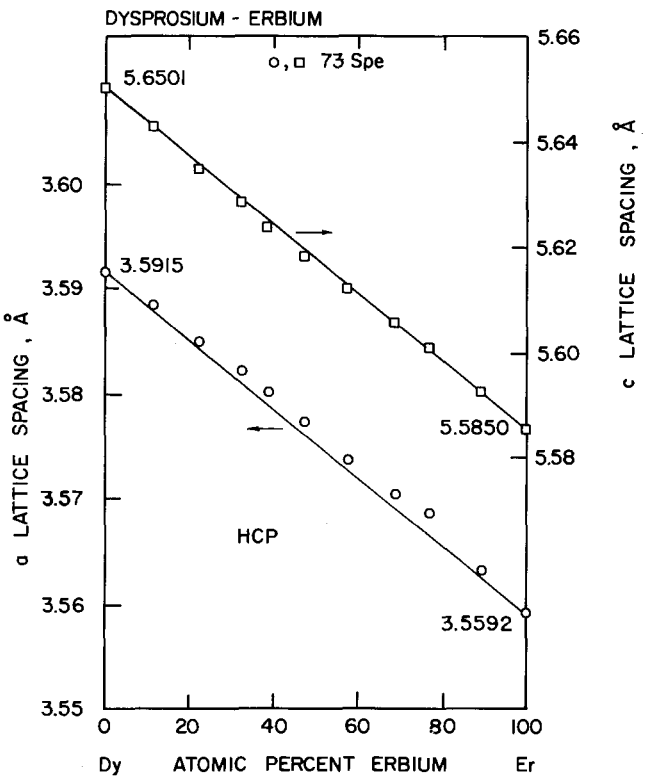

Fig. 106. Lattice spacings in the dysprosium–erbium system. The straight lines represent the Vegard's law relationships and are based on the accepted values for the pure metals as listed in table 2.

2.62. *Dy–Y: Dysprosium–yttrium*

2.62.1. *Phase diagram*

Markova et al. (1967) constructed a phase diagram for the dysprosium–yttrium system utilizing thermal analyses, X-ray diffraction, metallography, hardness and electrical resistance measurements. Their starting materials were distilled yttrium and dysprosium of 99.6 to 99.7(wt?)% purity. Both metals contained gaseous impurities as well as the metals Ca, Fe, Cu, Y, Gd, Dy and Ta. Alloys were prepared at approximately 10 at% intervals, arc-melted under purified helium and annealed at 850°C for 70 hr. The structure of all specimens was single phase with the hcp lattice. A continuous series of solid solutions between isomorphic modifications was observed.

The phase diagram as constructed by Markova et al. showed a minimum in the liquidus and solidus curves at about 1330°C and at a composition of about 45 at% Y. However, comparison with the work of Spedding et al. (1973) on Er–Y and related systems suggests that no minimum exists. Thus their diagram has been modified to the more likely construction shown in fig. 107. In this diagram there is a gradual nonlinear increase in the solidus and liquidus temperatures as the yttrium

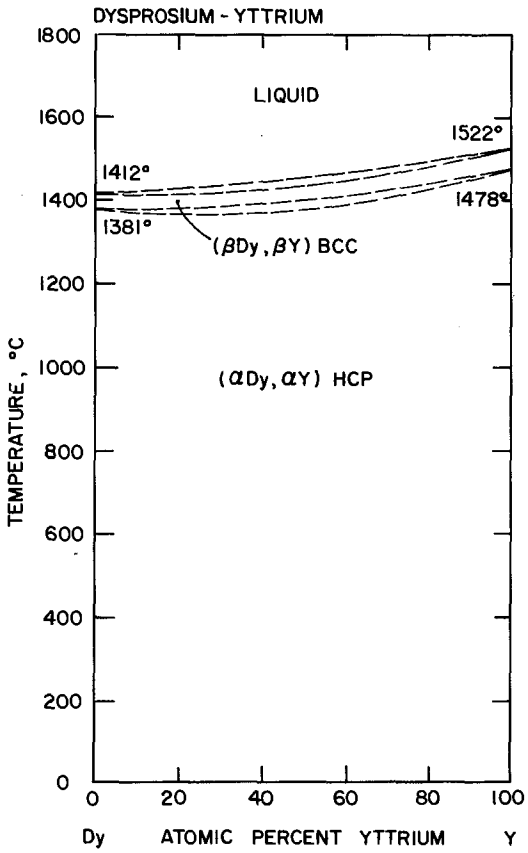

Fig. 107. Phase diagram of the dysprosium–yttrium system.

content of the alloys increase. A narrow two-phase region of liquid and bcc alloy is shown to exist just below the liquidus line. The solvus lines for the bcc ⇄ hcp structure transformation have a similar composition–temperature relationship. The temperature shown for the end-members on these phase diagrams for the melting point and transformation temperature are the accepted values for the pure metals taken from table 1 and not the temperatures given by Markova et al.

2.62.2. *Lattice spacings*

Lattice spacings for the dysprosium–yttrium system have been reported by Shafigullina et al. (1966) who investigated magnetic properties of these alloys from −269 to 27°C (4.2 to 300 K). Distilled metals of 99.6 (wt?)% purity were prepared in an arc furnace under purified helium and remelted several times to obtain homogeneity. Their lattice spacing data, reported in graphic form, have been adjusted to bring the observed spacings for dysprosium and yttrium into agreement with the accepted values for the pure metals listed in table 2. The adjusted *a* lattice spacings (fig. 108) show fairly good agreement with Vegard's law behavior despite some negative deviation at the Y-rich side of the graph. The *c* lattice spacings exhibit

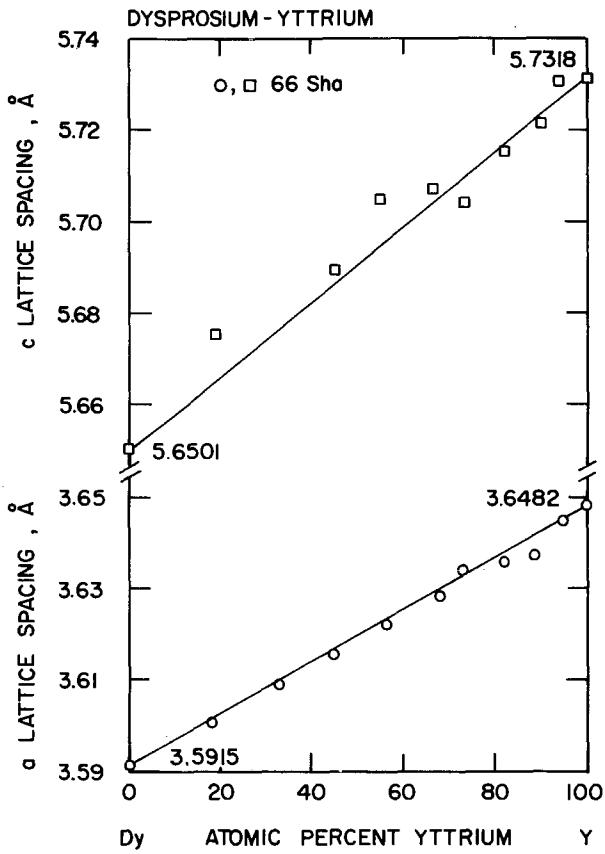

Fig. 108. Lattice spacings in the dysprosium–yttrium system. The straight lines, which show the Vegard's law relationship, are based on the accepted values for the pure metals shown in table 2.

considerable scatter showing a positive deviation from the Vegard's law line for Dy-rich alloys and a negative deviation (except for one point) in the Y-rich alloys containing more than 70 at% Y.

References

Markova, I.A., V.F. Terekhova and E.M. Savitskii, 1967, Izv. Akad. Nauk SSSR, Neorg. Mater. **3**, 392 [English transl.: Inorg. Mater. **3**, 343].

Shafigullina, G.A., V.I. Chechernikov and I.A. Markova, 1966, Fiz. Met. Metalloved. **22**, 838 [English transl.: Phys. Met. Metallogr. **22**, 35].

Spedding, F.H., B. Sandeen and B.J. Beaudry, 1973, J. Less-Common Met. **31**, 1.

2.63. *Ho–Er: Holmium–erbium*

2.63.1. *Phase diagram*

The Ho–Er phase system has been studied by Spedding et al. (1973) who employed thermal, X-ray and metallographic methods. The purified holmium metal contained (in at ppm): 816 H, 556 O, 59 each N and Si, 30 Fe, 27 C, 26 F, 22 Sc and

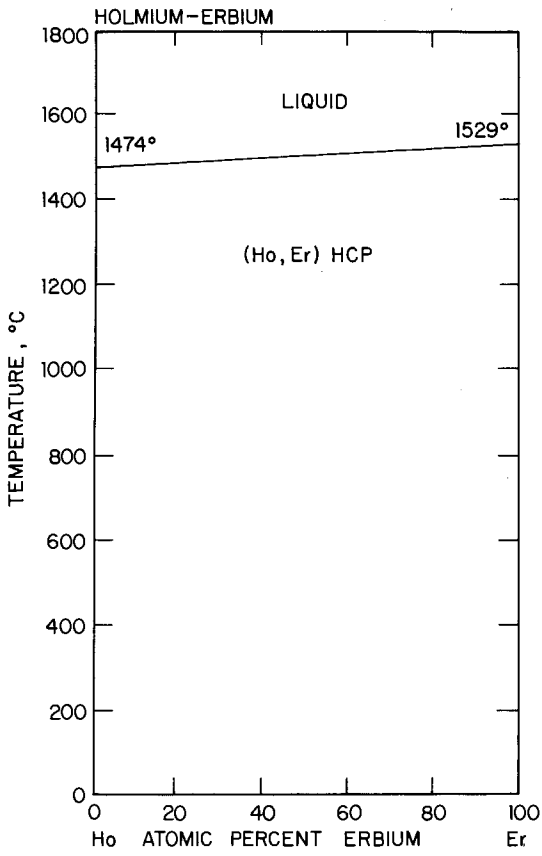

Fig. 109. Phase diagram of the holmium–erbium system.

20 each Cu and Er. Their erbium metal contained the following impurities (also in at ppm): 368 O, 331 H, 145 Cu, 97 C, 60 Ta, 28 Y and 26 F.

The same careful experimental techniques were used in the investigation of this system as were employed by these authors in their study of the Tb–Dy, Tb–Ho, Dy–Ho and Dy–Er systems (see sections 2.53, 2.54, 2.60 and 2.61, respectively). The addition of erbium to holmium increased the melting point linearly across the phase diagram as shown in fig. 109. Since neither metal has a bcc form, there is no bcc $\rightleftarrows$ hcp transition and the hcp structure exists for all compositions below the melting temperature with each metal being completely soluble in the other.

Shiflet et al. (1979) were quite successful in the calculation of the Ho–Er phase diagram using the Kaufman approach. Their calculated curve lay slightly above the experimentally determined liquidus–solidus curve and differed by no more than 2°C or by no more than 3 at%.

2.63.2. *Lattice spacings*

Spedding et al. (1973) determined lattice spacings for alloys in the Ho–Er system by applying a least squares fit to the extrapolation of back reflection X-ray data. The

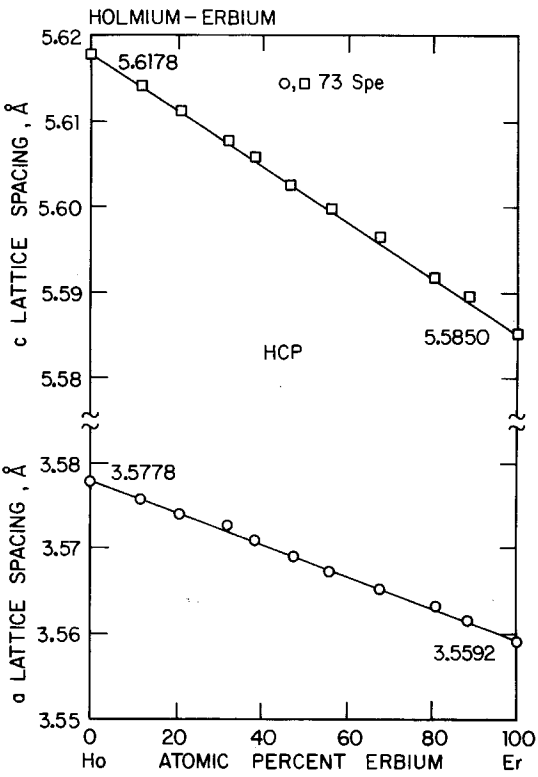

Fig. 110. Lattice spacings in the holmium–erbium system. The straight lines represent Vegard's law relationships and are calculated from the accepted values for the pure metals as listed in table 2.

specimens were cylinders of about 0.3 mm diameter that had been annealed at 550°C for 20 hr and electropolished to remove the cold-worked surface metal that had been introduced during shaping.

The lattice spacings determined by Spedding et al. are shown in fig. 110. The variation of a and c with composition in this binary system of adjacent elements is essentially linear within the limits of experimental error.

References

Shiflet, G.J., J.K. Lee and H.I. Aaronson, 1979, Calphad **3**, 129.
Spedding, F.H., B. Sandeen and B.J. Beaudry, 1973, J. Less-Common Met. **31**, 1.

2.64. *Ho–Sc: Holmium–scandium*

2.64.1. *Lattice spacings*

Cavin et al. (1967) have reported lattice spacings for five compositions in the holmium–scandium system. Details are not available on the purity of their metals, their alloy preparation procedures or the method used to determine the lattice parameters. Since their lattice spacing measurements for holmium and scandium metal were not included in their report, it is not known if the spacings for these

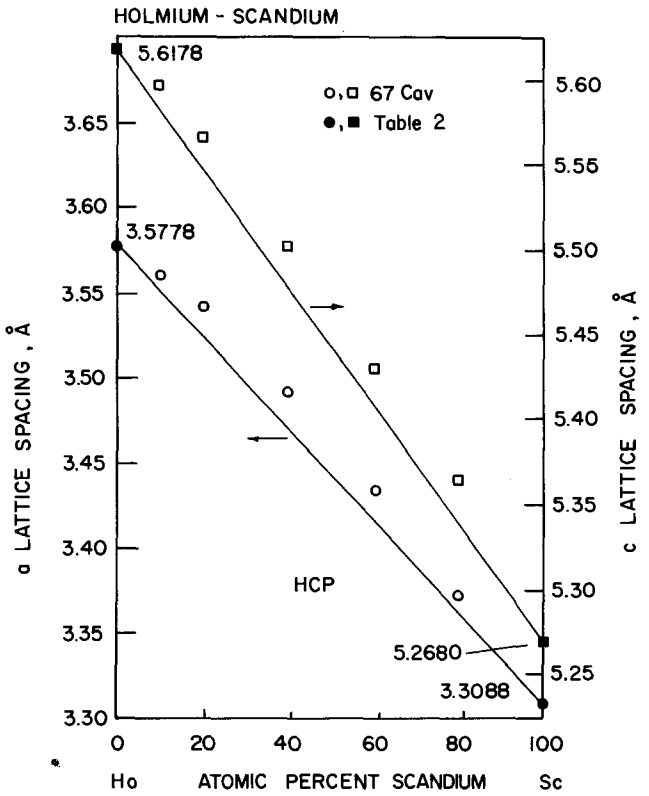

Fig. 111. Lattice spacings in the holmium–scandium system. The straight lines represent Vegard's law behavior based on the accepted values for the pure metals as listed in table 2.

end-members deviated from the accepted values for the pure metals given in table 2 and no adjustments to the observed values for their alloys are possible.

Their unadjusted data are shown in fig. 111 along with the lattice spacings for pure holmium and scandium taken from table 2. These data show a positive deviation from Vegard's law behavior in both the *a* and *c* spacings. In light of the behavior observed in the Gd–Sc and Tb–Sc systems (see sections 2.51.2 and 2.58.1), it appears likely that if the data could be adjusted for corrections to the spacings of the end-members, the data for these alloys would fall closer to the Vegard's law line.

Reference

Cavin, O.B., R.M. Steele, L.A. Harris and H.L. Yakel, 1967, Oak Ridge National Laboratory Rept. ORNL-4170 (November), Oak Ridge, TN.

2.65. *Ho–Y: Holmium–yttrium*

2.65.1. *Phase diagram*

The only phase diagram for the holmium–yttrium system found in the literature was that of Markova et al. (1967) who worked with distilled metals of 99.6 to 99.7 (wt?)% purity, both of which contained gaseous impurities. They state that the

solidus temperature for each alloy was observed with an optical pyrometer sighted on a hole in each sample. Their phase diagram shows a dashed liquidus line that passes through their data points while their solidus is indicated by a solid line that lies below and forms a narrow gap with the liquidus. Their diagram also shows solvus lines for the bcc ⇄ hcp transformation at all compositions. However, Spedding et al. (1973), who worked with high purity holmium metal, have shown that holmium does not have a high temperature bcc form.

A more likely configuration for the holmium–yttrium phase diagram is presented in fig. 112. Based on the investigation by Spedding et al. (1973) of phase equilibria in the Tb–Ho, Tb–Er, Dy–Ho, Dy–Er and Er–Y systems (see sections 2.54.1, 2.55.1, 2.60.1, 2.61.1 and 2.69.1, respectively), it would appear that no measurable gap would be found between the liquidus and solidus lines in the holmium–yttrium system when high purity metals are used. The shape of the solidus–liquidus line can only be determined by using sensitive experimental techniques and high purity metals; that is, it may be curved with a minimum (as found in the Er–Y system) or it may be linear (as found in the Dy–Ho system). Since holmium does not have the

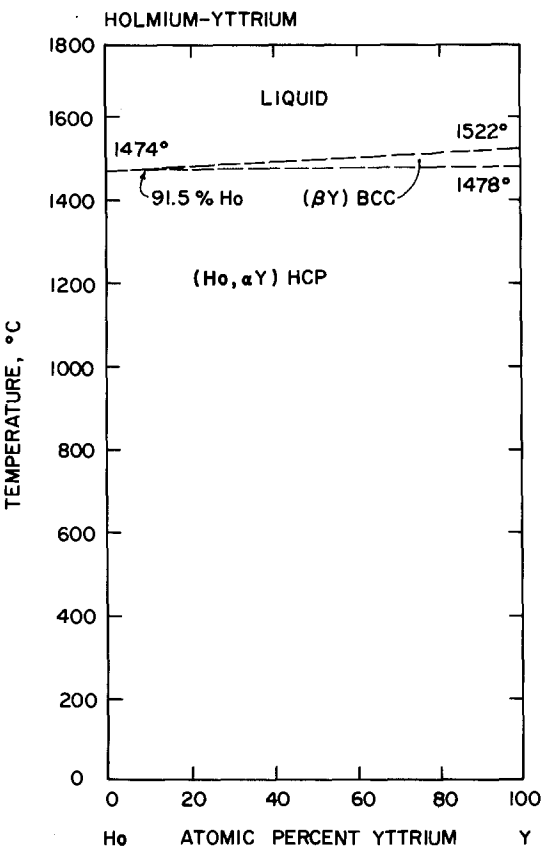

Fig. 112. Phase diagram of the holmium–yttrium system.

high temperature bcc form as does yttrium, the hcp solid solutions in the holmium-rich composition range will melt without undergoing a solid state transformation whereas alloys in the yttrium-rich composition range transform to the bcc structure before melting. A boundary of this bcc ⇄ hcp transformation was estimated from the behavior of the bcc structure in the five systems cited above. The estimated range of existence for the bcc phase in this system is from 8.5 to 100 at% Y. The estimate of the termination of the bcc phase at 8.5 at% Y is subject to rather wide error (i.e., the termination point could lie anywhere in the range 1 to 30 at% Y) and should be determined experimentally.

2.65.2. *Lattice spacings*

Markova et al. (1970) determined the ternary Dy–Ho–Y phase diagram using distilled metals of 99.5 to 99.7 (wt?)% purity but containing O, Ca, Cu, Fe and Ta as impurities. They reported lattice spacings for the system by means of triangular diagrams showing lines of equal value for the *a* and the *c* axes. Lattice spacings for the Ho–Y system were obtained by scaling one side of their ternary diagram. The lattice spacings for holmium and yttrium listed by Markova et al. have small deviations from the accepted values for the pure metals as listed in table 2, so adjustments have been made to the lattice spacings of their alloys. The adjusted data

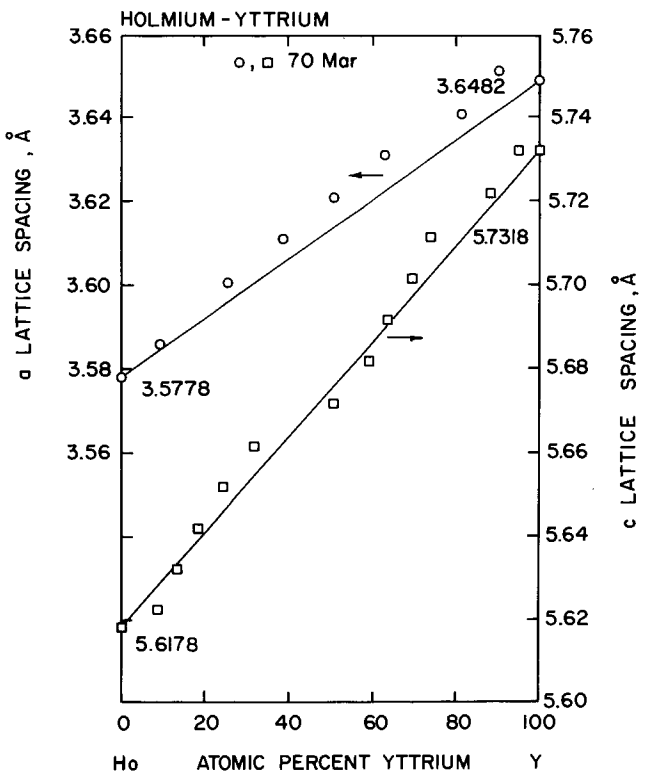

Fig. 113. Lattice spacings in the holmium–yttrium system. The straight lines representing Vegard's law behavior are based on the accepted values for the pure metals as given in table 2.

are shown in fig. 113. A positive deviation from Vegard's law behavior is seen for the a lattice constant at all alloy compositions. The adjusted c spacing data show scatter about the Vegard's law line with no general trend.

2.65.3. *Thermodynamic properties*

Nelson and Legvold (1961) calculated entropy changes involved in the demagnetization of Y–0.6 at% Ho and Y–1.0 at% Ho single crystals. These changes were found to be about 15% of that expected if the alloy behaved as an ideal paramagnetic substance. They observed a large contribution to the heat capacity in the range 0.7 to 1.2 K, which they attributed to magnetic spins.

References

Markova, I.A., V.F. Terekhova and E.M. Savitskii, 1967, Izv. Akad. Nauk SSSR, Neorg. Mater. **3**, 392 [English transl.: Inorg. Mater. **3**, 343].

Markova, I.A., V.F. Terekhova and E.M. Savitskii, 1970, Izv. Akad. Nauk SSSR, Met. [6], 170 [English transl.: Russ. Metall. [6], 106].

Nelson, D.T. and S. Legvold, 1961, Phys. Rev. **123**, 80.

Spedding, F.H., B. Sandeen and B.J. Beaudry, 1973, J. Less-Common Met. **31**, 1.

2.66. *Er–Tm: Erbium–thulium*

2.66.1. *Thermodynamic properties*

Satya and Wei (1971) measured the heat capacities of hcp erbium and thulium metals and three of their isostructural alloys from 1.3 and 4.2 K. They analyzed their data by a least squares method to fit the equation

$$C_v/T = \gamma + (\beta + \mu)T^2 + \nu T^{-3},$$

where C_v is the heat capacity at constant volume, T is the temperature (degrees Kelvin) and γ, β, μ and ν are, respectively, the electronic, lattice, magnetic and nuclear heat capacity coefficients. The various contributions for each of their samples were tabulated and the electronic heat capacity contributions were plotted as a function of composition.

Reference

Satya, A.V.S. and C.T. Wei, 1971, in Electronic Density of States, Nat. Bur. Stand. Spc. Publ. 323, U.S. Government Printing Office, Washington, p. 571.

2.67. *Er–Lu: Erbium–lutetium*

2.67.1. *Thermodynamic properties*

The heat capacity from −267 to 27°C (60 to 300 K) of 9.65 at% Er–Lu alloy has been measured by Taylor et al. (1972) using an adiabatic calorimeter and a platinum resistance thermometer. The metals used in preparing the alloy were vacuum sublimed in tantalum at 10^{-9} torr and 1600°C for lutetium and 1400°C for erbium, then analyzed for impurities. The alloy was remelted several times to insure homogeneity, cast to a cylindrical shape and machined. After heat capacity measure-

ments had been completed, the specimen was again analyzed for impurities, which were found to be the same as in the starting metals. Impurities included (in at ppm): 970 O, 350 H, 60 N, 400 C, 50 each Si, Fe and Ni, 150 Ta, 40 Cu, and 20 each Pt and W.

The heat capacity measurements were tabulated along with the standard entropy, enthalpy and free energy functions, which were calculated by numerical integration of the heat capacity results after numerically extrapolating C_p to 0 K.

Reference

Taylor, W.A., B.C. Gerstein, W.D. Shickell and F.H. Spedding, 1972, J. Chem. Phys. **56**, 2722.

2.68. *Er–Sc: Erbium–scandium*

2.68.1. *Phase diagram*

Naumkin et al. (1964) and Savitskii et al. (1965) have reported phase diagrams for the erbium–scandium system. These phase diagrams are identical and appear to be the product of the same research effort. The erbium metal used in their investigation

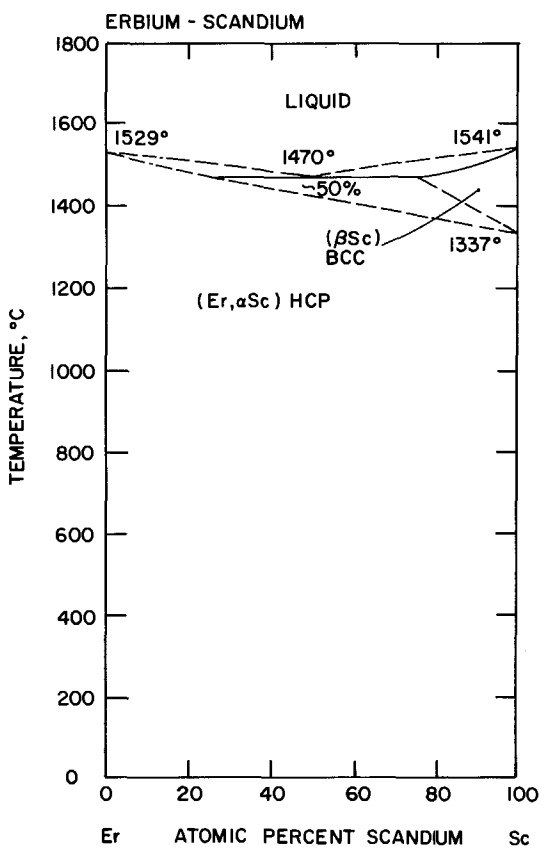

Fig. 114. Phase diagram of the erbium–scandium system.

was stated by Naumkin et al. to be 99.35(wt?)% pure. Their analysis showed the following impurity limits in the erbium (in wt ppm): < 2800 Ho, < 2000 Th, < 1000 each Nd, Tm and Y, < 200 Ca, < 100 Fe and < 70 Cu. Impurities in the 98.16 wt% pure scandium were (wt ppm): 1000 Th, 1600 C, 500 each Si, Yb, Y, Ti and Fe, 370 Ca and 100 each Al and Mo.

Alloys were arc-melted under purified helium and remelted three times, then annealed at 1000°C for 50 hr. The diagrams were established by thermal, microstructural and X-ray methods. Hardness, microhardness and densities were also measured.

The temperatures shown on their phase diagram for melting points of erbium and scandium were 29 and 11°C less, respectively, than the accepted values for the pure metals as listed in table 1. Also, the temperature shown for the bcc ⇄ hcp transformation in pure scandium is 13°C higher than the accepted value. In constructing fig. 114 the accepted values for the melting points of the pure metals and for the transformation temperature of pure scandium have been used. The eutectic temperature is shown here as 1470°C, an increase of 20°C over the temperature given by Naumkin et al. This 20°C increase for the eutectic temperature is the average of the difference between their melting point temperatures for the erbium and scandium metals and the accepted melting point of the respective pure metal.

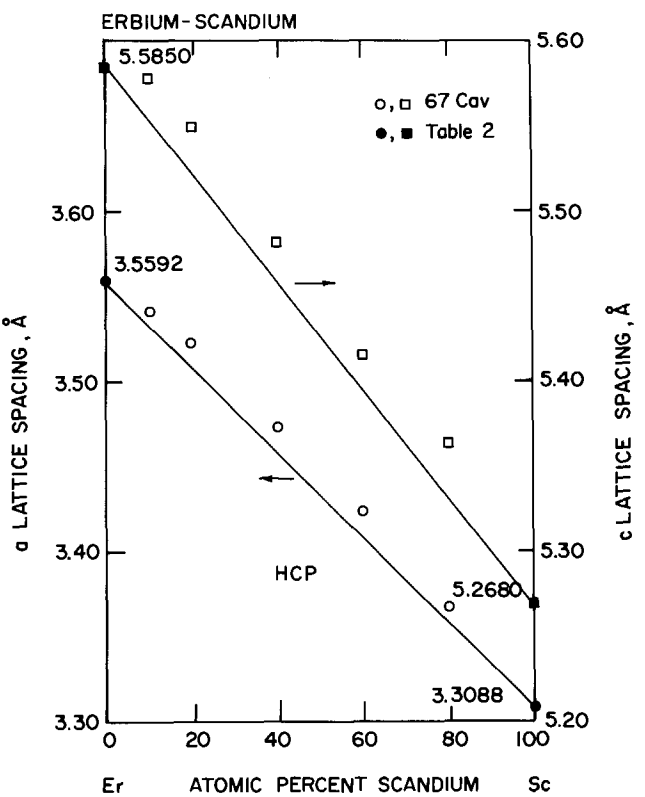

Fig. 115. Lattice spacings in the erbium–scandium system. The straight lines represent the Vegard's law relationships based on the accepted values for the pure metals as shown in table 2.

Naumkin et al. observed complete miscibility in the liquid state at all concentrations, and a continuous series of hcp solid solutions at room temperature. Since erbium has no bcc form, alloys rich in erbium pass directly from the hcp structure to the liquid state.

2.68.2. *Lattice spacings*

Cavin et al. (1967) reported a and c lattice spacings for five compositions in the erbium–scandium system. Information is not available on the purity of their alloys or their experimental techniques. Lattice spacing data for their pure metals were not included. Their data are plotted in fig. 115 along with the table 2 values for the lattice spacings of pure erbium and scandium. Small positive deviations from Vegard's law behavior are evident in both the a and c lattice spacings.

In view of the behavior observed in the Gd–Sc and the Tb–Sc systems (see sections 2.51.2 and 2.58.1) it appears likely that if the data could be adjusted for corrections to the spacings of the end-members, the lattice parameters for these alloys would fall near the Vegard's law lines.

References

Cavin, O.B., R.M. Steele and H.L. Yakel, 1967, Oak Ridge National Laboratory Rept. ORNL-4170 (November), Oak Ridge, TN.

Naumkin, O.P., V.F. Terekhova and E.M. Savitskii, 1964, Zh. Neorg. Khim. **9**, 2497 [English transl.: Russ. J. Inorg. Chem. **9**, 1347].

Savitskii, E.M., V.F. Terekhova, I.V. Burov, O.P. Naumkin and I.A. Markova, 1965, Izv. Akad. Nauk SSSR, Neorg. Mater. **1**, 1648 [English transl.: Inorg. Mater. **1**, 1503].

2.69. *Er–Y: Erbium–yttrium*

2.69.1. *Phase diagram*

Investigations of phase equilibria in the erbium–yttrium system have been conducted by Markova et al. (1964) and by Spedding et al. (1973). The first group used distilled yttrium metal of 99.6(wt?)% purity and erbium metal of about 98(wt?)% purity. The principal impurities included Ca, Fe, Cu, Ta and other rare earth metals. The alloys were arc-melted under purified helium and studied in the annealed state. Microscopy, differential thermal analyses and X-ray methods were utilized and measurements of hardness and electrical resistivity were performed on the alloy specimens. The main difficulty experienced in their thermal analysis was the narrow temperature interval between the melting of their alloys and the polymorphic transformations.

The investigation of this system by Spedding et al. was performed using metals of higher purity. The impurities found in their erbium metal were (in at ppm): 368 O, 331 H, 145 Cu, 97 C, 60 Ta, 28 Y and 26 F. Impurities in their yttrium metal (also in at ppm) were: 1251 O, 880 H, 421 F, 333 C, 49 Sc and 30 Al. Great care was taken in the design of experimental equipment and methods to avoid errors in the measurements of melting points and transition temperatures. Differential thermal analysis, X-ray diffraction and metallographic observations were used by Spedding et al. in the determination of the erbium–yttrium phase diagram, which is reproduced in fig. 116.

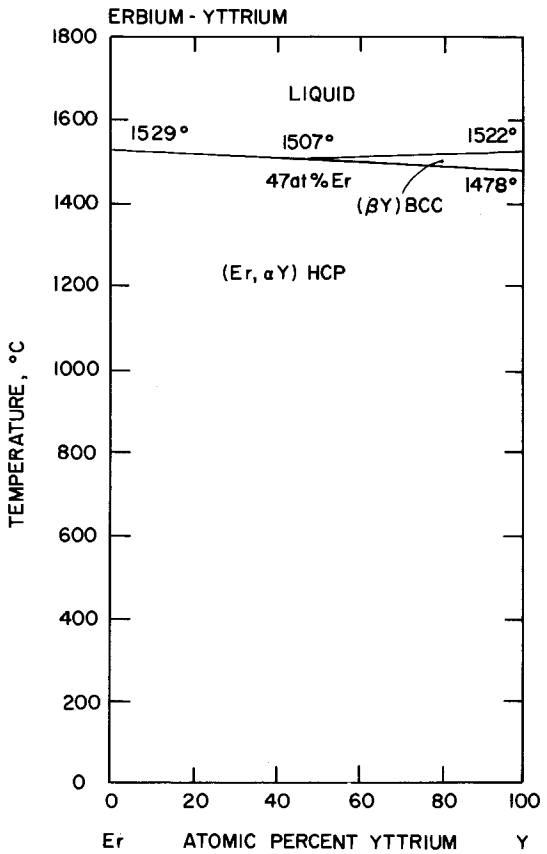

Fig. 116. Phase diagram of the erbium–yttrium system.

The thermal data points obtained by Spedding et al. were shown as single points for the melting temperatures and for the transition temperatures because the start and the stop of the thermal arrests on both heating and cooling curves were within 1.5°C, the same as for pure metals. The addition of erbium to yttrium or yttrium to erbium lowered the melting point to a minimum of 1507°C at 47 at% Y. Alloys containing more than 47 at% Y solidify to the bcc structure, which transforms at lower temperatures to hcp structure. Alloys with less than 47 at% Y crystallize directly to the hcp solid solution. The authors concluded that the wide separation between the liquidus and solidus lines for these alloys, reported in some earlier papers, was due, not to the enrichment of one rare earth over the other during freezing, but to the presence of impurities, particularly nonmetallic impurities. They also stated their belief that the pronounced minima in the melting point and transition temperature of the heavy lanthanide alloy series that have been reported, do not occur when the component rare earth metals are pure, but may well result if considerable impurities are present.

The phase diagram presented by Markova et al. showed melting temperatures for the pure metals that were lower than the accepted values listed in table 1 (Er: 1490°C and Y: 1515°C vs. the accepted values of 1529 and 1522°C, respectively). When their thermal analyses data are adjusted for the differences in the melting points of the pure metals, they generally agree quite well with those of Spedding et al.

2.69.2. *Lattice spacings*

Spedding et al. (1973) obtained lattice spacing data for the erbium–yttrium system by applying a least squares fit to the extrapolation of back reflection X-ray data. In addition to their plot of the lattice spacing data, which are shown in fig. 117, they compared their measured parameters with calculated values based on the spacings for the pure metals. They observed a slight positive deviation from linearity (Vegard's law) in both the *a* and *c* spacings, but this is hardly, if at all, evident in fig. 117.

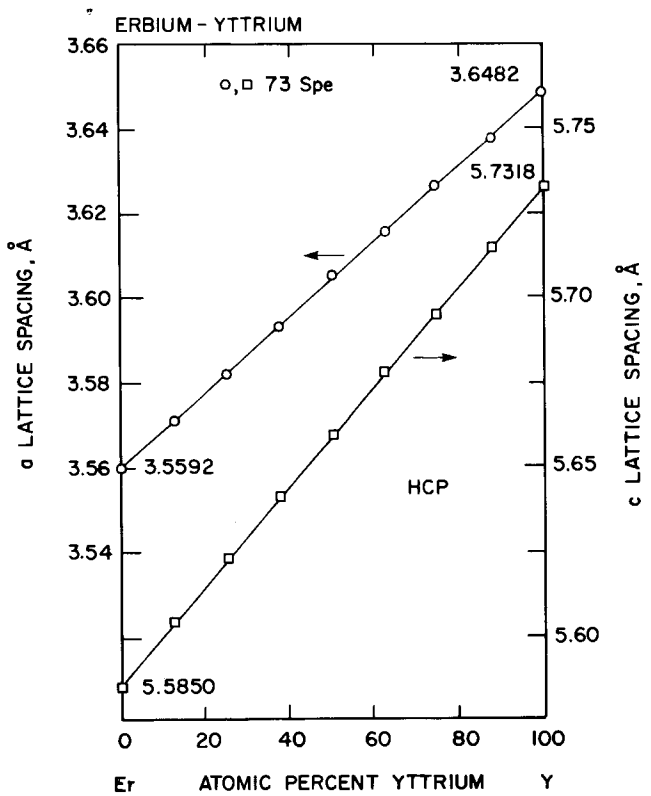

Fig. 117. Lattice spacings in the erbium–yttrium system. The straight lines represent the Vegard's law relationships based on the accepted values for the pure metals as listed in table 2.

References

Markova, I.A., V.F. Terekhova and E.M. Savitskii, 1964, Zh. Neorg. Khim. **9**, 2034 [English transl.: Russ. J. Inorg. Chem. **9**, 1098].

Spedding, F.H., B. Sandeen and B.J. Beaudry, 1973, J. Less-Common Met. **31**, 1.

2.70. *Yb–Lu: Ytterbium–lutetium*

2.70.1. *Phase diagram*

Beaudry and Spedding (1974) have studied the binary phase system between ytterbium metal, which is normally divalent, and lutetium metal, which is trivalent. The Yb–Lu system is representative of the systems between ytterbium and the rare earth metals that do not have a high temperature bcc form.

The ytterbium metal was prepared by the reduction–distillation method from a mixture of lanthanum metal and ytterbium sesquioxide, then purified by sublimation at 625°C. The impurities found in the ytterbium (in at ppm) were: 2570 H, 324 O, 210 Cl, 80 Ca, 62 N, 30 Dy, 29 C, 22 Fe and 20 each Mg and Lu. The lutetium metal

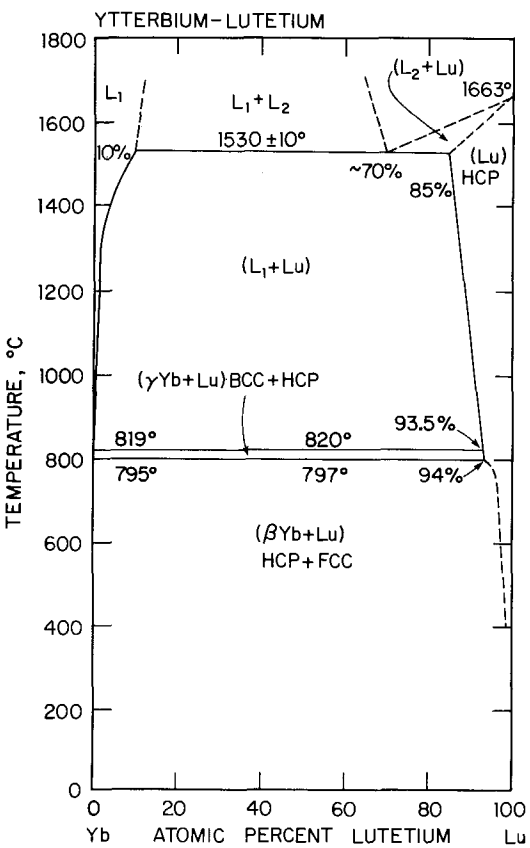

Fig. 118. Phase diagram of the ytterbium–lutetium system.

used in the study was prepared by the calcium reduction of lutetium fluoride in a tantalum crucible. The reduced metal was purified by vacuum casting at 1850°C for 10 min followed by sublimation at 1650°C into a tungsten-lined condenser under a vacuum of 10^{-8} torr. The principal impurities in the lutetium metal (in at ppm) were: 665 O, 520 H, 220 C, 50 W, 30 Fe and 28 F.

The effect of lutetium on the melting point and $\beta \rightleftarrows \gamma$ transformation of ytterbium and of ytterbium on the melting point of lutetium, as well as the temperature of the various horizontals in the system were determined by differential thermal analysis. The averages of the heating and cooling curve arrests were used to determine the horizontal temperature on both the Yb- and Lu-rich alloys since the arrests observed on heating and cooling were within experimental error of each other.

The phase diagram for the ytterbium–lutetium system as determined by Beaudry and Spedding is shown in fig. 118 with a slight adjustment to the melting point for pure ytterbium (raised from 816 to 819°C), the $\beta \rightleftarrows \gamma$ transformation temperature of pure ytterbium (dropped from 796 to 795°C), the peritectic horizontal temperature (raised from 817 to 820°C) and the peritectoid temperature (dropped from 798 to 797°C). These adjustments were made to bring the melting point and transition temperatures for pure ytterbium into agreement with table 1 values for this metal and to maintain the observed relationships between the melting and transition temperatures and the respective horizontals.

Extrapolation of the liquidus data to the 820°C peritectic horizontal indicates a solubility of about 0.2 at% Lu in Yb at that temperature. The decrease in the lattice parameter of a 10 at% Lu in Yb alloy heat-treated at 800°C and quenched indicated a solubility of 0.3 at% Lu in γYb. The solubility appears to drop to less than 0.1 at% Lu in βYb at 500°C since a sample equilibrated at 500°C and quenched to room temperature had the same lattice parameter as pure Yb. The solubility of Yb in Lu at 820°C (6.5 at% Yb) was obtained by extrapolating the solubility curve to the peritectic horizontal. Solubility of Yb in Lu at the 797°C peritectoid temperature was estimated to be 6 at%.

The authors concluded that the tendency to form trivalent ytterbium in lutetium is small. The small solubility of Yb in Lu is a result of the size disparity in this system.

2.70.2. *Thermodynamic data*

Beaudry and Spedding (1974) fitted the solubility of Lu in liquid Yb vs. temperature data by the least squares method to the equation $\log N = A + B/T$ where N is the concentration of Lu in at%, T is the absolute temperature and A and B are constants. The slope of the line B is equal to $-\Delta H/2.303R$ where ΔH is the heat of solution of Lu in Yb and R is the gas constant. There is considerable scatter in the data for the Lu–Yb system below 1200°C. A least squares fitting of the data from 1200 to 1500°C gave $A = 4.39$ and $B = 6258$, and from this a value of 120 kJ/mol was derived for the heat of solution over this temperature range.

Reference

Beaudry, B.J. and F.H. Spedding, 1964, Metall. Trans. **5**, 1631.

2.71. *Sc–Y: Scandium–yttrium*

2.71.1. *Phase diagram*

Beaudry and Daane (1963) investigated the scandium–yttrium system by thermal and X-ray methods. Impurities in their distilled scandium metal were (in wt ppm): 1100 O, 475 F, 400 Fe, 290 C, 250 Ta, 100 each Al, N and Cu, 75 each Ni and Cr, 50 each Si and Ca, 25 Mg and 20 Ti. Impurities in their yttrium metal (also in wt ppm): 530 O, 200 Fe, 159 F, 115 C, 100 Ta, 85 Ni, 56 N and 30 each Mg and Ca. Alloys were prepared by arc-melting the metals under an atmosphere of helium or argon, inverting and remelting five or more times to obtain homogeneity. During melting about 1.5 wt% of the metals were lost, but it was assumed that the intended compositions were not altered.

The solidus and the melting points of the alloys were determined by an optical pyrometer method. The temperature for the hcp ⇄ bcc transformations was determined by differential thermal analysis. Some solidus and liquidus points were also determined by this method and were in good agreement with those observed with the optical pyrometer.

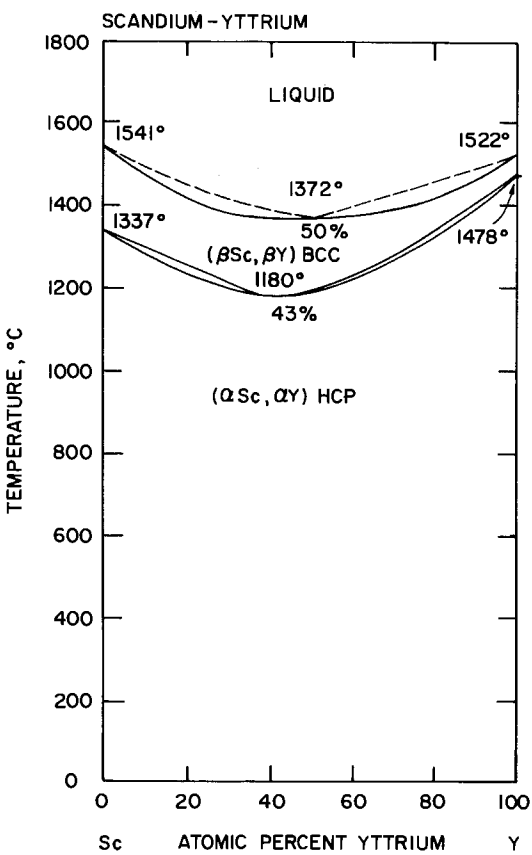

Fig. 119. Phase diagram of the scandium–yttrium system.

Markova et al. (1964) were in the process of investigating this system when the work of Beaudry and Daane was published. Markova et al. subsequently published some photomicrographs showing single-phase structure in scandium, yttrium and alloys containing 11, 43 and 67 at% yttrium, but did not show their phase diagram for the system. They stated that their measurements showed a continuous series of solid solutions of the isomorphous modifications of the components in this system, which confirms the work of Beaudry and Daane.

The phase diagram shown in fig. 119 is based on the thermal and X-ray studies made by Beaudry and Daane. The melting point temperatures and the $\alpha \rightleftarrows \beta$ transformation temperatures of the end-members did not agree with the accepted values for the pure metals as shown in table 1. Consequently these have been changed to agree with table 1 and the corresponding temperatures for each alloy specimen have been adjusted by prorating those deviations on the basis of the composition of the alloy. The minimum in the solidus and liquidus lines was therefore raised from 1365 to 1372°C and the minimum in the solvus lines was increased from 1175 to 1180°C. The liquidus on this phase diagram was shown as a dashed line since only a few points on this curve were determined experimentally. X-ray studies showed complete solid solubility of these alloys at room temperature.

Shiflet et al. (1979) attempted to calculate the phase diagram for the scandium–yttrium system by means of the Kaufman approach, which involves the differences in enthalpy and entropy between different crystal structures in the pure elements and the solution constant for the enthalpy of mixing. The composition of the congruently melting composition in the Sc–Y system was predicted with fair accuracy by this method, but the calculated melting temperature was about 150°C low. A particularly disturbing feature of this theoretical phase diagram was that the calculated liquid + bcc region crossed the calculated bcc + hcp area on the diagram.

2.71.2. *Lattice spacings*

Beaudry and Daane (1963) reported lattice spacings for the end-members and seven alloy compositions in the Sc–Y system using filings taken from heat-treated alloys. Their filings were sealed in tantalum capsules and annealed at 550°C for 15 hr then cooled at a rate of 5°C/min. The lattice spacings were calculated by a least squares method using the Nelson–Riley extrapolation function. Their data, as adjusted for deviations between the lattice spacings of the end-members and the corresponding accepted values for the pure metals as listed in table 2, are shown in fig. 120. The plotted data show a positive deviation from Vegard's law behavior for almost all compositions in both the a and c lattice spacings. Considering the high impurity contents of the metals from which these alloys were made, it is surprising that these deviations were not greater.

References

Beaudry, B.J. and A.H. Daane, 1963, Trans. Met. Soc. AIME **227**, 865.

Markova, I.A., V.F. Terekhova and E.M. Savitskii, 1964, Zh. Neorg. Khim. **9**, 2034 [English transl.: Russ. J. Inorg. Chem. **9**, 1098].

Shiflet, G.J., J.K. Lee and H.I. Aaronson, 1979, Calphad **3**, 129.

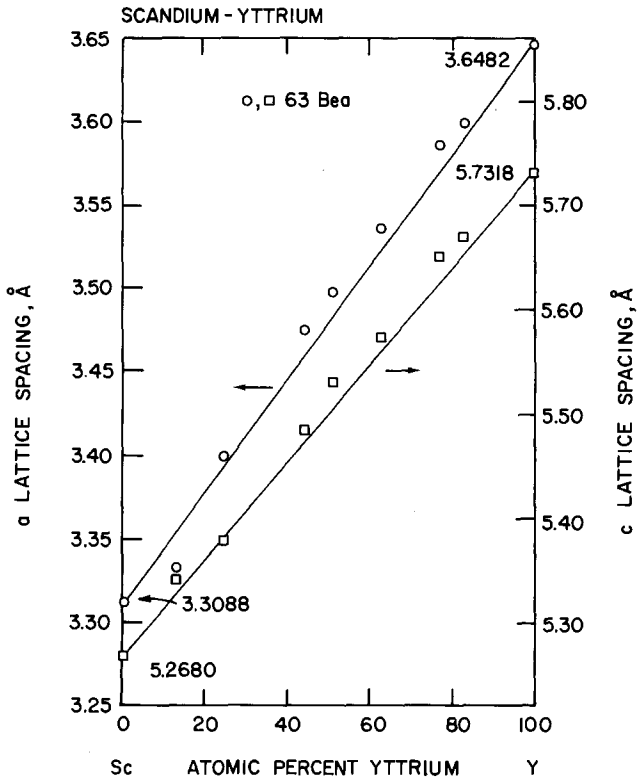

Fig. 120. Lattice spacings in the scandium–yttrium system. The straight lines represent the Vegard's law relationships and are based on the accepted values for the pure metals as listed in table 2.

3. Systematics

3.1. *Introduction*

Systematics is a process in which some property of the lanthanides, and sometimes the complete rare earth group, is examined in detail to see how it varies from one rare earth element to another. In general one examines the group as a whole, or at least a portion of the group (at least three members) to see the overall trend and anomalies from the trend. For the lanthanides the atomic number is usually the variable, but size is frequently used. For the rare earth group, which includes Sc and Y in addition to the lanthanides, the atomic or ionic size is the only logical variable on which the comparison is based.

As we will see systematics is a powerful tool. It gives us insight to and understanding of the chemical and physical natures of the rare earth metals, alloys and

compounds. It can be used to check the reliability of experimental results, i.e., to choose between two conflicting pieces of data or to question a result because it does not follow the trend established within the expected experimental error. It can also be used to predict unknown properties, especially by interpolation between known data. The use of systematics in evaluating RM binary phase diagrams (where R is rare earth and M is a non-rare earth metal) and RM crystallographic data have been described by Gschneidner and Calderwood (1983).

The smooth systematic variation of the physical properties of the lanthanides was recognized as soon as the first physical property measurements had been made on the entire group of lanthanide elements. The first such measurements were the lattice parameters of the rare earth oxides from which the ionic radii were deduced. In 1924, Goldschmidt, while compiling the ionic radii of the elements, noted that those of the lanthanide elements decreased in a regular and smooth fashion from La to Lu, and coined the words "lanthanide contraction" to describe this systematic trend (e.g. see Goldschmidt et al., 1925, von Hevesy, 1927 and Goldschmidt, 1954). He recognized that this contraction is due to the increased effective nuclear charge as an additional 4f electron is added as one proceeds along the lanthanide series in increasing atomic number. Since then, scientists have utilized systematics and deviations from the general trends to understand the natures and behaviors of lanthanide materials. For example, deviations in a plot of the metallic radii vs. the atomic number of the lanthanide elements indicate that Eu and Yb are divalent because of their much larger radii (see Beaudry and Gschneidner, 1978), and that αCe has a valence of ~ 3.7 because its radius lies below the established curve (see Koskenmaki and Gschneidner, 1978).

Properties that depend only upon the outer valence electrons will show similar regular variations when plotted against the atomic number. These include, in addition to the lattice constants of compounds, alloys, etc., the density, unit cell volume, melting point and most thermodynamic properties. Other properties, such as the magnetic susceptibility, moments, ordering temperatures, etc. and optical spectra, are due to the 4f electrons and thus the variations of these properties depend upon the S, L and J quantum numbers. These properties are not used in our systematic analysis of rare earth binary phase diagrams. Another set of related properties also behave anomalously—the boiling point, heat of sublimation at 298 K, the cohesive energy and any other thermodynamic quantity that involves the heat of sublimation in calculating a thermodynamic cycle, such as a Born–Haber cycle. The reason for this anomaly is that the boiling point, heat of sublimation, etc. not only involve the solids (which have three 6s5d valence electrons and a $4f^n$ configuration) but also the gaseous atoms (which have a $4f^{n+1}6s^2$ configuration except for La, Ce, Gd and Lu, which have $4f^n6s^25d$ configurations). The tendency to change electron configurations during evaporation or sublimation gives rise to a sawtooth-like variation in a plot of the property vs. atomic number (Beaudry and Gschneidner, 1978).

Yttrium and scandium data can also be examined along with those of the lanthanides. Generally the values for yttrium fall between those of dysprosium and

holmium, but this is not always true and some care and discretion must be used in the analysis. The data for scandium can be compared with those of the lanthanides by plotting the results as a function of the metallic radius, but again much care and discretion must be used if the scandium data deviate from the expected trends.

3.2. *Early work*

Work on correlating the crystal structure sequence in the pure metals and intra rare earth alloys started in about the mid-1960s, shortly after the discovery by Spedding et al. (1962) of the formation of the Sm-type structure in alloys between a light lanthanide metal and a heavy lanthanide (or yttrium) metal. The next major impetus was provided by the high pressure work of Bell Telephone Laboratory's research group (Jayaraman and Sherwood, 1964a, b; McWhan and Bond, 1964) who found that under pressure hcp Gd transformed to the Sm-type structure; Sm (rhombohedral, Sm-type structure) transformed to the dhcp structure; and dhcp La transformed to the fcc structure. Thus it became evident that the crystal structure sequence in the lanthanide series at 1 atm pressure varied from fcc → dhcp → Sm-type(or δ) → hcp, while pressure caused the reverse structure sequence.

The occurrence of these phases, especially the Sm-type structure, was discussed by a variety of investigators who tried to correlate these behaviors to c/a ratios (Spedding et al., 1962; Harris et al., 1966), size (Nachman et al., 1963), atomic volume (McWhan and Bond, 1964), 4f hybridization with conduction electrons (Gschneidner and Valletta, 1968; R.H. Langley, 1981), the average atomic number (Harris and Raynor, 1969), and the relative occupancy of s and d orbitals (Duthie and Pettifor, 1977; Skriver, 1983). Of these factors, all except size (and atomic volume) are valid and can be used with some modification to correlate the structure occurrences at atmospheric and high pressures. In the mid-1970s Johansson and Rosengren (1975) developed a generalized phase diagram for the rare earth elements by superimposing the individual pressure–temperature diagrams on one another by connecting their melting points and in some instances their hcp–bcc phase transformation temperatures. From this, one could correlate the general trends of the various phase transformations, but their generalized diagram is difficult to use, especially for binary alloys, because the temperature and pressure axes are displaced from one lanthanide to another.

3.3. *Generalized phase diagram at 1 atm*

Recently, by making use of systematics, Gschneidner (1985a) proposed a generalized phase diagram for the trivalent intralanthanide and yttrium–lanthanide binary alloys. This single diagram, shown in fig. 121a, represents a total of 91 phase diagrams. The diagram was constructed from the melting and transformation temperatures of the trivalent lanthanides, assuming Ce and Sm are trivalent. The data for Eu and Yb in this figure are for the hypothetical trivalent states. The various phase boundaries were estimated from the various intralanthanide phase diagrams. In order to accomplish this, each lanthanide was assigned a value called

the "systematization number" (SN), which is shown on the top of the diagram. It is seen that SN varies from zero for La to 14 for Lu, and is equal to the total number of 4f electrons for the respective trivalent lanthanide element. However, as Gschneidner (1985a) points out, this coincidence is fortuitous and no implication was intended that these two numbers are related. Yttrium was assigned an SN value of 9.5.

In order to estimate the location of a critical composition or phase boundary, x_B (mole fraction of B), in any intralanthanide alloy system between lanthanides A and B one uses the lever law

$$(1 - x_B)\mathrm{SN}_A + x_B\mathrm{SN}_B = \mathrm{SN}_{\mathrm{cp}}$$

and the systematization number of the critical point or phase boundary, $\mathrm{SN}_{\mathrm{cp}}$. In the above equation SN_A and SN_B are the respective systematization numbers of A and B. The $\mathrm{SN}_{\mathrm{cp}}$ values are listed in table 5.

The phase boundaries shown in fig. 121a are shown as narrow lines, but in the actual phase diagrams the two phase regions are generally between 2 and 10 at% wide; for neighboring lanthanides they may be as wide as 20 at%. Gschneidner (1985a) believed that the boundaries can be estimated to within 5 at% and the temperatures to within ± 25°C.

The dip at Ce in the melting point and two transformation points is due to the valence fluctuation character of Ce, and presents no problem when Ce is one of the end-members of a binary phase diagram. When Ce and R are alloyed the appropriate phases and the corresponding temperatures will be found as indicated in the generalized phase diagram.

This dip, however, is ignored in phase diagrams in which La is an end-member and the other end-member is any other lanthanide (or yttrium) except Ce. Since this dip is due to the 4f electron in Ce, a feature that cannot be mimicked by a pseudo-Ce composition made up by a La–R alloy with SN = 1, no dip is to be expected, and none is found in the known La–R systems (e.g., see section 2.4.1, fig. 5). For a La–R diagram, the melting points of La and R are connected with a straight line allowing for a liquidus–solidus separation at intermediate compositions. A shallow dip, however, is expected in the bcc → hcp transformation since this is due

TABLE 5
Systematization number for phase boundary limits or critical points on the generalized phase diagram.

Phase boundary limit or critical point	Temperature (°C)	Systematization number
fcc–dhcp	> 400	1.2
dhcp–δ(Sm)	25	4.4
δ(Sm) decomposition	Maximum	5.0
δ(Sm)–hcp	25	5.6
bcc–hcp–liquid	> 1200	9.8

to a eutectoid decomposition of the bcc phase to the dhcp plus fcc phases at SN = 1 (see section 2.4.1, fig. 5). For Y, the hcp–bcc and bcc–liquid transformation temperatures are about 50°C higher than the values shown on the generalized phase diagram at SN = 9.5. Thus the respective phase boundaries must be prorated upward accordingly when one is calculating a particular Y–R diagram.

The continuous phase transition from the dhcp phase at low SN values (< 5) to the hcp phase at high SN values (> 5) as shown in fig. 121a is consistent with our current understanding of binary intra rare earth alloys involving a light lanthanide metal ($0 \leq SN \leq 4$) with a heavy lanthanide or yttrium metal ($7 \leq SN \leq 14$). This has been discussed in section 2.1.4.

Although the generalized phase diagram may be used with confidence for most binary combinations, it appears it may not be valid with regard to the formation of the δ phase in lutetium alloys with the light lanthanides. On the basis of an X-ray study in both the La–Lu (section 2.8.1) and Nd–Lu (section 2.36.1) systems, no δ-phase structure was observed in the X-ray patterns of alloys that were expected to have this phase.

An analysis of the generalized binary alloy phase diagram showed that there are only 13 possible types of diagrams that can be formed (Gschneidner 1985a). Of the known phase diagrams, 11 of the 13 types have been observed experimentally. Using the scheme outline above, Gschneidner calculated the hypothetical diagrams of the other two types, La–Er, which represents type 5, and Sm–Ho, which represents type 11. A type 5 phase diagram is formed between one component having three polymorphic phases and a second monophasic component that is not isomorphic with any phase of the first component, but a region of complete miscibility is formed between the dhcp phase of the first component and hcp phase of the second component. A type 11 phase diagram is formed between Sm, which has three polymorphic forms, and the heavy lanthanides, which have only the hcp structure (Ho, Er, Tm and Lu).

3.4. *The high pressure generalized phase diagram*

In a second paper Gschneidner (1985b) extended the atmospheric generalized intra rare earth binary phase diagram to high pressures: 1, 2 and 4 GPa (see figs. 121b, c and d, respectively). The high pressure diagrams are almost entirely based on high pressure behaviors of the pure metals. The greatest uncertainty in these diagrams lies in the intermediate temperature range between room temperature and the hcp–bcc and bcc–liquid phase boundaries.

Examination of Fig. 121 shows that the fcc and Sm-type phase fields tend to expand at the expense of the dhcp- and hcp-phase fields, respectively, as the pressure is increased, and since the fcc-phase field is growing faster than the Sm-type phase field, the fcc structure is expected to be the stable phase at sufficiently high pressures.

The formation of the collapsed αCe phase from γCe is evident in figs. 121b and c. At higher pressure the transformation of the fcc αCe to the αU-type structure is noted in fig. 121d. The influence of these dense phases on the melting point is quite evident as the Ce dip becomes much more severe as the pressure increases.

Figs. 121–123

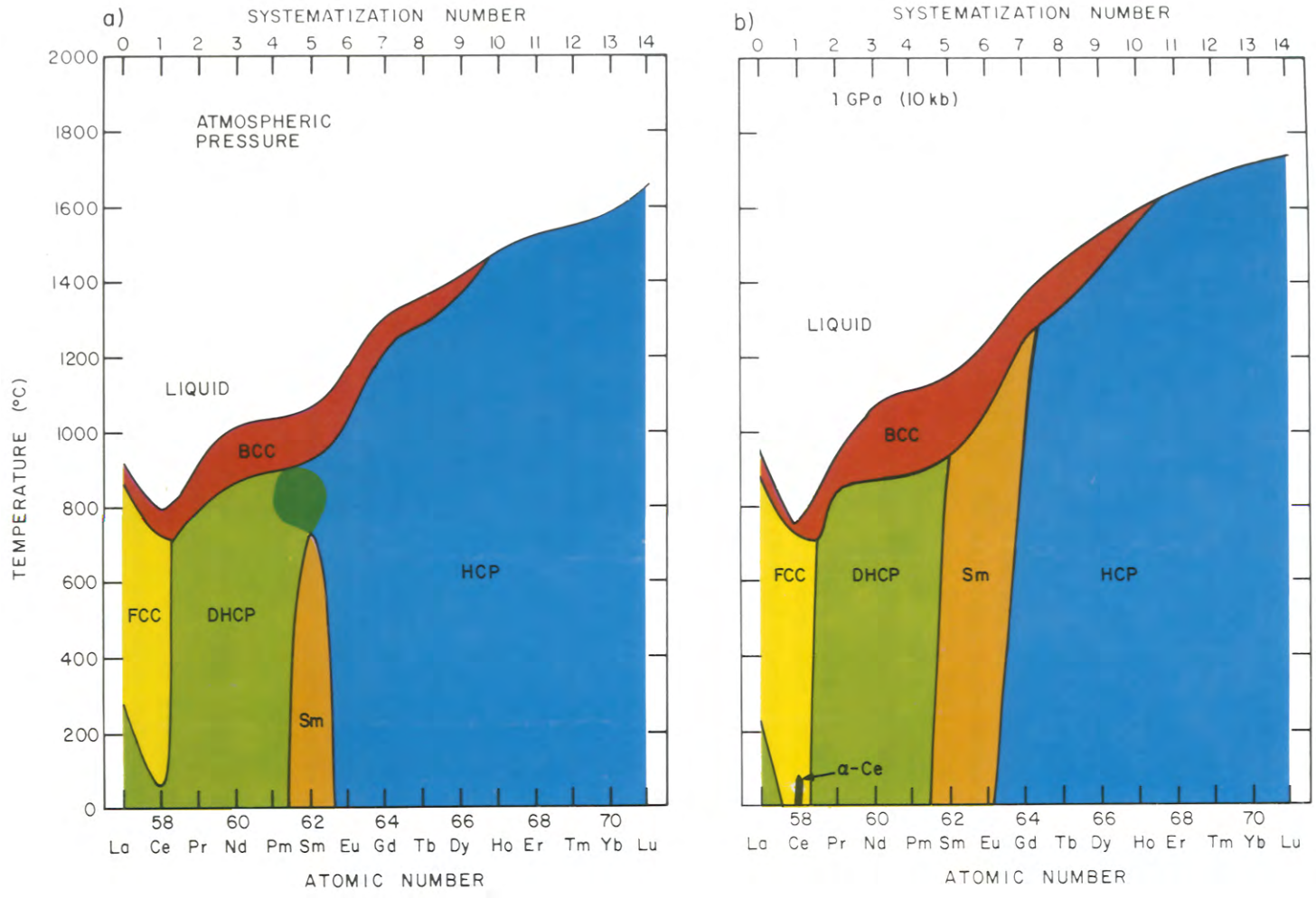
a)
SYSTEMATIZATION NUMBER
0 1 2 3 4 5 6 7 8 9 10 11 12 13 14
ATMOSPHERIC PRESSURE
LIQUID
BCC
FCC
DHCP
Sm
HCP
TEMPERATURE (°C)
2000
1800
1600
1400
1200
1000
800
600
400
200
0
58 60 62 64 66 68 70
La Ce Pr Nd Pm Sm Eu Gd Tb Dy Ho Er Tm Yb Lu
ATOMIC NUMBER
b)
SYSTEMATIZATION NUMBER
0 1 2 3 4 5 6 7 8 9 10 11 12 13 14
1 GPa (10 kb)
LIQUID
BCC
FCC
DHCP
Sm
HCP
α-Ce
58 60 62 64 66 68 70
La Ce Pr Nd Pm Sm Eu Gd Tb Dy Ho Er Tm Yb Lu
ATOMIC NUMBER

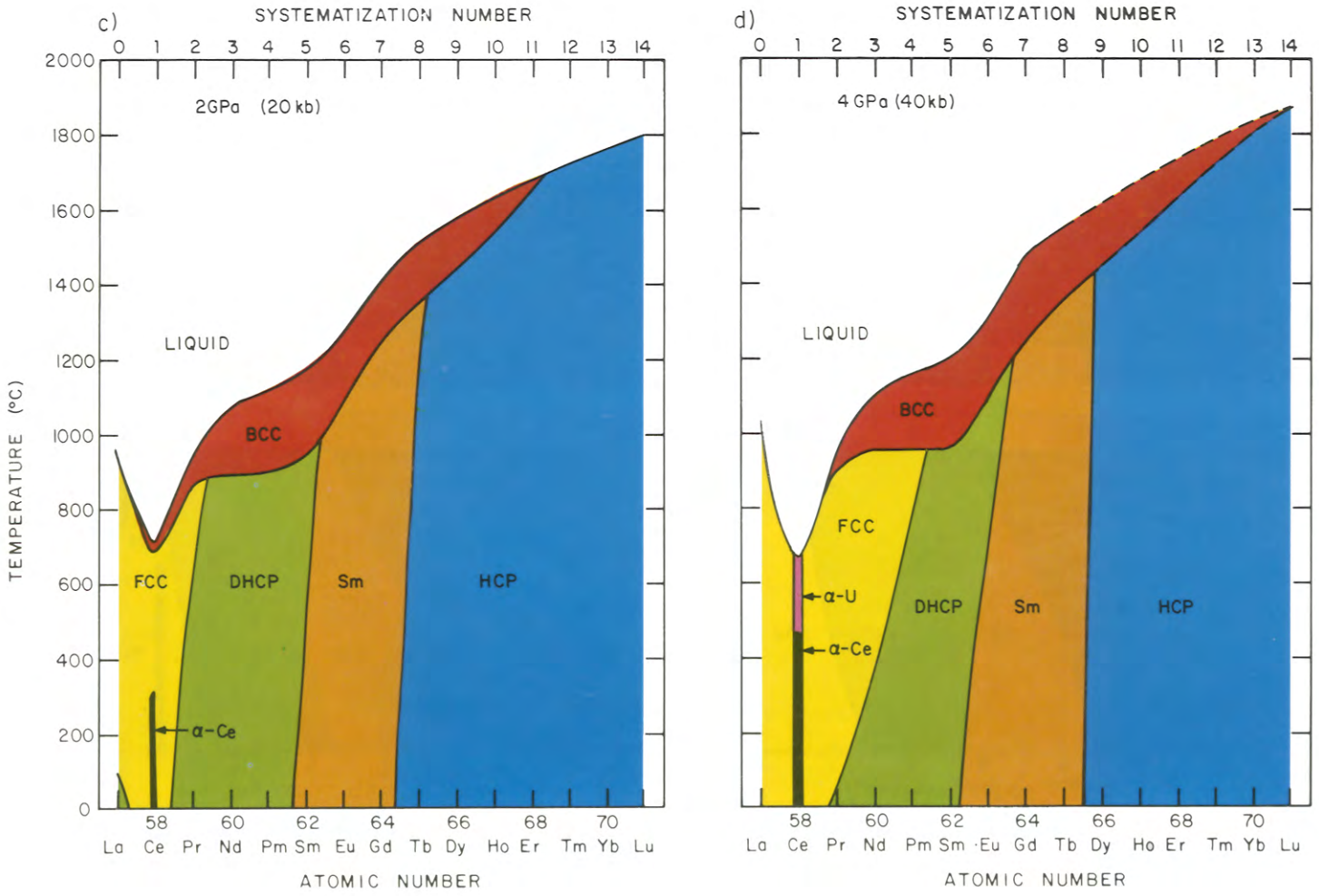

Fig. 121. The generalized phase diagram for trivalent intralanthanide alloys at various pressures: (a) the isopiestic section at atmospheric pressure; (b) the 1 GPa (10 kbar) isopiestic section; (c) the 2 GPa (20 kbar) isopiestic section; and (d) the 4 GPa (40 kbar) isopiestic section.

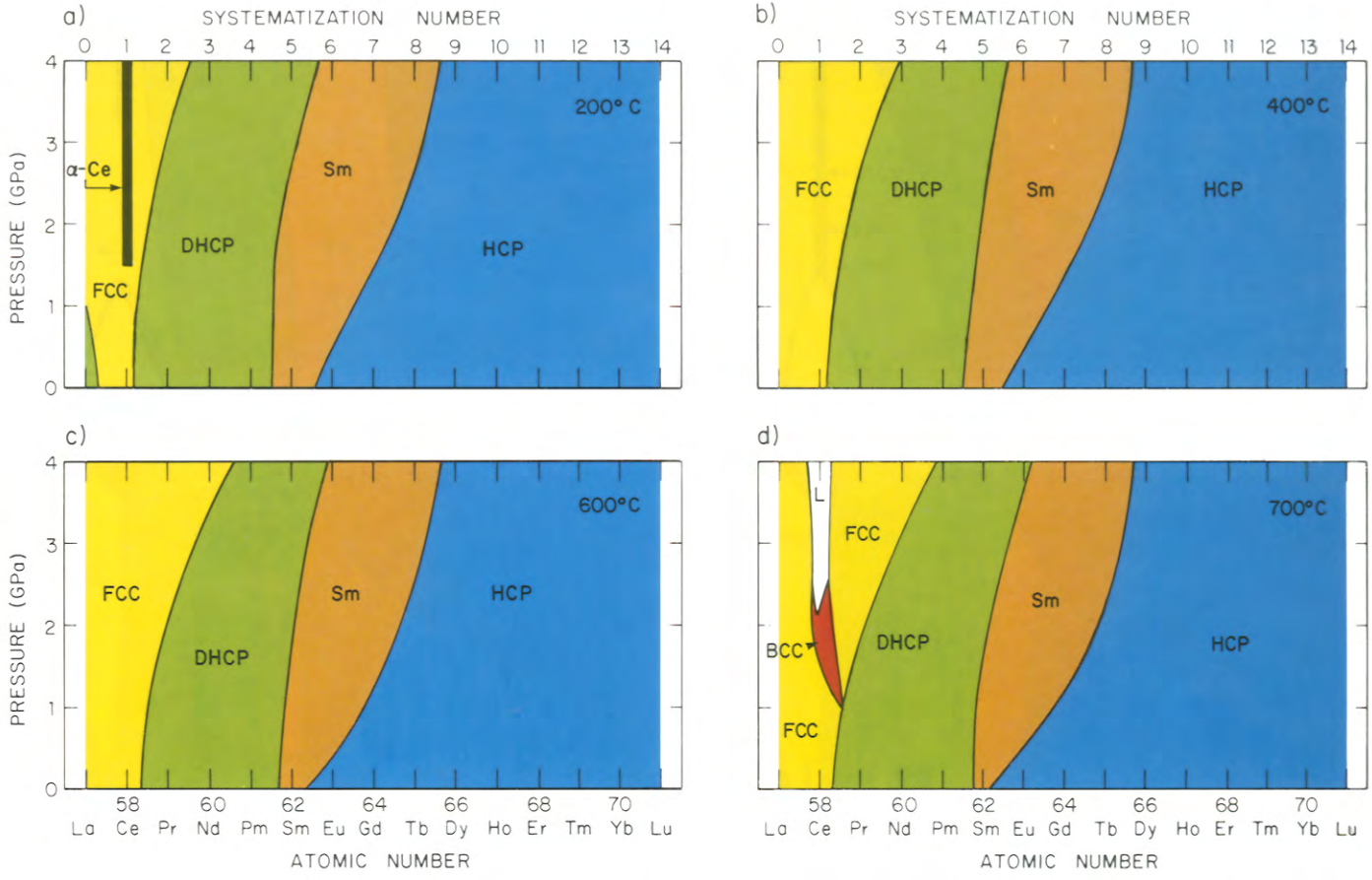
a)
SYSTEMATIZATION NUMBER
0 1 2 3 4 5 6 7 8 9 10 11 12 13 14
200° C
α-Ce
FCC
DHCP
Sm
HCP
PRESSURE (GPa)
0 1 2 3 4
b)
SYSTEMATIZATION NUMBER
0 1 2 3 4 5 6 7 8 9 10 11 12 13 14
400° C
FCC
DHCP
Sm
HCP
c)
600°C
FCC
DHCP
Sm
HCP
PRESSURE (GPa)
0 1 2 3 4
58 60 62 64 66 68 70
La Ce Pr Nd Pm Sm Eu Gd Tb Dy Ho Er Tm Yb Lu
ATOMIC NUMBER
d)
L
FCC
700°C
Sm
BCC
DHCP
HCP
FCC
58 60 62 64 66 68 70
La Ce Pr Nd Pm Sm Eu Gd Tb Dy Ho Er Tm Yb Lu
ATOMIC NUMBER

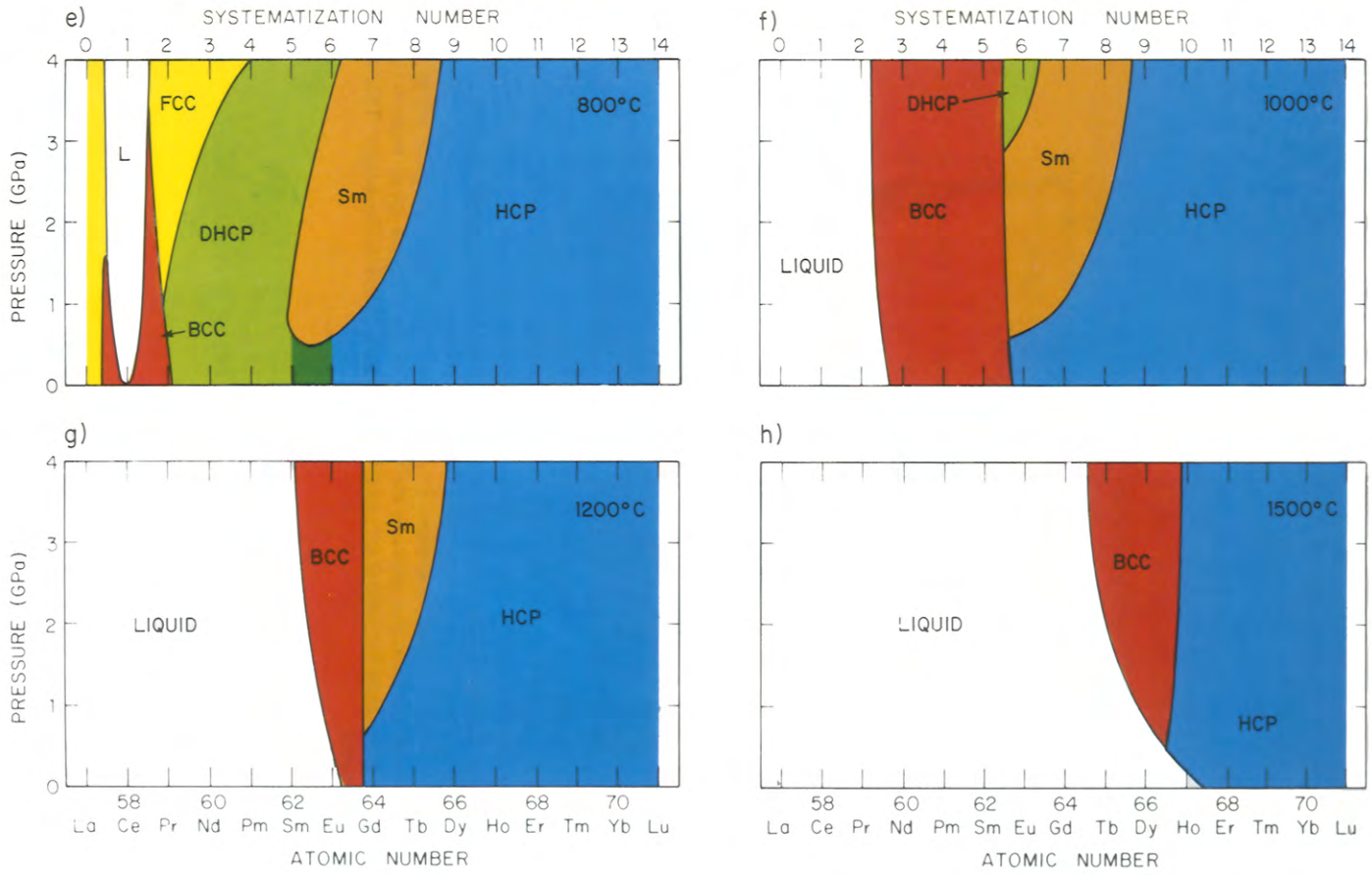

Fig. 122. Isothermal sections of the generalized intra rare earth binary alloy phase diagram from 0 to 4 GPa: (a) 200, (b) 400, (c) 600, (d) 700, (e) 800, (f) 1000, (g) 1200, and (h) 1500°C.

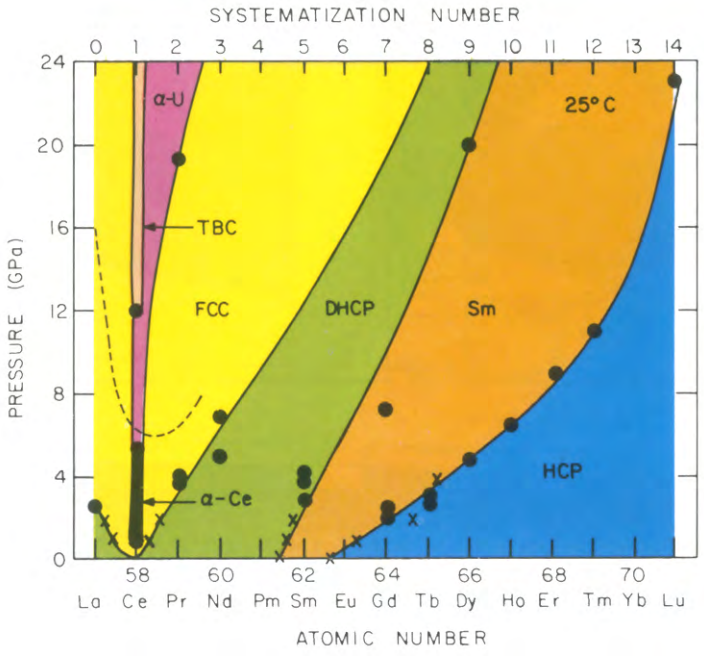

Fig. 123. The 25°C isothermal section of the intra rare earth generalized binary phase diagram from 0 to 24 GPa (0 to 240 kbar). The solid circles are transformation points observed in the pure metals and the × data points are taken from the phase boundaries given in the generalized phase diagrams shown in fig. 121. The dashed line in the fcc region indicates the formation of the distorted fcc or triple hexagonal close-packed (thcp) phase from the normal fcc phase with increasing pressure. The letters "TBC" mean tetragonal body-centered.

The pressure dependence of the bcc region is quite interesting: The region disappears with increasing pressure for La, Ce and Pr but grows with increasing pressure from Sm (SN = 5) to the end of the lanthanide series Lu, SN = 14. For Nd the bcc region expands as the pressure increases to 2 GPa and then contracts as more pressure is applied. Gschneidner (1985b) correlated this behavior of the bcc region with the d occupation number n_d (see table 6). Based on the disappearance of γLa (bcc) with pressure and the termination of the bcc phase at 1 atm between Dy and Ho, Gschneidner estimated that the bcc phase is stable over the range $1.6 \geq n_d \geq 2.2$. Since n_d increases with increasing pressure by about 0.1/GPa (Skriver, 1983), application of pressure causes the light lanthanides, which have high n_d values, to exceed the 2.2 upper limit and disappear, while for those elements which have small n_d values (< 1.6), pressure increases n_d so that it exceeds the 1.6 lower limit causing the bcc to form.

In order to determine the structure(s) of a given binary rare earth alloy system, one follows the procedures outlined in section 3.3 utilizing the appropriate isopiestic section shown in fig. 121. Unfortunately, it is difficult to make such estimates for pressures between the four isopiestic sections. In order to improve such estimations a set of eight isothermal sections at 200, 400, 600, 700, 800, 1000, 1200 and 1500°C is presented in fig. 122, where the ordinate extends up to 4 GPa. Since little if any high temperature data exist above 4 GPa the diagrams were cut off at this pressure. At room temperature, however, data extend up to higher pressures as shown in fig. 123.

With increasing temperature the αCe phase (seen in fig. 122a) disappears (absent in fig. 122b) because of the α–γ critical point at 327°C. The fcc phase is seen to grow at the expense of the dhcp as the temperature is raised (figs. 122a, b and c), but the formation of the bcc phase interrupts this process (fig. 122d). The bcc phase continues to expand with increasing temperature eliminating the dhcp between 1000 and 1200°C (figs. 122f and g) and also the Sm-type phase between 1200 and 1500°C (figs. 122g and h). The Sm-type phase region expands with increasing pressure and maintains its width of about three SN values with increasing temperature until about

TABLE 6
The d occupation number n_d for the trivalent rare earth metals (after Skriver, 1983).

R	n_d	R	n_d
La	1.99	Dy	1.64
Ce	1.97	Ho	1.60
Pr	1.93	Er	1.56
Nd	1.89	Tm	1.52
Pm	1.85	Yb[a]	1.48[b]
Sm	1.81	Lu	1.44
Eu[a]	1.77[b]	Sc	1.58
Gd	1.72	Y	1.60
Tb	1.68		

[a] Hypothetical trivalent R.
[b] Estimated by reviewers.

1000°C (figs. 122a–f) and it begins to narrow down and disappears as noted above. But at low pressures (< 0.5 GPa) this phase, which is about one SN value wide (fig. 122a and b) begins to narrow at 600°C (fig. 122c) and disappear between 700 and 800°C (figs. 122d and e). At high temperature the liquid phase becomes important for the light lanthanides at practically all pressures.

The extremely high pressure behavior of the lanthanides at room temperature, as shown in fig. 123, is quite interesting. The fcc and Sm-type phase fields expand with increasing pressure at the expense of the dhcp- and hcp-phase fields, respectively. The formation of the unusual αU-type structure for Ce and Pr and the body-centered tetragonal (bct) phase for Ce is evidence for delocalization of the 4f electron in these metals at high pressure (Koskenmaki and Gschneidner, 1978; Grosshans et al., 1983; Benedict et al., 1984).

The dashed line in fig. 123 in the fcc region represents the formation of a "distorted fcc" phase from the true fcc polymorph with increasing pressure (Grosshans et al., 1982). More recently, Smith and Akella (1984) suggested that this new phase has a triple hexagonal close-packed (thcp) structure, which had been predicted by McMahan and Young (1984).

The rapid rise of the hcp–Sm-type phase boundary beyond Tm (fig. 123), and the anomalous high pressures of transformation in Y (hcp → Sm-type, Sm-type → dhcp and dhcp → fcc) relative to lanthanide elements was cited by Gschneidner (1985b) as evidence for 4f valence electron hybridization having a significant role in determining the lanthanide crystal structure. He noted, however, that d occupation number probably is more important in determining which crystal structure would form, as had been proposed by others (e.g., see Duthie and Pettifor, 1977; Skriver, 1983).

3.5. *Lattice spacings and Vegard's law*

Lattice spacings have been reported for about 40% of the possible intra rare earth systems, and these have been summarized in earlier portions of this review. Several interesting trends have been noted by Gschneidner (1985a) and these are discussed below.

For systems wherein both end-members have the same structure at room temperature, either positive deviations from Vegard's law are found in either the a (25 systems) or c (10 systems) lattice parameter (e.g., see section 2.2.2 and fig. 2), or no deviations (22 systems) are observed. This behavior is consistent with the second order elasticity model of Gschneidner and Vineyard (1962) that predicts only positive deviations from Vegard's law regardless of the solute to solvent size ratio. Other models predict both positive and negative deviations from Vegard's law (Gschneidner and Vineyard, 1962).

When the end-members have different room temperature structures quite a different behavior is found. For a light lanthanide metal as a solvent the a parameter generally exhibits a negative deviation from Vegard's law, while the c parameter shows a positive deviation (e.g., see section 2.4.2 and figs. 6 and 7, respectively). This behavior was found in 28 of 33 systems for both the a and c lattice parameters. But if the solvent is a heavy lanthanide or Y or Sc, the a parameter deviates positively

from Vegard's law (15 of 18 systems) and the c parameter tends to exhibit a negative deviation (7 of 18 systems) or no deviation (7 of 18 systems). Typical examples can be found in section 2.38.2, figs. 67 and 68, respectively.

Gschneidner (1984a) found that these behaviors can be understood in terms of the d occupation numbers, which are smaller for the heavy lanthanides, Y and Sc than those of the light lanthanides (see table 6). It is known that an increase in the amount of d character results in a smaller c/a ratio (Legvold et al., 1977). Gschneidner (1984a) argued that when a heavy lanthanide (or Y or Sc) is added to a light lanthanide the amount of d character seen by the heavy lanthanide solute is larger than in the pure heavy lanthanide metal. This "excess" d character can be reduced by increasing the c/a ratio beyond that expected from a simple addition of atomic volumes and this leads to a negative deviation from Vegard's law in the a parameter of the matrix and also a positive deviation in the c parameter, which is the case when the dhcp and Sm phases are solvents. The opposite occurs when a light lanthanide is dissolved in a heavy lanthanide matrix: The light lanthanide sees a smaller amount of d character and this deficiency will be ameliorated by decreasing the c/a ratio. This causes a positive deviation from Vegard's law of the a lattice parameter and a negative deviation of the c lattice parameter, which is observed for a hcp solvent containing light lanthanide solutes.

Of course in addition to the dependence on the d occupation number, second order elasticity effects also apply. This probably accounts for the fact that for the heavy lanthanide solvents the departures from Vegard's law exhibited in the c lattice spacing are only slightly negative or do not occur because the electronic and second order elasticity effects tend to cancel one another.

Thus, the variation of lattice parameters in the intra rare earth alloys is reasonably well understood in terms of elasticity theory and electronic configurations (d occupation numbers). Exceptions to the above correlations are probably due to poor experimental data.

3.6. *Thermodynamics*

Lundin and Yamamoto (1967) investigated the Pr–Nd, Sm–Gd, Sm–Y and Gd–Y systems to further the understanding of alloy formation. Variables under consideration were electronic structure, crystal structure, atomic diameter, valences and electronegativity. The Pr–Nd system (see section 2.25) represented a system in which there were no significant differences in these parameters and their investigation revealed thermodynamic ideality in this system (see section 2.25.3, fig. 45). The Sm–Gd system (section 2.39) had one major variable, the crystal structure Sm-type vs. hcp, and showed large negative deviations from ideality (see section 2.39.3, fig. 71), which were attributed to lattice strain. The Gd–Y system (section 2.52), in which the crystal structures are the same, had a large difference in electronic structure between the two components but was found to be thermodynamically ideal (see section 2.52.4, fig. 91). The Sm–Y system (section 2.40) varies from the other systems in that the room temperature crystal structures (Sm-type vs. hcp) and the electronic structures [$(6s5d)^3 4f^5$ vs. $(5s4d)^3$] of the components are different while

the metallic radii (1.802 vs. 1.801 Å) and the electronegativities (1.26 vs. 1.27) are essentially equal. Large negative deviations, which were not as large as found in the Sm–Gd system, were observed (see section 2.40.3, fig. 75) and Lundin and Yamamoto concluded that this was due to the crystal structure difference between the components.

Although their conclusions may seem reasonable, the fact is that, in the two systems in which large negative deviations were observed in the activities (Sm–Gd and Sm–Y), the measurements were made at high temperatures (900°C) where the metals have the same hcp crystal structure. Thus it is unlikely that the crystal structure is the important factor in causing nonideal behaviors. A comparison with d occupation number (table 6) suggests that this cannot account for the departure from ideality. That is, the difference in d occupation numbers is 0.04 for Pr–Nd, 0.09 for Sm–Gd, 0.21 and Sm–Y and 0.12 for Gd–Y and if the two Sm systems deviate from ideality one would also expect the Gd–Y alloys to do the same. The major difference between the systems studied is the much higher vapor pressure of Sm compared with the other four metals (see table 4). This high vapor pressure is related to the tendency for Sm to become divalent, see section 7 in Beaudry and Gschneidner (1978). Thus the most reasonable conclusion is that the departures from ideality are due to the tendency of Sm to become divalent.

References

Beaudry, B.J. and K.A. Gschneidner, Jr., 1978, in: Gschneidner, Jr., K.A., and L. Eyring, eds., Handbook on the Physics and Chemistry of Rare Earths, Vol. 1 (North-Holland, Amsterdam) p. 173.

Benedict, U., L. Geward and J.S. Olsen, 1984, Acta Crystallogr. **A40** Suppl., C-413.

Duthie, J.C. and D.G. Pettifor, 1977, Phys. Rev. Lett. **38**, 564.

Goldschmidt, V.M., 1954, Geochemistry (Clarendon Press, Oxford) p. 306.

Goldschmidt, V.M., T. Barth and G. Lunde, 1925, Geochemische Verteilungsgesetze der Elemente V, in: Skrifter utgit av det norske Videnskaps-Akademi i Oslo, I. Matem.-Naturvid. Klasse [5], 5–24; abstracted in Chem. Abstr. **19** (1925) 3391.

Grosshans, W.A., Y.K. Vohra and W.B. Holzapfel, 1982, Phys. Rev. Lett. **49**, 1572.

Grosshans, W.A., Y.K. Vohra and W.B. Holzapfel, 1983, J. Phys. F **13**, L149.

Gschneidner, K.A., Jr., 1985a, J. Less-Common Met. **114**, 29.

Gschneidner, K.A., Jr., 1985b, J. Less-Common Met. **110**, 1.

Gschneidner, K.A., Jr. and F.W. Calderwood, 1983, Bull. Alloy Phase Diagrams **4**, 129.

Gschneidner, K.A., Jr., and R.M. Valletta, 1968, Acta Metall. **16**, 477.

Gschneidner, K.A., Jr., and G.H. Vineyard, 1962, J. Appl. Phys. **33**, 3444.

Harris, I.R. and G.V. Raynor, 1969, J. Less-Common Met. **17**, 336.

Harris, I.R., C.C. Koch and G.V. Raynor, 1966, J. Less-Common Met. **11**, 436.

Jayaraman, A. and R.C. Sherwood, 1964a, Phys. Rev. Lett. **12**, 22.

Jayaraman, A. and R.C. Sherwood, 1964b, Phys. Rev. **134**, A691.

Johansson, B. and A. Rosengren, 1975, Phys. Rev. B **11**, 2836.

Koskenmaki, D.C. and K.A. Gschneidner, Jr., 1978, in: Gschneidner, K.A. Jr., and L. Eyring, eds., Handbook on the Physics and Chemistry of Rare Earths, Vol. 1 (North-Holland, Amsterdam) p. 337.

Langley, R.H., 1981, J. Solid State Chem. **38**, 300.

Legvold, S., B.N. Harmon, B.J. Beaudry, P. Burgardt, D.R. Younkin and H.W. White, 1977, Phys. Rev. B **16**, 4986.

Lundin, C.E. and A.S. Yamamoto, 1967, Final Report, Denver Research Institute Rept. DRI-2437, University of Denver, Denver, CO.

McMahan, A.K. and D.A. Young, 1984, Phys. Lett. **105A**, 129.

McWhan, D.B. and W.L. Bond, 1964, Rev. Sci. Instrum. **35**, 626.
Nachman, J.F., C.E. Lundin and G.P. Rauscher, Jr., 1963, Denver Research Institute Rept. DRI-2082, University of Denver, Denver, CO.
Skriver, H.L., 1983, in: Sinha, S.P., ed., Systematics and the Properties of the Lanthanides (Reidel, Dordrecht, The Netherlands) p. 213.
Smith, G.S. and J. Akella, 1984, Phys. Lett. **105A**, 132.
Spedding, F.H., R.M. Valletta and A.H. Daane, 1962, Trans. Quarterly (Am. Soc. Met.) **55**, 483.
von Hevesy, G., 1927, Die Seltenen Erden von Standpunkte des Atombaues (Julius Springer, Berlin) p. 22.

Acknowledgments

The authors are indebted to L.H. Bennett, National Bureau of Standards, H. Baker, American Society for Metals and our co-workers B.J. Beaudry and O.D. McMasters for their critical and helpful comments.

Handbook on the Physics and Chemistry of Rare Earths, edited by K.A. Gschneidner, Jr. and L. Eyring

Chapter 55

POLAROGRAPHIC ANALYSIS OF THE RARE EARTHS

XIAOXIA GAO
Department of Chemistry, Peking University, Beijing, People's Republic of China

Contents

Symbols

ac = alternating current
dc = direct current
DPP = differential pulse polarography
EC = electrode and chemical reactions
$E_{1/2}$ = half-wave potential, V
E_p = peak potential, V

JP-1A = single-sweep oscillographic polarograph
LS = linear sweep (PAR 384-4)
M = mole/liter; metal
M303 = static mercury drop electrode, Model-303 (PAR 384-4)
M-79-1 = voltammetric analyzer, Model-79-1 (made in China)
NPP = normal pulse polarography
PAR 370 = electrochemistry system, Model 370, lock-in Model 174A, 175 (made by Princeton Applied Research Corp., USA)
PAR 384-4 = polarographic analyzer, Model 384-4 (made by Princeton Applied Research Corp., USA)
s = slope
SCE = saturated calomel electrode
SMDE = static mercury drop electrode
μC = microcoulomb
μg = microgram
V = volt
v = rate of scan, V/s or mV/s

1. Introduction

The unique chemical similarity of the rare earth group elements and their undesirable electrochemical properties make the determination of individual members of this group by polarographic analysis exceedingly difficult with only a few exceptions. Eu, Yb and Sm can be reduced at the dropping mercury electrode (DME) from the trivalent to the divalent states with half-wave potentials less negative than -1.8 V (vs. SCE), so that the waves are not obscured because of the reduction of hydrogen ions. The first study of the polarography of the rare earth group elements was made on Sc by Noddack et al. (1937), and they concluded that the reduction takes place in two stages, first to the 2+ state and then to the metal. However, in view of the experiments of Leach et al. (1937), this conclusion appears to be incorrect, and the first wave observed by Noddack et al. was probably due to the discharge of hydrogen ion. Kolthoff et al. (1952) surveyed the works done before 1952. Ryabchikov et al. (1966) wrote a monograph on "Analytical Chemistry of Ytterbium and the Lanthanide Elements", which was translated into English by Aladjem (1970), and where the analytical chemistry of the rare earth group elements before 1966 was very thoroughly reviewed. The recent review on this subject was written by O'Laughlin (1979) in chapter 37A of Volume 4 of this *Handbook*. From these reviews it may be seen that the most useful polarographic methods of analysis are only those of Eu and Yb with half-wave potentials equal to -0.67 and -1.41 V (vs. SCE), respectively. Until recently the development of polarographic analysis of the rare earths was rather slow, as noted by O'Laughlin (1979): "Polarographic methods are not as sensitive nor as accurate as spectrometric methods and are seldom employed at this present time."

Since 1960 our research group has investigated the polarographic catalytic waves of many metal ions. For example, in cooperation with the Chinese Academy of Geological Sciences, we have developed new catalytic waves for noble metals, such as Rh, Ir and Pt, which have sensitivities as high as 10^{-9} to 5×10^{-11} M and have

successfully applied them to the analyses of ores (Gao et al., 1977). Since China's rare earth resources are richly endowed by nature, we are urged to develop quick, sensitive and accurate analytical methods for rare earths using simple and inexpensive instruments. In 1978, in cooperation with the Chinese Academy of Geological Sciences, our group started to study the electroanalytical chemistry of the rare earth group elements, especially the polarographic methods. To date we have proposed more than ten sensitive systems for the analysis of the rare earths. We have also studied the mechanisms of these polarographic waves and found that they belong to several different types, which will be discussed in detail in the following section. The sensitivities of these waves in single-sweep polarography are 10^{-6} to 10^{-7} M, and in some systems, may be down to 10^{-8} M. They have been used for the determination of microamounts of individual or total rare earths in phosphors, alloys, minerals, ores and plants. It was found that these polarographic methods are simple and easy to perform, and the results are comparable with those obtained by other analytical methods.

2. Literature survey of the polarographic analysis of the rare earths

2.1. *Polarographic analysis in simple base electrolytes*

Europium can readily be determined polarographically and Eu and Yb can be determined by differential polarography as shown by Pomeroy et al. (1952). All published reports on the polarographic analysis of the rare earths in simple base electrolytes, such as $HClO_4$, HCl, KCl, LiCl, NH_4Cl, $NaClO_4$, etc., are limited almost exclusively to Eu(III) and Yb(III). Ilkova (1968) reported that Eu and Yb can be determined simultaneously in 0.2 M NH_4Cl by dc polarography with a sensitivity as high as 6×10^{-6} M. Steeman et al. (1977, 1978) used differential pulse polarography (DPP) for the quantitative determination of Eu in minerals and oxides of other lanthanides down to 0.2 ppm in an acetate buffer at pH 3.80; and in the supporting electrolyte LiCl (0.1–1 M) at pH 5, Yb can be determined down to 5×10^{-8} M. Steeman et al. (1978) discussed in detail the reduction waves of Eu(III), Yb(III) and Sm(III) in acidic sodium perchlorate solution in the presence of Et_4NClO_4, which yielded hydrogen waves with the formation of their hydroxy compounds. Sm(III) in LiCl solution at pH 3 exhibits a peculiar electrochemical behavior in dc polarography to give a peaked hydrogen wave with the formation of its basic salt or hydroxy compound (Kopanskaya et al., 1974). Kurbatov et al. (1979) reported that microamounts of Eu and Yb in samples of rare earth oxides may be determined in alkaline or alkaline earth salt solutions. The polarographic characteristics of Eu(III) in KSCN (Weaver et al., 1975) and Eu, Yb in $NaClO_4$, NaCl, LiCl, KI and tetraammonium salts were investigated by several authors. They demonstrated that the nature of the supporting electrolyte and the pH of the solution exert a great effect on their half-wave potentials and the magnitude of their reduction currents. Rare earth ions are readily hydrolyzed at a pH greater than 6 when no complexing agent is present, so that pH is a very important factor effecting the electrochemical behavior of the rare earth ions.

TABLE 1
$E_{1/2}$ of Dy(III) in water–ethanol mixtures containing 0.1 M LiCl or 0.1-M Et_4NBr

Ethanol (%)	Dielectric constant	$M^{3+}-3e=M$, $E_{1/2}$ (V SCE)
25	68	−1.894
50	48	−1.818
75	36	−1.723

The half-wave potentials of rare earth ions in nonaqueous media or mixtures of water and organic solvents will be shifted to less negative values than in aqueous solutions, and in some cases the reduction may be split into two steps. Table 1 shows the $E_{1/2}$ of Dy(III) in water–ethanol mixtures (Almagro et al., 1966).

In a nonaqueous medium, such as acetonitrile, Eu in metal Am can be determined because the $E_{1/2}$ for the first reduction step of Eu^{3+} to Eu^{2+} becomes −0.14 V SCE instead of −0.67 V in the aqueous solution, so that the reduction wave of Am(III) at the more negative potential does not interfere (Myasoedov, 1972). The polarographic waves of rare earth ions in formamide, benzonitrile, dimethylformamide or dimethylsulfoxide were reported by Aihara et al. (1976). For analytical purposes the sensitivity of the determination of rare earth ions in nonaqueous solutions is only about 10^{-4} to 10^{-3} M, because of the low conductivity of nonaqueous media.

2.2. *Polarographic analysis in complexing media*

Many spectrophotometric methods were reported in the literature based on the formation of rare earth complexes with organic reagents. Several institutes in China have synthesized some new organic reagents for the purpose of increasing the sensitivity and selectivity of the analysis of rare earths. But only a few complexing agents can be used in the polarographic analysis, because most complexes of the metals reduce at more negative potentials than the free or hydrated metal ions. Therefore only Eu complexes are suitable for polarographic analysis. EDTA is a widely used complexing agent for lanthanide ions with stability constants ranging from 10^{15} for La and 10^{20} for Lu. The stability constants of DTPA complexes of the lanthanides are even larger, ranging from 10^{20} to 10^{23} (Harder et al., 1958). A method for the analysis of Eu(III) in mixed rare earth oxides using the Eu–EDTA complex wave at −1.0 to −1.45 V SCE in square-wave polarography was reported (Kaplan, 1962). Other rare earth ions do not interfere at these potentials.

The Eu(III)–citric acid complex is reduced at $E_{1/2}=-0.89$ V SCE and can be used to determine Eu in rare earth phosphates which contain titanium (Ignatova, 1977). Eu(II) and Eu(III) also form complexes with ethylenediamine, malonic acid, succinic acid, glutaric acid, etc., and yield well-defined waves suitable for analysis.

Rare earth ions can displace In^{3+}, Mn^{2+}, Cu^{2+}, Cd^{2+}, etc., from their EDTA complexes. This property has been used for the indirect determination of rare earth ions by polarographically measuring the displaced metal ions. Thus Sc(III) (1–10 mg) in a solution of $In(EDTA)^-$ can be determined by measuring $InCl^{2+}$ polarographi-

cally, which is displaced by Sc^{3+} via the following reaction:

$$In(EDTA)^- + Sc^{3+} + Cl^- = InCl^{2+} + Sc(EDTA)^-.$$

Even in the presence of other rare earths in an amount up to 100 times that of Sc, the wave height of $InCl^{2+}$ displaced by Sc^{3+} can still be measured (Sevryukov et al., 1973). Th(IV) interferes in this determination. The total amount of Th and rare earths can be determined by the displacement of Mn^{2+} from the $Mn(EDTA)^{2-}$ complex (Sevryukov et al., 1973). Here In^{3+} or Mn^{2+} is called the "indicator ion". Rare earth ions can also be determined by single-sweep polarography in a solution containing 1-M $NaNO_3$ at pH 7, some 2,2′-dipyridyl (dipy), EDTA, and Cd^{2+} as indicator ion (Borishchak, 1978). Cd^{2+} forms complexes with both dipy and EDTA and the reduction wave of $Cd(dipy)^{2+}$ precedes that of $Cd(EDTA)^{2-}$. Upon addition of a small amount of rare earth ions, which form more stable complexes with EDTA than with Cd^{2+}, Cd^{2+} ions are set free forming the $Cd(dipy)^{2+}$ complex, whose wave height is thus increased. The increase of the wave height of $Cd(dipy)^{2+}$ is proportional to the concentration of rare earth ions, such as Sm(III), Ce(III) or Eu(III) in the range of 3×10^{-7} to 5×10^{-6} M. If individual lanthanides in their mixture are to be determined by this indirect polarographic method, the mixture must first be separated by liquid chromatography in an ammonium lactate solution (Inczedy, 1967); then the concentration of each individual lanthanide can be successively determined by displacement of $Cu(EDTA)^{2-}$ or $Zn(EDTA)^{2-}$ complexes.

2.3. *Polarographic adsorptive complex waves and catalytic waves*

Trivalent rare earth ions in aqueous solutions have electrochemical behavior somewhat like Al^{3+}, which gives no well-defined wave before the liberation of hydrogen. However, Willard et al. (1950) found that the analysis of Al could be carried out by the reduction of its complex with certain dyes. Similarly, Florence et al. (1960, 1962) studied the reduction waves of rare earth–Eriochrome violet B complexes by dc, ac and single-sweep polarography. This dye in an ammoniacal buffer solution at pH 9.5 exhibits a good wave with $E_{1/2} = -0.5$ V SCE. The original wave height is decreased by the addition of Y^{3+} or a trivalent lanthanide ion, and a new split wave appears at a more negative potential ($E_{1/2} = -0.7$ V SCE). The sum of the heights of the two waves is a little bit lower than the height of the free dye wave. The height of the discrete wave is proportional to the concentration of Y^{3+} or lanthanide ions. Since then, further studies have been focused on the mechanism of the split wave and in searching for other cations such as Al^{3+}, Ni^{2+}, etc., that form such discrete waves with similar dyes (Florence, 1974). Thakur (1974) obtained a split peak ($E_p = -0.95$ V) with a single-sweep polarograph when Gd^{3+} was added to a solution containing Solochrome violet RS. The height of this discrete peak is proportional to the concentration of Gd^{3+} in the range of 0.5 to 12 μg/ml. Other ions such as As(III), Rh(III), U(VI), Ho, Y and La interfere.

This kind of wave, obtained by the formation of metal–dye complexes in single-sweep polarography, is quite sensitive because in single-sweep polarography there is a rest period of 5 s before the potential scanning to facilitate the adsorption and accumulation of the electroactive complexes on the surface of the mercury electrode. If the adsorption process goes very fast, equilibrium may be reached within this period and a maximum current can be obtained during the 2 s sweep. By using the derivative single-sweep technique, the sensitivity of this method can be further enhanced and the separation between the two waves also improved. We call such waves formed due to the reduction of the ligand coordinated with a metal ion and adsorbed on the surface of the mercury electrode "adsorptive complex waves".

There is another kind of wave called "catalytic prewave". Many examples of the catalytic prewave are given in the book written by Tur'yan (1980). Certain ligands such as thiocyanate, tartrate, gallate ions and neutral organic reagents like pyridine may be adsorbed on the surface of the mercury electrode and react with some metal ions diffusing to the electrode to form some loose complexes or ion pairs or "active bridges", by which the reduction of the metal ions is facilitated and a prewave appears at a potential less negative than the $E_{1/2}$ of the simple metal ion. These prewaves may be used to determine small amounts of anion ligands.

An outstanding example is the prewave of Eu(III)–*o*-phenanthroline (Osipova, 1981) in ac polarography. In the base electrolyte NH_4Ac at pH 6–7, the reduction of Eu^{3+} to Eu^{2+} with a peak potential equal to -1.09 V SCE is irreversible. On addition of a small amount of phenanthroline, a prewave at $E_p = -0.81$ V SCE is observed, the height of which is proportional to concentration in the range 1×10^{-6} to 1×10^{-5} M Eu^{3+}. Pr, Nd, Sm, Gd, Tb, Y and La do not interfere. This method was applied to determine the Eu content in europium-doped ytterbium oxysulfide, which is a cathodoluminophor. This catalytic prewave is produced by a heterogeneous reaction between Eu^{3+} and *o*-phenanthroline on the electrode surface.

There are few papers that deal with the catalytic waves of rare earths. The wave of $La(NO_3)_3$ in the presence of H_2O_2 is catalytic in nature (Henne et al., 1964); that is, La^{3+} catalyzes the reduction of H_2O_2 by shifting its potential from -0.9 to -0.1 V SCE. This catalytic wave is, however, useless in analysis because it is unstable.

Zhdanov (1963) found that some anions exhibit an autocatalytic reduction wave in the presence of 0.1 M $La(NO_3)_3$ at pH 5. For example, in the presence of La^{3+}, the nitrate ion will reduce at a less negative potential to give NH_2OH or NH_4^+ as a product. The effect of a multivalent cation on the electrical double layer can be used to determine anions such as NO_3^-, NO_2^-, BrO_3^-, IO_3^- and NH_2OH. Particularly trace amounts of NO_3^- and NO_2^- can be determined by DPP in the presence of a definite amount of Yb^{3+} (Boese, 1977). The mechanism of this system, Yb^{3+}–NO_3^-(or NO_2^-)–NH_4Cl, was investigated by Gao (1982), and the wave was confirmed by several auxiliary experiments to be a catalytic wave of EC type (Heyrovsky, 1965), where NO_3^- or NO_2^- act as an oxidizing agent to regenerate Yb^{3+}. This forms a catalytic cycle known as a "catalytic wave of an electrode reaction in parallel with a chemical reaction". On the contrary, if Yb^{3+} is present in a definite amount, the reduction wave of NO_3^- or NO_2^-, catalyzed by Yb^{3+}, is known as an autocatalytic wave. In both cases the final reduction product is hydroxylamine. Wang et al. (1982)

studied the polarographic behavior of NO_3^-, NO_2^- and NH_2OH in both buffered and unbuffered solutions by DPP. It was ascertained that Yb^{3+} serving as a multivalent cation may electrocatalyze the nitrate and nitrite waves adjacent to the reduction wave of Yb^{3+} itself on the one hand, while on the other the electroreduction product Yb^{2+} may be reoxidized to Yb^{3+} to produce a kinetic wave (especially at higher concentrations of NO_3^- or NO_2^-). In the same year Boese et al. (1982) studied the mechanism of the reduction of nitrate ion in the presence of Yb^{3+} by using DPP in cyclic voltametric and coulometric techniques. The nitrate ion was found to be reduced via at least two mechanisms in Yb^{3+} solution with either KCl or NH_4Cl as the supporting electrolyte. The first mechanism, which is a catalytic cycle involving the Yb^{3+}–Yb^{2+} couple, causes a great enhancement of the Yb^{3+} peak current at -1.4 V SCE in both differential pulse polarograms at the DME and in the first cathodic scan of cyclic voltammograms at the hanging mercury drop electrode (HMDE). The second mechanism, which involves direct reduction of the nitrate ion at the mercury electrode coated with a small amount of $Y(OH)_3$, gives a new peak at -1.3 V SCE in the second cathodic scan of cyclic voltammograms. The magnitudes of both reduction peaks exhibit a marked pH dependence in the KCl supporting electrolyte, but are much greater and pH independent in the NH_4Cl supporting electrolyte. NH_4^+ appears to act as a proton donor in the reduction of NO_3^- by either mechanism. Current transients and coulometry at the DME indicate that the nitrate ion may be reduced via both mechanisms under ordinary polarographic conditions. These conclusions are in mutual accordance. This method is sensitive and specific to Yb^{3+}. Under optimum conditions it can be applied to analyze Yb in ores with no interference from other rare earth ions.

In this chapter only the sensitive polarographic methods for rare earths will be reviewed; other electroanalytical methods, such as indirect analysis by displacement reactions and anodic stripping methods, will not be included.

3. Recent developments of polarographic adsorptive complex waves and catalytic waves of the rare earths

Catalytic and catalytic hydrogen waves are generally considered as the most sensitive polarographic methods for analysis (Mairanovskii, 1968). However, the rare earth ions, with the exception of Eu and Yb, form either catalytic or catalytic hydrogen waves in aqueous solutions with difficulty. The only way to find sensitive polarographic waves is through the reduction of adsorptive complexes of rare earths in which the ligands are reducible. More than 10 recently suggested systems (Gao et al., 1983) will be reviewed.

3.1. *The Sc–cupferron–diphenylguanidine–NH_4Cl system*

Scandium is very scarce and generally occurs in very small amounts in minerals; therefore, it is desirable to develop a very sensitive and convenient method for its analysis. Yao et al. (1981) first suggested a system of Sc(III)–cupferron–diphenyl-

guanidine–NH_4Cl for the polarographic determination of Sc. The derivative single-sweep polarogram of this system is shown in fig. 1a. By measuring the height from peak to peak in this figure, the concentration of Sc in the range from 1×10^{-7} to 1×10^{-6} M may be determined with a limit of detection equal to 5×10^{-8} M. It is 100 times more sensitive than spectrophotometric methods and three times more sensitive than flameless atomic absorption spectroscopy.

Gao et al. (1982) studied the mechanism of this system and concluded that it is an adsorptive complex wave. The experimental evidence is: (a) In NH_4Cl electrolyte cupferron gives a small single-sweep wave at -1.5 V SCE, which is greatly enhanced by the addition of a trace amount of Sc^{3+} and the increase in height is proportional to the increments of Sc^{3+} added. Diphenylguanidine (DPG) does not reduce at this potential but stabilizes the peak and increases the sensitivity. Since Sc^{3+} cannot reduce at this potential, the peak current must be attributed to the reduction of cupferron in the mixed-ligand complex. (b) The electrocapillary curves of cupferron–NH_4Cl and Sc^{3+}–cupferron–diphenylguanidine–NH_4Cl systems show a great change in surface tension, indicating that adsorption occurs in these systems. The temperature coefficient is negative at higher temperatures. The wave peak disappears with the addition of a trace amount of a surfactant. At a prolonged period of standing before the potential scan, the sharp reduction peak at -1.5 V increases in

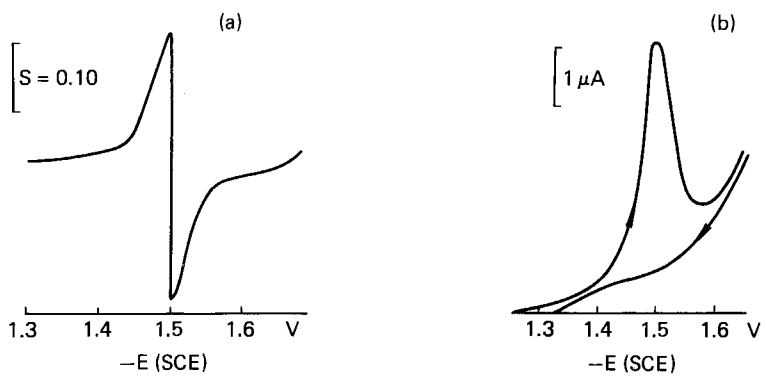

Fig. 1. (a) Derivative single-sweep wave and (b) cyclic voltametric curve in the Sc–cup–DPG system 0.1 M NH_4Cl + 6.5×10^{-4} M cupferron + 2×10^{-4} M diphenylguanidine + 1×10^{-6} M Sc^{3+}.

height but no wave appears during the backward scanning as shown in fig. 1b. These experimental facts indicate that the wave peak in this system is an adsorptive complex wave; its high sensitivity may be due to the strong adsorbability of the complex.

The composition of this mixed-ligand complex was determined by the following equation derived by Li et al. (1973):

$$1/i = 1/i_{max} + 1/i_{max}\beta(X)^m(Y)^n,$$

where i and i_{max} are the current and maximum current of a catalytic wave from dc polarograms, respectively, β is the stability constant of the complex MX_mY_n, (X) and (Y) are the concentrations of the two different ligands. If this equation is applied to the derivative single-sweep polarograms, i_{der} and $i_{der,max}$ should be used instead of i and i_{max}. Keep (Y) and other variables constant, vary (X) and plot $1/i_{der}$ versus $(X)^{-m}$ for a series of trial m values equal to $1, 2, 3, \ldots$. If a straight line is obtained for a certain value of m, then this value of m is just the number of molecules of ligand X in the complex MX_mY_n. Similarly, n can be found by plotting i/i_{der} versus $(Y)^{-n}$, keeping (X) constant. By applying this method, the composition of the complex was determined to be Sc^{3+} : cup : DPG = 1 : 1 : 1. According to Hantzch (1931), $K_{a,cup} = 5.3 \times 10^{-5}$; therefore cupferron at pH 5 will mainly exist in anionic form, while DPG is a basic compound, which will exist in cationic form. Therefore the complex $Sc(cup)(DPG)^{2+}$ carries two positive charges and two Cl^- ions must be coordinated with it in order to get a neutral molecule. The structural formula may be written as follows:

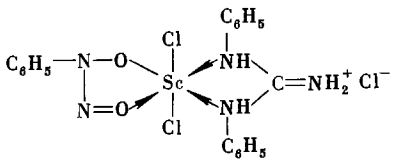

This complex compound is formed in solution and adsorbed on the surface of the DME. At a potential of -1.5 V, it may dissociate to give free cupferron and Sc^{3+}; the former reduces in a stepwise fashion to phenylhydrazine (Kolthoff et al., 1948) to give the wave and the latter may be complexed with cupferron and DPG and adsorbed again.

This sensitive adsorptive complex wave has been utilized to analyze Sc in ores (Yao et al., 1981). The procedure may be summarized as follows: Fuse the ore sample containing Sc and separate it from other ions by extraction with 0.01 M 1-phenyl-3-methyl-4-benzoylpyrazole-5–benzene solution. Strip Sc from the organic phase into water, add NH_4Cl, cupferron and DPG, adjust pH and take the single-sweep polarogram. More than 10 iron ores and 2 silicate rocks were analyzed and the results were in good agreement with those obtained from atomic absorption spectroscopy, when the content of Sc in ores was above 10^{-4}%. If the content is below 10^{-4}% (down to 10^{-5}%), it is beyond the limit of detection by atomic absorption spectroscopy, but this sensitive polarographic method can still be used.

3.2. *The Y–rhodamine B–diphenylguanidine–NH_4Cl system*

Rhodamine B is a basic dye, which forms complexes with rare earth ions. Its polarographic behavior has been studied and three examples of the adsorptive complex waves have been proposed.

Yang (1980) used rhodamine B as a ligand to coordinate with Y^{3+} and the adsorptive complex wave thus formed could be used to determine Y^{3+} in a narrow range of concentrations from 0.5 to 3.0 μg/ml with dc polarography. Jiao et al. (1982) suggested the Y(III)–rhodamine B–DPG–NH_4Cl system, which is more suitable for analysis.

In the ammonium chloride electrolyte, rhodamine B exhibits two peaks on the single-sweep polarogram just the same as the two reduction waves on the dc polarogram (Pályi et al. 1962), see fig. 2.

The peak potentials of the peaks P_1 and P_2 in fig. 2 are -0.96 and -1.5 V SCE, respectively. On the addition of DPG, P_1 does not change, while P_2 increases in height; see curves a_2 and b_2 in fig. 2. When a small amount of Y^{3+} is added to the system, P_1 remains unchanged but P_2 decreases in height considerably as shown by curves a_3 and b_3 in fig. 2. If the ratio of concentrations of rhodamine B to Y(III) is relatively small, a third ill-defined peak P_3 will appear after P_2. Under the condition that P_3 does not appear, i.e., a definite amount of rhodamine B and DPG are present, the decrease of P_2 is directly proportional to the concentration of Y(III) in the range of 10^{-7} to 10^{-6} M. Heavy rare earth ions behave similarly. If the separation is made between the cerium group and the yttrium group elements, the method can be used for the determination of the total concentration of the yttrium group elements.

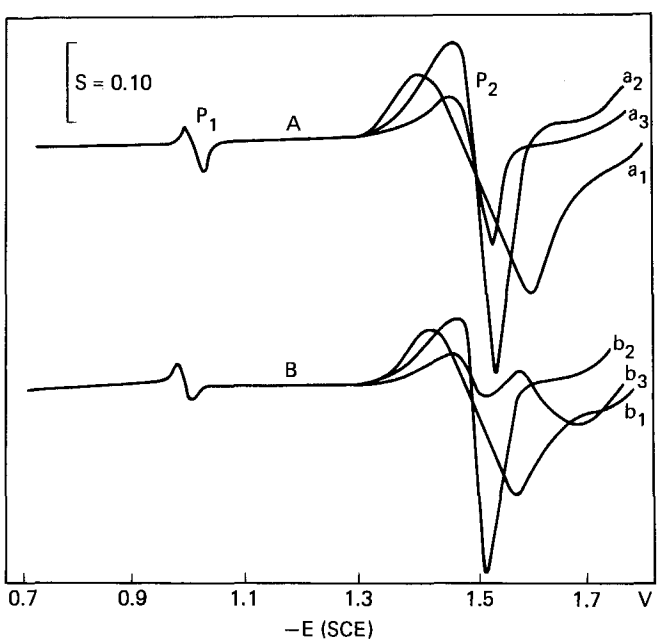

Fig. 2. Derivative single-sweep polarograms of the Y–rhod–DPG system. Curve A: a_1: 0.4 M NH_4Cl + 8.0×10^{-5} M rhodamine B; a_2: $a_1 + 1.0 \times 10^{-4}$ M diphenylguanidine; a_3: $a_2 + 1.0 \times 10^{-6}$ M Y^{3+}. Curve B: b_1: 0.4 M $NH_4Cl + 4.0 \times 10^{-5}$ M rhodamine B; b_2: $b_1 + 1.0 \times 10^{-4}$ M diphenylguanidine; b_3: $b_2 + 1.0 \times 10^{-6}$ M Y^{3+}.

Pályi et al. (1962) reported that the first wave produced by rhodamine B is a diffusion-controlled wave, while the second wave is an adsorptive wave. Various experiments were performed by Jiao et al. (1982) to verify that P_2 is adsorptive in nature. The logarithmic analysis of i–t curves showed that $\alpha = 0.24$ and 0.55 for P_1 and P_2, respectively. The greater value of α means that the corresponding wave is adsorptive. pH exerts a great influence on P_2. At pH 4.5–5.0, the addition of Y(III) causes a decrease of P_2 and makes the peak even sharper. This means that the adsorption of the Y(III)–rhodamine–DPG complex is stronger than that of rhodamine itself.

There is an equilibrium between the lactone and quinone forms of rhodamine B:

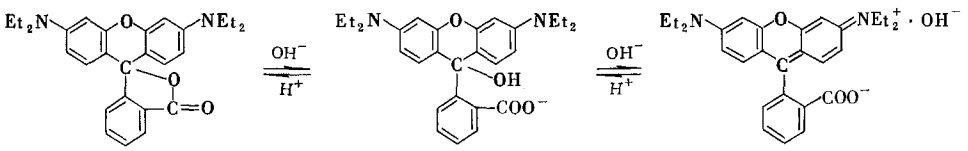

When pH $\geq$ 7.5, rhodamine B exists mainly in the quinone form, which is nonreducible in polarography and no P_2 can be found. Under the experimental conditions at pH 4.5 to 5.0, Y(III) may be coordinated with rhodamine anion to form $Y(rhod)_4^-$ and associated with the diphenylguanidine cation $(DPG)^+$. This associated ion pair reduces at a more negative potential than P_2 to give P_3. (Akhmedli et al., 1973, Menkov et al., 1977). For analytical purposes, measuring the decrease of P_2 is better than measuring the increase of P_3 for the determination of rare earth ions. Furthermore, P_2 and P_3 are so close together in dc and normal single-sweep polarography that derivative single-sweep polarography is recommended.

The polarographic behavior of rare earths with rhodamine B in ammonium chloride solution has been further studied with Sm^{3+} instead of Y^{3+}. In the presence of a small amount of DPG, the addition of Sm(III) decreases the height of the derivative peak P_2 (-1.45 V SCE) of rhodamine B as in the case of Y(III) (Ye et al., 1982). The decrease of peak height is proportional to the concentration of Sm(III) added in the range 3×10^{-7} to 2×10^{-6} M.

In an ammonium chloride solution containing 10% dioxane or ethanol, the Sm complex of rhodamine B exhibits a reductive dc polarogram at -1.70 V SCE. The wave height is directly proportional to the concentration of Sm(III) within the range of 2×10^{-6} to 2×10^{-5} M. Since there is a large adsorptive wave P_2 of rhodamine B, which precedes the complex wave, it is difficult to increase further the sensitivity either in dc or single-sweep polarography.

A comparison of the waves of rhodamine B complexes with various rare earth ions in aqueous solution containing 10% dioxane has been made. It was found that Eu is more sensitive than Sm and Er is the most sensitive. This also demonstrates the effect of adding the organic solvent dioxane on the adsorptive complex waves of the rare earths.

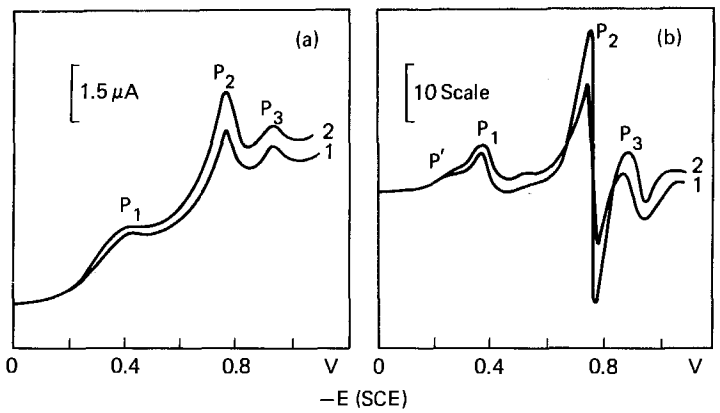

Fig. 3. The (a) normal and (b) derivative single-sweep polarogram of CNA and the Nd–CNA system. Curve 1: 0.1 M KNO_3 and 1×10^{-4} M CNA; curve 2: curve 1 + 5×10^{-6} M Nd^{3+}.

3.3. *The La,Nd–carboxynitrazo–KNO_3 system*

Carboxynitrazo (CNA) is a sensitive organic reagent for spectrophotometric determination of rare earths. It has been synthesized by the Analytical Chemistry Laboratory, Wuhan University, China. Jiao et al. (1984) investigated the polarographic behavior of CNA and its complexes with La and Nd in detail. The single-sweep polarograms of the Nd(III)–CNA–KNO_3 system are shown in fig. 3.

Carboxynitrazo in $NaClO_4$ electrolyte at pH 10–11 exhibits a differential pulse polarogram (PAR 384-4) at −0.68 V (vs. Ag/AgCl), which corresponds to the P_2 in derivative single-sweep polarography (fig. 3b), when KNO_3 is used as the electrolyte instead of $NaClO_4$. This P_2 peak increases its height with the addition of trace amounts of La(III), Nd(III) or Pr(III). In order to increase the sensitivity, the solution of CNA in $NaClO_4$ was taken as "blank" and the current measured in the "blank" was stored in the Instrument PAR 384-4 for subtraction from the peak height P_2 when La(III) was added to the solution; thus La(III) could be determined down to 10^{-8} M.

The mechanism of this system is different from those previously mentioned. Here the adsorptive complex does not give a new wave nor decrease the wave height of the free ligand, but it does increase the height of the peak P_2 at the same potential.

From more than 10 electrolytes tested, KNO_3 was chosen as the supporting electrolyte, in which the increase of peak height of La or Nd attains a maximum value and the potential difference between P_1 and P_2 is rather large. The calibration curves of some rare earth ions showed that the responses of La and Nd are more sensitive than other rare earth ions. After Gd(III), the responses become smaller and smaller reaching a minimum at Tm, but rise again for Lu. Among them, the linear relationship holds between the peak height of P_2 and the concentrations of Nd(III) from 5×10^{-7} to 8×10^{-6} M with a detection limit of 3×10^{-7} M.

Carboxynitrazo in 0.1 M KNO_3 at pH 5–12 exhibits waves on dc, ac and single-sweep polarograms, but they differ in their reduction mechanisms at different pH values. Jiao et al. (1984) studied a solution containing 0.1 M KNO_3 and 1×10^{-4}M CNA at pH greater than 8.8 by single-sweep polarography as shown in fig. 3a. It may be seen from fig. 3 that the wave consists of three peaks P_1, P_2 and P_3. P_1 is further split into P_1 and P_1'. Jiao et al. (1984) proved that they correspond to the stepwise reduction of CNA as follows:

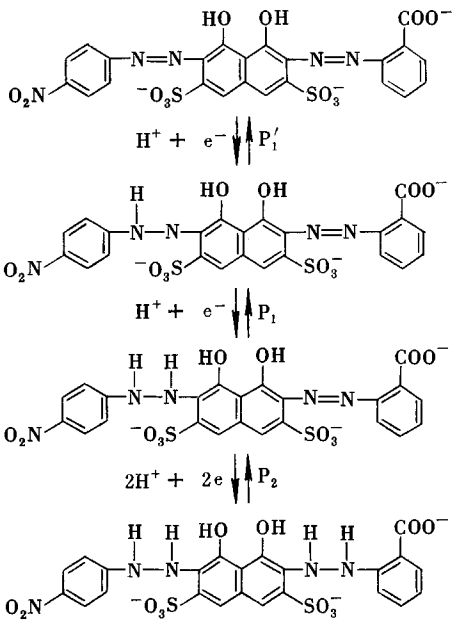

Due to the reduction of the $-NO_2$ group in the molecule, the P_2 peak is much higher than P_1; the small P_3 peak is due to the reduced product of P_2. Addition of a trace amount of Nd(III) increases the wave heights of the peaks (especially P_2). It was found by Job's method of continuous variations in both spectrophotometry and single-sweep polarography that the ratio of Nd(III) : CNA in the complex is 1 : 1. Based on the structure of CNA and following Callis et al. (1952) and Langmyhr et al. (1971), it was postulated that the complex may have the following structure:

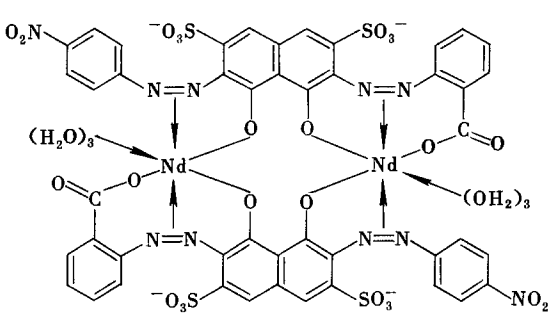

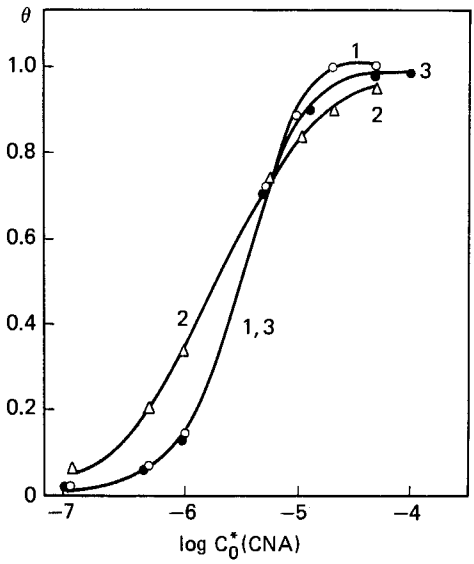

Fig. 4. Adsorption isotherms of CNA. Curve 1: experimental; curve 2: calculated from the Langmuir isotherm; curve 3: calculated from the Frumkin isotherm.

The adsorption of CNA and the Nd–CNA complex on a hanging mercury drop electrode (HMDE) was studied quantitatively as shown in fig. 4. Curve 1 is the adsorption isotherm determined experimentally, curves 2 and 3 are those calculated according to Langmuir and Frumkin isotherms, respectively. It may be seen that curve 1 fits curve 3 quite well, i.e., the Frumkin isotherm is satisfied. The Frumkin isotherm is represented by the following expression:

$$\theta/(1-\theta) = \beta C_0 \exp(2\gamma\theta)$$

The parameters in the Frumkin isotherm were determined to be $\beta = 1.21 \times 10^5$ and $\gamma = 1.01$, which means that there is an attractive force between the adsorbed CNA molecules. Furthermore, the fraction of the Nd(III)–CNA complex adsorbed on the HMDE surface already saturated with CNA was also determined and the result supports the assumption that the adsorbability of the Nd(III)–CNA complex is stronger than that of CNA. This is the reason why the rare earth–CNA complex increases the wave height of the free ligand and why the sensitivity is so high. This sensitive method has been applied to the determination of trace amounts of the light rare earths in the leaves of plants.

3.4. *The La,Pr–o-cresolphthalexon–NH_4Cl system*

Triphenylmethane dyes, such as xylenol orange and methylthymol blue, are widely used in spectrophotometric determination of rare earths. Véber (1979, 1981) studied several triphenylmethane dyes by polarographic methods. It was found that the quinoid group and the carbonium ion are responsible for the reduction wave in polarography. Zhang et al. (1984) investigated and compared the polarographic

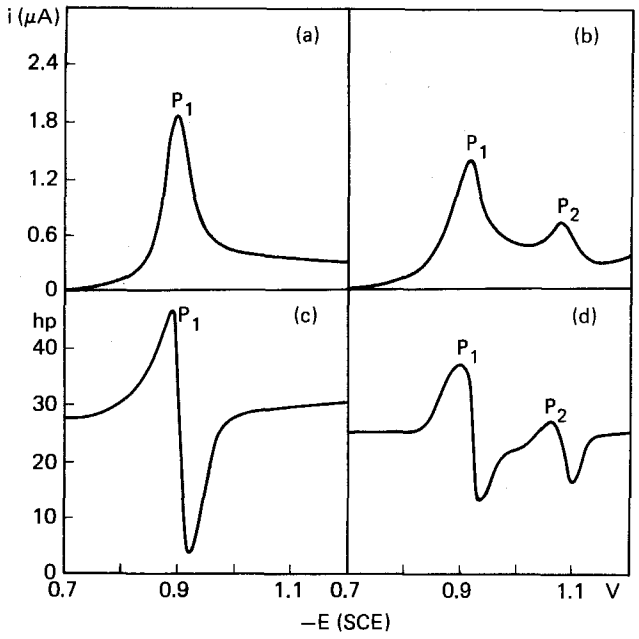

Fig. 5. (a), (b) Normal and (c), (d) derivative polarograms of OCP and the Pr–OCP system. (a), (c): 0.1 M NH_3–NH_4Cl + 1×10^{-4} M OCP, pH 9; (b), (d): same as (a), (c) + 1×10^{-5} Pr^{3+}.

behavior of two triphenylmethane dyes and their complexes with the rare earths. Kolthoff et al. (1948) studied the polarographic reduction of phenolphthalein. Since it did not form complexes with most metal ions, Zhang et al. (1984) tried to use *o*-cresolphthalein (OCP), which has a similar reducing group to phenolphthalein, but differs from the latter in having two additional amino-carboxylic groups that can form complexes with most cations. Figure 5 shows the reduction wave of OCP (P_1) and its complex with Pr^{3+} (P_2).

Addition of some light rare earth ions into a solution containing 1×10^{-4} M OCP and 0.1 M NH_3–NH_4Cl at pH 9, depresses the wave peak P_1 of OCP and a new peak P_2 ($E_p = -1.08$ V SCE) appears that is about 200 mV more negative than P_1. The height of P_2 is proportional to the concentration of the light rare earth ions.

Under these experimental conditions, if the concentration of OCP exceeds 5×10^{-4} M, its adsorption on the mercury electrode will reach a state of saturation, i.e., a complete coverage of the electrode occurs, which inhibits the reduction of the complex. Therefore the appropriate concentration of OCP to be used in the analysis should be considerably lower than 5×10^{-4} M, but about one order of magnitude greater than the estimated concentration of the rare earth ions. The pH value of the solution exerts a great influence on the shape of the wave; only at pH 9 does P_2 have a sufficient height even at very low of rare earth ions concentration. Under the conditions shown in fig. 5, the linear relationship holds between the heights of P_2 and the concentrations of La(III) or Pr(III) in the range of 5×10^{-7} to 1×10^{-5}. When the automatic subtraction technique is applied, the limit of detection is 1×10^{-7} M.

The polarographic behavior of the complexes of OCP with heavy rare earths is quite different from light rare earths. After Sm(III), the adsorptive complex waves gradually approach the OCP wave, until no more new wave appears. This phenomenon is very similar to the absorption spectra in which OCP has a maximum absorption at 580 nm; addition of La^{3+} increases this peak in height and a new peak appears at 400 nm. Ce gives no peak at 400 nm, while the peak produced by adding Pr or Nd is smaller than that due to La. After Sm, the peak at 400 nm gradually disappears, although the absorption peak at 580 nm still increases. Sc(III) has a negative absorption value. These phenomena may be explained by the lanthanide contraction of their ionic radii. The spatial arrangement of the OCP molecule favors complex formation with metal ions of larger ionic radii. Sc^{3+} has the smallest radius

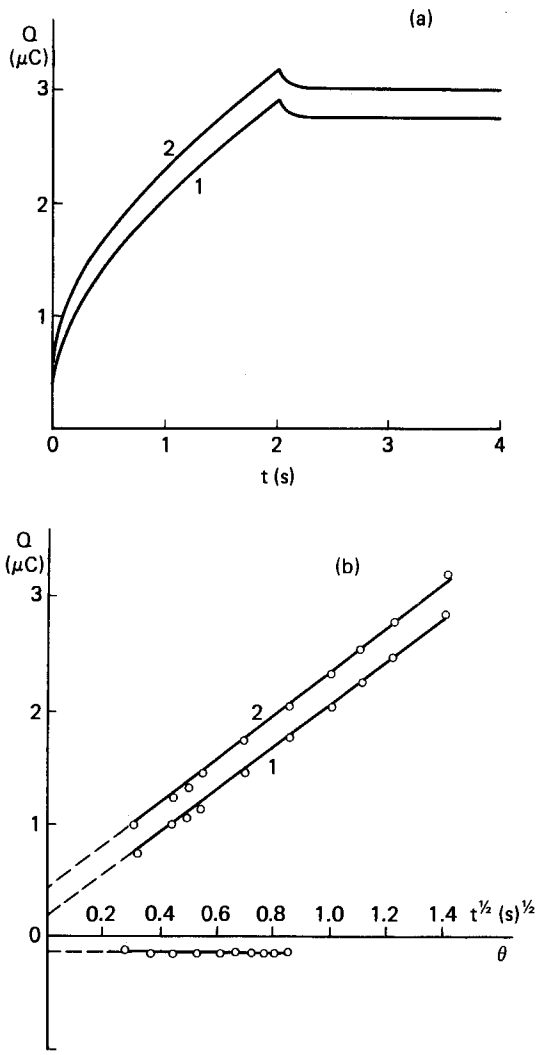

Fig. 6. (a) Q vs. t response of double-step chronocoulometry. $E_1 = -0.6$ V, $E_2 = -1.3$ V (vs. Ag/AgCl); HMDE, $S = 0.029\,cm^2$. Curve 1: 5×10^{-4} M OCP + 0.1 M NH_3–NH_4Cl, pH 9; curve 2: curve 1 + 5×10^{-4} M Pr^{3+}. (b) Linear plot of (a).

and therefore the least complex formation. This is an example of the inverse order of stability that is unusual in rare earth complexes.

The composition of the La(or Pr)–OCP complex was found by Job's method of continuous variation in spectrophotometry to be 1:1. The mechanism of this adsorptive complex wave was studied by several electrochemical methods as follows: (a) The plot of peak current against the square root of the rate of scanning is not a straight line but an upward curve. This indicates that there is adsorption of the reagent (Osteryoung et al., 1962). (b) Koryta (1953) made the assumption that if adsorption equilibrium is established as far as the complex reaching the electrode surface is concerned, the surface coverage θ at time t can be expressed as $\theta = (t/T)^{1/2}$, where T is the time required for complete coverage. Using the combination of PAR 174A and M303 electrodes, we may control the rest time before the potential scan in the linear-sweep polarograph at a wide range of values from several seconds to several hundred seconds. The experimental data showed that the peak heights of OCP and its complex are increased and the peak potentials are shifted to more negative values by lengthening the rest time. This kind of behavior is characteristic of adsorptive waves. (c) The comparison of the effects of OCP and La(III)–OCP on the electrocapillary curves showed that the adsorbability of the complex is larger than that of the free ligand OCP. This is the reason why the complex reduces at a more negative potential. (d) The double-step chronocoulometric plots Q vs. t and the corresponding linear plots Q vs. $t^{1/2}$ are shown in figs. 6a and 6b, respectively (Bard et al., 1980).

The equation of double-step chronocoulometry was given by Anson (1966) and Christie et al. (1967) as follows:

$$Q_f = 2nFAC_0(tD_0/\pi)^{1/2} + nFA\Gamma_0 + Q_{\mathrm{dl}}, \qquad t \le \tau,$$

where Q_{dl} is the charge on the double layer, Γ_0 is the amount of adsorption of OCP or its complex. From the data of fig. 6b, Q_{dl} was determined to be $0.108\,\mu$C, Γ_0 of OCP $= 2.1 \times 10^{-11}$ mol/cm^2 and Γ_0 of Nd–OCP $= 4.4 \times 10^{-11}$ mol/cm^2. This quantitatively proves that the adsorbability of OCP is smaller than that of its complex.

So far we have discussed the mechanism of this adsorptive complex wave, but there still remains one more question to be answered: whether or not this adsorptive complex dissociates before reduction. Florence et al. (1969) suggested the following criterion: If the adsorptive complex does not dissociate, it must satisfy the following equation (assuming the reduction involves two electrons):

$$\Delta E_{1/2} = E_{1/2,\mathrm{complex}} - E_{1/2,\mathrm{ligand}}$$

$$= -(RT/2F)\ln(\beta K_{a1}K_{a2}/\beta^* K_{a1}^* K_{a2}^*),$$

where β is the stability constant of the complex ML, K_{a1} and K_{a2} are the first and the second ionization constants of the dibasic ligand acid H_2L and the asterisk (*) denotes the reduction products. This equation means that $\Delta E_{1/2}$ depends only upon

β and the K_as. If the complex dissociates before reduction, then $\Delta E_{1/2}$ is given by the expression

$$\Delta E_{1/2} = -(RT/2F)\ln(M) - (RT/2F)\ln(\beta K_{a1}K_{a2}) + (RT/F)\ln(H^+).$$

Here $\Delta E_{1/2}$ depends not only upon β and the K_as but also upon the concentration of the metal ion and the pH of the solution.

According to these relationships, two sets of experiments were performed, in which the concentrations of OCP were varied from 10^{-6} to 10^{-4} M and the pH varied from 5.0 to 9.5. The differences of the peak potentials (ΔE_ps of OCP and its complex corresponding to $\Delta E_{1/2}$ in the above expressions) observed under such diversified conditions did not substantially change. Therefore it was concluded that the Pr or other light rare earth–OCP complex does not dissociate but reduces directly on the mercury electrode to give a new adsorptive wave via the following electrode process:

$$Pr^{3+} + (OCP)^{4-} = (PrOCP)^- \qquad \text{(in solution)},$$

$$(PrOCP)^- = (PrOCP)^-_{ads} \qquad \text{(on the surface of the electrode)},$$

$$(PrOCP)^-_{ads} + 2H_2O + 2e = (PrOCPH_2)^-_{ads} + 2OH^-.$$

The last electrode reaction results from the addition of two hydrogen atoms to the quinoid structure of OCP. This adsorptive complex wave can be used to determine the total amount of light rare earths after the separation from the heavy rare earths.

3.5. *The rare earths–thymolphthalexon–NH_3–NH_4ClO_4 system*

Thymolphthalexon (TP) is another triphenylmethane dye that has a similar structure to *o*-cresolphthalein but with two additional isopropyl groups in the molecule. In equilibrium it also exists in two forms; only the quinoid form is reducible. Zhang et al. (1984) found that the peak potentials of TP in 0.1 M $NaClO_4$ solutions are related to pH as follows: $E_p = -0.575 - 0.030$ pH. Since the slope of the plot E_p vs. pH is (Florence et al., 1969)

$$s = (m/n)(RT/F) = (m/n)(59\,\text{mV}) \qquad (\text{at } 25°\text{C}),$$

where m and n are the numbers of protons and electrons participating in the electrode reaction, respectively, and since the reduction of TP is similar to that of phenolphthalein, i.e., $n = 2$, we obtain $m = 1$; that is, one H^+ participates in the reaction.

Figure 7 shows the linear-sweep (LS) polarograms of TP. The wave peak is sharp and symmetrical. The normal pulse polarogram at low concentrations of TP is also peak-shaped. These facts indicate that the reactant is adsorbable (Flanagan et al., 1977). Under the optimum conditions for analysis (0.4 M NH_3–NH_4Cl and 1×10^{-4} M TP at pH 9), the presence of rare earth ions decreases the height of the TP peak linearly. If the amount of rare earth ions added is small, there is no new peak after the reduction peak of TP. If the concentrations of TP and the rare earth are

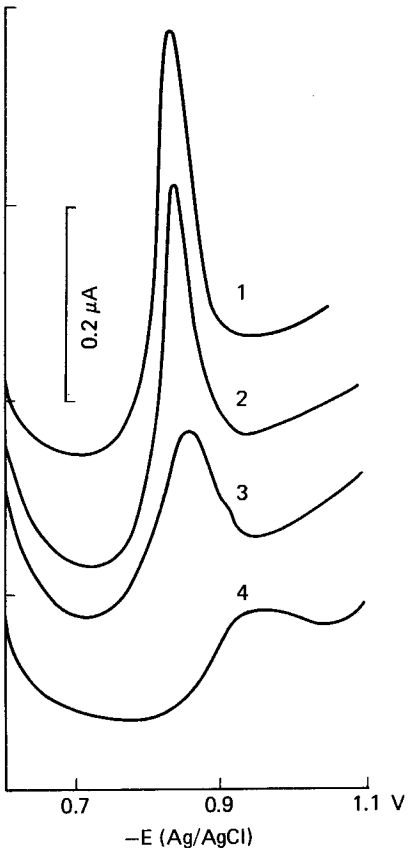

Fig. 7. LS polarogram of TP (PAR 384-4). $v = 20\,mV/s$. Curve 1: 0.4 M NH_3–$NH_4Cl + 1 \times 10^{-4}$ M TP, pH 9; curve 2: curve $1 + 1 \times 10^{-5}$ M Dy^{3+}; curve 3: curve $1 + 5 \times 10^{-5}$ M Dy^{3+}; curve 4: curve $1 + 1 \times 10^{-4}$ M Dy^{3+}.

equal, then the TP peak will vanish and a small flat wave will appear at a more negative potential. This is quite different from the rare earth–OCP system. All the rare earth ions decrease the height of the TP peak almost equally; therefore individual or total rare earths can be determined in the concentration range of 10^{-6} to 10^{-5} M. Most di- or trivalent cations do not interfere except In(III), whose behavior is similar to rare earth ions.

The electrocapillary curves of this system show that TP is strongly adsorbed on the surface of DME, but its complex only weakly. In ac polarography, the half-wave width of TP is 110 mV, indicating that the reduction is quasireversible. Adding Dy^{3+} depresses and greatly broadens the wave. This means that the reduction of the complex at a more negative potential is an irreversible process. Therefore the result of complex formation is to decrease the height of the ligand wave without forming new waves at low concentrations of the rare earth. The double-step chronocoulometric technique was applied to two systems containing 5×10^{-4} M TP and 5×10^{-4} M Dy(III)–TP. The linear plot (Q vs. $t^{1/2}$) of the forward potential step of the former system has an intercept greater than that of the latter system, indicating that TP is

more strongly adsorbed than Dy(III)–TP. Other experiments, such as rest period and $i_p v^{-1/2}$ vs. v plot, also proved that the complex is only weakly adsorbable.

In conclusion, the complexes of rare earth ions with OCP and TP are different in their adsorbability and their reduction mechanisms. Light rare earth–OCP complexes exhibit a new wave, which may be used to determine the concentration of the light rare earths. In contrast, TP complexes decrease the wave height of TP. This difference in polarographic behavior is due to the steric hindrance of the large substituted groups in the TP molecule, which renders its complex less stable and less adsorbable and causes the adsorptive complex wave to be less sensitive.

3.6. *The Sm–tetracycline–NH_4ClO_4 system*

Several polarographic methods have been reported for the quantitative analysis of the antibiotic tetracycline (TC). In a solution containing 0.2 M HAc–NaAc at pH 5.0, the content of TC in tablets, ointments and injections was successfully determined by single-sweep polarography and differential pulse polarography (Ye et al., 1983). Rare earth–tetracycline complexes have been used in the examination of brain tumors (Saiki et al., 1977). The cerium–tetracycline complex has been used for clinical antitumor experiments in China (Fu et al., 1983). Ye et al. (1984) studied the polarographic behavior of the rare earth–tetracycline complexes in order to develop an analytical method for the determination of trace amounts of the rare earth elements. In a solution containing 0.1 M NH_4ClO_4, 1×10^{-4} M NaF and

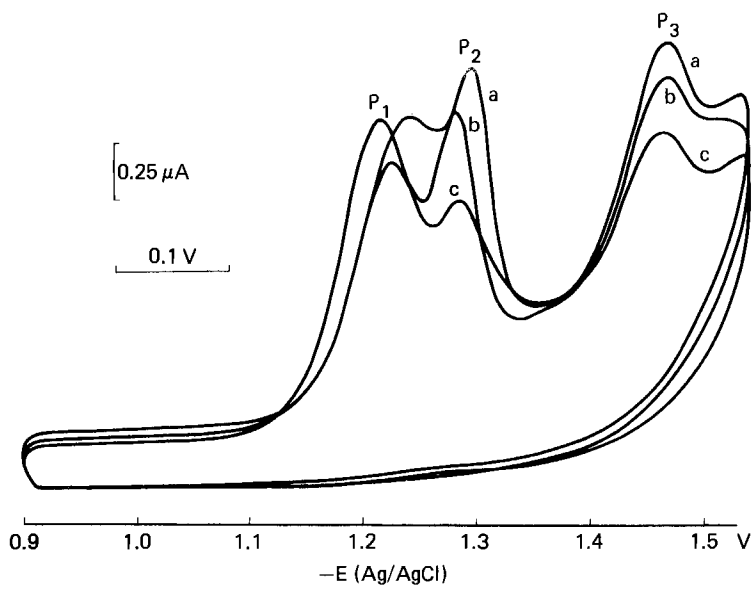

Fig. 8. Cyclic voltametric curves of TC. PAR 370,174A, 175; SMDE. Curve a: 0.1 M $NH_4ClO_4 + 1 \times 10^{-4}$ M $F^- + 3 \times 10^{-5}$ M TC, pH 7.5; curve b: curve a + 2×10^{-6} M Sm^{3+}; curve c: curve a + 5×10^{-6} M Sm^{3+}.

$3–5 \times 10^{-5}$ M TC at pH 7–8, Sm(III) can be determined in the concentration range of 1×10^{-6} to 1×10^{-5} M, with a detection limit of 2×10^{-7} M. This method is based on the formation of a Sm–TC complex, which diminishes the peak height of TC (P_3) in LS or DPP (see fig. 8). Among the rare earth elements, La and Pr have high responses but Eu has almost no response at all. The previous method has been used for the determination of La, Pr or Sm in some ores following separation of the individual light rare earths by a paper chromatographic method.

Tetracycline is a polybasic acid having the following structure:

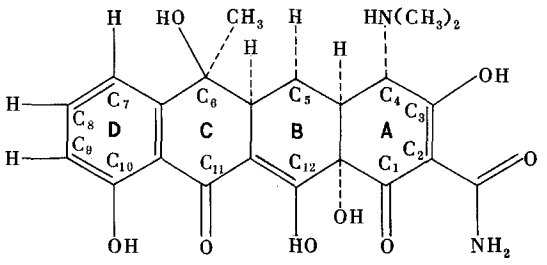

According to Sachan et al. (1980) and Fu et al. (1983), the first ionizable hydrogen atom belongs to C_3–OH of ring A, with $pK_1 = 3.42$; the second belongs to C_{10}–OH of ring D, with $pK_2 = 7.52$; the third belongs to $(CH_3)_2NH$ of ring A, with $pK_3 = 9.27$; and the fourth belongs to C_{12}–OH of ring B, with $pK_4 = 10.02$ (25°C) (Fu et al., 1983). Using these constants and $C_{TC} = 5 \times 10^{-5}$ M, the distribution of various species of TC ($L^{3-}, HL^{2-}, H_2L^-, H_3L, H_4L^+$, where L denotes the TC anion) at pH 3–10 was calculated by a TRS-80 microcomputer. It was found that the main constituents at pH 7–8 are HL^{2-} and H_2L^-. Since the addition of rare earth ions to the TC solution at pH 7–8 will diminish the peak heights in polarograms, it it reasonable to suppose that the coordination with the rare earth ions takes place at the position of C_{10}–O of ring D and the carbonyl group of ring C.

In the presence of NaF, the amount of decrease of P_3 (see fig. 8) is proportional to the concentration of Sm(III). The composition of the Sm–TC complex was found to be 1:2. Other experimental evidence shows that the Sm–TC complex is not adsorptive. The high sensitivity of the method is due to the reduction of TC to produce three peaks, of which peak P_3 is very sensitive in LS or DPP. This method is not applicable to Eu(III) because it will reduce to Eu(II), the TC complex of which is not as stable as that of the trivalent rare earth–TC complexes.

Jiang et al. (1984) investigated an Eu–tetracycline–NH_4SCN system and found that Eu(III) in concentrations ranging from 10^{-6} to 10^{-5} M may be quantitatively determined in a medium containing 0.1 M NH_4SCN and 1×10^{-5} M TC at pH 7. If we wish to determine 10^{-7} to 10^{-6} M Eu(III), the optimum medium is 0.05 M NH_4SCN and 2×10^{-6} M TC at pH 7. This method was used to determine Eu in the phosphor BaFCl:Eu in the *X*-ray intensifying screen with satisfactory results. The mechanism of this system is similar to that of the Sm–TC–NH_4ClO_4 system, except that the thiocyanate anion promotes the reduction of Eu(III) to Eu(II) more

reversibly (Weaver et al., 1975), and the Eu(II)–TC complex formed is more stable than that in the $NaClO_4$ medium.

3.7. *The Eu–DTPA–NaCl complex wave*

In common electrolytes such as HCl and NH_4Cl, Eu(III) gives a well-defined wave at $E_{1/2} = -0.67$ V SCE, which is suitable for analysis, but the sensitivity is not high. Three sensitive polarographic waves of Eu will be discussed in this and the following two sections.

Li et al. (1981) compared the ac polarographic behavior of Eu(III) in different electrolytes, such as NH_4SCN, EDTA–NaCl, DTPA–NaCl, etc., and found that DTPA–NaCl is a very good medium to given sensitive complex waves of Eu. When $C_{NaCl} \geq 0.3$ M, pH ≥ 6.5 and concentration of DTPA is large enough to complex all cations, the limit of detection of Eu is 2×10^{-6} M in LS and 2×10^{-7} M in DPP. Other rare earth ions do not interfere. The enhanced sensitivity is simply due to the formation of the extremely stable Eu(III)–DTPA complex (Misumi et al., 1966).

The preceding complex wave was used to analyze Eu_2O_3 in oxides of mixed rare earths. The procedure is: Dissolve the sample by heating with HCl and H_2O_2, neutralize the solution with NaOH to pH 8–9, add a suitable amount of DTPA and record the wave on an ac or a single-sweep polarograph. The calibration curve may be obtained by taking La_2O_3 as the total rare earth oxide. The results were in good agreement with those obtained by other methods.

3.8. *The Eu(III)–VO^{2+}–KI catalytic wave*

In the Eu(III)–VO^{2+}–KI system, Eu(III) reduces to Eu(II), which is reoxidized by VO^{2+} to give a sensitive catalytic wave (Li et al., 1981). Other oxidizing agents, such as NO_3^-, NO_2^-, ClO_3^-, BrO_3^-, H_2O_2, NH_2OH, etc., fail to produce such a catalytic wave. In acidic mediums, VO^{2+} itself gives a two-electron irreversible wave ($E_{1/2} = -0.85$ V SCE), while the reduction of Eu(III) takes place at a half-wave potential that is 200 mV more positive than the VO^{2+} wave. The addition of VO^{2+} to a solution containing Eu(III) increases the wave height of the latter, but the electrolyte greatly influences the separation of the Eu^{3+} and VO^{2+} waves. For this system 0.1 M KI at pH 1–3.5 is recommended as a suitable base electrolyte. The catalytic current i_c is proportional to the square root of the concentration of VO^{2+}. When the ratio of VO^{2+}/Eu^{3+} is kept between 10–15, a linear relationship between i_c and Eu^{3+} holds within the range of 2×10^{-5} to 1×10^{-4} M. The sensitivity is rather low. Since VO^{2+} is present in excess, the oxidation of Eu^{2+} may be considered as a pseudo first order reaction.

Espenson et al. (1969) investigated the kinetics of the oxidation of Eu^{2+} by VO^{2+},

$$VO^{2+} + Eu^{2+} + 2H^+ = V^{3+} + Eu^{3+} + H_2O,$$

and pointed out that, within a certain pH range, the rate of the reaction is independent of pH; therefore the reaction may be represented by two steps:

$$VO^{2+} + Eu^{2+} \xrightarrow{k} (VOEu^{4+}),$$

$$(VOEu^{4+}) + 2H^{+} \rightleftharpoons V^{3+} + Eu^{3+} + H_2O.$$

The rate of the second step is much greater than that of the first, so the first step is rate-controlling. At pH 1–3.7, the catalytic current and $E_{1/2}$ of this system are also independent of pH and i_c depends solely upon the rate of the first reaction. In KI solutions, the product V^{3+} is immediately reduced to V^{2+} on the surface of the electrode ($E_{1/2} = -0.46$ V SCE). Therefore, the overall reaction scheme of this catalytic wave may be summarized as

$$Eu^{3+} + e \rightleftharpoons Eu^{2+},$$

$$VO^{2} + Eu^{2+} \overset{k}{\rightleftharpoons} (VOEu^{4+}),$$

$$(VOEu^{4+}) + 2H^{+} \rightleftharpoons V^{3+} + Eu^{3+} + H_2O,$$

$$V^{3+} + e \rightarrow V^{2+}.$$

The rate constant k was determined (Li et al., 1981) by applying Koutecký's equation (Koutecký, 1953; Hyerovský et al., 1965),

$$\bar{i}_c/\bar{i}_d = 0.812\left(2k(VO^{2+})t_1\right)^{1/2},$$

where t_1 is the drop time of the mercury electrode. From the asymptotic line of the plot $\bar{i}_c/\bar{i}_d$ vs. (VO^{2+}), which passes through the origin, the average value of k was found to be $1.84 \times 10^3\,M^{-1}s^{-1}$, which is comparable with the value obtained by Espenson et al. (1969), $k = 2.64 \times 10^3\,M^{-1}s^{-1}$. The discrepency may be due to the difference in the solution compositions. Furthermore, according to the equation derived by Kao et al. (1963), in single-sweep polarography

$$i/i_p = (RT/nFv)^{1/2}(1/0.447)\left(kC_z^0\right)^{1/2}$$

where v is the rate of scanning (0.25 V/s), C_z^0 is the concentration of VO^{2+} and k was found to be $1.38 \times 10^3\,M^{-1}s^{-1}$. Since the value of k is small, the catalytic wave is not sensitive. In order to enhance the sensitivity, we must search for a system that has a large value of k. This is a general rule for catalytic waves.

3.9. *The Eu-xylenol orange–HAc–NaAc system*

Europium is an important element in the rare earth family. It is desirable to develop a sensitive method for its analysis. The previously mentioned methods are not sensitive enough.

Xylenol orange (XO) is a triphenylmethane dye, which is used as an indicator. It is widely used in spectrophotometry for the determination of rare earths. Véber et al. (1979) studied the polarographic behavior of XO and showed that the carbonyl group in the molecule reduces via two steps. In the first step a free radical is formed and in the second step this free molecule is reduced. At high acidity the free radical disproportionates into XO and a final product, so the second wave disappears. At pH 4–5, the rate of disproportionation is very slow, hence we may obtain two separate waves of approximately equal height.

Gao et al. (1982) investigated the reduction wave of the Eu(III)–xylenol orange–HAc–NaAc system. It can be seen from fig. 9a that P_1 and P_2 are the two peaks of XO and P_3 (-0.83 V SCE) is a new one developed by the Eu–xylenol complex, the height of which is directly proportional to the concentration of Eu in the range of 1×10^{-7} to 1×10^{-6} M, with a detection limit of 5×10^{-8} M.

The formation of the Eu–XO complex may be seen from the following experimental findings: The color of XO solution changes from orange to red upon addition of Eu^{3+}, and its absorption peak at 430 nm moves to 563 nm. The composition of the complex was determined by Job's method of continuous variation using both spectrophotometric and polarographic data to be $Eu^{3+}:XO = 1:1$. The degree of dissociation $\alpha = 0.134$ (Inczedy, 1976) and its apparent stability constant

$$K = (1 - \alpha)/C\alpha^2 = 7.2 \times 10^5 \quad \text{or} \quad \log K = 5.85.$$

The adsorptive nature of the complex was verified by cyclic voltametry. Therefore it is an adsorptive complex wave.

From fig. 9b, it may be seen that among the XO complexes of all 16 rare earth elements except Pm, the Eu–XO complex wave is the most sensitive, especially at pH 5. This is in contrast to other systems where the Eu complex wave is usually the most insensitive. This is because the Eu–XO wave is also catalytic in nature as may be seen from the following experimental facts: If the complex wave is purely adsorptive as in the case of the Gd–XO system, the wave height is independent of the concentration of XO within a certain concentration range, but the wave height of the Eu–XO system is proportional to the square root of the concentration of XO, indicating that the wave is also catalytic in nature. Furthermore, the temperature coefficient of the Gd–XO wave is 1.1% per °C in the temperature range of 5–40°C, while that of the Eu–XO wave is 5.3% per °C, indicating that the former is a diffusion-controlled process, while the latter is kinetic in nature. Therefore the P_3 peak has the dual properties of an adsorptive complex wave as well as a catalytic wave. This explains the exceptionally high sensitivity of the Eu–XO system. The

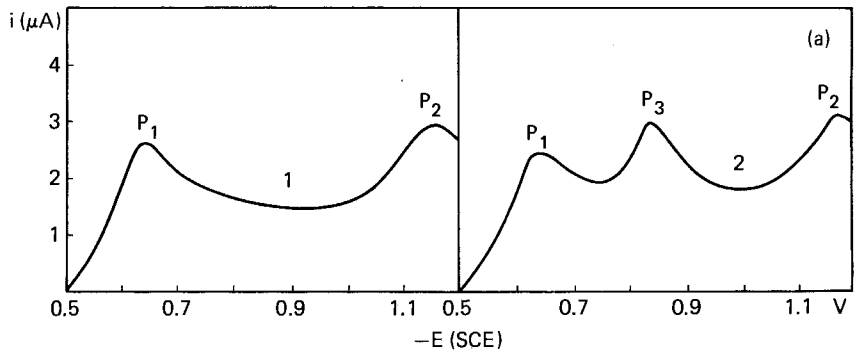

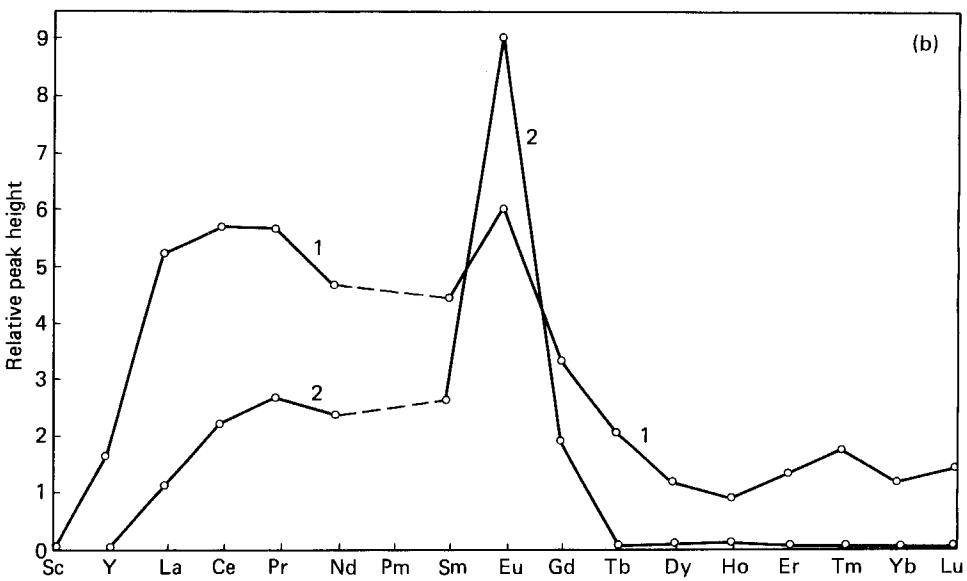

Fig. 9. (a) Normal single-sweep polarograms of XO and the Eu–XO system. Curve 1: 0.1 M HAc–NaAc $+ 1 \times 10^{-3}$ M XO; curve 2: curve $1 + 1 \times 10^{-5}$ M Eu^{3+}. (b) Comparison of the sensitivities of the adsorptive XO complex waves of various rare earth elements. 0.1 M HAc–NaAc, 3×10^{-4} M XO and 1×10^{-6} M R^{3+}. Curve 1: pH 4; curve 2: pH 5.

electrode processes in this system may be summarized as

$$XO + H^+ + e \rightarrow XH\dot{O} \qquad (P_1),$$
$$XH\dot{O} + H^+ - e \rightarrow XHOH \qquad (P_2),$$
$$Eu^{3+} + XO \rightleftarrows Eu^{3+} - XO \qquad \text{(in solution)},$$
$$Eu^{3+} - XO \rightleftarrows (Eu^{3+} - XO)_{ads} \qquad \text{(adsorption)},$$
$$(Eu^{3+} - XO)_{ads} \rightleftarrows Eu^{3+} + XO,$$
$$Eu^{3+} + e \rightleftarrows Eu^{2+}$$
$$\uparrow \text{——————} \downarrow$$
$$Eu^{2+} + XH\dot{O} + H^+ \rightleftarrows Eu^{3+} + XHOH \qquad \text{(reaction layer)}.$$

This sensitive polarographic method for Eu was used to determine Eu in the phosphor BaFCl : Eu used as an *X*-ray intensifying screen. The procedure is: Divide the sample into two portions; dissolve the first by heating with HCl under a nitrogen atmosphere; dissolve the second in HCl and H_2O_2. Prepare each portion in a solution containing 0.1 M HAc–NaAc and 1×10^{-4} M XO at pH 5 and take the polarograms. The first gives the amount of Eu^{3+} in the sample and the second gives the sum of Eu^{3+} and Eu^{2+}. The difference them gives the Eu^{2+} content in the sample. The results are satisfactory.

3.10. *The Gd–o-pyrocatechol violet–NH_4Cl–$(CH_2)_6N_4$ system*

The polarography of the complexes of metal ions with *o*-pyrocatechol violet (PV) were studied by Wang et al. (1966) and Véber et al. (1981). Tokano (1966) investigated the complexes of rare earths with PV by spectrophotometric methods. Zhang et al. (1983) studied the polarographic behavior of PV in several base electrolytes, such as NH_4Cl, NH_4SCN, $(CH_2)_6N_4$, etc., and found that it gives a wave peak P_1. On adding Gd(III), only at pH 5–6, a new complex wave peak P_2 (-0.85 V SCE) can be observed. The presence of NH_4^+ seems necessary for the reduction of PV; hexamethylene tetramine, $(CH_2)_6N_4$, also provides NH_4^+ through hydrolysis:

$$(CH_2)_6N_4 + 6H_2O + 4H^+ = 6HCHO + 4NH_4^+.$$

In order to have a well-shaped P_2 and a good separation between P_1 and P_2, a mixed electrolyte consisting of 0.3 M NH_4Cl and 0.003 M $(CH_2)_6N_4$ at pH 5.5 should be used. Under such conditions, Gd(III) in the concentration range of 1×10^{-6} to 1×10^{-5} M can be determined by measuring the height of P_2.

The adsorptive properties of this complex wave were confirmed by the following experiments.

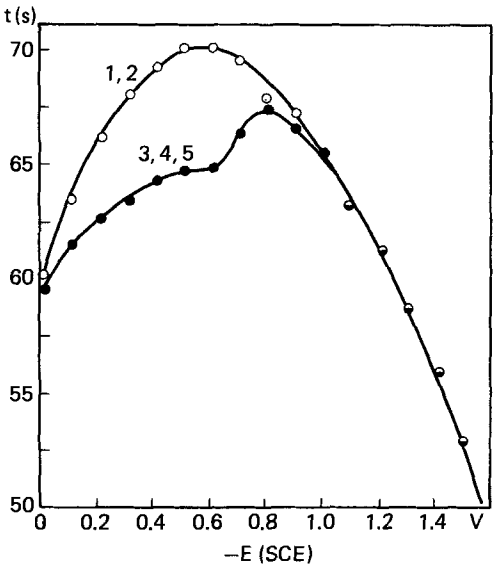

Fig. 10. Electricapillary curves of PV and the Gd–PV system. Curve 1: 0.3 M NH_4Cl, pH 5.5; curve 2: curve 1 + 0.003 M $(CH_2)_6N_4$; curve 3: curve 1 + 1×10^{-4} M PV; curve 4: curve 2 + 1×10^{-4} M PV; curve 5: curve 4 + 2×10^{-5} M Gd^{3+}.

(a) The electrocapillary curves shown in fig. 10 indicate that both the PV and the Gd–PV complexes depress the surface tension before −0.70 V, then a hump is formed at −0.8 V, just at the reduction peak of the complex, showing that the extent of adsorption of the PV and the Gd–PV complexes are at the same level.

(b) The rest-period before the scan can be varied by a JP-1A single-sweep polarograph. Cd^{2+} in KNO_3 was taken as a reference that is independent of rest time. It was found that the height of the Gd–PV peak linearly increases with rest time when the latter is less than 15 s, after which there is no further change in peak height, indicating that the adsorption equilibrium is reached after 15 s.

(c) The relationship between the wave heights and the drop time in the PAR-384-4 pulse polarograph is shown in table 2.

From the table, it can be seen that for the Cd^{2+}–KNO_3 system, i_p and E_p are practically constant at different drop times, indicating that it is a reversible diffusion wave without adsorption. For the PV and Gd–PV systems, i_p increases with the drop time, indicating that adsorption occurs. The NPP waves of PV and Gd–PV are both in peak form but the latter have a more negative E_p value.

(d) The cyclic voltametric curves of PV and Gd–PV show that the reduction of PV is irreversible, and that the complex is adsorbed more strongly than PV. This system is a typical example of adsorptive complex waves. All rare earth ions except Sc(III) give similar waves; therefore, an approximate estimation of the total concentration of all lanthanide ions and Y^{3+} can be made by this method.

The mechanism and application of this system were further studied by Gao et al. (1983). In acid medium, only the quinoid form of PV is reducible at −0.75 V SCE (C'ifka et al., 1956). The slight acidity of the NH_4Cl solution facilitates the reduction of PV; hence, it is a good supporting electrolyte. The addition of 0.003 M $(CH_2)_6N_4$

TABLE 2
The relationship between wave heights and drop time

System	Drop time (s)								
	0.5	0.7	0.9	1.1	1.3	1.5	1.7	1.9	2.1
No. 1 i (nA)	—	1582	1564	1490	1480	1480	1470	1460	1460
$-E_p$ (V)	—	0.662	0.662	0.662	0.662	0.662	0.662	0.662	0.662
No. 2 i (nA)	217	401	530	649	706	726	752	769	785
$-E_p$ (V)	0.826	0.798	0.786	0.786	0.782	0.786	0.786	0.786	0.786
No. 3 i (nA)	465	887	1160	1420	1490	1590	1600	1620	1620
$-E_p$ (V)	0.858	0.870	0.882	0.890	0.890	0.898	0.898	0.898	0.898

System No. 1: 0.1 M KNO_3 + 3×10^{-4} M Cd^{2+}
System No. 2: 0.3 M NH_4Cl + 0.003 M $(CH_2)_6N_4$ + 1×10^{-4} M PV, pH 5.5
System No. 3: No. 2 + 5×10^{-5} M Gd^{3+}

is necessary for two reasons. First, it acts as a buffer to absorb the proton liberated by PV, thus improving its wave shape. Second, it acts as a weak surfactant that inhibits the wave splitting and increases the wave height. The rare earth–PV system has been employed to determine La and Gd in some phosphors of the general formula $(La_xGd_{1-x})_2O_2S$:Eu synthesized by the Inorganic Chemistry Division of Peking University. This method is also useful in ore analysis for rare earths.

3.11. *The Gd–alizarin red S–NH_3–NH_4OH system*

Alizarin red S is a color reagent for rare earth ions (Munshi et al., 1963; Sangal, 1965). In single-sweep polarography, alizarin red S in 0.1 M NH_3–NH_4Cl solution at pH 8.9–9.7 exhibits a reversible reduction peak P_1 at −0.60 V SCE. On adding Gd(III) to the above solution, a second peak, P_2, appears at −0.68 V SCE, the height of which is proportional to the concentration of Gd(III) in the range from 1×10^{-7} to 1×10^{-6} M, with a detection limit equal to 6×10^{-8} M (Li et al., 1983). In dc polarography, 2×10^{-4} M alizarin red S gives a diffusion current $\bar{i}_d = 0.58\,\mu$A, when $m = 0.965$ mg/s, $t = 5.69$ s and $D = 4.0 \times 10^{-6}$ cm^2/s (Furman et al., 1948). According to these data and the Ilkovic equation, n was calculated to be 1.8 or approximately 2. Therefore, two electrons are involved in the reduction, i.e., the quinone group in the molecule is reduced to hydroxyquinone by adding two protons and two electrons. The wave shape is symmetrical as in fig. 11a of the next section. From the experiments of electrocapillary curves, the temperature coefficients and the plot of i_p vs. $v^{1/2}$, etc., its was proved that, at pH 9.6, anionic alizarin red S was adsorbed on the surface of the dropping mercury electrode and the Gd–arizarin red S complex was adsorbed even more strongly. The composition of the complex was determined by the method of Li et al. (1973) to be Gd : alizarin = 1 : 2 when the concentration of Gd is 1×10^{-5} to 7×10^{-5} M. If the concentration of Gd is equal to or greater than 8×10^{-5} M the ratio becomes 1 : 3. The corresponding stability constants are $\log \beta_{1:2} = 13.0$ and $\log \beta_{1:3} = 18.2$.

The electrode process of this adsorptive complex wave may be represented by the following equations:

$$Gd^{3+} + 3HL^{2-} + 3NH_3 \leftrightharpoons (GdL_3)^{6-} + 3NH_4^+ \quad \text{(chemical reaction)},$$

$$(GdL_3)^{6-} \leftrightharpoons (GdL_3)_{ads}^{6-} \quad \text{(surface process)},$$

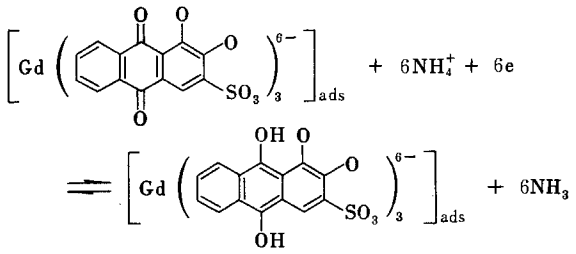

where L denotes the alizarin red S anion. Among the PV complexes of various rare earth ions, the Eu–PV complex is the most sensitive, probably because of the reducibility of Eu(III) to Eu(II) at the potential P_2. Other common cations such as 1×10^{-5} M Ca^{2+}, Al^{3+} seriously interfere with the measurement of P_2. 1×10^{-5} M Cu^{2+} does not interfere although it also produces a new wave at a more positive potential. Mg^{2+} and Fe^{3+} at concentrations of 1×10^{-5} M do not interfere.

3.12. *The Tb–oxine–$NaClO_4$ system*

Many metal ions coordinate with 8-hydroxyquinoline (oxine, HOx). Three species, namely Ox^-, HOx and H_2Ox^+, exist in aqueous solution and the two-step acid dissociation constants are $pK_1 = 5.16$ and $pK_2 = 9.63$ (Fujinaga et al., 1969). In the pH 3.5–5.0 range, oxine exists mainly as H_2Ox^+, which gives a reversible reduction wave peak P_1 at -1.60 V SCE in the single-sweep polarogram. Addition of Tb(III) decreases P_1 and a new peak P_2 appears at a more negative potential (about -1.7 V SCE) (Jiao et al., 1983). In a solution containing 0.1 M $NaClO_4$ and 8×10^{-5} M HOx at pH 4, a linear calibration curve was obtained by plotting the decrease of P_1 versus the concentration of Tb(III) added within the range 1×10^{-6} to 1×10^{-5} M, and the straight line passes through the origin. If the concentration of HOx is 2×10^{-4} M, a linear relationship holds between the peak height of P_2 and the concentration of Tb(III) within the range 3×10^{-6} to 3×10^{-5} M, but the straight line does not pass through the origin. Therefore, from an analytical point of view, it is better to measure the decrease of P_1. All rare earth ions with the exception of Eu(III) decrease the P_1 peak and give the P_2 peak. This is probably due to the reduction of Eu(III) to Eu(II) before P_1 and P_2. When the pH of the solution is greater than pK_2 of oxine (9.63), Ox^- is the predominant species, which is more difficult to reduce than H_2Ox^+, so both P_1 and P_2 disappear.

Experiments similar to those mentioned in the preceding sections were performed to show that oxine is weakly adsorbed while the Tb–oxine complex is adsorbed more strongly (Jiao et al., 1983). By a method suggested by Yatsimirskii et al. (1962), the stability constant of the Tb–oxine complex was found to be $\log K_1 = 10.35$. The

electrode process is described by the following equations (Jiao et al., 1983):

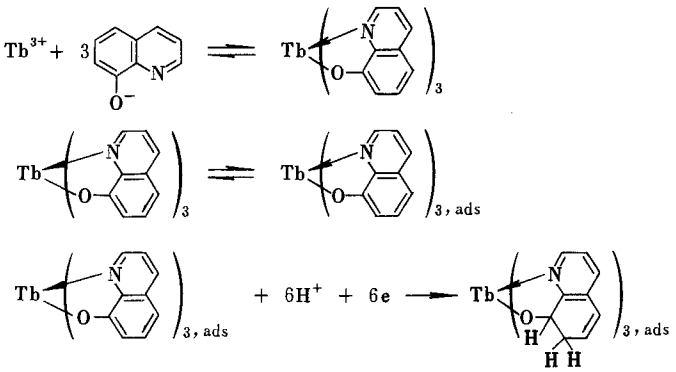

This is another example of the reduction of an adsorptive complex without prior dissociation.

Gao et al. (1983) tried to use La instead of Tb in this system, but the wave obtained in the La–oxine–$NaClO_4$ system is not sensitive. By addition of another ligand, maleic acid, the sensitivity of the wave was greatly enhanced. The optimum conditions are 0.08 M KCl, pH 4, 2×10^{-4} M HOx and 8×10^{-4} M maleic acid. By measuring the decrease of P_1 (−1.50 V SCE), 5×10^{-7} to 5×10^{-6} M La^{3+} can be determined; by measuring the increase of P_2 (−1.58 V SCE), 2×10^{-6} to 1×10^{-5} M La^{3+} can be analyzed. Maleic acid at pH 1–10 has two reduction waves with $E_{1/2} = -1.04$ and −1.37 V SCE, respectively. The addition of La^{3+} depresses the two wave heights, indicating the formation of a La(III)–oxine–maleic acid complex with a composition of La^{3+} : Ox : maleic anion = 1 : 3 : 1. The mixed-ligand complex formed was shown by ion-exchange experiments to be a large anion $(LaOx_3A)^-$ where A^- is the maleic acid anion. Finally it was shown that P_1 is due to the diffusion wave of oxine and P_2 (−1.58 V SCE) is the adsorptive reduction wave of the complex. The cyclic voltamogram shows two peaks corresponding to P_1 and P_2 but without an anoidic wave, indicating that the reduction of oxine is irreversible.

This system has been used to determine La in the phosphor $(La,Gd)_2O_2S$ with satisfactory results.

3.13. *The Tm–alizarin complexon–HAc–NaAc system*

Alizarin complexon is a color reagent in spectrophotometry and an indicator in complexometric titrations. It has a structure similar to alizarin red S but with two additional aminocarboxylic groups to facilitate the complexation with metal ions. In single-sweep polarography, alizarin complexon in a solution containing 0.1 M HAc–NaAc at pH 5.9 exhibits a reversible preadsorption wave with $E_{p1} = -0.43$ V SCE, followed by a reversible diffusion wave with $E_{p2} = -0.48$ V (Li et al., 1984). The process is reversible and adsorptive. Figure 11 shows the cathodic and anodic polarization curves obtained from a single-sweep polarograph. These polarization

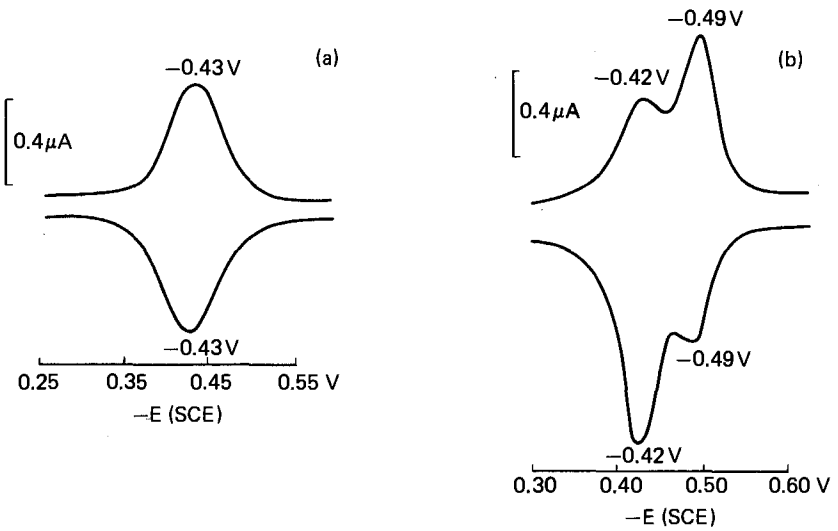

Fig. 11. Cathodic and anodic polarization curves of the alizarin complexon and the Tm–alizarin complexon system. (a) 0.1 M HAc–NaAc + 2×10^{-5} M alizarin complexon, pH 5.9. (b) 0.1 M HAc–NaAc + 3×10^{-5} M alizarin complexon + 1×10^{-5} M Tm^{3+}, pH 5.9.

curves are symmetrical in shape. The electrode reactions of alizarin complexon to produce P_1 and P_2 were investigated in detail and the amount of adsorption at P_1 was quantitatively determined. Under optimum conditions, 5×10^{-5} M of alizarin complexon is enough to establish a complete coverage, which is equal to 1.4×10^{-10} mol/cm^2, so the area of each alizarin complexon molecule may be calculated to be 118 Å^2. From an equation derived by Koryta (1953) for fast adsorption equilibrium the amounts of adsorption at different concentrations of alizarin complexon were calculated. Based on these data, an adsorption isotherm was drawn. The curve was best fitted to the Frumkin isotherm with adsorption constants $\beta = 2.9 \times 10^4$ and $\gamma = 1.27$, indicating that the adsorption of reactant is very strong because of the strong attraction between the adsorbed molecules.

At a concentration of alizarin complexon less than 5×10^{-5} M for the complete coverage of the electrode, an adsorptive peak of alizarin complexon ($E_p = -0.43$ V SCE) and an adsorptive complex peak ($E_p = -0.49$ V SCE) in the presence of Tm can be observed as shown in fig. 11. Since the redox reaction is reversible and adsorptive, the cathodic and anodic polarization curves are symmetrical.

The calibration curves were obtained in the concentration ranges of 1×10^{-8} to 1×10^{-7} and 1×10^{-7} to 1×10^{-6} M Tm(III). Tm is the most sensitive element in the lanthanide series.

The composition of the Ce(III)–alizarin complexon reported by Langmyhr et al. (1971) is 2:2, hence the Tm–alizarin complexon complex is probably also a 2:2 dinuclear complex. If the concentration of alizarin complexon is greater than that of Tm, an induced adsorption may occur and a film of $(TmL)_2L_2$ will be formed.

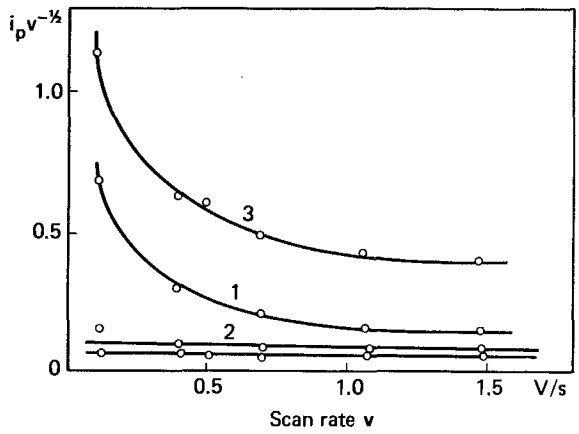

Fig. 12. Plot of $i_p v^{-1/2}$ vs. v of the Yb^{3+}–NO_3^- (or NO_2^-) system.

No.	Yb^{3+}, M	$(NO_3^-)/(Yb^{3+})$
1	1.5×10^{-5}	100
2	5×10^{-5}	0.4
		$(NO_2^-)/(Yb^{3+})$
3	3×10^{-6}	200
4	1.5×10^{-5}	1

Therefore, when this system is used for analysis, the concentration of the ligand should not exceed that for a saturated coverage of the mercury electrode.

3.14. *The Yb–NO_3^- (or NO_2^-)–NH_4Cl system*

Gao et al. (1982) developed a very sensitive catalytic wave of Yb(III) in a solution containing 0.1 M NH_4Cl, 5×10^{-2} M KNO_3 (or 5×10^{-4} M $NaNO_2$), 1×10^{-3} M KI and 0.02% polyvinylalcohol at pH 5.0. The limit of detection of Yb(III) is as low as 5×10^{-8} M. In dc polarography, $E_{1/2} = -1.45$ V SCE. The catalytic nature of this wave was proved by the following experiments.

(a) If the concentration ratio NO_3^-/Yb^{3+} is varied from 1 to 120, the current i_1 is proportional to the square root of (NO_3^-). When the concentration ratio is less than 1, then i_1 is proportional to (NO_3^-). In the former case the wave is catalytic in nature, while in the latter case the wave is diffusion-controlled. For the Yb^{3+}–NO_2^- system, when the concentration ratio NO_2^-/Yb^{3+} is greater than 20, the wave is catalytic; when the concentration ratio is below 20, the wave is diffusion-controlled.

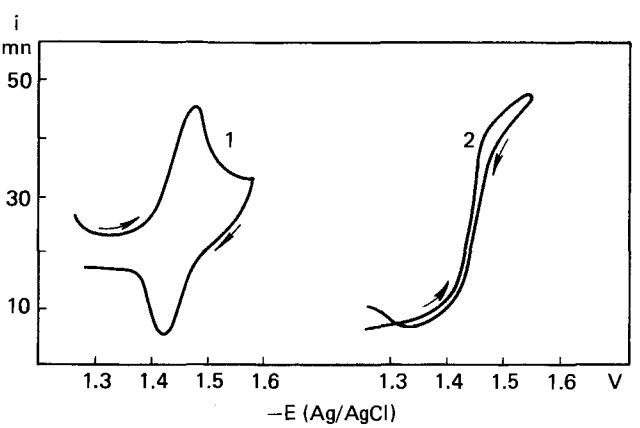

Fig. 13. Cyclic voltametric curves of Yb^{3+} and the Yb^{3+}–NO_2^- system. Curve 1: 0.1 M $NH_4Cl + 8.6 \times 10^{-4}$ M Yb^{3+}, pH 5.0; curve 2: curve $1 + 7.5 \times 10^{-3}$ M $NaNO_2$.

(b) According to Nicholson et al. (1964), the plot of $i_p v^{-1/2}$ vs. v, where v is the scan rate, may be used to test whether a wave is diffusion-controlled or a kinetic. Figure 12 shows the $i_p v^{-1/2}$ vs. v plot of the Yb^{3+}–NO_3^- (or NO_2^-) system. The horizontal straight lines 2 and 4 indicate that the waves are diffusion-controlled, while curves 1 and 3 indicate that the waves are kinetic.

(c) Figure 13 shows the cyclic voltametric curves from which is may be seen that Yb^{3+} in NH_4Cl solution reduces reversibly (curve 1), but in the presence of $NaNO_2$ only the reductive wave is observed (curve 2). This clearly indicates a catalytic wave with the EC mechanism, where the Yb^{2+} formed is immediately reoxidized by NO_3^- or NO_2^- into Yb^{3+}.

Under optimum conditions, this catalytic wave can be used to determine 1×10^{-7} to 1×10^{-6} M Yb^{3+} in dc polarography without the separation from other rare earth ions. The nitrate or nitrite ion in this system acts as an oxidizing agent, and itself is reduced to hydrazine. The addition of some polyvinyl alcohol is necessary, because it acts as a surfactant that stabilizes and improves the shape of the catalytic wave. This method has been used for the analysis of ores.

3.15. *The light rare earths–N,N′-di(2-hydroxy-5-sulphophenyl)–C-cyanformazan–KNO_3 system*

N,N′-di(2-hydroxy-5-sulphophenyl)–*C*-cyanformazan (DSPCF) forms colored complexes with many metal ions, which are used for spectrophotometric analysis (Yu et al., 1965). Campbell et al. (1956) studied the electrochemical properties of formazan compounds. Zhang et al. (1983) investigated in detail the complexes of DSPCF with light rare earth elements and suggested an adsorptive complex wave in KNO_3 supporting electrolyte at pH 4.0.

The polarographic behavior of DSPCF (10^{-5} M) with Sm^{3+} (10^{-5} M) was examined in 0.1 M solutions of various supporting electrolytes, such as KNO_3, KCl, LiCl, KI, NH_4Cl, $(CH_3)_4NCl$ and $(CH_2)_6N_4$ at pH 4.0. There is no wave in

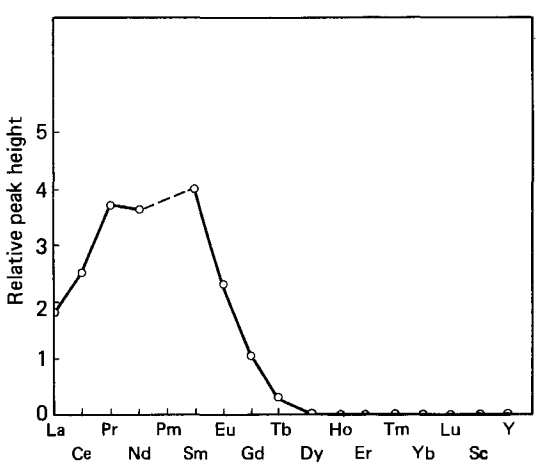

Fig. 14. Comparison of the sensibilities of the adsorptive DSPCF complex waves of various rare earth elements. 0.25 M KNO_3 + 1×10^{-5} M DSPCF + 2×10^{-6} M R^{3+}, pH 4.0.

urotropine and the waves in KI and NH_4Cl are not well-defined. In KNO_3, KCl, NaCl, LiCl and $(CH_3)_4NCl$, DSPCF has two peaks in single-sweep polarography at about -0.66 and -0.71 V SCE. When Sm^{3+} is added, a third peak appears at -0.73 V. A linear relationship holds between the derivative wave heights and the concentrations of 1×10^{-7} to 5×10^{-6} M Ce^{3+}, 3×10^{-7} to 3×10^{-6} M Pr^{3+}, 5×10^{-7} to 3×10^{-6} M Nd^{3+}, 5×10^{-7} to 5×10^{-6} M Eu^{3+}, La^{3+}, and 3×10^{-7} to 2×10^{-6} M Sm^{3+}. The complexes of DSPCF with other rare earth elements (from Gd to Lu, Sc and Y) have no electroactivity and do not interfere with the determination of light rare earths in 0.25 M KNO_3 at pH 4.0. Figure 14 shows the comparison of the electroactivities of DSPCF complexes with all the rare earth elements except Pm.

DSPCF is an organic coloring agent as well as an indicator. When the pH is < 5.5, DSPCF gives a yellow-orange color; when the pH is > 8.0, the solution becomes purple-red. At pH > 11.0, DSPCF is unstable and the solution turns colorless after long standing. From the plot between the peak potential E_p and the pH, the acid dissociation constants of DSPCF were calculated as

$$H^+ + H\Phi^{=-} \rightleftharpoons H_2\Phi^{=} \quad K_1 = \frac{[H_2\Phi^{=}]}{[H^+][H\phi^{=-}]} = 1.0\times10^9,$$

$$H^+ + H_2\Phi^{=} = H_3\Phi^{-} \quad K_2 = \frac{[H_3\Phi^{-}]}{[H^+][H_2\Phi^{=}]} = 6.3\times10^3.$$

Under the analytical condition of pH 4.0, $H_2\Phi^{=}$ is the essential form of DSPCF.

The cyclic voltametric curves of DSPCF have been recorded with an M-79-1 (fig. 15). There are three reduction peaks at -0.28, -0.70 and 1.20 V on the cathodic branch and only one oxidation peak at -0.23 V on the anodic branch. The longer the rest time before the potential scan, the higher the reduction peaks.

Campbell et al. (1956) determined the polarographic reduction potentials of triphenyl tetrazolium, triphenyl formazan and benylidene. Based on Campbell's

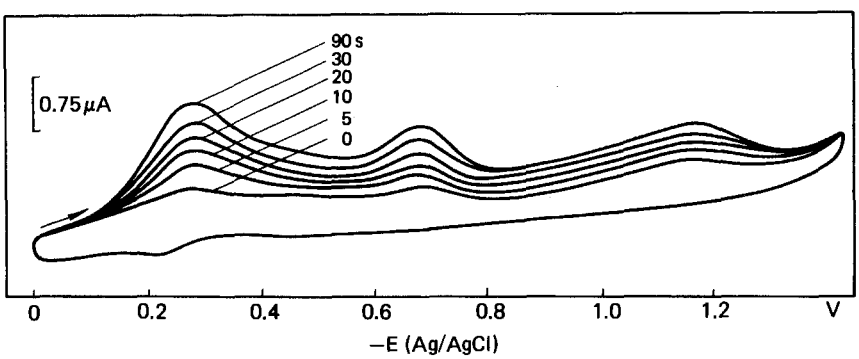

Fig. 15. Cyclic voltammograms of DSPCF. 0.25 M KNO_3 + 1×10^{-5} M DSPCF, 50% methanol, pH 4.0; $v = 250$ mV/s.

data, Zhang et al. (1983) suggested that the oxidation and reduction peaks obtained from cyclic voltametric curves (fig. 15) correspond to the following electrochemical processes.

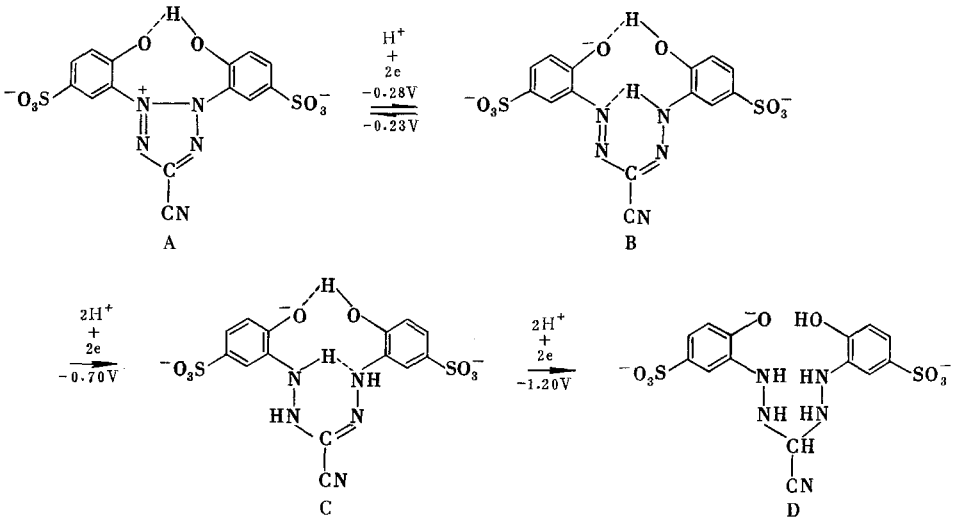

At pH 4.0 DSPCF mainly exists in the form of B. If the starting point of the scan is at 0.0 V, form B is oxidized to A on the electrode surface before the scan, and form A will in turn be reduced to B, C and D during the scan. The oxidation peak at -0.23 V corresponds to the reduction peak at -0.28 V, which shows that a reversible redox process exists between A and B, while further reduction of B and C is entirely irreversible.

Figure 15 shows cyclic voltametric curves at different rest times before the scan. The peak of the first cycle increases with increased rest time, but in the second and subsequent cycles, the peak is the same as that of zero rest time, and no more changes take place during the latter scans. This is because there is no more time interval between scans. By changing the starting potential, for instance, scanning from a potential more negative than -0.28 V, such as -0.30, -0.80 and -1.40 V the curves obtained are just the same as zero rest time.

Various experiments including the studies of electrocapillary curves, the effect of starting scan potential, the relationship between the peak height and the rest time and the temperature coefficients verified that the third peak in the system light rare earth–DSPCF is an adsorptive complex wave. The composition of the complex was determined to be $H_2Ln\Phi(NO_3)_2^=$, where Ln denotes light rare earths. This complex has electroactivity at pH 3.8–5.0, but has no characteristic color. As the pH becomes > 5.0, the electroactivity decreases but the color turns deeper and deeper. This means that another form of the complex is perhaps present in the solution. The variation of colors of DSPCF, DSPCF–La^{3+} and DSPCF–Lu^{3+} is summarized as follows (0.25 M KNO_3, 1.5×10^{-5} M DSPCF, 1.0×10^{-5} M Ln^{3+}):

TABLE 3
The apparent stability constants of light rare earth–DSPCF complexes $H_2Ln\Phi(NO_3)_2^{=}$

Element	La	Ce	Pr	Nd	Sm	Eu
β	1.7×10^6	7.7×10^6	3.8×10^7	4.8×10^7	8.3×10^7	1.1×10^8

The apparent stability constants of $H_2Ln\Phi(NO_3)_2^{=}$ are determined as shown in table 3.

The electrode process of this sensitive adsorptive complex wave ($E_p = -0.73$ V SCE at derivative single-sweep polarograph) may be represented by

$$H_2\Phi^{=} + Ln^{3+} + 2NO_3^- \rightleftharpoons H_2Ln\Phi(NO_3)_2^{=},$$

$$H_2Ln\Phi(NO_3)_2^{=} \rightarrow [H_2Ln\Phi(NO_3)_2^{=}]_{ads},$$

$$[H_2Ln\Phi(NO_3)_2^{=}]_{ads} \xrightarrow{2e} \text{products}.$$

The composition of the DSPCF complex with heavy rare earths was determined by spectrophotometry to be $Ln\Phi(H_2O)_2^{=}$, which has no electroactivity. The structural formulas of $H_2\Phi^{=}$ and $Ln\Phi(H_2O)_2^{=}$ are

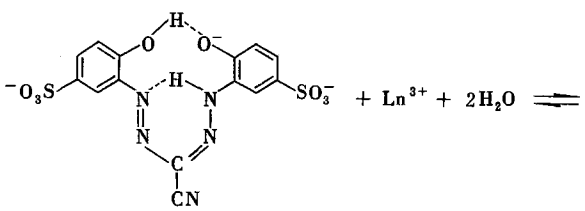

$H_2\Phi^{=}$

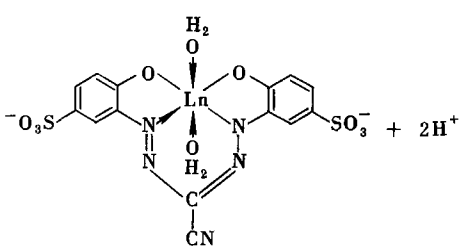

$Ln\Phi(H_2O)_2^{=}$

This light rare earth–DSPCF adsorptive complex wave has been used for the determination of La in the luminescent materials synthesized by the Inorganic Chemistry Division of Peking University, and the total amount of light rare earths in monazite and xenotime. The results are in agreement with those obtained by atomic absorption spectrometry.

The polarographic methods described above have been employed for the determination of rare earths in ores, minerals, phosphors and Eu in mixed rare earth oxides. Rare earth elements have been used in China since the 1970s for planting experiments on crops and some increasing yields have been observed (Wu et al., 1983). The application of a very small amount of mixed rare earth nitrate or chloride to seeds may accelerate the growth and development of crops and increase yield. In order to understand the functions of rare earth elements in plant growth, we must first establish a sensitive and convenient analytical method for the determination of trace amounts of rare earths in the plants. The following procedure was used: A plant sample, such as spinach, tea, pine leaves, wheat, corn, etc., was washed and dried at 80°C, crushed and sieved. A weighed sample of 2 g was ignited in a muffle furnace at a temperature of about 500°C for 6 hr. For the complete ashing, 1 ml of conc. HNO_3 was added to the ash powder and burned again until only a white residue remained. The residue was dissolved in HCl and the rare earth ions in the solution were separated from other elements by extraction with 1-phenyl-3-methyl-4-benzoylpyrazolone-5 in the presence of masking agents NH_4SCN and sulphosalicylic acid (Jensen, 1959; Peng et al., 1973). The rare earth contents in the organic phase were back-extracted into 1% HCl solution and determined by the adsorptive complex wave of rare earth–rhodamine B–diphenylguanidine system or rare earth–xylenol orange system (Jiao et al., 1982).

The regularity of the distribution of rare earth elements in plants was studied by the water culture method in which the nutrient materials can be controlled. Cucumber, the experimental plant, was treated with a solution of lanthanum chloride during its growth, and the rare earth content in different parts of the cucumber was analyzed. It was found that the tender part of the cucumber had more lanthanum than the tough part. This is in accordance with the regular distribution of essential nutrient elements in plants.

References

Aihara, M., K. Tmamure and Y. Eyuchi, 1976, Rev. Polarography **22**, 114.

Akhmedli, M.K., P.B. Granovskaya and R.A. Neimatova, 1973, Russ. J. Anal. Chem. **28**, 278.

Aladjem, A., 1970, Analytical Chemistry of Yttrium and the Lanthanide Elements (Ann-Humphrey Science, Ann Arbor, MI).

Almagro, V., F. Almagro and F. Sancho, 1966, in: Polarography, Vol. 1 ed. G.J. Hills, (Macmillan, New York) p. 667.

Anson, F.C., 1966, Anal. Chem. **33**, 54.

Bailar, J.C., Jr. and C.F. Callis, 1952, J. Am. Chem. Soc. **74**, 6018.

Bard, A.J. and L.R. Faulkner, 1980, Electrochemical Methods (Wiley, New York) pp. 535–536.

Boese, S.W. and V.S. Archer, 1977, Anal. Chem. **49**, 479.

Boese, S.W. and V.S. Archer, 1982, J. Electroanal. Chem. **138**, 273.

Borishchak, O.A., 1978, Russ. J. Anal. Chem. **33**, 2134.

Callis, C.F., N.C. Nielsen and J.C. Bailar, Jr., 1952, J. Am. Chem. Soc. **74**, 3461.

Campbell, H. and P.O. Kane, 1956, J. Am. Chem. Soc. **78**, 3130.

Christie, J.H., R.A. Osteryoung and F.C. Anson, 1967, J. Electroanal. Chem. **13**, 236.

C'ifka, J., C. Ryba, V. Suk and M. Malat, 1956, Collect. Czech. Chem. Commun. **21**, 1418.

Espenson, J.H. and R.J. Christensen, 1969, J. Am. Chem. Soc. **91**, 7311.

Flanagan, J.B., K. Takahashi and F.C. Anson, 1977, J. Electroanal. Chem. **85**, 258.

Florence, T.M., 1974, J. Electroanal. Chem. **52**, 115.

Florence, T.M. and G.H. Aylward, 1962, Aust. J. Chem. **15**, 65.

Florence T.M. and W.L. Belew, 1969, J. Electroanal. Chem. **21**, 157.

Florence, T.M. and L.E. Smythe, 1960, Nature **187**, 771.

Fu, S.R., L.M. Kao, L.M. Li and G.X. Xu, 1983, Beijing Daxue Xuebao **4**, 50.

Fujinaga, T, K. Izutzu, S. Okazaki and H. Swamoto, 1969, J. Electroanal. Chem. **21**, 187.
Furman, N.H. and K.G. Stone, 1948, J. Am. Chem. Soc. **70**, 3055.
Gao, X.X. and K. Jiao, 1982, Acta Chim. Sin. **40**, 611.
Gao, X.X. and X.R. Yao, 1977, Polarographic Catalytic Waves of Platinum Group Elements (Science Press, Beijing, China).
Gao, X.X. and L.Q. Zhang, 1982, Acta Chim. Sin. **40**, 621.
Gao, X.X. and M.P. Zhang, 1982, Sci. Sin. Ser. B **25**, 690 (in English).
Gao, X.X. and M.P. Zhang, 1984, Anal. Chem. **56**, 1912.
Gao, X.X., K. Jiao and S.V. Wu, 1983, Fenxi Huaxue **11**, 107.
Gao, X.X., R.L. Li, M.P. Zhang, K. Jiao and L.Q. Zhang, 1983, Kexue Tongbao 155 (special issue English).
Gao, X.X., N.Q. Li, K. Jiao, L.Q. Zhang and M.P. Zhang, 1983, Kexue Tongbao **15**, 914.
Gao, X.X., M.P. Zhang and T. Hu, 1983, Fenxi Huaxue **11**, 762.
Hantzsch, A., 1931, Ber. **64**, 695.
Harder, R. and S. Cheberek, 1958, J. Inorg. Nucl. Chem. **11**, 197.
Henne, M.T. and J.W. Collect, 1964, J. Electroanal. Chem. **7**, 359.
Heyrovsky, J. and Kuta, 1965, Principles of Polarography (in English) (Czechoslovak Academy of Science, Prague) pp. 380–392.
Ignatova, N.K., P.M. Zaitsev and V.G. Kazak, 1977, Russ. J. Anal. Chem. **32**, 708.
Ilkova, S.B., V.F. Barkovsky and E.A. Chistyakova, 1968, Russ. J. Anal. Chem. **23**, 1158.
Inczedy, J., 1967, Anal. Chem. Acad. Sci. Hung. **37**, 349.
Inczedy, J., 1976, Analytical Applications of Complex Equilibria (Ellis Horwood Press) p. 138.
Jensen, B.S., 1959, Acta Chim. Scand. **13**, 1668, 1890.
Jiang, Z.W. and X.X. Gao, 1985, Chinese J. Rare Earths **3**, 59.
Jiao, K. and X.X. Gao, 1982, Chem. J. of Chin. Univ. **3**, 327.
Jiao, K. and X.X. Gao, 1983, Acta Chim. Sin. **41**, 351.
Jiao, K. and X.X. Gao, 1985, Sci. Sin. B (4), 306.
Jiao, K., M.P. Zhang and X.X. Gao, 1982, Beijing Daxue Xuebao **12**, 77.
Kao, H., Z.X. Zhang and V.B. Zhang, 1963, J. Nanking Univ. (Chem. Ed.) **1**, 65.
Kaplan, B.Ya. and I.A. Sorkobekaya, 1962, Zavod. Lab. **28**, 1424.
Kolthoff, I.M. and J. Lehmicke, 1948, J. Am. Chem. Soc. **70**, 1879.
Kolthoff, I.M. and A. Liberti, 1948, J. Am. Chem. Soc. **70**, 1885.
Kolthoff, I.M. and J.J. Lingane, 1952, Polarography, 2nd ed. (Interscience, New York) pp. 435–440.
Kopanskaya, L.S., L.V. Mirovich and D.N. Knue, 1974, Russ. J. Anal. Chem. **29**, 71.
Koryta, J., 1953, Collect. Czech. Chem. Commun. **18**, 206.
Koutecky, J., 1953, Collect. Czech. Chem. Commun. **18**, 311.
Kurbatov, D.I. and V.I. Kostitsyna, 1979, Russ. J. Anal. Chem. **34**, 708.
Langmyhr, F.T., K.S. Klausen and M.H. Nouri-Nekoni, 1971, Anal. Chim. Acta **57**, 341.
Li, N.Q. and X.X. Gao, 1984, Acta Chim. Sin. **42**, 1062.
Li, N.Q. and L. Zhang and X.X. Gao, 1983, Acta Chim. Sin. **41**, 351.
Li, R.L. and X.X. Gao, 1981, Chem. J. Chin. Univ. **2**, 25.
Mairanovskii, S.G., 1968, Catalytic and Kinetic Waves in Polarography (Plenum, New York) Ch. 9.
Masuda, Y, T. Nakamor and E. Sekodo, 1978, Nippon Kagaku Kaishi **2**, 204.
Menkov, A.A. and N.A. Nepomnyashchaya, 1977, Russ. J. Anal. Chem. **32**, 1409.
Misumi, S. and A. Iwase, 1966, Modern Aspects of Polarography (Plenum, New York).
Munshi, K.N., S.N. Sinka, S.P. Songal and A.K. Dey, 1963, Microchem. J. **7**, 473.
Myasoedov, B.F., 1972, Radiochem. Radioanal. Lett. **10**, 123.
Nicholson, R.S. and I. Shain, 1964, Anal. Chem. **36**, 706.
Noddack, W. and A. Bruckel, 1937, Angew. Chem. **50**, 362.
O'Laughlin, J.W., 1979, in: Handbook on the Physics and Chemistry of Rare Earths, Vol. 4 eds., K.A. Gschneidner, Jr. and L. Eyring (North-Holland, Amsterdam) pp. 355–357.
Osipova, E.A., G.V. Prokhorova, P.K. Agasyan and E.D. Zhukova, 1981, Russ. J. Anal. Chem. **30**, 1738.
Osteryoung, R.A., G. Lauer and F.C. Anson, 1962, Anal. Chem. **34**, 1833.
Peng, C.L., 1973, Kexue Tongbao **4**, 170.
Pályi, GY., F. Péter and I. Szeberényi, 1962, Acta Chem. Acad. Sci. Hung. **32**, 387.
Pomeroy, P.R., R.A. White and G.H.R. Gwatkins, 1952, Metallurgia **46**, 157.
Pyatnitzky, I.B., 1946, Russ. J. Anal. Chem. **1**, 135.
Ryabichicov, D.I. and V.A. Ryabukhin, 1966, Analytical Chemistry of Rare Earth Elements (in Russian) (Institute of Geochemistry and Analytical Chemistry, Moscow).
Sachan, N.P. and C.M. Gupta, 1980, Talanta **27**, 457.
Saiki, M. and F.W. Lima, 1977, J. Radioanal. Chem. **36**, 435.
Sangal, S.P., 1965, Microchem. J. **9**, 38.
Sevryukov, N.N. and Gi.I. Doropeeva, 1973, Russ. J. Anal. Chem. **28**, 62, 77.
Steeman, E., E. Stemmerman and F. Verbeck, 1977, Bull. Soc. Chim. Belg. **86**, 491, 499.
Steeman, E., E. Stemmerman and F. Verbeck, 1978, J. Electroanal. Chem. **89**, 97, 113.
Thakur, M.L., 1974, Talanta **21**, 771.
Tsuneo Tokano, T., 1966, Bunseki Kagaku **15**, 1087.
Tur'yan, Ya.I., 1980, Chemical Reactions in Polarography (in Russian) (Chemistry, Moscow) Ch. 4.
Veber, M. and L.J. Csanyi, 1979, J. Electroanal. Chem. **101**, 419.

Veber, M. and L.J. Csanyi, 1981, J. Electroanal. Chem. **124**, 221.
Wang, E.K. and H.T. Hou, 1967, Annu. Rep. Inst. Appl. Chem., Acad. Sin. **15**, 30.
Wang, E.K. and X.Q. Lin, 1982, J. Electroanal. Chem. **136**, 311.
Wang, E.K. and W.J. Song, 1965, Annu. Rep. Inst. Appl. Chem., Acad. Sin. **13**, 18.
Weaver, M.J. and F.C. Anson, 1975, J. Electroanal. Chem. **65**, 759.
Willard, H.H. and J.A. Dean, 1950, Anal. Chem. **22**, 1264.
Wu, Z.M., X.K. Tang, X.X. Gao, K. Jiao and M.P. Zhang, 1983, J. Chin. Rare Earth Soc. **1**, 70.
Yang, J.Q., 1980, Proceedings of Polarographic Analysis Conference, China (Geological Publisher, Beijing, China) pp. 4–8.
Yao, X.R., J.X. Chou and M. Yin, 1981, Fenxi Huaxue **9**, 22.
Yatsimirskii, K.B. and L.I. Bularin, 1962, Russ. J. Inorg. Chem. **7**, 1090, 1824.
Ye, X.Z. and X.X. Gao, 1982, Chem. J. of Chin. Univ. **3**, 475.
Ye, X.Z. and X.X. Gao, 1985, Chinese J. Rare Earths **3**, 77.
Ye, X.Z., Z.W. Jiang, S.W. Zhou, Z.Y. Zhang and X.X. Gao, 1983, Beijing Daxue Xuebao **6**, 76.
Yu, R.J., P.Q. Li and J.W. Zhang, 1965, Kexue Tongbao **10**, 916.
Zhang, L.Q. and X.X. Gao, 1983, Sci. Sin. Ser. B. **26**, 351 (in English).
Zhang, M.P. and X.X. Gao, 1983, Acta Chim. Sin. **41**, 342.
Zhang, M.P. and X.X. Gao, 1984, Anal. Chem. **56**, 1917.
Zhdanov, S.I., 1963, Russ. J. Phys. Chem. **37**, 387.

Handbook on the Physics and Chemistry of Rare Earths, edited by K.A. Gschneidner, Jr. and L. Eyring

Chapter 56

INORGANIC COMPLEX COMPOUNDS I

M. LESKELÄ* AND L. NIINISTÖ
Department of Chemistry, Helsinki University of Technology, SF-02150 Espoo 15, Finland

Contents

1. Introduction

1.1. *Historical development*

During the period of discovery of the rare earths, which began with the separation of impure yttria by Gadolin in 1794 and ended with the discovery of the last stable rare earth lutetium by Urbain in 1907 (Weeks, 1968), research efforts were directed

*Present address: Dept. of Chemistry, University of Oulu, SF-90570 Oulu 57, Finland.

mostly toward finding improved methods of separation and purification. These methods, which may now be called classical, involved almost exclusively inorganic compounds; the oxalate precipitation discovered by Gadolin must be regarded as an exceptional use of organic reagents at this early stage. Studies on the occurrence of the rare earths in nature likewise were concerned with inorganic compounds, often ones of complicated composition, such as in the case of the silicate minerals.

The last years in the period of discovery and the some 30 years following it saw several developments in separation techniques; for example, the reduction process was introduced for certain rare earths. The variety of chemical methods developed was then applied on an ever increasing scale, sometimes to many kilograms of starting materials; especially large amounts were used in the search for the elusive element 61. As examples of the compounds used in the large-scale separation of the rare earths by fractional crystallization, ammonium nitrates and ferrocyanides may be mentioned. Spectroscopic methods were applied to evaluate the success of the separation. A review of the often very laborious separation procedures has been presented by Prandtl (1938).

In the course of the separational and analytical studies a wealth of information about rare earth inorganic compounds was obtained. Composition, solubility and thermal stability were investigated and reported in detail, for instance. The structures remained largely unknown, however, and even compounds of complicated composition were referred to simply as salts or, when containing an extra cation, as double salts.

In the late 1940s and in the 1950s a dramatic change in research emphasis occurred when ion exchange methods based on organic complexing agents were introduced, to be followed and later superceded by solvent extraction. The review by Bock (1950) gives notice of the dawn of a new era in separation techniques. These powerful new separation methods were applicable on an industrial scale, which increased interest in the organic complexes of the rare earths. The interest was strengthened by the unusual luminescent properties that some of the compounds, e.g., the β-diketones, were found to possess. New inorganic applications were emerging at the same time but, since they generally involved compounds of simple composition (and high stability) or intermetallics, they did not attract the attention of the coordination chemist to the same extent. Though structural chemistry in the solid state was steadily evolving with the increasing use of X-ray diffraction methods, the studies on rare earth complexes were largely focused on organic ligands and solution studies. The comprehensive reviews written by Moeller et al. (Moeller et al., 1965, 1968; Moeller 1972) and Thompson (1979) in this *Handbook* present a good overall view of the developments in rare earth complex chemistry emphasizing organic ligands in solution and the solid state.

Inorganic compounds of the rare earths are still used today in industrial separation processes, but only at early stages involving group separations and not for the purification of individual rare earths. There are, however, a number of other considerations suggesting that more attention should be paid to the area of inorganic rare earth complexes. These include their potential application in phosphors, unusual structural features such as high and varying coordination numbers, interesting

high temperature reactions and possibilities in synthesis and catalysis. The inorganic compounds are also of direct relevance to geochemistry and mineralogy and for comparative purposes in actinide chemistry.

1.2. *Scope of the review*

As mentioned above, the 190 years of rare earth research have generated a wealth of information. The experimental data are so extensive that it would be impossible to systematize and cover them in a single book or review. While in the 1930s it was possible to report all essential data in two volumes of the *Gmelin-Kraut Handbook* (1928–32), and still in the late 1950s the *Nouveau Traité de Chimie Minerale* (Pascal, 1959) provided good coverage of the important research results in less than 1500 pages, now a comprehensive attempt involves tens of volumes and thousands of pages, as manifested in the latest, still incomplete edition of the *Gmelin Handbook* (1938–). According to a computer search of *Chemical Abstracts*, more than 100 books and 600 reviews on some aspect of rare earth chemistry were published during the five year period 1977–81 alone. These figures reflect the growth of chemical literature in general and rare earth literature in particular.

Even if one limits oneself to a coverage of inorganic compounds of complex composition and structure, the task is formidable and has not been attempted lately outside the *Gmelin Handbook*.

The recent reviews on complexes of the rare earths focus on organic ligands, with inorganic complexes as occasional examples. In addition to the reviews by Moeller and Thompson previously mentioned and some volumes of the *Gmelin Handbook* (Gmelin, 1980, 1981, 1982), the reviews of Moseley (1975) and Sinha (1976) contain useful information classified according to coordination numbers. An earlier book by Sinha (1966) deals almost exclusively with organic ligands and solution studies. Porai-Koshits et al. (1976) have also reviewed the structural aspects of rare earth coordination compounds, emphasizing organic ligands but including some inorganic ligands in the discussion. The comprehensive work by Panyushkin et al. (1977), on the other hand, systematically covering the years 1965–1975 with nearly 500 references, mentions the inorganic complexes only in a minor way when discussing the spectroscopy of lanthanides. Particular aspects of inorganic complexes have been discussed in specialized monographs and reviews: Brown, for instance, has covered the structural chemistry of rare earth halides (1968) and nitrates (1975) up to the late 1960s and early 1970s, respectively. The only review entirely devoted to inorganic complexes, however, seems to be the recent overview of limited scope of Niinistö (1983).

In view of this, it is felt that a review on the inorganic complex compounds, even though selective in coverage, would fill an important need. In several instances it is only now that we are able to understand the fundamental structural characteristics of these compounds, thanks mainly to the X-ray diffraction studies performed in recent years. As an example it may be noted that the X-ray structures of the double sulfates of the trivalent lanthanides, used in rare earth separations since the last

century, were determined only in the early 1970s; the structures of the corresponding ammonium double nitrates were not solved until just a few years ago.

To keep the review to a reasonable size, the following guidelines have been followed in the selection and coverage of topics:

(i) Solid state aspects of the trivalent compounds are emphasized, including applications in science and industry. Complex formation in solution is discussed only when relevant to the solid state structure and composition; the important case of aqua complexes in solution and in the solid state is treated in a special section however.

(ii) In selection of ligands, those compounds (including closely related ones) already covered in the *Handbook* (e.g., the molybdates (VI), Brixner et al., 1975) are left out of the review. Likewise, complexes containing both organic and inorganic ligands, e.g., carboxylates with aqua ligands, are not considered as inorganic and fall outside of the scope of the review.

(iii) Discussion of the bonding, complex formation and other general characteristics of the rare earth complexes is kept to a minimum and the reader is referred to other parts of the *Handbook*.

It is often difficult to judge from the literature whether a compound should be classified as a complex or not. In borderline cases a systematic approach has been adopted, viz., on the basis of available data a decision has been made about the whole group of compounds. Thus, silicates were included, for instance, while the binary oxides were excluded. The literature coverage is necessarily selective owing to the multitude of data. There has been an attempt, nevertheless, to briefly mention the most important books and review articles. In the case of primary publications this could not be done. Currentness is attempted through a coverage extending wherever possible to the first half of 1984 and 1985 for parts I and II of the review, respectively.

1.3. *General properties of the rare earth ions*

The coordination chemistry of the rare earths is frequently oversimplified and discussed only in terms of ionic radii with possible mention of the unusual oxidation states of cerium and europium. In addition to the ionic size and oxidation state, several other factors contribute to the complex formation of the rare earth ions and to the properties of the complexes formed. These include: type of bonding to ligands, coordination number and geometry, thermodynamic and kinetic stability, ligand–ligand repulsions, and so on. Many of these factors are related to each other and to the electronic configuration of the central ion. The complex formation of rare earth ions has been discussed among others by Karraker (1970), Moeller et al. (1965), Moeller (1972), Panyashkin et al. (1977), Grenthe (1978) and Thompson (1979).

On a more fundamental level, the different aspects of rare earth chemistry have been treated by Jørgensen (1976, 1979) and Jørgensen and Reisfeld (1982).

In the following we shall briefly discuss only the magnitude and effects of the ionic radii, oxidation potentials and bonding.

1.3.1. *Ionic radii*

The first sets of ionic radii for the trivalent rare earths were based on a cation coordination number (CN) of 6 and a fixed value of the anion radius O^{2-} or F^-. The lanthanide contraction, viz., the gradual decrease of ionic size from lanthanum to lutetium, is clearly apparent in the early values presented by Goldschmidt et al. (1926), who also noted that the radii varied with CN.

At the present, several sets of ionic radii are available taking into account the different CNs, oxidation and spin states and the slight variation of anion radii with CN. Very comprehensive data have been published by Shannon and Prewitt (1969, 1970a) and revised by Shannon (1976). The most recent set includes the values of effective ionic radii for all stable trivalent rare earths with coordination numbers 6, 8 and 9. In addition, values corresponding to CN = 10 and 12 have been listed for La^{3+} and Ce^{3+}, and values for 12-coordinated Nd^{3+} and Sm^{3+} (Shannon, 1976).

Ordering by effective ionic radii, yttrium takes a position in the middle of the heavier lanthanides; the values of 6-coordinated Y^{3+} (0.900 Å) and Ho^{3+} (0.901 Å) are equal. The historical name of yttermetals for the heavier lanthanides (Tb–Lu) seems justified on the basis of ionic radii. Sc^{3+} (0.745 Å) on the other hand, is closer to some trivalent ions of the d block, Fe^{3+} (0.645 Å) and Ti^{3+} (0.670 Å), for example, than to the heavier lanthanides, where the lanthanide contraction ends in an ionic radius of 0.861 Å for Lu^{3+} (Shannon, 1976).

In general, the ionic radii give an indication of the expected coordination number in a rare earth complex, though this is more apparent in aqueous solutions than in the solid state, where bulky ligands and different coordination modes may result in unexpected CNs. Scandium with its smaller ionic size has a significantly lower average coordination number than the other rare earths. The properties of scandium and yttrium, which are partly due to the ionic radii, are discussed in relation to those of the lanthanides in section 1.3.4.

1.3.2. *Oxidation states*

The chemistry of rare earths is often discussed only in terms of the trivalent ions and indeed, contrary to the actinides, the oxidation states encountered in lanthanide compounds in the solid state and especially in solution are few in number. Standard electrode potentials E^0 M(II–III) and E^0 M(III–IV) indicate that, besides the trivalent rare earth ions, only Eu^{2+} (−0.35 V), Yb^{2+} (−1.15 V), Sm^{2+} (−1.55 V) and Ce^{4+} (+1.74 V) are sufficiently stable to exist in aqueous solutions (Nugent, 1975). It has long been known that alkaline conditions and many complexing anions such as nitrate, phosphate and sulfate stabilize Ce(IV) (Jørgensen, 1979) and recently it has been shown that large complex-forming ligands such as heteropolyanions also stabilize to some extent tetravalent praseodymium and terbium (Spitsyn, 1977).

The tetravalent cerium is interesting because of its high charge and relatively large size, which lead to high coordination numbers in the solid compounds and to a resemblance to thorium. In the following review the trivalent state will be em-

phasized, but cerium(IV) and europium(II) compounds will be discussed as well whenever reliable data are available.

1.3.3. *Bonding in complexes*

The properties of the complexes strongly suggest that the bonding between the rare earth ion and the ligand is mainly electrostatic in nature (Karraker, 1970; Moeller, 1972). The observed and calculated effects of covalency are very small. For instance, in contrast to d-block elements, the bonding has no directional character but rather preserves the spherical symmetry of the central ion. A closer look reveals that a number of ions (e.g., Sc^{3+}, Y^{3+}, La^{3+}) have a noble gas configuration and in cases where the 4f orbitals are partly filled they are well shielded from ligand orbital interaction. The nature of $R-L_n$ bonds has been discussed in detail earlier in this *Handbook* (Jørgensen, 1979, Thompson, 1979) as well as elsewhere (Jørgensen, 1976) and the reader is referred to those reviews.

Another aspect of the bonding in complexes is the low kinetic stability in solution. For instance, the kinetics of water exchange from the first hydration sphere of aqueous Gd^{3+} has been studied by NMR and EPR techniques and the rate constants are found to be higher than previously assumed, exceeding those for the transition metal ions (Southwood-Jones et al., 1980). The lability of the complexes limits the possibilities for isomerism and places the rare earth ions in the same category as the alkaline earth ions.

1.3.4. *Scandium, yttrium and promethium*

The three elements Sc, Y and Pm deserve special attention, though for different reasons. As pointed out in section 1.3.1, the smaller size of scandium leads to somewhat exceptional chemical and physical behaviour. A more fundamental difference, however, is the electronic configuration where the lack of f electrons separates Sc and also Y from the lanthanides. Promethium is a true representative of the 4f elements but, being the only unstable rare earth, it has enjoyed a special position in rare earth research.

The limited availability and relatively high price of scandium have been the major reasons for the small-scale technical applications so far (Youngblood and Gschneidner, 1975) and probably have also contributed to the limited amount of research on it as compared with the other rare earths. The last two decades have nevertheless seen a significant increase in the papers devoted to scandium (Horowitz, 1975a); these include a number of structural studies on the inorganic complexes especially in the 1970s (Valkonen, 1979). There are also two books dealing with scandium: The earlier work also includes yttrium but is based on the relatively limited data then available (Vickery, 1960), while the more recent compilation by Horowitz (1975b) aims at covering all major aspects of scandium research and includes comprehensive overviews on inorganic compounds (Melson, 1975a; Gschneidner, 1975). There are two reviews on the coordination chemistry of scandium: The review by Melson and Stotz (1971) emphasizes organic ligands but discusses also the ammine and halide complexes; the more recent work by Pushkina and Komissarova (1983) deals with scandium chelates formed by EDTA and its

analogues. An earlier review by Petrů and Hajek (1966) also contains useful information on the inorganic compounds of scandium.

Although scandium is one of the rare earths and behaves similarly in many respects, e.g., forms strong complexes with oxygen-donor ligands, its small ionic size brings it closer to the large trivalent d-element ions. In many instances scandium compounds, although having the same stoichiometries as the lanthanide compounds, are not isostructural with them. Scandium is also the only rare earth capable of forming alums in analogy with Fe^{3+} (see for instance Bashkov et al., 1972). The structural chemistry of scandium may be well discussed in conjunction with trivalent metals other than the lanthanides, as done in a recent discussion of sulfates and selenates (Voronkov et al., 1982).

The smaller ionic radius also leads to extensive hydrolysis, which helps to explain why scandium compounds are more difficult to crystallize than those of the lanthanides and why the number of basic compounds is large. In aqueous solutions, depending on the pH, the Sc^{3+} ion can be presented as $[Sc(H_2O)_6]^{3+}$, $[Sc(H_2O)_5OH]^{2+}$ and $[Sc(H_2O)_5(OH)]_2^{4+}$ (Komissarova, 1980); there is also evidence for the formation of other polymeric species (Biedermann et al., 1956). The main product of polynuclear hydrolysis for Sc^{3+}, Y^{3+} as well as for In^{3+} appears to be (hydrated) $R_2(OH)_2^{4+}$ according to Biedermann and Ferri (1982). The same authors have also compared the formation constants of hydrolysis products with the composition ROH^{2+} and found that Sc^{3+} has a much lower pK_1 value ($pK_1 = 5.1$) than Y^{3+} (9.1) or La^{3+} (10.1). The trend may be correlated with Allred's electronegativity values. For hydrolytic equilibria of Sc^{3+}, see also Brown et al. (1983).

There are other examples where scandium more closely follows the d-type transition metals (or large trivalent metals of the p-block) than the lanthanides. For instance, Silber and Mioduski (1984) found recently that in aqueous methanol this is the case with Sc^{3+} though not with Y^{3+}, which resembles La^{3+} in its coordination behavior. Furthermore, scandium strongly prefers octahedral coordination in its inorganic complexes (Valkonen, 1979); the maximum CN appears to be 9, which has been achieved only in the case of compact nitrato ligands (see section 6). This may be compared with the lighter lanthanides where 9 is the most common CN and values up to 12 are not rare (cf., section 1.4.2).

The higher degree of covalency in scandium complexes as compared with the corresponding lanthanide compounds is more obvious in the case of organic ligands where well-known examples include the stable and volatile acetylacetonates (Melson, 1975b; Thompson, 1979). The fluorocomplexes of scandium are the best-known examples of strong complexes formed by inorganic ligands (Melson and Stotz, 1971).

In the case of yttrium, the research has not been hampered by lack of pure starting materials or technical applications. Nevertheless, fundamental studies dealing with the relation of yttrium to the lanthanides are few in number. Siekierski and co-workers have looked at the position of yttrium in the lanthanide series and found evidence for the participation of 4f orbitals in bonding. Siekierski (1981a) determined the relative atomic number of yttrium (Z_Y) in 52 isostructural R_mX_n compounds where the Z_Y would be around 68 if no covalent effects were present. Z_Y was found to vary between 64.0 and 67.7 and was correlated with the R–X

electronegativity difference. The result was explained in terms of covalent shortening of the R–X bonds in lanthanide compounds. The studies were later extended to americium (Siekierski, 1981b) and, in the case of thermodynamic complex formation constants, covered both Am^{3+} and Y^{3+} (Alzahairi and Siekierski, 1984).

Studies on promethium have been few because of its radioactivity, which calls for special safety measures. All available information on oxidation states, structure of compounds, etc., is in full agreement with the expected behaviour of an element between neodymium and samarium. The chemistry of promethium has been authoritatively reviewed by Weigel (1969, 1978). Most of the some 40 compounds known today have been synthesized by Weigel and Scherer; they include a few complex inorganic compounds, e.g., carbonate and nitrate hydrates (Weigel, 1978).

1.4. *Inorganic complex compounds*

1.4.1. *Ligands and the preparation of complexes*

The rare earth ions are A-type acceptors as defined by Ahrland et al. (1958) or hard acids in the Pearson definition (1963). This behaviour distinguishes them from many d-block elements. Thus, it is not surprising that most inorganic complex compounds of rare earths, especially those isolated from aqueous solutions, are compounds with oxygen-donor ligands. Another strong donor atom is fluorine. Table 1 lists typical ligands where the donor atom is either oxygen or halogen.

Rare earth halides, especially the chlorides, have been extensively studied both in solution and in the solid state. Fluoride is an exceptional non-oxygen-donor ligand as it competes effectively with water molecules and enters the primary coordination sphere of the cation in aqueous solutions. The stoichiometry of the precipitated fluoride shows it to be nearly anhydrous, whereas the other halides prepared this way usually contain 6–9 water molecules. The removal of water from halide hydrates is difficult as oxyhalides are easily formed. Iodides are especially sensitive to decomposition.

The bond strengths in halide complexes follow the electronegativity order. The inner- vs. outer-sphere character may also be correlated with the basicity of the

TABLE 1
Typical inorganic oxygen- and halogen-donor ligands.

Ligand type	Examples
X	F^-, Cl^-, Br^-, I^-
XH	OH^-
XH_2	OH_2
XO_2	NO_2^-
XO_3	$CO_3^{2-}, NO_3^-, SO_3^{2-}, SeO_3^{2-}, ClO_3^-, BrO_3^-, IO_3^-$
XO_4	$VO_4^{3-}, NbO_4^{3-}, CrO_4^{2-}, MoO_4^{2-}, WO_4^{2-}$, $SiO_4^{4-}, GeO_4^{4-}, PO_4^{3-}, AsO_4^{3-}, SO_4^{2-}$, SeO_4^{2-}, ClO_4^-

ligands (Choppin and Bertha, 1973). Thus, fluoride forms predominantly inner-sphere complexes whereas chloride complexes are already of outer-sphere-type. The same is found in the structure of the rare earth trichloride hydrates, where part of the chloride ligands is not coordinated to the central ion.

The number of oxygen-donor ligands is large (cf., table 1) and the ligands represent a variety of molecular symmetries. The most important group is formed by the tetrahedral XO_4 oxoanions, which include the silicates, phosphates and sulfates. Among the XO_3-type ligands the carbonate and nitrate groups have a planar D_{3h} symmetry and those groups with a free electron pair have a pyramidal C_{3v} symmetry. In addition, several of the oxoanions may undergo condensation reactions in solution or in the solid-state, thereby increasing the number and variety of complexes formed. A well-known example is the R_2O_3–SiO_2 system where the condensation in the solid state may go as far as the ratio 1 : 6 (see section 4).

The polyanions and heteropolyanions, which represent extreme cases of condensed anions, are also capable of forming compounds with the rare earths; for instance $La_2V_{10}O_{28} \cdot 20H_2O$ has been structurally characterized (Safianov et al., 1978).

In solution the equilibrium between the different species may be "frozen" by precipitation and an unusual solid complex may be prepared. An example from the Pr^{3+}–SeO_3^{2-}–$HSeO_3^-$–$Se_2O_5^{2-}$–H_2O system is the $PrH_3(SeO_3)_2Se_2O_5$ complex compound where the praseodymium ion is nonacoordinated by six diselenite and three selenite oxygens (Koskenlinna and Valkonen, 1977). Possibly many solid phases of complicated composition described in the early literature in terms of empirical formulas are actually mixed ligand complexes.

The aqua ligand constitutes a special case of oxygen-donor ligands because it is a neutral ligand available for coordination in excess under preparative conditions employing aqueous solutions. It is also a strong hydrogen-bond donor contributing to the stability of the structures formed. The formation and structure of the aqua complexes will be treated in a separate section in the second part of this review.

Apart from the halogen-donor ligands, there are only a few examples of non-oxygen-donor ligands of practical importance (Moeller et al., 1973). Some complexes involving nitrogen-donor ligands have been prepared in anhydrous or nearly anhydrous conditions. These include rather unstable ammine complexes of type $RX_3 \cdot nNH_3$ and the hexacoordinated $[R(NCS)_6]^{3-}$ complexes stabilized in the solid state by large *n*-butylammonium counter ions. The N-donor complexes have been reviewed but most examples involve organic ligands (Forsberg, 1973; Gmelin, 1980, 1982).

A mixed ligand complexation with both inorganic and organic ligands is also possible and interesting combinations are often formed. The inorganic ligand may be the neutral aqua ligand or a counter ion to balance the charge. Examples of popular combinations include DMSO and crown ether complexes with the nitrato ligand; these compounds are left outside the scope of this review, however.

Basic information on the preparative conditions for the rare earth compounds, complete with phase diagrams and other relevant data, is available in a number of reference sources (Gmelin-Kraut, 1928–32; Pascal, 1959; Gmelin, 1938– ; Mellor,

1965). In addition, there are some books and series devoted to preparative chemistry covering the whole Periodic Table; the most noteworthy are Brauer (1980–1982) and *Inorganic Synthesis* (1939–).

When crystals suitable for X-ray analysis are desired, familiarity with different crystal growth techniques is required in addition to knowledge of the ligand equilibria in solution.

1.4.2. *Solid state structures: Coordination numbers and geometries*

An exceptionally wide range of coordination numbers has been found in the solid phase for rare earth complexes. The lowest coordination numbers (CN = 3–5) are exceptional and in many instances clearly caused by steric hindrance due to bulky ligands. The coordination numbers and geometries encountered in rare earth complexes have been reviewed by Moeller (1972), Moseley (1975), Sinha (1976), Porai-Koshits et al. (1976) and Thompson (1979); the reviews include many examples of both inorganic and organic complexes, dating to the late 1970s. The thesis and review on rare earth complexes by Albertsson (1972, 1978) should also be mentioned here. More recent reviews by Palenik (1983) and Niinistö (1983) discuss the organic and inorganic complexes, respectively.

The coordination number 6 was once thought to be characteristic for rare earth complexes (Moeller et al., 1965) but a recent survey of more than 500 crystal structures has revealed that this is the case only for scandium. Lanthanum has an average CN of 8.5 and the smallest lanthanide lutetium has a value of 7.1 (Leskelä and Niinistö, 1980).

TABLE 2
Coordination geometries for high (9–12) coordination numbers (Favas and Kepert, 1982; Milligan et al., 1984).

Coordination number	Geometry
9	Tricapped trigonal prism
	Monocapped square antiprism
10	Tetracapped trigonal prism
	Tetradecahedron
	Pentagonal antiprism
	Pentagonal prism
	Bicapped square prism
11	Pentacapped trigonal prism
	Monocapped pentagonal antiprism
	Interpenetrating pentagon
12	Icosahedron
	Cuboctahedron
	Truncated tetrahedron
	Hexagonal antiprism
	Bicapped pentagonal prism
	Anticuboctahedron
	Irregular icosahedron

In fact, high coordination numbers are quite common especially for the lighter lanthanides, viz., La and Ce. The recent interest in the high coordination geometries with CN = 8–12 has initiated a number of X-ray structural analyses and molecular geometry calculations on lanthanide complexes. Muetterties and Wright (1967) were the first to discuss the high coordination structures with CN = 7–12 and 10 years later Drew (1977) performed a critical analysis of structural data with CN = 8–12. Also Kepert and co-workers have in a series of articles analyzed the various coordination geometries with the results recently summarized by Kepert (1982).

The same trends are apparent in inorganic complex compounds as in organic complexes. The ionic size has a predominant effect on the coordination number but also the size, charge and bonding mode of the ligand are important. The effect of charge has been studied by Aslanov and Porai-Koshits (1975). A compact bidentate ligand with "a small bite" bonded to a large cation leads with high probability to a large CN. Such a combination is the nitrato ligand and La^{3+} or Ce^{3+} cation, and, indeed, in lanthanum nitrates the CN is 11 or 12 (see section 6).

It should be pointed out here that the concept of coordination number is not a very clear one and various approaches to determine it have recently been proposed (Batsanov, 1977; Carter, 1978; O'Keeffe, 1979). Jørgensen (1983, 1984a, b) has also discussed CN in relation to chemical bonding.

Table 2 lists the idealized coordination geometries for various high coordination ($CN \geq 9$) polyhedra. With the exception of CN = 11 the polyhedra have been analyzed and compared with actual structures (Drew, 1977; Favas and Kepert, 1981). The obvious reason of lack of sufficient data has prevented such an analysis for the undecacoordination. Since 1978, however, several examples of this coordination have been presented in the literature, in addition to the two thorium compounds known since the late 1960s, and all these compounds involve rare earths (table 3). Apparently, then, the 11 coordination is not so rare as previously thought and a first attempt to analyze the coordination polyhedra has recently been made (Milligan et al., 1984).

2. Rare earth borates

2.1. *Introduction*

Although the rare earth borates are easily prepared, for instance by hot-pressing of mixtures containing rare earth and boron oxides, their chemistry and physics have not been systematically explored. This is especially true for the ternary compounds that have an additional low valent cation in the structure and for borates of more complicated compositions. The binary $R_2O_3 \cdot B_2O_3$ compounds with R : B ratios of 3 : 1, 1 : 1 and 1 : 3, have been studied frequently, however, and most phases in this series have been structurally characterized by single crystal methods. The structures show the characteristic features of rare earth oxoanion complexes such as high coordination numbers. A summary of the structural data on rare earth borates is given in Table 4.

TABLE 3
Undecacoordinated rare earth complexes.

Formula	Complex	Chromophore	Reference
$La(NO_3)_3 \cdot 6H_2O$	$[La(NO_3)_3(H_2O)_5]$	RO_{11}	Eriksson et al., 1978, 1980b
$(NC_5H_4 \cdot C_5H_4NH)Ce(NO_3)_4(H_2O)_2(NC_5H_4 \cdot C_5H_4N)$	$[Ce(NO_3)_4(H_2O)_2(NC_5H_4 \cdot C_5H_4N)]$	$RO_{10}N$	Bukowska and Tosik, 1978
$Y(BH_4)_3(THF)_3$[a]	$[Y(BH_4)_3(THF)_3]$	RH_8O_3	Segal and Lippard, 1978
$C_{18}H_{36}O_6N_2Sm(NO_3)_6 \cdot H_2O$	$[Sm(NO_3)_5H_2O]$	RO_{11}	Burns, 1979
La(DAPBAH)$(NO_3)_3$[b]	[La(DAPBAH)$(NO_3)_3$]	RO_{11}	Thomas et al., 1979
Eu$(NO_3)_3$10C5[c]	[Eu$(NO_3)_3$10C5]	RO_{11}	Bünzli et al., 1982
La$(NO_3)_3$TEG[d]	[La$(NO_3)_3$TEG]	RO_{11}	Casellato et al., 1982
La$(NO_3)_3$1,8-naphtho-16C5	[La$(NO_3)_3$1,8-naphtho-16C5]	RO_{11}	Wang Genglin et al., 1982
Ce$(NO_3)_3$15C5	[Ce$(NO_3)_3$15C5]	RO_{11}	Lin Young-Hua and Xing Yan, 1983

[a] THF = tetrahydrofuran.
[b] DAPBAH = 2,6-diacetylpyridinebis (benzoic acid hydrazone).
[c] 10C5 = 10-crown-5 ether.
[d] TEG = tetraethyleneglycol.

TABLE 4
Summary of the structural data on rare earth borates.

Composition	R	Compound	Cell parameters				Z	Space group	Reference
			a	*b*	*c*	angle (°)			
RBO_3	La · · · Nd	La	5.10	8.25	5.38		4	Pmcn	Levin et al., 1961
	Sm · · · Lu, Y	Yb	3.73	(6.46)	8.74		2 (6)	$P6_3/mmc$	Bradley et al., 1966
	Lu, Sc	Lu	4.92		16.21		6	$R\bar{3}c$	Abrahams et al., 1971
	Sm	Sm	6.49	6.50	6.24	$\alpha = 107.8$ $\beta = 107.8$ $\gamma = 93.3$	4	P1	Palkina et al., 1976
	La, Ce	La	6.35	5.08	4.19	$\beta = 107.9$	2	$P2_1/n$	Böhlhoff et al., 1970
$R_2O_3 \cdot 3B_2O_3$	La · · · Gd	La	7.96	8.16	6.50	$\beta = 93.6$	4	I2/a	Ysker and Hoffman, 1970
$3R_2O_3 \cdot B_2O_3$	La · · · Nd	La	6.92	12.89	14.56	$\beta = 99.5$	8	$P2_1/c$	Bartram, 1964
	Sm · · · Yb, Y	Eu	18.57	3.77	14.26	$\beta = 120.0$	6	C2/m (C2 or Cm)	Bartram, 1964
	Lu	Lu	24.57	3.57	14.29	$\beta = 115.0$	8	C2/m (C2 or Cm)	Bartram, 1964
$R_3B_2O_6$	Eu	Eu	9.07		12.54		6	R3c	Hata et al., 1977
RB_2O_3	Eu	Eu	6.59	12.06	4.34		4	Pnca	Machida et al., 1979a
RB_4O_7	Eu	Eu	4.44	10.73	4.24		2	$Pnm2_1$	Machida et al., 1980a
$R_2B_5O_9X$ (X = Br, Cl)	Eu	Eu	11.50	11.38	6.48		4	Pnn2	Machida et al., 1980b, Machida et al., 1981b
$Li_3R_2(BO_3)_3$	Pr · · · Eu	Nd	8.81	14.14	5.78	$\beta = 103.8$	4	$P2_1/n$	Abdullaev and Mamedov, 1977a
$Li_6R(BO_3)_3$	Ho · · · Yb	Yb	7.12	6.58	16.32	$\beta = 105.1$	4	$P2_1/b$	Abdullaev and Mamedov, 1977b
$Na_3R_2(BO_3)_3$	La · · · Nd	Nd	5.12	11.23	7.11		4	Amm2	Mascetti et al., 1983
$Na_3R(BO_3)_2$	La · · · Nd	Nd	6.62	8.81	12.11	$\beta = 122.3$	4	$P2_1/c$	Mascetti et al., 1981
$MRBO_4$ (M = Ca, Sr)	La	La	5.20		8.72				Van der Spijker and Konijnendijk, 1978
(M = Ca)	Dy · · · Lu, Y, Sc	Y	3.58	9.59	10.42		4	Pmcn	Blasse, 1969
$Sr_3R_2(BO_3)_4$	La · · · Er	Pr	8.80	16.45	7.37		4	$Pc2_1n$	Palkina et al., 1973
$RCoB_5O_{10}$	La · · · Ho, Y	Sm	8.61	7.58	9.45	$\beta = 92.0$	4	$P2_1/n$	Abdullaev et al., 1974
$RMgB_5O_{10}$	La · · · Er, Y	Sm	8.72	7.51	12.49	$\beta = 131.3$	4	$P2_1/c$	Saubat et al., 1980
$RM_3(BO_3)_4$ (M = Al, Ga, Cr, Fe)	Nd, Gd, Y	Nd	9.34		7.31		3	R32	Hong and Dwight, 1974
	Nd	Nd	7.25	9.34	11.10	$\beta = 103.4$	4	C2/c	Jarcow et al., 1979
	Gd	Gd	7.23	9.32	16.18	$\beta = 90.6$	6	C2	Belokoneva et al., 1980
$RAl_{2.07}(B_4O_{10})O_{0.6}$	Nd	Nd	4.59		9.30		1	$P\bar{6}2m$	Pushcharovskii et al., 1978
$R_2O_3 \cdot B_2O_3 \cdot 2XO_3$ (X = Mo, W)	La	La	5.69	4.15	9.37	$\beta = 99.3$	1	$P2_1$	Palkina et al., 1979
$RCr(BO_3)_2$	Dy · · · Lu, Y	Y	4.76		15.52		3	$R\bar{3}$	Vicat and Alconard, 1968
$Ca_3R_3Ge_2BO_{13}$	Er	Er	10.45				4	F43m	Chenavas et al., 1981

The interesting properties of the rare earth borates, including their high thermal stability, glass formation and luminescence have encouraged a number of studies aimed at their practical use in refractories, optical glass and phosphors.

There appear to be neither short nor comprehensive Gmelin-type reviews devoted entirely to rare earth borates. Metal borates have been treated in some recent reviews emphasizing d-block elements, however (Farmers, 1982). The nomenclature of borates, as well as that of many other oxoanion compounds capable of different stoichiometries, is confusing and partially contradictory. For instance, $R_2O_3 \cdot 3B_2O_3$ is called metaborate because the formula can be written $R(BO_2)_3$, yet the structural data available indicate it to be hexaborate. In the present review, in order to facilitate comparisons between different compounds, empirical formulae based on stoichiometry are preferred to names; the generally accepted name orthoborate, which is not contradictory to the structural formula, is used, however.

2.2. *Binary rare earth borates*

2.2.1. *1 : 1 compounds*

The rare earth borate $R_2O_3 \cdot B_2O_3$, frequently called orthoborate and formulated as RBO_3, can be prepared from a stoichiometric mixture of the oxides. The powder is usually pressed into a pellet and heated twice to 1000–1400°C (Felten, 1961). The use of boric acid instead of boron oxide allows the use of lower temperatures in the firing (Levin et al., 1961). Since the rare earth borates have a tendency to decompose with volatilization of B_2O_3, crucibles should be sealed (Roth et al., 1964). RBO_3 is also formed in the fusion reaction between R_2O_3 and borax with suitable R : B ratio (Canneri, 1926). Tananaev et al. (1966) have prepared orthoborates for all rare earths except cerium by dissolving R_2O_3 in sodium borate melt (900°C). In boron oxide melt at temperatures above 850°C, R_2O_3 reacts to RBO_3 (Khodakov et al., 1980). In the system Na_2O–R_2O_3–B_2O_3 (R = Dy ··· Lu) with higher sodium concentration the solid obtained is orthoborate, whereas with lower sodium concentration the product is $R_2O_3 \cdot 3B_2O_3$ (Tananaev et al., 1965, 1966; Dzhurinskii et al., 1967). Single crystals of rare earth orthoborates have been grown in $PbO + PbO_2$, $PbO + PbO_2 + MoO_3$ and $PbO + PbO_2 + PbF_2$ fluxes (Wanklyn, 1973b, 1981). The formation of different rare earth orthoborates has been investigated by the differential thermal analysis method (Stransky, 1970). The kinetics of the preparation of $DyBO_3$ by sintering various mixtures of Dy_2O_3 and B_2O_3 have been determined by X-ray diffraction studies (Sheikh et al., 1970). The phase diagrams for the systems La_2O_3–B_2O_3 and Sc_2O_3–B_2O_3 have been presented in figs. 1 and 2.

Goldschmidt and Hauptman noticed as early as 1932 that $LaBO_3$ has an aragonite-like structure. A phase transformation of $LaBO_3$ from aragonite structure to calcite structure at higher temperatures was later detected by Keith and Roy (1954). Finally Weir and Lippincott (1961) and Levin et al. (1961) investigated the IR spectra and X-ray diffraction patterns of RBO_3 and $CaCO_3$ and showed that rare earth orthoborates display all three structure types of calcium carbonate, viz. aragonite, calcite and vaterite.

$LaBO_3$ and $NdBO_3$, and possibly $CeBO_3$ and $PrBO_3$, have aragonite structure at low temperatures (Levin et al., 1961). The structure is orthorhombic (Pmcn) contain-

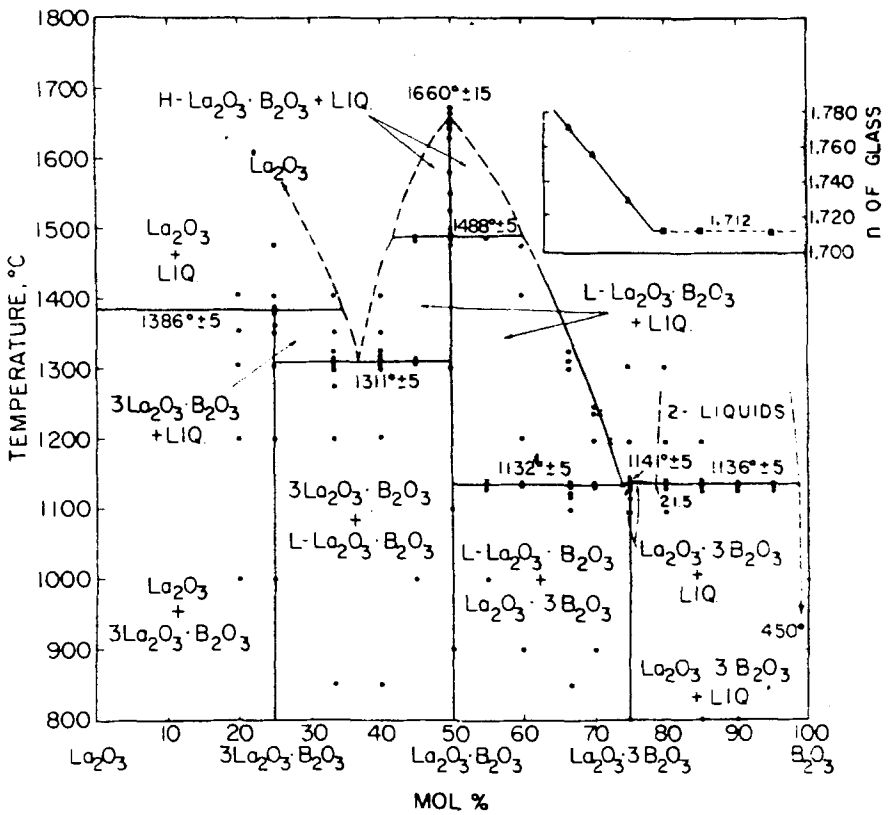

Fig. 1. Phase diagram for the system La_2O_3–B_2O_3. The refraction index for quenched glass vs. composition is presented at upper right corner (Levin et al., 1961). L = low-temperature polymorph; H = high-temperature polymorph.

ing isolated BO_3 triangles, joined by RO_9 polyhedra that share edges and corners forming columns (fig. 3) (Adbullaev et al., 1976).

The rare earths from Eu to Yb have stable vaterite structure, unlike the vaterite structure of $CaCO_3$ that is only metastable. $SmBO_3$ has the vaterite structure only between 1065 and 1285°C. Above this temperature range its structure is similar to $NdBO_3$ at high temperatures (Levin et al., 1961) and below 1065°C it is triclinic containing the 8-coordinated rare earth ions and planar BO_3 triangles (Palkina et al., 1976). The structure of the vaterite-type is hexagonal ($Z = 6$) but it can be described using rhombohedral setting ($Z = 2$). The structure contains 8-coordinated rare earth ions and three-membered rings of borate tetrahedra (fig. 3). The coordination of boron differs from that in vaterite $CaCO_3$, which is planar (Newhamn et al., 1963; Bradley et al., 1966). The tetrahedral coordination of boron in vaterite structure can be seen in the IR spectrum (Laperches and Tarte, 1966).

There is also a high temperature form of the vaterite structure where BO_3^{3-} assumes a planar structure (Bradley et al., 1966) and which is thus more similar to $CaCO_3$ vaterite than is the low-temperature form. In $YbBO_3$ the transition from the

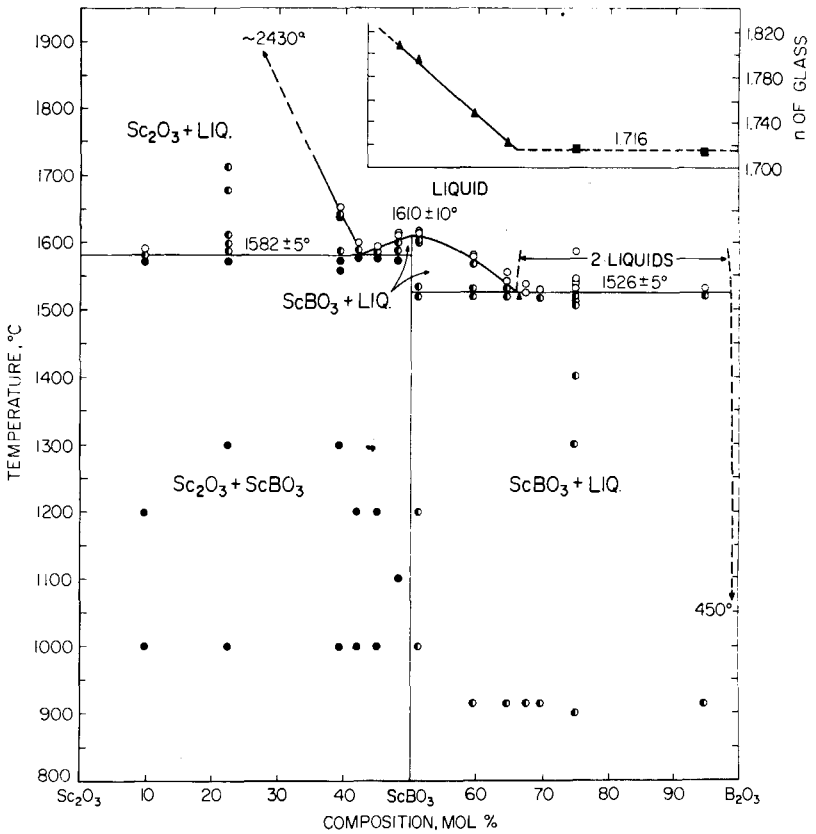

Fig. 2. Phase diagram for the system Sc_2O_3–B_2O_3. The refraction indices are presented as in Fig. 1 (Bowden and Thompson, 1980).

low-temperature to the high-temperature phase occurs below 1100°C: the *a* axis expands from 6.46 to 6.99 Å and the *c* axis shortens from 8.74 to 8.34 Å ($Z = 6$). The probable space group of the high-temperature form is $P6_322$.

$LuBO_3$ and $ScBO_3$ both have calcite structure at low temperatures (Levin et al., 1961; Biedl, 1966). The rare earth has sixfold coordination and the arrangement of the borate ions is triangular (Abrahams et al., 1971).

The orthoborates of lighter lanthanides (La · · · Eu) and $LuBO_3$ all have high-temperature modifications (fig. 4). Above 1310°C $LuBO_3$ transforms to vaterite structure. The aragonite-types of $LaBO_3$ and $NdBO_3$ have reversible transformations at 1488 and 1090°C, respectively. According to Roth et al. (1964) the high-temperature forms are isostructural and both have lower symmetry than the aragonite structure. In later studies Böhlhoff et al. (1970, 1971) reported the structure to be closely related to that of aragonite but with monoclinic lattice. The high-temperature forms of $LaBO_3$ and $NdBO_3$ were not found to be isostructural and $CeBO_3$ was found to have two high-temperature forms, one like $LaBO_3$ and one like $NdBO_3$.

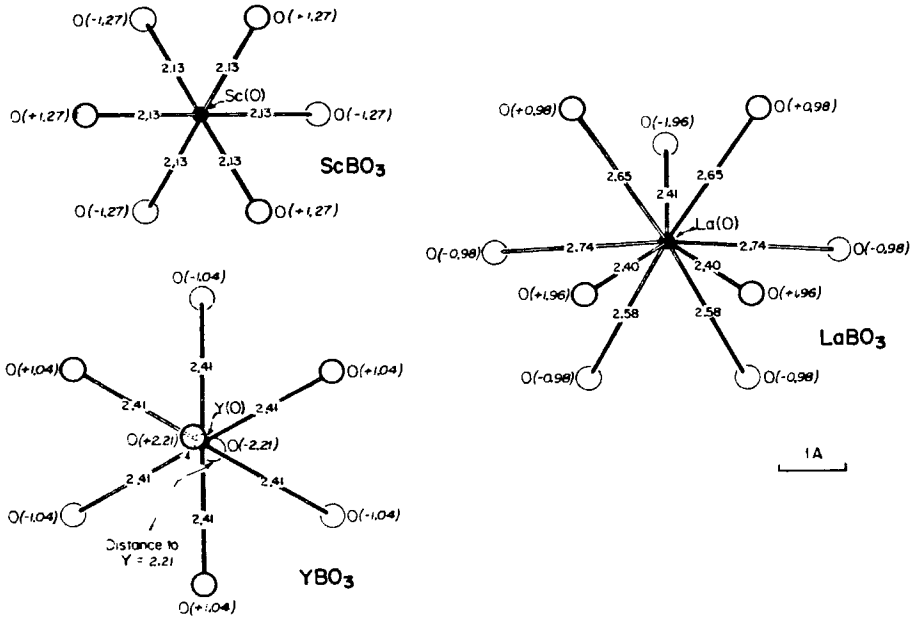

Fig. 3. Comparison of the cation environment in $LaBO_3$, YBO_3 and $ScBO_3$ showing the 9, 8 and 6 coordination, respectively. The bond distances and relative heights of the atomic sites are given in Å (Newnham et al., 1963).

The formation of solid solutions between different rare earth orthoborates changes the dominance of the different structure types (Roth et al., 1963, 1964). The mixing of La and Sm cations causes the high-temperature form of $LaBO_3$ and the low-temperature form of $SmBO_3$ to dominate instead of aragonite and vaterite. In the case of La and Lu a new hexagonal compound $LaLu(BO_3)_2$, which may have the dolomite structure, is formed.

Scandium has attracted comparatively little attention and there seems to be evidence only for the formation of $ScBO_3$ (Levin, 1967). The orthoborates of promethium have been prepared and their chemistry has been discussed by Weigel and Scherer (1967).

2.2.2. *1 : 3 compounds*

Rare earth borates with $R_2O_3 : B_2O_3$ ratio 1 : 3 can be synthesized in a similar way to the 1 : 1 compounds but with the concentration of boron increased to correspond to the ratio 1 : 3. The boron starting material may be boron oxide, boric acid or borax (Canneri, 1926; Weidelt, 1970). The reactions of R_2O_3 with molten B_2O_3 at 750°C and with $Na_2O \cdot 19B_2O_3$ at 600–700°C give $R_2O_3 \cdot 3B_2O_3$ (Tananaev et al., 1975; Khodakov et al., 1980). The 1 : 3 compounds are formed as well in the ternary systems R_2O_3–SrO–B_2O_3 at 1100°C and R_2O_3–Na_2O–B_2O_3 at 900°C with suitable concentration of the components. Orthoborate and strontium double borate are

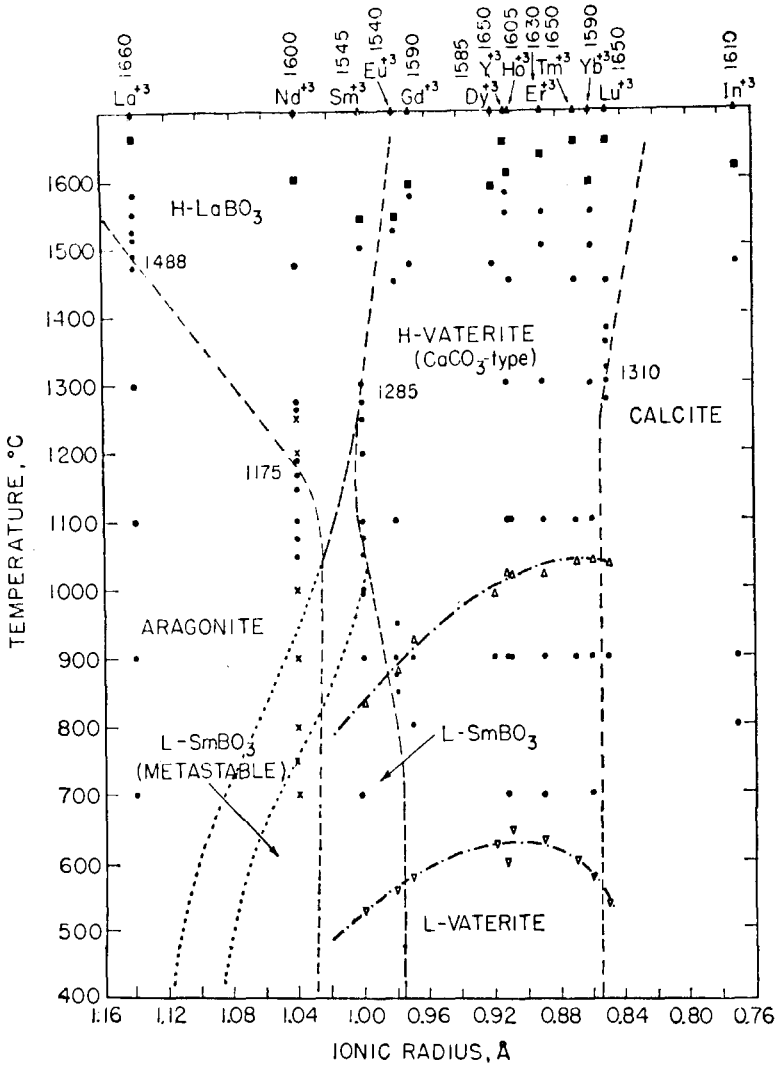

Fig. 4. Stability relationships of the RBO_3 borates as a function of temperature and ionic radius (Roth et al., 1964). ● subsolidus experiments; ■ liquidus values; × X-ray diffraction results; △ ▽ DTA results (heating, cooling).

obtained by changing the concentration (Dzhurinskii et al., 1967, 1968a, b, 1969a). Single crystals of $R_2O_3 \cdot 3B_2O_3$ have been grown in Na_2O–B_2O_3, SrO–B_2O_3 and B_2O_3 fluxes by slow cooling (Pakhomov et al., 1969).

RCl_3 solution reacts with borax solution at pH 6.5–6.9 to form a borate hydrate precipitate. Analysis of the dried powder indicated the composition $R(BO_2)_3 \cdot nH_2O$ ($n = 4$ or 6) (Vasilev and Serebrennikov, 1964; Pajakoff, 1969).

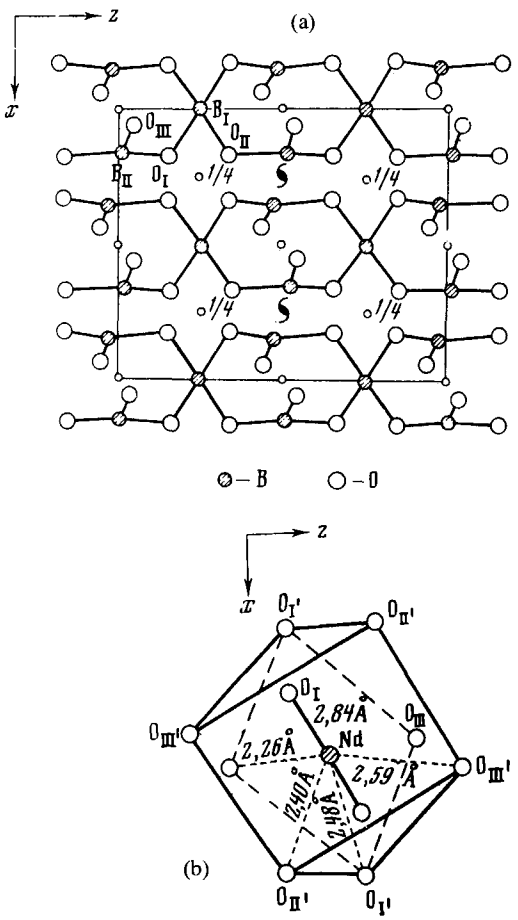

Fig. 5. A projection of the structure of $Nd(BO_2)_3$ on the (010) plane. Nd atoms at (0, 0.049, 1/4) are omitted for clarity but the coordination round them is shown in (b) (Pakhomov et al., 1972).

$R_2O_3 \cdot 3B_2O_3$ (R = La $\cdots$ Tb) compounds have been reported to be isostructural and to have monoclinic structure (I2/a) (Bambauer et al., 1968, 1969). According to Ysker and Hoffman (1970) LaB_3O_6 contains infinite $[B_3O_6]_\infty$ chains of BO_4 tetrahedra that are linked by two planar BO_3 groups. Pakhomov et al. (1972) report that $Nd(BO_2)_3$ contains chains of BO_4 tetrahedra and BO_3 triangles. The most recent determination of $R_2O_3 \cdot 3B_2O_3$ structure has been made by Abdullaev et al. (1975a), who reported the structure of the La compound to consist of chains of $[B_6O_{12}]_\infty$ radicals composed of two BO_4 tetrahedra and four BO_3 triangles. The chains are bonded to rare earth ions having tenfold coordination (fig. 5).

According to Tananaev et al. (1975), $R_2O_3 \cdot 3B_2O_3$ displays three structure types: the first, monoclinic-type, for La $\cdots$ Tb; the second for Dy $\cdots$ Tm, Y; and the third for Yb, Lu. The structure determinations of the two last forms have not been carried out. Pakhomov et al. (1971) propose that $Tb(BO_2)_3$ is not isomorphic with $R_2O_3 \cdot 3B_2O_3$ compounds of the lighter rare earths but is orthorhombic, with possible space

groups Pbnm and $Pbn2_1$. The difference in the structures of the monoclinic $R_2O_3 \cdot 3B_2O_3$ and $Tb_2O_3 \cdot 3B_2O_3$ was confirmed by luminescence spectra (Pakhomov et al., 1971).

2.2.3. *Other binary borates*

A third binary rare earth borate, $3R_2O_3 \cdot B_2O_3$, is formed from the oxides by heating the oxide mixture at 1350°C for 16 hr. $3R_2O_3 \cdot B_2O_3$ compounds have three different monoclinic structure types along the lanthanide series (Bartram, 1962). La $\cdots$ Nd borates have the space group $P2_1/c$ and the borates of Sm $\cdots$ Yb, Y have

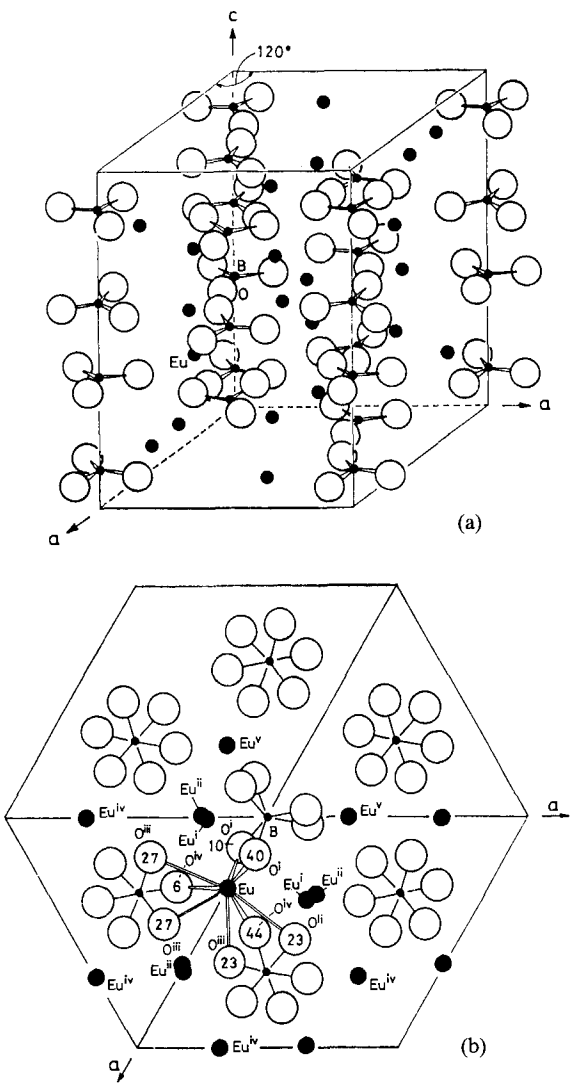

Fig. 6. The crystal structure of $Eu_3(BO_3)_2$. (a) Unit cell contents and (b) a projection of the structure ($0 \leq z \leq 0.5$) along the c axis (Machida et al., 1981a).

C2/m, C2 or Cm. One of the two space groups of $3Lu_2O_3 \cdot B_2O_3$ is of the second type and the other is unknown. Structurally these compounds may be orthoborates and the formula could be written as $(RO)_3BO_3$ (Bartram, 1964).

A series of europium(II) borates, viz. $Eu_3B_2O_6$, $Eu_2B_2O_5$, EuB_2O_5 and EuB_4O_7, have been prepared by solid state reaction of appropriate amounts of Eu_2O_3, B and H_3BO_3 (Hata et al., 1977; Machida et al., 1979b, c). Other preparation methods are the heating of EuO and B_2O_3 in air at 900–1000°C or the heating of Eu_2O_3 and B_2O_3 in H_2 atmosphere at 1000–1100°C (Churilova and Serebrennikov, 1971, 1973). The structure of $Eu_3B_2O_6$ ($Eu_3(BO_3)_2$) is hexagonal containing isolated planar BO_3^{3-} anions and 8-coordinated europium cations (fig. 6). EuB_2O_4 is orthorhombic and isostructural with $Ca_2B_4O_8$ (Hata et al., 1977). EuB_2O_4 contains $[BO_2]_\infty$ chains

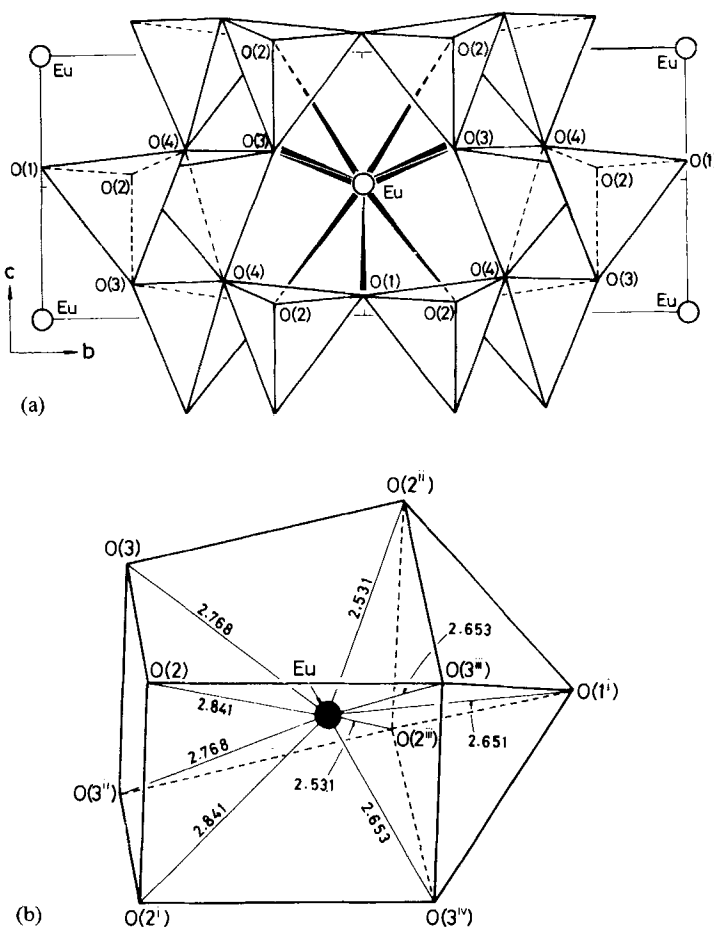

Fig. 7. Crystal structure of EuB_4O_7: (a) projection along the *a* axis and (b) the EuO_9 polyhedron with bond distances in Å (Machida et al., 1980a).

formed by corner-sharing BO_3 triangles along the c axis. Europium has eightfold coordination (Machida et al., 1979a). The structural framework of EuB_4O_7 consists of a three-dimensional $[B_4O_7]_\infty$ network of BO_4 tetrahedra. Each europium is surrounded by nine oxygen atoms (fig. 7) (Machida et al., 1980a).

A number of different haloborates are formed in the ternary system $MO-MX_2-B_2O_3$ (M = Ca, Sr, Ba, Eu, Pb; X = Cl, Br). For europium, for example,

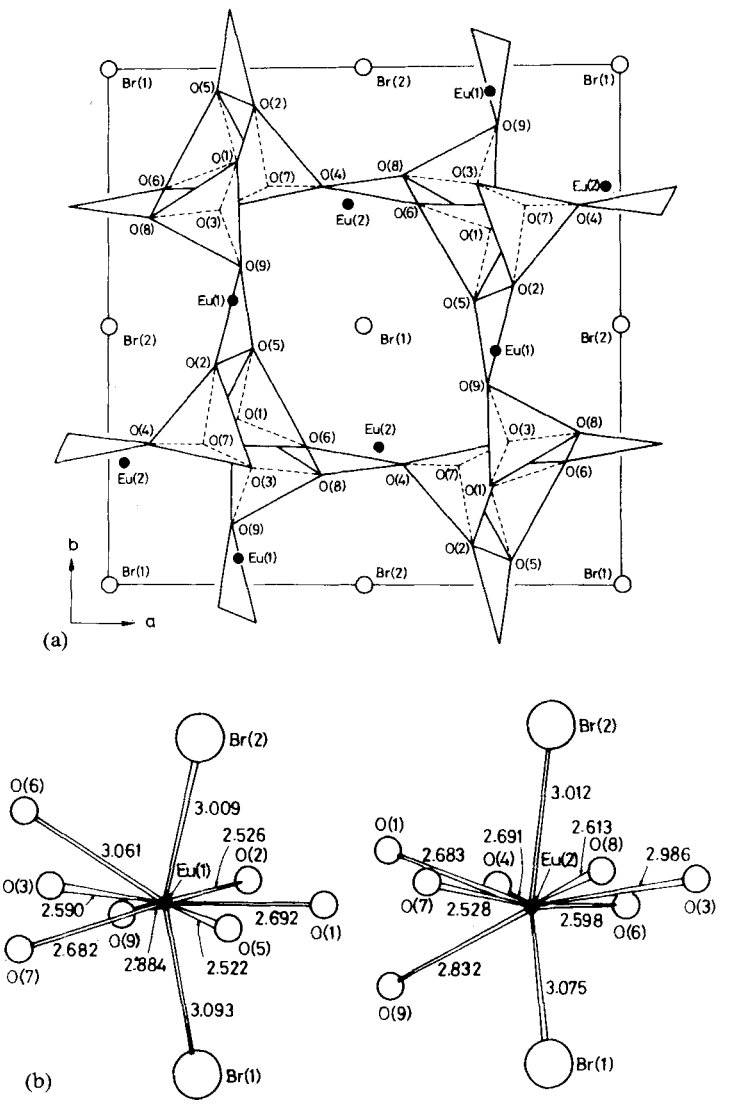

Fig. 8. Projection of the $Eu_2B_5O_9Br$ structure along the c axis (a) and environments of the Eu atoms with distances in Å (b) (Machida et al., 1980b).

the chloroborates $Eu_3B_7O_{13}Cl$ and $Eu_2B_5O_9Cl$ and bromoborate $Eu_2B_5O_9Br$ are known (Machida et al., 1979d). The structure of $Eu_2B_5O_9Cl$ is tetragonal, while $Eu_2B_5O_9Br$ is orthorhombic. Later on the chloroborate was shown to be also orthorhombic and isomorphic with bromoborate (Machida et al., 1981b). The structure of $Eu_2B_5O_9X$ consists of a three-dimensional $[B_5O_9]_\infty$ network in which B_5O_{12} groups of three BO_4 tetrahedra and two BO_3 triangles are linked together through shared corner oxygens. Eu and Br atoms are located in the tunnels of the $[B_5O_9]_\infty$ network (fig. 8). Each europium is surrounded by two bromine and seven oxygen atoms (Machida et al., 1980b).

2.3. *Ternary rare earth borates*

The only alkali rare earth double borates known are Li and Na borates. The larger ionic radii of the subsequent alkali ions obviously prevent them from forming stable double borates with the rare earths. The lithium borates $Li_6R(BO_3)_3$ and $Li_3R_2(BO_3)_3$ can be synthesized from the mixture Li_2O–R_2O_3–B_2O_3. The structure of $Li_6R(BO_3)_3$ contains discrete BO_3 triangles that are linked together by LiO_4, LiO_5 and RO_8 polyhedra (Abdullaev and Mamedov, 1977b; Abdullaev et al., 1978a). The structure of $Li_3R_2(BO_3)_3$ is monoclinic and the crystal structure has been determined for isomorphic Pr, Nd and Eu compounds (Abdullaev et al., 1977a, b; Adbullaev and Mamedov, 1977a). Isolated BO_3 triangles are joined to each other by LiO_4 and RO_9 polyhedra to form a three-dimensional network (fig. 9).

Mascetti et al. (1983) have found three new compounds with compositions $Na_3Nd_2(BO_3)_3$, $Na_3Nd(BO_3)_2$ and $Na_{18}Nd(BO_3)_7$ in the system M_2O–Nd_2O_3–B_2O_3. According to powder diffraction patterns the first compound forms orthorhombic crystals. The structure of $Na_3Nd(BO_3)_2$ is monoclinic and

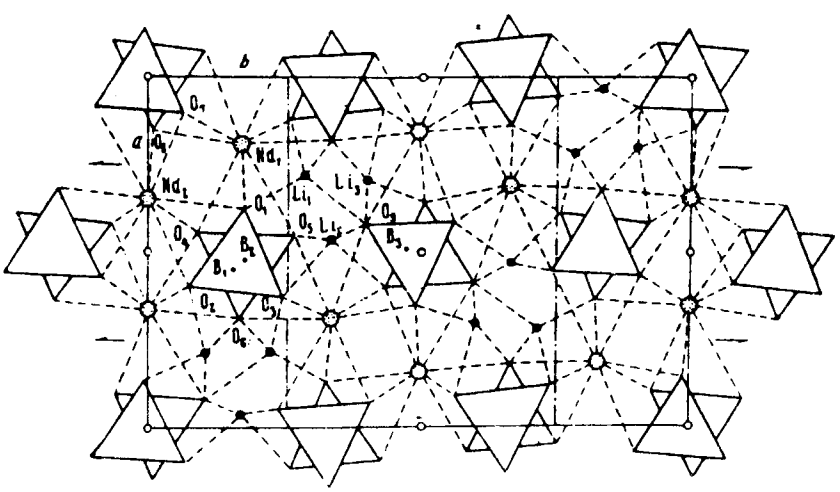

Fig. 9. Crystal structure of $Li_3Pr_2(BO_3)_3$ projected along the c axis (Abdullaev et al., 1977).

contains isolated BO_3 triangles linked by 8-coordinated Nd and Na atoms which have 7, 6 and unusual 3 + 1 coordinations (Mascetti et al., 1981). The structure of the third compound, $Na_{18}Nd(BO_3)_7$, is unknown.

When the additional cation is divalent, small size is no longer a prerequisite for stable structures. Thus, three types of ternary compounds have been reported in the system $MO-R_2O_3-B_2O_3$ (M = Ca, Sr, Ba). Blasse (1969) gives the crystallographic and luminescence data for $CaRBO_4$ (R = Dy $\cdots$ Lu, Y, Sc). The structure is orthorhombic and isomorphic with Y_2BeO_4. The compound $CaLaBO_4$ is isomorphic with $SrLaBO_4$ and the structure is hexagonal (van de Spijker and Konijnendijk, 1978). With strontium and barium, compounds of formula $M_3R_2(BO_3)_4$ are formed too, and isomorphism has been observed in $Sr_3R_2(BO_3)_4$ (R = La $\cdots$ Gd) and $Ba_3R_2(BO_3)_4$ (Dzhurinskii et al., 1969b; Palkina et al., 1972). The structure is orthorhombic containing isolated BO_3 triangles that are bonded by Sr^{2+} and R^{3+} ions into a three-dimensional network. The coordination number of R is 8 and that of Sr is 9 or 10 (Palkina et al., 1973; Abdullaev et al., 1973; Abdullaev and Mamedov, 1974, 1976, 1982).

Single crystals of $RCoB_5O_{10}$ and $RMgB_5O_{10}$ have been obtained by melting mixtures of the corresponding oxides at 1200°C and cooling. An excess of B_2O_3, MgO and CoO is useful to compensate for the volatilization losses (Abdullaev et al., 1974; Saubat et al., 1980). The compounds are isomorphic from lanthanum to holmium and erbium including yttrium (Abdullaev et al., 1975b, 1978b; Saubat et al., 1980). The structure is monoclinic ($P2_1/c$ or $P2_1/n$) with layers of $[B_5O_{10}^{5-}]_\infty$ ions containing three tetrahedrally and two triangularly coordinated boron atoms (fig. 10). The layers are joined by CoO_6 or MgO_6 and RO_{10} polyhedra (fig. 11). An interesting feature of the structure is that the R atom centered polyhedra form isolated chains (Abdullaev, 1976; Saubat et al., 1980). The R–R distance within the chain is around 4 Å but is between adjacent chains over 6.4 Å.

With the trivalent cations aluminium, gallium, chromium and iron, the rare earths form rhombohedral $RM_3(BO_3)_4$ crystals (Ballman, 1962). The compounds are formed by the reaction of the excess amounts of appropriate oxides in MoO_3 and

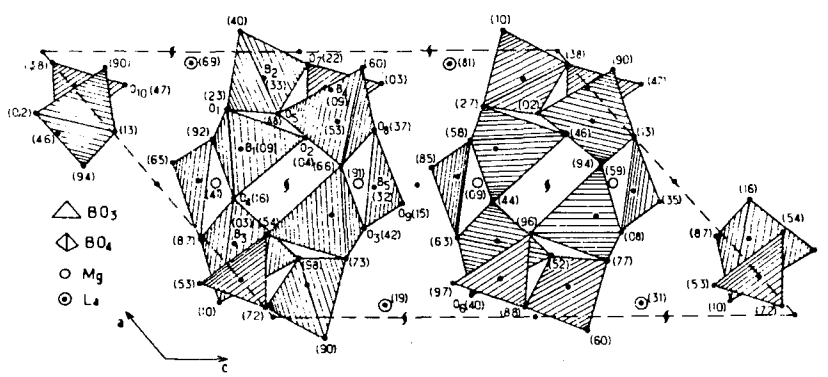

Fig. 10. Projection of the structure of $LaMgB_5O_{10}$ on the (010) plane (Saubat et al., 1980).

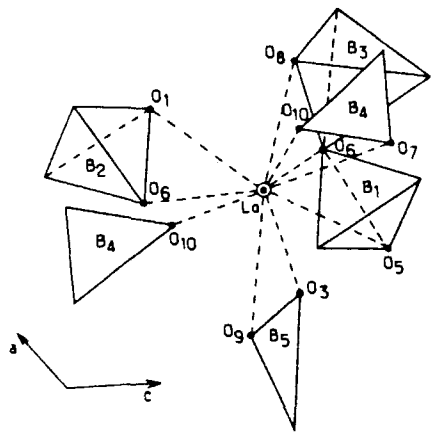

Fig. 11. A perspective view showing coordination of different borate groups to La atoms in $LaMgB_5O_{10}$ leading to an unsymmetric LaO_{10} polyhedron (Saubat et al., 1980).

K_2SO_4 fluxes (Tate and Oishi, 1981). The Al and Cr compounds can be crystallized more easily from a $Pb_3(BO_3)_2$ melt (Mills, 1962). The structure of $RM_3(BO_3)_4$ is similar to that of mineral huntite, $CaMg_3(CO_3)_4$ (fig. 12) (Hong and Dwight, 1974b; Belokoneva et al., 1978; Kuroda et al., 1981). Respectively, the R, M and B atoms occupy central positions in trigonal prisms, octahedra and triangles formed with oxygen atoms. Edge-sharing MO_6 octahedra form helices along the *c* axis, with the helices connected by isolated BO_3 triangles and RO_6 trigonal prisms. The R atoms can partly be replaced by Bi atoms (Belokoneva et al., 1979). At high temperatures the huntite structure is distorted and the lattice symmetry, for example in $NdAl_3(BO_3)_4$, is monoclinic C2/c (Jarchow et al., 1979; Belokoneva et al., 1980). The high-temperature form of $GdAl_3(BO_3)_4$, crystallized from $K_2Mo_2O_{10}$ flux, is

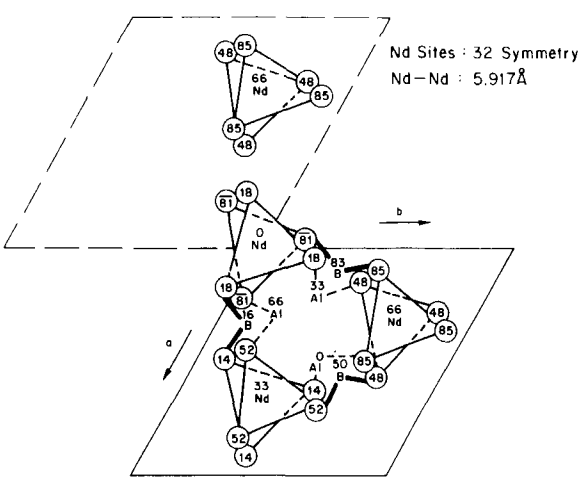

Fig. 12. A projection of the structure of $NdAl_3(BO_3)_4$ on the *ab* plane showing the Nd–Nd separation (Hong and Dwight, 1974).

not isomorphic with the corresponding neodymium compound, but has a monoclinic C2 structure (Belokoneva et al., 1981b; Timchenko et al., 1981).

In addition, aluminum forms with rare earth borates nonstoichiometric compounds with formula $RAl_{1.67+x0.67}(B_4O_{10})O_x$ where $x = 0 \cdots 1$. The crystals have been grown from potassium molybdate melt (Pashkova et al., 1981). Structure determination of the Nd compound with $x = 0.6$ has shown it to be hexagonal ($P\bar{6}2m$) with $[B_2O_5]_\infty$ chains. The arrangement of the cations is closely similar to that described for $RAl_3(BO_3)_4$ (Pushcharovskii et al., 1978b). This compound is formed for the lanthanides from lanthanum to neodymium (Bartsch and Jarchow, 1983).

The heavier lanthanides and yttrium form a double borate $RCr(BO_3)_2$ with trivalent chromium at 950–100°C. The structure of this compound is similar to dolomite (Vicat and Aleonard, 1968). At 1100–1150°C the compounds decompose to RBO_3, Cr_2O_3 and B_2O_3.

Complex structures containing additional anions are also possible. Rare earth borates with a second anion are known in the case of molybdate, wolframate and silicate. $La_2O_3 \cdot B_2O_3 \cdot 2MoO_3$ and $La_2O_3 \cdot B_2O_3 \cdot 2WO_3$ crystals are monoclinic ($P2_1$) and isomorphic (Palkina et al., 1979a). Other borate wolframates reported are $R(BO_2)WO_4$ and $R_2B_2WO_9$ (Dzhurinskii et al., 1980). The mineral stillwellite, whose idealized formula is $Ce_2O_3 \cdot B_2O_3 \cdot 2SiO_2$, is an example of borate silicates (Voronkov and Pyatenko, 1967).

2.4. *Properties and applications*

The rare earth orthoborates are extremely resistant to water and sodium hydroxide even at elevated temperature, but they are attacked by dilute hydrochloric acid (Isupova and Lileev, 1965). The 1 : 3 borates are attacked by both alkali and acids.

Thermoanalytical studies on rare earth orthoborates show that they do not decompose below 1400°C; only phase transitions can be observed (Sweeney, 1975). Orthoborates melt congruently at 1540°C (Eu)–1660°C (La) (Levin et al., 1961). In studies on glass formation in R_2O_3–B_2O_3 systems an area of liquid immiscibility has been observed. The extent of the immiscibility increases with decreasing ionic radius, from 21.5 mol% for the La_2O_3 system to 34.0 mol% for the Sc_2O_3 system. With the exception of La and Nd the temperature of the monotectics increases monotonically from 1136°C for Sm_2O_3 to 1526°C for Sc_2O_3 (Levin, 1966).

The thermal decomposition of $R_2O_3 \cdot 3B_2O_3$ (R = Dy $\cdots$ Lu) occurs at 850–950°C depending on the cation. The decomposition products are RBO_3 and B_2O_3 (Tananaev et al., 1975). The compounds of the lighter lanthanides melt congruently at about 1100°C (Levin et al., 1961). $3R_2O_3 \cdot B_2O_3$ compounds melt incongruently at about 1380°C.

Infrared spectra have been recorded for a number of borates. The different structure types of orthoborates can be identified from the spectra (Laperches and Tarte, 1966). Table 5 presents important IR frequencies recorded for selected orthoborates.

The luminescence properties have been investigated for binary 1 : 1 and 1 : 3 borates doped with Eu^{3+}. The phosphors show emission spectra characteristic of

TABLE 5
Infrared absorption frequencies (cm^{-1}) of selected rare earth orthoborates (Laperches and Tarte, 1966).

$ScBO_3$	$PrBO_3$	$ErBO_3$
1260		1066
1240	1285	1031
1220	1250	980
1200		927
	944	871
764	788	835
740	713	711
	610	565
637	590	401
422		365
285	300	267
262		

Eu^{3+}. In the gadolinium compound, energy transfer occurs between Gd^{3+} and Eu^{3+} ions (Bril and Wanmaker, 1964). The dependence of the emission intensity on temperature in rare earth borates has been studied by Blasse and de Vries (1967b). Besides europium, the luminescence spectra of Ce^{3+}- and Tb^{3+}-activated compounds have been determined – even for $ScBO_3$ (fig. 13) (Blasse and Bril, 1967c; Denisov et al., 1969; Hoshina and Kuboniwa, 1972). The binary 1 : 3 borates are possible phosphors for fluorescent lamps, particularly the Ce^{3+}- and Tb^{3+}-activated ones as green phosphors (Philips, 1976; Hitachi, 1981, 1982; Konijnendijk et al., 1981).

For gas-discharge display panels, phosphors having high efficiency under irradiation below 200 nm are required. It has been shown recently that europium and terbium in YBO_3 and $GdBO_3$ hosts can be excited by xenon discharge, which causes absorption in the BO_3 groups in the region 150–170 nm followed by an energy transfer to the rare earth ions (Veenis and Bril, 1978; Koike et al., 1979). The activated orthoborates may have applications in gas-discharge devices.

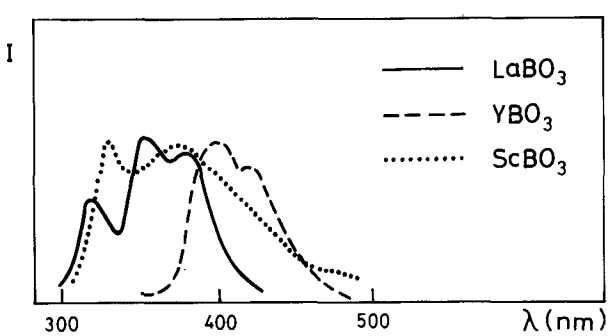

Fig. 13. The emission spectra of Ce^{3+} in $LaBO_3$, YBO_3 and $ScBO_3$. The emission of Ce^{3+} is due to the allowed electric dipole $5d \rightarrow 4f$ transition, which is dependent on the crystallographic environment of Ce^{3+} (Blasse and Bril, 1967c).

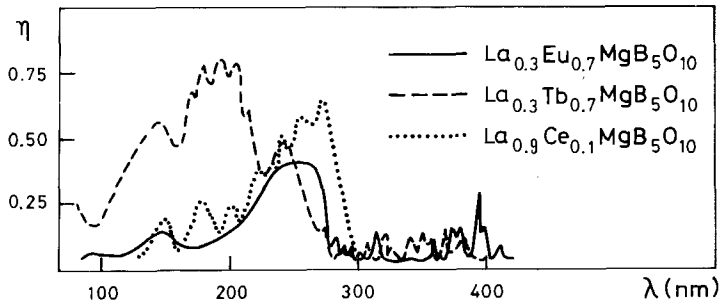

Fig. 14. The excitation spectra of Ce^{3+}, Eu^{3+} and Tb^{3+} in $LaMgB_5O_{10}$. The strong band in the cases of Eu^{3+} and Tb^{3+} are charge-transfer and 4f → 5d bands, respectively (Saubat et al., 1981).

The ternary borates can act as phosphor matrices too. In $LaMgB_5O_{10}:Eu^{3+}$ and $LaMgB_5O_{10}:Tb^{3+}$, saturation of the absorption in both the Eu^{3+} charge-transfer state and the Tb^{3+} f → d bands is almost reached for an activator concentration of close to 30%. The maximum of the charge-transfer state (CTS) band of Eu^{3+} lies at 255 nm (Saubat et al., 1981). As in the case of orthoborates, the fluorescence can be excited by short wavelength radiation in the vicinity of 150 nm, but the efficiency is low. The Tb^{3+}-activated borate shows an external quantum efficiency exceeding 75% when excited in 5d levels between 180 and 205 nm (fig. 14). The excitation range of high efficiency is extended to 290 nm when Ce^{3+} sensitization is used, which makes the material a good candidate for use as green component in low-pressure fluorescent lamps (Saubat et al., 1981; Looye et al., 1981).

The rare earth coordination polyhedra form isolated chains in $RMgB_5O_{10}$, so that interactions between R^{3+} ions are predominantly one-dimensional. Concentration quenching of the Eu^{3+} and Tb^{3+} emissions occurs only at high concentrations. The nonradiative losses result from energy migration within the chains, followed by energy transfer to energy sinks, viz. lattice defects and impurities (Fouassier et al., 1981). The emission spectra of Eu^{3+} and Tb^{3+} in $LaMgB_5O_{10}$ have been presented in fig. 15.

Energy transfer studies in $RMgB_5O_{10}$ have recently been carried out by de Hair and Kemenade (1983) and Saakes et al. (1984). $RMgB_5O_{10}$ (R = La, Gd) with Mn^{2+} at Mg^{2+} octahedral sites and sensitized with Bi^{3+} is an efficient red phosphor. Energy transfer from Ce^{3+} remains in the R^{3+} chains and cerium sensitizes Tb^{3+} (critical distance 5.5 Å) but not manganese. In the $GdMgB_5O_{10}$ matrix the excitation energy is able to migrate within the Gd^{3+} sublattice. Ce^{3+} is a good sensitizer for this host. If the Gd^{3+} sublattice is diluted with La^{3+} ions, the energy migration in Gd^{3+} chains is blocked and interchain energy transfer occurs. A very efficient phosphor is obtained by Ce^{3+} sensitization, Gd^{3+} intermediation and Tb^{3+} activation (Leskelä et al., 1984).

Yttrium aluminium borate, $YAl_3(BO_3)_4$, can be used as host lattice for several trivalent luminescent ions: Eu^{3+}, Tb^{3+}, Dy^{3+}, Gd^{3+} and Sm^{3+} (Kellendonk and Blasse, 1981a, b, 1982). Besides the rare earths, Bi^{3+} and Cr^{3+} can be used as

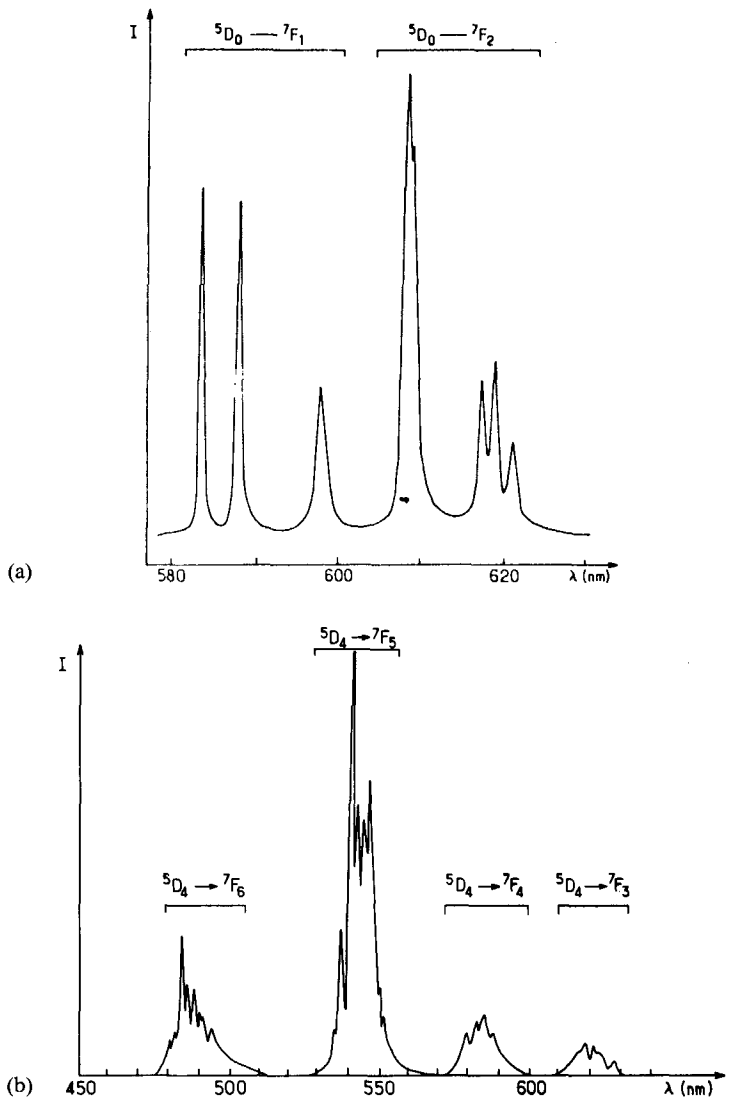

Fig. 15. The emission spectra of Eu^{3+} and Tb^{3+} in $LaMgB_5O_{10}$ showing the typical emissions from the $^5D_0$ and $^5D_4$ levels, respectively. The emissions from the higher levels are almost completely lacking in this host (Fouassier et al., 1982).

activator and, in the host, yttrium can be replaced by some other rare earth and aluminium by gallium (Blasse, 1967; Blasse and Bril, 1967d; Kellendonk et al., 1982). The earlier study by Blasse and Bril (1967d) showed that there is no concentration quenching in these phosphors. A reinvestigation of single crystals and powder samples (Kellendonk and Blasse, 1981a) has shown that the quenching temperature of crystals is lower than that of powder, due to the impurity centres

originating from the flux material used in the crystal growth. The study shows that a relatively large part of Eu^{3+} occupies nonregular crystallographical sites (fig. 16). $YAl_3(BO_3)_4$ activated with Ce^{3+} or Bi^{3+} has broad band spectra at room temperature. At 4.2 K the excitation spectra show a zero-phonon line. The concentration is much less pronounced in the Ce^{3+}-activated compound than in the Bi^{3+}-activated compound, because the quenching process is different. The energy transfer from Ce^{3+} to Tb^{3+} and from Bi^{3+} to Cr^{3+} is not efficient (Kellendonk et al., 1982). However, $CeAl_3(BO_3)_4:Tb^{3+}$ can be used as phosphor in various applications (Westinghouse, 1981). In $GdAl_3(BO_3)_4$ the transfer from Bi^{3+} to Tb^{3+} is very efficient due to the intermediate role of gadolinium (de Hair, 1979).

$NdAl_3(BO_3)_4$ and $KNdP_4O_{12}$ were the first high Nd concentration laser materials with acentric space group allowing second order nonlinear optical processes as well as linear ones (Chinn and Hong, 1976). In $NdAl_3(BO_3)_4$ the Nd concentration is 5.43×10^{21} cm^3, the lifetime $\tau_0(Nd_{0.01}Gd_{0.99}Al_3(BO_3)_4)$ is only 50 μs and $\tau(NdAl_3(BO_3)_4)$ is 19 μs (Hong and Dwight, 1974b). The emission spectrum of neodymium in aluminium borate is shown in fig. 17.

The luminescence properties of $CaLaBO_4$ and $SrLaBO_4$ have been reported by Blasse (1969). The spectral energy distribution of the emission of the Eu-activated compounds gives evidence of two crystallographic ions. Green emission is obtained when $R_2M_3(BO_3)_4$ (M = Ca, Sr, Ba) is activated with terbium (Philips, 1973). These phosphors have application in the luminescent screens of lamps. Lead-activated $MLaBO_4$ (M = Ca, Sr) phosphors show efficient luminescence under excitation with 254 nm radiation, the maximum in the emission being at about 470 nm with a half-width of 125 nm (van der Spijker and Konijnendijk, 1978, 1979).

Among the europium(II) borates the tetraborate has been found to give a strong emission with high quantum efficiency based on the $f \rightarrow d$ transition of Eu^{2+} (Machida et al., 1979b). EuB_2O_4 shows a similar emission to EuB_4O_7, viz. a peak at 372 nm with half-width of 20 nm (Machida et al., 1980b). The other binary borates do not show any luminescence, and the bromoborates emit blue light.

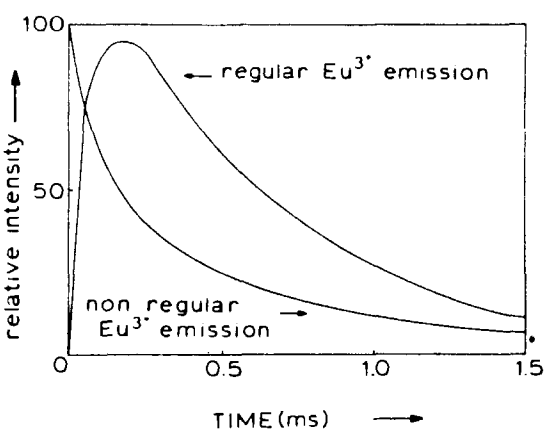

Fig. 16. Decay curves of the nonregular Eu^{3+} emission and regular Eu^{3+} emission after excitation of the nonregular Eu^{3+} ions in a $Gd_{0.3}Eu_{0.7}Al_3B_4O_{12}$ crystal at 115 K showing the energy transfer from nonregular sites to regular sites (Kellendonk and Blasse, 1981a).

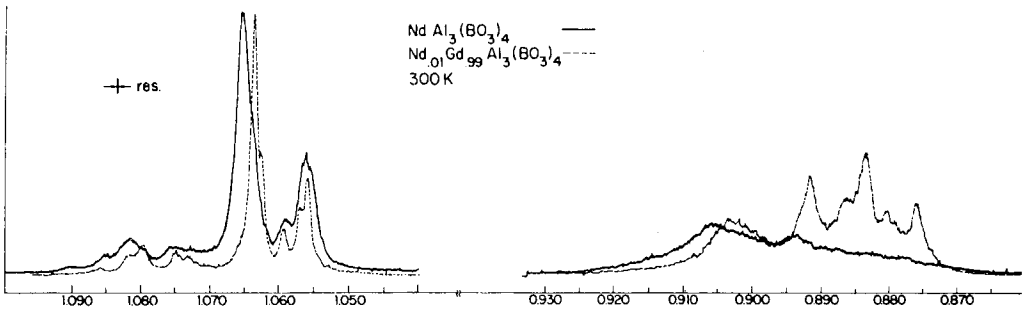

Fig. 17. Room temperature fluorescence spectra of the transitions $^4F_{3/2} \rightarrow {}^4I_{11/2}$ and $^4F_{3/2} \rightarrow {}^4I_{9/2}$ in $NdAl_3(BO_3)_4$ and $Nd_{0.01}Gd_{0.99}Al_3(BO_3)_4$ (Chinn and Hong, 1975).

Vitrification, glass formation and crystallization of glasses of rare earth borates have been studied by Mukhin and Shmatok (1968) and Gutkina et al. (1975). The rare earth borate glasses are of optical grade and their chemical resistance is good (Ohora, 1981).

3. Rare earth carbonates

3.1. *Introduction*

The rare earth carbonates constitute an important group of compounds from the geochemical and geological point of view. In geological systems hydrogen carbonate and carbonate ions may complex a rare earth either alone or together with a fluoro or hydroxo ligand and, indeed, more than 10 different carbonate minerals containing rare earths have been found in nature. The most important of these minerals are bastnaesite (La, Ce)(F, OH)CO_3, lanthanite (La, Ce)$_2(CO_3)_3 \cdot 8H_2O$ and calkinsite (La, Ce)$_2(CO_3)_3 \cdot 4H_2O$. Several double carbonates exist, too: among the more interesting are parisite $2CeFCO_3 \cdot CaCO_3$, synchysite $CeFCO_3 \cdot CaCO_3$ and ancylite (La, Ce)$_x$(Ca, Sr)$_{2-x}(CO_3)_2(OH)_x \cdot (2-x)H_2O$ (Donnay and Donnay, 1953; Wakita and Kinoshita, 1979; Gmelin, 1984a; Clark, 1984).

In the laboratory, the first rare earth carbonates were synthesized about 100 years ago. Their spectroscopic and thermal properties have been frequently studied and there are a number of studies dealing with complex formation, under normal conditions as well as in geological systems. X-ray structural studies are surprisingly few, obviously due to the difficulties of crystal growth. There are no reviews devoted to the rare earth carbonates alone, but several theses dealing with specific aspects of carbonato complexes in solution or in the solid state have recently appeared (Dexpert, 1976; Dumonceau, 1979; Spahiu, 1983).

Rare earth carbonates have few uses as such. They are used as a rare earth source in synthesis and in the preparation of microcrystalline oxide powders (Yukinori and Fumikazu, 1978). Cerium carbonates have been suggested for use in thermochemical cycles for the production of hydrogen from water (Peterson and Onstott, 1978).

Indirectly, the carbonates play a central role in the rare earth industry, as carbonatite ores are among the most important sources of rare earths. The immense bastnaesite deposit in Mountain Pass, California, for instance, has accounted for more than 80% of world rare earth production during recent years (Moore, 1980; Griffiths, 1984).

3.2. *Carbonate complexes in solution*

Studies on complex formation equilibria have revealed the predominating carbonato complexes in aqueous solution and given an indication of the composition of the solid phase. A review of older complex formation and other data for metal carbonates has been given by Krishnamurthy et al. (1970).

More recently the rare earth carbonate system has been studied by Dumonceau and co-workers as well as by Ciavatta, Ferri, and Grenthe et al. The former group has established by extraction studies the overall stability constant for the formation of the limiting tetracarbonato complex:

$$R^{3+} + 4CO_3^{2-} \rightleftarrows [R(CO_3)_4]^{5-}. \tag{1}$$

All rare earths except Ce and Pr were investigated (Dumonceau, 1977; Dumonceau et al., 1979).

Ciavatta et al. (1981) studied the formation of La(III) carbonate complexes in aqueous perchlorate medium (3 M) where the La(III) concentration ranged from 0.1 to 1 M and the partial pressure of CO_2 ranged from 0.1 to 0.98 atm. The emf data could be explained by assuming $[La_2CO_3]^{4+}$ and $[LaHCO_3]^{2+}$ as the predominant species while $[LaCO_3]^+$ is of minor importance in these concentration ranges. These studies were later extended by solubility measurements to a Ce(III)–CO_3^{2-}–H_2O system (Ferri et al., 1983) where a concentration range found in ground water was used. Data of this type are needed to decide whether the concentration of trivalent rare earths and actinides in ground water is limited by solubilities or not. The results indicate that rare earths should occur in ground water with a 100–200 ppm carbonate concentration as $[RCO_3]^+$ and $[R(CO_3)_2]^-$ complexes while $R_2(CO_3)_3$ is the most stable solid carbonate phase under these conditions. The method for evaluation of solubility equilibria has been described in detail for $La_2(CO_3)_3 \cdot 8H_2O(s)$ (Ferri and Salvatore, 1983).

Comparative studies between lanthanides and actinides have been carried out by Lundqvist (1982) who studied Eu(III) and Am(III) systems; his results concerning the predominating carbonate complexes in aqueous solution are in agreement with those reported above.

Spahiu (1983, 1985) has studied the Y(III)–H_2O–CO_2(g) system at 25°C by emf measurements at various perchlorate (0.3–3 M) and Y(III) (0.05–3 M) concentration levels. The acidity and partial pressure of CO_2(g) were in the range 10^{-3}–$10^{4.5}$ M and 0.09–0.99 atm, respectively. All the emf data may be explained by assuming the

equilibria:

$$Y^{3+} + H_2O + CO_2(g) \rightleftarrows [YHCO_3]^{2+} + H^+, \quad \log\beta^0_{111} = -5.4 \pm 0.1, \tag{2}$$

$$Y^{3+} + H_2O + CO_2(g) \rightleftarrows [YCO_3]^{+} + 2H^+, \quad \log\beta^0_{121} = -10.0 \pm 0.2, \tag{3}$$

$$2Y^{3+} + H_2O + CO_2(g) \rightleftarrows [Y_2CO_3]^{4+} + 2H^+, \quad \log\beta^0_{221} = -10.09 \pm 0.1. \tag{4}$$

The equilibrium constants were derived to zero ionic strength by using the specific interaction theory (SIT); see Biedermann (1975).

Sinha (1983) has undertaken a systematic study of the spectroscopic behaviour and complex formation characteristics of the rare earth carbonate systems. Preliminary results show some interesting features, for instance, the carbonate complex, which is assumed to be $[R(CO_3)_4]^{5-}$, increases the intensity of the $^5D_0 \rightarrow {}^7F_2$ hypersensitive transition of Eu(III) by a hundredfold as compared with the same transition in the Eu(III) aqua complex. This phenomenon has been exploited by Sinha (1982) to detect minor amounts (10^{-7} M) of Eu(III) in aqueous solutions (fig. 18). A further application is of geochemical nature. By the use of Eu(III) as a structural probe Sinha and Möller (1983) have studied the ternary R^{3+}–CO_3^{2-}–F^- system in order to obtain more information on the origin of the bastnaesite deposits found in some parts of the world. While in the La(III)–carbonate system only 1% of the La(III) ion can be transformed into complexes without the formation of solid carbonates (Ciavatta et al., 1981), the systems containing large amounts of F^- and CO_3^{2-} are capable of keeping the rare earths from precipitating for a long time (Sinha, 1983).

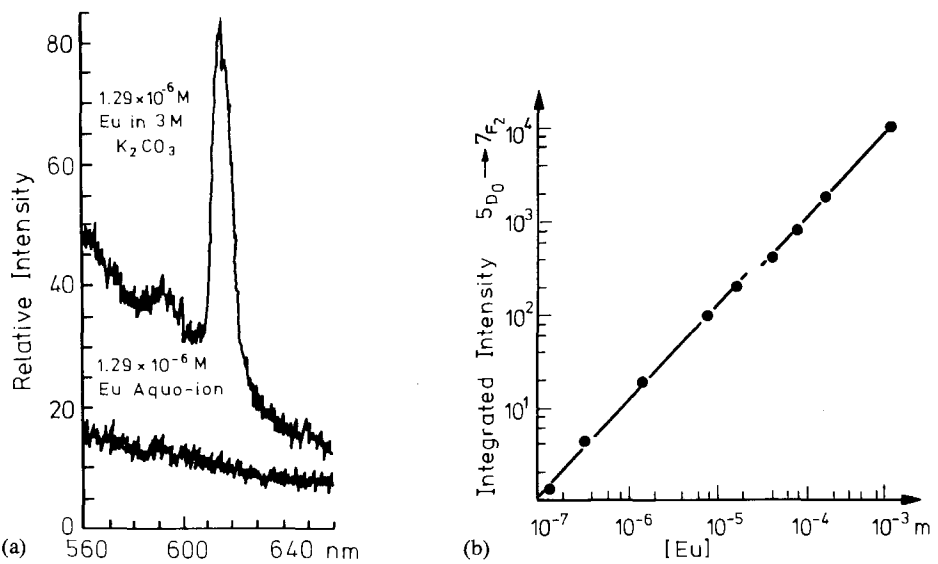

Fig. 18. Increase in intensity of the $^5D_0 \rightarrow {}^7F_2$ band of Eu(III) when a carbonato complex is formed in aqueous solution (a) and a logarithmic plot (b) showing the integrated intensity vs. the concentration of Eu(III).

3.3. *Preparation and structure of solid binary carbonates*

Solid rare earth carbonates, like the carbonates of most metals, can be prepared by the following two precipitation methods: (1) by adding alkali or ammonium carbonate or hydrogen carbonate to a solution of the metal salt and (2) by passing carbon dioxide through an aqueous suspension of the metal hydroxide (Preiss and Dussik, 1923; Vickery, 1953; Su and Shih, 1980; Trofimovich and Sedelnikov, 1963; Jordanov and Havezov, 1966; Deineka et al., 1972).

Precipitates of the heavier lanthanides prepared by these techniques usually appear amorphous (Salutsky and Quill, 1950; Charles, 1965; Sastry et al., 1966). Pure crystalline carbonates of the rare earths are generally obtained through the hydrolysis of trichloroacetates. To obtain the theoretical ratio of CO_3^{2-} and R^{3+} ions, it is necessary that the hydrolysis be carried out under a pressure of CO_2 (Head and Holley, 1964, 1965). The rare earth carbonates are also obtained as crystalline precipitate when the rare earth salt of an organic acid is dissolved in water and the solution placed in a beaker inside a pressure vessel where the atmosphere is purged with CO_2. The reaction time is 2–15 hr and temperature is 30–90°C (Head, 1967, 1968). Nagashima et al. (1973) have prepared pure crystalline rare earth carbonates in a solution of RCl_3 and urea in an autoclave.

In general, the principal factors influencing the crystallization from aqueous solutions are the nature of the precipitant, temperature and pressure, concentrations and the ageing period (fig. 19). When the experimental conditions are suitable, crystalline $R_2(CO_3)_3 \cdot xH_2O$ can be prepared by the alkali carbonate, trichloroacetic

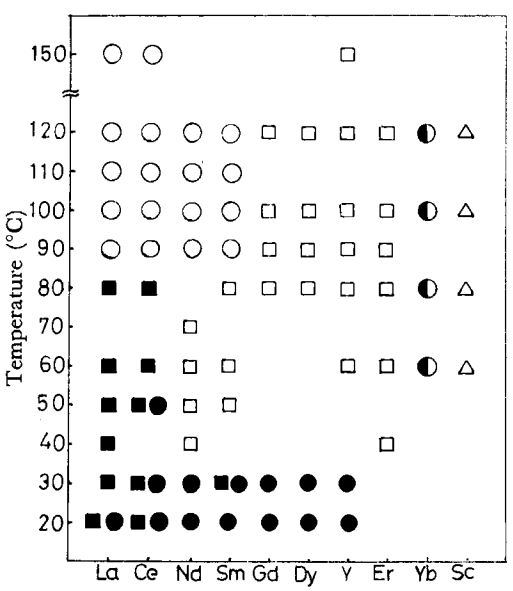

Fig. 19. The phases formed by carbonate precipitation for different rare earth elements at various temperatures (Nagashima et al., 1973). ○ monooxocarbonate, ● double carbonate, ◐ amorphous, □ tengerite type, ■ lanthanite type, △ hydroxide.

acid and urea autoclaving methods (Nagashima et al., 1973). The single crystals of slightly soluble materials can be grown by means of silica gel technique, and Wakita (1978) has grown $R_2(CO_3)_3 \cdot nH_2O$ crystals using sodium metasilicate.

Rare earth elements with ionic radii larger than neodymium crystallize in lanthanite-type hydrated normal carbonates, $R_2(CO_3)_3 \cdot 8H_2O$, whereas rare earth elements with ionic radii smaller than Nd crystallize in tengerite-type hydrated normal carbonates, $R_2(CO_3)_3 \cdot 2\text{–}3H_2O$. Neodymium itself crystallizes as hydrate containing 4.54 water molecules and having calkinsite structure (Wakita and Nagashima, 1972; Wakita, 1978). The number of water molecules in the tengerite-type varies between 2 and 3: Head and Holley (1964) have reported the values 2.5 for Sm, 2.2 for Eu and 2.44 for Gd carbonates, for example. Some authors have reported, however, that the tengerite-type contains three water molecules (Karapetyants et al., 1977a; Chai and Mroczkowski, 1978). Ytterbium and lutetium carbonates, which usually are amorphous, contain six water molecules (Caro et al., 1968). In addition to these values, five molecules have been reported for lanthanum and cerium (Ambrozhii et al., 1960), six for cerium (Maier et al., 1972), eight for neodymium (Caro and Lemaitre-Blaise, 1969), four for neodymium (Baskova et al., 1974), seven for neodymium and five for yttrium (Faucherre et al., 1966) and four for yttrium (Kokhanovskii and Pavlyuchenko, 1976). Temperature and other experimental conditions determine the amount of water in the solid precipitate. In the studies of thermal decomposition of rare earth carbonates still other hydrated phases have been observed, e.g., containing 5.5, 2.5, 1 and 0.5 mol of water (Dabkowska and Kalbowiak, 1971), but these are obviously unstable intermediates.

Pure scandium carbonate hydrate is difficult to prepare. Crookes (1909) reported the preparation of $Sc_2(CO_3)_3 \cdot 12H_2O$ but this has not been confirmed by later studies. In the high-pressure method described by Head and Holley (1965) and Head (1968, 1971), for example, the product is a mixture mainly of $Sc_2(CO_3)_3 \cdot 5H_2O$ and $Sc_2(CO_3)_3 \cdot 4H_2O$ corresponding to the formula $Sc_2O_3 \cdot 2.64CO_2 \cdot 4.54H_2O$. The tendency of scandium to hydrolyze leads to the formation of hydroxocarbonates in the precipitation methods (Sterba-Bohm and Sterba-Bohm, 1938; Komissarova et al., 1971a).

Anhydrous lanthanum carbonate has been prepared by heating $La_2(CO_3)_3 \cdot 8H_2O$ in vacuum at 180°C for 5 hr and then raising the temperature to 430°C with a simultaneous increase of CO_2 pressure to 100 kPa. Keeping the sample in these conditions for 100 hr gave tetragonal $La_2(CO_3)_3$ crystals (Samuskevich et al., 1975).

According to Shinn and Eick (1968), $R_2(CO_3)_3 \cdot 8H_2O$ crystallizes in the space group Pccn with orthorhombic structure and is isomorphic with mineral lanthanite, $(La, Ce)_2(CO_3)_3 \cdot 8H_2O$. A slightly different space group has been reported by Dal Negro et al. (1977). The layered structure consists of alternating rows of R^{3+} and CO_3^{2-} ions running parallel to the x axis. In the two distinct 10-coordinated metal polyhedra of the structure the coordination sites are occupied both by water molecules and by bidentate and unidentate carbonato ligands (fig. 20). One fourth of the water molecules are not bonded to the metal ions but are situated between the layers, holding them together by hydrogen bonds (Shinn and Eick, 1968).

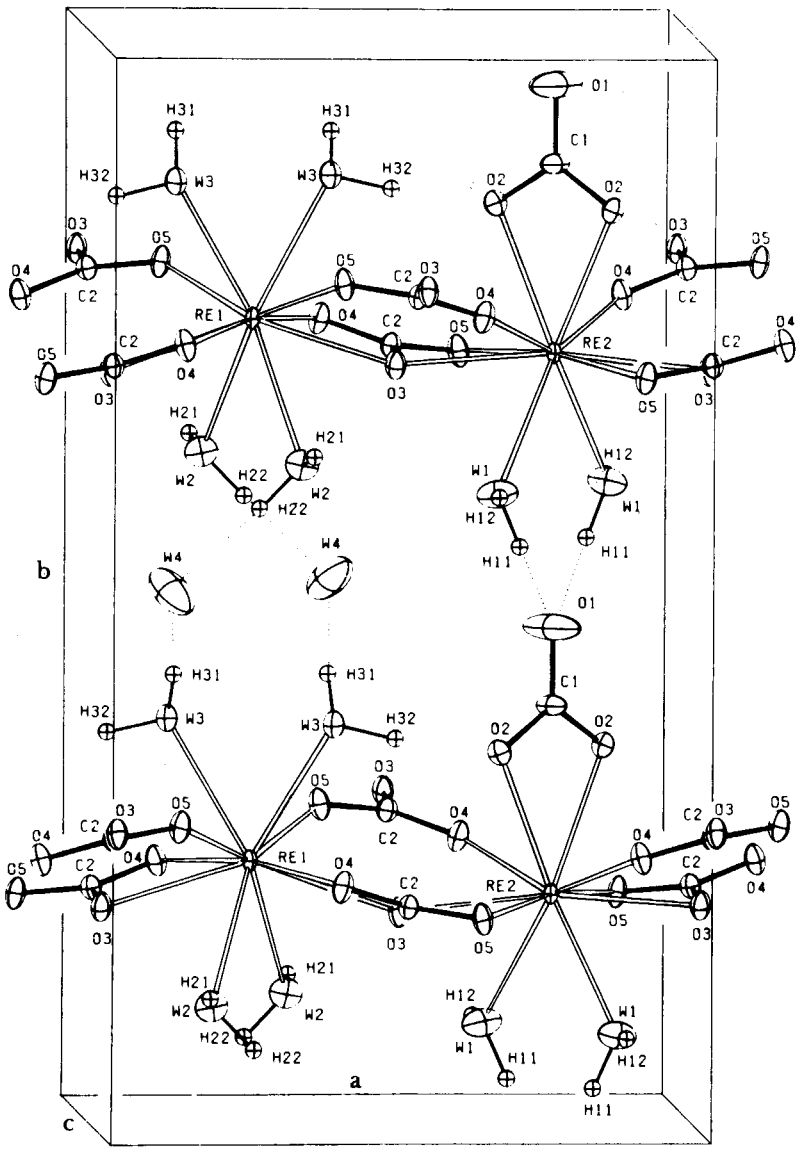

Fig. 20. The unit cell of $(La,Ce)_2(CO_3)_3 \cdot 8H_2O$ showing the coordination of rare earth ions to carbonate groups and water molecules (Dal Negro et al., 1977).

Holmium hydrogen carbonate hydrate crystals can be prepared by slow evaporation of acidified carbonate solution or of a saturated holmium sucrose solution. The gradual degradation of sucrose to hydrogen carbonate in the acidic solution coupled with slow evaporation yielded $Ho(HCO_3)_3 \cdot 6H_2O$ crystals (Rohrbaugh and Jacobson, 1974). The structure of this compound is triclinic containing 10-coordinated holmium atoms linked by bidentate HCO_3 groups and aqua ligands. According to the X-ray study its formula should be given as $[Ho(HCO_3)_3(H_2O)_4] \cdot 2H_2O$.

The evaporation of aqueous gadolinium formate solution led to formation of hydrogen carbonate pentahydrate, $Gd(HCO_3)_3 \cdot 5H_2O$ (Furmanova et al., 1981). The Gd atoms have coordination number 10 with three bidentately coordinated hydrogen carbonato ligands and four oxygen atoms from water molecules in its coordination kernel, thus leading to the formula $[Gd(HCO_3)_3(H_2O)_4] \cdot H_2O$ (fig. 21). The structure is linked together by hydrogen bonds in which all the hydrogen atoms are involved.

The diffraction diagrams of $R_2(CO_3)_3 \cdot 2\text{–}3H_2O$ powders can be indexed as orthorhombic (Wakita and Nagashima, 1972). The unit cell resembles that of tengerite $CaY_3(OH)_3(CO_3)_4 \cdot 3H_2O$ but the details of the structure are unknown even though single crystals of $Y_2(CO_3) \cdot nH_2O$ have been grown (Tareen et al., 1980a, b). The unit cell dimensions determined by different authors differ somewhat (Caro et al., 1972; Nagashima et al., 1973). Caro and Coutures (1974) have obtained $Ho_2(CO_3)_3 \cdot 2.25H_2O$ with monoclinic structure (C2/m) at 60°C.

Europium in divalent state forms the carbonate $EuCO_3$. This lemon yellow material can be obtained by digesting $EuSO_4$ in a solution of NaOH and $NaHCO_3$ (Cooly and Yost, 1946). The structure of $EuCO_3$ is orthorhombic (Pmcn) and shows some structural similarities with KNO_3 (Mayer et al., 1964). The material decomposes in air at about 500°C and an oxycarbonate is formed where europium has

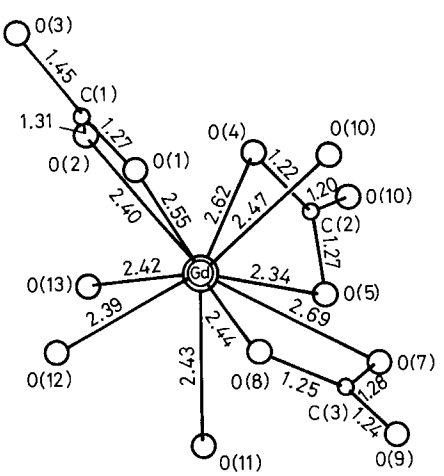

Fig. 21. A perspective view of the $[Gd(HCO_3)_3(H_2O)_4]$ complex showing the bond distances in Å (Furmanova et al., 1981).

been oxidized into the trivalent state. The oxycarbonate decomposes further to Eu_2O_3 at 750°C (Stroganova and Rousaikina, 1970).

3.4. *Thermal decomposition of binary rare earth carbonates*

Most of the papers dealing with the preparation of rare earth carbonate hydrates also contain an account of their thermal decomposition. Thermal studies have been carried out with thermobalance (TG) and differential scanning calorimetry (DSC) or differential thermal analysis (DTA), in air, vacuum, carbon dioxide, carbon monoxide, hydrogen, nitrogen, oxygen and helium (Wendlandt and George, 1961; Head and Holley, 1964, 1965; Tselik et al., 1968a, b; Caro et al., 1970; Kokhanovskii et al., 1971; Nagashima et al., 1973; Wakita, 1978).

In spite of the different initial water content of samples obtained in different preparative approaches, there is good agreement among authors on the dehydration mechanism. The water molecules are released in a single stage somewhere between 150 and 300°C, depending on the rare earth in question and the experimental conditions used in thermal studies (fig. 22). Only one report has suggested the existence of intermediate hydrates during the thermal decomposition of $R_2(CO_3)_3 \cdot 8H_2O$ (Dabkowska and Kalbowiak, 1971).

The thermal decomposition of anhydrous rare earth carbonate to oxide occurs via intermediate oxycarbonate phases. The particular oxycarbonate formed depends on the experimental conditions. The stoichiometric oxycarbonates are monoxydicarbonate, $R_2O(CO_3)_2$, and dioxymonocarbonate, $R_2O_2CO_3$. Monoxydicarbonate can also be prepared in hydrated form at higher temperatures in rare earth carbonate solutions (Nagashima et al., 1973).

The decomposition of anhydrous rare earth carbonates begins above 350°C. In air and CO_2 atmosphere the formation of $R_2O(CO_3)_2$ has been reported for the

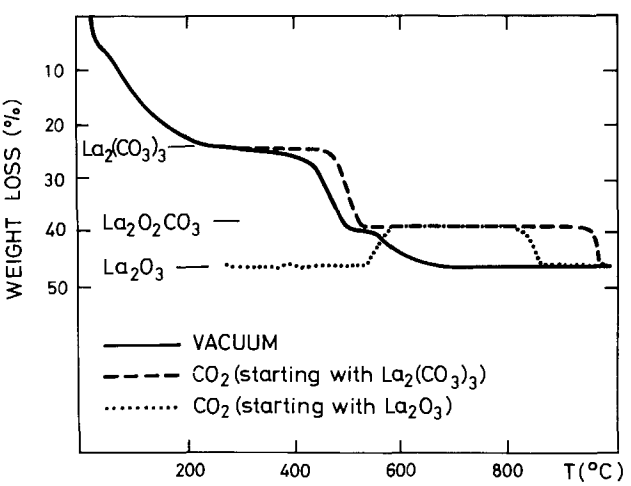

Fig. 22. Thermal decomposition of $La_2(CO_3)_3 \cdot 8H_2O$ in different atmospheres and the formation of $La_2O_2CO_3$ (Head and Holley, 1964).

lighter lanthanides (Preiss and Rainer, 1923; Wakita, 1978), though Head and Holley (1964) have not detected this phase in any experiment. At about 450°C the monoxydicarbonate begins to decompose to dioxymonocarbonate. The $R_2O_2CO_3$ phase exists for all rare earths except lutetium and scandium (Chai and Mroczkowski, 1978). The stability of the oxycarbonate phase in air decreases with increasing atomic number of the rare earth. $Nd_2O_2CO_3$, for example, is stable in air up to 750°C. The thermal decomposition of the rare earth carbonates proceeds more rapidly in H_2O, O_2 and H_2 atmospheres than in vacuum, CO and CO_2 atmospheres (Kokhanovskii et al., 1971). $La_2O_2CO_3$ is stable in carbon monoxide up to nearly 1000°C (Caro et al., 1970).

There are many reports in the literature on the nonstoichiometric oxycarbonates. The compounds are usually represented by the formula $R_2O_3 \cdot yCO_2$ where y is normally less than 1, but Hiroyuki et al. (1977) have prepared $Gd_2O_3 \cdot 2.5CO_2$ which is stable in a CO_2 atmosphere. According to Sawyer et al. (1971) the thermal decomposition of oxycarbonates yields $R_2O_{2+x}(CO_3)_{1-x}$ phases, where $x = 0$ only in the case of La and Pr, and x increases with the atomic number in the lanthanide series. Preiss and Rainer (1923) and Ambrozhii et al. (1960) have found the compound $Nd_2O_3 \cdot 0.5CO_2$. Head and Holley (1964), on the other hand, found the following compounds in CO_2 atmosphere: $Nd_2O_3 \cdot 0.75CO_2$, $Sm_2O_3 \cdot 0.8CO_2$, $Eu_2O_3 \cdot 0.12CO_2$ and $Gd_2O_3 \cdot 0.87CO_2$; in the case of all the other rare earths they found the decomposition of $R_2O_2CO_3$ to be a one-stage process. According to Wakita (1978), $Nd_2O_2CO_3$ decomposes in a single step to oxide. In studies of the thermal decomposition of $R_2O(CO_3)_2 \cdot nH_2O$, nonstoichiometric compounds have also been observed for the lighter lanthanides: compounds containing 0.8 and 0.4 mol of CO_2 in the case of lanthanum and 0.9 and 0.7 mol in the case of neodymium (Nagashima et al., 1973). The dioxycarbonate phase was not detected. It is possible that the nonstoichiometric phases in reality are mixtures of dioxycarbonates and oxides (Sawyer et al., 1971).

The kinetics of the decomposition reactions of rare earth carbonates have been studied by Kokhanovskii et al. (1971) and Eiji et al. (1976). Though the reactions seem to be of first order, one should be cautious about placing too much physical significance on the results, as solid state decompositions are complicated and dependent on experimental conditions.

The decomposition of the carbonates of cerium is a special case. The thermal decomposition product is not trivalent oxide but tetravalent cerium dioxide. Analysis of the gas evolved during the decomposition shows the presence of H_2, CO and CO_2, with the quantity of each dependent on the amount of water present during the decomposition. Hydrogen is produced via the water gas shift reaction. The equilibrium data indicate that CeO_2 exhibits catalytic activity with respect to this reaction. It is possible to manipulate the $CO : H_2$ ratio in the gas mixture so that introduction to a suitable catalyst will yield methane, methanol or higher hydrocarbons (Onstott et al., 1976; Peterson et al., 1978).

The thermal dissociation of praseodymium carbonate in an O_2 atmosphere yields an intermediate tetravalent carbonate. This decomposes at much lower temperature (295–310°C) than tetravalent cerium carbonate (Pajakoff, 1968).

3.5. *Hydroxide carbonates of the rare earths*

The heating of aqueous solutions of the rare earth trichloroacetates in acidic medium leads to the formation of carbonate hydrates as described above. In neutral medium the product is hydroxide-containing carbonate, $ROHCO_3 \cdot nH_2O$ (Sklyarenko and Ruzaikina, 1970). The preparation of rare earth carbonates with CO_2 does not give hydroxide carbonate, but when alkali carbonates are used the situation is different. When $CO_3^{2-} : R^{3+}$ is 1.5 with ytterbium, $YbOHCO_3$ is formed; for europium the ratio must be 2 and for neodymium > 4.

The neutral carbonates hydrolyze slowly in warm water and rapidly in boiling water, forming $ROHCO_3$ (Preiss and Dussik, 1923). The hydrolysis rates in boiling solution have been investigated by Brinton and James (1921). Hydrolysis also occurs when the partial pressure of carbon dioxide is reduced below 1 kPa (Caro and Lemaitre-Blaise, 1969). The phases formed in this pressure method are of variable composition $R_2(CO_3)_x(OH)_{2(2-x)} \cdot nH_2O$, where for $x = 2.3$, $n = 0.5$ and for $x = 1$, $n = 2$–5 (Caro et al., 1972). The hydroxide carbonate phase has also been prepared by hydrolysis of urea in hot $R(NO_3)_3$ solution by gradually increasing the pH and CO_2 concentration (Sawyer et al., 1973). Carbonation of oxychloride produces the hydroxide carbonate phase at least in the case of cerium ($CeOHCO_3$) (Peterson and Onstott, 1978).

Crystalline rare earth hydroxide carbonate can be prepared by hydrothermal methods. Christensen (1970a) succeeded in growing for yttrium single phase $Y_2O(OH)_2CO_3$ crystals, by keeping the $Y(OH)_3$ solution in a CO_2 atmosphere at 260–300°C and pressure of 20 MPa. Later the formula was corrected to $Y_2(OH)_4CO_3$ (Christensen and Hazell, 1984). Rare earth carbonates (La $\cdots$ Er, Y) form stable $ROHCO_3$ crystals in the presence of 6 M NH_4Cl in the temperature range 250–500°C and under pressures of 100–200 MPa. The thermal stability of these compounds decreases systematically with decreasing ionic radius of the R element. In the presence of 6 M K_2CO_3 the stability region for $ROHCO_3$ is further reduced (Chai and Mroczkowski, 1978). At higher temperatures and pressures the dioxycarbonates, $R_2O_2CO_3$, are formed. In the experiments of Chai and Mroczkowski yttrium appeared also as oxide hydroxide carbonate. In the case of erbium an orthorhombic hydroxide carbonate is formed. The chemical formula of this compound is $Er_2(OH)_4CO_3 \cdot nH_2O$, which has been determined also by Caro and Lemaitre-Blaise (1969) for neodymium.

Scandium hydroxide carbonate, $ScOHCO_3 \cdot nH_2O$ ($n = 1$ or 3), has been obtained by adding sodium or ammonium carbonate to a solution of scandium chloride (Sterba-Bohm and Sterba-Bohm, 1938; Komissarova et al., 1971a). From NMR data Komissarova et al. (1972) suggested the formula $Sc_2O(OH)_2(HCO_3)_2 \cdot nH_2O$ ($n = 3$ or 5) for the product obtained from Sc_2O_3 and M_2CO_3.

The rare earth hydroxide carbonates, $ROHCO_3$, have two different structure types. The first type is hexagonal ($P\bar{6}$) and most of the rare earths (La $\cdots$ Er, Y) form a compound of this type (Caro et al., 1971; Haschke and Eyring, 1971; Christensen, 1973b). The structure is isomorphic with mineral bastnaesite ($RFCO_3$),

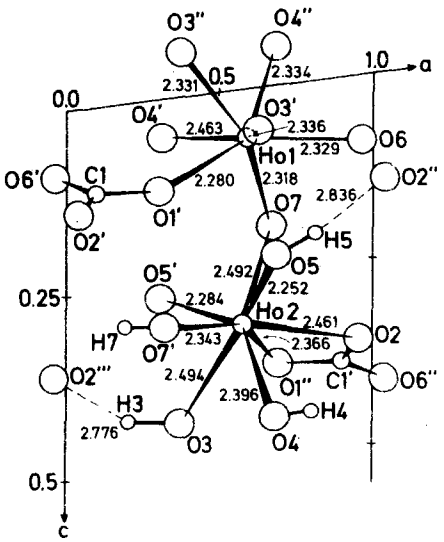

Fig. 23. Coordination of hydroxo and carbonato ligands resulting in 7- and 8-coordinated Ho atoms in $Ho_2(OH)_4CO_3$ (Christensen and Hazell, 1984).

containing ROH^{2+} ions held together in layers by the carbonate ions. The rare earth atom has a ninefold coordination.

The second $ROHCO_3$ structure type is orthorhombic and it is more difficult to prepare in hydrothermal conditions than the hexagonal modification (Caro and Lemaitre-Blaise, 1969). According to Tareen et al. (1980a, b) formic acid is a promising mineralizer for hydrothermal growth of rare earth carbonates and hyroxide carbonates. Though the structure of the orthorhombic $ROHCO_3$ is closely related to the mineral ancylite $(Ce, La)_4(Sr, Ca)_3(CO_3)_7(OH)_4 \cdot 3H_2O$ (Sawyer et al., 1973), slightly different structural models have been proposed (Dexpert and Caro, 1974; Dal Negro et al., 1975). Furthermore, two different orthorhombic space groups have been proposed for this $ROHCO_3$-type: Pmcn by Dexpert and Caro (1974) and Dexpert et al. (1975) for powder samples and $P2_12_12_1$ by Beall et al. (1976) for a single crystal sample. However, both groups report that the rare earth atoms in orthorhombic hydroxide carbonates are 9-coordinated to two OH and seven CO_3^{2-} oxygen atoms. The carbonate group chelates two R atoms (fig. 23).

The structures of rare earth hydroxide carbonates can also be described by means of different $CaCO_3$ structure types. The orthorhombic $ROHCO_3$ and the mineral ancylite structures can be derived from aragonite-type $CaCO_3$. Hexagonal $ROHCO_3$ has structural similarities to vaterite-type calcium carbonate (Dexpert et al., 1972, 1982).

The structure of $R_2(OH)_4CO_3$ is monoclinic and contains layers of metal atoms close to the *yz* plane. The metal atoms are 7- and 8-coordinated (fig. 24). The layers are held together by carbonate ions and hydrogen bonds (Christensen and Hazell, 1984).

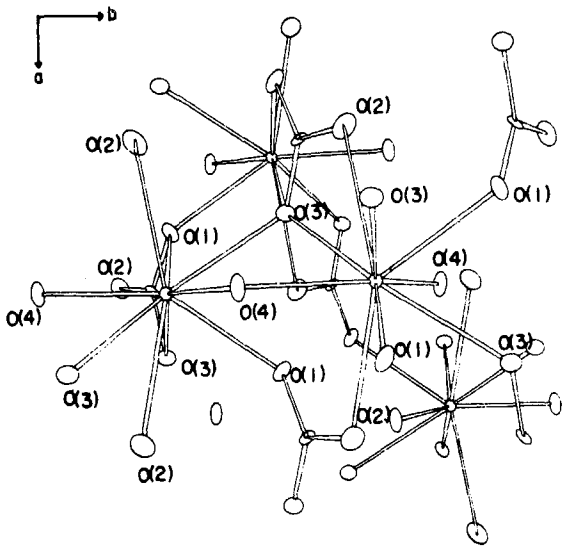

Fig. 24. The joining of 9-coordinated Y atoms in the structure of $YOHCO_3$ (Beall et al., 1976).

Not only the hydroxide ion but also the fluoride and chloride ions can combine with rare earth carbonates, as is the case in the mineral bastnaesite (Aumont et al., 1971). Synthetically the fluoride carbonates can be obtained by precipitation from rare earth carbonate solutions with potassium fluoride or by the action of a stoichiometric amount of hydrogen fluoride in an aqueous suspension of normal carbonates (Fridman and Gorokhov, 1967, 1969a). The fluoride carbonates may also contain water.

Anhydrous RCO_3F decomposes around 600°C to rare earth oxyfluoride (Fridman and Goroknov, 1969b). The solubility of RCO_3F in water at 20°C varies between 2 and 4×10^{-5} mol dm^{-3}.

3.6. *Rare earth oxycarbonates*

The rare earth dioxymonocarbonate (abbreviated oxycarbonate) is formed as a stable intermediate during the thermal decomposition of carbonate hydrates in air. The decomposition reaction leading to oxycarbonate may have one or two steps as described earlier. Thermoanalytical studies have established that the thermal decomposition of rare earth oxalates in an air or CO_2 atmosphere is another simple way to prepare oxycarbonates (Ropp and Gritz, 1965). The decomposition of rare earth formates likewise leads to oxycarbonates (Petru et al., 1966).

The rare earth hydroxide carbonates decompose to oxide via the oxycarbonate phase. The hexagonal form of $ROHCO_3$ transforms to hexagonal $R_2O_2CO_3$. This topotactic reaction as well as the further decomposition of oxycarbonate to hexagonal A-type oxide has been followed by electron microscopy (Dexpert et al., 1975; Schiffmacher et al., 1977; Dexpert and Caro, 1978). The decompositions are typical

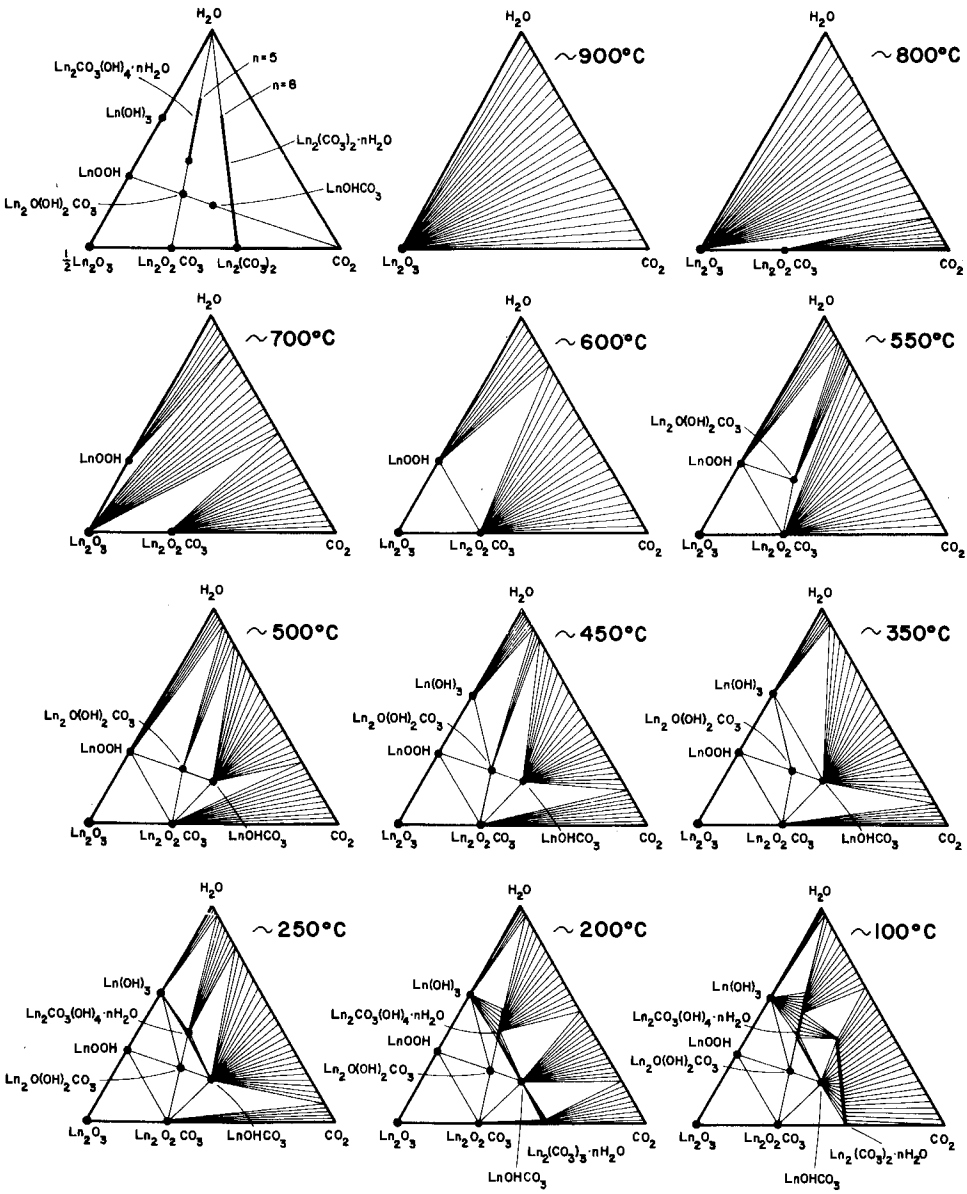

Fig. 25. The phase relationships among the R_2O_3–H_2O–CO_2 systems at various temperatures up to 900°C (Chai and Mroczkowski, 1978).

solid state reactions involving a very small displacement of cations and thus there is no extensive reconstruction of the structure.

Gd, Er and Y oxycarbonates can be prepared in hydrothermal conditions from carbonates in NH_4Cl or K_2CO_3 solution (Chai and Mroczkowski, 1978). The hexagonal form of the known $R_2O_2CO_3$ structure types is formed under these conditions and, in addition, at temperatures about 250°C, $Er_2O_2CO_3$ and $Y_2O_2CO_3$ crystallize with an unknown structure. The phase relationship in the system R_2O_3–H_2O–CO_2 at three temperatures has been presented in fig. 25.

The rare earth oxycarbonates form three different structure types: tetragonal I ($I4/mmm$) (La · · · Er), monoclinic IA (La · · · Nd) and hexagonal II ($P6_3/mmc$) (La · · · Yb) (Turcotte et al., 1968; Sawyer et al., 1971; Christensen, 1973a; Chai and Mroczkowski, 1978). In the decomposition reaction of carbonates and oxalates the forms I and IA appear at 400–500°C. A phase transition to hexagonal II form occurs between 520 and 670°C depending on the rare earth.

The crystal structure of hexagonal oxycarbonate has been determined by Christensen (1970b). The structure contains RO_8 polyhedra packed in hexagonal layers of $(RO)_2^{2+}$ ions. The layers are held together by carbonate ions that are slightly disordered. The tetragonal $R_2O_2CO_3$-type was first suggested to be cubic (Petru et al., 1966), but X-ray powder diffraction data and the IR spectrum now indicate structural similarities with $Bi_2O_2CO_3$. The structure of the bismuth compound is known to be tetragonal (Sawyer et al., 1971).

3.7. *Ternary rare earth carbonates*

The rare earth double carbonates with alkali metals have been known since the beginning of this century. $MR(CO_3)_2 \cdot nH_2O$ where M = K, NH_4^+, R = La · · · Nd and $n = 4$–12 was first prepared by Meyer (1904). Zambonini and Carobbi (1924) extended the studies to sodium compounds. The ternary compounds are obtained by adding an excess of alkali carbonate to rare earth solutions at pH about 5. In the case of $(NH_4)_2CO_3$–RCl_3 the ratio $CO_3^{2-}:R^{3+}$ needs to be more than 2 before the double compound will form (Tselik et al., 1969). The number of water molecules in $MR(CO_3)_2$ varies between two and six (depending on the rare earth) according to more recent studies (de Polignac et al., 1971; Mochizuki et al., 1974). The lithium rare earth carbonate hydrates are formed only below room temperature (Kalz and Seidel, 1980).

Scandium alkali carbonates having the general composition $MR(CO_3)_2 \cdot nH_2O$ can also be prepared. Besides the sodium, potassium and ammonium compounds, the corresponding rubidium and cesium compounds have been reported too (Spitsyn et al., 1960; Fromage, 1968; Komissarova et al., 1972). Another composition where the ratio $M^+:R^{3+}$ is 5:1 is known for scandium and for ytterbium and lutetium (Faucherre et al., 1966; Komissarova et al., 1971b). This corresponds to the $[R(CO_3)_4]^{5-}$ complex found in solution. The number of water molecules in these $M_5R(CO_3)_4 \cdot nH_2O$ compounds is 2, 11 or 18 for sodium and 5 for potassium.

TABLE 6
Summary of structural data for rare earth carbonates.

Composition	R	Compound	Cell parameters				Z	Space group	Reference
			a	*b*	*c*	angle (°)			
$R_2(CO_3)_3 \cdot 8H_2O$	La · · · Pr	La	9.98	8.58	17.00		4	Pccn	Shinn and Eick, 1968
$R_2(CO_3)_3 \cdot 2\text{–}3H_2O$	Sm · · · Tm, Y	Y	9.20	11.32	7.59		4		Wakita and Nagashima, 1972
$R_2(CO_3)_3$	La	La	8.69		9.72		4		Samuskevich et al., 1975
$ROHCO_3$	La · · · Er, Y	Sm	12.23		9.86		18	$P\bar{6}$	Christensen, 1973b
	Y	Y	4.81	6.96	8.47		4	$P2_12_12_1$	Beall et al., 1976
$R_2(OH)_4CO_3$	Ho · · · Yb, Y	Ho	6.27	6.04	15.42	$\beta = 97.4$	4	$P2_1/c$	Christensen and Hazell, 1984
$R_2O_2CO_3$	La · · · Nd	La	4.07	4.07	13.49	$\beta = 91.0$			Sawyer et al., 1971
	La · · · Er	La	4.06		13.50		2	14/mmm	Sawyer et al., 1971
	La · · · Yb	Dy	3.97		15.16		2	$P6_3/mmc$	Christensen, 1973a
$R(HCO_3)_3 \cdot 6H_2O$	Ho	Ho	9.18	11.59	6.73	$\alpha = 88.9$ $\beta = 112.5$ $\gamma = 71.5$	2	$P\bar{1}$	Rohrbaugh and Jacobson, 1974
$R(HCO_3) \cdot 5H_2O$	Gd	Gd	6.88	9.58	18.87	$\beta = 102.6$	4	$P2_1/a$	Furmanova et al., 1981
RCO_3	Eu	Eu	5.10	8.42	6.03		4	Pmcn	Maier et al., 1964
$LiR(CO_3)_2$	La · · · Gd	Nd	8.29	7.74	6.82	$\beta = 97.8$	4		Kalz and Seidel, 1980
	Tb · · · Lu, Y	Er	6.63	13.63	10.37	$\beta = 72.6$	4		Kalz and Seidel, 1980
$NaR(CO_3)_2$	La · · · Sm	Nd	6.35	5.10	7.07		2		Schweer and Seidel, 1981
	Tb · · · Lu, Y	Er	6.21	13.07	6.12	$\beta = 102.7$	4		Schweer and Seidel, 1981
$KR(CO_3)_2$	La · · · Nd	Pr	4.89	6.48	8.61		2		Kalz and Seidel, 1982
	Sm · · · Lu, Y	Er	8.48	9.41	6.90	$\beta = 111.0$	4		Kalz and Seidel, 1982
$LiROCO_3$	Sm · · · Lu, Y	Ho	3.41	7.53	7.40	$\beta = 102.8$	2		Kalz and Seidel, 1980
$Na_5R(CO_3)_4 \cdot 2H_2O$	Sc	Sc	7.46		11.60		2	$P\bar{4}2_1c$	Zhdanova et al., 1972
$KR(CO_3)_2 \cdot 3H_2O$	Pr · · · Gd	Gd	13.30	6.26	9.23	$\beta = 94.0$	4	$P2_1/c$	Delaunay et al., 1971
$KR(CO_3)_2 \cdot 6H_2O$	Pr · · · Eu	Pr	13.34	6.35	13.4	$\beta = 95.2$			de Polignac et al., 1971
$KR(CO_3)_2 \cdot 4H_2O$	Gd · · · Lu	Gd	12.21	5.77	12.26	$\beta = 90.4$			de Polignac et al., 1971
$KR(CO_3)_2 \cdot 2\text{–}3H_2O$	La	La	13.11	8.53	7.47	$\beta = 60.0$			de Polignac et al., 1971
$Na_6(R(CO_3)_5) \cdot 12H_2O$	Ce	Ce	9.53	9.84	13.58	$\alpha = 90.5$ $\beta = 104.5$ $\gamma = 95.4$	2	$P\bar{1}$	Voliotis and Rimsby, 1975
$(C(NH_2)_3)_6(R(CO_3)_5) \cdot 4H_2O$	Ce	Ce	16.05	16.63	13.14	$\gamma = 108.1$	4	Bb	Voliotis et al., 1975

X-ray diffraction diagrams have been recorded for some ternary alkali carbonate hydrate powders. According to de Polignac et al. (1971), their structure is monoclinic. Five structure types have been detected for the sodium compounds and four for the potassium compounds (table 6). The structure of $K[Gd(CO_3)_2(H_2O)_3]$ contains 8-coordinated Gd atoms having three bonded water molecules in the coordination sphere. The Gd atoms form chains and are bonded together by carbonate groups (Delaunay et al., 1971). The structure of $Na_5[Sc(CO_3)_4] \cdot 2H_2O$ has been determined as hexagonal ($P\bar{4}2_1c$) containing 8-coordinated scandium (Zhdanova et al., 1972).

The anhydrous alkali double carbonates of the rare earths have been synthesized from mixtures of M_2CO_3 (M = Li, Na, K) and rare earth oxalate hydrate under carbon dioxide pressure of 200–300 MPa and at temperatures of 350–500°C (fig. 26). The sodium and potassium compounds can also be synthesized by dehydration of $MR(CO_3)_2 \cdot nH_2O$ under the same experimental conditions. At lower pressures (20 MPa) lithium forms an oxycarbonate, $LiROCO_3$ (Kalz and Seidel, 1980). The compounds have been characterized from powder samples by IR and X-ray investigations and by thermal decomposition studies.

Two structure types have been found in each series. The lithium-containing carbonate types are both monoclinic, whereas the double carbonates with sodium and potassium form orthorhombic structures with the lighter rare earths and monoclinic structures with the heavier (Schweer and Seidel, 1981; Kalz and Seidel, 1982).

$LiR(CO_3)_2$ starts to decompose at temperatures between 400 and 500°C, depending on the rare earth, to Li_2CO_3, $R_2O_2CO_3$ and CO_2. In the second stage lithium carbonate decomposes to oxide and as the last step R_2O_3 is formed between 800 and 1100°C. In sodium compounds the second and third stages are reversed: $R_2O_2CO_3$ decomposes before sodium carbonate (fig. 27) (Schweer and Seidel, 1981).

Among the ternary carbonates of rare earths with alkaline earth metals the minerals synchysite, parisite and roentgenite are the most important. These minerals contain fluoride in addition to the carbonate anion. $CeFCO_3$ and $CaCO_3$ are

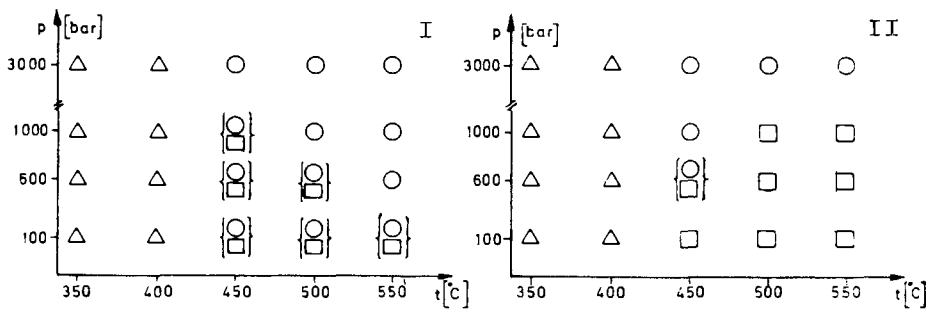

Fig. 26. The effect of CO_2 pressure and temperature on the formation of $LiR(CO_3)_2$ and $LiROCO_3$ (Kalz and Seidel, 1980). Starting materials: I, Li_2CO_3, $Nd_2(C_2O_4)_3 \cdot xH_2O$; II, Li_2CO_3, $Lu_2(C_2O_4)_3 \cdot xH_2O$. Products: △ starting materials, ○ $LiR(CO_3)_2$, □ $LiROCO_3$.

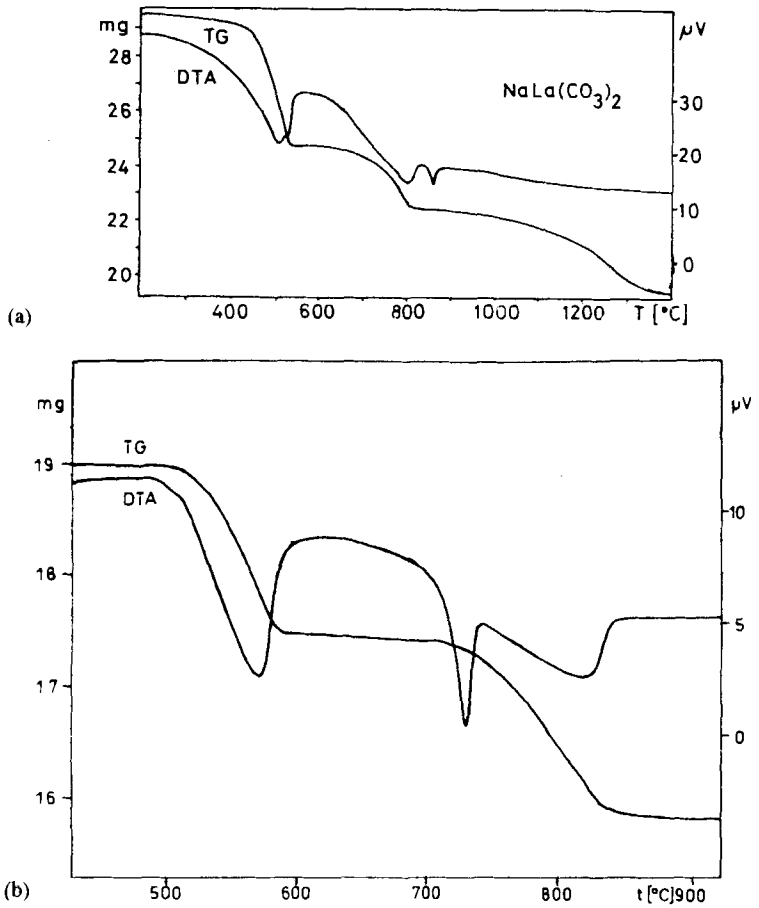

Fig. 27. The TG and DTA curves for $NaLa(CO_3)_2$ and $LiYbOCO_3$ heated in air (Kalz and Seidel, 1980; Schweer and Seidel, 1981). The exothermic peak in the DTA curve without any weight change is due to the melting of alkali carbonate.

TABLE 7

Solubilities of some rare earth carbonates in water (mol dm^{-3}) (Sklyarenko and Ruzaikina, 1970; Trofimovich and Sedelnikov, 1963; Jordanov and Havezov, 1966).

Compound	Solubility
$La_2(CO_3)_3$	2.4×10^{-7}
$Ce_2(CO_3)_3$	1.0×10^{-6}
$Nd_2(CO_3)_3$	1.1×10^{-6}
$Eu_2(CO_3)_3$	2.0×10^{-6}
$Y_2(CO_3)_3$	2.5×10^{-6}
$Yb_2(CO_3)_3$	5.0×10^{-6}

contained in proportions 1:1, 2:1 and 3:2, respectively. The structures of the minerals resemble the structure of bastnaesite and the diffraction diagrams can be indexed as hexagonal. Synchysite is probably orthorhombic but a pseudohexagonal unit cell has been presented for it too (Donnay and Donnay, 1953).

The crystals of some double carbonates of tetravalent cerium have been prepared and their structures determined by Dervin et al. (1973), Voliotis et al. (1975) and Voliotis and Rimsky (1975). The counter-ion in the compounds has been sodium or guanidine.

3.8. *Properties of rare earth carbonates*

The rare earth carbonates are only sparingly soluble in water, the solubility increasing with increasing atomic number (Sklyarenko and Ruzaikina, 1970). Table 7 lists the solubilities of some rare earth carbonates in water.

The solubility values of hydroxide carbonates are similar to those of normal carbonates. The solubility of alkali rare earth double carbonates decreases in the series $NH_4^+ < Na^+ < K^+$.

Karapetyants et al. (1977a, b) have studied the thermodynamic properties of rare earth carbonates and have calculated the standard Gibbs energies, entropies and heats of formation for each compound. For $La_2(CO_3)_3 \cdot 8H_2O$ the $\Delta H°$, $\Delta G°$ and $\Delta S°$ values at 298 K are -5683 kJ/mol, -4954 kJ/mol and -2445 kJ/K mol, respectively.

The infrared absorption spectra of different rare earth carbonates have been recorded by several authors. The spectra can be used to identify the various structure types although the assignment of the bonds is not unambiguous in all cases. As a summary of the results, values observed for some neodymium carbonates are presented in table 8.

4. Rare earth silicates

4.1. *Introduction*

Because of the lithophilic nature of the rare earths the silicates are among the most important rare earth minerals found in nature. Among them the most abundant are the silicates with simple composition, e.g., the disilicates like thortveitite and thalenite (Strunz, 1970). Thortveitite has an unusual distribution of rare earths where scandium is strongly enriched and it is considered one of the very few true scandium minerals.

Recently, synthetic studies have increased the number of known silicates and shown that the reaction between R_2O_3 and SiO_2 leads mainly to 1:1, 2:3 and 1:2 compositions although lower $R_2O_3 : SiO_2$ ratios are also known but not studied in detail (figs. 28 and 29). The number of possible structures is further increased by the fact that polymorphism is a common feature for instance among the disilicates and that additional cations may be present.

TABLE 8

Infrared absorption frequencies (cm^{-1}) and their assignments for neodymium carbonates (Caro et al., 1972; Dexpert et al., 1982)[a)]

Compound	ν_4	ν_1	ν_2	ν_6	ν_3	ν_5	Additional bands
$Nd_2(CO_3)_3 \cdot 8H_2O$	1470s(sp)	1370s(sp) 1340m(sh)	1080m(sp)	847s(sp)	748m(sp)	675m(sp)	3200–3300s(b) (H_2O) 1630w(sh) (HOH bending)
$Nd_2(CO_3)_3 \cdot 2H_2O$	1480s(b)	1410s(b)	1070m(b)	863m 834s	782w(sh) 761m(sp) 730w(sp)	695m(b)	3200–3500s(b) (H_2O)
$Nd_2(CO_3)_x(OH)_{2(3-x)} \cdot nH_2O$	1495s(sp)	1425s(sp)	1078m(sp)	856m(sp) 810m(b)	723s(sp) 712m(sh)	697s(sp)	3450s(sp) 1805w 1770w } (OH)
$NdOHCO_3$ (orthorhombic)	1495	1450	1081	858 820	718	700	3450 388 356 } ν_{OH} ; 729 δ_{OH}
$NdOHCO_3$ (hexagonal)	1500	1440 1410	1100 1087	878 852 876 848 805 788	743 732	694	3615 3635 3465 3485 368 340 } ν_{OH} ; 668 620 } δ_{OH}

[a)] s = strong, m = medium, w = weak, sp = sharp, b = broad, sh = shoulder.

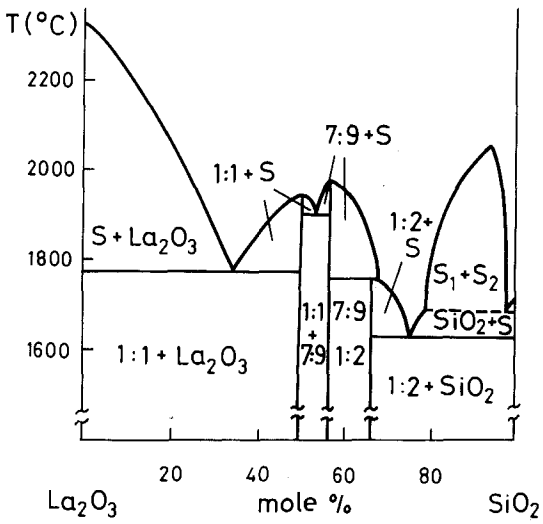

Fig. 28. Phase diagram for the system La_2O_3–SiO_2 after Felsche (1973).

Studies on rare earth silicates have mainly been directed towards syntheses involving high temperatures and pressures and X-ray structural characterization. Quite often the thermally and chemically stable structure has also been proved suitable for luminescent and other physical applications.

The present review will focus on the synthetic and structural studies as well as on applications. The mineralogical and geochemical aspects of the rare earth silicates are only briefly summarized as there is a comprehensive review in English on the silicate minerals (Gmelin, 1984b). The structural chemistry of the silicates has also been reviewed earlier but a lot of new data have accumulated since the appearance of the authorative review by Felsche (1973).

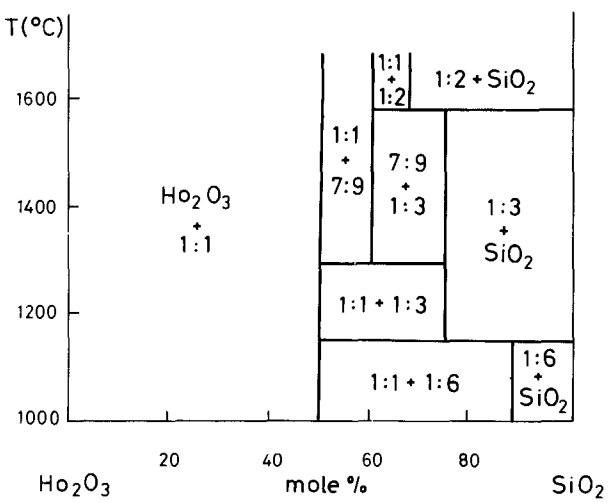

Fig. 29. Phase diagram for the system Ho_2O_3–SiO_2 indicating the solid phases formed in the temperature range 1000–1600°C (Montorsi, 1982).

4.2. *Oxyorthosilicates*

The 1 : 1 compound between R_2O_3 and SiO_2 is called rare earth oxyorthosilicate with a formula $R_2(SiO_4)O$ because it contains isolated SiO_4 tetrahedra and extra oxygen atoms that are not bonded to silicon. The oxyorthosilicates can be prepared directly by a solid state reaction between rare earth oxides and silicon dioxide. The reaction is slow and high temperatures are needed (1700°C) to get 100% conversion in a reasonable time (Keler and Kuznetsov, 1962). The kinetics of the reaction between Y_2O_3 and SiO_2 have been studied and the reaction appears to proceed via diffusion (Keler and Kuznetsov, 1962; Leskelä and Niskavaara, 1982). The polymorphic transitions of SiO_2 complicate the interpretation of the reaction mechanism, however.

The formation of rare earth silicates can be accelerated by the addition of flux material to the reaction mixture. The accelerators may be halides, carbonates, sulfates or oxides of alkali metals, earth alkaline metals, lead, zinc, bismuth, etc. (Leskelä and Niskavaara, 1981). The amount of the accelerator represents only a few percent of the total weight of the reaction mixture. For example, using alkali fluorides it is possible to reach a complete conversion to silicate in the temperature range 1000–1300°C (Watanabe and Nishimura, 1978; Leskelä and Niskavaara, 1981).

The growth of $R_2(SiO_4)O$ single crystals has been performed mainly by crystallization from a solution in a melt. Various compounds, similar to those mentioned as reaction accelerators, have been used as flux materials (Harris and Finch, 1965; Buisson and Michel, 1968; Wanklyn et al., 1974, 1975). Crystals of $Y_2(SiO_4)O$ of superior optical quality have been obtained from melts by zone refining in an optical furnace (Arsenev et al., 1972) and by the IKAN method (Bagdasarov et al., 1973). Ananeva et al. (1981) have prepared large single crystals of all rare earth oxyorthosilicates by the Czochralski method.

The crystal structure of the rare earth oxyorthosilicates has been determined from single crystals prepared using Bi_2O_3 as a flux material (Buisson and Michel, 1968). The oxyorthosilicates from praseodymium to terbium are isomorphic and crystallize in the monoclinic space group $P2_1/c$ with $Z = 4$. According to Ananeva et al. (1981) dysprosium can also have this structure type (A) too, but more often has another structure type (B). It is not clear whether or not lanthanum has a structure of its own. The unit cell dimensions of lanthanide oxyorthosilicates, except those of cerium and promethium compounds, are presented in table 9.

An accurate crystal structure determination of the A oxyorthosilicate-type has been carried out for $Gd_2(SiO_4)O$ (see fig. 30). Gadolinium atoms have two crystallographically different sites. The first Gd atom is 9-coordinated with eight oxygen atoms from the SiO_4^{4-} groups and one of the extra oxygens not bonded to silicon. The other Gd atom shows sevenfold oxygen coordination: three of the oxygen atoms are not silicon-bonded and the remaining four are silicate oxygens from different groups. The average Gd–O bond length to the isolated oxygen atoms is clearly shorter than that to the silicate oxygens. Four gadolinium atoms form a tetrahedron around the extra oxygen. The three-dimensional structure may be described in terms

TABLE 9
The unit cell dimensions of rare earth oxyorthosilicates (Felsche, 1973).

	a_0 (Å)	b_0 (Å)	c_0 (Å)	β (°)	V (Å^3)
$La_2[SiO_4]O$	9.420 (9)	7.398 (7)	7.028 (7)	108.21 (6)	465.2 (9)
$Pr_2[SiO_4]O$	9.253 (9)	7.301 (8)	6.934 (8)	108.15 (9)	445.1 (8)
$Nd_2[SiO_4]O$	9.250 (11)	7.258 (10)	6.886 (9)	108.30 (11)	439.3 (6)
$Sm_2[SiO_4]O$	9.161 (9)	7.112 (9)	6.821 (7)	107.51 (9)	424.4 (7)
$Eu_2[SiO_4]O$	9.142 (8)	7.054 (6)	6.790 (6)	107.53 (9)	417.9 (8)
$Gd_2[SiO_4]O$	9.131 (7)	7.045 (6)	6.749 (5)	107.52 (7)	414.0 (9)
$Tb_2[SiO_4]O$	9.083 (22)	6.990 (11)	6.714 (10)	107.31 (21)	406.1 (42)
	a (Å)	b (Å)	c (Å)	γ (°)	V (Å^3)
$Dy_2[SiO_4]O$	14.38 (2)	10.42 (2)	6.74 (1)	122.0 (3)	856.5 (72)
$Ho_2[SiO_4]O$	14.35 (2)	10.37 (2)	6.71 (1)	122.2 (3)	843.0 (38)
$Er_2[SiO_4]O$	14.32 (2)	10.35 (2)	6.69 (1)	122.3 (3)	836.7 (41)
$Tm_2[SiO_4]O$	14.302 (9)	10.313 (9)	6.662 (6)	122.21 (9)	828.5 (9)
$Yb_2[SiO_4]O$	14.28 (1)	10.28 (1)	6.653 (5)	122.2 (1)	824.0 (7)
$Lu_2[SiO_4]O$	14.254 (9)	10.241 (8)	6.641 (7)	122.20 (8)	819.3 (10)

of a two-dimensional network formed by the OR_4 tetrahedra with the silicate tetrahedra situated in the wide meshes of the net (Smolin and Tkachev, 1969).

The B-type oxyorthosilicate is also monoclinic with a space group of B2/b and there are eight formula units in a unit cell approximately double the size of the A-type cell. This structure type is characteristic of the heavier lanthanides (Dy $\cdots$ Lu) and yttrium. Crystal structures have been determined for the yttrium and ytterbium

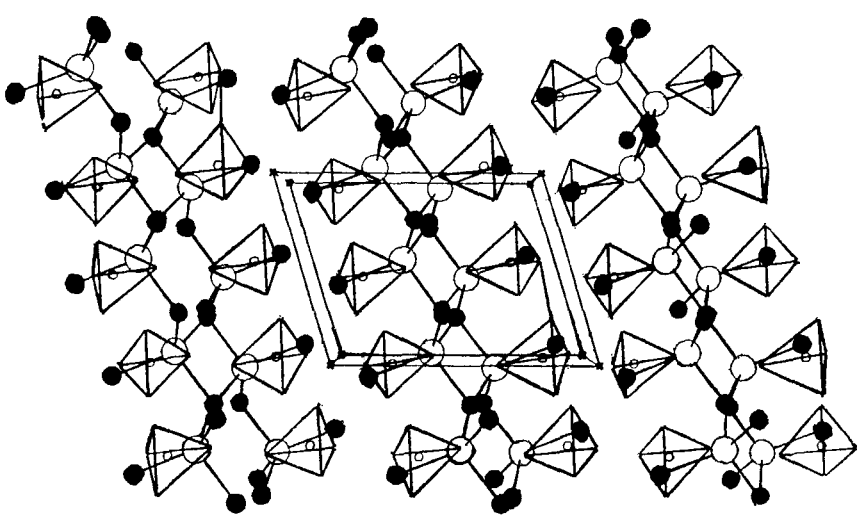

Fig. 30. The crystal structure of $Gd_2(SiO_4)O$ projected on the xz plane. Gd atoms are marked with solid circles (Felsche, 1973; Smolin and Tkachev, 1969).

compounds (Maksimov et al., 1968b; Smolin, 1969). The structure of the B-type closely resembles that of the A-type and can be described in terms of the arrangements of SiO_4^{4-} and OR_4 tetrahedra. The packing in the unit cell is not as efficient as in the A-type and the coordination around the heavy atoms is different. The two crystallographically independent rare earth atoms have coordination numbers 7 and 6. Each has two oxygen atoms not bonded to silicon in its coordination sphere, and five or four silicon-bonded oxygen atoms, respectively. The original suggestion for the coordination number for the first rare earth atom was 6, but accurate study of the structure showed that the number must be 7 although the seventh R–O distance is somewhat longer than the others (Maksimov et al., 1968b; Felsche, 1973).

In addition to the well-established A and B forms, Wanklyn et al. (1975) have found a new form of oxyorthosilicate for gadolinium, terbium and dysprosium. Single crystals have been obtained by the flux growth method from a mixture containing PbF_2, R_2O_3 and SiO_2. Only the X-ray powder patterns of these crystals have been published. It should also be noted that the new structure was obtained from only 4 of 40 batches prepared. Wanklyn et al. concluded that the structure must be somewhat unstable, yet upon heating to 1700°C the diffraction pattern remained unchanged. The crystals contained lead only as a trace impurity.

According to Warshaw and Roy (1964), Lazarev et al. (1968) and Ananeva et al. (1981), lanthanum oxyorthosilicate has a structure of its own that is not similar to the monoclinic A-type of the lighter lanthanides. Felsche, however (table 9), did not place lanthanum oxyorthosilicate into a separate group but included it among the A-type structures. As no structural study is available for $La_2(SiO_4)O$ the question of its separate structure cannot yet be resolved.

Reports of scandium oxyorthosilicates are limited to an IR spectroscopic study from the early 1960s (Lazarev et al., 1963).

4.3. *Binary silicates with oxyapatite structure*

Of all the binary and ternary rare earth silicates, those having the apatite-type structure form the only isostructural series comprising all lanthanides and yttrium (Felsche, 1972b). The rare earth silicates with oxyapatite structure can be prepared by solid state reaction by heating a mixture of rare earth and silicon oxide in molar proportions of 7 : 9. Fluxes can be used to accelerate the reaction and to lower the reaction temperature (Felsche, 1972b). Preparation of the oxyapatite silicates of the heavier rare earths (Tb $\cdots$ Lu) is difficult owing to the metastability of the compounds. The reaction product obtained from a $7R_2O_3 \cdot 9SiO_2$ mixture with Tb_2O_3, Gd_2O_3 and Dy_2O_3 always contains small amounts (up to 20%) of disilicates (Felsche, 1970). In the case of the heaviest lanthanides the product contains only a small amount of oxyapatite silicate, with the greatest part being oxyorthosilicate and disilicates (Buisson and Michel, 1968). The formation reaction proceeds as follows:

$$5(7R_2O_3 + 9SiO_2) \rightarrow 15R_2(SiO_4)O + 6R_2Si_2O_7 + 3R_{9.33}\square_{0.67}(SiO_4)_6O_2.$$

The binary rare earth silicates with oxyapatite structure crystallize in the hexagonal space group $P6_3/m$. The unit cell dimensions are presented in table 10. These

TABLE 10
Unit cell dimensions of $R_{9.33}\square_{0.67}(SiO_4)_6O_2$ (Felsche, 1973).

R	a_0 (Å)	c_0 (Å)	V (Å^3)
La	9.713	7.194	587.8
Ce	9.657	7.121	575.1
Pr	9.607	7.073	565.3
Nd	9.563	7.029	556.9
Sm	9.493	6.946	542.0
Eu	9.472	6.905	536.6
Gd	9.431	6.873	529.4
Tb	9.401	6.825	522.4
Dy	9.373	6.784	516.2
Ho	9.346	6.744	510.3
Er	9.324	6.686	503.4
Tm	9.300	6.666	499.3
Yb	9.275	6.636	494.4
Lu	9.260	6.621	491.6

silicates have been used as examples in studies of the changes in crystallographic properties of the lanthanides along the series and also for calculations of ionic radii of 9- and 7-coordinated rare earth ions (Felsche, 1973).

Single crystal X-ray studies have confirmed the cation-deficient structure $R_{9.33}\square_{0.67}(SiO_4)_6O_2$ (Kuzmin and Belov, 1965, Smolin and Shepelev, 1969). Taking into account all atoms in the unit cell the best way to describe the formula is

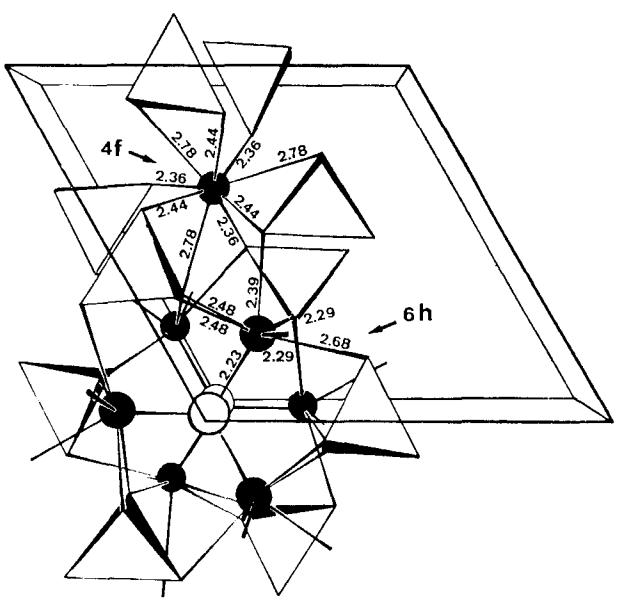

Fig. 31. A perspective view of $(Gd_{3.33}\square_{0.67})Gd_6(SiO_4)_6O_2$ along the b axis showing the bond distances around Gd atoms (Felsche, 1973).

$^{IX}(R_{3.33}\square_{0.67})^{VII}R_6(^{IV}Si^{IV}O_4)_6{}^{III}O_2$, where the superscript Roman numerals preceding the element symbol indicate the coordination number. Thus the structure contains two crystallographically different rare earth ions. The first rare earth ion is situated in a special position, occupying only $3\frac{1}{3}$ of the cation positions, and leaving $\frac{2}{3}$ cation holes per unit cell. It is surrounded by nine oxygen atoms all bonded to silicon atoms. The second rare earth ion is 7-coordinated to oxygen atoms, of which only one is not bonded to silicon. The bond distance between the rare earth ion and the oxygen atom not bonded to silicon is clearly shorter than the other R–O distances and is even shorter than the sum of the ionic radii (fig. 31). The extra oxygen atom, not bonded to silicon, is surrounded by three rare earth atoms with a bond angle of 120°.

4.4. *Disilicates*

Compounds with composition $R_2O_3 \cdot 2SiO_2$ are known for all binary rare earth silicate systems. Seven polymorphic forms have been observed at ambient pressure (fig. 32). All are of the type $R_2Si_2O_7$ with the exception of $R_4(Si_3O_{10})(SiO_4)$, which is stable only for the lanthanides of medium size (Felsche, 1972a).

The preparation of rare earth disilicates occurs by heating the mixture of corresponding oxides in molar ratio 1 : 2. The reaction is slow and the use of higher temperatures to accelerate the reaction is not possible when the polymorphic modifications of lower temperature are desired. Bocquillon et al. (1977) have used a precipitation method for the preparation of rare earth disilicates. A gel was precipi-

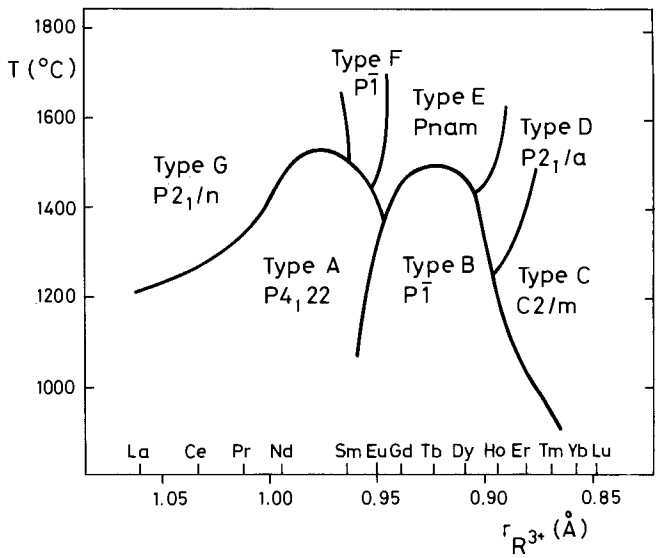

Fig. 32. The structure types of rare earth disilicates and the phase relationships between different polymorphs after Felsche (1970).

tated from the solution of rare earth chloride and silicic acid and a complete reaction to solid disilicate was achieved when the gel was heated a few hours at 1200°C.

Single crystals of rare earth disilicates can be prepared by extended annealing of powder samples (100 hr) in a suitable temperature range (1300–1600°C) (Felsche, 1970). Though the crystals obtained are purer than those prepared by flux methods, flux methods have been widely used in the preparation of large single crystals. The flux materials used are potassium fluoride (Bondar et al., 1965a), a mixture of lead oxide and fluoride (Wanklyn, 1978) and the mixtures ($PbO + PbF_2$)–($SiO_2 + MoO_3$) and Bi_2O_3–($SiO_2 + V_2O_5$); in some cases boron oxide and potassium fluoride have been employed as flux (Maqsood et al., 1979). Wanklyn pointed out the need for an excess of the acidic component in starting compositions for the flux growth of compounds consisting of a refractory oxide and an acidic oxide. Therefore Maqsood et al. used SiO_2 in excess. Rare earth disilicate single crystals have also been prepared by the Verneuil method (Smolin and Shepelev, 1970a) and by vapour flux technique (Wanklyn et al., 1974).

Ito and Johnson (1968), Warshaw and Roy (1964) and Bocquillon et al. (1973) used Greek letters to distinguish the polymorphic forms of rare earth disilicates. Felsche (1970, 1973) followed the nomenclature of the polymorphs of the rare earth sesquioxides, designating the various structure types by the capital letters A, B, C, D, E, F, G. This method of naming is followed in the present review.

The polymorphism of the rare earth disilicates in the temperature range 900–1800°C is presented in fig. 32. The lighter lanthanides (La · · · Nd) have two structure types: tetragonal A at lower temperatures and pseudoorthorhombic G at higher temperatures. The low-temperature form of $Ce_2Si_2O_7$ has not been obtained, even in reducing atmosphere in long-time annealing experiments (Felsche, 1973). $Sm_2Si_2O_7$ has the A-type as a low-temperature form but it has two high-temperature forms: triclinic F and pseudoorthorhombic G. A second low-temperature form of the rare earth disilicates, triclinic B, appears from europium to erbium. Thulium,

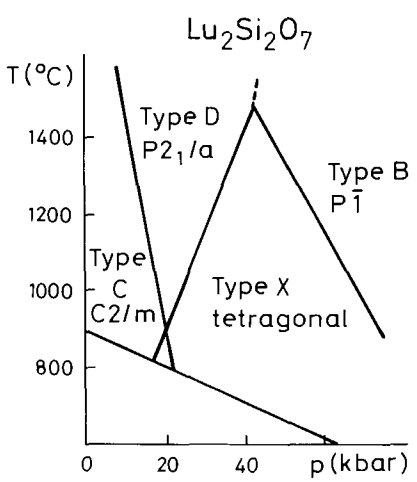

Fig. 33. The p–T phase diagram for $Lu_2Si_2O_7$ after Bocquillon et al. (1980).

ytterbium and lutetium have the disilicate of B-type too, but it forms only at high temperatures and pressures (Bocquillon et al., 1977). At lower temperatures $Eu_2Si_2O_7$ has the A-type in addition to the B-type. At higher temperatures it has two polymorphs: triclinic F and orthorhombic E. A third low-temperature disilicate form, monoclinic C, has been met for the heaviest lanthanides from holmium to lutetium. This structure type is the only one in the family of rare earth disilicates that is stable from room temperature up to the melting point of the compound. The high-temperature form, monoclinic D, appears at ambient pressure for the holmium and erbium compounds but at higher pressures also for $Tm_2Si_2O_7$, $Yb_2Si_2O_7$ and $Lu_2Si_2O_7$. The three last lanthanides have a high-pressure form of their own: tetragonal X (Bocquillon et al., 1977, Loriers et al., 1977). Eu, Ho, Tm, Yb and Lu have the greatest number of disilicate polymorphs, viz. four (fig. 33).

Felsche (1973) has investigated the phase transitions of different disilicates and observed a large time constant for the transitions between high- and low-temperature forms. Owing to the low rate of diffusion, mixed phases can be obtained over a wide temperature range. In cases where a single rare earth has three or four polymorphs, not all phase transitions could be observed.

4.4.1. *Structure type A (La $\cdots$ Eu)$_2Si_2O_7$*

The single crystal X-ray study of this structure type has been carried out for $Pr_2Si_2O_7$ (Felsche, 1971b), $Sm_2Si_2O_7$ (Smolin and Shepelev, 1970b) and $La_2Si_2O_7$ (Dago et al., 1980b), which crystallize in the tetragonal space group $P4_122$. The structure is similar to that found for β-$Ca_2P_2O_7$. The acentric structure consists of

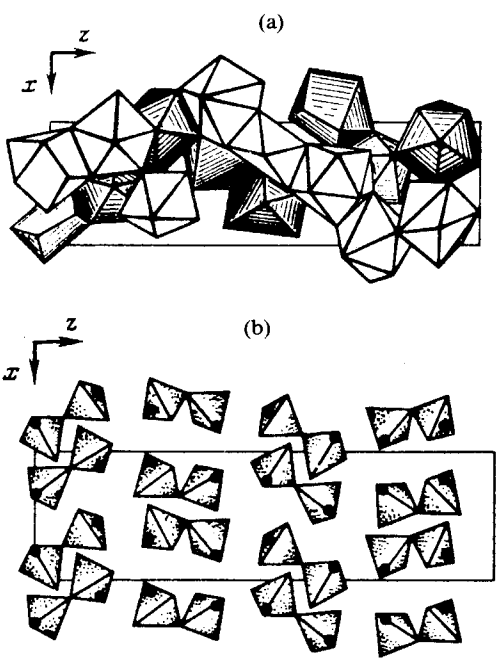

Fig. 34. The crystal structure of $La_2Si_2O_7$ (A-type) showing a packing diagram of the polyhedra (a) and a projection of the structure on the *xz* plane (b). Lanthanum atoms are indicated as solid black circles (Dago et al., 1980b).

isolated $Si_2O_7^{6-}$ double tetrahedra and rare earth ions arranged in four sheets perpendicular to the *c* axis and related through 90° rotation. Within each of the sheets the $Si_2O_7^{6-}$ units and the rare earth ions form parallel rows. The heavy atoms are attached to either side of the sheets and provide a connection to the adjacent sheet (fig. 34). The anion $Si_2O_7^{6-}$ tetrahedra pair is essentially of eclipsed configuration, but the ideal point symmetry is destroyed by the marked distortion of the tetrahedra in bond lengths and angles and by the twisting of the Si–O–Si in the double tetrahedra.

One unit cell contains four crystallographically different rare earth atoms, of which two have ninefold, one eightfold and one sevenfold coordination. The coordination polyhedra around the cations can best be described as monocapped square antiprism, dodecahedron and monocapped trigonal prism, respectively. Dago et al. (1980b) have observed in $La_2Si_2O_7$ only one 9-coordinated and two 8-coordinated rare earth atoms. The heavy atoms are usually coordinated to the terminal oxygen atoms of the $Si_2O_7^{6-}$ anion but the 7-coordinated and one of the 9-coordinated atoms have one bond to a bridging oxygen atom of the double tetrahedra.

4.4.2. *Structure type B (Eu · · · Er)$_4$(Si$_3$O$_{10}$)(SiO$_4$)*

Structures of the triclinic rare earth disilicate type B have been determined from single crystal data for the holmium compound (Felsche, 1972b). It contains isolated chain-like $Si_3O_{10}^{8-}$ groups and additional SiO_4 tetrahedra, whereas all the other rare earth disilicates contain double tetrahedra groups of either staggered or eclipsed configuration. The B-type rare earth disilicate is isotypic with the digermanates of the large rare earth cations.

The structure of holmium disilicate can be described in terms of holmium–oxygen polyhedra chains formed by edge-sharing, and the silicon atoms might be thought of as accommodated in the holes of these chains (fig. 35). All four heavy atoms in the structure have the coordination number 8. The coordination polyhedron is very

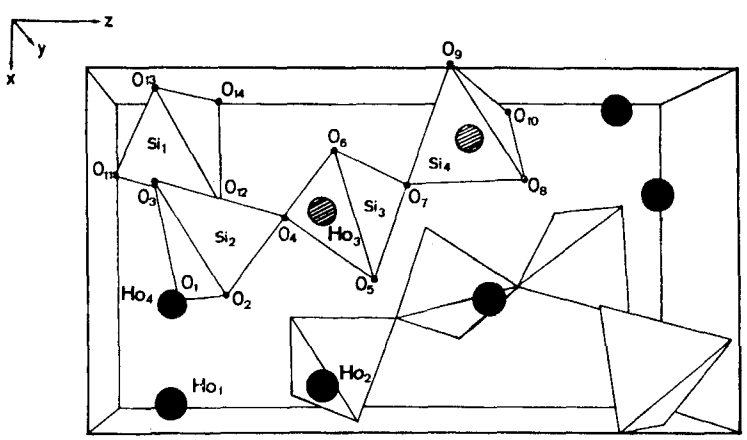

Fig. 35. The crystal structure of $Ho_4(Si_3O_{10})(SiO_4)$ (B-type) (Felsche, 1972).

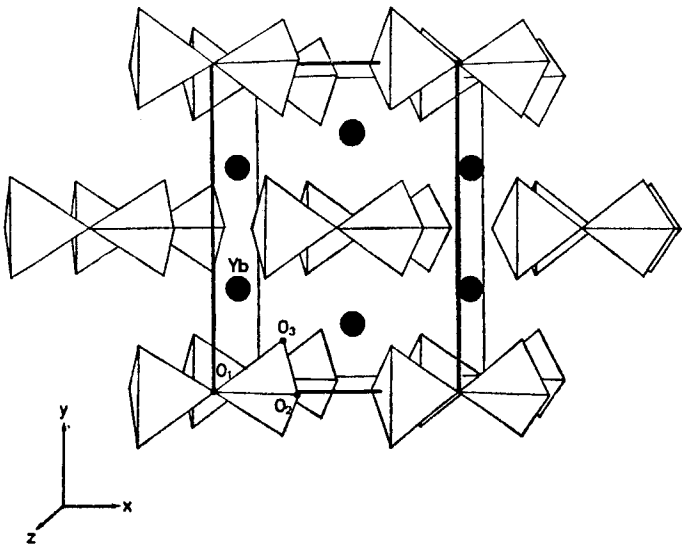

Fig. 36. The crystal structure of $Yb_2Si_2O_7$ (C- or the thortveitite-type; Felsche, 1973).

distorted. The RO_8 chains are connected together by corner-sharing at every second polyhedron of each chain.

The silicate tetrahedra belonging to the $Si_3O_{10}^{8-}$ chain are quite regular but the isolated SiO_4 tetrahedron is very distorted. The degree of distortion is the largest observed in rare earth silicate structures. The Si–O distances vary between 1.54 and 1.78 Å, while in other isolated SiO_4 tetrahedra the difference in distances is usually less than 0.1 Å.

4.4.3. *Structure type C (Ho · · · Lu)$_2$Si$_2$O$_7$*

The stability range of the disilicate type-C along the lanthanide series is extended beyond the smallest rare earth, lutetium, to scandium (Shannon and Prewitt, 1970b). This structure type is named after the corresponding scandium mineral, thortveitite.

The crystal structure has been solved for $Sc_2Si_2O_7$ (Cruickshank, et al., 1962) and $Yb_2Si_2O_7$ (Smolin and Shepelev, 1970a). The space group of these crystals is monoclinic C2/m. The oxygen atoms are packed in nearly hexagonal arrangement, with rare earth atoms in the octahedral and silicon atoms in the tetrahedral holes in alternating parallel layers (fig. 36). This arrangement of the atoms may be the reason for the high stability of the structure. Both the silicate tetrahedra and the RO_6 octahedra show a very low degree of distortion. In the $Si_2O_7^{6-}$ double tetrahedra the Si–O–Si angle is 180° by space group symmetry requirements.

4.4.4. *Structure type D (Ho · · · Er)$_2$Si$_2$O$_7$*

The crystal structure of monoclinic D-type rare earth disilicate was first presented for $Y_2Si_2O_7$ (Batalieva and Pyatenko, 1967) and later it was noticed that it is

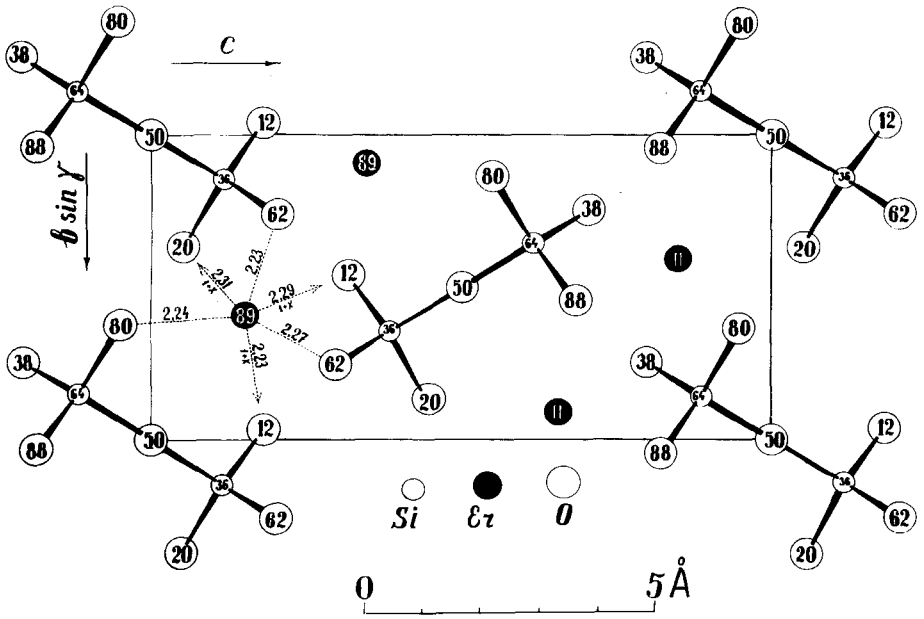

Fig. 37. The structure of $Er_2Si_2O_7$ (D-type) projected down the *a* axis (Smolin and Shepelev, 1970a).

isostructural with holmium and erbium disilicates (Smolin and Shepelev, 1970a). (See fig. 37.)

Some structural correlation can be seen in the D- and C-type rare earth disilicates. In both types the $Si_2O_7^{6-}$ double tetrahedra have a staggered orientation with a Si–O–Si angle of 180° and the rare earth atoms have sixfold coordination. In the D-type the octahedra around the rare earth atoms are strongly distorted, however. The structure of the D-type differs from that of the C-type in orientation of the Si_2O_7 groups relative to each other and their connection to the RO_6 octahedra, and the coordination of the heavy atoms does not result in a network as in the C-type but in a ribbon-like arrangement along the *b* axis.

4.4.5. *Structure type E (Eu ··· Ho)$_2$Si$_2$O$_7$*

This rare earth disilicate type was first determined for $Gd_2Si_2O_7$ (Smolin and Shepelev, 1970a) and later also for $Eu_2Si_2O_7$ (Felsche, 1973). (See fig. 38.) The orthorhombic structure can be described in terms of alternating layers of eclipsed Si_2O_7 double tetrahedra and rare earth atoms parallel to the [001] direction. The crystallographically independent heavy atoms have sevenfold oxygen coordination. The layer structure is generated by the coordination of the bridging oxygen atom and two terminal oxygen atoms of the $Si_2O_7^{6-}$ group to both rare earth atoms. The RO_7 polyhedra share two edges and three corners, causing a wave-like packing of the polyhedra parallel to the [010] direction.

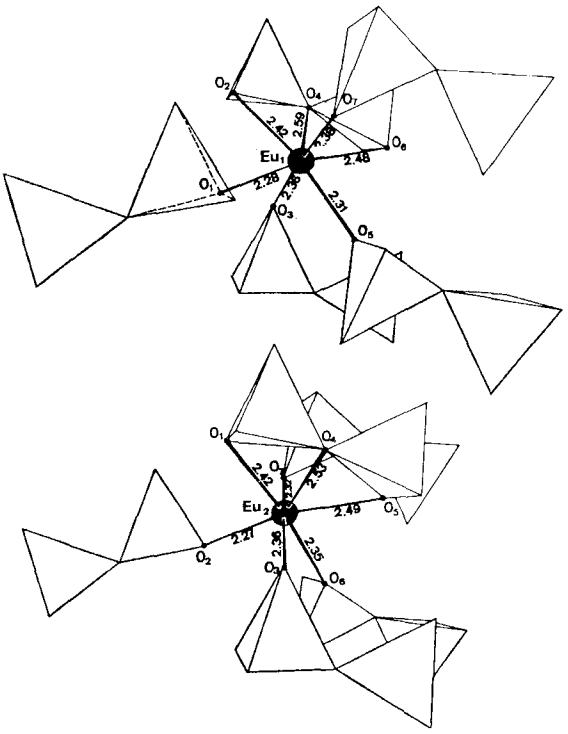

Fig. 38. The coordination of the disilicate anions to europium atoms in the E-type $Eu_2Si_2O_7$ (Felsche, 1973).

4.4.6. *Structure type F (Sm $\cdots$ Eu)$_2Si_2O_7$*

This is the only rare earth disilicate formed at ambient pressure for which crystallographic information is based only on the powder diffraction data. The preparation of single crystals has not been successful. However, the cell dimensions and the diffraction intensities are closely similar to those of the structure type G (Felsche, 1970) and it may be assumed that there is a structural similarity between the F and G-types.

4.4.7. *Structure type G (La $\cdots$ Sm)$_2Si_2O_7$*

The structure type G has been determined for $Nd_2Si_2O_7$ as orthorhombic (Smolin and Shepelev, 1970a) and for $Pr_2Si_2O_7$ as monoclinic with $\beta = 90°$ (pseudoorthorhombic) (Felsche, 1971b). Otherwise the structural determinations are in good internal agreement. The structure is built of Si_2O_7 columns packed back-to-back. The Si–O–Si angle is only 131°. The rare earth atoms are 8-coordinated with a markedly distorted coordination polyhedra. The RO_8 polyhedra have an arrangement similar to that of fluoride-type rare earth dioxides.

4.4.8. *Structure type X (Tm $\cdots$ Lu)$_2Si_2O_7$*

The most recently discovered structure type of rare earth disilicate is tetragonal X. It has been prepared at high pressures and at quite low temperatures from a mixture

of $R_2Si_2O_7$, $R_2(SiO_4)O$ and SiO_2 (Bocquillon et al., 1977). The p–T phase diagrams of the disilicates of the heavier lanthanides have also been presented. The structural information available for the X-type is limited to the unit cell parameters.

4.5. *Higher silicates*

Montorsi (1982) has studied the phase equilibrium relations in the Ho_2O_3–SiO_2 system within the temperature range 1100–1600°C. Four silicates were identified: the previously known monoclinic 1 : 1 and hexagonal 2 : 3 compounds and two new phases having compositions 1 : 3 and 1 : 6. Two crystalline modifications have been found for $Ho_2O_3 \cdot 3SiO_2$: one stable between 1150 and 1250°C and the other stable above 1250°C. Both have a monoclinic structure according to powder diffraction data. $Ho_2O_3 \cdot 6SiO_2$ is only stable up to 1150°C and its structure is unknown.

4.6. *Ternary rare earth silicates*

Mixed cation rare earth silicates are known for all three types of rare earth silicates: ortho-, oxyapatite- and disilicates. The second cation is usually alkali or earth alkaline metal but other divalent metals like Zn, Cd and Pb are suitable for apatite structures. The easiest way to prepare mixed silicates is through solid state reaction of the corresponding oxides at temperatures of 1000–1300°C (Harris and Finch, 1965; Cockbain and Smith, 1968). Compounds decomposing to oxides upon heating can also be used as starting material. The single crystals of mixed cation silicates are obtained by hydrothermal methods (Chichagov et al., 1969b; Maksimov et al., 1969), by flux growth methods using alkali halides or wolframates in long-time slow cooling experiments (Bondar et al., 1965b; Wanklyn et al., 1975; Ito, 1968; Fedorov et al., 1975a) or by crystal pulling methods (Hopkins et al., 1971b).

4.6.1. *Ternary $RMSiO_4$ silicates*

Rare earths silicates with univalent cations in molar ratio 1 : 1 are known for lithium and sodium. Their preparation has been carried out by hydrothermal methods at high pressure in the system M_2O–R_2O_3–SiO_2–H_2O (Chichagov et al., 1969b). Analogous potassium-containing compounds have not been obtained during corresponding experiments.

Three different structure types are known for the sodium compound $RNaSiO_4$. Structurally all types are related to polymorphic Ca_2SiO_4, which supports the general $Na^{1+}R^{3+} \leftrightarrow 2Ca^{2+}$ substitution phenomenon often described in geochemical processes.

Cerium, praseodymium and neodymium form ternary silicates of the first type with sodium. The structure is orthorhombic with space group $Pna2_1$. The unit cell is large because $Z = 12$. The crystal structure of $NaNdSiO_4$ has been solved from X-ray diffraction film data and shown to contain olivine-like ribbons constructed of a core of R polyhedra and edges of Na polyhedra (Chichagov and Belov, 1968). The ribbons are linked by SiO_4 tetrahedra and by shared corners (fig. 39). The three crystallographically different rare earth atoms have eightfold coordination. The use

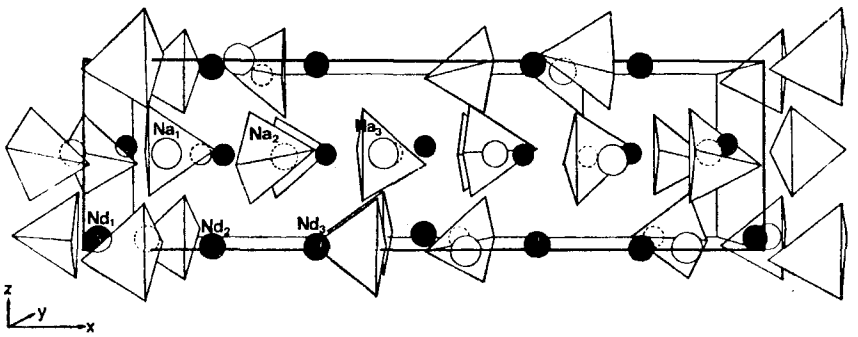

Fig. 39. A perspective view of the structure of $NaNdSiO_4$ showing the unit cell contents (Chichagov and Belov, 1968; Felsche, 1973).

of high pressure also allows the preparation of the first type structures with smaller ions such as yttrium (Chenavas et al., 1969).

The second type of $RNaSiO_4$ compound exists for lanthanides from neodymium to holmium. The structure is tetragonal, with space group I4/m or $I\bar{4}$. Structure refinement has been carried out for the Sm compound from film data and for the Gd compound from single crystal data (Chichagov et al., 1967; Fallon and Gatehouse,

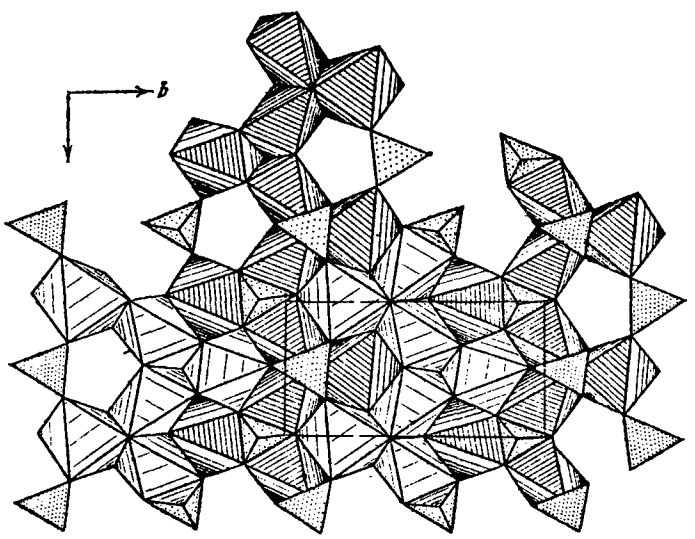

Fig. 40. A packing diagram of $NaYSiO_4$ projected on the *yz* plane. The olivine bonds at different levels are indicated by different shadings (Demianets et al., 1982).

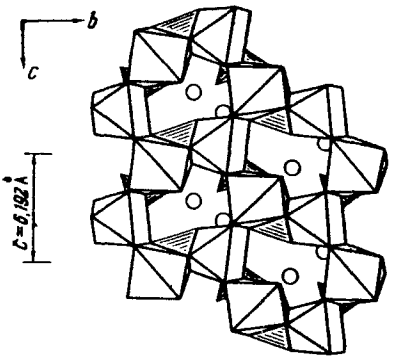

Fig. 41. A perspective view of the structure of $LiYSiO_4$ on the *yz* plane showing the arrangement of YO_7 and SiO_4 polyhedra and the location of Li ions (circles) (Nikolskii et al., 1976).

1982). The low-temperature phase of $NaYSiO_4$ appears to be of this type too (Shannon et al., 1980). The second harmonic generation test of $NaGdSiO_4$ implies that the space group is noncentrosymmetric $I\bar{4}$ rather than centrosymmetric I4/m (Shannon et al., 1980). The structure comprises 8-coordinated R polyhedra sharing corners with three and edges with two SiO_4 tetrahedra, as well as faces with two and corners with three other RO_8 polyhedra (fig. 40). The sodium atoms have 7 and 10 coordination (Fallon and Gatehouse, 1982). The structure descriptions in different reports are somewhat contradictory (Chichagov et al., 1967; Avetisyan et al., 1970; Fallon and Gatehouse, 1982).

A third group of sodium rare earth silicates is formed by the smallest lanthanides from erbium to lutetium and yttrium. The original description of the structures as $Pbn2_1$ (Maksimov et al., 1967) was later changed to $Pcn2_1$, for $NaYSiO_4$ (Merinov et al., 1979) after a different choice of axes. This structure is isostructural with Ca_2SiO_4, but with the octahedrally coordinated calcium atoms replaced by sodium and rare earth atoms.

The mixed cation lithium compounds $RLiSiO_4$, are hexagonal (La $\cdots$ Dy) and orthorhombic (Ho $\cdots$ Lu, Y). Blasse and deVries (1976a) have suggested that the latter phase is isostructural with the sodium compounds of C-type, but Nikolskii et al. (1976) reported from single crystal work that $LiYSiO_4$ is monoclinic, with space group $P2_1/b$ (see fig. 41). Possibly the crystal used by Nikolskii et al. was a high-pressure form of the compound, since it was prepared hydrothermally at high pressure. Blasse and deVries heated the mixture of oxides and Li_2CO_3 at ambient pressure.

The crystal structure of $LiScSiO_4$ is very interesting because it is isotypic with olivines and closely resembles the Mg_2SiO_4 structure (Steele et al., 1978). It is the first known univalent–trivalent silicate with an olivine structure.

4.6.2. *Ternary silicates with oxyapatite structure*

The following types of ternary rare earth oxyapatite silicates are known: $MR_9(SiO_4)_6O_2$ (M = Li, Na, K), $M_2R_8(SiO_4)_6O_2$ (M = Mg, Ca, Sr, Ba, Mn, Zn, Cd, Pb) and $M_4R_6(SiO_4)_6(OH)_2$ (M = Ca, Sr, Ba, Mn, Pb). In addition, several

TABLE 11
The unit cell dimensions of the compounds $LiR_9(SiO_4)_6O_2$ and $NaR_9(SiO_4)_6O_2$ (Felsche, 1972).

$LiR_9[SiO_4]_6O_2$			$NaR_9[SiO_4]_6O_2$		
a_0 (Å)	c_0 (Å)	V (Å^3)	a_0 (Å)	c_0 (Å)	V (Å^3)
9.681	7.160	581.2	9.687	7.180	583.5
9.623	7.091	568.7	9.628	7.117	571.3
9.575	7.040	558.8	9.580	7.080	562.6
9.529	6.994	550.1	9.535	7.027	553.4
9.464	6.918	536.6	9.472	6.943	539.6
9.437	6.876	530.3	9.456	6.912	535.2
9.413	6.852	525.8	9.419	6.878	528.4
9.381	6.803	522.0	9.390	6.840	522.2
9.362	6.769	513.9	9.362	6.800	516.2
9.337	6.736	508.6	9.337	6.760	510.4
9.316	6.696	503.3	9.321	6.728	506.2
9.301	6.672	499.8	9.310	6.688	502.0
9.270	6.637	493.8	9.300	6.661	498.8
9.265	6.615	490.9	9.290	6.635	495.9

compounds are known where a part of the silicate is replaced by borate or phosphate ions (Ito, 1968). All the structures are similar to those described for binary rare earth oxyapatite silicates (see section 4.3). In the Russian papers the reduced formula $MR_4(SiO_4)_3O$ is used for the ternary compounds with divalent cations.

Ternary oxyapatite compounds with sodium and lithium exist for all rare earths (Felsche, 1973). Their unit cells are given in table 11. Information about the corresponding potassium compounds is scanter. The oxyapatite structure has two cation sites: 9-coordinated 4f and 7-coordinated 6h. In the mixed rare earth silicates it is not clear in which position the alkali and earth alkaline atoms lie or whether they are randomly distributed in both positions. The single crystal studies with X-ray diffraction do not show any disorder of the cations. The problem has been investigated by looking for the changes in unit cell dimensions of oxyapatite compounds along the lanthanide series. It has been suggested that lithium occupies the 6h position. In sodium compounds where $r_{Na^+} > r_{R^{3+}}$ sodium lies at the 4f position; otherwise it is at the 6h position (Felsche, 1973). This rule is confirmed with $NaY_9(SiO_4)_6O_2$ single crystals where Y occupies the 6h sites and Na and Y together the 4f sites (Gunawardane et al., 1982b). Pushcharovskii et al. (1978a) have concluded, on the basis of single crystal data, that in the structure of $KNd_9(SiO_4)_6O_2$ the potassium atoms occupy the 9-coordinated 4f position.

The ternary rare earth oxyapatite silicates with divalent cations are listed in table 12. The cation ordering in these compounds has likewise been a problem. Felsche (1973) has drawn conclusions about the cation distributions on the basis of changes in the unit cell dimensions, emphasizing the role of the ionic radii of the cations (fig. 42). Urusov and Khudolozhkin (1974), on the other hand, have shown by energetic analysis that the type of cation–anion bond is more important than the size of the

TABLE 12
Ternary rare earth oxyapatite silicates of type $M_2R_8(SiO_4)_6O_2$ and $M_4R_6(SiO_4)_6(OH)_2$ for which unit cell data are available.

Formula	R[a)]	Reference
$Mg_2R_8(SiO_4)_6O_2$	La · · · Er, Y	Ito, 1968
$Ca_2R_8(SiO_4)_6O_2$	La · · · Lu, Y	Ito, 1968; Fedorov et al., 1975a; Bondar et al., 1974
$Sr_2R_8(SiO_4)_6O_2$	La · · · Er, Y	Ito, 1968
$Ba_2R_8(SiO_4)_6O_2$	La · · · Sm	Ito, 1968
$Mn_2R_8(SiO_4)_6O_2$	La · · · Er, Y	Ito, 1968
$Zn_2R_8(SiO_4)_6O_2$	La · · · Ho	Fedorov et al., 1976
$Cd_2R_8(SiO_4)_6O_2$	La · · · Yb	Fedorov et al., 1975b
$Pb_2R_8(SiO_4)_6O_2$	La · · · Dy, Y	Ito, 1968
$Ca_4R_6(SiO_4)_6(OH)_2$	La · · · Lu, Ce, Y	Ito, 1968
$Sr_4R_6(SiO_4)_6(OH)_2$	La · · · Lu, Ce, Y	Ito, 1968
$Ba_4R_6(SiO_4)_6(OH)_2$	Nd · · · Dy	Ito, 1968
$Mn_4R_6(SiO_4)_6(OH)_2$	La · · · Er, Y	Ito, 1968
$Pb_4R_6(SiO_4)_6(OH)_2$	La · · · Lu, Ce, Y	Ito, 1968

[a)] Data for Ce, Pr, Tb and often for Eu are lacking.

cation for distribution. Schroeder and Matthew (1978) have solved the crystal structure of $Ca_2La_8(SiO_4)_6O_2$ and established that, in spite of their smaller size, the calcium atoms occupy a part of the 9-coordinated 4f sites.

Besides the compounds presented in table 12, rare earths form numerous mixed cation oxyapatite silicates where the silicate anion is partly replaced by phosphate or borate anion (Ito, 1968). Some mixed systems of rare earths with di- and tetravalent lead are known as well and they also have the oxyapatite structure. One unusual structure of ternary lead compound has been reported by Ansell and Wanklyn (1976). The formula of this compound is $Er_6Pb_3(SiO_4)_6$ and its structure is apatite-like but without any extra oxygen atoms. The lead atoms partially fill the 4f positions.

4.6.3. *Ternary rare earth disilicates*

The rare earth elements form mixed disilicates with alkali metals of $M_3RSi_2O_7$. There are two different structure types – hexagonal and orthorhombic. $K_3EuSi_2O_7$ is the only example that has been found of the first type (Bondar et al., 1965b). Mixed disilicates with sodium and lanthanides from erbium to lutetium, yttrium and scandium exhibit the second structure type (Maksimov et al., 1969). The structure is similar to that of the sheet-like silicates of vermiculite, nontronite, etc., and consists of isolated Si_2O_7 groups joined together by NaO_5, NaO_4 and RO_6 polyhedra (Skshat et al., 1969) (fig. 43).

$Na_3YSi_2O_7$ has a hexagonal high-pressure form, which has been prepared hydrothermally at 400°C and a pressure of 100 MPa (Shannon et al., 1980; Merinov et al., 1981). Part of the yttrium atoms can be replaced by scandium atoms and the

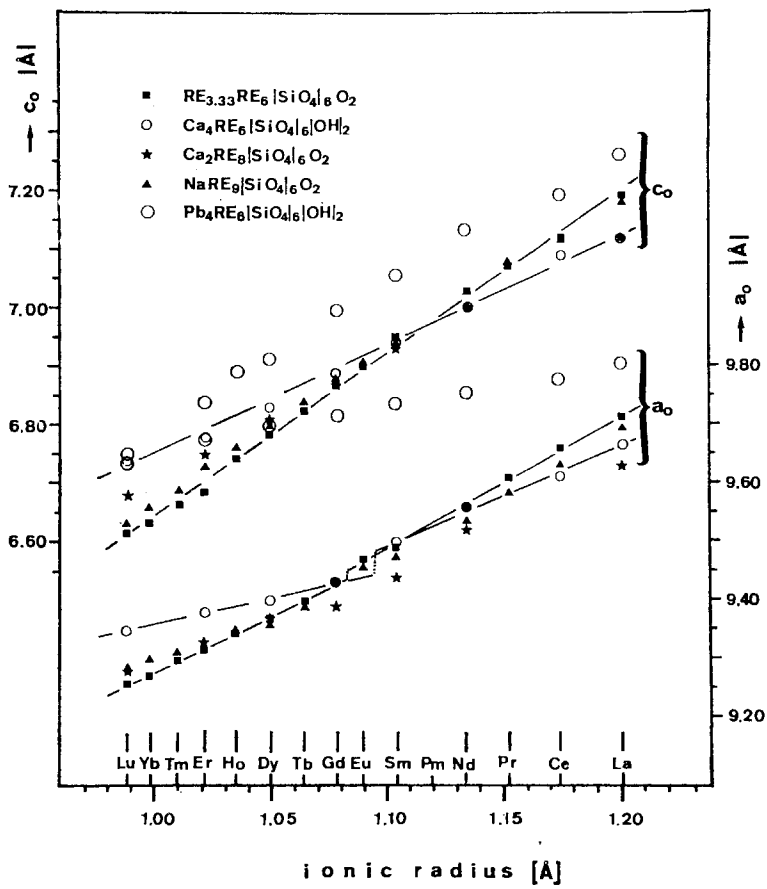

Fig. 42. Unit cell dimensions vs. ionic radii in some ternary rare earth silicates having oxyapatite structure (Felsche, 1973).

structure is still hexagonal (Maksimov et al., 1979b; Zhdanova et al., 1980). The cations are randomly ordered.

A new type of mixed cation disilicate has been reported by Ragimov et al. (1980). Besides univalent potassium, the compound contains divalent cobolt, leading to the formula $KHoCoSi_2O_7$. The crystals have been prepared at high pressure. The structure is monoclinic and differs from the structure of the ternary alkali rare earth disilicates.

4.6.4. *Other ternary rare earth silicates*

The sodium silicates of type $Na_3RSi_3O_9$ (R = Gd, Dy, Y) show structural similarities with $Na_4CaSi_3O_9$ (Shannon et al., 1980). Their unit cell is orthorhombic ($P2_12_12_1$) and the structure contains $Si_3O_{10}^{8-}$ groups that are further joined into $Si_{12}O_{36}^{24-}$ rings (Maksimov et al., 1980a).

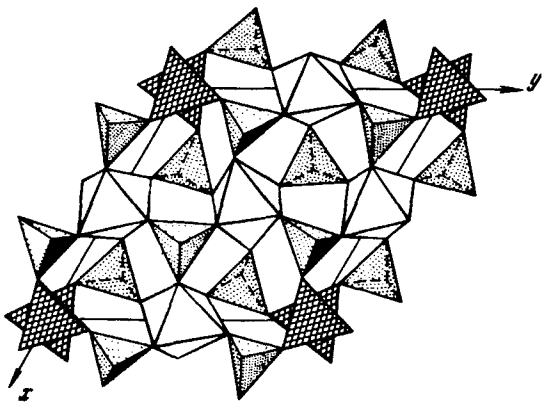

Fig. 43. A perspective view of the structure $Na_3(Y, Sc)Si_2O_7$ projected on the *xy* plane. The figure shows only the isolated RO_6 octahedra that are linked by $Si_2O_7^{6-}$ double tetrahedra. The polyhedra around the sodium atoms are omitted (Maksimov et al., 1979b).

TABLE 13
The unit cell dimensions of hexagonal compounds with $Na_5YSi_4O_{12}$ structure (Shannon et al., 1978; Maksimov et al., 1979a).[a]

Compound	*a* (Å)	*c* (Å)
$Na_5ScSi_4O_{12}$	21.672(3)	12.437(2)
$Na_5LuSi_4O_{12}$	21.920(2)	12.576(2)
$Na_5YbSi_4O_{12}$	21.940(2)	12.567(2)
$Na_5TmSi_4O_{12}$	21.958(3)	12.579(2)
$Na_5ErSi_4O_{12}$	21.989(2)	12.610(2)
$Na_5HoSi_4O_{12}$	22.034(2)	12.607(2)
$Na_5YSi_4O_{12}$	22.035(1)	12.604(1)
$Na_5DySi_4O_{12}$	22.058(2)	12.623(3)
$Na_5TbSi_4O_{12}$	22.083(1)	12.627(1)
$Na_5GdSi_4O_{12}$	22.126(5)	12.650(4)
$Na_5SmSi_4O_{12}$	22.164(4)	12.661(4)
$Ag_5YSi_4O_{12}$	22.175(1)	12.859(1)
$Ag_5GdSi_4O_{12}$	22.269(2)	12.912(1)

[a] Slightly different values for the Sc, Lu, Yb and Y compounds have been reported by Merinov et al. (1978a).

Hexagonal sodium rare earth silicates, $Na_5RSi_4O_{12}$, are known for the heavier lanthanides (Sm $\cdots$ Lu) as well as for yttrium and scandium (Shannon et al., 1978). They are isostructural with the corresponding germanates. The sodium atoms in the structure can also be replaced by silver atoms (table 13). The crystal structures of sodium metasilicates have been presented for yttrium (Maksimov et al., 1973; Maksimov and Belov, 1984), lutetium (Merinov et al., 1978a) and scandium compounds (Merinov et al., 1980a). The structure is characterized by SiO_4 tetrahedra joined into puckered $Si_{12}O_{36}^{24-}$ rings, separated by Na tetrahedra and octahedra and stacked into large rigid columns parallel to the *c* axis (fig. 44). The columns are linked together by RO_6 octahedra. Part of the sodium atoms are tightly bound in the

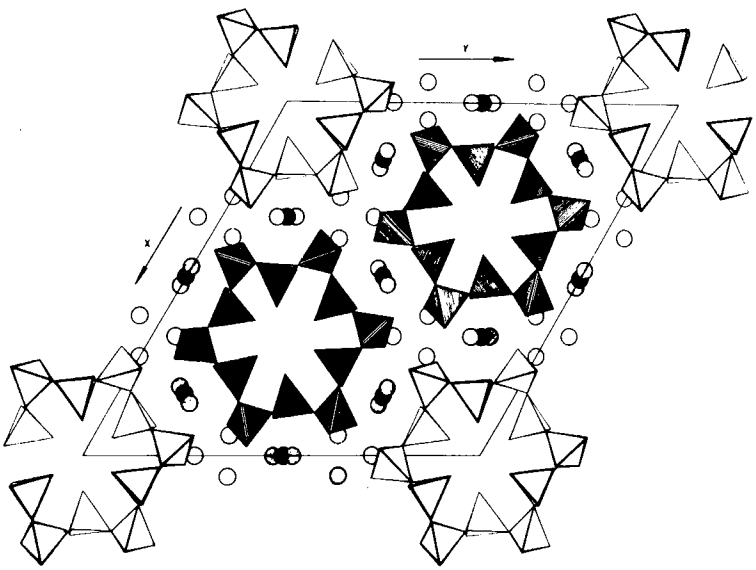

Fig. 44. A projection of the $Na_5YSi_4O_{12}$ structure on the xy plane showing the location of $Si_{12}O_{36}$ rings, YO_6 octahedra and the mobile Na^+ ions. Unshaded $Si_{12}O_{36}$ rings are located at $z = 0$ and $1/2$, medium shaded at $z = 1/6$ and $2/3$, and fully shaded at $z = 1/3$ and $5/6$ (Shannon et al., 1978).

columns and are immobile, but it is difficult to locate the rest of the sodium atoms. Possibly they are moving freely in the large open channels contained in the structure. The ionic conductivity of these compounds is high (Beyeler and Hibma, 1978; Shannon et al., 1978; Maksimov et al., 1979a). The conductivity mechanism has been presented by Maksimov et al. (1982).

Besides the compounds presented above, the compound $Na_2O \cdot R_2O_3 \cdot 12SiO_2$, also written as $NaRSi_6O_{14}$ (Dimitrova et al., 1976), exists in the system Na_2O–R_2O_3–SiO_2–H_2O (R = La $\cdots$ Nd) at 400–550°C and at 60–120 MPa. The lattice is orthorhombic I. The crystal structure of the praseodymium compound has been solved by Karpov et al. (1976). The structure is characterized by a wall of $(Si_3O_7)_n^{2n-}$ with a thickness of three SiO_4 tetrahedra perpendicular to the z axis. The walls are tied together by rare earth octahedra and sodium polyhedra.

The high-pressure system of neodymium silicate containing potassium produces crystals of formula $K_3NdSi_6O_{15}$ (Pushcharovskii et al., 1977). The unit cell is orthorhombic (Pbam). The structure consists of layers of $(Si_2O_5)_n^{2n-}$ parallel to the (101) plane with a chain of $(Si_6O_{17})_n^{10n-}$ along the x axis. The neodymium atoms are octahedrally coordinated and lie between the layers. A ternary silicate of the same composition, $Na_2LiYSi_6O_{15}$, is formed upon crystallization of its glassy mixture at ambient pressure. The structure is built of corrugated double silicate chains that have a six-tetrahedral repeat in the c direction. LiO_4, YO_6 and NaO_n polyhedral chains link the silicate chains to form a three-dimensional structure (fig. 45) (Gunawardane et al., 1982a).

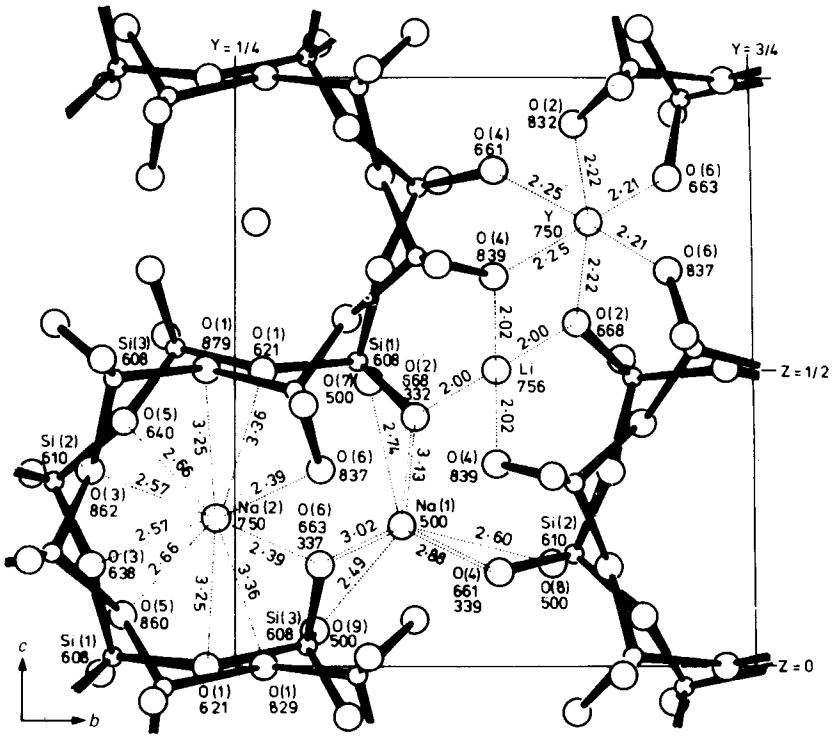

Fig. 45. Partial structure of $Na_2LiYSi_6O_{15}$ projected along the *a* axis showing the coordination of the Li, Na, Y and Si atoms (Gunavardane et al., 1982a).

Hydrated silicates form in M_2O–R_2O_3–SiO_2–H_2O systems particularly at higher pressures. The crystal structures of the following hydrated mixed cation silicates are known: $K_3YSi_3O_8(OH)_2$ (Maksimov et al., 1968a), $Na_2Pr(SiO_4)(OH)$ (Pushcharovskii et al., 1976), $NaNdSi_6O_{13}(OH)_2 \cdot nH_2O$ (Karpov et al., 1977b), $K_3Sc_2(Si_4O_{12})(OH)_2$ (Pyatenko et al., 1979), $Na_2CeSi_6O_{16}(OH) \cdot nH_2O$ (Shumyatskaya et al., 1980) and $K_8Yb_3(Si_6O_{16})_2(OH)$ (Pushcharovskii et al., 1981). The first compound is built of $Si_3O_8(OH)_2^{6-}$ groups; the second has olivine-like structure; the third is built of $Si_2O_5^{2-}$ and $Si_6O_{17}^{10-}$ groups; and the fourth has $Si_4O_{12}^{9-}$ rings. The fifth structure contains chains of SiO_4^{4-} and the last of $Si_6O_{16}^{8-}$ rings (fig. 46). In the structures the rare earth ions are 6-, 7- or 8-coordinated.

With potassium silicate tetravalent cerium forms crystals of formula $K_2CeSi_6O_{15}$. The structure consists of a $(Si_2O_5)_n^{2n-}$ framework. Cerium is octahedrally coordinated. Large channels in the structure give it a zeolite character (fig. 47) (Karpov et al., 1977a).

In addition to $Na_3ScSi_2O_7$ and $Na_5ScSi_4O_{12}$ the sodium–scandium silicate system includes crystalline phases with formulas $NaScSi_2O_6$ (Ito and Frondell, 1968) and $Na_4Sc_2Si_4O_{13}$ (Maksimov et al., 1980b). $NaScSi_2O_6$, as well as the corre-

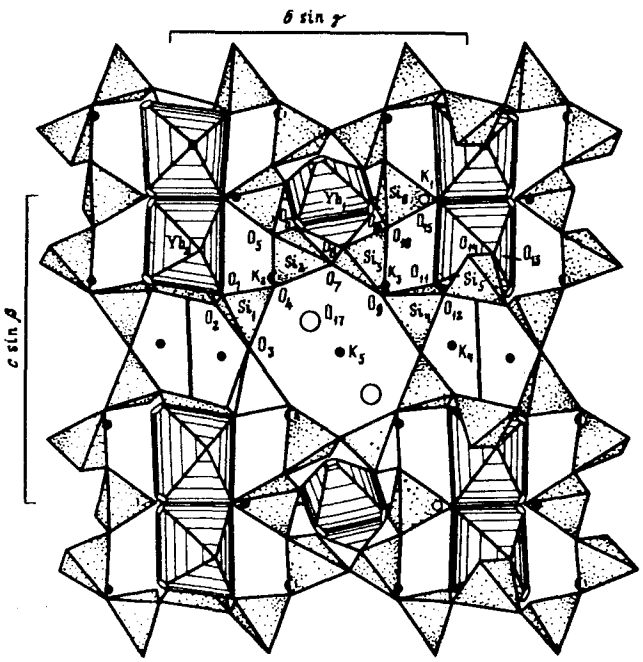

Fig. 46. The structure of $K_8Yb_3(Si_6O_{16})_2(OH)$ projected along the *a* axis. The hydroxide ions are marked with large open circles and K^+ ions with solid circles. The YbO_6 octahedra are hatched while SiO_4 tetrahedra are dotted (Puscharovskii et al., 1981).

sponding lithium compound $LiScSi_2O_6$, have the monoclinic alkali pyroxene structure (fig. 48) (Hawthorne and Grundy, 1973, 1977). $Na_4Sc_2Si_4O_{13}$ is orthorhombic and it contains $Si_4O_{13}^{10-}$ chains and $Sc_2O_{10}^{14-}$ double octahedra.

The main phase in ternary silicates of the rare earths with divalent cations is the oxyapatite structure, for example $M_2R_8(SiO_4)_6O_2$ or $M_4R_6(SiO_4)_6(OH)_2$. Ito (1967) has succeeded in hydrothermally synthesizing magnesium rare earth silicates,

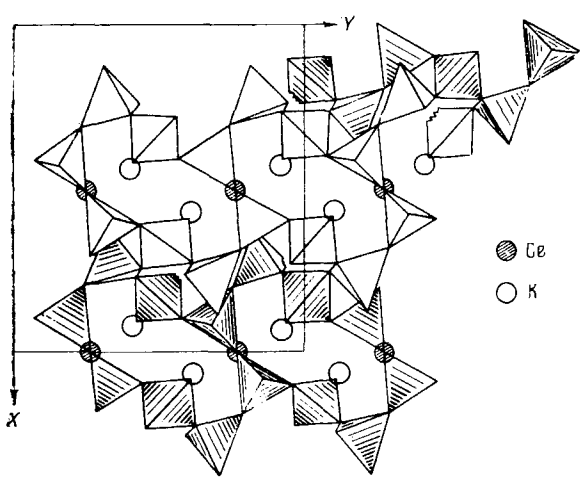

Fig. 47. A projection of the structure of $K_2CeSi_6O_{15}$ on the *xy* plane. The octahedrally coordinated Ce(IV) ions and the 7-coordinated K^+ ions are marked with shaded and open circles, respectively (Karpov et al., 1977a).

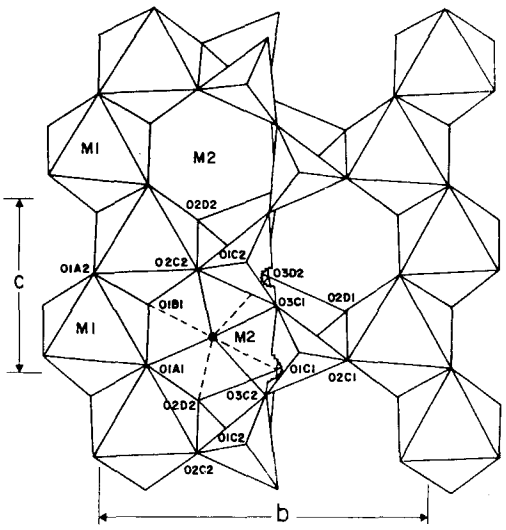

Fig. 48. An *a* axis projection of $LiScSi_2O_6$ having pyroxene structure (Hawthorne and Grundy, 1977).

$Mg_3R_2(SiO_4)_3$. This cubic garnet structure is stable only for smaller rare earths (Ho $\cdots$ Lu, Y). The crystals prepared by Ito were too small for single crystal studies and therefore the exact structure is unknown. Andreev et al. (1975) have reported on triclinic $Ca_3R_2Si_6O_{18}$ ($R = Er \cdots Lu$) compounds but their exact structure is unknown. Ansell and Wanklyn (1975) have determined the crystal structure of monoclinic $Er_4PbSi_4O_{17}$, which contains both $Si_3O_{10}^{8-}$ and $Si_2O_7^{6-}$ groups. The erbium atoms are 6-coordinated. A similar structure has been found for dysprosium and yttrium (Wanklyn et al., 1975).

With trivalent aluminium a hydrated $R_2Al(SiO_4)_2(OH)$ is formed at 800°C and at pressure of 150 MPa (Jarchow et al., 1982). The compound is also known as mineral törnebohmite (Shen and Moore, 1982). The structure is monoclinic $P2_1/c$. According to Bettermann et al. (1983) aluminium can be replaced by iron without structural change.

4.7. *Silicates containing divalent rare earths*

In the binary system $RO-SiO_2$ the existence of silicates of composition R_2SiO_4 and $RSiO_3$ has been established by X-ray diffraction and IR studies for Sm, Eu and Yb. In addition, Eu and Yb form the silicates $R_3Si_2O_7$ and $R_3(SiO_4)O$ (fig. 49) (Bondar et al., 1965c, 1967; Shafer, 1965). A strong similarity to the alkaline earth silicates has been found. Single crystal work has been carried out for the dimorphic Eu_2SiO_4 (Busch et al., 1970; Felsche, 1971a; Marchand et al., 1978) and for $Eu_3(SiO_4)O$ (Felsche, 1973).

The low-temperature form of Eu_2SiO_4 is monoclinic and single crystals can be prepared by chemical transport reaction (Kaldis and Verreault, 1970). The structure that is related to that of β-Ca_2SiO_4 consists of isolated silicate tetrahedra and two

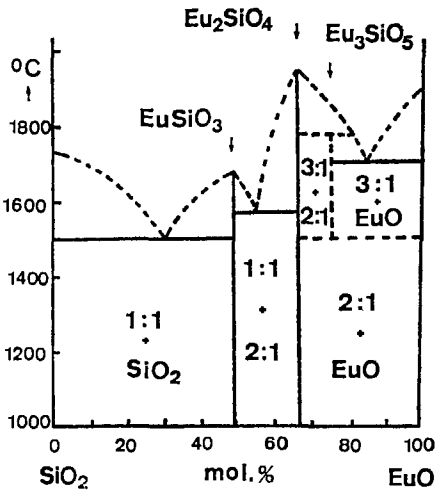

Fig. 49. Phase diagram for the system EuO–SiO_2 (Shafer, 1965).

kinds of europium ions, of which the first has eightfold and the second tenfold coordination. Viewing along the direction [010] reveals a pseudohexagonal arrangement of strings containing SiO_4 tetrahedra alternating with the 10-coordinated europium atoms. The 8-coordinated cations lie in the channels between these strings (fig. 50) (Felsche, 1971a).

The high-temperature form of Eu_2SiO_4 is orthorhombic and isotypic with β-K_2SO_4 (Marchand et al., 1978). Like the low-temperature form the structure is built of isolated SiO_4^{4-} tetrahedra linked together by europium atoms. Europium has seven- and tenfold coordination.

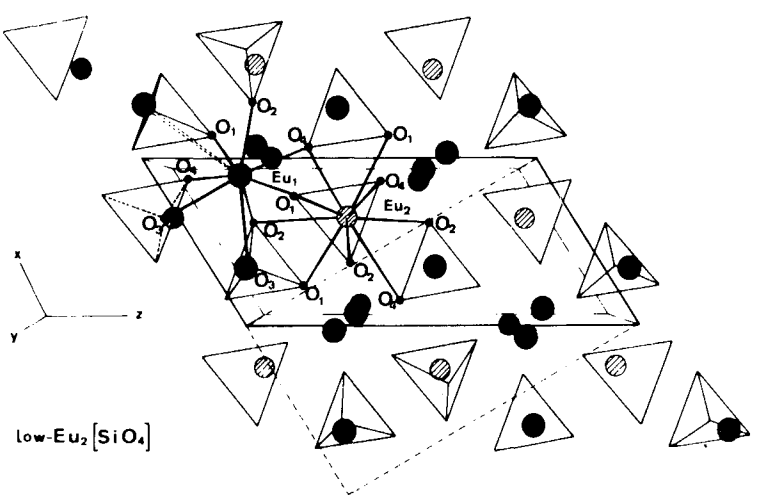

Fig. 50. The structure of low temperature modification of Eu_2SiO_4 (Felsche, 1971a).

The crystal structure of $Eu_3(SiO_4)O$ has tetragonal symmetry. Like the oxyorthosilicates of the trivalent rare earths, it has two types of anions: SiO_4 tetrahedra and oxygens not bonded to silicon. Both crystallographically independent europium atoms are octahedrally coordinated. The octahedra form a three-dimensional framework in which the anions are located to achieve charge balance (Felsche, 1973).

Like the alkaline earth metasilicates, europium metasilicate, $EuSiO_3$, has high-pressure phases. At ambient temperature $EuSiO_3$ is monoclinic (C2) but at pressure of 6 GPa and temperature of 1000°C it transforms to triclinic ($P\bar{1}$). At still higher pressure (7 GPa) and temperature (1200°C) the structure is again monoclinic ($P2_1/c$) (Machida et al., 1981d).

4.8. *Mixed anion silicates*

The rare earth elements form numerous compounds where, in addition to the silicate anion, there is another anion, viz. borate, carbonate, phosphate and aluminate (Voronkov and Pyatenko, 1967; Ito, 1968; Rumanova et al., 1968; Wanklyn et al., 1974; Malinovskii, 1983). These compounds can also contain cations other than rare earths. Interesting compounds among the mixed anion rare earth silicates are the halosilicates and silicate nitrides. The halosilicates are of type R_3SiO_4Cl (Diehl and Brandt, 1974) or $RSiO_3X$ (X = F, Cl, Br) (Lehmann and Isaacs, 1978). Both structures are orthorhombic but only the structure of $Yb_3(SiO_4)_2Cl$ has been solved (Ayasse and Eick, 1973). The structure consists of YbO_7Cl dodecahedra, YbO_6Cl_2 square antiprisms and SiO_4 tetrahedra (fig. 51).

The rare earth silicate nitrides, also called silicon rare earth nitrides, have been found for the ternary system R_2O_3–SiO_2–Si_3N_4 and the binary system R_2O_3–Si_3N_4. The following compounds are formed: $R_{10}(SiO_4)_6N_2$ with hexagonal oxyapatite structure (Gaude et al., 1975), monoclinic $R_4Si_2O_7N_2$ and tetragonal $R_2Si_2O_3N_4$ (Willis et al., 1976a; Guha, 1980). In addition, lanthanum and ytterbium have compounds not reported for the other rare earths, viz. orthorhombic $La_2Si_6O_3N_8$, monoclinic $LaSiO_2N$ and tetragonal $Yb_2Si_3O_5N_2$ (Willis et al., 1976b; Mitomo et al., 1982).

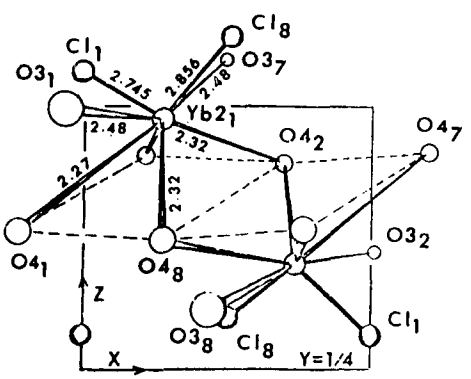

Fig. 51. Perspective view of the coordination of Yb(2) in $Yb_3(SiO_4)_2Cl$ (Ayasse and Eick, 1973).

TABLE 14
Summary of structural data on rare earth silicates.

Composition	R	Compound	Cell parameters				Z	Space group	Si radical	Reference
			a (Å)	b (Å)	c (Å)	angle (°)				
$R_2(SiO_4)O$	Pr · · · Tb	Sm	9.16	7.11	6.82	$\beta = 107.5$	4	$P2_1/c$	$[SiO_4]$	Felsche, 1973
	Dy · · · Lu, Y	Er	14.32	10.35	6.69	$\beta = 122.3$	8	$B2/b$	$[SiO_4]$	Buisson and Michel, 1968
$R_{9.33}\square_{0.67}(SiO_4)_6O_2$	La · · · Lu	Gd	9.43		6.87		1	$P6_3/m$	$[SiO_4]$	Felsche, 1972
$R_2Si_2O_7$	La · · · Eu	Sm	6.69		24.38		8	$P4_122$	$[Si_2O_7]$	Felsche and Hirsiger, 1969
	Eu · · · Lu	Dy	6.64	6.69	12.15	$\alpha = 94.0$ $\beta = 89.8$ $\gamma = 91.7$	4	$P\bar{1}$	$[SiO_4][Si_3O_{10}]$	Felsche, 1970; Bocquillon et al., 1977
	Ho · · · Lu	Tm	6.82	9.10	4.68	$\beta = 101.8$	2	$C2/m$	$[Si_2O_7]$	Felsche, 1970
	Ho · · · Lu	Tm	5.54	10.78	4.68	$\beta = 96.1$	2	$P2_1/a$	$[Si_2O_7]$	Felsche, 1970
	Eu · · · Ho	Gd	13.87	5.05	8.30		4	Pnam	$[Si_2O_7]$	Felsche, 1970
	Sm · · · Eu	Eu	8.52	12.85	5.39	$\alpha = 91.7$ $\beta = 92.2$ $\gamma = 90.4$	4	$P\bar{1}$	$[Si_2O_7]$	Felsche, 1969
	La · · · Sm	Nd	8.63	12.95	5.39	$\beta = 90.0$	4	$P2_1/n$	$[Si_2O_7]$	Felsche and Hirsiger, 1969
	Tm · · · Lu	Yb	6.57		11.99		4	tetrag. C		Bocquillon et al., 1977
$R_2O_3 \cdot 3SiO_2$	Ho	Ho	6.84	8.92	9.34	$\beta = 102.1$				Montorsi, 1982
	Ho	Ho	5.58	10.83	4.69	$\beta = 96.2$				Montorsi, 1982
$NaRSiO_4$	Ce · · · Nd	Nd	20.0	9.28	5.45		12	$Pna2_1$	$[SiO_4]$	Chichagov and Belov, 1968
	Nd · · · Ho	Sm	11.84		5.45		8	$I4/m$	$[SiO_4]$	Chichagov et al., 1968
	Er · · · Lu	Er	5.09	10.96	6.35		4	$Pbn2_1$	$[SiO_4]$	Maksimov et al., 1967
	Y	Y	5.13	6.93	11.14		4	$Pc2_1n$	$[SiO_4]$	Merinov et al., 1979
$LiRSiO_4$	La · · · Dy	La	9.69		7.15					Blasse and deVries, 1967
	Ho · · · Lu, Y	Y	4.96	10.68	6.29					Blasse and deVries, 1967.
	Y	Y	5.37	10.81	6.19	$\beta = 113.4$		$P2_1/b$	$[SiO_4]$	Nikolskii et al., 1976
	Sc	Sc	4.82	10.44	5.97			Pbnm	$[SiO_4]$	Steele et al., 1978
$MR_9(SiO_4)_6O_2$	La · · · Lu	$NaGd_9$	9.42		6.88		1	$P6_3/m$	$[SiO_4]$	Felsche, 1972
		$LiGd_9$	9.41		6.85		1	$P6_3/m$	$[SiO_4]$	Felsche, 1972
		KNd_9	9.58		7.01		1	$P6_3/m$	$[SiO_4]$	Pushcharovskii et al., 1978
$Me_2R_8(SiO_4)_6O_2$	La · · · Lu	Ca_2La_8	9.65		7.16		1	$P6_3/m$	$[SiO_4]$	Ito, 1968; Fedorov et al.,
Me = Mg, Ca, Sr,	(not in all									1975c; Fedorov et al., 1976
Ba, Mn, Zn, Cd, Pb	cases)	Pb_2Y_8	9.42		6.80		1	$P6_3/m$	$[SiO_4]$	Sidorov et al., 1977
$Me_4R_6(SiO_4)_6(OH)_2$	La · · · Lu	Ca_4La_6	9.63		7.12		1	$P6_3/m$	$[SiO_4]$	Ito, 1968
Me = Ca, Sr, Ba,	(not in all	Mn_4Er_6	9.28		6.63		1	$P6_3/m$	$[SiO_4]$	Ito, 1968
Mn, Pb	cases)									

Composition	R	Compound	Cell parameters				Z	Space group	Si radical	Reference
			a (Å)	b (Å)	c (Å)	angle (°)				
$Pb_3R_6(SiO_4)_6$	Er	Er	9.64		6.78		1	$P6_3/m$	$[SiO_4]$	Ansell and Wanklyn, 1976
$M_3RSi_2O_7$	Eu	K_3Eu	9.98		14.44		4	$P6_3/mcm$	$[Si_2O_7]$	Bondar et al., 1965b
	Er · · · Lu, Y, Sc	Na_3Sc	5.35	9.35	13.09			Pbnm	$[Si_2O_7]$	Maksimov et al., 1969
	Y(Y, Sc)	Na_3Y	9.42		13.79		4	$P6_3/m$	$[Si_2O_7]$	Shannon et al., 1980
$Na_3RSi_3O_9$	Gd, Dy, Y	Y	15.03	15.14	15.21		16	$P2_12_12_1$	$[Si_{12}O_{36}]$	Maksimov et al., 1980a
$Na_5RSi_4O_{12}$	Sm · · · Lu, Y, Sc	Y	22.04		12.60		18	$R\bar{3}c$	$[Si_{12}O_{36}]$	Shannon et al., 1978
$NaRSi_6O_{14}$	Na · · · Nd	Nd	7.67	15.39	19.68		8	Ibam	$[Si_3O_7]_\infty$	Dimitrova et al., 1976
$K_3RSi_6O_{15}$	Nd	Nd	16.01	14.98	7.28		4	Pban	$[Si_2O_5]_\infty$ $[Si_6O_{17}]_\infty$	Pushcharovskii et al., 1977
$MRSi_2O_6$(M = Li, Na)	Sc	Li, Sc	9.80	8.96	5.35	$\beta = 110.3$	4	C2/c	$[Si_2O_6]_\infty$	Hawthorne and Grundy, 1977
$Na_4R_2(Si_4O_{13})$	Sc	Sc	14.44	5.29	14.22		4	Pnam	$[Si_4O_{13}]$	Maksimov et al., 1980b
$K_2RSi_6O_{15}$	Ce	Ce	13.06	11.85	8.70	$\beta = 90.2$	4	B2/b	$[Si_2O_5]_\infty$	Karpov et al., 1977a
$NaRSi_6O_{16}(OH)_2nH_2O$	Nd	Nd	30.87	7.39	7.12		4	Cmm2	$[Si_2O_5]_\infty$ $[Si_6O_{17}]_\infty$	Karpov et al., 1977b
$K_4R_2(Si_4O_{12})(OH)_2$	Sc	Sc	12.73	12.74	8.44		8	Pban	$[Si_4O_{12}]$	Pyatenko et al., 1979
$Na_2RSi_6O_{16}(OH)nH_2O$	Ce	Ce	7.50	15.62	7.35		4	Pmm2	$[SiO_4]$	Shumyatskaya et al., 1980
$K_8R_3(Si_6O_{16})(OH)$	Yb	Yb	6.81	11.43	11.45	$\alpha = 88.5$ $\beta = 90.9$ $\gamma = 100.1$	1	$P\bar{1}$	$[Si_6O_{16}]$	Pushcharovskii et al., 1981
$Mg_3R_2(SiO_4)_3$	Ho · · · Lu, Y	Y	12.12				8	Ia3d	$[SiO_4]$	Ito, 1967
$Ca_3R_2Si_6O_{18}$	Er · · · Lu	Er	8.08	8.29	7.81	$\alpha = 113.3$ $\beta = 89.9$ $\gamma = 100.4$				Andreev et al., 1975
$PbR_4Si_4O_{17}$	Dy, Er, Y	Er	5.53	10.58	6.96	$\beta = 107.2$	4	$P2_1/n$	$[Si_2O_7]$ $[Si_2O_{10}]$	Ansell and Wanklyn, 1975
$Na_2R(SiO_4)(OH)$	Pr	Pr	9.68	7.44	6.60		4	Pnma	$[SiO_4]$	Puschcharovskii et al., 1976
$Na_2LiRSi_6O_{15}$	Y	Y	14.51	17.60	10.38		8	Cmca	$[SiO_4]$	Gunawardane et al., 1982a
$K_3R(Si_3O_8(OH)_2)$	Y	Y	13.57	13.17	5.87					Maksimov et al., 1968a
$R_2AlSi_2O_8(OH)$	La · · · Nd	La	7.03	5.78	17.20	$\beta = 110.6$	4	$P2_1/c$	$[SiO_4]$	Jarchow et al., 1982
$Ca_2R_2(Si_4O_{12})CO_3 \cdot H_2O$	Y	Y	12.93	14.30	6.73		4	Pmnb	$[Si_4O_{12}]$	Rumanova et al., 1966
$R_3(SiO_4)_2Cl$	Yb	Yb	6.73	17.56	6.13		4	Pnma	$[SiO_4]$	Ayasse and Eick, 1973
$Na_2BaR_2(Si_4O_{12})CO_3$	Nd	Nd	6.95	13.46	14.03		4	$Pna2_1$	$[Si_4O_{12}]$	Malinovskii, 1983
$NaBa_3R_3(Si_2O_7)(Si_4O_{12})$	Nd	Nd	5.59	24.14	14.83		4	Cmcm	$[Si_2O_7]$ $[Si_4O_{12}]$	Malinovskii et al., 1983

TABLE 15
Some physical properties of rare earth silicates

Composition	Density ($g\,cm^{-3}$)	Melting temp. (°C)	Reference
$Eu_2(SiO_4)O$	6.63	1980	Toropov and Bondar, 1964
$Gd_2(SiO_4)O$	6.77	2170	Ananeva et al., 1981
$Ho_2(SiO_4)O$	6.80	2190	Ananeva et al., 1981
$Lu_2(SiO_4)O$	7.41	2320	Ananeva et al., 1981
$Y_2(SiO_4)O$	4.45	2200	Ananeva et al., 1981
$Y_{9.33}\square_{0.67}(SiO_4)_6O_2$	4.63	1950	Toropov and Bondar, 1961
$Y_2Si_2O_7$	4.09	2090	Ananeva et al., 1982
$La_2Si_2O_7$	4.71	2010	Ananeva et al., 1982
$Sc_2Si_2O_7$	3.50	2200	Ananeva et al., 1982
$Ca_2La_8(SiO_4)_6O_2$	5.10	2180	Fedorov et al., 1975a
$Ca_2Y_8(SiO_4)_6O_2$	4.41	2050	Fedorov et al., 1975a
$La_2Y_5Eu_3(SiO_4)_6O_2 : Ho^{3+}, Tm^{3+}$	4.50		Hopkins et al., 1971a
$Cd_2La_8(SiO_4)_6O_2$	5.63	1800	Fedorov et al., 1975b
$Cd_2Dy_8(SiO_4)_6O_2$	6.86	1800	Fedorov et al., 1975b
$Zn_2La_8(SiO_4)_6O_2$	5.27	1680	Fedorov et al., 1975b
$Zn_2Gd_8(SiO_4)_6O_2$	6.29	1730	Fedorov et al., 1975b

4.9. *Properties of rare earth silicates*

The main focus of research on the rare earth silicates has been their preparation and structure. A summary of the structural data available is presented in table 14. In many cases the physical properties are unknown. An important application of the rare earth silicates is the use of yttrium oxyorthosilicate activated with terbium as a luminescent material in fluorescent lamps. Several patents have been published in this field.

Among the general characteristics of rare earth silicates high melting points (table 15) and high refraction indices may be mentioned. The hardness of oxyorthosilicates is 6–6.5 (Ananeva et al., 1981) and that of oxyapatite silicates with divalent metals 6.6–7 in Mohs' scale (Hopkins et al., 1971a, b).

4.9.1. *IR spectra*

Lazarev et al. (1961, 1962, 1963, 1965, 1968) and Toropov et al. (1971) have recorded the infrared spectra of several rare earth silicates in connection with their studies of different structure types. They did not succeed, however, in assigning all frequencies

TABLE 16
Frequencies (cm^{-1}) observed in the IR spectra of yttrium silicates (Lazarev et al., 1961).[a)]

$Y_2(SiO_4)O$	$Y_{9.33}\square_{0.67}(SiO_4)_6O_2$	$Y_2Si_2O_7$
1153vw	1112vw	1024s
1083vw	1026vw	982vs
993vs	983vs	954s
964s	942s	915m
918vs	908vs	870s
892s	872vs	850s
843vs	857s	635m
597vs	633w	587m
583s	590s	555vs
547vs	554vs	541s
532vs	536s	508vs
513s	510vs	481m
466m	481m	452m
448m	448m	432m

[a)] vs = very strong, s = strong, m = medium, w = weak, vw = very weak.

that may have included combination bands. The asymmetric and symmetric stretching frequencies of the SiO_4 group are found at 850–1000 and 840 cm^{-1}, respectively. The corresponding deformation vibrations lie at 450–600 cm^{-1}. In disilicates the asymmetric stretching of the Si–O–Si bond lies at 1000–1100 cm^{-1} and the symmetric stretchings at 630–730 cm^{-1}. The asymmetric and symmetric stretching frequencies of SiO_4 groups are at 900–1000 and 800–900 cm^{-1}, respectively. The vibrations caused by R–O bonds can be found at 600–700 and 400–500 cm^{-1}. IR data for some yttrium silicates are presented in table 16.

4.9.2. *Luminescence properties*

Rare earth oxyorthosilicates activated with Nd^{3+}, Ho^{3+} and Er^{3+} ions emit in the infrared region. The compounds can be used for laser beam production with wavelength of about 2 μm (Arsenev et al., 1972; Bagdasarov et al., 1973; Morozov et al., 1976). The emission of Nd^{3+} in $Y_2(SiO_4)O$ has a shorter wavelength of 0.9 μm (Ananeva et al., 1981).

The rare earth silicates with divalent cations and oxyapatite structure can be used as high energy storage laser hosts for Nd^{3+} (Hopkins et al., 1971b). The emission wavelength is about 1.05 μm and the line is broader in these compounds than in yttrium aluminium garnets activated with Nd^{3+}. The $Ca_2Y_8(SiO_4)_6O_2$ crystals doped with Ho^{3+}, Er^{3+} and Tm^{3+} produce a laser action at 2.06 μm (Hopkins et al., 1971a). Erbium and thulium ions act as sensitizers and the final emission originates from the holmium ions (fig. 52).

The silicates of divalent europium are ferromagnetic semiconductors. Magnetic measurements of $Eu_3(SiO_4)O$ have revealed a transition temperature of 9 K and

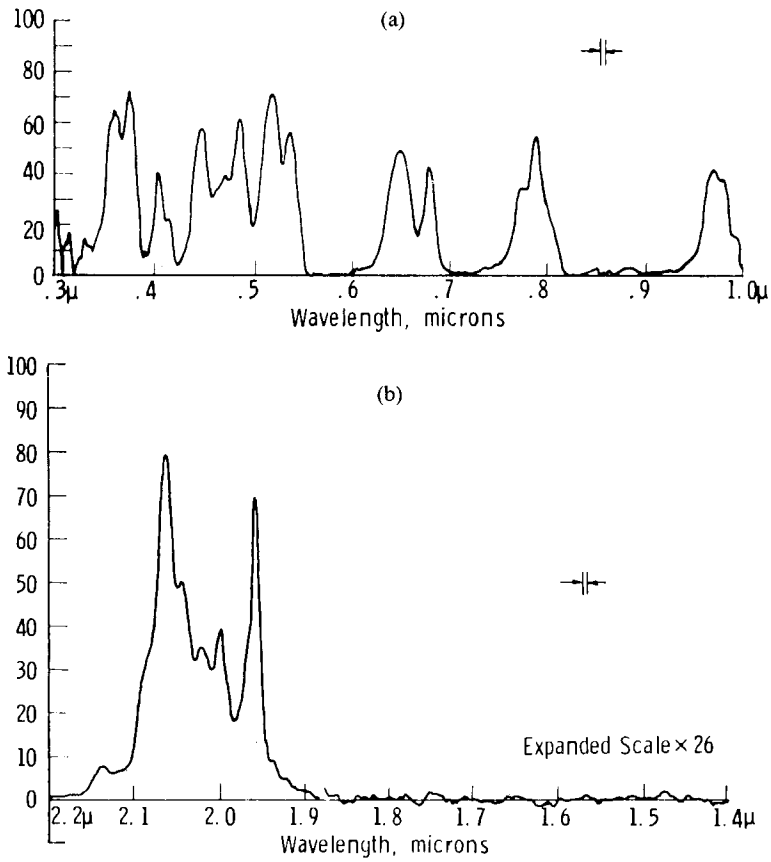

Fig. 52. The emission and excitation spectra of Er^{3+}-, Tm^{3+}- and Ho^{3+}- doped $CaY_4(SiO_4)_3O$ at 77K (Hopkins et al., 1971a).

saturation magnetization of $9\mu_B$/Eu ion (Kaldis et al., 1974). The photoluminescence spectrum of the pure compound has a single emission band in the red region with a high quantum yield (fig. 53). The crystals of the low-temperature form of Eu_2SiO_4 are transparent with a characteristic yellow colour. Depending on the growth conditions some crystals have green colour. The polymorphic change at 165°C causes a change in colour too: the yellow crystals become deep orange and the green ones take on a brownish appearance (Busch et al., 1970). A strong yellow luminescence has been found in these substances at room temperature under UV illumination. A small spectral shift can be observed within the polymorphic transition (Kaldis and Verreault, 1970).

The luminescence properties of trivalent lanthanide ions in rare earth silicate matrices are quite well known. Most materials studied include oxyortho-, di-, halo- and alkali double silicates of yttrium, lanthanum, gadolinium and lutetium.

Trivalent cerium emits in the UV region, either blue or blue-green light depending on the silicate matrix and Ce^{3+} concentration (Klasens, 1956; Bril et al., 1971). The emission originates from the allowed transition from the 5d state to the ground state doublet $^2F_{7/2}$ and $^2F_{5/2}$ (Gomes de Mesquita and Bril, 1969). Because of the allowance of the transition its lifetime is short and the Ce^{3+}-activated silicates can be used in cathode ray tubes, display screens and flying spot tubes (Watanabe and Sumita, 1973; Fukuda et al., 1974).

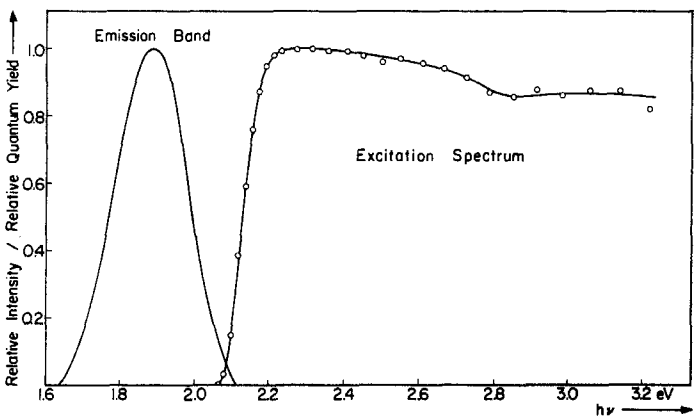

Fig. 53. The photoluminescence spectra of $Eu_3(SiO_4)O$ at 4.2 K (Kaldis et al., 1974).

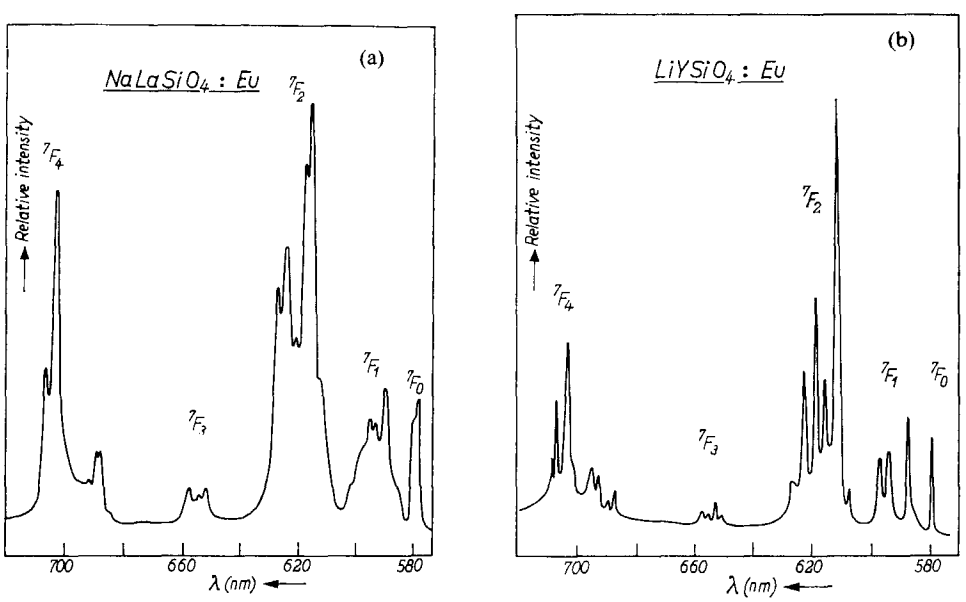

Fig. 54. Emission spectra of Eu^{3+} in $LiYSiO_4$ and $NaLaSiO_4$ matrices excited with 254 nm (Blasse and Bril, 1967a).

A green emission can be obtained from Tb^{3-}-activated rare earth silicates upon excitation with cathode rays. The transition showing the intense green is $^5D_4 \rightarrow {}^7F_5$ (Fukushima et al., 1975). The other less intense peaks in the blue, yellow and orange regions of the emission spectrum of Tb^{3+} are caused by the transitions $^5D_4 \rightarrow {}^7F_6$, $^5D_4 \rightarrow {}^7F_4$ and $^5D_4 \rightarrow {}^7F_3$ (Peters, 1969).

Red colour is produced in rare earth phosphors by Eu^{3+} activators. In rare earth silicates the emission intensity of trivalent europium seems to be weak (McAllister, 1969). Shiokawa and Adachi (1979) have activated the rare earth silicates with divalent europium and found the typical emission colour of Eu^{2+}-activated phosphors: blue or blue-green. Blasse and Bril (1967a) have studied the luminescence properties of Eu^{3+}-activated $MRSiO_4$ (M = Li, Na) (fig. 54). In all compounds the orange transition $^5D_0 \rightarrow {}^7F_2$ had the highest intensity. The fluorescence spectra have been used as a structural probe and the crystallographical position of the activator ion has been predicted from the sharpness and number of the emission peaks.

Of the other rare earth ions, Ho^{3+} and Nd^{3+} emit in the IR region in the rare earth silicate matrix (Morozov et al., 1976). The rare earth silicates activated with Dy^{3+}, Er^{3+} and Tm^{3+} have been prepared but information about their luminescence has not been given (Gomes de Mesquita and Bril, 1969; Schuil, 1976).

The luminescence of Tb^{3+} can be sensitized with Ce^{3+} ions: The cerium ions absorb the electromagnetic radiation and transfer the energy to the Tb^{3+} ions. The very efficient green emission obtained in oxyortho- and disilicates (Watanabe et al., 1978; Tokyo Shibaura Electric Co., 1980) gives these materials a use in fluorescent lamps. In $Y_2(SiO_4)O:Tb^{3+}$ the excitation band ($4f \rightarrow 5d$) is situated at 250 nm whereas the Ce^{3+} sensitized phosphors can be most effectively excited with the 360 nm wavelength (fig. 55).

Ce^{3+}, Tb^{3+} and Eu^{3+} have their typical luminescence properties in rare earth halosilicate matrices (Lehmann and Isaacs, 1978; Yamada et al., 1978). The Ce^{3+}, Tb^{3+}-activated compounds can be used in flying spot tubes (Yamada et al., 1974).

Along the double rare earth silicates only the luminescence properties of $BaY_4Si_5O_{17}$ have been investigated (Sumita and Watanabe, 1973). Ce^{3+} emits blue light, Pr^{3+} in the UV region and Tb^{3+} green light with high quantum yield (de Hair, 1980).

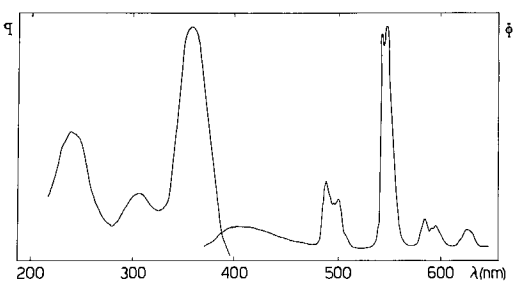

Fig. 55. The excitation and emission spectra of Ce, Tb-activated yttrium oxyorthosilicate (Leskelä and Suikkanen, 1985).

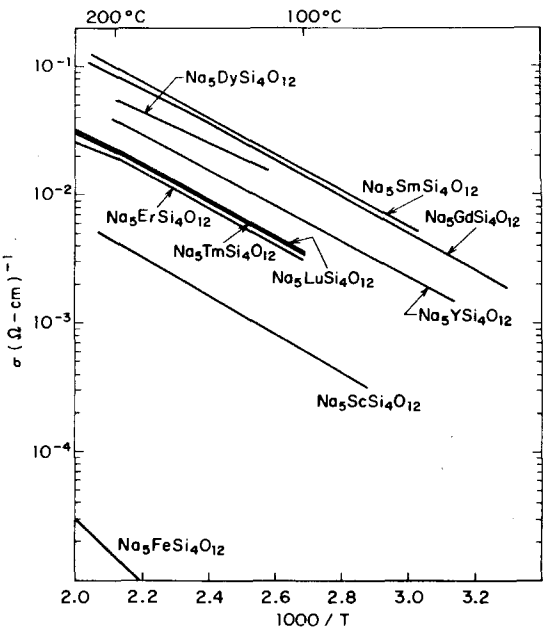

Fig. 56. Conductivity (log scale) vs. $1/T$ for selected $Na_5RSi_4O_{12}$ compounds (Shannon et al., 1978).

4.9.3. *Other properties*

Maqsood et al. (1979) have measured the magnetic properties of erbium disilicates. C–$Er_2Si_2O_7$ and D–$Er_2Si_2O_7$ become antiferromagnetic at 2.50 and 1.71 K, respectively. In $PbDy_4Si_5O_{17}$ the transition to the antiferromagnetic state occurs at 1.2 K (Wanklyn et al., 1975).

The ionic conductivity in sodium rare earth silicates with the formula $NaRSi_4O_{12}$ is high due to the channels in the structure where the sodium ions can move. The conductivity values of these compounds are of the same order of magnitude as that of β-Al_2O_3 ($2 \times 10^{-1}\,\Omega\,cm^{-1}$ at 300°C), which is known to be a good conductor (fig. 56) (Shannon et al., 1978).

5. Rare earth germanates

5.1. *Introduction*

Germanium belongs to the fourth main group in the periodic system of elements and its nearest relative, both chemically and physically, is silicon. In view of this, it is not surprising to find that in most of its compounds germanium behaves like silicon. Many germanates, and many rare earth germanates, are isostructural with the corresponding silicates. The similarity to silicon also means that the structural chemistry of germanates is not simple and straightforward, but a multitude of compounds and structures are possible (fig. 57).

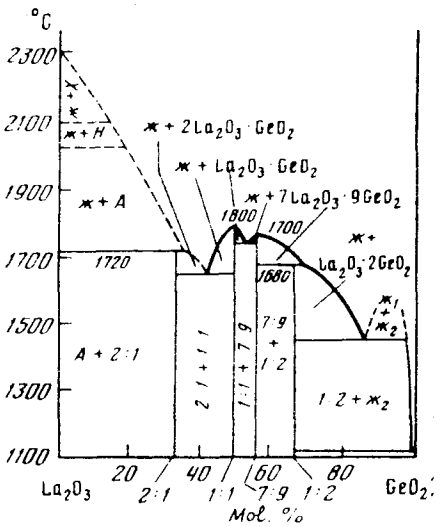

Fig. 57. Phase diagram for the system La_2O_3–GeO_2 (Bondar, 1982).

A characteristic feature of the structural chemistry of silicates and germanates is the tetrahedral coordination of four oxygens around Si or Ge. In some cases, the larger size of Ge^{4+} ($r_{IV}^{4+} = 0.44$ Å) compared with Si ($r_{IV}^{4+} = 0.39$ Å) provides enough space for octahedral coordination, leading to a more metal-like behaviour.

Several applications of rare earth silicates in solid state technology have undoubtedly encouraged a closer look at the structurally related and stable germanates. No large scale applications have yet been found, but then the chemistry of germanates has only been partially explored. Russian scientists have been especially active in the research on rare earth germanates and have written authoritative reviews in the field. Deserving mention is the recent review of Demianets et al. (1980b), which is based on a comprehensive book in Russian by the same authors (Demianets et al., 1980a).

5.2. *Binary rare earth germanates*

5.2.1. *Oxyorthogermanates*

The formation of binary rare earth germanates from the corresponding oxides in solid state reactions is a slow process, as in the case of silicates. The addition of a flux material is useful, even in the preparation of powder samples (Glushkova et al., 1967; Shannon and Sleight, 1968). Single crystals have been prepared in several ways: from melt or flux and by different hydrothermal techniques. The use of melt is limited by the volatility of GeO_2 and incongruency in melting of many rare earth germanates. The most common flux material for single crystal preparation is Bi_2O_3 (Buisson and Michel, 1968; Bondar and Petrova, 1969), but lead and potassium fluorides have been used as well (Wanklyn, 1973a; Emelchenko et al., 1975a). The temperatures needed in flux growth vary between 800 and 1500°C. A number of papers describe the preparation of rare earth germanate crystals by hydrothermal

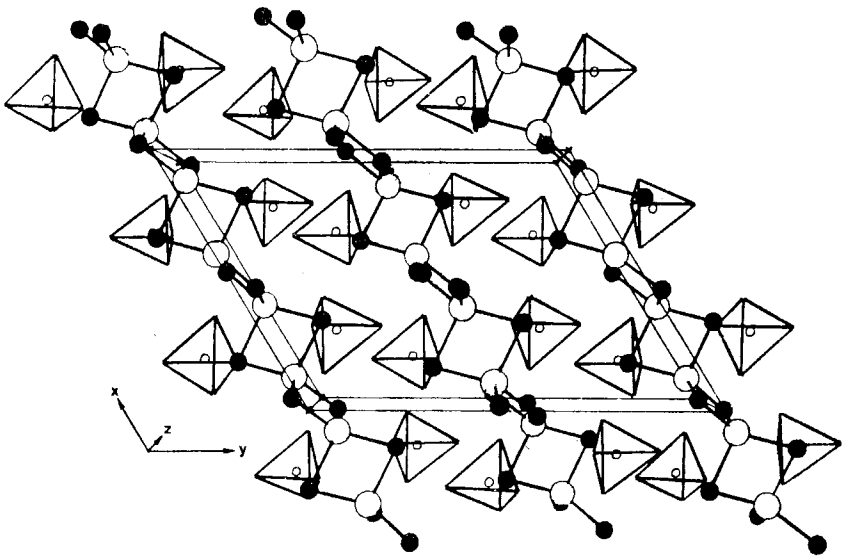

Fig. 58. The crystal structure of $Yb_2(SiO_4)O$ which is isostructural with the second type of oxyorthogermanates. Yb atoms are marked as solid circles (Felsche, 1973).

methods (Emelchenko et al., 1974a, b, d; Emelchenko, 1974; Demianets et al., 1974, 1976, 1980b). These methods are particularly suitable for alkali double germanates but they can also be applied for binary germanates (Emelchenko et al., 1975b).

The structures of rare earth oxyorthogermanates can be divided into three groups. The monoclinic structure (La $\cdots$ Gd) with primitive unit cell is isostructural with the corresponding oxyorthosilicate structure (Buisson and Michel, 1968; Lazarev, 1968). Likewise, the second type of structure (Gd $\cdots$ Lu) is analogous to the corresponding silicate structure (fig. 58). In germanates the structure change occurs at Gd, whereas in silicates it occurs at Dy. Both structural modifications are met in $Gd_2(GeO_4)O$ (Demianets et al., 1980b). The third, monoclinic structure type, which exists in $Sc_2(GeO_4)O$, has no analogue among the silicates (Gorbunov et al., 1974b).

Contradictory results have been published for the crystal structure of these oxyorthogermanates with the lighter rare earths. According to Leonov and Bondar (1973) they are orthorhombic, whereas in a recent single crystal work Kato et al. (1979) have shown that the structure of $Eu_2(GeO_4)O$ is monoclinic with space group $P2_1/c$ (fig. 59). Both europium atoms have seven coordination and the structure thus differs from the oxyorthosilicates of A-type (Michel and Buisson, 1967) where the second rare earth has nine coordination (Smolin and Thachev, 1969). Rare earth oxyorthogermanates where the ratio between rare earth and germanium oxide is 2 : 1 can be prepared by the same techniques as described above but with the proportion of $R_2O_3 : GeO_2$ in the starting mixture ≥ 2 (Wanklyn, 1973a). The single crystals have also been obtained by hydrothermal methods (Demianets et al., 1980a).

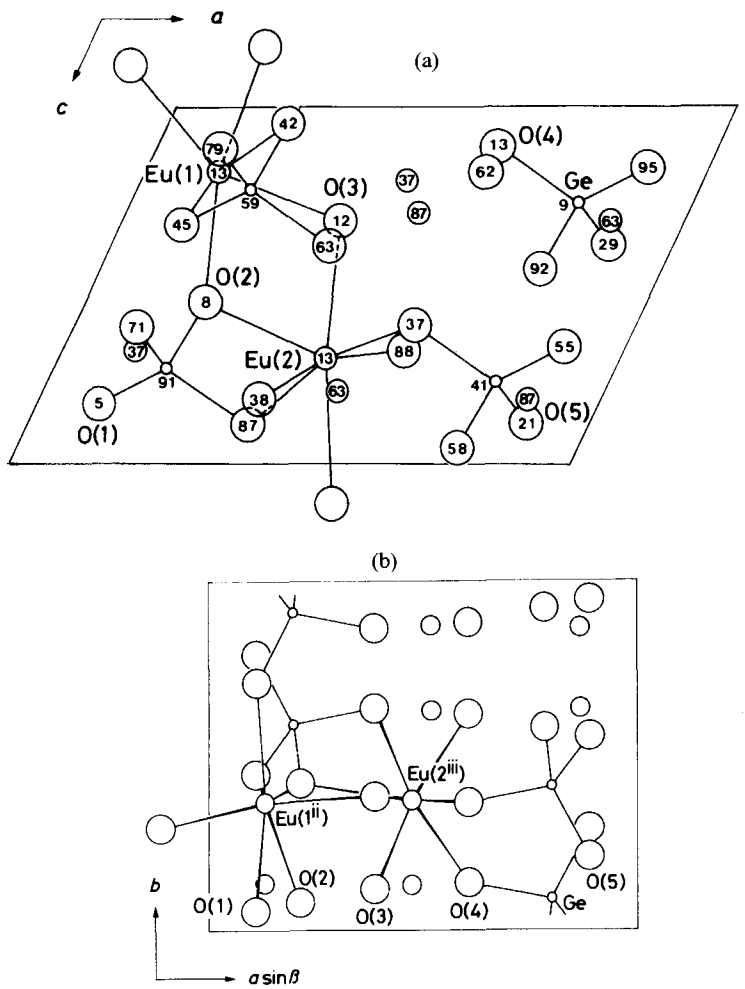

Fig. 59. Two projections of the crystal structure of $Eu_2(GeO_4)O$. (a) A projection on the xz plane (numbers indicate the heights of atoms in hundredths of the b axis). (b) A projection along the c axis (Kato et al., 1979).

The rare earth oxyorthogermanates R_4GeO_8 can be divided into at least two structural subgroups according to the X-ray diffraction powder patterns. The lighter rare earths from lanthanum to gadolinium form a hexagonal crystal structure containing isolated GeO_4 tetrahedra. Thus the formula of these compounds may best be written $R_4(GeO_4)O_4$ (Toropov et al., 1971). The structure of the orthogermanates of the heavier rare earths is unknown. A single crystal study of $Nd_4(GeO_4)O_4$ has shown, however, that Nd has another modification besides the hexagonal one. The crystals were obtained hydrothermally and found to be orthorhombic with space group $Pmc2_1$ (Merinov et al., 1978b). The coordination numbers of the neodymium

atoms are 7 and 8 and the neodymium oxygen polyhedra are connected together through their edges to form a rigid three-dimensional skeleton. The GeO_4 tetrahedra are situated in the holes.

5.2.2. *Binary germanates with oxyapatite structure*

In the proportion 7 : 9, rare earth and germanium oxides form crystals with hexagonal oxyapatite structure (Bondar et al., 1967; Lazarev, 1968). The formula of this compound can be written $R_{4.67}(GeO_4)_3O$, or as presented for silicates $R_{9.33}\square_{0.67}(GeO_4)_6O_2$, when the defect structure and whole content of the unit cell are taken into account. Contrary to the case of oxyapatite silicates, not all rare earth elements form oxyapatite germanate. This structure has been observed only with the lighter cations (La · · · Dy) (Belokoneva et al., 1972). Cockbain and Smith (1965) have reported a lanthanum germanate having the oxide proportion 2 : 3. Since the structure was hexagonal, however, and identical to that found in oxyapatites, they presumably made a mistake in the chemical analysis and the correct oxide proportion was 7 : 9. A similar error was made before 1967 for silicates.

5.2.3. *Digermanates*

The structures of rare earth digermanates can be divided into six groups, of which one is a high-temperature form and one a high-pressure form (Demianets et al., 1980a; Bocquillon et al., 1980). (1) The first low-temperature subgroup is triclinic and appears with lanthanum and praseodymium (Smolin et al., 1969). (2) The second subgroup (Nd · · · Gd) is also triclinic but the unit cell is noncentrosymmetric and larger than in the first group (Smolin et al., 1971). According to Vetter et al. (1982) the structure of $Nd_2Ge_2O_7$ is centrosymmetric and the *a* axis is twice as long as presented by Smolin et al. (1971). (3) The heavier rare earths (Tb · · · Lu) form tetragonal digermanates with space group $P4_12_12$ (Smolin, 1970). (4) Scandium digermanate crystallizes in a group of its own and has a thortveitite-like structure with monoclinic unit cell (Shannon and Prewitt, 1970). (5) A cubic high-temperature

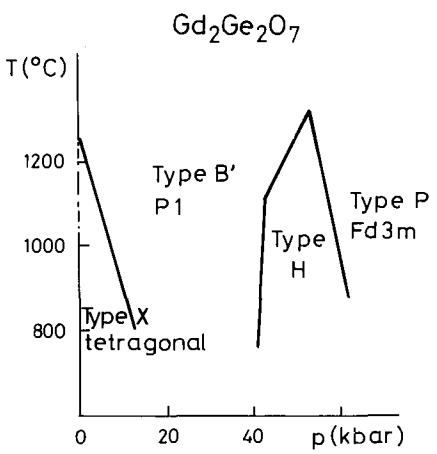

Fig. 60. The p–T diagram for $Gd_2Ge_2O_7$. P indicates pyrochlore structure, H hexagonal high-pressure form, B′ triclinic structure and X tetragonal structure (Bocquillon et al., 1980).

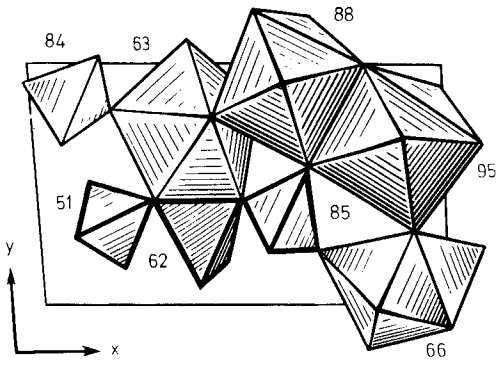

Fig. 61. The structure of $La_2Ge_2O_7$ ($La_4(Ge_4O_{10})GeO_4$) projected on the *xy* plane. The numbers correspond to hundredths of the *c* axis (Demianets et al., 1980b).

form of digermanate has been detected for ytterbium and scandium (Demianets et al., 1980a). Since the same structure was found for the rare earths from gadolinium to lutetium at high pressure, this structure has been named the high-pressure pyrochlore phase (Shannon and Sleight, 1968; Bocquillon et al., 1978; Chateau and Loriers, 1979). (6) Bocquillon et al. (1980) have reported a new hexagonal high-pressure phase of RGe_2O_7 (R = Sm, Gd) that differs from all other digermanate and disilicate phases (fig. 60). The new phase is an intermediate phase and transforms to the pyrochlore phase with increasing pressure.

Only the third and fourth structure types are really digermanates, in the sense of containing separate $Ge_2O_7^{4-}$ groups. The other structures do not contain diorthogermanate radicals. In the two first types germanium forms a triortho group $Ge_3O_{10}^{4-}$ and isolated GeO_4^{4-} tetrahedra (fig. 61, table 17). The coordination of germanium atoms in the sixth digermanate group is unknown. The octahedron is the form of germanium radical in the high-temperature modification of $R_2Ge_2O_7$ (Shannon and Sleight, 1968).

The first structure type of the digermanates is isotypic with the rare earth disilicate of B-type (Smolin et al., 1969; Felsche, 1972a). The scandium digermanate shows the same thortveitite structure as scandium disilicate and the third structure type of digermanates is identical to the tetragonal high-pressure disilicate of X-type (Jouhet-Vetter and Queyroux, 1975; Bocquillon et al., 1977, 1978). No structural analogies with the rare earth disilicates have been found for the remaining digermanate structures.

In addition to the sufficiently characterized digermanates, there are reports of the existence of lanthanum metagermanate ($La_2O_3 \cdot 3GeO_2$ or $La_2Ge_3O_9$) (Kornilova et al., 1965; Tenisheva et al., 1965). The discovery was based on IR spectra and X-ray data. Attempts of later investigators to detect the compound ended in failure (Glushkova et al., 1967; Toropov et al., 1971; Bondar, 1979).

5.2.4. *Binary germanates containing hydroxide ions*

Two types of rare earth germanates containing hydroxide anion have been found: $R_{13}(GeO_4)_6(OH)_3 \cdot [O, (OH, F)]$ (R = Nd $\cdots$ Eu) and $R_4Ge_3O_9(OH, F)_6$ (R = Sm,

TABLE 17
Symmetry of structure data for the rare earth germanates.

Composition	R	Compound	Cell parameters				Z	Space group	Ge radical	Reference
			a (Å)	b (Å)	c (Å)	angle (°)				
$R_2(GeO_4)O$	La · · · Tb	Nd	9.32	7.74	6.81	$\beta = 105.4$	4	$P2_1/c$	$[GeO_4]$	Bondar, 1979
	Dy · · · Lu, Y	Y	14.94	10.58	6.87	$\gamma = 122.0$	8	$B2/b$	$[GeO_4]$	Buisson and Michel, 1967
	Sc	Sc	10.93	10.66	10.49	$\gamma = 94.0$	12	$B2/b$	$[GeO_4]$	Gorbunov et al., 1974
$R_{9.33}\square_{0.67}(GeO_4)_6O_2$	La · · · Dy	Nd	9.75		7.15		1	$P6_3/m$	$[GeO_4]$	Demianets et al., 1980a
$R_4(GeO_4)O_4$	Nd	Nd	7.48	5.73	17.93		4	$Pmc2_1$	$[GeO_4]$	Merinov et al., 1978b
$R_2Ge_2O_7$	La, Pr	La	12.76	7.07	7.00	$\alpha = 91.0$ $\beta = 90.4$ $\gamma = 94.1$	4	$P\bar{1}$	$[Ge_3O_{10}]$ $+[GeO_4]$	Smolin et al., 1969
	Nd · · · Gd	Gd	18.50	6.80	6.86	$\alpha = 87.9$ $\beta = 91.5$ $\gamma = 94.5$	6	P1	$[Ge_3O_{10}]$ $+[GeO_4]$	Smolin et al., 1971
	Tb · · · Lu	Er	6.78		12.34		4	$P4_12_12$	$[Ge_2O_7]$	Smolin, 1970
	Sc	Sc	6.55	8.69	4.90	$\beta = 102.0$	2	$C2/m$	$[Ge_2O_7]$	Shannon and Prewitt, 1970b
	Gd · · · Lu, Y, Sc	Yb	9.83				8	$Fd3m$	$[GeO_6]$	Shannon and Sleight, 1968
	Sm, Gd	Sm	11.20		31.80			Pc/mmm		Bocquillon and Padiou, 1980
$R(OH)_3 \cdot 6R_2(GeO_4)$ $\cdot[O, (OH, F)_2]$	Nd · · · Eu	Sm	15.90		6.98		2	$P6_3/m$	$[GeO_4]$	Emelchenko and Ilyukhin, 1974
$R_4Ge_3O_9(OH)_6$	Sm	Sm	15.20	10.91	7.16		8	Cmcm	$[Ge^{VI}Ge_2^{IV}O_9]_\infty$	Nikolskii et al., 1977
$NaR(GeO_4)$	La · · · Nd, Eu	Eu	11.75		5.45		8	$I4/m$	$[GeO_4]$	Chichagov et al., 1969b
	Sm · · · Lu, Y	Sm	5.27	11.70	6.50		4	$Pbn2_1$	$[GeO_4]$	Kharakh et al., 1970

Composition	R	Compound	Cell parameters				Z	Space group	Ge radical	Reference
			a (Å)	b (Å)	c (Å)	angle (°)				
$LiR(GeO_4)$	Nd	Nd	5.10	11.92	5.40		4	Pbcn	$[GeO_4]$	Merinov et al., 1980b
$Na_4R_2(Ge_4O_{13})$	Ho · · · Lu, Sc	Yb	14.45	5.60	15.35		4	$Pna2_1$	$[Ge_4O_{13}]$	Gorbunov et al., 1973b
$NaR_3Ge_4O_{13}$	Pr, Nd	Pr	7.18	11.61	7.04	$\alpha = 98.9$ $\beta = 91.6$ $\gamma = 102.5$	2	$P\bar{1}$	$[Ge_2O_7]$ $[Ge_4O_{12}]$	Gorbunov et al., 1974
$Na_5RGe_4O_{12}$	Gd · · · Lu, Y	Gd	22.78		12.99		18	$R\bar{3}c$	$[Ge_{12}O_{36}]$	Shannon et al., 1978
$MRGe_2O_6$ (M = Na, K)	Sc	Sc	10.12	9.14	4.73	$\beta = 108.0$	2	C2/c	$[Ge_2O_6]$	Maksimov et al., 1973
(M = Li)	Sc	Sc	18.82	9.09	5.48		4	Pbca	$[Ge_2O_6]$	Grotepass et al., 1983
$NaR_3(GeO_4)_2(OH)_2$	Nd · · · Gd	Nd	5.26	12.25	13.93	$\alpha = 90.3$	4	I2/c	$[GeO_4]$	Chichagov et al., 1969a
$NaR(GeO_4)OH$	La, Pr, Gd	La	9.57	7.55	7.00		4	Pnma	$[GeO_4]$	Pushcharovskii et al., 1976
	Sc	Sc	12.34	13.78	5.53		8	Pmab	$[GeO_4]$	Zhdanova et al., 1975
$NaR_4(GeO_4)_2O_2OH$	Ho	Ho	6.75	21.67	6.91		4	Pnma	$[GeO_4]$	Christensen, 1972
$K_2R_2(Ge_2O_7)(OH)_2$	Sc	Sc	7.06	11.35	10.67		4	Pbcn	$[Ge_2O_7]$	Gorbunov et al., 1973a
$K_2R_4(Ge_4O_{13})(OH, F)_4$	Pr · · · Gd	Nd	6.82	7.44	17.69	$\beta = 121.0$	2	$P2_1$	$[Ge_4O_{13}]$	Klimentova et al., 1975
$K_4R_2(Ge_8O_{20})(OH, F)_2$	Yb	Yb	12.11	11.90	8.58	$\beta = 112.1$	2	$P2_1/m$	$[Ge_8O_{20}]_\infty$	Nikolskii et al., 1975
$Me_3R_2Ge_4O_{12}$ (Me = Mg, Ca, Sr, Mn, Co, Ni, Zn, Cd)	Eu · · · Lu, Y	Gd	12.36				8	Ia3d	$[GeO_4]$	Bayer, 1971
$Me_4R_6(GeO_4)_6Cl_2$ (Me = Mg, Ca, Sr, Ba)	La, Ce	Ce	6.47		7.00		1	$P6_3/m$	$[GeO_4]$	Cockbain and Smith, 1965
MgR_2GeO_6	La	La	3.90				1	Pm3m	$[GeO_4]$	Roy, 1954
$Sr_2R_8(GeO_4)_6O_2$	La · · · Dy	Nd	9.78		7.13		1	$P6_3/m$	$[GeO_4]$	Fedorov et al., 1982
$RMGeO_5$ (M = Al, Gd)	Eu, Sm, Y	Sm	7.38	8.52	5.12		4	Pbam	$[GeO_5]$	Jarchow et al., 1981b
$RM(Ge_2O_7)$ (M = Al, Ga)	La · · · Eu	Nd	7.21	6.60	12.82		4	$P2_1/c$	$[Ge_2O_7]$	Jarchow et al., 1981a
$R_2AlGe_2O_8(OH)$	La, Nd	La	7.63	5.78	17.20	$\beta = 110.6$	4	$P2_1/c$	$[GeO_4]$	Jarchow et al., 1982

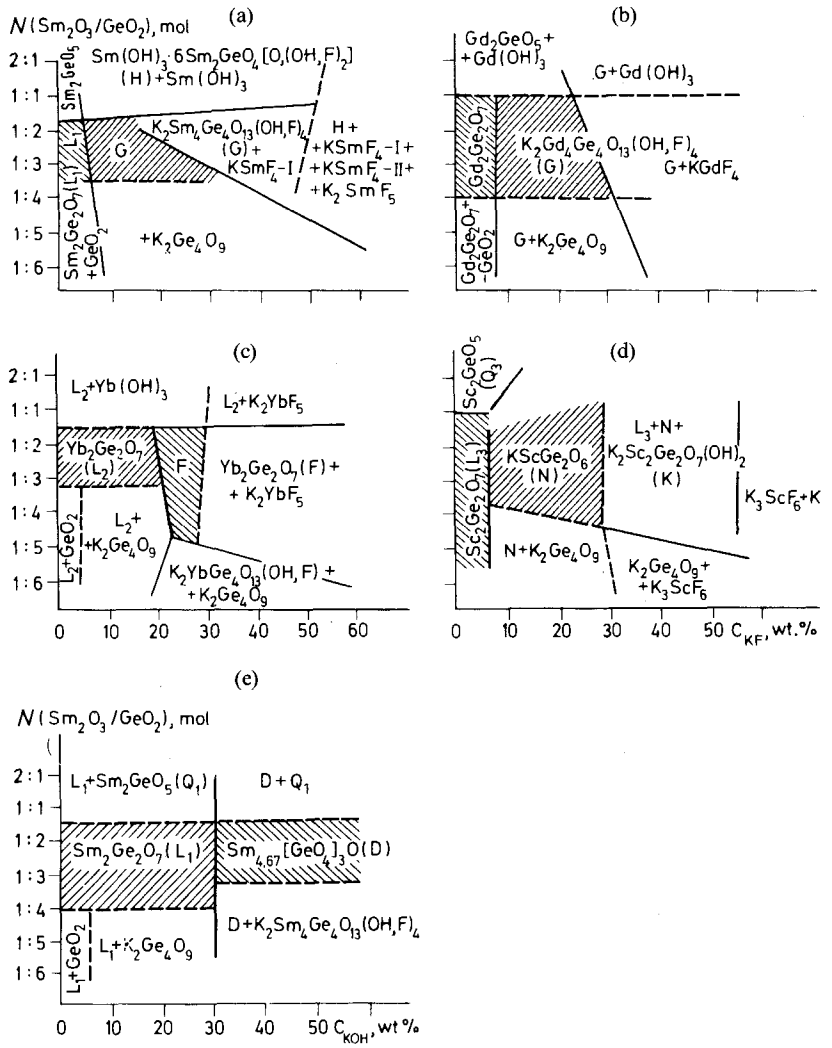

Fig. 62. Phase diagrams for crystallization in the R_2O_3–GeO_2–KF–H_2O systems (a)–(d). In (e) KOH is used as a mineralizer (Demianets et al., 1980b).

Er, Yb). The first compound can also contain fluoride ions, in which case the formula is $R(OH)_3 \cdot 6R_2(GeO_4) \cdot [O, (OH, F)]$ (Emelchenko and Iluykhin, 1974). The structure is hexagonal with the same space group as in oxyapatites and reveals a close relationship to the apatite structure. $R_{13}(GeO_4)_6(OH)_3 \cdot [O, (OH, F)]$ is prepared hydrothermally in the R_2O_3–GeO_2–H_2O system using a $R_2O_3 : GeO_2$ ratio of more than 1 and KF as the mineralizer (fig. 62) (Demianets et al., 1980b).

$R_4Ge_3O_9(OH, F)_6$ powder and crystals can be hydrothermally prepared in the same system R_2O_3–GeO_2–H_2O with KOH as the mineralizer (Demianets et al.,

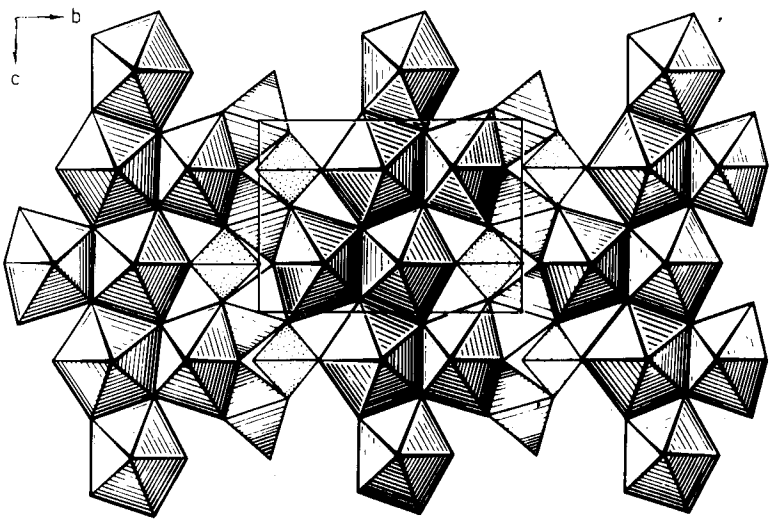

Fig. 63. A projection of the structure of $Sm_4Ge_3O_9(OH)_6$ on the *yz* plane. Bands of Sm polyhedra and GeO_4 lie above and below the plane $x = 0$ whereas the GeO_6 octahedra lie on this plane (Nikolskii et al., 1977).

1980a). In the structure of $Sm_4Ge_3O_9(OH)_6$ the germanium atoms occupy two types of coordination polyhedra: tetrahedra and octahedra. The GeO_6 octahedra are joined in an infinite chain through GeO_4 tetrahedra: each octahedron is linked to two tetrahedra (fig. 63). The coordination of the radical $Ge_3O_9^{6-}$ may be presented as $Ge^{VI}Ge_2^{IV}O_9$ (Nikolskii et al., 1977). The rare earth atoms are 7- and 8-coordinated. The skeletons of cation oxygen polyhedra show olivine-like bands (Dago et al., 1980a; Pushcharovskii et al., 1980).

5.3. *Ternary rare earth germanates*

5.3.1. *Alkali rare earth germanates*

The most common alkali rare earth germanate is the type $ARGeO_4$ where A is lithium or sodium. There are two structure types: tetragonal for the lighter rare earths (La $\cdots$ Nd, Eu) and orthorhombic for the heavier ones (Sm $\cdots$ Lu, Y) (Chichagov et al., 1967, 1969b; Emelchenko et al., 1974c). These structures, like nearly all the alkali rare earth germanates, show olivine-like band structure in the orientation of the cation polyhedra.

In the tetragonal $NaRGeO_4$ structure RO_6 octahedra are located in the gaps of the NaO_6 octahedra bands. The RO_6 octahedra appear in rings of four surrounded by the sodium atoms. The structure is isomorphic with B-type $NaRSiO_4$ (Chichagov et al., 1967). The orthorhombic $NaRGeO_4$, isomorphic with C-type $NaRSiO_4$, contains linear olivine-like bands of Na and R octahedra (Kharakh et al., 1970). The germanium atoms occupy the triangular holes in these bands. Blasse and Bril (1967a)

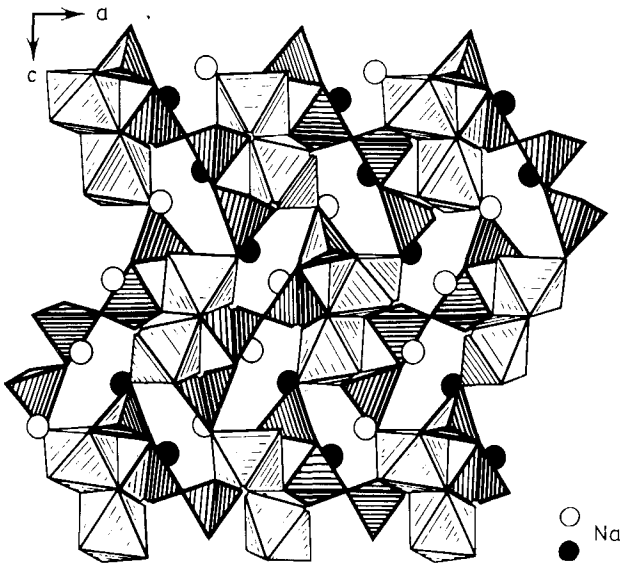

Fig. 64. The crystal structure of $Na_4Sc_2Ge_4O_{13}$ on the *xz* plane. Germanium octahedra are drawn with thicker lines (Gorbunov et al., 1973b).

presume on the basis of the luminescence spectrum that replacement of sodium with lithium does not change the structure. Merinov et al. (1980b) have solved the crystal structure of $LiNdGeO_4$, however, and found it to differ from the sodium compound. The space group is Pbcn and the structure contains octahedrally coordinated neodymium atoms and tetrahedrally coordinated lithium and germanium atoms.

The smallest rare earths (Yb, Lu, Sc) form a sodium germanate with composition $Na_4R_2Ge_4O_{13}$ (Gorbunov et al., 1973b). The structure contains linear $Ge_4O_{13}^{10-}$ radicals, which are unknown in silicates. The radicals are linked together by pairs of RO_6 octahedra having common edges. The $Ge_4O_{13}^{10-}$ germanate anion has also been found in $NaR_3Ge_4O_{13}$ compounds but structural studies have shown that the correct presentation of the composition is $Na_2R_6(Ge_2O_7)_2(Ge_4O_{12})$ (Gorbunov et al., 1974a). The structure contains $Ge_4O_{12}^{8-}$ in rings of four tetrahedra and discrete diorthogermanate groups (fig. 64).

The crystal structure of $Na_5RGe_4O_{12}$ is isomorphic with the corresponding silicate (Demianets et al., 1976; Shannon et al., 1978) having $Ge_{12}O_{36}$ rings joined into infinite columns.

The $NaScGe_2O_6$ and $KScGe_2O_6$ compounds are characterized by an endless chain of Ge_2O_6 radicals (Maksimov et al., 1973). The structure is similar to that found in monoclinic pyroxene and in corresponding silicates (Hawthorne and Grundy, 1977). $LiScGe_2O_6$ is not isomorphic with the corresponding silicate but has an orthorhombic structure (Grotepass et al., 1983).

5.3.2. *Alkali rare earth germanates containing hydroxide ions*

The formation of alkali rare earth hydroxide germanates occurs in hydrothermal conditions in R_2O_3–GeO_2–NaOH(KOH, KF)–H_2O mixtures (Demianets et al.,

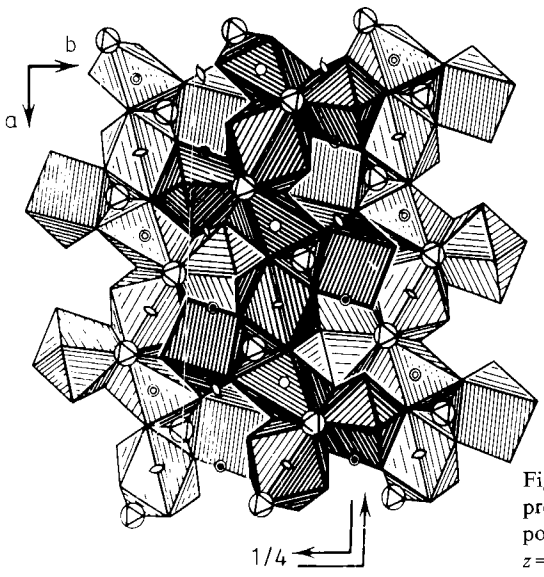

Fig. 65. The structure of $NaSm_3(GeO_4)_2(OH)_2$ projected on the *yz* plane. The lighter bands of polyhedra correspond to $z = 0$ and the darker to $z = 0.75$ (Emelchenko et al., 1975b).

1980b). Single crystals can also be prepared by this method. The composition obtained depends on the proportion of starting material. At least six different structures are known for basic alkali rare earth germanates. In some of these part of the hydroxide ions can be replaced by fluoride ions.

The monoclinic structure type $NaR_3(GeO_4)_2(OH)_2$ is obtained for the rare earths from neodymium to gadolinium (Chichagov et al., 1969a, b). The NaO_6 and RO_7 polyhedra alternate in an infinite olivine-like band parallel to direction (100) (fig. 65). One of the hydroxide ions is coordinated to two rare earth atoms, and the other to three cations (one Na and two R) (Emelchenko et al., 1975b).

A cationic band of olivine–montichellite-type lies at the base of the structure of $Na_2R(GeO_4)OH$ (R = La, Pr, Gd) (Pushcharovskii et al., 1976). The order of the bands of cationic polyhedra is the reverse of that in montichellite ($CaMgSiO_4$). Scandium forms a germanate of the same composition ($Na_2Sc(GeO_4)OH$) but the structure differs from that of the lanthanide compound. In the scandium compound the cationic band pattern is built of ScO_6 octahedra with common cis vertices. The other vertices are common with vertices of GeO_4 tetrahedra (fig. 66) (Zhdanova et al., 1975).

Holmium forms orthorhombic crystals of composition $NaHo_4(GeO_4)O_2OH$ in hydrothermal conditions. The structure contains 7-coordinated rare earth atoms forming a polyhedral band. The germanate groups are linked to the holmium and sodium coordination polyhedra (Christensen, 1972).

$K_2Sc_2(Ge_2O_7)(OH)_2$ is the only known alkali rare earth digermanate. The compound contains potassium, which is not common in rare earth germanates. ScO_6 octahedra sharing edges again form olivine-like bands in the structure (fig. 67). The GeO_4 groups in digermanate ions have an angle of only about 120° (Gorbunov et al., 1973a).

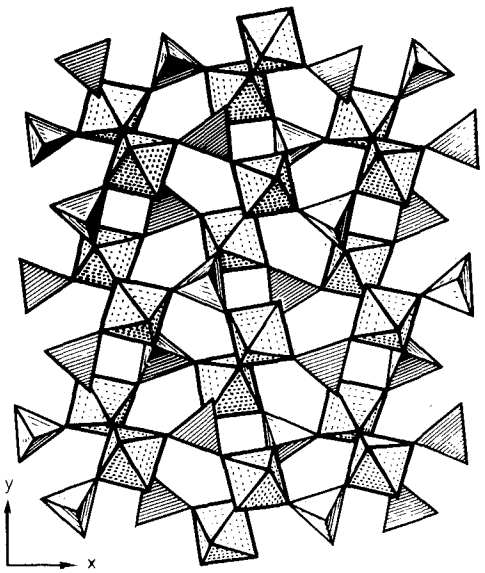

Fig. 66. The crystal structure of Na_2ScGeO_4OH projected on the *xy* plane: infinite bands of ScO_6 octahedra linked by GeO_4 tetrahedra (Zhdanova et al., 1975).

A bent chain of four GeO_4 tetrahedra and rings of six rare earth oxygen octahedra with shared edges are characteristic for the structure of $K_2R_4Ge_4O_{13}(OH, F)_4$ (Demianets et al., 1975). The rare earth–oxygen octahedra form rings containing six polyhedra with shared edges. The ring pattern is parallel to the direction [010] (Klimentova et al., 1975).

A complex infinite radical band $(Ge_8O_{20})^{8-}_{\infty}$ is formed in the germanate $K_2YbGe_4O_{10}(OH, F)$. With this form of the radical the formula of the compound should be doubled and written as $K_4Yb_2Ge_8O_{10}(OH, F)_2$. The repeating band contains a ring of eight GeO_4 tetrahedra. The YbO_6 octahedra are connected through their vertices and form a column along the *c* axis (Nikolskii et al., 1975).

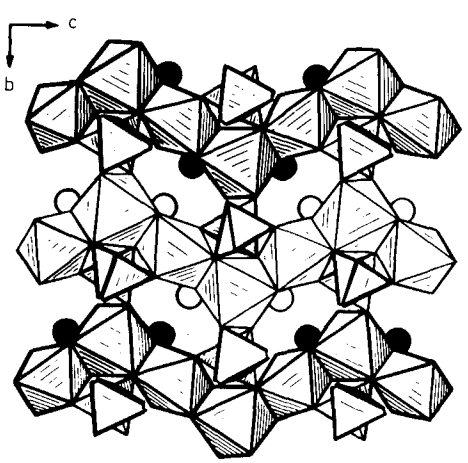

Fig. 67. The structure of $K_2Sc_2Ge_2O_7(OH)_2$ on the *yz* plane. The darker octahedra and open K circles are located at $x = 0$ whereas the lighter octahedra and full K circles are at $x = 0.5$ (Gorbunov et al., 1973a).

5.3.3. *Rare earth germanates containing divalent cations*

Three different structure types of ternary rare earth germanates with divalent cations are known: garnet, apatite and perovskite. The rare earth garnets have been studied widely because of their interesting optical, magnetic and electric properties (Geller et al., 1960; Mill, 1966; Geller, 1967). In the ideal garnet structure the trivalent cations occupy the dodecahedral site, the divalent cation the octahedral site and the tetravalent atoms (Si, Ge) the tetrahedral site.. In some cases the divalent cations partly occupy the dodecahedral site (Reinen, 1964). In germanates the divalent cations can also be partly tetrahedrally coordinated; then a part of the germanium atoms have octahedral coordination (Bayer, 1971; Mill and Roniger, 1973).

The structure of apatite-type mixed cation rare earth germanates is similar to that described for mixed cation silicate apatites. The structure is capacious toward isomorphic substitutions and preserves itself in various substitutions, in the cation as well as in the anion structure (Cockbain and Smith, 1965; Ito, 1968; Fedorov et al., 1982).

$MgLa_2GeO_6$ has a perovskite structure containing 12-coordinated rare earth atoms and 6-coordinated magnesium and germanium atoms. The lattice is simple cubic with lanthanum atoms at the corners, oxygen atoms on the faces and magnesium and germanium atoms at the center of the cube (Roy, 1954).

5.3.4. *Germanates containing trivalent cation*

Two types of germanates containing trivalent aluminium or gallium have been obtained for the rare earths: $RMGeO_5$ and $RMGe_2O_7$. Both compounds can be crystallized by hydrothermal methods. The structure of $RMGeO_5$ contains chains of MO_6 octahedra that are held together by RO_8 polyhedra and GeO_5 pyramids (Jarchow et al., 1981b). In the digermanate structure the isolated $Ge_2O_7^{6-}$ double tetrahedra are linked by strongly distorted MO_5 trigonal prisms and RO_9 polyhedra (Jarchow et al., 1981a).

5.4. *Properties of rare earth germanates*

Densities and melting temperatures of selected rare earth germanates are listed in table 18. The binary rare earth germanates seem to have high melting temperatures and refraction indices and, for alkali-containing germanates, lower values are reported.

5.4.1. *IR spectra*

The infrared spectra of rare earth germanates have been investigated by Toropov et al. (1971) and Demianets et al. (1975). Results from those studies are collected in table 19. Exact assignments could not be made for all frequencies observed.

5.4.2. *Electrical and magnetic properties*

The rare earth oxyorthogermanates and digermanates have been classified as dielectric materials. At room temperature they have high specific resistance (10^{-13}–$10^{-14}\,\Omega\,cm^{-1}$). The character of the conductivity is ionic (Popov and Petrova, 1973).

TABLE 18
Densities and melting temperatures of some rare earth germanates according to Glushkova et al., 1967, Bondar, 1979 and Demianets et al., 1980b.

Composition	Density ($g\,cm^{-3}$)	Melting temp. (°C)
$La_2(GeO_4)O$	5.97	1800
$Gd_2(GeO_4)O$	7.07	1880
$Y_2(GeO_4)O$	4.83	1975
$La_{4.67}(GeO_4)_3O$	5.89	1770
$La_4(GeO_4)O_4$	6.30	172[a]
$Gd_4(GeO_4)O_4$	7.77	1650[a]
$Y_4(GeO_4)O_4$	5.10	2000
$La_2Ge_2O_7$	5.67	1680[a]
$Gd_2Ge_2O_7$	6.70	1770
$Y_2Ge_2O_7$	4.69	1800
$Sc_2Ge_2O_7$	4.46	1860

[a] Melting with decomposition.

Like their silicate analogues the sodium rare earth germanates of composition $Na_5RGe_4O_{12}$ show high ionic conductivity. The alkali cations can move freely in the structure. The conductivity values observed in the germanates lie between 10^{-2} and $10^{-3}\,\Omega\,cm^{-1}$ (Shannon et al., 1978; Hong et al., 1978).

The temperatures of the magnetic transitions of some rare earth germanates have been studied by Fournier and Kohemüller (1968) and Wanklyn (1973a). In oxyorthogermanates the temperatures are 1.25–2.50 K and in digermanates 1.15–2.15 K.

5.4.3. *Luminescence properties*

Among the activated binary rare earth germanates, only the luminescence properties of $Y_2(GeO_4)O:Tb^{3+}$ have been recorded. In this compound, terbium shows its usual intense yellow-green emission at wavelength 550 nm (Bondar, 1979).

More detailed work has been carried out with Eu^{3+}- and Tb^{3+}-activated alkali (Li, Na) rare earth (La, Gd, Lu, Y) germanates (Blasse and Bril, 1967a). The luminescence of the unactivated compounds has been studied as well. The excitation spectrum of Eu^{3+}-activated $ARGeO_4$ phosphors contains a broad charge transfer band between 230 and 280 nm, varying in position with the host cation. In the Tb^{3+}-activated compounds the excitation band lies at about 250 nm (Blasse and Bril, 1967a, b). The quantum efficiency of these phosphors is quite good and increases with decreasing excitation band wavelength (Blasse, 1966; Blasse and Bril, 1967b). Energy transfer from the Gd^{3+} ion to the activator has been observed in the $NaGdGeO_4$ matrix (Bril and Wanmaker, 1964). The emission spectra of Eu^{3+}- and Tb^{3+}-activated $ARGeO_4$ compounds contain the normal peaks of these activators. In europium-activated compounds the most intense peaks are originating from the $^5D_0 \rightarrow {}^7F_2$ transition, situated in the orange-red region (600–625 nm). The transitions from the $^5D_1$ level in the green region are exceptionally lacking in these materials

TABLE 19

IR frequencies (cm^{-1}) of some rare earth germanates according to Toropov et al., 1971 and Demianets et al., 1975, 1980b.[a)]

$Tb_2(GeO_4)O$		$La_{4.67}(GeO_4)_3O$		$La_2Ge_2O_7$		$Nd_4(GeO_4)O_4$		$NaSmGeO_4$	
ν	Assignment	ν	Assignment	ν	Assignment	ν	Assignment	ν	Assignment
870vs	ν_s GeO_4	855s	ν_s GeO_4	880m	ν_{as} GeOGe	915vw		840m	ν_s GeO_4
830vw		830vs		840s		890vw	ν_s GeO_4	785vs	ν_{as} GeO_4
790vs		795vs		805vs		850w		735s	
750s	ν_{as} GeO_4	770vs	ν_{as} GeO_4	770s	ν_s GeO_3	800m		670s	
700vs		645w		740s		770sh	ν_{as} GeO_4	495s	δ_{as} GeO_4
515sh		580w		630m	ν_s GeOGe	750vs		475s	
495m	δ_{as} GeO_4	490s	δ_{as} GeO_4	525w		550m	δ_{as} GeO_4	450sh	
445m		440vs		495m	δ GeO_3	450vs			
				460m					
				440sh	ν La–O				
				410s					

$NaSm_3(GeO_4)_2(OH)_2$		$K_2Sc_2Ge_2O_7(OH)_2$		$Na_4Yb_2Ge_4O_{13}$		$Na_2Nd_6(Ge_2O_7)_2(Ge_4O_{12})$		$NaScGe_2O_6$	
ν	Assignment	ν	Assignment	ν	Assignment	ν	Assignment	ν	Assignment
930–850m	δ Sm–OH	790sh		870s		895m		920m	
795		775vs	ν_s GeO_3	840w	ν_{as} GeOGe	840m	ν_{as} GeOGe	885sh	ν_{as} GeOGe
775	ν_{as} GeO_4	760vs		820w	ν_{as} GeO_2	830m		870s	ν_s GeO_2
755s		720s		790vs	ν_s GeO_2	800		815vs	ν_{as} GeO_2
685s		570s	ν_s GeOGe	780vs	ν_{as} GeO_3	780sh	ν_{as} GeO_2	785vs	
570vw	γ Sm–OH	475vs	δ GeO_3	750s	ν_s GeO_3	755vs	ν_s GeO_2	510s	ν_s GeOGe
465m		450sh	ν Sc–O	725s		740sh	ν_{as} GeO_3	490m	δ Ge–O
430m	δ_{as} GeO_4			580m	ν_s GeOGe	715sh	ν_s GeO_3	465s	δ Sc–O
410m				550m		690m	ν_s GeOGe	425vs	
				500sh	ζ GeO_3	565sh			
				465sh	ζ GeO_2	550m	ν_s' GeOGe		
				440m	δ GeOGe	475sh	ζ GeO_3		
				425m	ν Yb–O	455sh			
				415m		440m	δ GeOGe		
						410m	δ Nd–O		

[a)] Symbols follow tables 8 and 16.

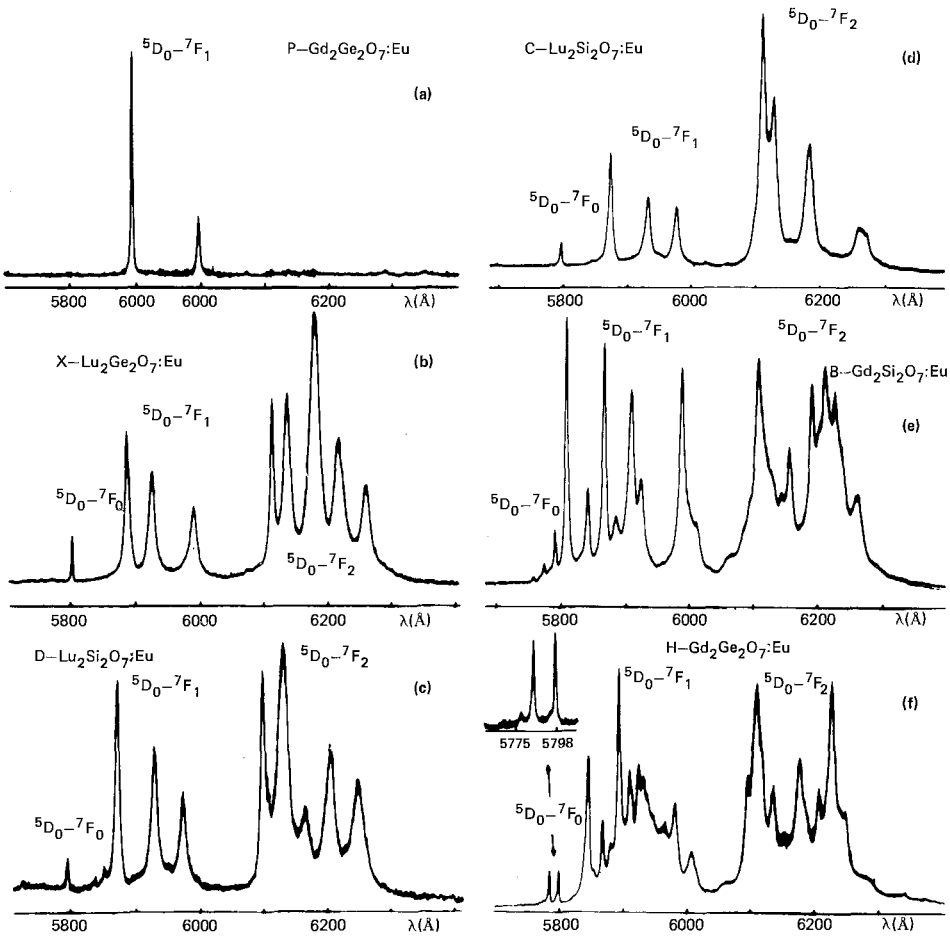

Fig. 68. Part of the emission spectra of Eu^{3+} in different digermanate and disilicate hosts (coded as in fig. 60) (Bocquillon et al., 1980).

because of the nonradiating transition $^5D_1 \rightarrow {}^5D_0$ (Baumik and Nuget, 1966; Blasse and Bril, 1967b). In terbium-activated compounds the most intense transition is $^5D_4 \rightarrow {}^7F_5$ emitting in the yellow-green region.

A detailed analysis of the luminescence spectra of alkali rare earth germanates has been made by Emelchenko et al. (1976). The crystal field parameters have been calculated.

Eu^{3+}-activated rare earth digermanates have been investigated by Bocquillon et al. (1980). The main interest in their work was the use of europium as a structural probe and special attention was paid to the new hexagonal digermanate phase they discovered (fig. 68).

The luminescence spectrum of Nd^{3+}-activated $NaGdGeO_4$ crystals has been studied by Kaminskii et al. (1980). The compound is a promising laser material. The

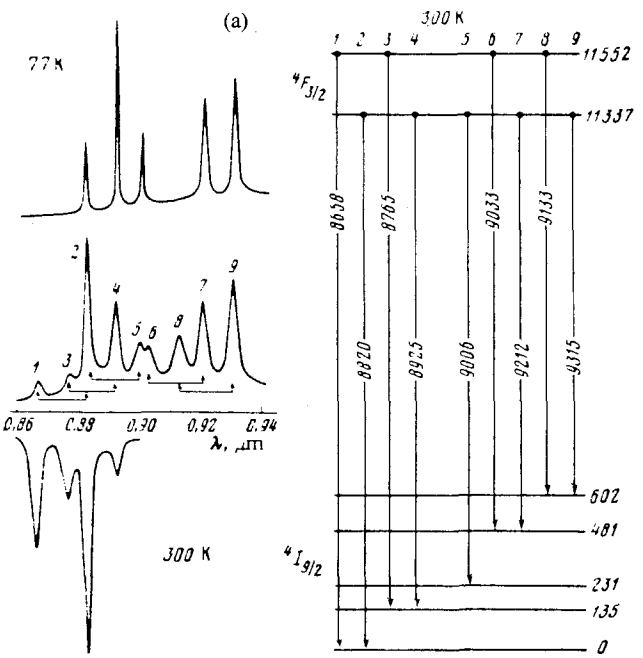

Fig. 69. (a) The luminescence and absorption spectra of Nd^{3+} in $NaNdGeO_4$ and the splitting of the $^4F_{3/2}$ and $^4I_{9/2}$ multiplet.

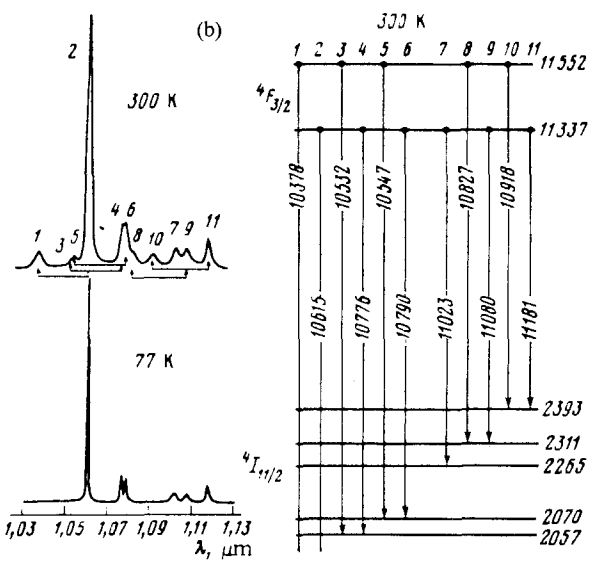

Fig. 69. (b) The luminescence spectra and splitting of the $^4F_{3/2}$ and $^4I_{11/2}$ multiplet of Nd^{3+} in the same host (Kaminskii et al., 1980).

stimulated emission is based on the Nd^{3+} transitions $^4F_{3/2} \rightarrow {}^4I_{11/2}$ and $^4F_{3/2} \rightarrow {}^4I_{13/2}$ having room temperature wavelengths 1.0615 and 1.3334 μm, respectively (fig. 69). The width of these lines is about 12 cm^{-1}. With low Nd concentrations the lifetime of the metastable $^4F_{3/2}$ state is about 180 μs with a quantum yield close to unity (Kaminskii et al., 1981).

6. Rare earth nitrates

6.1. *Introduction*

The nitrates are among the few readily soluble and easily prepared inorganic compounds of the rare earths. This has led to their use as starting materials for the synthesis of rare earth complexes, in a similar way to the chlorides (Garnovskii et al., 1981). Sufficient solubility has also encouraged a large number of studies dealing with complex equilibria and solubility (Siekierski et al., 1983). The growth of good quality single crystals has allowed X-ray, optical and other studies of the thermodynamically stable phases to be carried out. Until the late 1950s rare earth nitrates were extensively used in the separation and purification of individual rare earth elements by fractional crystallization and the nitrate solutions still are used in liquid–liquid separation processes (Greinacher and Reinhardt, 1982).

The literature on rare earth nitrates is voluminous, extending over 100 years and into hundreds of primary articles. A number of reviews have appeared too. The Gmelin nitrate volume (1974) and its Gmelin-Kraut (1928–1932) predecessor and the handbooks by Pascal (1959) and Mellor (1965) all contain invaluable information. There is a review by Brown (1975) on actinide and lanthanide nitrates emphasizing literature between the years 1969 and 1972, and there are recent reviews by Eriksson (1982a) and Niinistö (1982), though more limited in scope.

The present review, while providing an overall picture of complex rare earth nitrates, will focus on recent literature and on solid state structural data. Thermal and spectroscopic data will be discussed and the composition and structural data from solution studies will be compared with the data from solid state studies. As in the previous sections, mixed ligand complexes with organic ligands and counter-ions will generally be excluded from the discussion.

6.2. *Interaction between rare earth and nitrate ions*

The interaction between R^{3+} and NO_3^- ions in aqueous solutions has been studied by several techniques during the past 20 years. A literature survey up to the early 1970s is presented in Gmelin (1974). The main question that has been debated concerns the nature of the complexation: is it inner or outer sphere? From thermodynamic considerations, Choppin (1971) arrived at a predominantly outer-sphere model; see also Choppin and Bertha, 1973. However, in a recent study of fluorescence spectra and lifetimes, Bünzli and Yersin (1979) suggested inner-sphere complexation for europium nitrate, in contrast to the corresponding perchlorate system, see fig. 70. After studying the effect of various ligands on the $^7F_0 \rightarrow {}^5D_0$ transition,

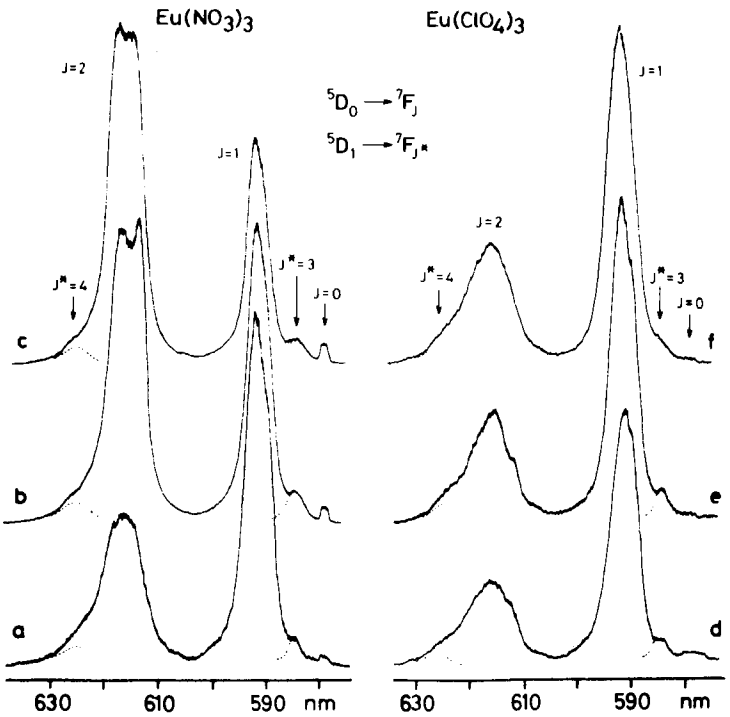

Fig. 70. Part of the fluorescence spectra of $Eu(NO_3)_3$ and $Eu(ClO_4)_3$ in water. Curve labels: a 0.01 M, b 1 M, c 0.1 M + Me_4NNO_3 5 M, d 0.01 M, e 1 M, f 0.05 M + $NaClO_4$ 0.5 M (Bünzli and Yersin, 1979).

Breen and Horrocks (1983) also concluded the Eu^{3+}–NO_3^- interaction to be of inner-sphere nature.

On the other hand, Marcantonatos et al. (1981, 1982) have pointed out that luminescence studies are concerned with excited state behavior that may be different from that of ground state systems; see also a recent discussion by Choppin (1984).

It is interesting to note, however, that the stability constants calculated on the basis of different models and different techniques deviate very little. As an example, the association constant for $[Eu(NO_3)]^{2+}$ at $I = 0.5$ M $NaClO_4$ may be quoted as $\beta_1 = 1.5 \pm 0.7$ and 2.7 ± 0.2 when determined by luminescence (Breen and Horrocks, 1983) and thermodynamic (Choppin, 1984) techniques, respectively.

Since a very recent luminescence study again clearly favors the inner-sphere model (Tanaka and Yamashita, 1984), it seems reasonable to assume that the inner-sphere contribution cannot be neglected. Judging from the solid state structures, moreover, this would be the preferred model. There is an obvious need for an X-ray diffraction, neutron diffraction or EXAFS study in solution to settle this question.

Besides the 1 : 1 complexes, there are reports indicating the existence of higher complexes, especially in concentrated aqueous solutions. According to Marcus and Givon (1964), n may be as high as 7 for the $[R(NO_3)_n]^{3-n}$ complexes. The existence

of the pentanitrato complex $[R(NO_3)_5]^{2-}$ has been well established by solution studies (Gmelin, 1974) as well as by the isolation of solid pentanitrate complexes. The solubility data on rare earth nitrates, including the compositions of precipitating solid phases, have recently been tabulated by Siekierski et al. (1984) as part of a IUPAC project.

In most solution studies, the bonding mode of the nitrate group has not been discussed. A Raman and IR study of gadolinium nitrate solutions indicated that in the $[Gd(NO_3)_2]^+$ complex the nitrate groups are not equal; one is bound in bidentate and the other in unidentate mode (Nelson and Irish, 1971). In the solid state, several bonding modes are observed for metal nitrates: These Addison et al. (1971) have classified into four main groups: symmetrically bidentate, unsymmetrically bidentate, unidentate and bridging. The bonding modes involve either C_s or C_{2v} symmetry of the nitrato group. Leclaire (1979) has used seven classes, noting that the most frequent case is the bidentate. This is also the favored mode of bonding for the solid rare earth nitrates, as will be seen below. The dimensions of the nitrate group in solid R^{3+} and R^{4+} structures have been discussed briefly by Brown (1975) and in more detail, using Leclaire's criteria, by Eriksson (1982a).

6.3. *Rare earth trinitrates*

Evaporation at room temperature of aqueous nitric acid solutions containing R^{3+} yields a crystalline precipitate $R(NO_3)_3 \cdot nH_2O$ where n is usually 5 or 6, depending on R and on the preparative conditions. The heavier rare earths and yttrium tend to form pentahydrate precipitates more easily and this tendency can be promoted by seeding with $Bi(NO_3)_3 \cdot 5H_2O$ crystals (Marsh, 1941). A recent study on the crystallization of the penta- and hexahydrates has been published by Odent et al. (1975).

Scandium differs in its behavior by forming, under normal conditions, the tetrahydrate phase (Pushkina and Komissarova, 1963). For the other rare earths, lower hydrates can be prepared at higher temperatures or by varying the composition of the initial solution (Gmelin, 1974; Siekierski et al., 1983). Another preparative possibility is careful dehydration.

Although large single crystals have been grown by the slow evaporation method for many rare earths (e.g., Richardson et al., 1959), difficulties due to viscous solutions and metastable phases (O'Brien and Bautista, 1975) or to "nitrosolvates" (Popov and Mironov, 1968; Mironov et al., 1969) have been reported. A crystallization procedure yielding stoichiometric $Nd(NO_3)_3 \cdot 6H_2O$ crystals has been discussed recently in detail by Caro et al. (1977) and by Quarton and Svoronos (1982).

6.3.1. *The hexahydrates*

Solubility data for the systems R^{3+}–HNO_3–H_2O and $R(NO_3)_3$–H_2O (Siekierski et al., 1983) indicate the existence of the hexahydrate phase for yttrium and all lanthanides except promethium, which has not been studied. Hexahydrate crystals were studied by optical crystallography as early as the turn of the century (Groth, 1908) and found to be triclinic. X-ray diffractometric studies have confirmed these early results and shown that there exist two isostructural series, both crystallizing in

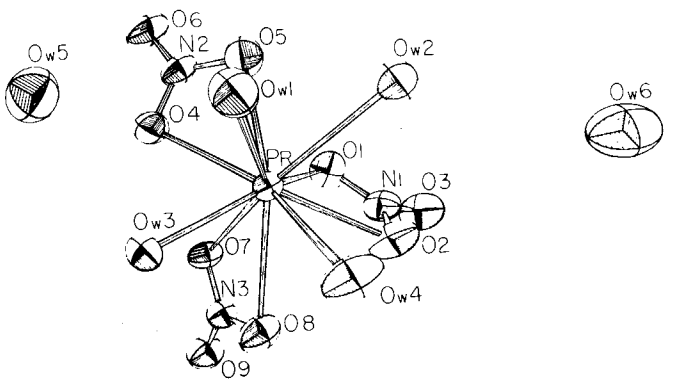

Fig. 71. A perspective drawing showing the coordination around Pr^{3+} in the structure of $Pr(NO_3)_3 \cdot 6H_2O$ (Fuller and Jacobson, 1976).

the space group $P\bar{1}$: La and Ce belong to the first series, and Pr $\cdots$ Lu and Y to the second (Iveronova et al., 1951, 1955). On the other hand, the early reports on the existence of α and β polymorphs for $La(NO_3)_3 \cdot 6H_2O$ and $Nd(NO_3)_3 \cdot 6H_2O$ (Friend, 1935a, b; Brunisholz et al., 1964) have not yet found corroboration through X-ray studies. DSC studies (Eriksson, 1982a) have likewise failed to provide any indication of phase transitions.

Representatives of the second isostructural series were the first to be studied by single crystal X-ray diffraction methods. The structure of $Pr(NO_3)_3 \cdot 6H_2O$ was determined by Volodina, Rumanova, and Belov in 1961 and refined a few years later (Rumanova et al., 1964). Another refinement was carried out by Fuller and Jacobson (1976). The praseodymium atom is decacoordinated by three bidentate nitrate groups and by four water molecules (fig. 71). The Pr–O(NO_3) distances range from 2.56 to 2.72 Å but the Pr–O(H_2O) range is much shorter, 2.45–2.47 Å (Fuller and Jacobson, 1976). It is interesting to note that $[Pr(H_2O)_4(NO_3)_3] \cdot 2H_2O$ is isostructural with the holmium bicarbonate complex $[Ho(H_2O)_4(HCO_3)_3] \cdot 2H_2O$ (Rohrbaugh and Jacobson, 1974).

Besides reports giving unit cell data for other members of the second isostructural series Pr $\cdots$ Lu, Y, there are two papers presenting a full structural determination. Ribar et al. (1980) have determined the structure of $Y(NO_3)_3 \cdot 6H_2O$ and Rogers et al. (1983) have studied the structure of the Nd compound. In the latter report, the hydrogen atom positions are given, showing how the $[R(H_2O)_4(NO_3)_3]$ complexes and the two outer-sphere water molecules are joined into a three-dimensional structure by hydrogen bonds.

The first isostructural series, represented only by La and Ce, exhibits interesting structural features. The structure of $La(NO_3)_3 \cdot 6H_2O$ was solved only recently (Eriksson et al., 1978, 1980b). X-ray study revealed that La^{3+} is surrounded by 11 oxygens, from three bidentate NO_3^- groups and from five H_2O molecules, making this the first example of undecacoordination in a trivalent rare earth complex. The bond distance ranges are 2.53–2.67 and 2.62–2.88 Å for La–O(H_2O) and La–O(NO_3)

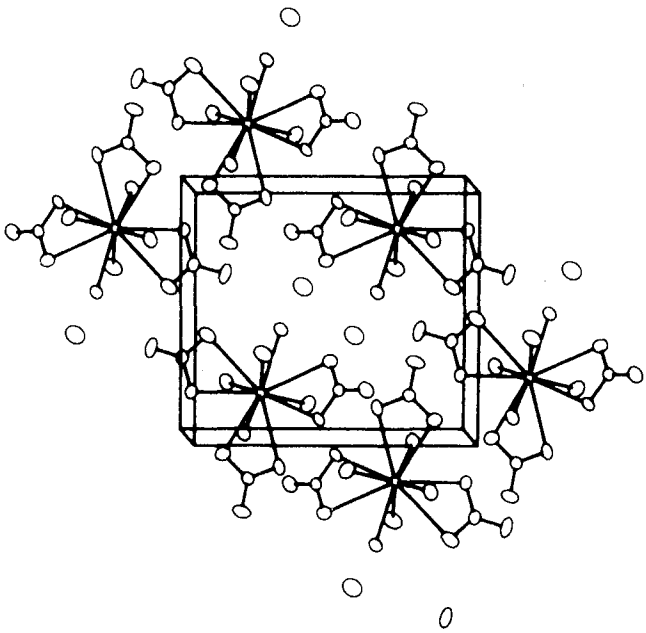

Fig. 72. A perspective view of the unit cell packing in the structure of $La(NO_3)_3 \cdot 6H_2O$ (Eriksson et al., 1980b).

bonds, respectively. The unit cell packing and coordination polyhedron are shown in figs. 72 and 73.

Although 11-coordination is not often encountered in the Periodic Table, there are now several examples among the R^{3+} complexes (section 1, table 1); however, $La(NO_3)_3 \cdot 6H_2O$ (and its cerium analogue; Milinski et al., 1980) still remains the only purely inorganic compound among them.

6.3.2. *The pentahydrates*

Unlike the hexahydrates, the pentahydrates appear to be thermodynamically unstable (Siekierski et al., 1983). Single crystals and polycrystalline powder of $R(NO_3)_3 \cdot 5H_2O$ have nevertheless been prepared. Three different preparative approaches have been employed: (i) use of higher temperatures and nitric acid concentrations (e.g., Mironov and Popov, 1966), (ii) dehydration over H_2SO_4, P_2O_5 or NaOH (e.g., Löwenstein, 1909), and (iii) seeding with $Bi(NO_3)_3 \cdot 5H_2O$ (Marsh, 1941). In addition, the pentahydrate phase appears as an intermediate during the thermal degradation of the hexahydrates and this provides an additional, although difficult, preparative possibility.

In accordance with the preparative difficulties, the pentahydrates are structurally poorly characterized. Odent et al. (1975) showed that, as for the hexahydrates, two isostructural series, viz. La–Ce and Pr–Lu, Y, exist for the pentahydrates. They have also published the X-ray powder pattern for $Yb(NO_3)_3 \cdot 5H_2O$ and line diagrams for the isostructural Gd–Yb and Y compounds. Earlier, Mironov et al. (1969) had

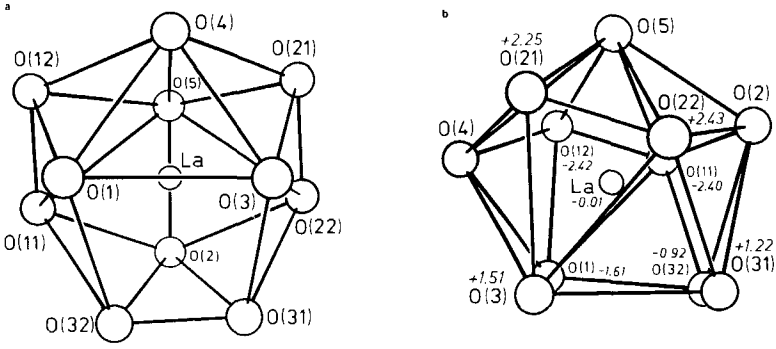

Fig. 73. Two views of the 11-coordinated polyhedron around La in the structure of $La(NO_3)_3 \cdot 6H_2O$ (Eriksson et al., 1980b).

published X-ray powder patterns for the pentahydrates, R = La–Sm, and their data also indicate a structural break between Ce and Pr. In addition, the JCPDS (Joint Committee on Powder Diffraction Standards) file contains powder patterns from diverse sources. As pointed out by Eriksson (1982b), one should be careful in identifying the nitrate phases on the basis of published X-ray patterns only.

In the pentahydrate series, the only compound to have been characterized by single crystal methods is $Y(NO_3)_3 \cdot 5H_2O$ (Eriksson, 1982). As in the corresponding hexahydrate, the crystals are triclinic ($P\bar{1}$) and the coordination number is 10. The unit cell is slightly smaller (583 vs. 610 Å^3), in accordance with its smaller content. Although the formula of the complex is the same as the hexahydrate, $[Y(H_2O)_4(NO_3)_3]$, the coordination about the Y^{3+} ion is different, as seen in fig. 74. Rather, the environment of Y^{3+} in $Y(NO_3)_3 \cdot 5H_2O$ resembles that of La^{3+} in the structure $La(NO_3)_3 \cdot 6H_2O$ (cf. figs. 72 and 73).

6.3.3. *The tetra- and lower hydrates*

Apart from that of scandium, the tetrahydrate phase appears to be metastable and difficult to obtain in the solid phase as an isolated product (Gmelin, 1974). This is even truer for the lower hydrates ($n \leqq 3$), whose existence has not even been claimed in the literature for all rare earths. For a critical evaluation of the solubility data concerning the nitrate hydrates, see Siekierski et al. (1983).

The solubility isotherm of Sc_2O_3–N_2O_5–H_2O at 0°C (Komissarova and Pushkina, 1967) indicates that $Sc_2(NO_3)_3 \cdot 4H_2O$ is formed in a wide concentration range. It should be noted that at lower HNO_3 concentrations hydroxo complexes are formed, indicating the tendency of Sc^{3+} to hydrolysis. Furthermore, the crystals of $Sc(NO_3)_3 \cdot 4H_2O$ are very hygroscopic and easily degrade in air. These properties and difficulties in growing crystals have prevented a full structural analysis, although the monoclinic unit cell constants are known (Pushkina and Komissarova, 1967).

The tri- and dihydrates of $Sc(NO_3)_3$ have also been obtained as crystalline precipitates from highly concentrated HNO_3 solutions (Chuvaev et al., 1967). Another route is slow dehydration of the tetrahydrate over concentrated H_2SO_4 or P_2O_5 (Komissarova and Pushkina, 1967; Pushkina and Komissarova, 1967). Accord-

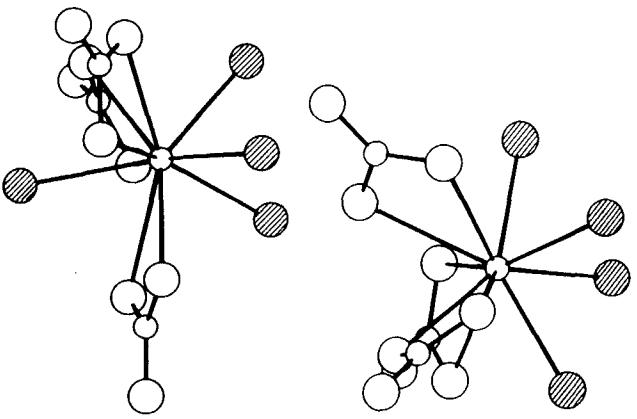

Fig. 74. A comparison of the coordination around yttrium in the two $[Y(NO_3)_3(H_2O)_4]$ complexes in the structures of $Y(NO_3)_3 \cdot 5H_2O$ (left) and $Y(NO_3)_3 \cdot 6H_2O$ (right). The shaded atoms are water oxygens (Eriksson, 1982a).

ing to Komissarova and Pushkina, the crystals of $Sc(NO_3)_3 \cdot 3H_2O$ are monoclinic but the plate-shaped crystals of the dihydrates have not been studied in detail. The hydrates of $Sc(NO_3)_3$ melt into their water of crystallization at relatively low temperatures. The observed melting points are 50, 90 and 75°C for the 4-, 3- and 2-hydrates, respectively (Komissarova et al., 1963; Chuvaev et al., 1967).

No single crystal X-ray data appear to be available for the lower hydrates of rare earth nitrates except those of scandium. The conditions for the preparation of several of these other hydrates have been established, however. Thus, in the system $La(NO_3)_3$–H_2O, the 6-, 5-, 4- and 3-hydrates appear as crystalline phases (Mironov and Popov, 1966). In the system Lu_2O_3–HNO_3–H_2O, the trihydrate was obtained and its powder diffraction pattern, refractive indices, IR and thermal data were determined (Molodkin et al., 1977). For $R(NO_3)_3 \cdot 4H_2O$ (R = La–Sm), see Mironov et al. (1969).

6.3.4. *Anhydrous trinitrates*

Anhydrous nitrates $R(NO_3)_3$ have been observed as intermediate phases during the thermal decomposition of the hydrates for all rare earths except scandium, which tends to decompose directly to the oxynitrate phase (see section 6.7).

A more practical route to anhydrous nitrates employs the reaction of N_2O_4 with the sesquioxides (Moeller and Aftandilian, 1954; Moeller et al., 1957) or, when dissolved in ethyl acetate, with the appropriate metal (Walker and Ferraro, 1965).

Apart from IR spectroscopic and thermoanalytical investigations, to be discussed later, the anhydrous phases have not been structurally characterized.

6.4. *Complex nitrates*

Anionic nitrato complexes, with mono- or divalent cations as counter-ions, have been known since the last century. These double nitrates have lower solubilities than the simple nitrates previously discussed and they were extensively used until the end of the 1950s for the separation of the individual rare earths (Callow, 1967).

Especially popular compounds in the fractional crystallization processes were the ammonium and magnesium nitrates, viz. $(NH_4)_2R(NO_3)_5 \cdot nH_2O$ and $Mg_3R_2(NO_3)_{12} \cdot 24H_2O$.

Among the complex nitrates, the pentanitrato series, corresponding to the anion $[R(NO_3)_5]^{2-}$, is the most extensive because several low valent cations may serve as counter-ions leading to a large number of solid structures. Furthermore, water plays an active role and may enter the inner coordination sphere, especially in the case of the larger R^{3+} ions, and/or may be included in the solid structures as water of crystallization. In the case of the dodecanitrato series, $M^{II}R_2(NO_3)_{12} \cdot 24H_2O$, M^{II} may be varied, but the number and role of water molecules is fixed.

Here we shall discuss only the purely inorganic structures, leaving the large number of organic counter-ions (e.g., Ph_3EtP, Ph_4As) and additional ligands (e.g., urea, DMSO) outside the scope of this review. Data for these other complexes can be found in Brown (1975), Gmelin (1974) and Palenik (1983). As an example of very recent studies involving nitrato complexes with organic ligands or counter-ions, the interesting ESR study by Urland and Kremer (1984) on $(Ph_4As)_2[Yb(NO_3)_5]$ may be mentioned.

6.4.1. *Pentanitrato complexes*

Solid pentanitrato complexes correspond to the formula $M^I_2R(NO_3)_5 \cdot nH_2O$, where M^I is most commonly an alkali (Li–Cs) or ammonium ion but may also be some other monovalent inorganic (e.g., Tl^+, NO^+) or organic ion. The formation of pentanitrato species has been studied extensively in systems R^{3+}–M^+–HNO_3–H_2O (Gmelin, 1974; Siekierski et al., 1983). In recent years, Molodkin and co-workers have made a systematic investigation and reported the formation and properties of $M_2[R(NO_3)_5] \cdot nH_2O$ phases in the case of several rare earths (La, Pr $\cdots$ Lu) and alkali metals (Li, Na, K, Rb, Cs) (Molodkin et al., 1976a, b, 1977, 1978a, b, 1979a, b, 1981a, b, 1982, 1983). As an example, the solubility diagram in the system $CsNO_3$–$La(NO_3)_3$–H_2O is depicted in fig. 75. Besides the stoichiometries of the hydrated phases ($n = 1$–4), X-ray powder patterns, IR and thermal decomposition curves are usually given.

Scandium behaves differently, since from aqueous solutions of $Sc(NO_3)_3 \cdot 4H_2O$ and MNO_3 (M = K, Rb, Cs) only mixtures of original nitrates are obtained (Komissarova et al., 1971c). At high HNO_3 concentrations (34–37%) it is possible to obtain the pentanitrato complexes, but then only as anhydrous compounds. These form single biaxial crystals that are very hygroscopic. Nevertheless, powder X-ray diffraction, IR and TG/DTA data have been obtained.

Although there are reports on the preparation of anhydrous pentanitrate complexes (other than those of scandium) by precipitation (e.g., $(NH_4)_2Gd(NO_3)_5$; Babievskaya and Perel'man, 1965), the most convenient method is the use of MNO_3/R_2O_3 melts. By this method Carnall et al. (1973) have prepared $K_2[Er(NO_3)_5]$; its structure has been reported by Gebert Sherry (1978).

The known crystal structures of inorganic pentanitrate complexes are summarized in table 20. The bidentate bonding mode of the nitrato groups leads to a minimum coordination number of 10, which is easily exceeded if water molecules are bonded

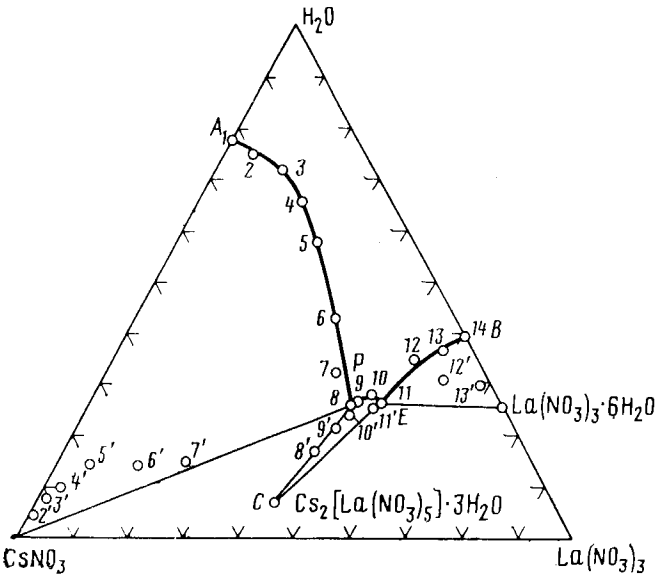

Fig. 75. $CsNO_3$–$La(NO_3)_3$–H_2O solubility diagram at 25°C (Molodkin et al., 1976a).

to the central ion. Only in the case of $(NO)_2[Sc(NO_3)_5]$ is the coordination number exceptionally nine; obviously for steric reasons one of the nitrato groups is monodentate. Even this coordination number is exceptionally high for scandium, which in most of its inorganic compounds has an octahedral coordination (Valkonen, 1979). It is interesting to note that although the unit cell dimensions in the complexes $(NO)_2[R(NO_3)_5]$, R = Sc, Y, Ho, are similar, the coordination around Sc^{3+} is different (Addison et al., 1978; Toogood and Chieh, 1975), cf. fig. 76.

The hydrated pentanitrato complexes all have a dodecacoordinated central ion $[R(NO_3)_5(H_2O)_2]^{2-}$. An interesting case is the ammonium complex $(NH_4)_2La(NO_3)_5 \cdot nH_2O$ ($n = 3$ or 4) (Eriksson et al., 1982). The two hydrates are structurally closely related because the removal of water does not bring about the collapse of the structure and the coordination geometry and crystal symmetry are preserved. The only significant change is the contraction of the unit cell when there is one water molecule less. The ammonium ions are involved in the network of hydrogen bonds with the complex anions and the noncoordinated water molecules.

The coordination polyhedron for the potassium (Eriksson et al., 1980a) and the ammonium compounds is a slightly distorted icosahedron; in both cases the water molecules occupy the *trans* positions of the capping atoms (see figs. 77 and 78). In the ammonium compounds each of the five nitrato groups contributes one oxygen atom to each of the two five-membered rings in the icosahedron (fig. 77), whereas in the potassium compound one of the nitrate groups belongs entirely to one of the rings. Symmetry is lower than in the case of the 12-coordinated Ce(IV) in the structure of $(NH_4)_2[Ce(NO_3)_6]$ where, however, all the ligands are similar (see section 6.6).

TABLE 20
Summary of structural determinations of rare earth nitrates.

Compound	Cell parameters			Angle (°)			Z	Space group	Structure	Reference
	a (Å)	b (Å)	c (Å)	α	β	γ				
$La(NO_3)_3 \cdot 6H_2O$	8.933	10.723	6.664	78.86	77.92	87.91	2	$P\bar{1}$	$[La(O_2NO)_3(H_2O)_5] \cdot H_2O$	Eriksson et al., 1978, 1980b
$Ce(NO_3)_3 \cdot 6H_2O$	8.886	10.671	6.612	78.76	102.19	92.08	2	$P\bar{1}$	$[Y(O_2NO)_3(H_2O)_5] \cdot H_2O$	Milinski et al., 1980
$Pr(NO_3)_3 \cdot 6H_2O$	9.234	11.770	6.778	91.17	110.72	69.48	2	$P\bar{1}$	$[Pr(O_2NO)_2(H_2O)_4] \cdot 2H_2O$	Fuller and Jacobson, 1976
$Nd(NO_3)_3 \cdot 6H_2O$	9.307	11.747	6.776	91.11	112.24	109.15	2	$P\bar{1}$	$[Nd(O_2NO)_2(H_2O)_4] \cdot 2H_2O$	Rogers et al., 1983
$Y(NO_3)_3 \cdot 6H_2O$	9.151	12.097	6.723	104.52	112.39	104.05	2	$P\bar{1}$	$[Y(O_2NO)_3(H_2O)_4] \cdot 2H_2O$	Ribár et al., 1980
$Y(NO_3)_3 \cdot 5H_2O$	6.652	9.558	10.563	63.59	84.62	76.06	2	$P\bar{1}$	$[Y(O_2NO)_3(H_2O)_4] \cdot H_2O$	Eriksson, 1982b
$(NO)_2Sc(NO_3)_5$	8.074	11.581	14.128		102.15		4	$P2_1/c$	$(NO)_2[Sc(O_2NO)_4ONO_2]$	Addison et al., 1978
$(NO)_2Y(NO_3)_5$	8.055	11.981	14.160		104.80		4	$P2_1/c$	$(NO)_2[Y(O_2NO)_5]$	Addison et al., 1978
$(NO)_2Ho(NO_3)_5$	8.094	11.979	14.170		104.7		4	$P2_1/c$	$(NO)_2[Ho(O_2NO)_5]$	Toogood and Chieh, 1975
$K_2La(NO_3)_5 \cdot 2H_2O$	11.335	21.621	12.355				8	Fdd2	$K_2[La(O_2NO)_5(H_2O)_2]$	Eriksson et al., 1980a
$(NH_4)_2La(NO_3)_5 \cdot 4H_2O$	11.152	8.966	17.881		101.6		4	C2/c	$(NH_4)_2[La(O_2NO)_5(H_2O)_2] \cdot 2H_2O$	Eriksson et al., 1982
$(NH_4)_2La(NO_3)_5 \cdot 3H_2O$	10.969	9.012	17.439		100.1		4	C2/c	$(NH_4)_2[La(O_2NO)_5(H_2O)_2] \cdot H_2O$	Eriksson et al., 1982
$K_2Er(NO_3)_5$	7.954	11.943	14.269		102.85		4	$P2_1/c$	$K_2[Er(O_2NO)_5]$	Gebert Sherry, 1978
$Mg_3Ce_2(NO_3)_{12} \cdot 24H_2O$	11.004		34.592				3	$R\bar{3}$	$[Mg(H_2O)_6]_3[Ce(O_2NO)_6] \cdot 6H_2O$	Zalkin et al., 1963
$K_3Pr_2(NO_3)_9$	13.52						4	$P4_332$	$[K_3Pr_2(NO_3)_9]_n$	Carnall et al., 1973
$Pr(OH)_2NO_3$	6.449	3.881	7.747		98.73		2	$P2_1$	$[Pr(OH)_2(O_2NO)]_n$	Lundberg and Skarnulis, 1976
$(NH_4)_2Ce(NO_3)_6$	13.061	6.842	8.183		91.34		2	$P2_1/n$	$(NH_4)_2[Ce(N_2NO)_6]$	Beineke and Delgaudio, 1968

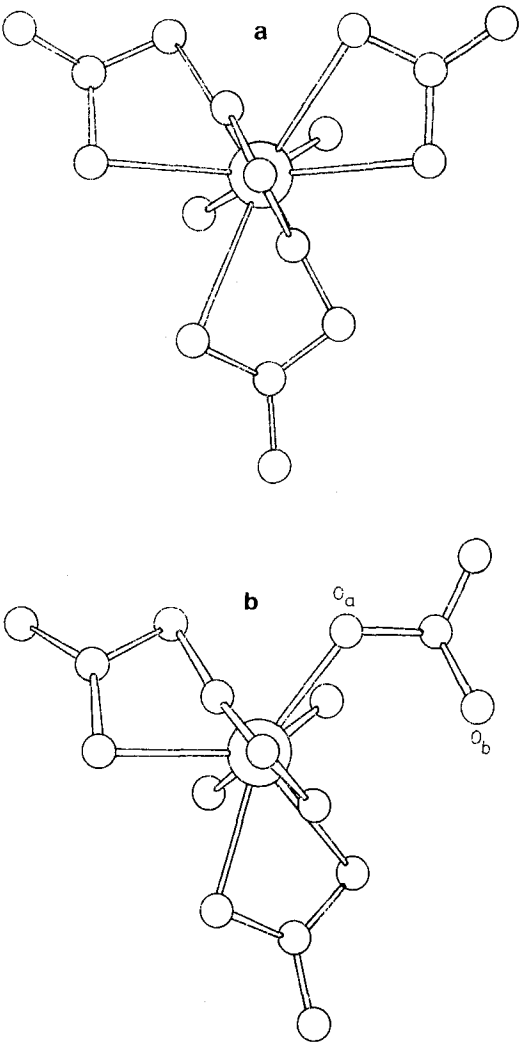

Fig. 76. Perspective views of the anions in the structure of $(NO_2)[R(NO_3)_5]$. R = Y (a) and Sc (b) (Addison et al., 1978).

6.4.2. *Other complex nitrates*

A second major type of hydrated nitrato complex is the $M^{II}_3R_2(NO_3)_{12} \cdot 24H_2O$ series, where M^{II} is Mg, Zn, Cd, Mn, Fe, Co, Ni or Cu, and R is most commonly La or Ce, though the series may extend as far as Er (Pascal, 1959).

The cerium magnesium compound (CMN) is best known and because of its magnetic transition it is used for low-temperature calibration. The good quality crystals it forms were investigated by single crystal methods as early as 1963 (Zalkin et al.). The central ion is 12-coordinated by six bidentate nitrato ligands at an average Ce–O(NO_3) distance of 2.64 Å (fig. 79). The divalent metal ions are

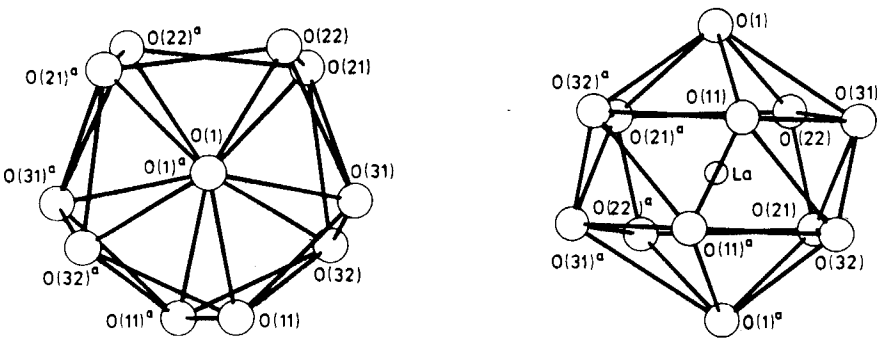

Fig. 77. Coordination polyhedron around the lanthanum atom in the structure of $(NH_4)_2[La(NO_3)_5(H_2O)_2] \cdot 2H_2O$. A view along the capping atoms (left) and a view perpendicular to it (right) (Eriksson et al., 1982).

octahedrally surrounded by water molecules; in addition there are six water molecules per unit cell that are held in the structure by hydrogen bonds.

Another interesting series is $K_3R_2(NO_3)_9$ recently prepared and characterized by Carnall et al., 1973. The compounds are prepared from $LiNO_3$–KNO_3 melts containing up to 2 M R^{3+} at 170–190°C. Isostructural compounds (R = Pr, Nd, Sm) were obtained and a single crystal analysis for the Pr compound showed them to be cubic.

The Pr atoms are surrounded by 12 oxygens from six bidentate NO_3 groups, at the corners of a distorted icosahedron. The Pr–O bond range is 2.577–2.745 Å. In notable contrast to all other known rare earth nitrato complexes, the structure of $K_3Pr_2(NO_3)_9$ contains no discrete $[R(NO_3)_n]^{m+}$ complexes but is continuous, with an unusually high crystal symmetry; site symmetry for Pr^{3+} is not especially high, however.

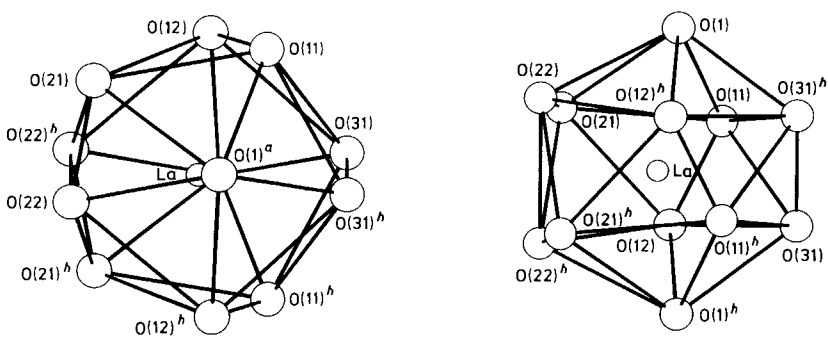

Fig. 78. Coordination around lanthanum in the structure of $K_2[La(NO_3)_3 \cdot (H_2O)_2] \cdot 2H_2O$. Note the difference in respect to fig. 77 (Eriksson et al., 1980a).

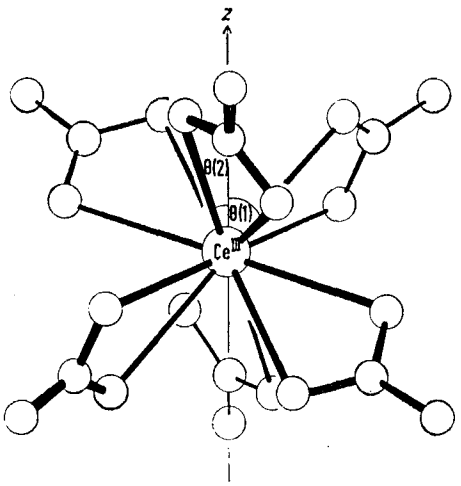

Fig. 79. Coordination around Ce^{4+} in the structure of $Mg_3Ce_2(NO_3)_{12} \cdot 24H_2O$ (Zalkin et al., 1963).

Although the structure is continuous and there is only one crystallographic site for Pr, the nitrate configurations fall into two groups, A and B. In the A-type the nitrate group is bridging bidentate to two Pr atoms, whereas in the B-type bonds are formed to only one Pr atom at significantly shorter distance (cf. fig. 80).

Recent preparative and thermoanalytical data suggest that the phase $M^I_3R_2(NO_3)_9$ is rather stable and is also formed in solutions and during thermal decomposition of complex nitrates (Riikonen, 1978; Niinistö and Kyläkoski, 1985).

Trivalent metals seem to not interact with the rare earth nitrates in solution. For instance, solubility isotherms in the system $Al_2(NO_3)_3$–$Y(NO_3)_3$–H_2O indicate that only separate nitrate hydrates of Al^{3+} and Y^{3+} are formed (Kuznetsova et al., 1981).

6.5. *Oxy- and hydroxynitrates*

Several investigators have noted the formation of the oxynitrate phase $RONO_3$ during the thermal decomposition of rare earth nitrates (see section 6.7). Daire and Lehuede (1970) studied the decomposition of $La(NO_3)_3 \cdot 6H_2O$ in both air and water vapor atmospheres and noticed that in the latter case the hydroxo compounds $La(OH)_2NO_3$ and $La_2O_3 \cdot 2La(OH)_2NO_3$ are formed, whereas in air only $LaONO_3$ could be seen. X-ray powder data are reported for the three compounds and the data for $La(OH)_2NO_3$ obtained at 350°C were indexed with an orthorhombic cell ($a = 8.26$, $b = 7.20$ and $c = 10.75$ Å); the limited number of diffraction maxima renders these results unreliable, however. A similar caution applies to the indexing of $LaONO_3$ (cubic, $a = 9.24$ Å).

There are several studies on the formation of hydroxynitrates in $R(NO_3)_3$ solutions when NaOH is added (Gmelin, 1974), but the first systematic investigation was that by Haschke and Eyring (1971). They studied the Pr_2O_3–$Pr(NO_3)_3$–H_2O system under hydrothermal conditions up to 700°C, above which oxidation occurs. The

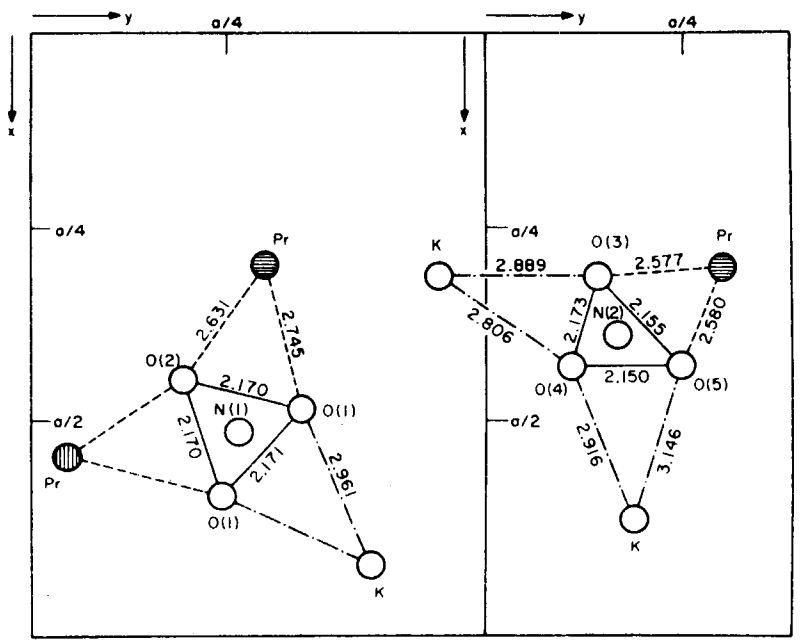

Fig. 80. Projection of the two types of nitrate environments in the structure of $K_3Pr_2(NO_3)_9$. Distances are given in Å (Carnall et al., 1973).

existence of two hydroxynitrate phases could be firmly established: monoclinic $Pr(OH)_2NO_3$ ($a = 6.442$, $b = 3.874$, $c = 7.742$ Å and $\beta = 98.75°$), space group $P2_1$ or $P2_1/m$ and hexagonal $Pr_2(OH)_5NO_3$ ($a = 18.410$, $c = 3.804$ Å), space group $P6_3$ or $P6_3/m$. An interesting relationship between the lattice parameters and those of $Pr(OH)_3$ was noted, suggesting a structural similarity and a possibility for anion substitution in the series $Pr_2(OH)_{6-n}(NO_3)_n$ with $Pr(OH)_3$ ($n = 0$) as the terminal member. The studies in the Pr system were later extended to cover most of the lanthanides and yttrium by Haschke (1974) who reported crystal data for several other phases, including partially substituted $R_2(OH)_{6-n}(NO_3)_n$ ($n = 0.9$ for La, 0.6 for Sm and Tb) and the hydrated phases $Yb(OH)_2NO_3 \cdot 2H_2O$, $Yb_2(OH)_5NO_3 \cdot 2H_2O$.

The crystal structure of $Pr(OH)_2NO_3$ was later determined by Lundberg and Skarnulis (1976) and the results confirm the unit cell and space group data obtained by Haschke and Eyring (1971). The compound has a layer structure where the layers are formed by PrO_9 polyhedra having a distorted tricapped trigonal prismatic symmetry. The corners of the polyhedra are occupied by six oxygens from the OH groups and the remaining positions are filled by oxygens from bidentate nitrate groups (fig. 81). The Pr–O(OH) distances, 2.425–2.574 Å, are significantly shorter

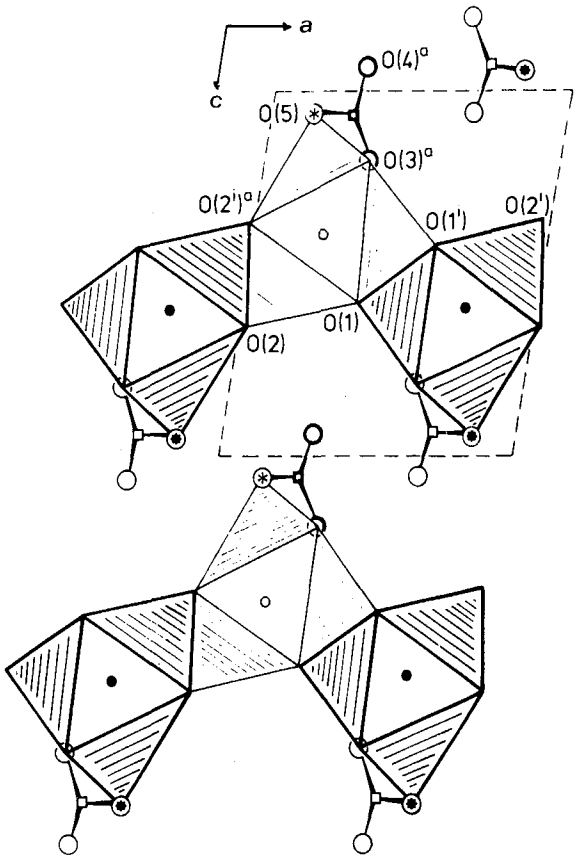

Fig. 81. The crystal structure of $Pr(OH)_2NO_3$ projected on the *ac* plane (Lundberg and Skarnulis, 1976).

than the Pr–O(NO_3) distances, which range from 2.656 to 2.693 Å. There exists a very close structural similarity to the monoclinic form of $Y(OH)_2Cl$; for a review of the hydroxohalide compounds, see Haschke (1975).

Scandium also forms several oxy- and hydroxynitrates. $ScOH(NO_3)_2 \cdot 3H_2O$ forms large enough crystals for single crystal studies and its triclinic unit cell has been determined (Pushkina and Komissarova, 1967). For the oxynitrates formed when $Sc(NO_3)_3 \cdot 4H_2O$ is heated, see section 6.7.

6.6. *Nitrates of tetravalent cerium*

The higher charge: radius ratio of Ce^{4+} compared with R^{3+} ions leads to a different behavior of cerium in the nitrate systems. In the system CeO_2–N_2O_5–H_2O,

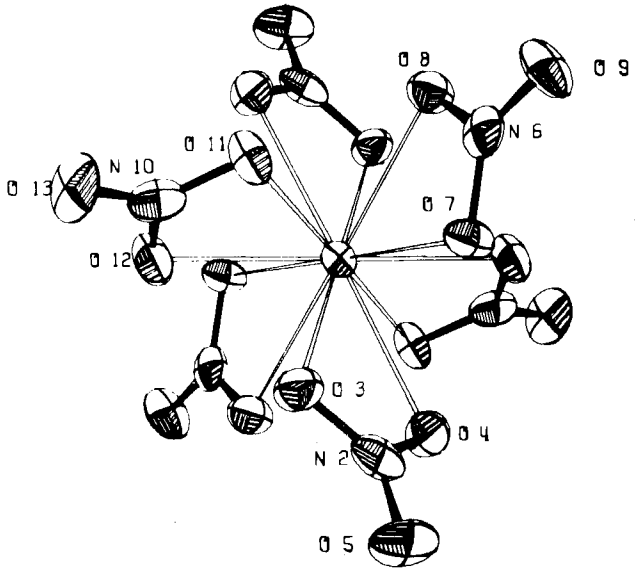

Fig. 82. The hexanitratocerium(IV) ion in the structure of $(NH_4)_2[Ce(NO_3)_6]$ (Beineke and Delgaudio, 1968).

there is one well-characterized phase, $Ce(NO_3)_4 \cdot 5H_2O$, and two phases, $Ce(NO_3)_4$ and $Ce(OH)(NO_3)_3 \cdot nH_2O$ ($n \simeq 3$), that are frequently reported in the literature but not yet studied in detail (Gmelin, 1974).

The published unit cell data for $Ce(NO_3)_4 \cdot 5H_2O$ (Staritzky, 1956) suggest that the compound is isostructural with $Th(NO_3)_4 \cdot 5H_2O$ (Ueki et al., 1966; Taylor et al., 1966) where the Th^{4+} ion is 11-coordinated by four bidentate nitrato groups and three of the five water molecules.

Among the complex nitrates of tetravalent cerium the well-known compound $(NH_4)_2[Ce(NO_3)_6]$ has been structurally characterized by single crystal methods (Beineke and Delgaudio, 1968) (see fig. 82). This compound was earlier used in industrial separation processes aimed at the production of pure cerium oxide (Smith et al., 1936). It also is used in quantitative analytical determinations for the preparation of standard cerium solutions (Petzold, 1955).

The corresponding potassium compound $K_2[Ce(NO_3)_6]$ has not yet been studied by single crystal X-ray methods although it is reported to form well-formed crystals. IR data and preparative details are available (Gatehouse et al., 1957, 1958). Also the hydrated hexanitratocerium(IV) complex $M^{II}Ce^{IV}(NO_3)_6 \cdot 8H_2O$ (M^{II} = Mg, Zn, etc.) has been reported (Pascal, 1959). The structure of the possibly isomorphous Th(IV) complex has been determined (Scavincar and Prodic, 1964).

6.7. *Properties of rare earth nitrates*

6.7.1. *Thermal stability*

Wendlandt (1956) was the first to systematically study the thermal stability of rare earth nitrates. He found by TG studies in air that a sequence of reactions $R(NO_3)_3 \cdot$

$6H_2O \rightarrow R(NO_3)_3 \rightarrow RONO_3 \rightarrow$ R oxide takes place for Sc, La, Pr, Nd and Sm. Cerium behaved differently by decomposing directly to CeO_2 without the $R(NO_3)_3$ or $RONO_3$ intermediates. Later the studies were extended to cover the heavier rare earths and the DTA technique (Wendlandt and Bear, 1960).

Subsequent systematic studies by Dabkowska and co-workers (Dabkowska and Boksa, 1973; Dabkowska and Broniszowska, 1973; Dabkowska, 1974–5) have corroborated the main reaction mechanism, but the combination of TG/DTG/DTA techniques has revealed additional details of the decomposition scheme (e.g., intermediate hydrates and oxynitrate phases).

Individual rare earth nitrate hydrates have been studied by several authors using a variety of thermoanalytical techniques. Yttrium nitrate, which was not included in the systematic investigations by Wendlandt and Dabkowska, has been studied by Odent and Autrusseau-Duberray (1976a, b). Claudel et al. (1963) investigated the decomposition of $Ce(NO_3)_3 \cdot 6H_2O$ in nitrogen and found that with an extremely slow heating rate (5°C/day) the anhydrous phase forms between 98 and 110°C. The oxynitrate phase was not found, in agreement with the results of Wendlandt (1956). If heating is performed in air, however, a Ce(IV) oxynitrate $CeO(NO_3)_2$ is formed; the formation of this phase at 150–180°C involves the evolution of nitrogen oxides (Pajakoff, 1964).

Scandium nitrate tetrahydrate seems to behave differently from the other rare earths upon heating, and formation of the dihydrate phase and several oxynitrate intermediates has been reported. The oxynitrates include $Sc_4O(NO_3)_{10} \cdot nH_2O$, $Sc_4O_3(NO_3)_6 \cdot nH_2O$ and the anhydrous $Sc_4O_5(NO_3)_2$. On the basis of the ^1H NMR and IR spectra, Sc–O–Sc chain-type structures with hydroxo bridges have been proposed (Komissarova et al., 1963, 1967; Chuvaev et al., 1967).

As a representative example, the thermal decomposition schemes of europium trinitrate hydrates are presented in table 21. It should be noted that the partially different results are probably largely due to somewhat different experimental conditions (sample size, heating rate, crucible and oven geometry, etc.).

When the nitrato complex includes an extra cation in the structure, as in the series $M^I_2[R(NO_3)_5] \cdot nH_2O$ for example, the thermal decomposition scheme becomes more complex. In the case of ammonium compounds the final product, at temperatures well below 1000°C, is R_2O_3 (or equivalent oxide) but in the case of alkali metals stable double oxides of type MRO_2 may be formed. The TG/DTG/DTA patterns for several complex nitrates have been determined by Molodkin and co-workers.

As an example of the decomposition schemes for the complex ammonium nitrates the TG and DTA curves for $(NH_4)_2[La(NO_3)_5(H_2O)_2] \cdot 2H_2O$ are depicted in fig. 83 (Riikonen, 1978). Figure 84 shows the TG, DTG and DTA curves for a lutetium pentanitrato complex $Na_2[Lu(NO_3)_5] \cdot 3H_2O$. The final product at 925°C is $NaLuO_2$ (Molodkin et al., 1978a).

The thermal stabilities of the hydroxynitrates (Haschke and Eyring, 1971; Haschke, 1974) and nitrates of tetravalent cerium (Brezina and Rosický, 1962) have also been studied. Figure 85 shows the TG curves for some of the oxynitrate phases studied by Haschke (1974).

TABLE 21
Thermal decomposition of $Eu(NO_3)_3 \cdot nH_2O$ in air.

Starting material and author	Reaction	Temperature range (°C)	Remarks
$Eu(NO_3)_3 \cdot 4H_2O$ (= A)	A → $EuONO_3$	75–450	No clear plateau
Wendlandt and Bear,	→ $EuONO_3 \cdot Eu_2O_3$	500–615	
1960	→ Eu_2O_3	615–730	
$Eu(NO_3)_3 \cdot 6H_2O$ (= B)	B → $Eu(NO_3)_3$	61–387	Stepwise dehydration via
Mironov et al., 1971	→ $EuONO_3$	387–482	5-, 4-, 3-, 2- and 1-hydrates
	→ Eu_2O_3	482–625	
$Eu(NO_3)_3 \cdot 5H_2O$ (= C)	C → $Eu(NO_3)_3$	80–425	Stepwise dehydration via
Dabkowska, 1974–5	→ $EuONO_3 \cdot Eu_2O_3$	425–500	2-hydrate
	→ Eu_2O_3	550–600	
$Eu(NO_3)_3 \cdot 6H_2O$ (= B)	B → $nEu_2O_3 \cdot mN_2O_5 \cdot pH_2O$	60–405	5-hydrate as an intermediate
Odinets et al., 1983	→ $nEu_2O_3 \cdot mN_2O_5$	405–560	
	→ Eu_2O_3	560–680	

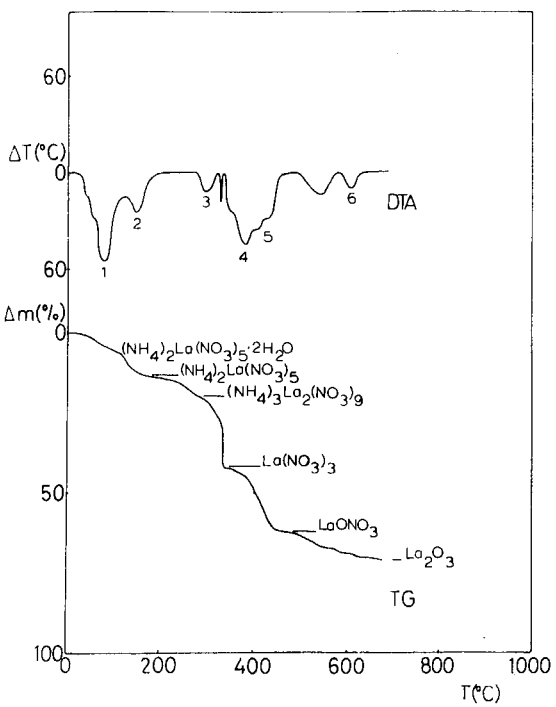

Fig. 83. TG and DTA curves for the thermal decomposition of $(NH_4)_2[La(NO_3)_3(H_2O)_2] \cdot 2H_2O$ (Riikonen, 1978).

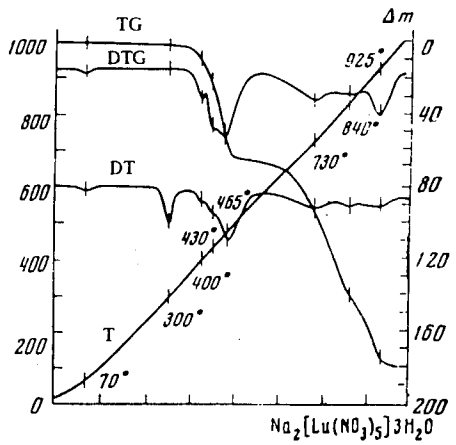

Fig. 84. TG, DTG and DTA curves for the thermal decomposition of $Na_2[Lu(NO_3)_5] \cdot 3H_2O$ (Molodkin et al., 1978a).

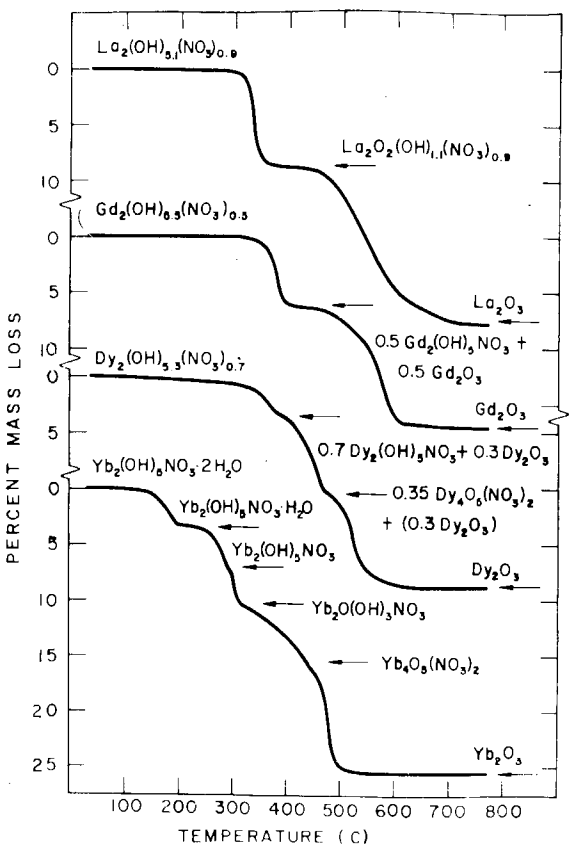

Fig. 85. TG curves for selected $La_2(OH)_{6-x}(NO_3)_x$ phases (Haschke, 1974).

6.7.2. *Spectroscopic properties: Vibrational spectra*

Ionic and coordinated nitrate groups can be distinguished simply on the basis of the number of IR or Raman active bands present in vibrational spectra (Gatehouse et al., 1957). However, to distinguish between the various types of nitrate coordination requires a more detailed analysis, which also takes into account the positions of the bands and the far-IR region (Addison et al., 1971).

In addition to the routine characterizations of the rare earth nitrates by IR spectroscopy, there are a few detailed investigations on the subject. Walker and Ferraro (1965) studied the IR spectra of anhydrous nitrates (R = Pr $\cdots$ Lu), prepared by the reaction of the corresponding metal and N_2O_4. The spectra were also recorded in the far-IR region down to 100 cm^{-1}. No evidence for the presence of ionic nitrato groups was found, in contrast to the result of Vratny and Honig (1960) for $Pr(NO_3)_3$. No definite conclusion about the mode of bonding could be reached but the authors felt there was a strong possibility of bidentate or bridging coordination. James and Kimber (1969) studied both the IR and Raman spectra, the latter also in solution, for $(NH_4)_2[Ce(NO_3)_6]$. In this case the crystal structure was known (Beineke and Delgaudio, 1968) but a factor group analysis was not possible due to the large number of atoms. The authors analyzed the spectra in detail and noted the similarity between the Raman spectra in the solid state and solution. In the solid state IR spectra there are, however, some unpredictable components, which in the absence of suitable criteria render the spectra of little use for the prediction of the detailed stereochemistry.

$K_3R_2(NO_3)_9$ is another compound for which spectral and structural data are available and a comparison between the two is possible (Carnall et al., 1973). Additional splitting was observed here, too, but the main features of the coordination could be derived from the spectra: the absence of ν_3 vibration around 1390 cm^{-1} excludes the ionic-type and the large separation between the nitrate stretching fundamentals (ν_1–ν_4) indicates bidentate and/or bridging mode of bonding; see table 22.

In other nitrato complexes even larger ν_1–ν_4 separations were observed, e.g., in $K_2[Lu(NO_3)_5] \cdot 3H_2O$ the $\Delta\nu$ is 295 cm^{-1} (Molodkin et al., 1978a). It would seem that $\Delta\nu$ increases with the decreasing size of the central ion and is also larger for the complex nitrates than for the trinitrates where the typical values are below 200 cm^{-2}; cf., data for $R(NO_3)_3 \cdot 6H_2O$ by Ivanov-Emin et al. (1972, 1974). $YONO_3$ has a value of 135 cm^{-1}, which is less than in $Y(NO_3)_3 \cdot 5H_2O$ (Odent and Autrusseau-Duperray, 1976b).

6.7.3. *Optical absorption spectra*

The optical absorption spectrum for single crystals of $Nd(NO_3)_3 \cdot 6H_2O$ has been recorded and interpreted by Caro et al. (1977). The measurements were carried out between 10 000 and 30 000 cm^{-1} at 4.2 K. The same group has also measured the spectrum of Gd^{3+} in several dilute (0.1 M) solutions, including nitrate solution (Svoronos et al., 1981). The UV absorption band of the nitrate makes interpretation in this case difficult. The absorption spectrum of Tm^{3+} in dilute nitrate solutions has

TABLE 22

IR and Raman spectra with assignments[a] for $K_3R_2(NO_3)_9$ (R = Pr, Nd) (Carnall et al., 1973).

Assignment	Frequencies[b]	
	IR	Raman
	$K_3Pr_2(NO_3)_9$	
$\nu_2 + \nu_3$	1788m	
	1768sh	
$\nu_2 + \nu_5$	1762m	
		1504vvs
ν_1 (a_1)	1465vs	1461vs
		1406vw
	1358vs	1366m
	1330vs	1341m
		1333sh
ν_4 (b_1)	1311s	
ν_2 (a_1)	1047vs	1048vs
	1041vs	1042s
	818vs	
ν_6 (b_2)	810sh	
ν_3 (a_1)	750vw	753m
		745s
ν_5 (b_1)	730m	727m
		719m
	$K_3Nd_2(NO_3)_9$	
	1804sh	
$\nu_2 + \nu_3$	1790m	
	1788sh	
$\nu_2 + \nu_5$	1762m	
		1502w
ν_1 (a_1)	1480vs	1453w
		1405w
	1358sh	
ν_4 (b_1)	1333s	1335s
ν_2 (a_1)	1048sh	1040vs
	1043vs	
ν_6 (b_2)	815vs	
	810sh	
ν_3 (a_1)	750vs	754vs
		746vs
ν_s (b_1)	729w	727m
		720m

[a] Assignments according to nomenclature established by Addison et al. (1971) for bidentate nitrate.

[b] Symbols follow tables 8 and 16.

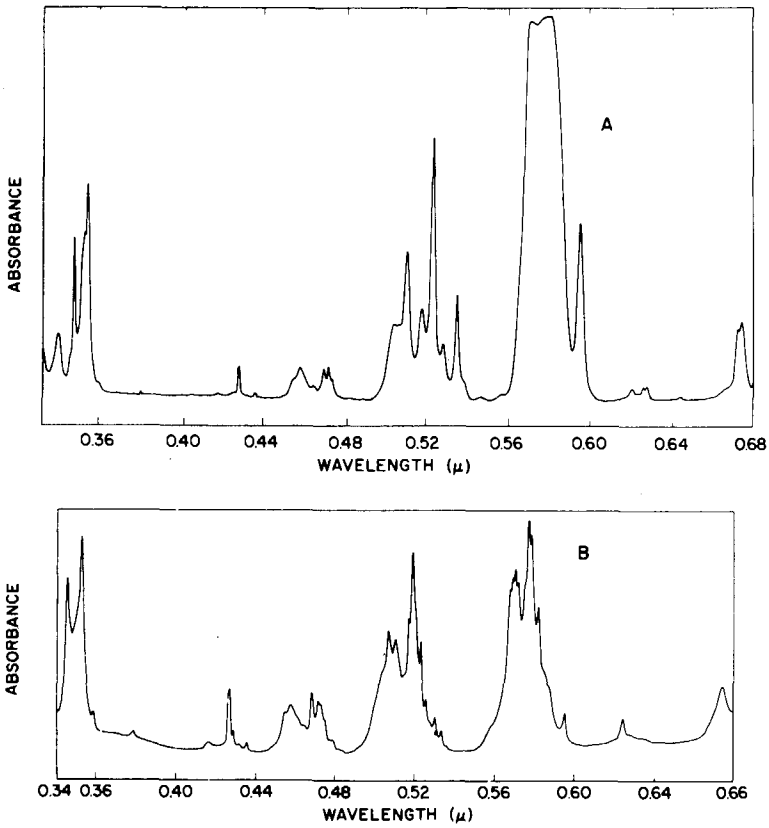

Fig. 86. The absorption spectra of thin single crystal samples of $K_3Nd_2(NO_3)_9$ (a) and $Nd^{3+}:LaF_3$ (b) (Carnall et al., 1973).

been also recently recorded and the spectral intensities and transition probabilities evaluated (Lakshman and Jayasankar, 1982).

Absorption spectra have also been measured for single crystals of $K_3R_2(NO_3)_9$ at ambient and high pressure. The Nd compound was chosen because in Pr^{3+} the hypersensitive transition bands lie in the near-IR region where absorption due to H_2O is strong. The enhancement of hypersensitive transitions was noted and compared with other crystals where Nd^{3+} has a low site symmetry (Carnall et al., 1973) (see fig. 86).

References

Abdullaev, G.K. 1976, Zh. Strukt. Khim. **17**, 1128.
Abdullaev, G.K. and K.S. Mamedov, 1974, Zh. Strukt. Khim. **15**, 157.
Abdullaev, G.K. and K.S. Mamedov, 1976, Zh. Strukt. Khim. **17**, 188.
Abdullaev, G.K. and K.S. Mamedov, 1977a, Kristallografiya **22**, 154.

Abdullaev, G.K. and K.S. Mamedov, 1977b, Kristallografiya **22**, 220.
Abdullaev, G.K. and K.S. Mamedov, 1982, Kristallografiya **27**, 795.
Abdullaev, G.K., K.S. Mamedov and S.T. Amirov, 1973, Kristallografiya **18**, 1075.
Abdullaev, G.K., K.S. Mamedov and G.G. Dzhafarov, 1974, Kristallografiya **19**, 737.
Abdullaev, G.K., K.S. Mamedov and G.G. Dzhafarov, 1975a, Kristallografiya **20**, 265.
Abdullaev, G.K., K.S. Mamedov and G.G. Dzhafarov, 1975b, Zh. Strukt. Khim. **16**, 71.
Abdullaev, G.K., G.G. Dzhafarov and K.S. Mamedov, 1976, Azerb. Khim. Zh. 117.
Abdullaev, G.K., K.S. Mamedov, I.R. Amiraslanov and A.I. Magerranov, 1977, Zh. Strukt. Khim. **18**, 410.
Abdullaev, G.K., K.S. Mamedov and G.G. Dzhafarov, 1978a, Azerb. Khim. Zh. 125.
Abdullaev, G.K., K.S. Mamedov, I.R. Amiraslanov, G.G. Dzhafarov, O.A. Aliev and B.T. Usubaliev, 1978, Russ. J. Inorg. Chem. **23**, 2332.
Abdullaev, G.K., K.S. Mamedov, G.G. Dzhafarov and O.A. Aliev, 1980, Russ. J. Inorg. Chem. **25**, 198.
Addison, C.C., N. Logan, S.C. Wallwork and C.D. Garner, 1971, Quant. Rev. Chem. Soc. **25**, 289.
Addison, C.C., A.S. Greenwood, M.J. Haley and N. Logan, 1978, J. Chem. Soc. Chem. Commun. 580.
Ahrland, S., J. Chatt and N.R. Davies, 1958, Q. Rev. (London) **12**, 265.
Albertsson, J., 1972, Thesis, University of Lund, Lund, Sweden.
Albertsson, J., 1978, Kem.-Kemi **5**, 229.
Alzahairi, T.J.M. and S. Siekierski, 1984, Radiochem. Radioanal. Lett. **57**, 301.
Ambrozhii, M.N., E.F. Luchnikova and M.I. Sidorova, 1960, Russ. J. Inorg. Chem. **5**, 366.
Ananeva, G.V., A.M. Korovkin, T.T. Merkulyaeva, A.M. Morozova, M.V. Petrov, I.R. Savinova, V.R. Startsev and P.P. Feofilov, 1981, Inorg. Mater. **17**, 754.
Ananeva, G.V., V.E. Karapetyan, A.M. Korovkin, T.I. Merkulyaeva, I.A. Peschanskaya, I.R. Savinova and P.P. Feofilov, 1982, Inorg. Mater. **18**, 442.
Andreev, I.F., A.M. Shevyakov, T.P. Smorodina and N.E. Semenov, 1975, Russ. J. Inorg. Chem. **20**, 1303.
Ansell, G.B. and B. Wanklyn, 1975, J. Chem. Soc. Chem. Commun. 794.
Ansell, G.B. and B.M. Wanklyn, 1976, J. Chem. Soc. Chem. Commun. 706.
Arsenev, P.A., I.N. Raiskaja and R.K. Sviridova, 1972, Phys. Status Solidi (a) **13**, K45.
Aslanov, L.A. and M.A. Porai-Koshits, 1975, Koord. Khim. **1**, 416.
Aumont, R., F. Genet, M. Passaret and Y. Thudie, 1971, C.R. Hebd. Seances Acad. Sci. Ser. C **272**, 314.
Avertisyan, E.I., A.V. Chichagov and N.V. Belov, 1970, Kristallografiya **15**, 1066.
Ayasse, C. and H.A. Eick, 1973, Inorg. Chem. **12**, 1140.
Babievskaya, I.A. and F.M. Perel'man, 1965, Zh. Neorg. Khim. **10**, 681 [English transl.: Russ. J. Inorg. Chem. **10**, 366].
Bagdasarov, K.S., A.A. Kaminskii, A.M. Kevorkov, A.M. Prokhorov, S.E. Sarkisov and T.A. Tevosyan, 1973, Dokl. Akad. Nauk. SSSR **212**, 1326.
Ballman, A.A., 1962, Am. Mineral. **47**, 1380.
Bambauer, H.V., J. Weidelt and J.S. Ysker, 1968, Naturwissenschaften **55**, 81.
Bambauer, H.V., J. Weidelt and J.S. Ysker, 1969, Z. Krist. **130**, 207.
Bartram, S.F., 1962, U.S. Atomic Energy Commission Conference 20-28, 22p.
Bartram, S.F., 1964, Rare Earth Research II, ed. K.S. Vorres (Gordon and Breach, New York) p. 165.
Bartsch, H.H. and O. Jarchow, 1983, Z. Krist. **162**, 14.
Bashkov, B.I., L.N. Komissarova, F.M. Spiridonov and V.M. Shatskii, 1972, Vestn. Mosk. Univ. Khim. **13**, 598.
Baskova, N.A., A.I. Maier and M.K. Karapetyants, 1974, Inorg. Mater. **10**, 1054.
Batalieva, N.G. and Yu.A. Pyatenko, 1967, Zh. Strukt. Khim. **8**, 548.
Batsanov, S.S., 1977, Zh. Neorg. Khim **22**, 1155 [English transl.: Russ. J. Inorg. Khim. **22**, 631].
Baturin, S.V., I.A. Malinovskii and O.S. Bondareva, 1983, Dokl. Akad. Nauk. SSSR **271**, 349.
Baumik, M.L. and L.J. Nuget, 1965, J. Chem. Phys. **43**, 1680.
Bayer, G., 1971, Naturwissenschaften **58**, 622.
Beall, G.W., W.O. Milligan and S. Mroczkowski, 1976, Acta Crystallogr. Sect. B **32**, 3143.
Beineke, T.A. and J. Delgaudio, 1968, Inorg. Chem. **7**, 715.
Belokoneva, E.L., T.L. Petrova, M.A. Simonov and N.V. Belov, 1972, Kristallografiya **17**, 490.
Belokoneva, E.L., L.I. Alshinskaya, M.A. Simonov, N.I. Leonjuk, T.I. Timchenko and N.V. Belov, 1978, Zh. Strukt. Khim. **19**, 382.
Belokoneva, E.L., L.I. Alshinskaya, M.A. Simonov, N.I. Leonjuk, T.I. Timchenko and N.V. Belov, 1979, Zh. Strukt. Khim. **20**, 461.
Belokoneva, E.L., M.A. Simonov, A.V. Pashkova, T.I. Timchenko and N.V. Belov, 1980, Dokl. Akad. Nauk SSSR **255**, 854.
Belokoneva, E.L., A.V. Pashkova, T.I. Timchenko and N.V. Belov, 1981, Dokl. Akad. Nauk. SSSR **261**, 361.
Bettermann, P., J. Lexow, F. Liebau and F. Seifert, 1983, Mater. Res. Bull. **18**, 507.
Beyeler, H.U. and T. Hibma, 1978, Solid State Commun. **27**, 641.
Biedermann, K., 1975, Phys. Chem. Sci. Res. Rep. (Nat. Seawater, Rep. Dahlem Workshop) 339.
Biedermann, G. and D. Ferri, 1982, Acta Chem. Scand. A **36**, 611.
Biedermann, G., M. Kilpatrick, L. Pokras and L.G. Sillen, 1956, Acta Chem. Scand. **10**, 1327.
Biedl, A., 1966, Am. Mineral. **51**, 521.

Blasse, G., 1966, J. Chem. Phys. **45**, 2356.
Blasse, G., 1969, J. Inorg. Nucl. Chem. **31**, 1519.
Blasse, G. and A. Bril, 1967a, J. Inorg. Nucl. Chem. **29**, 2231.
Blasse, G. and A. Bril, 1967b, Philips Res. Rep. **22**, 481.
Blasse, G. and A. Bril, 1967c, J. Chem. Phys. **47**, 5139.
Blasse, G. and J. de Vries, 1967a, J. Inorg. Nucl. Chem. **29**, 1541.
Blasse, G. and J. de Vries, 1967b, J. Electrochem. Soc. **114**, 875.
Bock, R., 1950, Angew. Chem. **62**, 375.
Bocquillon, G., C. Loriers-Susse, M. Dellalian and J. Loriers, 1973, C.R. Hebd. Seances Acad. Sci. Ser. C **276**, 543.
Bocquillon, G., C. Chateau, J. Loriers and J. Loriers, 1977, J. Solid State Chem. **20**, 135.
Bocquillon, G., J. Maugrion and J. Loriers, 1978, C.R. Hebd. Seances Acad. Sci. Ser. C **287**, 5.
Bocquillon, G., C. Chateau and J. Loriers, 1980, Rare Earths Mod. Sci. Technol. **2**, 209.
Bondar, I.A., 1979, Inorg. Mater. **15**, 793.
Bondar, I.A., 1982, Ceramurgia Int. **8**, 83.
Bondar, I.A., L.N. Koroleva and N.A. Toropov, 1965a, Rost Kristallov, Vol. 6 (Inst. Krist., Akad. Nauk. SSSR, Moscow) p. 111.
Bondar, I.A., T.F. Tenisheva, N.A. Toropov and Yu.F. Shepelev, 1965b, Dokl. Akad. Nauk SSSR **160**, 1069.
Bondar, I.A., N.A. Toropov and L.N. Koroleva, 1965c, Inorg. Mater. **1**, 561.
Bondar, I.A., N.A. Toropov and L.N. Koroleva, 1967, Inorg. Mater. **3**, 2034.
Bondar, I.A. and M.A. Petrova, 1969, Russ. J. Inorg. Chem. **14**, 1231.
Bowden, G.H. and R. Thompson, 1980, in: Mellors Comprehensive Treatise on Inorganic and Theoretical Chemistry. Vol. V, ed. R. Thompson and A.J.E. Welch (Longman, London) p. 597.
Bradley, W.F., D.L. Graf and R. S. Roth, 1966, Acta Crystallogr. **20**, 283.
Brauer, G., 1980–2, Handbuch der präparativen anorganischen Chemie, Vols. I–III (Enke, Stuttgart).
Breen, P.J. and W.D. Horrocks, Jr., 1983, Inorg. Chem. **22**, 536.
Brezina, F. and J. Rosický, 1962, Monatsh. Chem. **94**, 306.
Bril, A. and W.L. Wanmaker, 1964, J. Electrochem. Soc. **111**, 1363.
Bril, A., G. Blasse, A.H. Gomes de Mesquita and J.A. de Poorter, 1971, Philips Tech. Rev. **32**, 125.
Brinton, P.H.M. and C. James, 1921, J. Am. Chem. Soc. **43**, 1446.
Brixner, L.H., J.R. Barkley and W. Teitschko, 1979, Rare Earth Molybdates (VI), in: Handbook on the Physics and Chemistry of Rare Earths, Vol. 3, eds. K.A. Gschneidner, Jr. and L. Eyring (North-Holland, Amsterdam) Ch. 30, pp. 609–654.
Brown, D., 1975, MTP Int. Rev. Sci. Inorg. Chem. Ser. II **7**, 111.
Brown, D., 1968, Halides of the Lanthanides and Actinides (Wiley-Interscience, London).
Brown, T.A., J. Ellis and R.N. Sylva, 1983, J. Chem. Soc. Dalton Trans., 35.
Brunisholz, G., J.P. Quiche and A.M. Kalo, 1964, Helv. Chim. Acta **47**, 14.
Buenzli, J.-C. and J.-R. Yersin, 1979, Inorg. Chem. **18**, 605.
Buenzli, J.-C., B. Klein, G. Chapuis and K.J. Schenk, 1982, Inorg. Chem. **21**, 808.
Buisson, G. and C. Michel, 1968, Mater. Res. Bull. **3**, 193.
Bukowska-Strzyzewska, M. and A. Tosik, 1978, Inorg. Chim. Acta **30**, 189.
Burns, J.H., 1979, Inorg. Chem. **18**, 3044.
Busch, G., E. Kaldis, R. Verreault and J. Felsche, 1970, Mater. Res. Bull. **5**, 9.
Böhlhoff, R., H.V. Bambauer and W. Hoffmann, 1970, Naturwissenschaften **57**, 129.
Böhlhoff, R., H.V. Bambauer and W. Hoffmann, 1971, Z. Krist. **133**, 386.
Callow, R.S., 1967, The Industrial Chemistry of the Lanthanons, Yttrium, Thorium and Uranium (Pergamon, Oxford) p. 124.
Canneri, G., 1926, Gazz. Chim. Ital. **56**, 460.
Carnall, W.T., S. Siegel, J.R. Ferraro, B. Tani and E. Gebert, 1973, Inorg. Chem. **12**, 560.
Caro, P. and M. Lemaitre-Blaise, 1969, C.R. Hebd. Seances Acad. Sci. Ser. C **278**, 861.
Caro, P., M. Lemaitre-Blaise and F. Tromba, 1968, C.R. Hebd. Seances Acad. Sci. Ser. C **267**, 1594.
Caro, P., J.C. Achard and O. de Pous, 1970, Les elementes des terres rares. Colloques Intern. du CNRS No. 180, Vol. 1, p. 287.
Caro, P., M. Lemaitre-Blaise, H. Dexpert and J.O. Sawyer, 1971, C.R. Hebd. Seances Acad. Sci. Ser. C **272**, 57.
Caro, P.E., J.O. Sawyer and L. Eyring, 1972, Spectrochim. Acta A **28**, 1167.
Caro, P., D.R. Svoronos, E. Antic and M. Quarton, 1977, J. Chem. Phys. **66**, 5284.
Carter, F.L., 1978, Acta Crystallogr. Sect. B **34**, 2962.
Casellato, V., G. Tomat, P. Di Bernando and R. Graziani, 1982, Inorg. Chim. Acta **62**, 181.
Chai, B.H.T. and S. Mroczkowski, 1978, J. Cryst. Growth **44**, 84.
Charles, R.G., 1965, J. Inorg. Nucl. Chem. **27**, 1498.
Chateau, C. and J. Loriers, 1979, C.R. Hebd. Seances Acad. Sci. Ser. C **288**, 421.
Chenavas, J., A. Waintal, J.J. Capponi and M. Gondrand, 1969, Mater. Res. Bull. **4**, 425.
Chichagov, A.V. and N.V. Belov, 1968, Geokhim. SSSR **12**, 1456.
Chichagov, A.V., V.V. Ilyukhin and N.V. Belov, 1967, Dokl. Akad. Nauk. SSSR **177**, 574.
Chichagov, A.V., V.S. Kovalenko, V.I. Ponomarov and N.V. Belov, 1969a, Dokl. Akad. Nauk. SSSR **189**, 88.
Chichagov, A.V., B.N. Litvin and N.V. Belov, 1969b, Kristallografiya **14**, 119.
Chinn, S.R. and H.Y.-P. Hong, 1976, Opt. Commun. **18**, 87.
Choppin, G.R., 1971, Pure Appl. Chem. **27**, 23.
Choppin, G.R., 1984, J. Less-Common Met. **100**, 141.
Choppin, G.R. and B.L. Bertha, 1973, J. Inorg.

Nucl. Chem. **35**, 1309.
Christensen, A.N., 1970a, Les elementes des terres rares. Colloques Intern. du CNRS No. 180, Vol. 1, p. 279.
Christensen, A.N., 1970b, Acta Chem. Scand. **24**, 2440.
Christensen, A.N., 1972, Acta Chem. Scand. **26**, 1955.
Christensen, A.N., 1973a, Acta Chem. Scand. **27**, 1835.
Christensen, A.N., 1973b, Acta Chem. Scand. **27**, 2976.
Christensen, A.N. and R.G. Hazell, 1984, Acta Chem. Scand. A **38**, 157.
Churilova, N.N. and V.V. Serebrennikov, 1971, Tr. Tomsk. Gos. Univ. **204**, 277.
Churilova, N.N. and V.V. Serebrennikov, 1973, Tr. Tomsk Gos. Univ. **237**, 96.
Chuvaev, V.F., G.Ya. Pushkina, L.N. Komissarova and V.I. Spitsyn, 1967, Zh. Neorg. Khim. **12**, 2899 [English transl. Russ. J. Inorg. Chem. **12**, 1535].
Ciavatta, L., D. Ferri, I. Grenthe, F. Salvatore and K. Spahiu, 1981, Acta Chem. Scand. A **35**, 403.
Clark, A.M., 1984, Rare Earth Element Geochemistry, ed. P. Henderson (Elsevier, Amsterdam) p. 33.
Claudel, B., Y. Trambouze and J. Veron, 1963, Bull. Soc. Chim. Fr. 409.
Cockbain, A.G. and G.V. Smith, 1968, Mineral. Mag. **36**, 411.
Cooly, R.A. and A.M. Yost, 1946, Inorganic Syntheses, Vol. II (McGraw-Hill, New York) p. 70.
Crookes, W., 1909, Z. Anorg. Allg. Chem. **61**, 349.
Cruickshank, D.W.J., H. Lynton and G.A. Barclay, 1962, Acta Crystallogr. **15**, 491.
Dabkowska, M., 1974–1975, Ann. Univ. Mariae Curie-Sklodowska Sect. AA **29–30**, 49.
Dabkowska, M. and H. Boksa, 1973, Ann. Univ. Mariae Curie-Sklodowska Sect. AA **28**, 119.
Dabkowska, M. and A. Broniszewska, 1973, Ann. Univ. Mariae Curie-Sklodowska Sect. AA **28**, 133.
Dabkowska, M. and M. Kalbowiak, 1971, Ann. Univ. Mariae Curie-Sklodowska Sect. AA **26**, 321.
Dago, A.M., D.Yu. Pushcharovskii, E.A. Pobedimskaya, E.E. Strelkova and N.V. Belov, 1980a, Dokl. Akad. Nauk. SSSR **250**, 857.
Dago, A.M., D.Yu. Pushcharovskii, E.E. Strelkova, E.A. Pobedimskaya and N.V. Belov, 1980b, Dokl. Akad. Nauk. SSSR **252**, 1117.
Daire, M. and P. Lehuede, 1970, Compt. Rend. **270**, 1405.
Dal Negro, A.D., G. Rossi and V. Tazzoli, 1975, Am. Mineral. **60**, 280.
Dal Negro, A.D., G. Rossi and V. Tazzoli, 1977, Am. Mineral. **62**, 142.
de Hair, J.T.W., 1979, J. Lumin. **18**, 797.
de Hair, J.T.W., 1980, J. Solid State Chem. **33**, 33.
de Hair, J.T.W. and J.T.G. van Kemenade, 1983, 3rd Int. Conf. Sci. Technol. Light Sources, Toulouse, paper 54.
Deineka, G.F., I.N. Tselik and E.P. Ilinskaya, 1972, Russ. J. Inorg. Chem. **17**, 670.
Delaunay, J., A. de Polignac, F. Fromage and J. Despujols, 1971, C.R. Hebd. Seances Acad. Sci. Ser. C **273**, 692.
Demianets, L.N., G.A. Emelchenko and A.N. Lobachev, 1974, High Temp. High Pressures **6**, 699.
Demianets, L.N., G.A. Emelchenko and A.N. Lobachev, 1975, Koord. Khim. **1**, 1205.
Demianets, L.N., Yu.A. Gorbunov, B.A. Maksimov, V.V. Ilyukhin and N.V. Belov, 1976, Inorg. Mater. **12**, 126.
Demianets, L.N., A.N. Lobachev and G.A. Emelchenko, 1980a, Germanates of Rare Earth Elements (Nauka, Moscow).
Demianets, L.N., A.N. Lobachev and G.A. Emelchenko, 1980b, Crystals, Vol. 4 (Springer-Verlag, Berlin) p. 101.
Demianets, L.M., O.K. Melnikov, B.A. Maksimov, U.S. Borovkov, A.K. Ivanov-Shits, A.N. Lobachev, J.I. Filippov, B.V. Merinov and N.V. Belov, 1982, Kristallografiya **26**, 735.
Denisov, Yu.V., B.F. Dzhurinskii and V.A. Kizel, 1969, Inorg. Mater. **5**, 1240.
Dervin, J., J. Faucherre, P. Herpin and S. Voliotis, 1973, Bull. Soc. Chim. Fr., 2634.
Dexpert, H., 1976, Cristallochimie des systemes Ln_2O_3–CO_2–H_2O. Thesis, L'Universite Pierre et Marie Curie, Paris 6, France, 116 pp.
Dexpert, H. and P. Caro, 1974, Mater. Res. Bull. **9**, 1577.
Dexpert, H. and P. Caro, 1978, Phys. Status Solidi (a) **45**, 297.
Dexpert, H., M. Lemaitre-Blaise and P. Caro, 1972, International Conference on Reactivity of Solids. (Chapman and Hall, London) p. 758.
Dexpert, H., G. Schiffmacher and P. Caro, 1975, J. Solid State Chem. **15**, 301.
Dexpert, H., E. Antic-Fidanaev, J.P. Coutures and P. Caro, 1982, J. Crystallogr. Spectrosc. Res. **12**, 129.
Diehl, R. and G. Brandt, 1974, Mater. Res. Bull. **9**, 421.
Dimitrova, O.V., O.G. Karpov, B.N. Litvin, D.Yu. Pushcharovskii, E.A. Pobedimskaya and N.V. Belov, 1976, Kristallografiya **21**, 403.
Donnay, G. and J.D.H. Donnay, 1953, Am. Mineral. **38**, 928.
Drew, M.G.B., 1977, Coord. Chem. Rev. **24**, 179.
Dumonceau, J., 1977, Stabilite des tetracarbonatolanthanidates (III). Application a l'etude des carbonates complexes mixtes. Thesis, L'Universite de Reims, Reims, France, 217 pp.
Dumonceau, J., S. Bigot, M. Trevil, J. Faucherre and F. Fromage, 1979, Rev. Chim. Miner. **16**, 583.
Dzhurinskii, B.F., I.M. Belyakov and I.V. Tananeav, 1967, Inorg. Mater. **3**, 1876.
Dzhurinskii, B.F., I.V. Tananaev and O.A. Aliev, 1968a, Inorg. Mater. **4**, 641.
Dzhurinskii, B.F., I.V. Tananaev and O.A. Aliev, 1968b, Inorg. Mater. **4**, 846.
Dzhurinskii, B.F., I.A. Tananaev and O.A. Aliev, 1969a, Inorg. Mater. **5**, 832.

Dzhurinskii, B.F., I.V. Tananaev and O.A. Aliev, 1969b, Inorg. Mater. **5**, 1978.
Dzhurinskii, B.F., E.M. Reznik and I.V. Tananaev, 1980, Russ. J. Inorg. Chem. **25**, 2981.
Eiji, I., K. Yukihiro, S. Kenichi and Y. Tomotsu, 1976, Zairgo **25**, 389.
Emelchenko, G.A., 1974, Inorg. Mater. **12**, 427.
Emelchenko, G.A. and V.V. Ilyukhin, 1974, Dokl. Akad. Nauk. SSSR **217**, 824.
Emelchenko, G.A., L.N. Demianets, V.V. Ilyukhin and A.N. Lobachev, 1974a, Kristallografiya **19**, 434.
Emelchenko, G.A., L.N. Demianets, V.V. Ilyukhin and A.N. Lobachev, 1974b, Kristallografiya **19**, 781.
Emelchenko, G.A., L.N. Demianets and A.N. Lobachev, 1974c, Mater. Res. Bull. **9**, 1151.
Emelchenko, G.A., L.N. Demianets, V.V. Ilyukhin and A.N. Lobachev, 1974d, Kristallografiya **19**, 1272.
Emelchenko, G.A., L.N. Demianets and A.N. Lobachev, 1975a, J. Solid State Chem. **14**, 209.
Emelchenko, G.A., A.I. Gusev, Yu.A. Sokolov and V.V. Ilyukhin, 1975b, Dokl. Akad. Nauk. SSSR **222**, 343.
Emelchenko, G.A., B.N. Grechushnikov and V.V. Ilyukhin, 1976, Spectroscopy in Crystals (Nauka, Moscow) p. 265.
Eriksson, B., 1982a, Chem. Commun. Univ. Stockholm **3**.
Eriksson, B., 1982b, Acta Chem. Scand. A **36**, 186.
Eriksson, B., L.O. Larsson and L. Niinistö, 1978, J. Chem. Soc. Chem. Commun., 616.
Eriksson, B., L.O. Larsson, L. Niinistö and J. Valkonen, 1980a, Acta Chem. Scand. A **34**, 567.
Eriksson, B., L.O. Larsson, L. Niinistö and J. Valkonen, 1980b, Inorg. Chem. **19**, 1207.
Eriksson, B., L.O. Larsson and L. Niinistö, 1982, Acta Chem. Scand. A **36**, 465.
Fallon, G.O. and B.M. Gatehouse, 1982, Acta Crystallogr. Sect. B **38**, 919.
Farmer, J.B., 1982, Advances in Inorganic Chemistry and Radiochemistry, Vol. 25, eds. H.J. Emeleus and A.G. Sharpe (Academic, New York)
Faucherre, J., F. Fromage and R. Gobron, 1966, Rev. Chim. Miner. **3**, 953.
Favas, M.C. and D.L. Kepert, 1981, Prog. Inorg. Chem. **28**, 309.
Fedorov, N.F., I.F. Andreev and N.S. Meliksetyan, 1975a, Inorg. Mater. **11**, 1137.
Fedorov, N.F., T.A. Tunik, P.M. Sidorov and S.N. Razumovskii, 1975b, Russ. J. Inorg. Chem. **20**.
Fedorov, N.F., I.F. Andreev and I.L. Lukashov, 1982, Kristallografiya **27**, 384.
Felsche, J., 1969, J. Appl. Cryst. **2**, 1380.
Felsche, J., 1970, J. Less-Common Met. **21**, 1.
Felsche, J., 1971a, Naturwissenschaften **58**, 218.
Felsche, J., 1971b, Z. Krist. **133**, 304.
Felsche, J., 1972a, Naturwissenschaften **59**, 35.
Felsche, J., 1972b, J. Solid State Chem. **5**, 266.
Felsche, J., 1973, Struct. Bonding (Berlin) **13**, 99.
Felsche, J. and W. Hirsinger, 1969, J. Less-Common Met. **18**, 131.
Felten, E.J., 1961, J. Inorg. Nucl. Chem. **19**, 61.
Ferri, D. and F. Salvatore, 1983, Acta Chem. Scand. A **37**, 531.
Ferri, D., I. Grenthe, S. Hietanen and F. Salvatore, 1983, Acta Chem. Scand. A **37**, 359.
Forsberg, J.A., 1973, Coord. Chem. Rev. **10**, 195.
Fouassier, C., B. Saubat and P. Hagenmuller, 1981, J. Lumin. **23**, 405.
Fournier, J. and R. Kohemueller, 1968, C.R. Hebd. Seances Acad. Sci. Ser. C **266**, 1361.
Fridman, Ya.D. and S.D. Gorokhov, 1967, Russ. J. Inorg. Chem. **12**, 1798.
Fridman, Ya.D. and S.D. Gorokhov, 1969a, Inorg. Mater. **5**, 515.
Fridman, Ya.D. and S.D. Gorokhov, 1969b, Russ. J. Inorg. Chem. **14**, 1440.
Friend, J.N., 1935a, J. Chem. Soc., 824.
Friend, J.N., 1935b, J. Chem. Soc., 1430.
Fromage, F., 1968, Ann. Chim. (Paris) Ser. 14 **3**, 457.
Fuller, C.C. and R.A. Jacobson, 1976, Cryst. Struct. Commun. **5**, 349.
Fukuda, Y., F. Fukushima, Y. Tsujimoto, M. Fukai and S. Sugai, 1974, Ger. Offen. 2-409-953.
Fukushima, F., Y. Fukada, M. Fukai, Y. Tsujimoto and S. Sugai, 1975, Japan. Kokai 75-45-789.
Furmanova, N.G., L.V. Soboleva and L.M. Belyaev, 1981, Kristallografiya **26**, 312.
Garner, C.D., P. Lambert and F.E. Mabos, 1972, J. Chem. Soc. Dalton Trans., 91.
Garnovskii, A.D., V.T. Panyushkin and T.V. Gritsenko, 1981, Koord. Khim. **7**, 483.
Gatehouse, B.M., S.E. Livingstone and R.S. Nyholm, 1957, J. Chem Soc., 4222.
Gatehouse, B.M., S.E. Livingstone and R.S. Nyholm, 1958, J. Inorg. Nucl. Chem. **8**, 75.
Gaude, J., P. L'Haridon, C. Hamon, R. Marchand and Y. Laurent, 1975, Bull. Soc. Fr. Mineral. Cristallogr. **98**, 214.
Gebert Sherry, E., 1978, J. Inorg. Nucl. Chem. **40**, 257.
Geller, S. 1967, Z. Krist. **125**, 1.
Geller, S., C.E. Miller and R.G. Freuting, 1960, Acta Crystallogr. **13**, 179.
Glushkova, V.B., I.A. Davtjan and E.K. Keler, 1967, Inorg. Mater. **3**, 96.
Gmelin Handbuch der anorganischen Chemie, 1938, 8th Ed., Sc, Y, La–Lu, Vol. 39A (Springer-Verlag, Berlin).
Gmelin Handbuch der anorganischen Chemie, 1974, 8th Ed., Sc, Y, La–Lu, Vol. 39 C2 (Springer-Verlag, Berlin).
Gmelin Handbuch der anorganischen Chemie, 1980, 8th Ed., Sc, Y, La–Lu, Vol. 39 D1 (Springer-Verlag, Berlin).
Gmelin Handbook of Inorganic Chemistry, 1981, 8th Ed., Sc, Y, La–Lu, Vol. D3 (Springer-Verlag, Berlin).
Gmelin Handbook of Inorganic Chemistry, 1982, 8th Ed., Sc, Y, La–Lu, Vol. D2 (Springer-Verlag, Berlin).
Gmelin Handbook of Inorganic Chemistry, 1984a, 8th Ed., Sc, Y, La–Lu, Vol. 39 A7 (Springer-Verlag, Berlin) p. 69.
Gmelin Handbook of Inorganic Chemistry, 1984b, 8th Ed., Sc, Y, La–Lu, Vol. 39 A8

(Springer-Verlag, Berlin).
Gmelin Handbook of Inorganic Chemistry, 1984c, 8th Ed., Sc, Y, La–Lu, Vol. 39 D2 (Springer-Verlag, Berlin).
Gmelin-Krauts Handbuch der anorganischen Chemie, 1928–1932, Band VI, Abt. 1–2 (Carl Winters Universitätsbuchhandlung, Heidelberg).
Goldschmidt, V.M., T. Barth, G. Lunde and W. H. Zachariasen, 1926, Skr. Nor. Vidensk. Akad. Mat.-Nat. Kl. **2**.
Gomes de Mesquita, A.H. and A. Bril, 1969, Mater. Res. Bull. **4**, 643.
Gorbunov, Yu.A., B.A. Maksimov and N.V. Belov, 1973a, Dokl. Akad. Nauk. USSR **208**, 91.
Gorbunov, Yu.A., B.A. Maksimov and N.V. Belov, 1973b, Dokl. Akad. Nauk. SSSR **221**, 591.
Gorbunov, Yu.A., B.A. Maksimov, V.V. Ilyukhin and N.V. Belov, 1974a, Dokl. Akad. Nauk. SSSR **219**, 91.
Gorbunov, Yu.A., B.A. Maksimov, Yu.A. Kharitonov and N.V. Belov, 1974b, Kristallografiya **19**, 1081.
Greinacher, E. and K. Reinhardt, 1982, in: Chemische Technologie, 4th Ed., Vol. 2, eds. H. Harrisch, R. Steiner and K. Winnacker (Hanser, Munich) pp. 678–707.
Grenthe, I., 1978, Kem.-Kemi **5**, 234.
Griffiths, J., 1984, Ind. Miner. **199**, 19.
Grotepass, M., M. Behruzi and T. Hahn, 1983, Z. Krist. **162**, 90.
Groth, P., 1908, Chemische Crystallographie, Vol. II (Engelmann, Leipzig) pp. 1129–133.
Gschneidner, K.A., Jr., 1975, In: Scandium, ed. C.T. Horowitz (Academic Press, London) Ch. 8, pp. 152–251.
Guha, J.P., 1980, J. Mater. Sci. **15**, 262.
Gunawarde, R.P., R.A. Howie and F.P. Glasser, 1982a, Acta Crystallogr. Sect. B **38**, 1405.
Gunawardane, R.P., R.A. Howie and F.P. Glasser, 1982b, Acta Crystallogr. Sect. B **38**, 1564.
Gutkina, N.G., I.I. Kozhina and L.K. Shmatok, 1975, Inorg. Mater. **11**, 721.
Harris, L.A. and C.B. Finch, 1965, Am. Mineral. **50**, 1493.
Haschke, J.M., 1974, Inorg. Chem. **13**, 1812.
Haschke, J.M., 1975, J. Solid State Chem. **14**, 238.
Haschke, J. and L. Eyring, 1971, Inorg. Chem. 10, 2267.
Hata, H., G. Adachi and J. Shiokawa, 1977, Mater. Res. Bull. **12**, 811.
Hawthorne, F.C. and H.D. Grundy, 1973, Acta Crystallogr. Sect. B **29**, 2615.
Hawthorne, F.C. and H.D. Grundy, 1977, Can. Mineral. **15**, 50.
Head, E.L., 1967, U.S. Patent 3-374-069.
Head, E.L., 1968, U.S. Patent 3-401-008.
Head, E.L., 1971, J. Inorg. Nucl. Chem. **33**, 1201.
Head, E.L. and C.H. Holley, Jr., 1964, in: Rare Earth Research II, ed. K.S. Vorres (Gordon and Breach, New York) p. 51.
Head, E.L. and C.H. Holley, Jr., 1965, in: Rare Earth Research III, ed. L. Eyring (Gordon and Breach, New York) p. 707.
Hiroyuki, K., S. Yanitoski, V. Mitsutoshi and N. Koji, 1977, Nippon Kagaku Kaishi 798.
Hitachi, Ltd., 1981, Jpn. Kokai Tokyo Koho 81-70-085.
Hitachi, Ltd., 1982, Jpn. Kokai Tokyo Koho JP 82-83-581.
Hong, H.Y.-P and K. Dwight, 1974, Mater. Res. Bull. **9**, 1661.
Hong, H.Y.-P., J.A. Kafalas and M. Bayard, 1978, Mater. Res. Bull. **13**, 757.
Hopkins, R.H., N.T. Melamed, T. Henningsen and G.W. Roland, 1971a, J. Cryst. Growth **10**, 218.
Hopkins, R.H., G.W. Roland, K.B. Steinbruegge and W.D. Parflow, 1971b, J. Electrochem. Soc. **118**, 637.
Horowitz, C.T., 1975a, in: Scandium, ed. C.T. Horowitz (Academic, London), Ch. 1, pp. 1–17.
Horowitz, C.T., 1975b, Scandium (Academic, London).
Hoshina, T. and S. Kuboniwa, 1972, J. Phys. Soc. Jpn. **32**, 771.
Inorganic Syntheses, 1939–1984, Vols. 1–24 (McGraw-Hill, New York).
Isupova, E.N. and I.S. Lileev, 1965, Inorg. Mater. **1**, 222.
Ito, J., 1967, Mater. Res. Bull. **2**, 1093.
Ito, J., 1968, Am. Mineral. **53**, 890.
Ito, J. and C. Frondel, 1968, Am. Mineral. **53**, 1276.
Ito, J. and H. Johnson, 1968, Am. Mineral. **53**, 1940.
Ivanov-Emin, B.N., Z.K. Odinets, B.E. Zaitsev, A.I. Ezhov and K. Del'Pino, 1972, Zh. Neorg. Khim. 17, 2888 [English transl.: Russ. J. Inorg. Chem. **17**, 1517].
Ivanov-Emin, B.N., Z.K. Odinets, B.E. Zaitsev, V.M. Akimov, M. Avias de Pasqual and A.I. Ezhov, 1974, Zh. Neorg. Khim. **19**, 2319 [English transl.: Russ. J. Inorg. Chem. **19**, 1266].
Iveronova, V.I., V.P. Tarasova and M.M. Umanskij, 1951, Izv. Akad. Nauk. SSSR Ser. Fiz. **15**, 164.
Iveronova, V.I., V.P. Tarasova, Z.K. Zolina, G.V. Markhasin and I.M. Sukhodreva, 1955, Zh. Fiz. Khim. **29**, 314.
James, D.W. and G.M. Kimber, 1969, Aust. J. Chem. **22**, 2287.
Jarchow, O., F. Lutz and K.-H. Klaska, 1979, Z. Krist. **149**, 162.
Jarchow, O., K.-H. Klaska and H. Schenk, 1981a, Naturwissenschaften **67**, 475.
Jarchow, O., K.-H. Klaska and M. Werk, 1981b, Naturwissenschaften **68**, 92.
Jarchow, O., K.-H. Klaska and M. Werk, 1982, Z. Krist. **159**, 66.
Jordanov, N. and I. Havezov, 1966, Z. Anorg. Allg. Chem. **347**, 101.
Jørgensen, C.K., 1976, Gmelins Handbuch der anorganischen Chemie, Seltene Erden, Vol. 39 B1 (Springer-Verlag, Berlin) p. 17.
Jørgensen, C.K., 1979, Theoretical Chemistry of Rare Earth, in: Handbook on the Physics and Chemistry of Rare Earths, Vol. 3, eds. K. Gschneidner and L. Eyring (North-Holland, Amsterdam), Ch. 23, pp. 111–169.
Jørgensen, C.K., 1983, Rev. Chim. Miner. **20**,

533.
Jørgensen, C.K., 1984a, Chimia **38**, 75.
Jørgensen, C.K., 1984b, Top. Curr. Chem. **124**, 1.
Jørgensen, C.K. and R. Reisfeld, 1982, Top. Curr. Chem. **100**, 127.
Jouhet-Vetter, G. and F. Queyroux, 1975, Mater. Res. Bull. **10**, 1201.
Kaldis, E. and R. Verreault, 1970, J. Less-Common Met. **20**, 177.
Kaldis, E., P. Streit, S. Vaccani and P. Wachter, 1974, J. Phys. Chem. Solids **35**, 231.
Kalz, H.-J. and H. Seidel, 1980, Z. Anorg. Allg. Chem. **465**, 92.
Kalz, H.-J. and H. Seidel, 1982, Z. Anorg. Allg. Chem. **486**, 221.
Kaminskii, A.A., N.R. Agamalyan, S.E. Sarkisov, L.N. Demianets, A.N. Lobachev and G.A. Emelchenko, 1980, Inorg. Mater. **16**, 2185.
Kaminskii, A.A., V.A. Timoteeva, N.R. Agamalyan and A.B. Bykov, 1981, Inorg. Mater. **17**, 1703.
Karapetyants, M.K., A.I. Maier and N.A. Baskova, 1977a, Inorg. Mater. **13**, 858.
Karapetyants, M.K., A.I. Maier and N.A. Baskova, 1977b, Inorg. Mater. **13**, 1032.
Karpov, O.G., D.Yu. Pushcharovskii, E.A. Pobedimskaya and N.V. Belov, 1976, Dokl. Akad. Nauk. SSSR **228**, 88.
Karpov, O.G., E.A. Pobedimskaya and N.V. Belov, 1977a, Kristallografiya **22**, 382.
Karpov O.G., D.Yu. Pushcharovskii, E.A. Pobedimskaya and N.V. Belov, 1977b, Dokl. Akad. Nauk. SSSR **236**, 593.
Karraker, J.D., 1970, J. Chem. Educ. **47**, 424.
Kato K., M. Sekita and S. Kimura, 1979, Acta Crystallogr. Sect B **35**, 2201.
Keith, M.L. and R. Roy, 1954, Am. Mineral. **39**, 1.
Keler, E.K. and A.K. Kuznetsov, 1962, Zh. Prikl. Khim. **35**, 250.
Kellendonk, F. and G. Blasse, 1981a, J. Chem. Phys. **75**, 561.
Kellendonk, F. and G. Blasse, 1981b, Phys. Status Solidi b **108**, 541.
Kellendonk, F. and G. Blasse, 1982, J. Phys. Chem. Solids **43**, 481.
Kellendonk, F., T. van den Belt and G. Blasse, 1982, J. Chem. Phys. **76**, 1194.
Kepert, D.L., 1982, Inorganic Stereochemistry (Springer-Verlag, Berlin).
Kharakh, E.A., A.V. Chichagov and N.V. Belov, 1970, Kristallografiya **15**, 1064.
Khodakov, G.S., N.E. Kharkov and N.L. Kudryavtseva, 1980, Dokl. Akad. Nauk. SSSR **254**, 1183.
Klasens, H.A., 1956, Ger. Patent 942 344.
Klimentova, G.P., B.A. Maksimov, V.V. Ilyukhin, A.N. Kornev and N.V. Belov, 1975, Dokl. Akad. Nauk. SSSR **224**, 817.
Koike, J., T. Kojima, R. Toyonaga, A. Kagami, T. Hase and S. Inaho, 1979, J. Electrochem. Soc. **126**, 1008.
Kokhanovskii, V.V., M.M. Pavlyuchenko and E.A. Prodau, 1971, Russ. J. Inorg. Chem. **16**, 1403.
Kokhanovskii, V.V. and M.M. Pavlyuchenko, 1976, Russ. J. Inorg. Chem. **21**, 325.
Komissarova, L.N., 1980, Zh. Neorg. Khim. **25**, 143 [English transl.: Russ. J. Inorg. Chem. **25**, 75].
Komissarova, L.N. and G.Ya. Pushkina, 1967, Zh. Neorg. Khim. **12**, 1365.
Komissarova, L.N., G.Ya. Pushkina, V.I. Spitsyn, 1963, Zh. Neorg. Khim. **8**, 1884 [English transl.: Russ. J. Inorg. Chem. **8**, 719].
Komissarova, L.N., G.Ya. Pushkina and E.G. Teterin, 1967, Zh. Neorg. Khim. **12**, 2586 [English transl.: Russ. J. Inorg. Chem. **12**, 1366].
Komissarova, L.N., Z.N. Prozorovskaya, V.F. Chuvaev and N.M. Kosinova, 1971a, Russ. J. Inorg. Chem. **16**, 23.
Komissarova, L.N., V.F. Chuvaev, U.M. Shatskii, V.A. Zhorov and Z.N. Prozorovskaya, 1971b, Russ. J. Inorg. Chem. **16**, 1410.
Komissarova, L.N., G.Ya. Pushkina and V.I. Spitsyn, 1971c, Zh. Neorg. Khim. **16**, 2367 [English transl.: Russ. J. Inorg. Chem. **16**, 1262].
Komissarova, L.N., E.G. Teterin, V.M. Shatskii and V.A. Zhorov, 1972, Russ. J. Inorg. Chem. **17**, 367.
Konijnendijk, W.L., P.J.M. Willemsen and R.C. Peters, 1981, Patent Ger. Offen. 3-024-476.
Kornilova, E.I., M.E. Prikhodko and I.S. Lileev, 1965, Inorg. Mater. **1**, 227.
Koskenlinna, M. and J. Valkonen, 1977, Acta Chem. Scand. A **31**, 638.
Krishnamurthy, K.V., G.M. Harris and V.S. Sastri, 1970, Chem. Rev. **70**, 171.
Kuroda, R., S.F. Mason and C. Rosini, 1981, J. Chem. Soc. Faraday Trans. **77**, 2125.
Kuzmin, E.A. and N.V. Belov, 1965, Dokl. Akad. Nauk. SSSR **165**, 88.
Kuznetsova, G.P., Z.P. Yakimono, L.F. Yashebova and B.D. Stepin, 1981, Zh. Neorg. Khim. **26**, 3161 [English transl.: Russ. J. Inorg. Chem. **26**, 1692].
Lakshman, S.V.J. and C.K. Jagsankar, 1982, Proc. Indian Acad. Sci. (Chem. Sci.) **91**, 521.
Laperches, J.P. and P. Tarte, 1966, Spectrochim. Acta **22**, 1201.
Lazarev, A.N., 1968, Inorg. Mater. **4**, 1287.
Lazarev, A.N. and T.F. Tenisheva, 1961, Izv. Akad. Nauk. SSSR Otd. Khim. Nauk. 964.
Lazarev, A.N., T.F. Tehisheva, I.A. Bondar and L.N. Koroleva, 1962, Izv. Akad. Nauk. SSSR Otd. Khim. Nauk. 557.
Lazarev, A.N., T.F. Tenisheva, I.A. Bondar and N.A. Toropov, 1963, Izv. Akad. Nauk. SSSR Ser. Khim. 1220.
Lazarev, A.N., T.F. Tenisheva and I.A. Bondar, 1965, Inorg. Mater. **1**, 1104.
Lazarev, A.N., T.F. Tenisheva, I.A. Bondar, L.N. Koroleva and N.A. Toropov, 1968, Inorg. Mater. **4**, 1128.
Leclaire, A., 1979, J. Solid State Chem. **28**, 235.
Lehmann, W. and T.J. Isaacs, 1978, J. Electrochem. Soc. **125**, 445.
Leonov, A.I. and I.A. Bondar, 1973, Inorg. Mater. **9**, 50.
Leskelä, M. and L. Niinistö, 1980, unpublished data.
Leskelä, M. and J. Suikkanen, 1985, to be published.
Leskelä, M. and H. Niskavaara, 1981, Oulun

Yliopiston Kem. Laitoksen Raporttisar. 4, 12 pp.
Leskelä, M. and H. Niskavaara, 1982, Finn. Chem. Lett. **29**.
Leskelä, M., M. Saakes and G. Blasse, 1984, Mater. Res. Bull. **19**, 151.
Levin, E.M., 1966, Phys. Chem. Glasses **7**, 90.
Levin, E.M., 1967, J. Am. Ceram. Soc. **50**, 53.
Levin, E.M., R.S. Roth and J.B. Martin, 1961, Am. Mineral. **46**, 1030.
Lin Yong-Hua and Xing Yan, 1983, Acta Chim. Sin. **41**, 97.
Looye, B., J.T.W. de Hair and C. Bakker, 1981, European Patent Application No. 23-068.
Loriers, J., G. Bocquillon, C. Chateau and D. Colaities, 1977, Mater. Res. Bull. **12**, 403.
Löwenstein, E., 1909, Z. anorg. allg. Chem. **63**, 69.
Lundberg, M. and A.J. Skarnulis, 1976, Acta Crystallogr. Sect. B **32**, 2944.
Lundqvist, R., 1982, Acta Chem. Scand. A **36**, 741.
Machida, K., G. Adachi and J. Shiokawa, 1979a, Acta Crystallogr. Sect. B **35**, 149.
Machida, K., G. Adachi and J. Shiokawa, 1979b, J. Lumin. **21**, 101.
Machida, K., H. Hata, K. Okuno, G. Adachi and J. Shiokawa, 1979c, J. Inorg. Nucl. Chem. **41**, 1425.
Machida, K., T. Ishino, G. Adachi and J. Shiokawa, 1979d, Mater. Res. Bull. **14**, 1529.
Machida, K., G. Adachi and J. Shiokawa, 1980a, Acta Crystallogr. Sect. B **36**, 2008.
Machida, K., G. Adachi and J. Shiokawa, 1980b, Inorg. Chem. **19**, 3807.
Machida, K.I., G.Y. Adachi, H. Hata and J. Shiokawa, 1981a, Bull. Chem. Soc. Jpn. **54**, 1052.
Machida, K.I., G.Y. Adachi, Y. Moriwaki and J. Shiokawa, 1981b, Bull. Chem. Soc. Jpn. **54**.
Machida, K.I., G.Y. Adachi, Y. Moriwaki and J. Shiokawa, 1981c, Bull. Chem. Soc. Jpn. **54**, 1048.
Machida, K., G. Adachi, J. Shiokawa, M. Shimada, M. Koizumi, K. Suito and A. Onodera, 1981d, Chem. Lett., 1111.
Maier, A.I., Yu.L. Suponitskii, M.K. Karapetyants and N.A. Baskova, 1972, Inorg. Mater. **8**, 540.
Maksimov, B.A. and N.V. Belov, 1981, Dokl. Akad. Nauk. SSSR **261**, 623.
Maksimov, B.A., V.V. Ilyukhin and N.V. Belov, 1967, Kristallografiya **12**, 214.
Maksimov, B.A., V.V. Ilyukhin and N.V. Belov, 1968a, Dokl. Akad. Nauk. SSSR **181**, 591.
Maksimov, B.A., Yu.A. Kharitonov, V.V. Ilyukhin and N.V. Belov, 1968b, Dokl. Akad. Nauk. SSSR **183**, 1072.
Maksimov, B.A., B.N. Litvin, V.V. Ilyukhin and N.V. Belov, 1969, Kristallografiya **14**, 498.
Maksimov, B.A., Yu.A. Karitonov and N.V. Belov, 1973, Dokl. Akad. Nauk. SSSR **213**, 1072.
Maksimov, B.A., B.V. Merinov, V.S. Borovkov, A.K. Ivanovshits, Yu.A. Kharitonov and N.V. Belov, 1979a, Kristallografiya **24**, 265.
Maksimov, B.A., T.A. Zhdanova, A.A. Voronkov, G.S. Miranova, V.V. Ilyukhin and N.V. Belov, 1979b, Dokl. Akad. Nauk. SSSR **247**, 103.
Maksimov, B.A., V.R. Kalinin, B.V. Merinov, V.V. Ilyukhin and N.V. Belov, 1980a, Dokl. Akad. Nauk. SSSR **252**, 875.
Maksimov, B.A., O.K. Melnikov, T.A. Zhdanova, V.V. Ilyukhin and N.V. Belov, 1980b, Dokl. Akad. Nauk. SSSR **251**, 98.
Maksimov, B.A., I.V. Petrov, A. Rabenau and H. Schulz, 1982, Solid State Ionics **6**, 195.
Malinovskii, L.A., 1983, Dokl. Akad. Nauk SSSR **272**, 1375.
Malinovskii, L.A., S.V. Baturin and O.S. Bondareva, 1983, Dokl. Akad. Nauk. SSSR **272**, 865.
Maqsood, A., B.M. Wanklyn and G. Garton, 1979, J. Cryst. Growth **46**, 671.
Marcantonatos, M.D., M. Deschaux and J.J. Vuillenmier, 1981, Chem. Phys. Lett. **82**, 36.
Marcantonatos, M.D., M. Deschaux and J.J. Vuillenmier, 1982, Chem. Phys. Lett. **91**, 149.
Marchand, R., P. L'Haridon and Y. Laurent, 1978, J. Solid State Chem. **24**, 71.
Marcus, Y. and M. Givon, 1964, J. Phys. Chem. **68**, 2230.
Marsh, J.K., 1941, J. Chem. Soc. 561.
Mascetti, J., M. Vlasse and C. Fouassier, 1981, J. Solid State Chem. **39**, 288.
Mascetti, J., C. Fouassier and P. Hagenmuller, 1983, J. Solid State Chem. **50**, 204.
Mayer, I., E. Levy and A. Glasner, 1964, Acta Crystallogr. **17**, 1071.
McAllister, W.A., 1969, Patent Ger. Offen. 1-804-546.
Mellor, J.W., 1965, A Comprehensive Treatise on Inorganic and Theoretical Chemistry, Vol. 5, New Impression (Longmans, Green and Co., London) Ch. 37, pp. 494–709.
Melson, G.A., 1975a, in: Scandium, C.T. Horowitz (Academic, London), Ch. 6, pp. 111–138.
Melson, G.A., 1975b, in: Scandium, C.T. Horowitz (Academic, London), Ch. 10, pp. 323–384.
Melson, G.A. and R.W. Stotz, 1971, Coord. Chem. Rev. **7**, 133.
Merinov, B.V., B.A. Maksimov, Yu.A. Kharitonov and N.V. Belov, 1978a, Dokl. Akad. Nauk. SSSR **240**, 81.
Merinov, B.V., B.A. Maksimov, L.N. Demianets and N.V. Belov, 1978b, Dokl. Akad. Nauk. SSSR **241**, 353.
Merinov, B.V., B.A. Maksimov, V.V. Ilyukhin and N.V. Belov, 1979, Dokl. Akad. Nauk. SSSR **248**, 1108.
Merinov, B.V., B.A. Maksimov and N.V. Belov, 1980a, Dokl. Akad. Nauk. SSSR **225**, 577.
Merinov, B.V., B.A. Maksimov, L.N. Demianets and N.V. Belov, 1980b, Dokl. Akad. Nauk. SSSR **250**, 357.
Merinov, B.V., B.A. Maksimov and N.V. Belov, 1981, Dokl. Akad. Nauk. SSSR **260**, 1128.
Meyer, R.J., 1904, Z. Anorg. Allg. Chem. **41**, 97.
Milinski, N.B. Ribar and M. Sataric, 1980, Cryst. Struct. Commun. **9**, 473.
Mill, B.V., 1966, Russ. J. Inorg. Chem. **7**, 1533.
Mill, B.V. and G. Roniger, 1973, Kristallografiya **18**, 126.

Milligan, W.O., D.F. Mullica, H.O. Perkins, D.A. Grossic and C.K.C. Lok, 1984, Inorg. Chim. Acta **86**, 33.
Mills, A.O., 1962, Inorg. Chem. **1**, 960.
Mironov, K.E. and A.P. Popov, 1966, Rev. Roum. Chim. **11**, 1373.
Mironov, K.E., A.P. Popov and E.M. Moroz, 1969, Russ. J. Inorg. Chem. **14**, 165.
Mironov, K.E., A.P. Popov, V.Ya. Vorob'eva and Z.A. Grankina, 1971, Zh. Neorg. Khim. **16**, 2769 [English transl.: Russ. J. Inorg. Chem. **16**, 1476].
Mitomo, M., Z. Izumi, S. Horiuchi and Y. Matsui, 1982, J. Mater. Sci. **17**, 2359.
Mochizuki, A., K. Nagashima and H. Wakita, 1974, Bull. Chem. Soc. Jpn. **47**, 355.
Moeller, T., 1972, MTP Int. Rev. Sci. Ser. I **7**, 275.
Moeller, T. and V.D. Aftandilian, 1954, J. Am. Chem. Soc. **76**, 5249.
Moeller, T., V.D. Aftandilian and G.W. Cullen, 1957, in: Inorganic Syntheses (McGraw-Hill, New York) p. 37.
Moeller, T., D.R. Martin, L.C. Thompson. R. Ferris, G.R. Feistel and W.I. Randall, 1965, Chem. Rev. **65**, 1.
Moeller, T., E.R. Birnbaum, J.H. Forsberg and R.B. Gayhart, 1968, Prog. Sci. Tech. Rare Earths **3**, 61.
Moeller, T., R.L. Dieck and J.E. McDonald, 1973, Rev. Chim. Miner. **10**, 177.
Molodkin, A.K., Z.K. Odinets and O. Vargas Ponse, 1976a, Zh. Neorg. Khim. **21**, 2590 [English transl.: Russ. J. Inorg. Chem. **21**, 1425].
Molodkin, A.K., Z.K. Odinets and V. Pereira Paveze, 1976b, Zh. Neorg. Khim. **21**, 2794 [English transl.: Russ. J. Inorg. Chem **21**, 1540].
Molodkin, A.K., Z.K. Odinets and A.V. Chuvelev, 1977, Zh. Neorg. Khim. **22**, 1520 [English transl: Russ. J. Inorg. Chem. **22**, 827].
Molodkin, A.K., Z.K. Odinets, A.V. Chuvelev and T.N. Ivanova, 1978a, Zh. Neorg. Khim. **23**, 2250 [English transl.: Russ. J. Inorg. Chem. **23**, 1239].
Molodkin, A.K., Z.K. Odinets, A.V. Chugaev and T.N. Ivanova, 1978b, Zh. Neorg. Khim. **23**, 2355 [English transl.: Russ. J. Inorg. Chem. **23**, 1298].
Molodkin, A.K., Z.K. Odinets, T.V. Sedina and T.N. Ivanova, 1982, Zh. Neorg. Khim. **27**, 3064 [English transl.: Russ. J. Inorg. Chem. **27**, 1736].
Molodkin, A.K., Z.K. Odinets, A.V. Chuvelev, T.N. Ivanova and A.I. Ezhov, 1979a, Zh. Neorg. Khim. **24**, 2637 [English transl.: Russ. J. Inorg. Chem. **24**, 1464].
Molodkin, A.K., Z.K. Odinets, A.V. Chugaev, T.N. Ivanova and A.I. Ezhov, 1979b, Zh. Neorg. Khim. 24, 2402 [English transl.: Russ. J. Inorg. Chem. **24**, 1332].
Molodkin, A.K., Z.K. Odinets, Yu.A. Grigoriev and A.I. Ezhov, 1981a, Zh. Neorg. Khim. **26**, 2389 [English transl.: Russ. J. Inorg. Chem. **26**, 1286].
Molodkin, A.K., Z.K. Odinets, T.V. Sedina, T.N. Ivanova and A.I. Ezhov, 1981b, Zh. Neorg. Khim. **26**, 2395 [English transl.: Russ J. Inorg. Chem. **26**, 1289].
Molodkin, A.K., Z.K. Odinets, T.V. Sedina and T.N. Ivanova, 1983, Zh. Neorg. Khim. **28**, 103 [English transl.: Russ. J. Inorg. Chem. **28**, 56].
Montorsi, M., 1982, J. Less-Common Met. **84**, 25.
Moose, G.M., 1980, Mineral Facts and Problems, United States Department of Interior, Bureau of Mines, Washington, DC., p. 737.
Morozov, A.M., M.V. Petrov, V.R. Startsev, A.M. Tkachuk and P.P. Feofilov, 1976, Opt. Spektr. **41**, 1086.
Moseley, P.T., 1975, MTP Int. Rev. Sci. Ser. II **7**, 65.
Muetterties, E.L. and C.M. Wright, 1967, Quart. Rev. **21**, 109.
Mukhin, E.Ya. and L.K. Shmatok, 1968, Inorg. Mater. **4**, 1938.
Nagashima, K., H. Wakita and A. Mochizuki, 1973, Bull. Chem. Soc. Jpn. **46**, 152.
Nelson, D.I. and D.E. Irish, 1971, J. Chem. Phys. **54**, 4479.
Newham, R.E., M.J. Redman and R.P. Satoro, 1963, J. Am. Ceram. Soc. **46**, 253.
Niinistö, L., 1983, in: Systematics and the Properties of the Lanthanides, ed. S.P. Sinha (Reidel, Dordrecht) pp. 125–152.
Niinistö, L. and P. Kyläkoski, 1985, unpublished results.
Niinistö, L., J. Valkonen and P. Ylinen, 1980, Inorg. Nucl. Chem. Lett. **16**, 13.
Nikolskii, Yu.V., B.A. Maksimov and N.V. Belov, 1975, Dokl. Akad. Nauk. SSSR **222**, 87.
Nikolskii, Yu.V., B.A. Maksimov and N.V. Belov, 1976, Dokl. Akad. Nauk. SSSR **230**, 331.
Nikolskii, Yu.V., B.A. Maksimov, L.N. Demianets, V.V. Ilyukhin and N.V. Belov, 1977, Dokl. Akad. Nauk. SSSR **233**, 362.
Nugent, L.J., 1975, MTP Int. Rev. Sci. Inorg. Chem. Ser. II **7**, 195.
O'Brien, W. and R.G. Bautista, 1975, J. Less-Common Met. **41**, 191.
O'Keeffe, M., 1979, Acta Crystallogr. Sect. A **35**, 772.
Odent, G. and M.-H. Autrusseau-Duperray, 1976a, Rev. Chim. Miner. **13**, 196.
Odent, G. and M.-H. Autrusseau-Duperray, 1976b, Rev. Chim. Miner. **13**, 624.
Odent, G., E. Charetteur and M.-H Duperray, 1975, Rev. Chim. Miner. **12**, 17.
Odinets, Z.K., O. Vargas Ponse, B.E. Zaitsev and A.K. Molodkin, 1983, Zh. Neorg. Khim. **28**, 2784 [English transl.: Russ. J. Inorg. Chem. **28**, 1580].
Ohora Optical Glass Mfg. Co., Ltd., 1981, Jpn. Kokai Tokyo Koho 81-41-850.
Onstott, E.I., W.G. Witteman and M.G. Bowman, 1976, 12th Rare Earth Research Conference, Vail, Colorado, July 1976, p. 1.
Pajakoff, S., 1964, Monatsh. Chem. **95**, 1108.
Pajakoff, S., 1966, Monatsh. Chem. **97**, 733.
Pajakoff, S., 1968, Monatsh. Chem. **99**, 484.
Pajakoff, S., 1969, Monatsh. Chem. **100**, 1350.
Pakhomov, V.I., G.B. Silnitskaya, A.V. Medveder and B.F. Dzhuringskii, 1969, Inorg. Mater. **5**, 1409.

Pakhomov, V.I., G.B. Silnitskaya and B.F. Dzhurinskii, 1971, Inorg. Mater. **7**, 539.
Pakhomov, V.I., G.B. Silnitskaya, A.V. Medveder and B.F. Dzhurinskii, 1972, Inorg. Mater. **8**, 1259.
Palenik, G.J., 1983, in: Systematics and the Properties of the Lanthanides, ed. S.P. Sinha (Reidel, Dordrecht) pp. 153–206.
Palkina, K.K., V.G. Kuznetsov, B.F. Dzhurinskii and L.G. Moruga, 1972, Russ, J. Inorg. Chem. **17**, 341.
Palkina, K.K., V.G. Kuznetsov and L.G. Moruga, 1973, Zh. Strukt. Khim. **14**, 1053.
Palkina, K.K., V.G. Kuznetsov, L.A. Butman and B.F. Dzhurinskii, 1976, Koord. Khim. **2**, 286.
Palkina, K.K., V.Z. Saifuddinov, V.G. Kuznetsov, B.F. Dzhurinskii, G.V. Lysanova and E.M. Reznik, 1979, Russ. J. Inorg. Chem. **24**, 1193.
Panyashkin, V.T., Yu.A. Afanaslev, A.D. Garnovskii and O.A. Osipov, 1977, Usp. Khim. **46**, 2105; [English. transl.: Russ. Chem. Rev. **46**, 1109].
Pascal, P. (ed.), 1959, Nouveau Traite de Chimie Minerale (Masson & Cie, Paris) Tome VII.
Pashkova, A.V., O.V. Sorokina, N.I. Leonjuk, T.I. Timchenko and N.V. Belov, 1981, Dokl. Akad. Nauk. SSSR **258**, 103.
Pearson, R.G., 1963, J. Am. Chem. Soc. **85**, 3533.
Peters, T.E., 1969, J. Electrochem. Soc. **116**, 985.
Peterson, E.J. and E.I. Onstott, 1978, J. Inorg. Nucl. Chem. **40**, 1951.
Peterson, E.J., E.I. Onstott, M.R. Johnson and M.G. Bowman, 1978, J. Inorg. Nucl. Chem. **40**, 1357.
Petru, F. and B. Hajek, 1966, Chem. Listy **60**, 721.
Petru, F., F. Kutek and J. Satava, 1966, Collection Czech. Chem. Commun. **31**, 4459.
Petzold, N., 1955, Die Cerimetrie (Verlag Chemie, Weinheim/Bergstrasse) p. 32.
Philips N.V. Gloeilampenfabrieken, 1973, Patent Neth. Appl. 73-03-538.
Philips N.V. Gloeilampenfabrieken, 1976, Patent Neth. Appl. 76-07-724.
Polignac de, A., J. Delaynay, F. Fromage and J. Despeyols, 1971, C.R. Hebd. Seances Aead. Sci. Ser. C **273**, 735.
Popov, A.P. and R.E. Mironov, 1968, Rev. Roum. Chim. **13**, 765.
Popov, V.P. and M.A. Petrova, 1973, Inorg. Mater. **9**, 61.
Porai-Koshits, M.A., L.A. Aslanov and E.F. Korotnyi, 1976, Nauk. Tekh. Kristallokhim. **11**, 5.
Prandtl, W., 1938, Z. Anorg. Allg. Chem. **238**, 321.
Preiss, J. and A. Dussik, 1923, Z. Anorg. Allg. Chem. **131**, 275.
Pushcharovskii, D.Yu., E.A. Pobedimskaya, O.V. Kudryavtseva and B. Gettash, 1976, Kristallografiya **21**, 1126.
Pushcharovskii, D.Yu., O.G. Karpov, E.A. Pobedimskaya and N.V. Belov, 1977, Dokl. Akad. Nauk. SSSR **234**, 1323.
Pushcharovskii, D.Yu., G.I. Dorokhova, E.A. Pobedimskaya and N.V. Belov, 1978a, Dokl. Akad. Nauk. SSSR **242**, 835.
Pushcharovskii, D.Yu., O.G. Karpov, N.I. Leonjuk and N.V. Belov, 1978b, Dokl. Akad. Nauk. SSSR **241**, 91.
Pushcharovskii, D.Yu., A.M. Dago, E.A. Pobedimskaya and N.V. Belov, 1980, Dokl. Adad. Nauk. SSSR **251**, 334.
Pushcharovskii, D.Yu., A.M. Dago, E.A. Pobedimskaya and N.V. Belov, 1981, Dokl. Akad. Nauk. SSSR **258**, 1111.
Pushkina, G.Ya. and L.N. Komissarova, 1963, Russ. J. Inorg. Chem. **8**, 777.
Pushkina, G.Ya and L.N. Komissarova, 1967, Zh. Neorg. Khim. **12**, 2852.
Pushkina, G.Ya. and L.N. Komissarova, 1983, Koord. Khim. **9**, 3 [English transl. Coord. Chem. **8**, 1].
Pyatenko, Yu.A., T.A. Zhdanova and A.A. Voronkov, 1979, Dokl. Akad. Nauk. SSSR **248**, 868.
Quarton, M. and D. Svoronos, 1982, J. Solid State Chem. **42**, 325.
Ragimov, K.G., M.I. Chiragov and K.S. Mamedov, 1980, Dokl. Akad. Nauk. SSSR **253**, 1130.
Reinen, D., 1964, Z. anorg. allg. Chem. **327**, 238.
Reinhardt, K., 1984, Chemie unserer Zeit **18**, 24.
Ribar, B., N. Milinski and Z. Budovalcev, 1980, Cryst. Struct. Commun. **9**, 203.
Richardson, J.W., Q.W. Choi, F.V. Vratny and J.M. Honig, 1959, Anal. Chem. **31**, 1599.
Riikonen, P., 1978, M.Sc. Thesis, Helsinki University of Technology, Espoo, Finland, 133 pp.
Rogers, D.J., N.J. Taylor and G.E. Toogood, 1983, Acta Crystallogr. Sect. C **39**, 939.
Rohrbaugh, W.J. and R.A. Jacobson, 1974, Inorg. Chem. **13**, 2535.
Ropp, R.C. and E.E. Gritz, 1965, in: Rare Earth Research III, ed. L. Eyring (Gordon and Breach, New York) p. 719.
Roth, R.S., J.L. Waring and E.M. Levin, 1963, U.S. Atomic Energy Commission Conference 20-8.
Roth, R.S., J.L. Waring and E.M. Levin, 1964, in: Rare Earth Research II, ed. K.S. Vorres (Gordon and Breach, New York) p. 153.
Roy, R., 1954, J. Am. Ceram. Soc. **37**, 581.
Rumanova, I.M., G.F. Volodina and N.V. Belov, 1964, Kristallografiya **9**, 642 [English transl.: Sov. Phys. Crystallogr. **9**, 545].
Rumanova, I.M., G.F. Volodina and N.V. Belov, 1966, Kristallografiya **11**, 549.
Saakes, M., M. Leskelä and G. Blasse, 1984, Mater. Res. Bull. **19**, 83.
Safianov, Yu.N., E.A. Kuzmin and N.V. Belov, 1978, Dokl. Akad. Nauk. SSSR **242**, 603.
Salutsky, M.L. and L.L. Quill, 1950, J. Am. Chem. Soc. **72**, 3306.
Samuskevich, V.V., E.A. Prodan and M.M. Pavlyuchenko, 1975, Dokl. Akad. Nauk. B SSSR **19**, 144.
Sastry, R.L.N., S.R. Yoganarisimhan, P.N. Mehrota and C.N.R. Rao, 1966, J. Inorg. Nucl. Chem. **28**, 1165.
Saubat, B., M. Vlasse and C. Foussier, 1980, J. Solid State Chem. **34**, 271.
Saubat, B., C. Fouassier, P. Hagenmuller and J.C. Bourcet, 1981, Mater. Res. Bull. **16**, 193.
Sawyer, J.O., P. Caro and L. Eyring, 1971, Monatsh. Chem. **102**, 333.
Sawyer, J.O., P. Caro and L. Eyring, 1973, Rev. Chim. Miner. **10**, 93.

Scavingar, S. and B. Prodic, 1974, Acta Crystallogr. **18**, 698.
Schiffmacher, G., H. Dexpert and P. Caro, 1977, in: Reactivity of Solids, eds. J. Wood, O. Lindqvist, C. Helgesson and N.-G. Vannerberg (Plenum, New York) 641 pp.
Schroeder, L.W. and M. Mathew, 1978, J. Solid State Chem. **26**, 383.
Schuil, R.E., 1976, Patent Ger. Offen. 2-608-514.
Schweer, H. and H. Seidel, 1981, Z. Anorg. Allg. Chem. **477**, 196.
Segal, B.G. and S.J. Lippard, 1978, Inorg. Chem. **17**, 844.
Shafer, W.M., 1965, J. Appl. Phys. **36**, 1145.
Shannon, R.D., 1976, Acta Crystallogr. Sect. A **32**, 751.
Shannon, R.D. and C.T. Prewitt, 1969, Acta Crystallogr. Sect. B **25**, 925.
Shannon, R.D. and C.T. Prewitt, 1970a, Acta Crystallogr. Sect. B **26**, 1096.
Shannon, R.D. and C.T. Prewitt, 1970b, J. Solid State Chem. **2**, 199.
Shannon, R.D. and A.W. Sleight, 1968, Inorg. Chem. **7**, 1649.
Shannon, R.D., B.E. Taylor, T.E. Gier, H.-Y. Chen and T. Berzins, 1978, Inorg. Chem. **17**, 958.
Shannon, R.D., T.E. Gier, C.M. Foris, J.A. Nelen and D.E. Appleman, 1980, Phys. Chem. Miner. **5**, 245.
Sheikh, P.A., R. Winand and A.J. Flipot, 1970, J. Less-Common Met. **22**, 234.
Shen, J. and P.B. Moore, 1982, Am. Mineral. **67**, 1021.
Shinn, D.B. and H.A. Eick, 1968, Inorg. Chem. **7**, 1340.
Shiokawa, J. and G. Adachi, 1979, Jpn. Kokai Tokyo Koho 79-62-988.
Shumyatskaya, N.G., A.V. Voronkov and Yu.A. Pyatenko, 1980, Kristallografiya **25**, 728.
Sidorov, P.M., E.L. Belokoneva, N.F. Fedorov, T.A. Tunik, M.A. Simonov and N.V. Belov, 1977, Zh. Strukt. Khim. **18**, 397.
Siekierski, S., 1981a, J. Solid State Chem. **37**, 279.
Siekierski, S., 1981b, Inorg. Nucl. Chem. Lett. **17**, 169.
Siekierski, S., T. Miodowski and M. Salomon (eds.), 1983, IUPAC Solubility Data Series, Vol. 13: Scandium, Yttrium, Lanthanum and Lanthanide Nitrates (Pergamon, Oxford).
Silber, H.B. and T. Mioduski, 1984, Inorg. Chem. **23**, 1577.
Sinha, S.P., 1966, Complexes of the Rare Earths (Pergamon, London).
Sinha, S.P., 1976, Struct. Bond. (Berlin) **25**, 69.
Sinha, S.P., 1982, Fresenius Z. Anal. Chem. **313**, 238.
Sinha, S.P., 1983, NATO Adv. Sci. Inst. Ser. C **109**, 451.
Sinha, S.P. and P. Möller, 1983, J. Less-Common Met. **93**, 238.
Sklyarenko, Yu.S. and L.V. Ruzaikina, 1970, Russ. J. Inorg. Chem. **15**, 399.
Skshat, S.M., V.I. Simonov and N.V. Belov, 1969, Dokl. Akad. Nauk. SSSR **184**, 337.
Smith, B.F., Sullivan, V.R. and G. Frank, 1936, Ind. Eng. Chem. Anal. Educ. **8**, 449.
Smolin, Yu.I., 1969, Kristallografiya **14**, 985.
Smolin, Yu.I., 1970, Kristallografiya **15**, 47.
Smolin, Yu.I. and Yu.F. Shepelev, 1969, Inorg. Mater. **5**, 1823.
Smolin, Yu.I. and Yu.F. Shepelev, 1970a, Acta Crystallogr. Sect. B **26**, 484.
Smolin, Yu.I. and Yu.F. Shepelev, 1970b, Kristallografiya **15**, 256.
Smolin, Yu.I. and S.P. Tkachev, 1969, Kristallografiya **14**, 22.
Smolin, Yu.I., Yu.F. Shepelev and T.V. Upatova, 1969, Dokl. Akad. Nauk. SSSR **187**, 322.
Smolin, Yu.I., Yu.F. Shepelev and I.K. Butikova, 1971, Kristallografiya **16**, 911.
Southwood-Jones, R.V., W.L. Earl, K.E. Newman and A.E. Merbach, 1980, J. Chem. Phys. **73**, 5909.
Spahiu, K., 1983, Thesis, Royal Institute of Technology, Stockholm, Sweden.
Spahiu, K., 1985, Acta Chem. Scand. A **39**, 33.
Spitsyn, V.I., L.N. Komissarova, V.M. Shatskii and G.Ya. Pushkina, 1960, Russ. J. Inorg. Chem. **5**, 2223.
Spitsyn, V.I., 1977, Z. Chem. **17**, 353.
Staritzky, E., 1956, Analyt. Chem. **28**, 2022.
Steele, I.M., J.J. Pluth and J. Ito, 1978, Z. Krist. **147**, 119.
Sterba-Bohm, J.S. and J.P. Sterba-Bohm, 1938, Collection Czech. Chem. Commun. **16**, 8.
Stransky, E., 1970, Z. Phys. Chem. **243**, 86.
Stroganova, N.S. and L.V. Rousaikina, 1970, Les elementes des terres rares. Colloques Intern. du CNRS No. 180, Vol. 1, p. 297.
Su, C. and I.I. Shih, 1960, Russ. J. Inorg. Chem. **5**, 372.
Sumita, T. and M. Watanabe, 1973, Japan. Patent 73-38-316.
Svoronos, D.R., E. Antic-Fidancev, M. Lemaitre-Blaise and P. Caro, 1981, Nouv. J. Chim. **5**, 547.
Sweeney, M., 1975, Thermochim. Acta **11**, 397.
Tanaka, F. and S. Yamashita, 1984, Inorg. Chem. **23**, 2044.
Tananaev, I.V., I.M. Belyakov, B.F. Dzhurinskii and S.I. Berul, 1965, Inorg. Mater. **2**, 165.
Tananaev, I.V., B.F. Dzhurinskii and I.M. Belyakov, 1966, Inorg. Mater. **2**, 1791.
Tananaev, I.V., B.F. Dzhurinskii and V.I. Chistova, 1975, Inorg. Mater. **11**, 69.
Tareen, J.A.K., M.N. Viswanathiah and K.V. Krishnamurthy, 1980a, Rev. Chim. Miner. **17**, 51.
Tareen, J.A., T.R. Kutty and K. Krishnamurty, 1980b, J. Cryst. Growth **49**, 761.
Tate, I. and S. Oishi, 1981, Chem. Lett., 1301.
Taylor, J.C., M.H. Mueller and R.C. Hitterman, 1966, Acta Crystallogr. **20**, 842.
Tenisheva, T.F., A.N. Lazarev and T.M. Pavlyukovich, 1965, Izv. Akad. Nauk. SSSR Ser. Khim., 1553.
Thomas, J.E., R.C. Palenik and G.J. Palenik, 1979, Inorg. Chim. Acta **37**, L459.
Thompson, L.C., 1979, Complexes, in: Handbook on the Physics and Chemistry of Rare Earths, Vol. 3, eds. K.A. Gschneidner, Jr. and L. Eyring (North-Holland, Amsterdam) Ch. 25, pp. 209–297.
Timchenko, T.I., A.V. Pashkova, A.V. Azizov and A.Yu. Troshin, 1981, Dokl. Akad. Nauk. SSSR **258**, 106.
Tokyo Shibaura Electric Co., 1980, Jpn. Kokai Tokyo Koho 80-52-378.

Toogood, G.E. and C. Chieh, 1975, Can. J. Chem. **53**, 831.
Toropov, N.A. and I.A. Bondar, 1964, Dokl. Akad. Nauk. SSSR **158**, 173.
Toropov, N.A., I.A. Bondar, A.N. Lazarev and Yu.I. Smolin, 1971, Silicates of Rare Earth Elements and Their Analogues (Nauka, Leningrad) 230 pp.
Trofimovich, A.A. and G.S. Sedelnikov, 1963, Russ. J. Inorg. Chem. **8**, 1259.
Tselik, I.N., V.Ya. Shvartsman and V.D. Fedorenko, 1968a, Russ. J. Inorg. Chem. **13**, 106.
Tselik, I.N., G.R. Reineka, V.Ya. Shvartsman and V.D. Fedorenko, 1968b, Russ. J. Inorg. Chem. **13**, 669.
Tselik, I.N., G.F. Deineka, V.D. Fedorenko and V.Ya. Shvartsman, 1969, Russ. J. Inorg. Chem. **14**, 1238.
Turcotte, R.P., J.O. Sawyer and L. Eyring, 1969, Inorg. Chem. **8**, 238.
Ueki, T., A. Zalkin and D.H. Templeton, 1966, Acta Crystallogr. **20**, 836.
Urland, W. and R. Kremer, 1984, Inorg. Chem. **23**, 1550.
Urusov, V.S. and V.O. Khudolozhkin, 1974, Geochem. Int. **10**, 1048.
Valkonen, J., 1979, Ann. Acad. Sci. Fenn. Ser. AII, **188**, 34 p.
Valkonen, J. and P. Ylinen, 1979, Acta Crystallogr. Sect. B **35**, 2378.
van der Spijker, W.H.M.M. and W.L. Konijnendijk, 1978, Inorg. Nucl. Chem. Lett. **14**, 389.
van der Spijker, W.H.M.M. and W.L. Konijnendijk, 1979, Patent Ger. Offen. 2-915-623.
Vasilev, G.I. and V.V. Serebrennikov, 1964, Russ. J. Inorg. Chem **9**, 2490.
Veenis, A.W. and A. Bril, 1978, Philips J. Res. **33**, 124.
Vetter, G. F. Queyrouk, P. Labbe and M. Goreaud, 1982, J. Solid State Chem. **45**, 293.
Vicat, J. and S. Aleonard, 1968, Mater. Res. Bull. **3**, 611.
Vickery, R.C., 1953, Chemistry of Lanthanons (Butterworths, London) p. 218.
Vickery, R.C., 1960, The Chemistry of Yttrium and Scandium (Pergamon, London).
Voliotis, S. and A. Rimsby, 1975, Acta Crystallogr. Sect. B **31**, 2620.
Voliotis, S., A. Rimsky and J. Faucherre, 1975, Acta Crystallogr. Sect. B **31**, 2607.
Volodina, G.F., I.M. Rumanova and N.V. Belov, 1961, Kristallografiya **6**, 919 [English transl.: Sov. Phys. Crystallogr. **6**, 741].
Voronkov, A.A. and Yu.A. Pyatenko, 1967, Kristallografiya **12**, 214.
Voronkov, A.A., N.V. Kadoshnikova, N.V. Mukhtarova, R.K. Rastsvetaeva, N.A. Shumyatskaya and V.V. Ilyukhin, 1982, Probl. Teor. Kristallokhim. Slozhnykh. Oksidov., ed. A.N. Lazarev (Nauka, Leningrad) pp. 5–43; Ref. CA 99: 46077C.
Vratny, F. and J.M. Honig, 1960, Trans. Faraday Soc. **56**, 1061.
Wakita, H., 1978, Bull. Chem. Soc. Jpn. **51**, 2879.
Wakita, H. and K. Nagashima, 1972, Bull. Chem. Soc. Jpn. **45**, 2476.
Wakita, H. and S. Kinoshita, 1979, Bull. Chem. Soc. **52**, 428.
Walker, A. and J.R. Ferraro, 1965, J. Chem. Phys. **43**, 2689.
Wang Genglin, Yan Shiping, Li Xueyao, Yao Xinkan, Wan Zhuli, Rao Zihe and Liang Dongcai, 1981, Sci. Sin. Ser. B. **25**, 916.
Wanklyn, B.M., 1973a, J. Mater. Sci. **8**, 649.
Wanklyn, B.M., 1973b, J. Mater. Sci. **8**, 1055.
Wanklyn, B.M., 1978, J. Cryst. Growth **43**, 336.
Wanklyn, B.M., 1981, J. Cryst. Growth **54**, 610.
Wanklyn, B.M., F.R. Wondre, G.B. Ansell and W. Davison, 1974, J. Mater. Sci. **9**, 2007.
Wanklyn, B.M., F.R. Wondre, G.B. Ansell and W. Davison, 1975, J. Mater. Sci. **10**, 1494.
Warshaw, I. and R. Roy, 1964, Progress in the Science and Technology of the Rare Earths, Vol. I (Pergamon, Oxford) p. 203.
Watanabe, M. and T. Nishimura, 1978, Japan. Kokai 78-64-685.
Watanabe, M. and T. Sumita, 1973, Japan Kokai 73-34-787.
Watanabe, M., T. Nishimura, T. Omi, K. Komoto, T. Kobya and K. Shimizu, 1978, Patent Ger. Offen. 2-816-069.
Weeks, M.E., 1968, Discovery of the Elements, 7th Ed. (J. Chem. Educ., Easton), Ch. 16, pp. 667–699.
Weidelt, J., 1970, Z. Anorg. Allg. Chem. **374**, 26.
Weigel, F., 1969, Fortschr. Chem. Forsch. **12**, 539.
Weigel, F., 1978, Chem. Z. **102**, 339.
Weigel, F. and V. Scherer, 1967, Radiochim. Acta 7, 50.
Weir, C.E. and E.R. Lippincott, 1961, J. Res. Natl. Bur. Stan. 65A, 173.
Wendlandt, W.W., 1956, Anal. Chim. Acta **15**, 439.
Wendlandt, W.W. and J.L. Bear, 1960, J. Inorg. Nucl. Chem. **12**, 276.
Wendlandt, W.W. and T.D. George, 1961, Texas J. Sci. **13**, 316.
Westinghouse Electric Corp., 1981, Jpn. Kokai Tokyo Koho JP 81-163-185.
Willis, R.R., S. Homqvist, J.M. Wimmer and J.A. Cunningham, 1976a, J. Mater. Sci. **11**, 1305.
Willis, R.R., R.W. Stewart, J.A. Cunningham and J.M. Wimmer, 1976b, J. Mater. Sci. **11**, 749.
Yamada, H., T. Kano and M. Tanabe, 1974, Japan. Kokai 74-36-588.
Youngblood, D.H. and K.A. Gschneidner, Jr., 1975, in: Scandium, ed. C.T. Horowitz (Academic, London) Ch. 12, pp. 484–496.
Ysker, J.S. and W. Hoffmann, 1970, Naturwissenschaften **57**, 129.
Yukinori, M. and Y. Fumikazu, 1978, Japan Kokai Tokyo Koho 78-95-900.
Zalkin, A., J.D. Forrester and D.H. Templeton, 1963, J. Chem. Phys. **39**, 2881.
Zambonini, F. and G. Carobbi, 1924, Gazz. Chim. Ital. **54**, 53.
Zhdanova, T.A., A.A. Voronkov, L.N. Komissarova and Yu.A. Pyatenko, 1972, Dokl. Akad. Nauk. SSSR **196**, 1076.
Zhdanova, T.A., L.N. Demianets, A.A. Voronkov and Yu.A. Pyatenko, 1975, Dokl. Akad. Nauk. SSSR **224**, 1069.
Zhdanova, T.A., B.A. Maksimov, A.A. Voronkov, V.V. Ilyukhin and N.V. Belov, 1980, Kristallografiya **25**, 708.

Handbook on the Physics and Chemistry of Rare Earths, edited by K.A. Gschneidner, Jr. and L. Eyring

Chapter 57

IMPLICATIONS IN ORGANIC SYNTHESIS

JOHN R. LONG
Aldrich Chemical Company, Milwaukee, Wisconsin, USA

Contents

Symbols and definitions

Me = CH_3
Et = C_2H_5
Pr = *n*-C_3H_7
Bu = *n*-C_4H_9
Ph = C_6H_5
Cp = C_5H_5
Ac = $CH_3-\overset{O}{\overset{\|}{C}}-$

TES = triethylsilyl-
TBS = *tert*-butyldimethylsilyl-
THF = tetrahydrofuran
TFA = trifluoroacetic acid
L = an unspecified organic group
R = an unspecified rare earth species

The family of rare earths as described in this chapter consists of the elements in the lanthanide series plus scandium and yttrium. Formula representations of rare earth salts refer to the most common hydration state unless specifically noted otherwise.

Given that some of the chemistry presented herein deals with the preferential formation of one isomer over another during synthesis, certain definitions need to be established for the terms selectivity and specificity, especially when preceded by the terms stereo-, regio- and enantio-. A concise overview of this deceptively complex topic has been prepared by Ault (1984) and is particularly recommended.

In general, selectivity refers to the exclusive or predominant formation of one isomer out of a set of isomers possible for the given reaction, e.g., eq. (a).

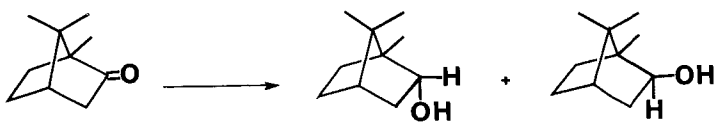

minor major (a)

In the example below, specificity is demonstrated in the exclusive formation of product isomer, A, from cis reactant I, while the opposite isomer, B, is produced from trans reactant isomer II.

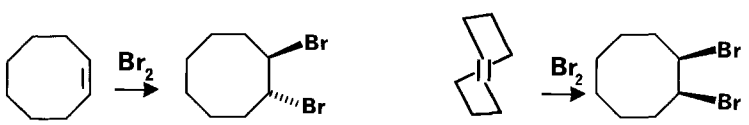

(I) (A) (II) (B) (b)

Adding the prefex stereo- to either of the above terms changes nothing. Stereo is simply a general term referring to any type of spatial isomerism.

The prefix regio- refers to the actual pattern of substituents. Regioselectivity means that the reaction is selective with regard to the physical positioning of the atoms involved.

The term enantio- pertains to optical activity, and is frequently designated as enantiomeric excess (e.e.), a ratio showing the predominance of a given optical isomer (enantiomer) preferentially formed.

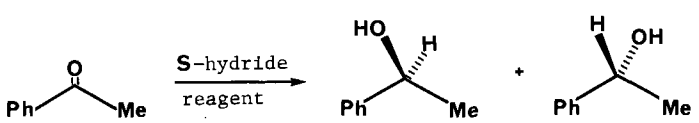

major (S) minor (R) (c)

However, there is sufficient confusion in the area of stereochemical nomenclature that new efforts to separate the concepts of local geometry and stereoisomerism are getting serious attention (Mislow and Siegel, 1984). Accordingly, in this chapter usage of terms described above must consider the context from which they were taken and the intent and understanding of the original authors.

1. Introduction

In 1983, the Rare Earth Society of Japan published a literature guide to the organic chemistry of rare earth elements that included the section "Organic Reactions and Syntheses by Using Rare Earth Elements as Reagents and Catalysts" (Uemura, 1983). Covering more than 60 years of research, this compilation is notable for several reasons:

(i) Of the 409 references cited, 346 pertained specifically to the element cerium, most frequently as ceric ammonium nitrate (CAN), while the 13 remaining lanthanides were featured in only 63 citations.

(ii) Several of the latter group of articles included descriptions of cerium(III) compounds as reagents of choice in selected organic transformations.

(iii) Of these same non-cerium references, 25 described heterogeneous/catalytic chemistry and/or patent literature, areas of marginal interest to the topic at hand.

(iv) Of the 63 papers, 19 were published between 1980 and 1982.

Accordingly, one is tempted to assume that there are relatively few ways in which the lanthanides can be applied to organic transformations; indeed, the most comprehensive and definitive compilation of data on reagents useful to the synthetic chemist, the Fiesers' "Reagents for Organic Synthesis" (L.F. Fieser and M. Fieser, 1967–1984), made infrequent mention of lanthanides other than CAN before 1977. In one case, it was to recommend cerous hydroxide for the destruction of peroxides (Ramsay and Aldridge, 1955).

Other instances included the use of ceric acetate in the synthesis of lactones, although preparation of the reagent was not trivial, and preferable alternatives were subsequently devised (Heiba and Dessau, 1971). Also, a combination of cerium(IV) oxide and hydrogen peroxide was found to oxidize phenols, possibly through the formation of singlet oxygen in situ (Barton et al., 1975).

Cerium(IV) trifluoroacetate was applied to the oxidation of certain arenes, but the reaction suffered from poor yields and complex product mixtures (Norman et al., 1973). As with the acetate, reagent preparation was an involved procedure.

In contrast to the scant attention given during most of the 1970s to the role of lanthanides in organic synthesis, aspects of f-element organometallic chemistry (featuring σ- and π-bonded derivatives) have been thoroughly reviewed by Marks (1976a, 1976b, 1978) as well as Schumann and Genthe (1984). While the chemistry of complexes having lanthanide–carbon bonds is only briefly considered in this chapter, the background information provided by these reviews is extremely instructive.

For example, the unique spatial distribution and energy of f-valence orbitals combines with the considerable size of the lanthanides to afford the potential for unusual coordination geometries. The shielding of the 4f electrons by the filled $5s^2$ and $5p^6$ shells means that the bonding orbitals are relatively unexposed to any electrostatic or covalent character introduced by the coordination environment compared with transition metal d-orbital interactions.

The f–f spectral lines show energies and intensities that are relatively insensitive to ligand changes, in direct contrast to transition metal d–d-absorption spectra.

The lanthanides are hard acids (Pearson, 1973) and form complexes with considerable ionic character due to the poor overlap exhibited by the contracted f orbitals. This character, as well as other properties, changes little with increasing atomic number.

Most lanthanide ions are paramagnetic, a property first exploited in the mid-1950s when it was found that the dysprosium(III) ion accelerated the rate of decarboxylation of phenylmalonic acid (Pitzer and Gelles, 1953). This "magnetic catalysis" was considered a minor effect (Gelles and Pitzer, 1955), and not until 1960 was this phenomenon applied to the resolution of the inadvertent overlap of NMR spectral resonances (Jackson et al., 1960).

Within 10 years, a variety of lanthanide–dionate complexes were being specifically designed to induce sizeable, clean proton NMR shifts (Cockerill et al., 1973). However, within the framework of this rapidly developing field, the unique coordinating ability of the lanthanide shift reagents was essentially ignored as far as applications in organic synthesis were concerned, and until recently, the application of the entire spectrum of rare earth elements (lanthanides plus scandium and yttrium) and compounds to organic processes has suffered from the lack of an investigative effort such as that generated in the development of the NMR shift reagents.

Within a year of Uemura's survey, however, the chemical literature witnessed at least two major reviews (Imamoto et al., 1984a; Natale, 1983) as well as a cascade of research articles that described new and surprising uses for lanthanides in organic synthesis. A review article on organolanthanoid complexes by Schumann (1984) speculated on the potential of such complexes in catalysis and organic synthesis, and complemented a recent chapter in this *Handbook* (Schumann and Genthe, 1984).

Our present objective is to complement these studies, as well as Kagan and Namy's chapter in this *Handbook* (1984), and put into focus the diverse chemistry reflected in this rapidly growing field.

2. Interactions of shift reagents with organic substrates

2.1. *Preliminary indications of catalytic activity*

Modest synthetic utility has been shown for certain shift reagents, initially attributed to their ability to induce conformational changes or to selectively stabilize complexes in a desirable coordination scheme.

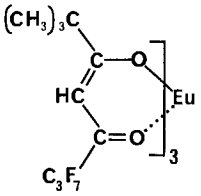

Fig. 1. Tris(2,2-dimethyl-6,6,7,7,8,8,8-heptafluoro-3,5-octanedionato) europium(III) [Eu(fod)$_3$].

The Lewis acid character of Eu(fod)$_3$ [tris(2,2-dimethyl-6,6,7,7,8,8,8-heptafluoro-3,5-octanedionato)europium(III), fig. 1] provided optimum regioselectivity in the conversion of the oxaspiropentane, C, to the cyclobutanone, D (Trost and Bogdanowicz, 1973).

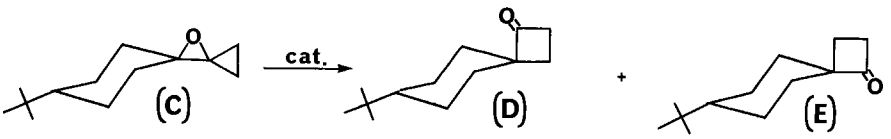

(1)

cat. = H^+:	82	18
cat. = Li^+:	91	9
cat. = Eu^{3+}:	99+	<<1

Catalysis via aqueous acid or a lithium perchlorate/benzene reflux was far less effective.

Ring opening was initiated by Lewis acid complexation with the epoxide oxygen, imparting a positive character to the adjacent carbon atom. It apparently is the nature of the oxygen–Lewis acid bond that determines the relative rates of bond migration (leading to D) vs. bond rotation (leading to E).

Europium and (to a lesser extent) lithium form a more ionic bond with the oxygen atom than do protons. This results in a greater negative charge on the oxygen and enhances bond migration and the formation of D through the scheme below.

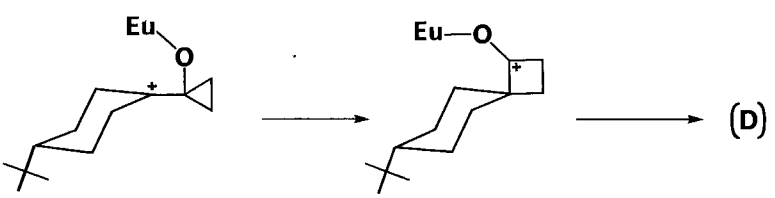

(2)

This rearrangement occurred in deuterochloroform at 37°C.

The contrasting catalysis with protonic acids results in covalent bonding with oxygen that minimizes the negative charge and allows significant bond rotation, leading to E.

Shortly after that report, a study of novel aspects of shift reagents in proton magnetic resonance analysis revealed the unexpected catalysis by $Eu(tfn)_3$ of the Diels–Alder reaction shown in eq. (3) (Morrill et al., 1975).

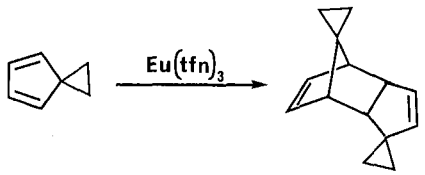

(3)

[tfn = tris(1,1,1,2,2,3,3,7,7,8,8,9,9,9-tetradecafluoro-4,6-nonanedionato)]

In 1977, spectral studies of cycloalkanones gave evidence of conformational changes between the free state when the rings were large enough to allow the substrate to act as a bidentate ligand toward the metal (Dunkelblum and Hart, 1977).

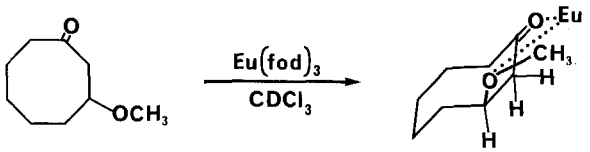

(4)

Similar observations of stereoselective rearrangements of camphorato-ligands (fig. 2) have been observed upon adduct formation with formamide and acetamide derivatives (Brittain, 1982).

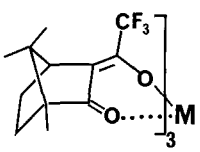

Fig. 2. Tris[3-(trifluoromethylhydroxymethylene)-*d*-camphorato], metal complex $[M(tfc)_3]$.

2.2. *Shift reagents as hetero-Diels–Alder catalysts*

In one of the first examples of a specific synthetic application of a lanthanide shift reagent, $Eu(fod)_3$ acted as a mild Lewis acid catalyst in hetero-Diels–Alder reactions (Bednarski and Danishefsky, 1983a).

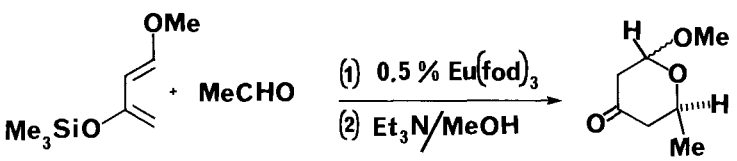

(5)

In this scheme, the character of the aldehyde is altered by the lanthanide cation so that it can act as a potent heterodienophile. This promotion can be attributed to the oxophilicity of the europium species, which, appropriately complexed, can exploit favorable solubility properties.

The resulting cyclocondensations represent a method for the stereospecific synthesis of carbon-branched pyranose derivatives [eq. (6)] where endoselectivity is maintained through a wide range of aromatic and aliphatic aldehydes.

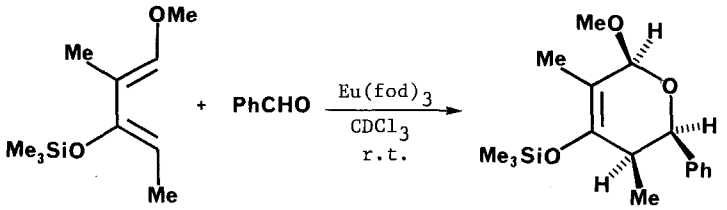

(6)

Extension of this chemistry to chiral europium(III) ligands shows promise for asymmetric induction and enantioselectivity in organic synthesis. The latter feature is possible through the use of a chiral catalyst such as $Eu(hfc)_3$, tris[3-(heptafluoropropylhydroxymethylene)-*d*-camphorato] europium (fig. 3).

Described as "interactivity of chiral auxiliaries with chiral catalysts" (Bednarski and Danishefsky, 1983b), this technique can be applied to the synthesis of optically pure saccharides, including L-glycosides, while avoiding formal resolution or glycosylation.

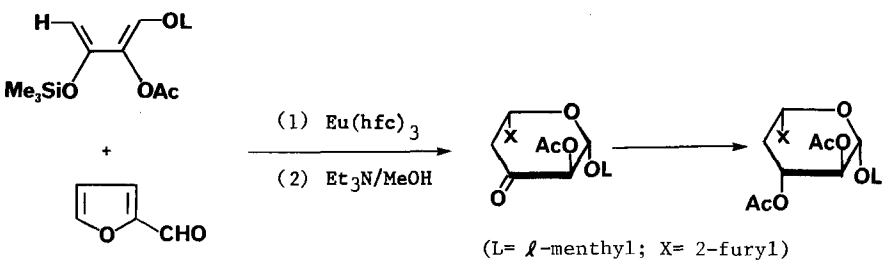

(L= ℓ-menthyl; X= 2-furyl)

(7)

The $Eu(hfc)_3$ complex also promotes the cyclocondensation of aldehydes with siloxydienes with considerable asymmetric induction (Bednarski et al., 1983).

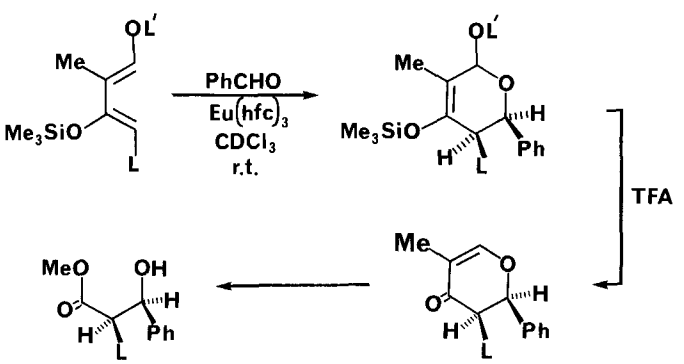

(8)

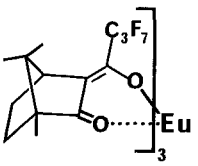

Fig. 3. Tris[3-(heptafluoropropylhydroxymethylene)-*d*-camphorato], europium(III) derivative [$Eu(hfc)_3$].

A systematic study designed to improve the initially observed enantiomeric enhancement of 18% led to more favorable reaction conditions. Over 50% e.e. could be realized by running the reaction at $-10°C$ in the absence of solvent. Increasing the proportion of the europium complex to 10 mol% dramatically improved the reaction rate but left the e.e. approximately the same. With such a large and complex lanthanide catalyst, the reason for the asymmetric induction is not well understood; based upon observation of a variety of shift reagent catalytic processes, it appears that the role of the catalyst is much more important than a general medium effect.

Ytterbium shift reagents also can promote cycloaddition reactions, in some cases more efficiently than the europium analogs (Danishefsky and Pearson, 1983). In chemistry applicable to the synthesis of milbemycin/avermectin targets, $\lesssim 5\%$ $Yb(fod)_3$ catalyzed the diene–acetaldehyde cyclocondensation [eq. (9)], whereas one equivalent of zinc chloride was required to effect similar conversions in like yields.

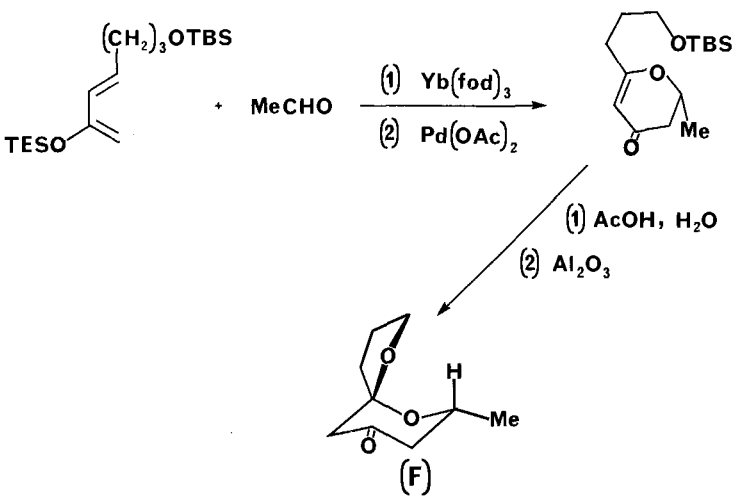

(9)

The lone isomer, F, was produced in 48% yield following desilylation and alumina-induced spirocyclization.

This mode of catalysis is especially attractive for dienes having sensitive functionalities. Cycloaddition of substrates bearing acid-labile components has been effected using $Yb(fod)_3$ at only 5 mol% levels (Danishefsky and Bednarski, 1984).

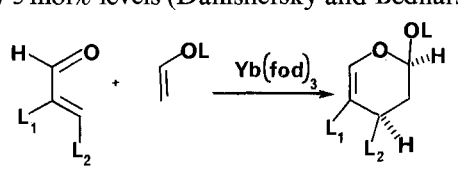

(10)

It was also possible to condense acrolein with dihydropyran in 55% yield (after distillation).

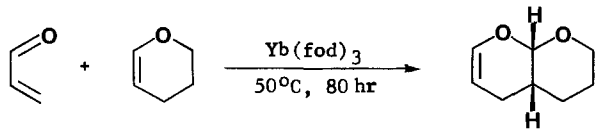

(11)

Immediately following Danishefsky's pioneering work, several reports of cyclocondensations promoted by lanthanide shift reagents appeared in the literature. The $Eu(fod)_3$/hetero-Diels–Alder methodology offers a novel approach to highly functionalized δ-lactones (Castellino and Sims, 1984a). Such a scheme provides access to natural products via synthetically useful intermediates.

A convenient and efficient synthesis of the α-pyrone kawain was also described that used 1.7 mol% Eu(fod) to give a 75% isolated yield (based on diene) (Castellino and Sims, 1984b). Catalysis by the corresponding complex of ytterbium, a stronger Lewis acid than europium, gave an 84% yield, while use of a stoichiometric amount of zinc chloride resulted in a 78% yield.

Substituting Ag(fod) as the catalyst afforded condensation to two acyclic diastereoisomers. Absence of catalyst is manifested by little differentiation between dienophilic sites and poor combined yield.

The use of simple aryl or alkyl ketones in the synthesis of a variety of substituted δ-lactones via Lewis acid-catalyzed cyclocondensations has been reported (Midland and Graham, 1984). In addition, it was shown that changes in substitution pattern on the diene (1,1-dialkoxy- in the case of Brasard's diene, single alkoxy substitution at the 1-position of Danishefsky's diene) were reflected in changes in diastereoselectivity induced by particular Lewis acids. Europium(III) catalysts improved diastereoselectivity in the cyclocondensation of Brasard's diene, implying a chelation-controlled addition that was much more efficient than additions catalyzed by zinc chloride or boron trifluoride etherate.

2.3. *Other effects of shift reagents*

An additional novel use of lanthanide shift reagents emerged from studies of metal-catalyzed light emission and decomposition of dioxetans (McCapra and Watmore, 1982). In the case of dioxetan, G (see fig. 4), the pseudo first-order

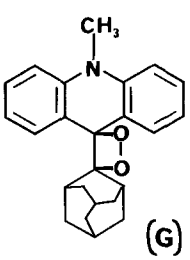

(G)

Fig. 4. Dioxetan, G, obtained from the oxidation of 9-(2-adamantylidene)-*N*-methylacridan.

reaction rate decreases as the Lewis acidity of the lanthanides decreases across the Periodic Table.

Again, the mechanism proposed for this process features interaction between the lanthanide ion and two oxygen atoms on the organic donor molecule:

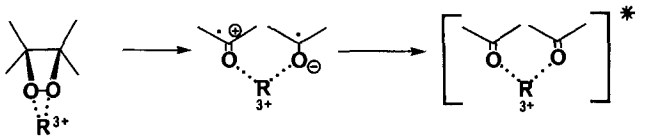

(12)

This interaction may serve to increase the oxidation potential of the peroxide on complexing with the Lewis acid represented by R^{3+}. The relative rates can be described by the ratios $Pr(fod)_3$, 65 : $Eu(fod)_3$, 30 : $Dy(fod)_3$, 6.5 : $Yb(fod)_3$, 1.0 (rate with no catalyst is 6.5×10^{-4}).

The use of shift reagents as a component of a gas–liquid chromatographic stationary phase applied to the resolution of racemic epoxides has also been reported (Golding et al., 1977). Effective separation of the enantiomers of epoxypropane was obtained at 40°C in less than 10 min with a nitrogen carrier. The efficiency of the lanthanide complexes in this role can be attributed to the energy differences between diastereoisomeric adducts. Accentuation of these differences by appropriate adjustments in ligand substitution, solvent properties and metal ion selection would be necessary to develop such chromatographic systems to their fullest potential.

3. Catalytic effects of lanthanide(III) salts

3.1. *Lanthanide-assisted nitrations and oxidations*

An early report of a catalytic oxidation of an organic substrate by a simple lanthanide salt focused on the oxidizing ability of the nitrate anion, which was promoted by various R^{3+} ions (Girard and Kagan, 1975). Of the lanthanides studied (La, Sm, Eu, Tm, Yb), ytterbium nitrate gave the highest yield of benzils from benzoins:

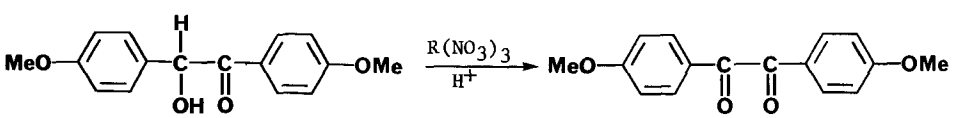

(13)

Given NO_3^- as the oxidizing agent, the presence of the ytterbium ion catalyzes the oxidation of nitrite back to nitrate by molecular oxygen (air). Variations in reaction conditions showed that the reaction required the presence of oxygen, the oxyanion and the lanthanide salt for best results. (See fig. 5.) As before, the ytterbium ion is

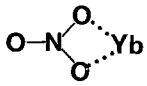

Fig. 5. Proposed ytterbium-nitrate ion intermediate in the lanthanide-assisted oxidation of benzils.

presumed to coordinate to two of the oxygen atoms of the nitrate ion, facilitating electron transfer followed by reoxidation of the anion.

Extension of this chemistry eventually led to the development of a new method for the high-yield nitration of phenols using one equivalent of sodium nitrate as nitrating agent in excess HCl (Ouertani et al., 1982); lanthanide catalysis was effective under mild conditions, which leave many other aromatic systems unaltered. Three particular aspects of this study should be emphasized:

(i) An acid medium is required (in 1 : 3 water/ethyl ether), but the method is potentially suitable for acid-sensitive compounds since reasonable reactivity is observed in a medium as weak as 0.5 mol eq HCl.

(ii) The ortho : para ratio of products is a function of the acidity: greater acidity favors ortho-nitration (para-substituted phenols undergo 80–90% nitration at the ortho position).

(iii) Small quantities of lanthanide catalyst are required (0.01 mol eq) and other lanthanum salts work as well as the nitrate; also effective are nitrates of Nd, Sm, Eu, Tb, Yb, and Tm.

The accompanying reactions represent typical product distributions.

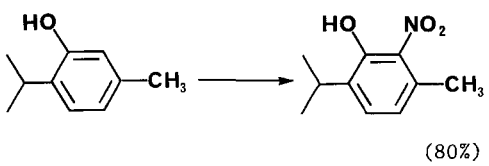

(14)

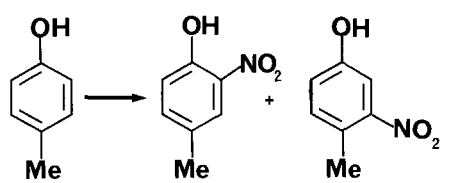

(15)

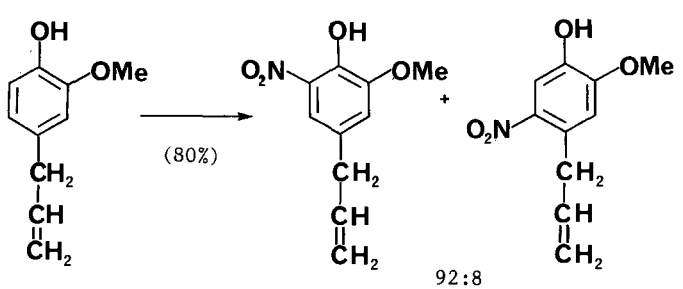

(16)

This procedure is selective for the nitration of phenol rings in the presence of those having substituents other than –OH, a property not observed under HNO_3/H_2SO_4 nitration conditions (Coombes et al., 1968).

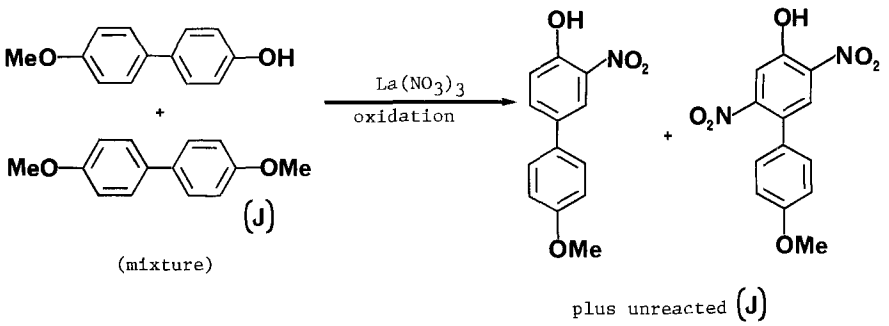

(17)

3.2. *Lanthanum perchlorate catalysis with nitrogen bases*

Lanthanum(III) perchlorate has also been developed as a catalyst in organic synthesis, specifically in the formation of 4-substituted-2,6-dimethylpyrimidines from cyclic secondary amines and acetonitrile (Forsberg et al., 1976).

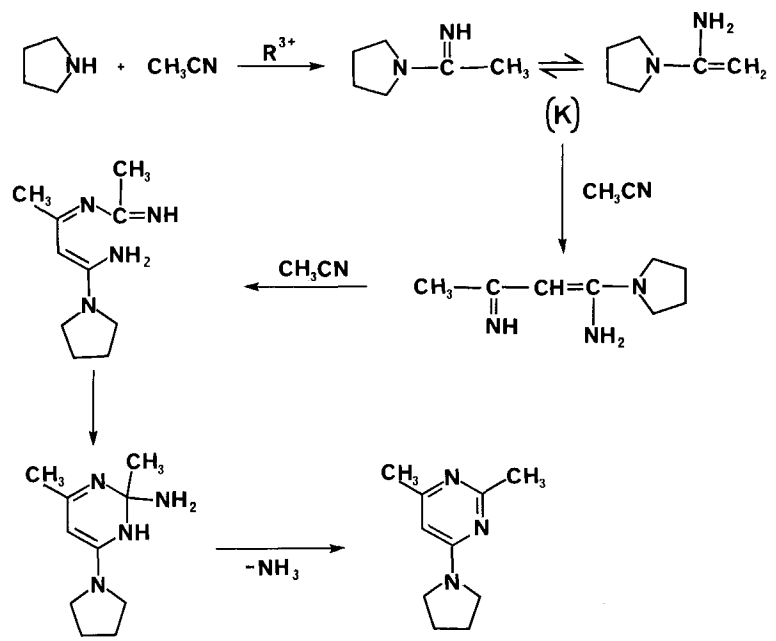

(18)

The lanthanum ion promotes the formation of amidine K (possibly by increasing the polarization of the C≡N bond to promote attack by the amine) and also appears to be necessary for the ring closure.

The implication of active lanthanide ion participation in labile ligand–metal interactions is rather unexpected, considering the thermodynamic stability of complexes formed between R^{3+} ions and polydentate aliphatic amines in acetonitrile (Forsberg, 1973).

3.3. *Catalytic effects of lanthanide chlorides in the acetalization of aldehydes*

A variety of lanthanide chloride salts effect aldehyde acetalization rapidly and under mild conditions (Luche and Gemal, 1978). With trimethyl orthoformate as a water scavenger, the reaction proceeds in minutes at room temperature with no side-products.

$$\mathrm{LCHO} + \mathrm{MeOH} \xrightarrow[\mathrm{HC(OMe)_3}]{\mathrm{RCl_3}} \mathrm{LCH(OMe)_2} \qquad (\mathrm{R} = \mathrm{La, Ce, Nd, Er, Yb}). \qquad (19)$$

Yields greater than 90% are typical, with lanthanum, cerium and neodymium chlorides being effective for aliphatic linear aldehydes while erbium and ytterbium chlorides are superior for aromatic and cyclic aldehydes (under the given experimental conditions, zinc chloride was ineffective).

The difference in activity among the lanthanide salts was further demonstrated by the fact that para-nitrobenzaldehyde was not acetalized after 20 hr in the presence of erbium chloride, but was completely converted when ytterbium chloride was the catalyst. This is consistent with the observation that acetalization yields increased with increasing atomic number (decreasing ionic radius), a phenomenon related to the Lewis acidity (or degree of hardness) of the cations. The role of the lanthanide catalyst is not well-defined, however.

As before, the reaction conditions are mild enough to accommodate sensitive functionalities that would be adversely affected by higher temperatures or stronger acids.

As part of a study of the cleavage of carbon–carbon bonds with a hard acid/soft nucleophile system, several lanthanide chlorides were evaluated to see if their Lewis acidity would promote a reaction similar to Luche's aldehyde acetalization (Fuji et al., 1981). Unfortunately, the reaction of lanthanum, ytterbium and cerium chlorides with α-cyano-α, β-unsaturated esters yielded varying amounts of Michael adduct and unreacted starting material after several days of reaction.

Other Lewis acids such as aluminum chloride, aluminum bromide, boron trifluoride etherate and ferric chloride converted these substrates into dithioacetals, frequently in less than an hour.

Significantly, the authors speculated that the conversion was activated by the interaction of the Lewis acid with the nitrile nitrogen atom, a process apparently requiring an orbital flexibility (capacity to hybridize) or other electronic character inconsistent with properties found in lanthanide species.

4. Cerium compounds in organic synthesis

4.1. *Recent and representative cerium(IV) applications*

The first indication of the strength of the interaction between the ceric ion (Ce^{4+}) and alcohols was described in 1901 (Meyers and Jacoby), and for decades the ceric ammonium nitrate (CAN) salt has held a premier position among lanthanide oxidants useful in organic synthesis (Ho, 1973).

While a thorough treatment of cerium(IV) chemistry is clearly beyond the scope of this chapter, presentation of selected and recent reports of its use is appropriate because of the background it provides for the subsequent examination of the cerous (Ce^{3+}) ion as a catalyst in organic reductions.

One of the few disadvantages of CAN lies in the quantity of material sometimes required to oxidize alcohols; in addition, such processes may not be as systematic or consistent as other methods. However, both ceric ammonium sulfate and CAN have been used as catalysts in the sodium bromate oxidation of secondary alcohols to ketones (Tomioka et al., 1982).

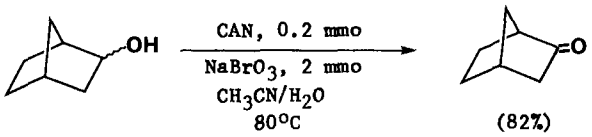

(20)

The preference for secondary alcohols is quite pronounced:

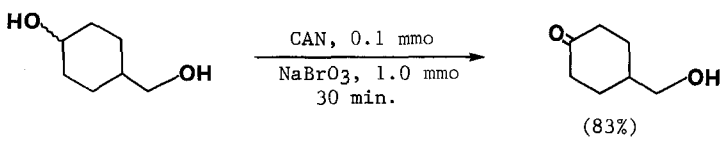

(21)

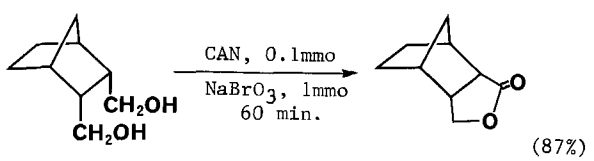

(22)

Cerium(IV) sulfate exhibits similar selectivity: 4-dodecanol is converted to 4-dodecanone in 98% yield, but 1-dodecanol undergoes only 3% conversion.

Ceric sulfate also can act as a cyclodehydrogenation reagent (Kropf and von Wallis, 1983).

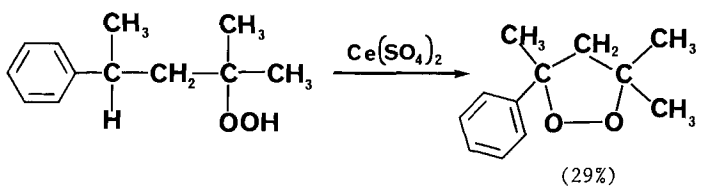

(23)

Studies of Ce(IV) oxidation of cyclic alcohols indicated that, in sulfuric acid/perchloric acid systems, the most reactive of the cerium(IV) sulfate complexes present in solution was $CeSO_4^{2+}$ (Hintz and Johnson, 1967). The same species was similarly identified in a study of oxidative decarbonylations (Hanna and Moehlenkamp, 1983).

A novel cerium(IV) reagent, cerium pyridinium chloride (CPC), promoted side-chain methoxylation of higher polymethylbenzenes (Maini et al., 1978). However, such reactions using CPC are extremely slow when run in alcohols other than methanol; this and other considerations led to the development of a more convenient and general procedure for benzylic alkoxylation of methylarenes (DallaCort et al., 1983).

Another new cerium(IV) reagent, ceric triethylammonium nitrate (CTEAN), has been prepared for use in the mild high-yield oxidation of benzylic alcohols and α-hydroxy ketones to the corresponding carbonyl compounds (Firouzabadi and Iranpoor, 1983). This CAN analog is stable, soluble in methylene chloride, acetonitrile, acetone, alcohols and water; it gives high yields in simple, nonacidic solvents and produces minimal secondary products from carbon–carbon bond cleavage.

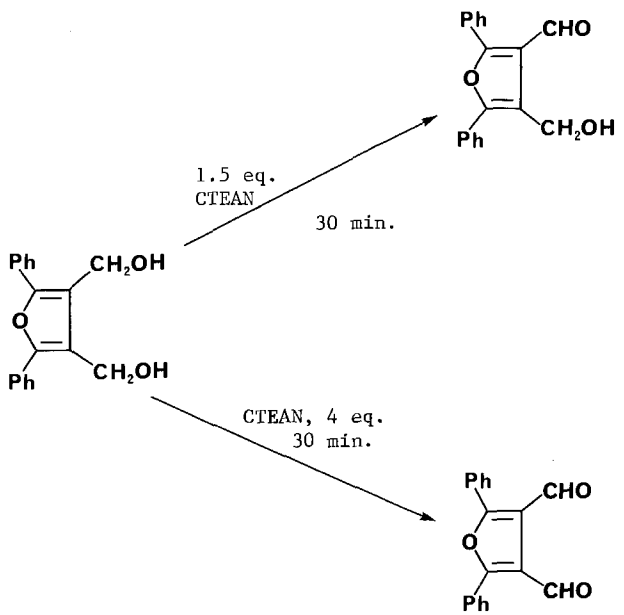

(24)

(25)

Further adjustments to the environment about the cerium(IV) ion allow the formulation of additional reagents having mild oxidizing capacities: bis[trinitratocerium(IV)] chromate, $[Ce(NO_3)_3]_2CrO_4$ (Firouzabadi et al., 1984a); dinitratocerium(IV) chromate dihydrate, $[Ce(NO_3)_2]CrO_4 \cdot 2H_2O$ (Firouzabadi et al., 1984b); and ceric trihydroxy hydroperoxide, $Ce(OH)_3O_2H$ (Firouzabadi and Iranpoor, 1984), which has the advantage of being stable and regenerable.

Cerium(IV) acetate, a relatively weak oxidant of limited stability, has shown somewhat less selectivity than CAN in the oxidation of alkyl aromatic compounds (Baciocchi, 1983). It best performs with substrates of relatively low ionization potential to give ring and/or side-chain acetoxylated compounds.

4.2. *Mechanistic aspects of aromatic nitromethylations involving cerium*

A variety of cerium(IV) salts were evaluated as alternatives to manganese(III) acetate in aromatic nitromethylations (Kurz and Ngoviwatchai, 1981). While CAN effected high-yield conversions, persistent side reactions were attributed to the presence of cerium(III) nitrate. In contrast, cerium(IV) acetate generated in situ gave high yields of nitromethylation products free of side-products.

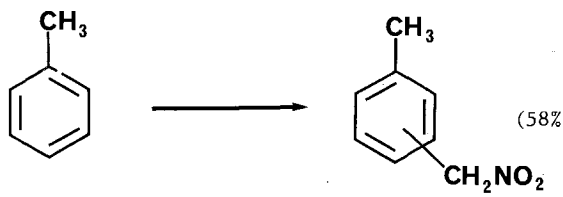

(58%) (26)

o:m:p::52.1:22.7:25.2

The mechanism suggested by kinetic data involved generation of nitromethyl radicals by Ce^{4+}, followed by radical attack on the aromatic substrate and oxidative rearomatization.

$$CH_3NO_2 + Ce^{4+} \rightarrow Ce^{3+} + H^+ + \dot{C}H_2NO_2, \quad (27)$$

$$\dot{C}H_2NO_2 + ArH \rightarrow H\text{–}\dot{A}r\text{–}CH_2NO_2, \quad (28)$$

$$H\text{–}\dot{A}r\text{–}CH_2NO_2 + Ce^{4+} \rightarrow Ce^{3+} + H^+ + ArCH_2NO_2. \quad (29)$$

One can infer from this mechanism that a chelating effect (fig. 6) governs the key intermediate; this is similar to the mechanism later applied to cerium(III)-assisted reductions, and is also closely related to the intermediate proposed as part of the first example of a cross-aldol reaction of cerium enolates (section 4.4).

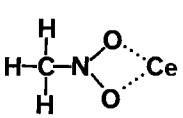

Fig. 6. Proposed cerium-nitromethane intermediate in the cerium-assisted nitromethylation of aromatic hydrocarbons.

4.3. *Early evidence of cerium(III) catalysis*

The scope of the catalytic potential of the cerium(III) ion was intimated by Pratt (1962) in an investigation of the addition of aromatic amines to quinones. Use of hydrated cerous chloride in place of cupric acetate as an oxygen carrier in the oxidation of byproduct hydroquinone resulted in improved yields and easier product separation from metal complexes.

The citation history of this chemistry leads ultimately to a German patent (Lucius and Bruning, 1911) issued only 10 years after Meyers and Jacoby's paper on cerium(IV)/alcohol oxidations.

In addition to improving product yields and shortening reaction times, cerous chloride promoted the regioselective addition of *p*-toluidine to the 6-position of 5,8-quinolinequinone [eq. (30)].

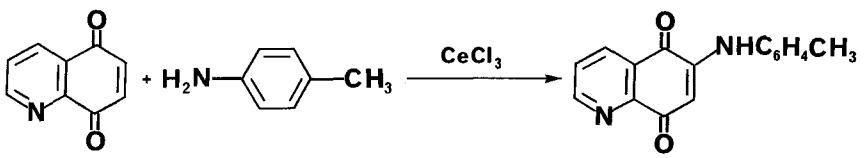

(30)

To more fully elucidate the role of the cerium(III) ion in these additions, Pratt suggested that the influence of the Lewis acid catalyst in reactions of 6-chloro-5,8-quinolinequinone was exerted primarily through the heterocyclic nitrogen atom; the resulting N–Ce interaction also allows the cerium ion to assume a position in close proximity to the 8-carbonyl oxygen, with concomitant 6-position activation.

In the case of the addition of *p*-nitroaniline to 1,4-naphthoquinone, or the replacement of the methoxy group in 2-methoxy-1,4-naphthoquinone, the catalytic effect was ascribed to coordination of cerium to a carbonyl group.

4.4. *Aldol couplings having an intermediate cerium(III) complex*

Lithium bis(trimethylsilyl)amide or (more frequently) lithium diisopropylamide, upon reaction with ketones, produces an enolate that reacts with anhydrous cerium(III) chloride at −78°C to afford a cerium enolate (Imamoto et al., 1983).

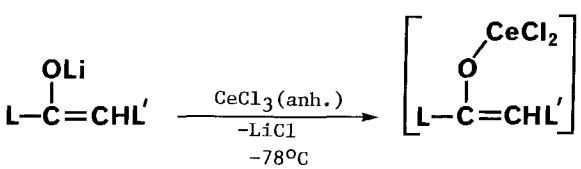

(31)

This transmetallation product, when applied to aldol couplings as shown below, exploits the stronger chelation of the cerium ion (relative to lithium) in the

six-membered intermediate. This suppresses retro-aldol and/or cross-enolization and gives higher yields than reaction with corresponding lithium enolates.

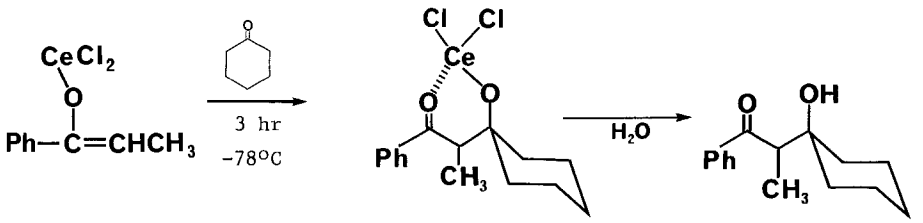

(32)

Generally, no differences in stereoselectivities were observed between the two enolate systems.

Cerium enolates also provide favorable routes to α-bromo-β-hydroxy ketones, important intermediates to α,β-epoxy ketones.

4.5. *Catalytic oxidation of phenols*

Recent attempts to apply cerium(III) chloride (hydrate) and lanthanum(III) acetate to the Lewis acid-catalyzed oxidation of phenols with hydrogen peroxide proved futile; in fact, they provided the worst results of over 20 metal salts studied (Ito et al., 1983). Ruthenium trichloride was even better than boron trifluoride, presumably activating the peroxide molecule rather than serving as a one-electron oxidant.

By far the widest application in organic synthesis for the cerium(III) species has involved its striking effects in selective reductions with sodium borohydride (section 5).

5. Application of lanthanide(III) salts to selective reductions

5.1. *Lanthanide chlorides and sodium borohydride reductions of unsaturated ketones*

In the late 1970s, Jean-Louis Luche and co-workers began to evaluate the role of lanthanide salts in selective organic reductions. Even with the extensive arsenal of available reagents, including sodium cyanoborohydride, diisobutylaluminum hydride and 9-borabicyclononane (9-BBN), there has remained room for improvement in yield, selectivity and reaction conditions in reductions of carbonyl groups in complex organic molecules.

In his first publication in this area, Luche found samarium trichloride and cerium trichloride (hydrated forms) to be especially effective in the selective conversion of α,β-unsaturated ketones to allylic alcohols (Luche, 1978), even in the case of 2-cyclopentenone, which tends to undergo 1,4-addition (essentially 100% reduction was observed with all reagent systems).

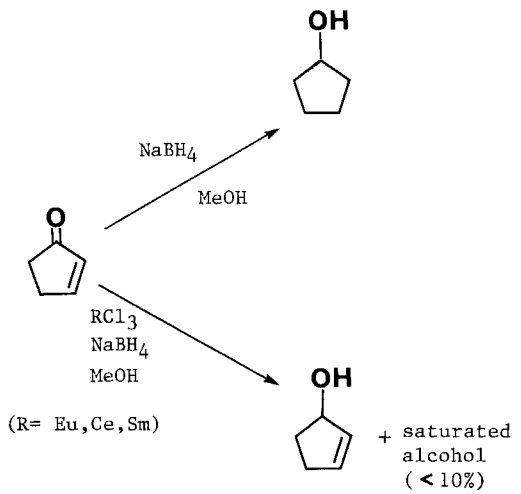

(33)

(34)

Advantages to the lanthanide chloride/sodium borohydride tandem include:

(i) Almost exclusive 1,2-reduction occurs under mild conditions that do not affect carboxylic acids, esters, amides, halides, as well as cyanide and nitro groups.

(ii) The reactions require no special atmospheric conditions and may be run at room temperature in a few minutes.

(iii) The amount of water present in the commercially available hydrated lanthanide salts has little effect on selectivity.

This method was also applied to the reduction of natural products, using cerium(III) chloride with sodium borohydride to minimize the formation of saturated alcohols and give good yields of allylic alcohols with good stereoselectivity (Luche et al., 1978).

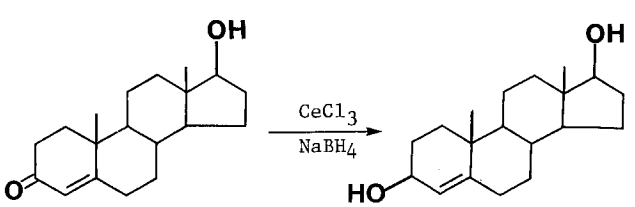

(35)

Application of this method to enones of the prostanoid series resulted in an equimolar mixture of alcohols.

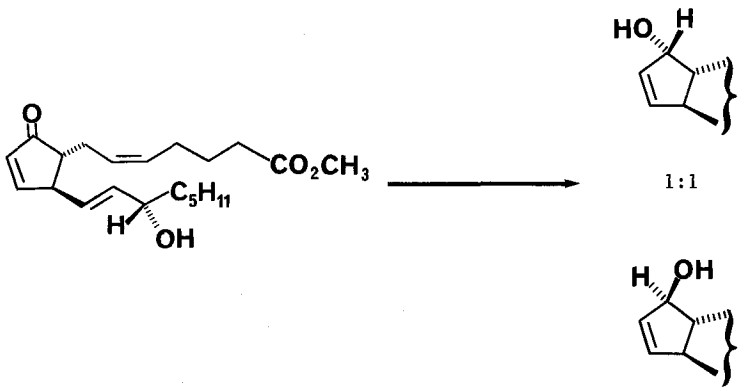

(36)

The sodium borohydride/cerium trichloride system can be used in a broad pH range without significant loss of regioselectivity; it is also efficient in the presence of pyridine, which is known to induce 1,4-reductions under a variety of conditions (Kupfer, 1961).

Reactions using erbium trichloride also exhibited the same regioselectivity in diethyl ether solution.

Extending this technique to the reduction of the dione, L, demonstrated an intramolecular selectivity attributable to conversion of the more reactive C-3 carbonyl to a monoketal intermediate (Gemal and Luche, 1979). This allows the preferential reduction at C-17, and also demonstrates the sharp contrast between aldehyde and ketone ketalization using lanthanide chlorides as catalysts.

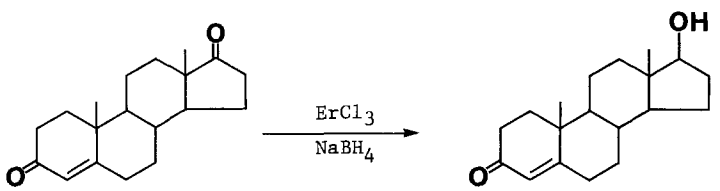

(L) (37)

This system typically allows the convenient, one-pot selective reduction of a less-reactive carbonyl group in the presence of a more reactive one.

Also noteworthy was the dependence of the ketal yield upon the choice of lanthanide salt. Lighter lanthanide ions (Ce^{3+}, Nd^{3+} – softer Lewis acids) having larger ionic radii were preferred in cases where the aldehyde–ketone discrimination became more difficult. Several examples were cited by the authors, and the subject of selective reduction of ketones in the presence of aldehydes is treated in section 5.2.

In the case of the reduction of progesterone, M, use of sodium borohydride alone produces N as the primary product, while cerium trichloride promotes the conversion (in 40% yield) to 3-β-hydroxypregnen-20-one, O, possibly through the in situ

protection of the C-20 carbonyl group as shown in the hypothesized intermediate below:

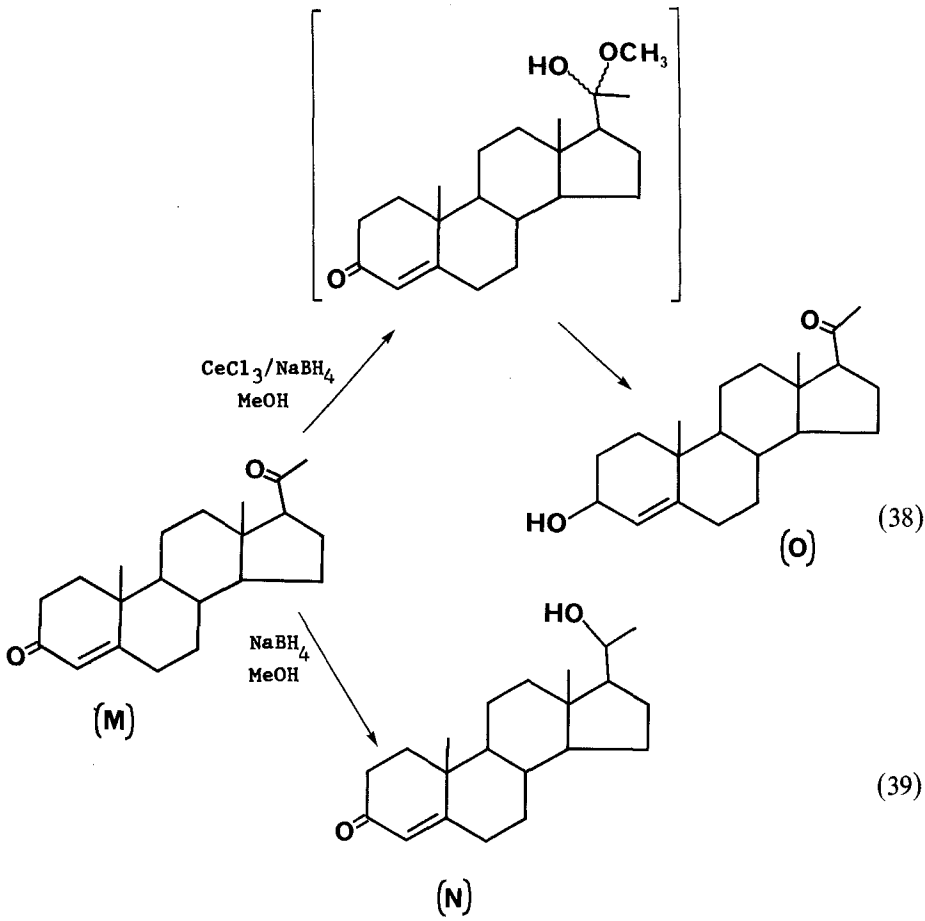

(38)

(39)

A similar intermolecular selectivity is also seen with the sodium borohydride/ lanthanide trichloride process shown in eq. (40).

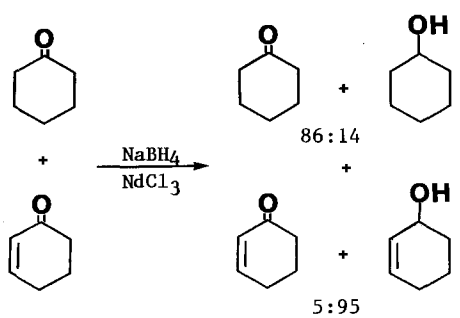

(40)

In addition, there are some mixtures that do not lend themselves to this synthetic procedure:

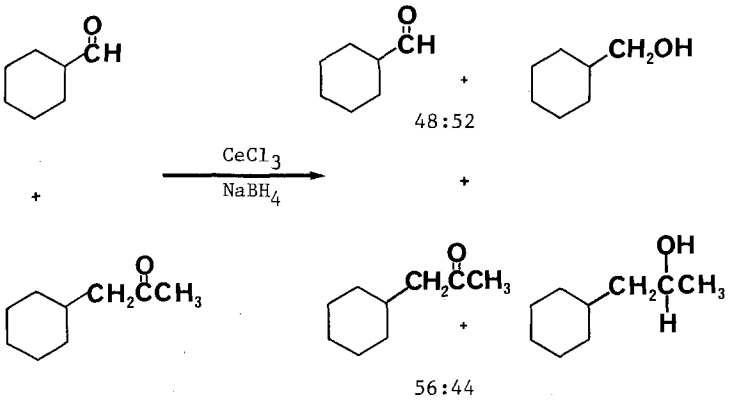

(41)

However, the large number of cases in which it is applicable makes this a very attractive method.

5.2. *Cerium(III)/sodium borohydride reduction of ketones in the presence of aldehydes*

Further study of the role of lanthanides in the reduction of carbonyl groups demonstrated the potential for selectively reducing ketones in the presence of aldehydes (Luche and Gemal, 1979). This reverse selectivity has resulted in the development of the first direct process that can be used in place of multistep procedures that gave low yields and/or separation problems caused by insufficiently selective catalysts.

In a typical reaction, two carbonyl compounds, or a dicarbonyl compound (two equivalents), are dissolved with cerium trichloride in water/ethanol; sodium borohydride is added at −15°C to give the selective reduction of the ketone, leaving the aldehyde group intact.

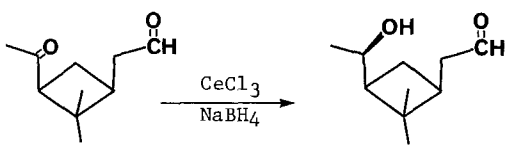

(42)

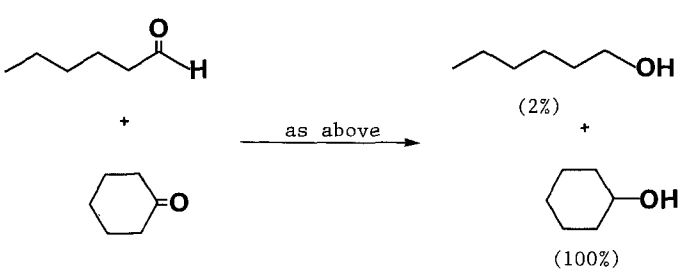

(43)

The reaction mixture in eq. (43) showed conversions of 7 and 93%, respectively, when erbium trichloride was used.

In general, selectivity is excellent for nonconjugated aliphatic and alicyclic carbonyl compounds, but diminishes for conjugated aldehydes. This preference can be exploited in the reduction of mixtures of aldehydes, however.

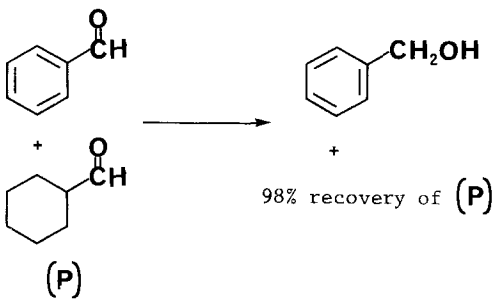

(44)

Given the hypothesis that the formation of a geminal diol is critical to nonconjugated aldehyde function protection, it was subsequently shown by NMR study that cerium(III) enhances diol stability better than any other cation tested. This implies that the cerium ion is large enough to provide protection during reduction, but still allows ready recovery of the aldehyde during workup. The utility of the cerium ion is also fortuitous in that it is one of the least expensive of the lanthanides.

5.3. *Other applications of cerium and lanthanum chlorides*

Other examples of cerium(III)-assisted reductions include reactions of derivatives of biologically active principals from *Podocarpus* plants (Hayashi and Matsumoto, 1982), and the preparation of precursors of stable carbocations derived from α-ethylene naphthalenium ions (Olah and Singh, 1982):

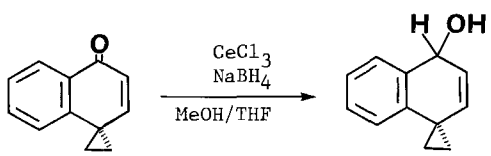

(45)

The selective reduction of the carbonyl function of a [4.4.4.]-propellatrienone to an allylic alcohol has been carried out with cerium(III) chloride-doped sodium borohydride (Paquette et al., 1984) en route to a unique tetraene derivative.

Cerium chloride has also been used to accelerate the oxidation of 10-decenal to the acid by the action of hydrogen peroxide in the presence of ammonium molybdate and potassium carbonate (Trost and Masuyama, 1984). This supports the contention that the hydrate of the alcohol is the species being oxidized (Luche and Gemal, 1979). Further study is required to establish the general utility of the method, however.

Other boron hydride reductions may be promoted by a variety of metal salts, and the enhanced cis selectivity shown by strong Lewis acids such as ferric chloride and lanthanum trichloride was described for the reduction of 3,3,5-trimethylcyclohexanone by tetrabutylammonium octahydrotriborate (Tamblyn et al., 1983).

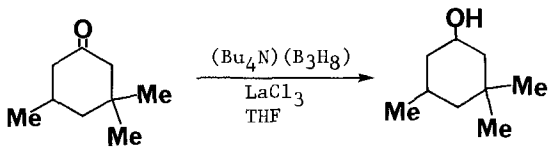

(46)

trans:cis = 57.8:42.2

5.4. *Cerium(III) nitrate/sodium borohydride systems*

The application of a sodium borohydride/cerium(III) nitrate reagent to a pyrone reduction produced results that departed somewhat from the 1,2-additions observed by Luche. Catalytic reductions of γ-pyrones can lead to complex mixtures of products via nonselective processes; however, the lanthanide/borohydride system provided a good yield of the specifically reduced dihydropyrone, Q, from the unsaturated precursor, while preserving the carbonyl function adjacent to the double bond (Poulton and Cyr, 1980).

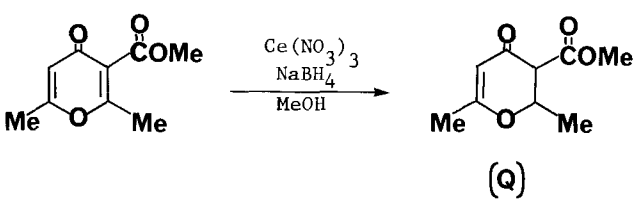

(47)

(Q)

5.5. *Other selective reductions*

5.5.1. *α-Enones*

While many metal salts have been shown to be effective in modifying sodium borohydride reductions, the use of lanthanides in the selective 1,2-reduction of α-enones (fig. 7) is potentially a very widely applicable synthetic tool. For this reason, an extensive and systematic study of the mechanistic and stereochemical

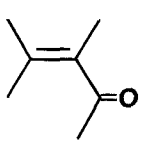

Fig. 7. Structural representation of α-enones.

aspects of this procedure was undertaken (Gemal and Luche, 1981a). The following were considered to be the salient points:

(i) Cerium(III) remains the recommended lanthanide species, best used as 0.4 M methanolic $CeCl_3 \cdot 6H_2O$ with 1 mol eq of sodium borohydride, usually at room temperature.

(ii) Reaction rate and selectivity were sensitive to changes in solvent as well as metal ion; methanol was by far the best solvent, and non-lanthanide metal ions were not effective.

(iii) A specific catalytic effect was demonstrated, with the lanthanide-catalyzed decomposition of the borohydride anion by the solvent appearing to be the rate determining step; this implies that BH_4^- is not the actual reducing species, rather one or more alkoxyborohydrides:

$$BH_4^- + MeOH \rightarrow H_3B(OMe)^- + H_2, \tag{48}$$

$$H_3B(OMe)^- + MeOH \rightarrow H_2B(OMe)_2^- + H_2, \tag{49}$$

$$H_2B(OMe)_2^- + MeOH \rightarrow HB(OMe)_3^- + H_2. \tag{50}$$

Arbitrarily taking one of these species as the appropriate intermediate, the following reaction scheme becomes possible:

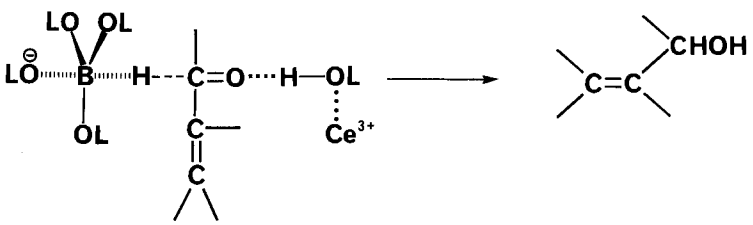

(51)

This is consistent with the observation that alkoxyborohydrides are more reactive than the borohydride ion; this is also borne out by the observation that reactions run in isopropyl alcohol give poor results because the respective alkoxy-borane species are more slowly formed, viz. $[H_{4-n}B(O-{}^iPr)_n]^-$.

The role of the lanthanide cation appears to be to modify electron density and hence the reactivity of the environment of the carbonyl group. Subsequent attack at the adjacent carbon atom is enhanced.

The utility of the selective reduction techniques described in these sections is so pronounced that the term "Luche reduction" is essentially generic. Natale's review (1983) is recommended for a more extensive examination of the types of synthetic methodology that have evolved from this base.

5.5.2. *Conjugative reductions with lanthanides other than cerium*

In systems using lanthanides other than cerium (which is too insoluble in THF to be effective), samarium triiodide or erbium trichloride demonstrated similar lanthanide ion control of selective reductions (Gemal and Luche, 1981a); this was in

particular contrast to reductions carried out in the presence of lithium or sodium ions (Handel and Pierre, 1975; Boone and Ashby, 1979). The utility of SmI_3 is also interesting in view of the extensive chemistry developed for SmI_2 reductions (section 6.2).

In a subsequent study of reaction parameters, lanthanide ions were found to promote the selective reduction of conjugated aldehydes in the presence of nonconjugated aldehydes in aqueous ethanol. Erbium trichloride was the preferred catalyst, usually where the solubility of cerium trichloride in solvents such as isopropyl alcohol was unfavorable (Gemal and Luche, 1981b). The authors described the interaction between the lanthanide and the intermediate substrate as a "chelating effect".

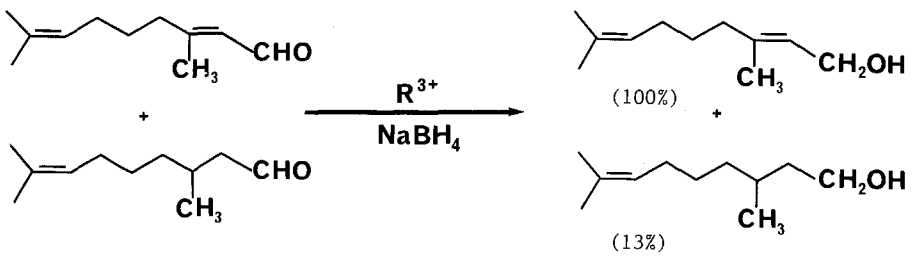

(52)

Chromium(III) was also effective in several selective reductions, although with lesser yields. The chromium ion is also undesirable from the standpoint of spent catalyst disposal.

6. Zero-valent and low-valent reductions

6.1. *Ytterbium–ammonia systems*

Reduction of a variety of organic functional groups has long been carried out using ammonia solutions of alkali metals (Birch and SubbaRao, 1972). Given the strongly electropositive character of lanthanides such as ytterbium (which features a $4f^{14}6s^2$ electron configuration), it follows that ytterbium/ammonia solutions should convert α,β-unsaturated ketones to saturated ketones, alkynes to trans-alkenes and aromatics to 1,4-dihydroaromatics (White and Larson, 1978).

The ammonia-solvated electron is stable for several hours at $-33°C$, and is a powerful reducing agent (Salot and Warf, 1968).

$$Yb^0 + NH_3 = Yb^{2+} + 2e^-(NH_3)_x. \tag{53}$$

Careful manipulation of reaction conditions is required to effect the high-yield conversions below:

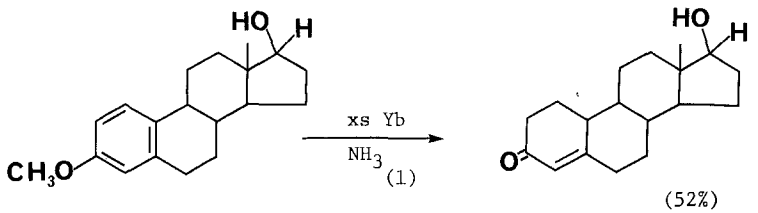

(54)

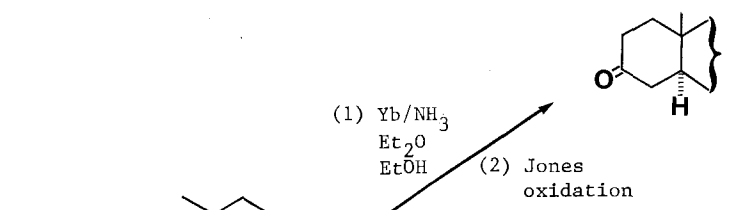

(55)

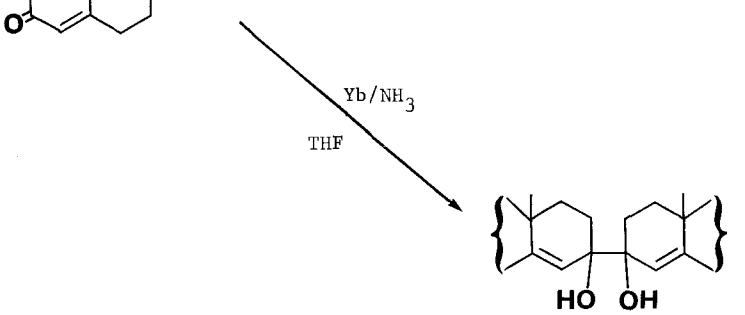

(56)

In addition, the Yb/NH_3 system is able to selectively reduce certain double bonds [eq. (57)].

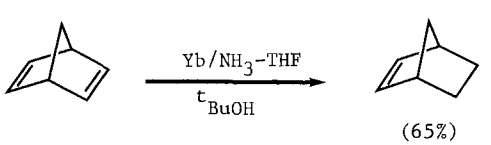

(57)

Advantages of the ytterbium/ammonia system include the inertness of ytterbium to water and air relative to alkali metal reagents, and the fact that strongly basic hydroxides can be avoided.

6.2. *Applications of divalent samarium and ytterbium species*

Since the initial report in 1977 of the preparation of stable solutions of diiodides of samarium and ytterbium (Namy et al., 1977) according to eq. (58), an extensive

$$R + ICH_2CH_2I \xrightarrow{THF} RI_2 + C_2H_4 \qquad (R = Sm, Yb) \tag{58}$$

and systematic chemistry has been developed for these systems (Kagan and Namy, 1984); this includes deoxygenation (epoxides and sulfoxides), dimerizations (benzyl halides), and reductions (imines and nitro groups to amines; aldehydes to alcohols; alkyl halides and sulfonate esters to hydrocarbons; α,β-unsaturated esters to saturated esters via conjugate reduction). The conversion of aldehydes and ketones to pinacols is rapid and clean (Namy et al., 1983).

The fact that this seemingly limited topic merited its own chapter in the sixth volume of the *Handbook on the Physics and Chemistry of Rare Earths* attests to its significance and synthetic potential. In light of Kagan and Namy's treatment of this subject, this discussion will be limited to recent and novel uses typified by the reductive cleavage of isoxazoles (Natale, 1982) shown in eq. (59).

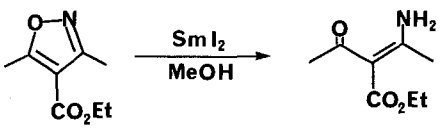

(96%) (59)

Advantages of the diiodosamarium method included the lack of competing olefin reductions, and the suitability of aprotic media for the reactions.

The effectiveness of the diiodide as a one-electron transfer reagent can be attributed to a high reduction potential [E_0(aq) Sm^{2+}/Sm^{3+} equal to 1.55 V] that is unusual for species soluble in organic solvents.

Souppe et al. (1984) have also elucidated mechanistic aspects of diiodosamarium/acid chloride reaction systems that produce symmetrical α-diketones via acyl anions. Nucleophilic acylation occurs through in situ trapping when an acid chloride is reduced by samarium(II) iodide in the presence of aldehydes or ketones.

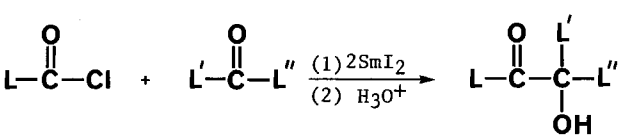

(60)

The SmI_2 reagent was the key to overcoming a serious obstacle to the synthesis of tetracyclic precursors of indole alkaloids (Exon et al., 1983). The inability of

traditional reducing agents to convert the 2-chloroethyl carbamate to the amine, R, was thereby overcome.

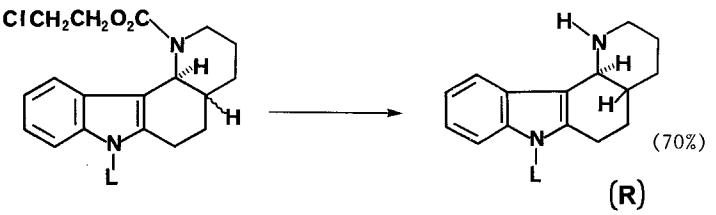

(61)

The selective deprotection of xanthates had been previously reported (Ananthanarayan et al., 1982).

Other applications include a new method for the hydroxymethylation of carbonyl compounds (Imamoto et al., 1984b):

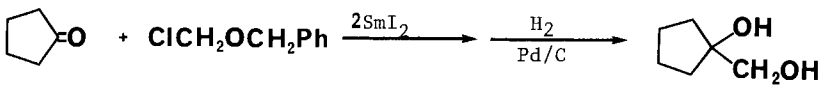

(62)

The addition of tetraethylene glycol to a THF solution of SmI_2 changes the characteristic green color to purple. The reducing power of the probable SmI_2/glycol complex was tempered in its affinity for the carbonyl oxygen, thereby suppressing pinacol coupling and allowing the eventual isolation of the desired diol in good yield.

Samarium(II) iodide has also been applied to intramolecular Barbier-type syntheses of five- and six-membered rings (Molander and Etter, 1984):

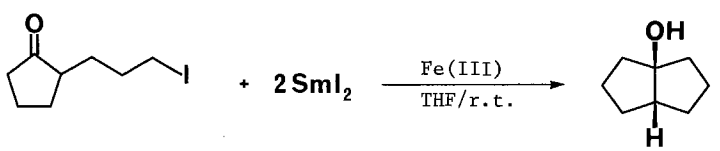

(63)

90% yield by gc
60% isolated yield

cis:trans 99.5:0.5

Not all cyclizations showed a pronounced cis effect; moreover, using YbI_2 (or Yb metal in some cases) instead of SmI_2 resulted in predominant formation of a single ring fused isomer. In spite of these successes, the ytterbium(II) iodide reagent has been ineffective in inducing intermolecular alkylations. Speculations regarding the relatively short Yb–O bond compared with that involving the larger, less polarizing Sm^{3+} ion do not sufficiently explain the contrasting behavior observed for the two divalent lanthanide reagents.

6.3. *Applications involving low-valent cerium*

In contrast to ytterbium and samarium, activation of the metal is required in the case of cerium, which is less reactive toward alkyl or aryl halides. The in situ generation of an allylcerium iodide in the presence of a ketone produces a homoallylic alcohol in good yield (Imamoto et al., 1981).

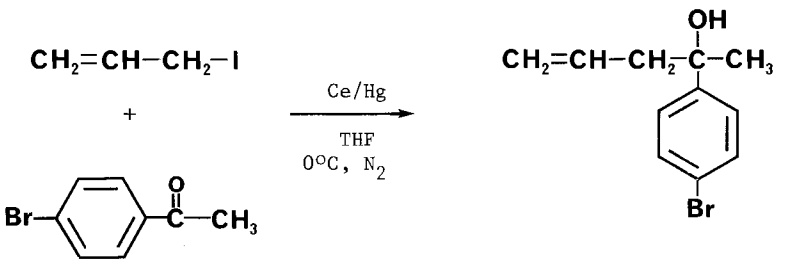

(64)

Reactions with benzyl iodide proceeded similarly in a chemoselective, one-step procedure. Other functional groups such as ester, nitrile, and aryl bromide were unaffected.

Additionally, several low-valent cerium reagents transform aldehydes and ketones into pinacols via reductive dimerization (Imamoto et al., 1982a):

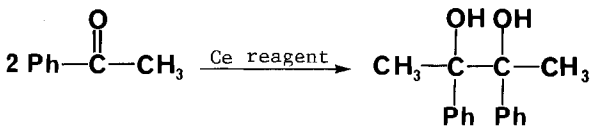

(65)

Reagent system	Yield (%)	Comment
Ce/I_2	88	Acetophenone/Ce mixture was treated with a THF solution of iodine
Ce/ICH_2CH_2I	79	
CeI_3/K	96	
Ce/C_6H_5I	95	
$Ce/TiCl_4$	68	Also prepared in situ

The failure of either cerium metal alone or cerium(III) iodide to effect the desired coupling implies that a divalent cerium species is responsible for driving the reaction. Some (but not all) aliphatic carbonyls undergo similar conversions.

One particular advantage of this method, as seen previously, is the efficiency and selectivity in the presence of functional groups such as ester, nitrile, and vinyl halide.

Imamoto et al. (1984c) reported a detailed investigation of carbon–carbon bond formation promoted by cerium amalgam and by organocerium(III) reagents gener-

ated from organolithiums and cerium(III) halides. Study of over 100 reactions demonstrated the utility of these reagent systems in a variety of addition reactions including Reformatsky-type and Barbier-type reactions.

6.4. *Other lanthanide–iodide systems*

Another method of producing useful organocerium reagents involved the treatment of organolithium compounds with cerium(III) iodide (Imamoto et al., 1982b):

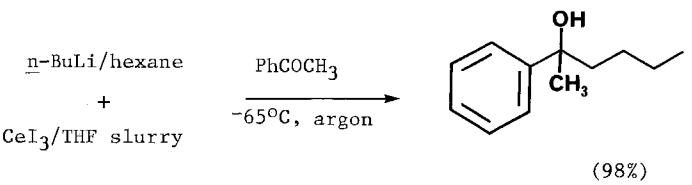

(66)

Samarium(III) iodide was also effective. Reaction temperatures of $-65°C$ appeared to give the cleanest conversions for all organocerium reagents used (i.e., with *n*-BuLi, sec-BuLi, MeLi and PhLi in combination with CeI_3). At temperatures above 0°C, reagents having beta-hydrogens converted acetophenone to 2,3-dihydroxy-2,3-diphenylbutane and/or phenethyl alcohol; use of methyllithium (having no beta-hydrogen) resulted in nucleophilic addition to the carbonyl group.

The synthetic potential of these particular lanthanide reagents lies in their distinctive reactivities relative to organolithium reagents: there is very little competing enolization that would result in unreacted ketone.

New methods of synthesis of samarium alkoxides catalytically active in Meerwein–Ponndorf–Verley reductions and Oppenauer oxidations resulted from careful reexamination of diiodosamarium-promoted alkylations of aldehydes (Namy et al., 1984).

Once it was shown that samarium(III) iodide (SmI_3) reacts with magnesium alkoxides to form a diiodosamarium alkoxide having reducing properties, it followed that a more direct route to these synthetically useful catalytic intermediates would be highly desirable [eq. (67)].

$$^{t}Bu\text{–}O\text{–}O\text{–}{}^{t}Bu + 2SmI_2 \xrightarrow[\text{r.t.}]{\text{THF}} 2\,{}^{t}Bu\text{–}O\text{–}SmI_2 \qquad (67)$$

The reaction of cerium metal, iodine and isopropyl alcohol in THF produced a similar cerium species. The only major limitation of these reagents is the fact that they can be deactivated by small amounts of water.

Ho attacked the problem of hydrodehalogenating α-haloketones by identifying CeI_3 as an appropriate combination of hard acid and soft base moieties for the

attack on the carbonyl and halide groups, respectively (Ho, 1979):

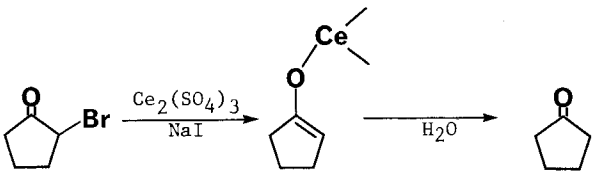

(68)

Reaction conditions called for mixing a THF solution of the α-haloketone with an aqueous mixture of cerium(III) sulfate and sodium iodide to produce the cerium iodide intermediate.

6.5. *Applications of organolanthanide(II) complexes*

The first definitive descriptions of organometallic divalent lanthanide complexes (Evans et al., 1970, 1971) also alluded to applications similar to Grignard methodology [eq. (69)].

$$\mathrm{Ph{-}\overset{\overset{O}{\|}}{C}{-}Ph} \xrightarrow{\mathrm{PhYbI}} \mathrm{Ph_3COH}. \tag{69}$$

More recently, it was shown that ytterbium metal reacts with alkyl or aryl iodides to give solutions of L–Yb–I species that react smoothly with ketones (Fukagawa et al., 1981). Similar reactions could be carried out with europium and samarium, which also have well-defined divalent forms (Asprey and Cunningham, 1960; Marks, 1978).

Diorganomercurials, upon reaction with ytterbium metal, form L_2Yb complexes that convert carbonyl compounds to alcohols via reductive coupling (Deacon and Tuong, 1981).

Some substrates have higher reactivity with phenylytterbium iodide than with analogous Grignard reagents (Fukagawa et al., 1982).

$$\mathrm{Ph{-}\overset{\overset{O}{\|}}{C}{-}Cl} \xrightarrow[-20^\circ C,\ THF]{\text{inverse addition of PhYbI; } FeCl_3} \mathrm{Ph{-}\overset{\overset{O}{\|}}{C}{-}Ph} \qquad (20\text{–}25\%), \tag{70}$$

$$\mathrm{Ph{-}\overset{\overset{O}{\|}}{C}{-}OCH_3} \xrightarrow[-20^\circ C,\ THF]{\mathrm{PhYbI}} \mathrm{Ph{-}\overset{\overset{O}{\|}}{C}{-}Ph} + \mathrm{Ph_3COH} \qquad (\text{each} < 20\%\ \text{yield}). \tag{71}$$

In addition, the higher reactivity of esters relative to ketones is unusual and opposite to that observed with Grignard reactions. Extension of this atypical reactivity resulted in the development of methods for selective ketone synthesis. Addition of benzoyl chloride or methyl benzoate to phenylytterbium iodide (in

THF) produces both triphenylcarbinol and benzophenone in significant amounts (the carbinol is the predominant Grignard product). However, benzophenone is consistently formed with 80% selectively when phenylytterbium iodide is added to benzoyl chloride. Addition of small amounts of a Lewis acid such as ferric chloride suppressed alcohol formation but introduced traces of biphenyl as a secondary product while cutting the overall yield by at least 50%.

The authors suggested that the ytterbium reagent was less reactive with bulky substrates than the L–Mg–I species because the ytterbium ionic radius is almost 50% larger than that of Mg^{2+}.

Reaction of LYbI complexes with α,β-unsaturated carbonyl compounds selectively produces 1,2-addition products (Yokoo et al., 1983), in spite of the large ytterbium(II) ionic radius.

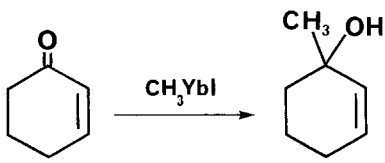

(39%)

(no 1,4-addition) (72)

A similar Grignard reaction gives product ratios of 2.57 : 1 with respect to 1,2-addition vs. 1,4-addition.

The reaction of PhYbI with chalcone encounters some steric effects that reverse the product ratio for the respective L–M–I reactions: 1,2-addition is 50% for M = Yb, 6% for M = Mg; 1,4-addition is 10% for M = Yb, 94% for M = Mg.

This regioselectivity was explained by the preferred attraction of the C-2 "hard site" to the harder lanthanide complex [eq. (73)].

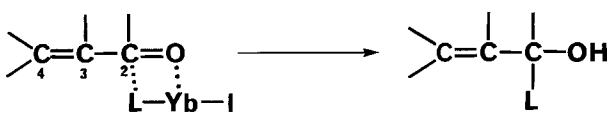

(73)

More recent studies included the low-temperature phenylytterbium iodide-induced cross-coupling with organic halides in the presence of transition metal catalysts (Yokoo et al., 1984a) and the use of methylytterbium iodide to convert active hydrogen compounds such as phenylacetylene or fluorene to corresponding acids or alcohols (Yokoo et al., 1984b).

The reactivity of methylytterbium iodide was markedly better than that of methylmagnesium iodide in similar reactions.

6.6. *Other low-valent techniques and applications*

In their chapter on organometallic compounds of rare earths, Schumann and Genthe (1984) provide a detailed examination of a variety of techniques and

products that may develop into reagent systems for organic synthesis; a condensed report of these studies has also been published (Schumann, 1984).

A good example of such a system would be the cocondensation of lanthanide metals with organic substrates (Evans et al., 1978), a technique which has afforded complexes capable of activating molecular hydrogen (Evans et al., 1979) and carbon monoxide (Evans et al., 1981a). Extension of this method to the preparation of soluble divalent organosamarium compounds (Evans et al., 1981b) is an especially promising development, especially in light of a later report of a vapor deposition method for preparing bis(pentamethylcyclopentadienyl)samarium(II) free of coordinating solvent molecules or other bases (Evans et al., 1984a). The unusually high degree of coordinative unsaturation in such a strongly reducing species makes this decamethylsamarocene a very reactive molecular model for unique organosamarium chemistry.

The study of catalytic processes involving rare earths has been advanced by the synthesis and characterization of alkyl and hydride complexes of yttrium (Evans et al., 1984b), which in part were investigated because they provided NMR information via Y–H and Y–C coupling. Although yttrium is not considered a lanthanide, that row of elements exhibits reactivities similar to yttrium, and subsequent comparisons are reasonably valid.

Similar divalent metallocene complexes of ytterbium, i.e., $(Cp)_xYb(base/ligand)_y$, were also shown to act as mild, one-electron reducing agents toward transition metal carbonyl compounds such as $Co_2(CO)_8$ (Tilley and Andersen, 1981), $CpCo(CO)_2$ (Boncella and Andersen, 1984) and other organometallic derivatives of cobalt.

In closing, Schumann and Genthe's chapter is recommended for an overview of rapidly developing synthetic organometallic chemistry that promises to have implications in the areas of homogeneous as well as heterogeneous organic synthesis.

7. Implications for future research

7.1. *Activation of hydrogen bonds*

Schumann and Genthe also deal extensively with the carbon–hydrogen activation by lutetium-hydride and lutetium-methyl complexes investigated by Watson and co-workers (Watson, 1982, 1983a, 1983b). The principal thrust of Watson's work has been to demonstrate the kinetic and thermodynamic feasibility of activating carbon–hydrogen bonds using homogeneous organometallic complexes. Given that the method is effective with methane, which has been the most difficult alkane C–H bond to activate, the scientific import may extend to commercial exploitation, as well as possibilities in the area of catalyst control using rare earth complexes.

7.2. *Carbon and hydrogen bonded to rare earths*

Introducing carbon and hydrogen atoms into the inner (bonding) coordination sphere of the rare earths continues to be a matter of high priority. Solvated, silylated

metallocene borohydride derivatives of scandium, yttrium and ytterbium exhibited bidentate borohydride coordination, while similar derivatives of lanthanum, praseodymium, neodymium and samarium exhibited tridentate bonding of the BH_4^- hydrogens to the lanthanide (Lappert et al., 1983).

Salts of hexamethyl derivatives of most of the rare earths have been prepared due largely to the stabilizing effects of tetramethylethylenediamine coordinated to a lithium cation: $[Li(tmed)]_3[R(CH_3)_6]$ (Schumann et al., 1984).

Interesting phosphorus ylide chemistry involving most of the rare earth elements was included in a recent review by Schmidbaur (1983).

7.3. *Coordination sphere modification*

Modifying the environment about the lanthanide ion in order to exploit coordination properties and chemical reactivity is another active area of spectroscopic and synthetic research, with implications for lanthanide separations.

At one extreme, a derivative free of coordination by water or anions has been prepared by the reaction of europium metal with $NOBF_4$ in dry acetonitrile (Albin et al., 1983). The resulting $Eu(CH_3CN)_n(Y)$ species ($Y = BF_4$, PF_6) reacts further with two equivalent ionophoric ligands to give bis(ligand) complexes.

The use of bulky ligands such as 2,6-di-tert-butyl-4-methylphenol allows isolation of the rare three- and four-coordinate forms of a variety of rare earths (Hitchcock et al., 1983). Theoretical aspects of the environment surrounding lanthanide complexes have been treated in calculations of steric interactions between NMR shift reagents and substituted pyridines (LaPlanche and Vanderkooi, 1983). This provided some insight into the steric factors that induce conformational alterations in these multifaceted species.

Another area of intense study is the complexation of rare earths (and other metal ions) with multidentate oxygen- and nitrogen-bearing ligands; these include cryptates (Pizer and Selzer, 1983; Yee et al., 1983), polyethylene glycols and glymes (Hirashima et al., 1983), crown ethers (Massaux and Desreux, 1982; Bunzli, 1986), derivatives of diazatetraoxacyclooctadecane-*N*,*N*′-diacetic acid (Chang and Rowland, 1983) and triaminotriethylamine (Johnson and Forsberg, 1976), with studies of reactivities and kinetic properties.

7.4. *Porphyrin and phthalocyanine derivatives*

Two specific metal-ligand systems merit mention because of the comprehensive research being carried out currently in the area of transition metal complexes: metalloporphyrin derivatives of the lanthanide and actinide groups (Wong et al., 1974; Wong and Horrocks, 1975; Horrocks and Wong, 1976); and phthalocyanine derivatives of most of the rare earths prepared and characterized over the last 20 years (Kirin et al., 1965).

One of the most interesting aspects of this group has been the incorporation of β-diketonate rare earth complexes with the phthalocyanine macrocycle radical anion

by their reaction with lithium phthalocyanine in dry THF (Sugimoto et al., 1983a, b).

Considering the catalytic potential demonstrated by transition metal complexes of porphyrins and phthalocyanines, it seems safe to predict a similarly rich and varied chemistry to be discovered for rare earth derivatives, including aspects pertinent to both catalysis and organic synthesis.

7.5. *Outlook*

Well into the 1980s, we have seen a dramatic increase in the number of articles dealing with many new aspects of lanthanide chemistry. For example, new systems of NMR shift reagents have recently been prepared specifically to allow the extension of this critically useful tool to aqueous solutions (Peters et al., 1983). Europium and ytterbium complexes of *S*-carboxymethyloxysuccinate were of primary interest.

New synthetic techniques are also available for application to the unique properties of the rare earths. The development of ultrasound as a synthetic tool in the preparation of colloidal potassium and its subsequent reaction with organic substrates (Luche et al., 1984) is such an event that could be adapted to organic synthesis using rare earths.

Vacuum deposition techniques have already been extended to the synthesis of samarium and ytterbium hydrogenation catalysts in low-temperature matrices (Imamura et al., 1984). This method produced solvated metal particles, e.g., Sm–THF, that were 15–20 nm across, porous (no preferred orientation), and had a BET surface area of 5.6 m^2/g.

By applying new vacuum line technology to liquid ammonia techniques, one can carry out clean high-yield syntheses of pentamethylcyclopentadienyl europium(II) and ytterbium(II) complexes from the respective metals (Wayda et al., 1984). The authors concluded that their reaction conditions produced genuinely stable metal–ammonia solutions, although the behavior of the two lanthanides differed in one particular aspect: while there was no evidence for an isolable Eu–NH_3 bond, it was possible to prepare and characterize an unusual ytterbium complex coordinated to both a THF moiety and an ammonia molecule.

Other imaginative uses of rare earths include the reduction of alkenes, aldehydes and ketones with intermetallic compounds containing absorbed hydrogen, viz. $LaNi_5H_6$ (Imamoto et al., 1984d). The use of duPont's Nafion® polymer as a support for Cr(III) and Ce(IV) reagents useful in the oxidation of alcohols has also been reported (Kanemoto et al., 1984). Such conversions also involved the use of *t*-butylhydroperoxide or sodium bromate as cooxidant.

It is becoming increasingly apparent that the synthetic organic chemist will be able to draw from a broad spectrum of reagents and methodology attributable to the novel chemistry of the rare earths.

Acknowledgment

The timely services of Mel Long, Dr. William Szabo and Dr. Howard Black in the preparation of this chapter are deeply appreciated.

Note added in proof: Recently a comprehensive review by H.B. Kagan was published, entitled: 4f-elements in organic synthesis, in: Fundamental and Technological Aspects of Organo-f-element Chemistry, eds. T.J. Marks and I.L. Fragala (Reidel, Boston, 1985) pp. 49–76.

References

Albin, M., A.C. Goldstone, A.S. Withers and W.D. Horrocks, Jr., 1983, Inorg. Chem. **22**, 3182.
Ananthanarayan, T.P., T. Gallagher and P. Magnus, 1982, Chem. Commun., 709.
Asprey, L.B. and B.B. Cunningham, 1960, Prog. Inorg. Chem. **2**, 267.
Ault, A., 1984, J. Chem. Educ. **61**, 614.
Baciocchi, E., C. Rol and G.V. Sebastiani, 1983, J. Chem. Res. (S), 232.
Barton, D.H.R., P. Magnus and J.C. Quinney, 1975, J. Chem. Soc. Perkin I, 1610.
Bednarski, M. and S. Danishefsky, 1983a, J. Am. Chem. Soc. **105**, 3716.
Bednarski, M. and S. Danishefsky, 1983b, J. Am. Chem. Soc. **105**, 6968.
Bednarski, M., C. Maring and S. Danishefsky, 1983, Tetrahedron Lett. **24**, 3451.
Birch, A.J. and G. SubbaRao, 1972, Advances in Organic Chemistry, Methods and Results, Vol. 8 (Wiley, New York) p. 1.
Boncella, J.M. and R.A. Andersen, 1984, Chem. Commun., 809.
Boone, J.R. and E.C. Ashby, 1979, Top. Stereochem. **11**, 53.
Brittain, H.G., 1982, J. Chem. Soc. Dalton Trans., 2059.
Bunzli, J.-C.G., 1986, in: Handbook on the Physics and Chemistry of Rare Earths, eds. K.A. Gschneidner, Jr. and L. Eyring (North-Holland, Amsterdam) to be published.
Castellino, S. and J.J. Sims, 1984a, Tetrahedron Lett. **25**, 2307.
Castellino, S. and J.J. Sims, 1984b, Tetrahedron Lett. **25**, 4059.
Chang, C.A. and M.E. Rowland, 1983, Inorg. Chem. **22**, 3866.
Cockerill, A.F., G.L.O. Davies, R.C. Harden and D.M. Rackham, 1973, Chem. Rev. **73**, 553.
Coombes, R.G., R.B. Moodie and R. Schofield, 1968, J. Chem. Soc. B, 800.
DallaCort, A., A. La Barbera and L. Mandolini, 1983, J. Chem. Res. (S), 44.
Danishefsky, S. and M. Bednarski, 1984, Tetrahedron Lett. **25**, 721.
Danishefsky, S. and W.H. Pearson, 1983, J. Org. Chem. **48**, 3865.
Deacon, G.B. and T.D. Tuong, 1981, J. Organometal. Chem. **205**, C4.
Dunkelblum, E. and H. Hart, 1977, J. Org. Chem. **42**, 3958.
Evans, D.F., G.V. Fazakerley and R.F. Phillips, 1970, Chem. Commun., 244.
Evans, D.F., G.V. Fazakerley and R.F. Phillips, 1971, J. Chem. Soc. A, 1931.
Evans, W.J., S.C. Engerer and A.C. Neville, 1978, J. Am. Chem. Soc. **100**, 331.
Evans, W.J., S.C. Engerer, P.A. Piliero and A.L. Wayda, 1979, Chem. Commun., 1007.
Evans, W.J., D.J. Wink, A.L. Wayda and D.A. Little, 1981a, J. Org. Chem. **46**, 3925.
Evans, W.J., I. Bloom, W.E. Hunter and J.L. Atwood, 1981b, J. Am. Chem. Soc. **103**, 6507.
Evans, W.J., J.H. Meadows, W.E. Hunter and J.L. Atwood, 1984a, J. Am. Chem. Soc. **106**, 1291.
Evans, W.J., L.A. Hughes and T.P. Hanusa, 1984b, J. Am. Chem. Soc. **106**, 4270.
Exon, C., T. Gallagher and P. Magnus, 1983, J. Am. Chem. Soc. **105**, 4739.
Fieser, L.F. and M. Fieser, 1967–1984, Reagents for Organic Synthesis (Wiley, New York).
Firouzabadi, H. and N. Iranpoor, 1983, Synth. Commun. **13**, 1143.
Firouzabadi, H. and N. Iranpoor, 1984, Synth. Commun. **14**, 875.
Firouzabadi, H., N. Iranpoor and H. Parham, 1984a, Synth. Commun. **14**, 631.
Firouzabadi, H., N. Iranpoor, F. Kiaeezadeh and J. Toofan, 1984b, Synth. Commun. **14**, 973.
Forsberg, J.H., 1973, Coord. Chem. Rev. **10**, 195.
Forsberg, J.H., T.M. Balasubramanian and V.T. Spaziano, 1976, Chem. Commun., 1060.
Fuji, K., T. Kawabata, M. Node and E. Fujita, 1981, Tetrahedron Lett. **22**, 875.
Fukagawa, T., Y. Fujiwara, K. Yokoo and H. Taniguchi, 1981, Chem. Lett., 1771.
Fukagawa, T., Y. Fujiwara and H. Taniguchi, 1982, Chem. Lett., 601.
Gelles, E. and K.S. Pitzer, 1955, J. Chem. Soc. **77**, 1974.
Gemal, A.L. and J.-L. Luche, 1979, J. Org. Chem. **44**, 4187.
Gemal, A.L. and J.-L. Luche, 1981a, J. Am.

Chem. Soc. **103**, 5454.
Gemal, A.L. and J.-L. Luche, 1981b, Tetrahedron Lett. **22**, 4077.
Girard, P. and H.B. Kagan, 1975, Tetrahedron Lett., 4513.
Golding, B.T., P.J. Sellars and A.K. Wong, 1977, Chem. Commun., 570.
Handel, H. and J.L. Pierre, 1975, Tetrahedron **31**, 2799.
Hanna, S.B. and M.E. Moehlenkamp, 1983, J. Org. Chem. **48**, 826.
Hayashi, Y. and T. Matsumoto, 1982, J. Org. Chem. **47**, 3421.
Heiba, E.I., R.M. Dessau, 1971, J. Am. Chem. Soc. **93**, 995.
Hintz, H.L. and D.C. Johnson, 1967, J. Chem. Soc. **32**, 556.
Hirashima, Y., K. Kanetsuki, I. Yonezu, K. Kanekura and J. Shiokawa, 1983, Bull. Chem. Soc. Jpn. **56**, 738.
Hitchcock, P.B., M.F. Lappert and A. Singh, 1983, Chem. Commun., 1499.
Ho, T.-L., 1973, Synthesis, 347.
Ho, T.-L., 1979, Synth. Commun. **9**, 241.
Horrocks, W.D., Jr. and C.P. Wong, 1976, J. Am. Chem. Soc. **98**, 7157.
Imamoto, T., Y. Hatanaka, Y. Tawarayama and M. Yokoyama, 1981, Tetrahedron Lett. **22**, 4987.
Imamoto, T., T. Kusumoto, Y. Hatanaka and M. Yokoyama, 1982a, Tetrahedron Lett. **23**, 1353.
Imamoto, T., T. Kusumoto and M. Yokoyama, 1982b, Chem. Commun., 1042.
Imamoto, T., T. Kusumoto and M. Yokoyama, 1983, Tetrahedron Lett. **24**, 5233.
Imamoto, T., Y. Tawarayama, T. Kusumoto and M. Yokoyama, 1984a, J. Synth. Org. Chem. Jpn. **42**, 143.
Imamoto, T., T. Takeyama and M. Yokoyama, 1984b, Tetrahedron Lett. **25**, 3225.
Imamoto, T., T. Kusumoto, Y. Tawarayama, Y. Sugiura, T. Mita, Y. Hatanaka and M. Yokoyama, 1984c, J. Org. Chem. **49**, 3904.
Imamoto, T., T. Mita and M. Yokoyama, 1984d, Chem. Commun., 163.
Imamura, H., A. Ohmura and S. Tsuchiya, 1984, Chem. Lett., 203.
Ito, S., K. Aihara and M. Matsumoto, 1983, Tetrahedron Lett. **24**, 5249.
Jackson, J.A., J.F. Lemons and H. Taube, 1960, J. Chem. Phys. **32**, 553.
Johnson, M.F. and J.H. Forsberg, 1976, Inorg. Chem. **15**, 734.
Kagan, H.B. and J.L. Namy, 1984, in: Handbook on the Physics and Chemistry of Rare Earths, eds. K.A. Gschneidner, Jr. and L. Eyring (North-Holland, Amsterdam) Ch. 50.
Kanemoto, S., H. Saimoto, K. Oshima and H. Nozaki, 1984, Tetrahedron Lett. **25**, 3317.
Kirin, I.S., P.N. Moskalev and Y.A. Makashev, 1965, Russ. J. Inorg. Chem. **10**, 1605.
Kropf, H. and H. von Wallis, 1983, Liebigs Ann. Chem., 610.
Kupfer, D., 1961, Tetrahedron **15**, 193.
Kurz, M.E. and P. Ngoviwatchai, 1981, J. Org. Chem. **46**, 4672.
LaPlanche, L.A. and G. Vanderkooi, 1983, J. Chem. Soc. Perkin Trans. II, 1585.
Lappert, M.F., A. Singh, J.L. Atwood and W.E. Hunter, 1983, Chem. Commun., 206.
Luche, J.-L., 1978, J. Am. Chem. Soc. **100**, 2226.
Luche, J.-L. and A.L. Gemal, 1978, Chem. Commun., 976.
Luche, J.-L. and A.L. Gemal, 1979, J. Am. Chem. Soc., **101**, 5848.
Luche, J.-L., L. Rodriguez-Hahn and P. Crabbe, 1978, Chem. Commun., 601.
Luche, J.-L., C. Petrier and C. Dupuy, 1984, Tetrahedron Lett. **25**, 753.
Lucius and Bruning (1911), German Patent 262, 180 [Chem. Abstr. 7, 3423 (1913)].
Maini, S., L. Mandolini and C. Rol, 1978, J. Org. Chem. **43**, 3236.
Marks, T.J., 1976a, Acc. Chem. Res. **9**, 223.
Marks, T.J., 1976b, Adv. Chem. Ser. **150**, 232.
Marks, T.J., 1978, Prog. Inorg. Chem. **24**, 51.
Massaux, J. and J.F. Desreux, 1982, J. Am. Chem. Soc. **104**, 2967.
McCapra, F. and D. Watmore, 1982, Tetrahedron Lett. **23**, 5225.
Meyers, R.J. and R. Jacoby, 1901, Z. Anorg. Chem. **27**, 359.
Midland, M.M. and R.S. Graham, 1984, J. Am. Chem. Soc. **106**, 4294.
Mislow, K. and J. Siegel, 1984, J. Am. Chem. Soc. **106**, 3319.
Molander, G.A. and J.B. Etter, 1984, Tetrahedron Lett. **25**, 3281.
Morrill, T.C., R.A. Clark, D. Bilobran and D.S. Youngs, 1975, Tetrahedron Lett., 397.
Namy, J.L., P. Girard and H.B. Kagan, 1977, Nouv. J. Chim. **1**, 5.
Namy, J.L., J. Souppe and H.B. Kagan, 1983, Tetrahedron Lett. **24**, 765.
Namy, J.L., J. Souppe, J. Collin and H.B. Kagan, 1984, J. Org. Chem. **49**, 2045.
Natale, N.R., 1982, Tetrahedron Lett. **23**, 5009.
Natale, N.R., 1983, Org. Prep. Proc. Int. **15**, 387.
Norman, R.O.C., C.B. Thomas and P.J. Ward, 1973, J. Chem. Soc. Perkin I, 2914.
Olah, G.A. and B.F. Singh, 1982, J. Am. Chem. Soc. **104**, 5168.
Ouertani, M., P. Girard and H.B. Kagan, 1982, Tetrahedron Lett. **23**, 4315.
Paquette, L.A., H. Jendralla and G. DeLucca, 1984, J. Am. Chem. Soc. **106**, 1518.
Pearson, R.G., ed., 1973, Hard and Soft Acids and Bases (Dowden, Hutchinson and Ross, Stroudsburg, PA).
Peters, J.A., C.A.M. Vivjerberg, A.P.G. Kieboom and H. van Bekkum, 1983, Tetrahedron Lett. **24**, 3141.
Pitzer, K.S. and E. Gelles, 1953, J. Chem. Soc. **75**, 5132.
Pizer, R. and R. Selzer, 1983, Inorg. Chem. **22**, 1359.
Poulton, G.A. and T.D. Cyr, 1980, Synth. Commun. **10**, 581.
Pratt, Y.T., 1962, J. Org. Chem. **27**, 3905.
Ramsey, J.B. and F.T. Aldridge, 1955, J. Am. Chem. Soc. **77**, 2561.
Salot, S. and J.C. Warf, 1968, J. Am. Chem. Soc. **90**, 1932.
Schmidbaur, H., 1983, Angew. Chem. Int. Ed. Engl. **22**, 907.
Schumann, H., 1984, Angew. Chem. Int. Ed.

Engl. **23**, 474.
Schumann, H. and W. Genthe, 1984, in: Handbook on the Physics and Chemistry of Rare Earths, eds. K.A. Gschneidner, Jr. and L. Eyring (North-Holland, Amsterdam) Ch. 53.
Schumann, H., J. Muller, N. Bruneks, H. Lanke and J. Pickardt, 1984, Organometallics **3**, 69.
Souppe, J., J.L. Namy and H.B. Kagan, 1984, Tetrahedron Lett. **25**, 2869.
Sugimoto, H., T. Higashi and M. Mori, 1983a, Chem. Lett., 1167.
Sugimoto, H., T. Higashi, A. Maeda, M. Mori, H. Masuda and T. Taga, 1983b, Chem. Commun., 1234.
Tamblyn, W.H., R.E. Aquardo, O.D. DeLuca, D.H. Weingold and T.V. Dao, 1983, Tetrahedron Lett. **24**, 4955.
Tilley, D.T. and R.A. Andersen, 1981, Chem. Commun., 985.
Tomioka, H., K. Oshima and H. Nozaki, 1982, Tetrahedron Lett. **23**, 539.
Trost, B.M. and M.J. Bogdanowicz, 1973, J. Am. Chem. Soc. **95**, 5321.
Trost, B.M. and Y. Masuyama, 1984, Tetrahedron Lett. **25**, 173.
Uemura, S., 1983, Literature Guide to Organic Chemistry of Rare Earth Elements. Part I: Organic Reactions and Syntheses by using Rare Earth Elements as Reagents and Catalysts (Rare Earth Society of Japan, Osaka).
Watson, P.L., 1982, J. Am. Chem. Soc. **104**, 337.
Watson, P.L., 1983a, J. Am. Chem. Soc. **105**, 6491.
Watson, P.L., 1983b, Chem. Commun., 276.
Wayda, A.L., J.L. Dye and R.D. Rogers, 1984, Organometallics **3**, 1605.
White, J.D. and G.L. Larson, 1978, J. Org. Chem. **43**, 4555.
Wong, C.P. and W.D. Horrocks, Jr., 1975, Tetrahedron Lett., 2637.
Wong, C.P., R.F. Ventichler and W.D. Horrocks, Jr., 1974, J. Am. Chem. Soc. **96**, 7149.
Yee, E.L., J.T. Hupp and M.J. Weaver, 1983, Inorg. Chem. **22**, 3465.
Yokoo K., Y. Yamanaka, T. Fukagawa, H. Taniguchi and Y. Fujiwara, 1983, Chem. Lett., 1301.
Yokoo, K., T. Fukagawa, Y. Tamanaka, H. Taniguchi and Y. Fujiwara, 1984a, J. Org. Chem. **49**, 3237.
Yokoo, K., Y. Kijima, Y. Fujiwara and H. Taniguchi, 1984b, Chem. Lett., 1321.

ERRATA

Vol. 1, ch. 2, Beaudry and Gschneidner

Page 225, table 2.15:

1. The boiling point for Eu should be: 1527°C.
2. The heat of sublimation at 25°C for Eu should be: 175.3 kJ/mol.
3. The melting point for Tb should be: 1356°C.

Vol. 2, ch. 17, Fulde

1. Page 311, eqs. (17.30), Γ_3 (second equation) should read: $Q_3^2(m) = \frac{1}{2}\sqrt{15}\,(\varepsilon_{xx}^m - \varepsilon_{yy}^m)$.
2. Page 311, last line should read: "except for $\alpha = 4$ (rotational part, see eq. 17.30) and $\alpha = 1$ where the lowest degree in $\boldsymbol{J}$ is $d = 4$."
3. Page 312, eq. (17.34): replace $a_{q\mu}^+$ by $a_{-q\mu}^+$.
4. Page 313, eqs. (17.37) should read: $Q_{\alpha\beta}^+ = \frac{1}{2}[e_\alpha(\boldsymbol{q}\mu)q_\beta + e_\beta(\boldsymbol{q}\mu)q_\alpha]$.

Vol. 3, ch. 23, Jørgensen

1. Page 112, list of symbols, right-hand column: $\nu_{\text{e.t.}}$ = wave*number* of first....
2. Page 114, last line: *electron*–nuclear distance....
3. Page 129, eq. (23.3): 8065.*48* cm^{-1}....
4. Page 144, line 14 from below: and is $21E^3$ for ....
5. Page 155, table 23.4, right-hand column: PrSb *4.6*....
6. Page 158, eq. (23.26) should start: *gaseous* R^{+2} < *gaseous* R^0 < RI_2....
7. Page 160, line 10: octahedral.
8. Page 162, line 14: configuration $4f^{13}6s^2$ of Yb^+.
9. Page 166, references: Broer, L.J.F., ... and J. Hoogschagen....

Vol. 4, ch. 40, Haley

1. Page 553, line 9: cadmium instead of "cadnium".
2. Page 558, last line: atrophy instead of "atropy".
3. Page 562, line 2: alveolar instead of "aleveolar".
4. Page 567, line 10: resorption instead of "resoprtion".
5. Page 567, line 15: administration instead of "administartion".
6. Page 572, lines 3 and 20 of sect. 5.9. Carcinogenicity: metastases instead of "metastes".

Vol. 5, ch. 44, Boulesteix

1. Page 331 (table 2) column heading: d_{020}/d_{111} should be d_{202}/d_{111}.
2. Page 377, lines 5 and 6: "or even... $\langle 111 \rangle$ axis" should be deleted.
3. Page 379, fig. 53: The upper set of triangles is fig. 53a, while the middle and lower sets of triangles make up fig. 53b. The dot–dashed line represents a mirror plane between the middle and lower sets of triangles. From the printed version some may interpret the middle and upper triangles as making up fig. 53a. (See figure below for a correct representation of p. 379.)

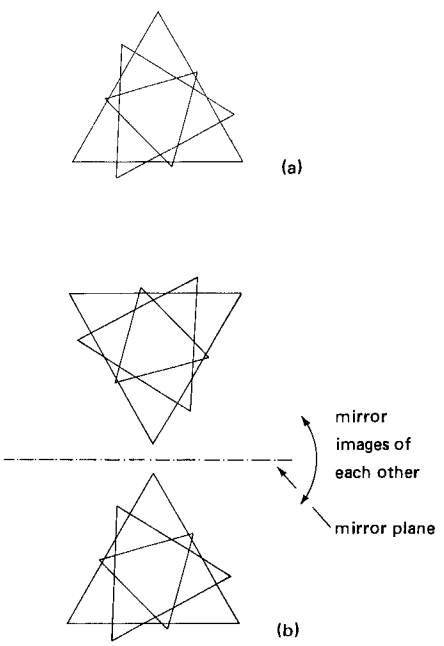

Vol. 6, ch. 48, Parthé and Chabot

1. Page 137, footnote, second last line: change (KuS, 73) to (KuSt, 73).
2. Change ChEP, 83 to ChEP, 84 in the following places:
   Page 145, 6067 Sc_2CoSi_2, footnote a,
   Page 149, 6360 $Sc_3Co_2Si_3$, footnote a,
   Page 160, 6750 ScRhSi, footnote e.
3. Page 202, 7646 $Sc_4Rh_7Ge_6$: change EnCP, 83 (heading and first line) to EnCP, 84.
4. Page 223, footnote e: change ChP, 83a to ChP, 84.
5. Page 226, 8244 $Sc_2Ru_5B_4$: change Ro, 83 (cited twice) to Ro, 84,
   and change $a = 8.452$ to $a = 8.4859$,
   $b = 3.004$ to $b = 3.0001$,
   $c = 9.953$ to $c = 9.9833$.
6. Page 239, 8380 $YCrB_4$: add to $RReB_4$ series R = Sm[r] and to footnotes [r]MiKS, 80.
7. Page 269, 8975 $CeCr_2B_6$: change KuS, 73 to KuSv, 73.
8. Page 271: insert a new entry before 92(17) $YNi_{10}Si_2$:

   [**9180**] **$CeFe_2Al_8$**, oP44, Pbam, $a = 12.51$, $b = 14.48$, $c = 4.07$ Å, is a new structure type, related to the structures shown in fig. 67, determined by YaRZ, 74.
9. Page 283, last line, footnote a: change KuCG, 81 to KuCC, 81.
10. Page 327, Chabot, Engel and Parthé (1983): change 1983 to 1984 and page 339 to 340.
11. Page 327, Chabot and Parthé (1983a): change 1983a to 1984 and submitted to **97**, 285–290.
12. Page 327, Engel, Chabot and Parthé: change 1983 to 1984.
13. Page 329, Kotur, B. Ya., O. I. Bodak and B. Ya. Kotur, 1980: correct initial of third author to O. Ya. Kotur.
14. Page 329, Kotur, B. Y. and M. Sikirica, 1982a: correct initial of first author to Kotur, B. Ya.
15. Page 332: change Rogl 1983, J. Less-Common Metals, in press to Rogl, P., 1984, J. Solid State Chem., submitted.
16. Add the following omitted references:
    Page 328: Grin', Yu. N., Ya. P. Yarmolyuk, V. I. Rozhdestvenskaya and E. I. Gladyshevskii, 1982, Sov. Phys. Crystallogr. **27**, 418–419.
    Page 330: Kuzma, Yu. B., N. S. Bilonizhko, N. F. Chaban and G. V. Chernyak, 1983, J. Less-Common Metals **90**, 217–222.

Page 331: Mikhalenko, S. I., Yu. B. Kuzma and O. K. Shchur, 1980, Poroshk. Metall. **9**, 50–52.

Page 334: Yarmolyuk, Ya. P., R. M. Rykhal and O. S. Zarechnyuk, 1974, Tezisy Dokl. Vses. Konf. Kristallokhim. Intermet. Soedin, 2nd Ed., ed. R. M. Rykhal (L'vov Gos. Univ., L'vov, USSR) pp. 39–40.

Vol. 6, ch. 49, Rogl

1. Chaban, N. F., Yu. B. Kuz'ma, ..., N. V. Petriv: (1980) should be (1979):
   p. 387, line 10,
   p. 426, line 20,
   p. 444, line 1.
2. Chaban et al. (1980) should be Chaban et al. (1979):
   p. 386, lines 2 and 17,
   p. 425, last line, just above fig. 38,
   p. 442, second last line,
   p. 443, line 7 from bottom of text above "References".

SUBJECT INDEX